LA-9737-MS

UC-20d
Issued: July 1983

LA--9737-MS

DE84 002268

The Modular Stellarator Reactor: A Fusion Power Plant

R. L. Miller
C. G. Bathke
R. A. Krakowski
F. M. Heck*
L. Green*
J. S. Karbowski*
J. H. Murphy*
R. B. Tupper*
R. A. DeLuca**
A. Moazed**
R. A. Terry**

*Westinghouse Electric Corporation, Madison, PA 15663.
**Stone & Webster Engineering Corporation, Boston, MA 02107.

Los Alamos National Laboratory
Los Alamos, New Mexico 87545

DISCLAIMER

CONTENTS

THE MODULAR STELLARATOR REACTOR: A FUSION POWER PLANT

by

The Stellarator Reactor Design Team

ABSTRACT

A comparative analysis of the modular stellarator and the torsatron concepts is made based upon a steady-state ignited, DT-fueled, reactor embodiment of each concept for use as a central electric-power station. Parametric tradeoff calculations lead to the selection of four design points for a ~4-GWt plant based upon Alcator transport scaling in $\ell = 2$ systems of moderate aspect ratio. The four design points represent high- (0.08) and low- (0.04) beta versions of the modular stellarator and torsatron concepts. The physics basis of each design point is described together with supporting engineering and economic analyses. The primary intent of this study is the elucidation of key physics and engineering tradeoffs, constraints, and uncertainties with respect to the ultimate power reactor embodiment.

---

1. EXECUTIVE SUMMARY

1.1. Introduction

As a generic class, the stellarator/torsatron/heliotron (S/T/H) represents one of the earliest approaches to magnetic confinement[1] and the first approach to be subjected to a serious conceptual reactor study.[2] Unlike the tokamak, S/T/H achieves the rotational transform, ι, required for equilibrium/stability by means of external windings alone, rather than by means of internal plasma currents, resulting in disruption-free, steady-state operation with a reduced recirculating-power fraction. Recently renewed interest in the reactor potential of the S/T/H (Sec. 2.) results from encouraging theoretical and experimental progress[3] and the application of innovative coil configurations.[4,5] The present effort is the culmination of an

initial assessment[6] of the reactor potential of the Modular Stellarator Reactor (MSR). Configurations with $\ell = 2$ poloidal field periods are emphasized to reduce coil mass, facilitate the blanket/shield design, and provide significant transform on-axis. Potentially attractive reactor design points were identified (Sec. 3.) by means of a parametric survey[7,8] that characterized global reactor performance subject to conservatively applied engineering constraints and target performance values (e.g., thermal power output, P_{TH}). Parameters for the MSR-IIB and the analogous continuous-helical-coil (ultimate torsatron) TR-B3 are summarized in Table 1-1. With

TABLE 1-1

COMPARISON OF MODULAR-STELLARATOR AND TORSATRON REACTOR DESIGN POINTS FOR $\langle\beta\rangle = 0.08$

PARAMETER	MSR-IIB	TR-B3
Edge rotational transform, $\iota(r_p)$	0.80	1.85
Plasma radius, r_p (m)	0.81	0.57
Coil radius, r_c (m)	3.3	2.3
Major toroidal radius, R_T (m)	23.0	23.0
Plasma volume, V_p (m^3)	298	149
Average density, $\langle n\rangle$ ($10^{20}/m^3$)	3.64	4.32
Average temperature, $\langle T\rangle$ (keV)	8.0	8.0
Lawson parameter, $\langle n\rangle\tau_E$ (10^{20} s/m^3)	3.43	3.43
Average beta, $\langle\beta\rangle$	0.08	0.08
DT plasma power density (MW/m^3)	12.4	24.9
On-axis magnetic field, B_o (T)	6.56	7.64
Peak field at coil, B_{CM} (T)	11.6	12.14
Neutron current, I_w (MW/m^2)	2.0	3.0
Thermal power, P_{TH} (MWt)	4000	4000
Net power, P_E (MWe)	1302	1302
System power density, P_{TH}/V_c (MWt/m^3)[(a)]	0.60	1.13
Mass utilization, M/P_{TH} (tonne/MWt)[(b)]	6.6	4.9
Recirculating power fraction, ε	0.07	0.07
Net plant efficiency, η_p ($\eta_{TH} = 0.35$)	0.33	0.33

(a) $V_c \equiv$ volume enclosing the first-wall/ blanket/shield/coils (FW/B/S/C).

(b) $M \equiv$ mass of Fusion Power Core (FPC) (i.e., FW/B/S/C).

similar power output, these S/T/H systems would share most features of the Balance of Plant (BOP) with the STARFIRE[9] tokamak and Elmo Bumpy Torus Reactor (EBTR)[10] conceptual designs, allowing concentration of the present design effort on the Fusion Power Core (FPC). Pumped-limiter impurity control is invoked here for the S/T/H, in common with the STARFIRE and EBTR, sacrificing the natural magnetic divertor available in S/T/H systems for improved volume utilization. This design effort is summarized below by treating the physics basis (Sec. 1.2.), engineering design (Sec. 1.3.), and technical/economic assessment (Sec. 1.4.).

1.2. Physics Basis

The physics basis of the S/T/H reactor incorporates the interrelated aspects of vacuum magnetics; equilibrium/stability beta limits; transport; and ignited, steady-state burn. These aspects are considered in turn.

Extensive parametric, tradeoff, and optimization studies of MSR vacuum magnetics were performed in the course of this study using the three-dimensional computer code TORSIDO (Sec. 4.). These computations were guided by and iterated with the results of the parametric studies[8] to identify the reactor design points to be subjected to detailed engineering design (Sec. 5.) and economic analysis (Sec. 7.). Coil deformation allows a single MSR coil set to produce both toroidal- and poloidal-field components without interlocked/interfering poloidal-field (PF) and toroidal-field (TF) coils, as in tokamak designs. To improve performance (i.e., transform, shear, magnetic-well depth, ripple, forces, etc.), the basic sinusoidal lateral deformation of the original Rehker-Wobig coil configuration[4] has been modified to include asymmetric, higher harmonic components in the winding law, thereby allowing the coil set to be "tuned" to reach specified objectives. The resulting $\ell = 2$ configuration yields significant positive shear at the plasma edge, while avoiding major rational-q surfaces and magnetic islands within the plasma. Best overall results (i.e., reduced coil peak fields and forces) are obtained with m = 4 toroidal-field periods and a relatively large number (N = 36) of identical coils with modest lateral distortion ($d/r_c \simeq 0.28$) and moderate coil aspect ratio ($A_c \equiv R_T/r_c \simeq 7$). Magnetics results for the MSR-IIB and TR-B3 cases are summarized in Table 1-2. Generally, both systems are designed to preserve the same major radius (R_T = 23 m) and peak coil field ($B_{CM} \simeq 12$ T). The MSR-IIB produces significantly lower rotational transform but has lower radial forces and lower stored magnetic energy. The MSR-IIB plasma cross

TABLE 1-2

MODULAR STELLARATOR AND TORSATRON
MAGNETICS COMPARISONS[a]

PARAMETER	MSR-IIB	TR-B3
Coil type	Modular[b]	Torsatron[c]
Pitch parameter, γ	NA	0.388
Normalized coil distortion, d/r_c	0.28	NA
Conductor major radius, R_T (m)	23.0	23.0
Conductor minor radius, r_c (m)	3.31	2.3
Conductor aspect ratio, $A_c = R_T/r_c$	6.95	10.0
Total coil current, I (MA)	21.0	35.7
Conductor cross section (m × m)	1.051 × 1.051	0.994 × 1.889
Conductor length, L_c (m)	22.916	461.57
Poloidal field period number, ℓ	2	2
Toroidal field period number, m	4	25
Number of coils, N	36	1
Plasma major radius, R_p (m)	23.02	22.989
Plasma minor radius, r_p (m)	0.81	0.573
Plasma volume/coil-bore volume	0.30	0.34
Magnetic axis, R_M (m)	23.04	23.001
Semiminor plasma radius[d] (m)	0.479(0.500)	0.446(0.559)
Semimajor plasma radius[d] (m)	1.406(1.425)	0.721(1.612)
Maximum plasma radius (m)	1.526	0.762
On-axis field, B_o (T)	6.47(6.56)[e]	7.64
Magnetic well depth (%)	-0.049	-0.16
Peak field at coil, B_{CM} (T)	11.59	12.14
On-axis ripple, $\varepsilon(0)$%	<2.89	<4.62
Edge ripple, $\varepsilon(r_p)$%	11.32	10.23
On-axis transform, $\iota(0)$	0.626	1.479
Edge transform, $\iota(r_p)$	0.804	1.847
Stored magnetic energy, E_M (GJ)	108	252
Peak radial force, f_r (MN/m)	78.36	112.25
Peak lateral force, f_ℓ (MN/m)	38.21	11.82
Coil surface area coverage at r_c	0.40	0.51

[a] Coil conductor/internal-structure current density, j_c = 19 MA/m^2.

[b] Distortion coefficients: $a_1 = 0.2111$, $a_2 = 0.0955$, $a_3 = 0.0534$, $a_4 = 0.0304$, $a_5 = 0.0160$: and $a_6 = 0.0066$ for use in the winding law: $d/r_c = \sum_{i=1}^{6} a_i \sin [i(\ell\theta + 2\pi m_j/N)]$.

[c] Winding law: $\phi = (\ell/m)(\theta + \gamma \sin \theta) - (\pi\ell/m)$.

[d] Under a coil (half a field period away).

[e] Performance requirement predicted from the parametric code (Ref. 8 and Sec. 3.4.7.).

section is more elongated, which, for circular-bore coils, results in reduced volume utilization of plasma within the coil bore. A larger fraction of the torus surface area is covered by coils for the TR-B3, somewhat reducing

accessibility. Generally, the idealized magnetics performance of the MSR is inferior to that of the torsatron, but overriding engineering considerations related to coil fabrication/repair/replacement dictate a preference for modular reactors (Sec. 6.2.).

The traditional, if approximate, scaling relationship for both equilibrium and stability beta limits is $\langle\beta\rangle \simeq \iota^2/A$, where $A \equiv R_T/r_p$ is the plasma aspect ratio. This limit implies an outward radial shift, Δ, of the core plasma relative to its radius, r_p, of about 50%. Strict application of this relationship would suggest that only the TR-B3 case in Table 1-2 is capable of achieving the target value[8] of $\langle\beta\rangle = 0.08$, although numerical computations also support this level of beta for MSR-IIB-like cases.[11] Achievement of these beta values is arguably the key prerequisite of competitive reactor performance from the viewpoint of FPC cost, mass, and power density and remains the central issue of the near-term S/T/H theoretical and experimental effort worldwide.

Radial transport of energy in a nonaxisymmetric S/T/H plasma is receiving intense attention. Rather than incorporate a tentative transport model, an empirical (Alcator-like) relationship was imposed, such that $\tau_E = 3(10)^{-21} \langle n\rangle r_p^2$. This approach[8] leads directly to an "engineering Lawson criterion" for ignition that requires $\langle\beta\rangle B_o^2 r_p \simeq 3\ T^2\ m$ for $\langle T\rangle \simeq 10$ keV. Under this convenient and conservative assumption, $P_{TH}/R_T \simeq 200$ MWt/m and $I_w(r_p/x) \simeq 3.8$ MWt/m, where P_{TH} is the thermal power of the reactor and I_w is the 14.1-MeV-neutron first-wall loading at the circularized first-wall radius, r_w, and $x \equiv r_p/r_w$. The general result of this transport scaling is moderate-aspect-ratio systems (i.e., $A \equiv R_T/r_p \simeq 20$) for $P_{TH} \simeq 4$-5 GWt. Application of neoclassical transport theory, corrected for ambipolar electric fields in realistic magnetic configurations, may be expected to result in favorable reductions in overall reactor size.[12]

1.3. Engineering Design

The present MSR-IIB design effort (Sec. 5.) focused on the FPC. Particular emphasis was placed on accommodating the mechanical design to the unique geometric constraints imposed by the magnet configuration. A credible first-wall/blanket (FW/B) maintenance approach was outlined that does not require routine coil movement, as has been considered in a parallel study of the UWTOR-M.[13]

A sector of the MSR-IIB reactor torus is illustrated in Fig. 1-1. In contrast to the UWTOR-M vacuum building, the MSR-IIB fixed-coil set surrounds a permanent vacuum boundary, which is penetrated by access hatches through which blanket/shield (B/S) modules are inserted or removed as part of the routine FW/B maintenance scheme. The square-cross-section coil conductor ($j_c \simeq 19$ MA/m^2) is graded radially in three sectors with cryostable Nb_3Sn in the inboard region to accommodate 8 T < B_c < 12 T; NbTi is incorporated in the outer sectors.

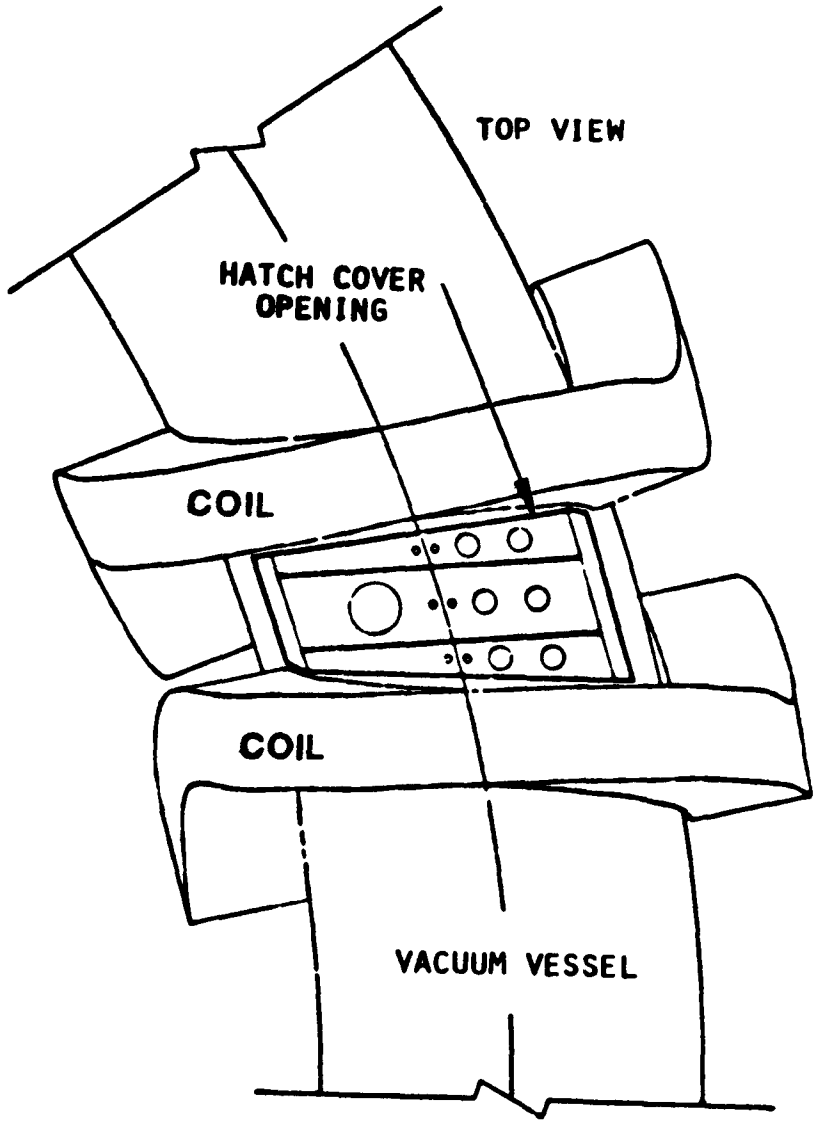

Fig. 1-1. MSR-IIB torus sector illustrating the $\ell = 2$ modular coil set and a typical access port through the permanent vacuum boundary.

An elevation view of the MSR-IIB is shown in Fig. 1-2. Coils (~390 tonnes each) are individually supported from below on columns resting on oil-pad bearings to permit movement during cooldown/heatup cycles. Coil failure and replacement would necessitate breaking the vacuum torus and would involve a protracted shutdown, as with the STARFIRE design.[9] Radial Lorentz forces on the coils are reacted by a 0.47-m-thick steel backing that conforms to the coil shape, and lateral forces are reacted by the 0.20-m-thick steel sidewalls of the coil case, allowing a maximum strain of 0.35% in the Nb_3Sn conductor. Centering forces are reacted by a pair of steel bucking rings and a central concrete cylinder.

The FW/B/S cross section is illustrated in Fig. 1-3. The blanket consists of a primary candidate alloy stainless steel (PCASS) structure and Li_2O solid breeder matrix with embedded pressurized-water (15 MPa, T_{IN} = 550 K, T_{OUT} = 590 K) coolant tubes. A helium purge stream removes tritium from the blanket. The FW/B/S cross section accommodates the elongated ℓ = 2 plasma cross section at the expense of thin beryllium neutron reflector regions located at the ends of the plasma semimajor axis, covering ~25% of the available FW surface area. The plasma chamber opening within each module has a quasi-rectangular cross section and projects straight through a given FW/B/S module. The opening tracks the helical precession of the plasma cross section by a stepped (~7°) precession of the openings of successive modules. A

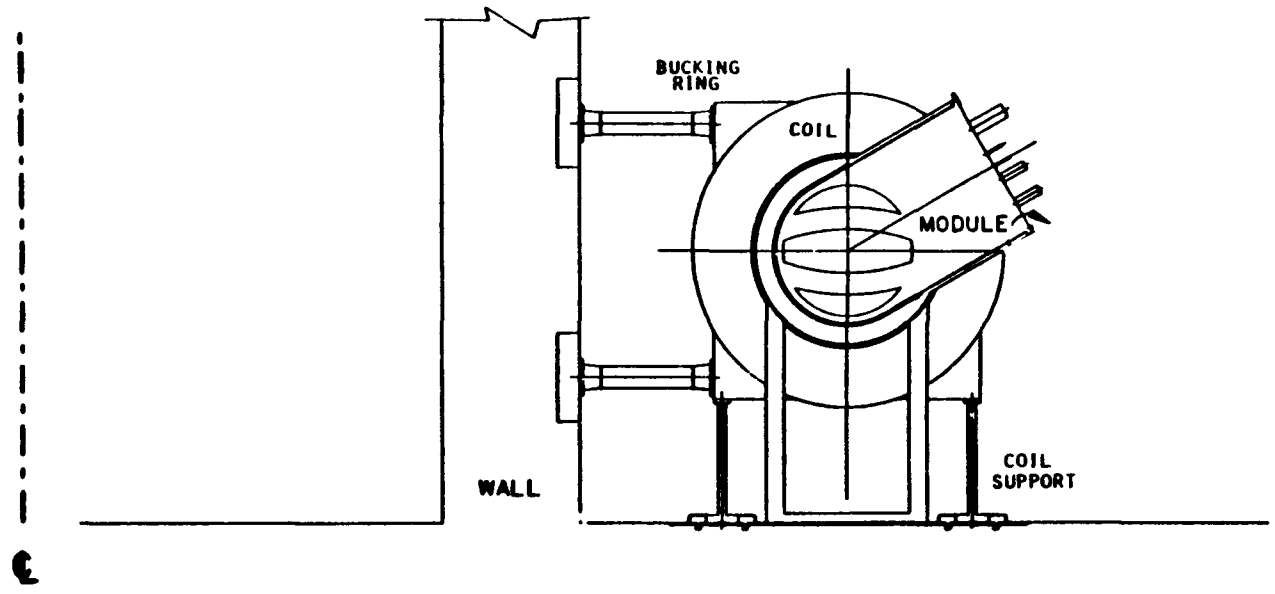

Fig. 1-2. MSR-IIB reactor elevation view with a typical module orientation.

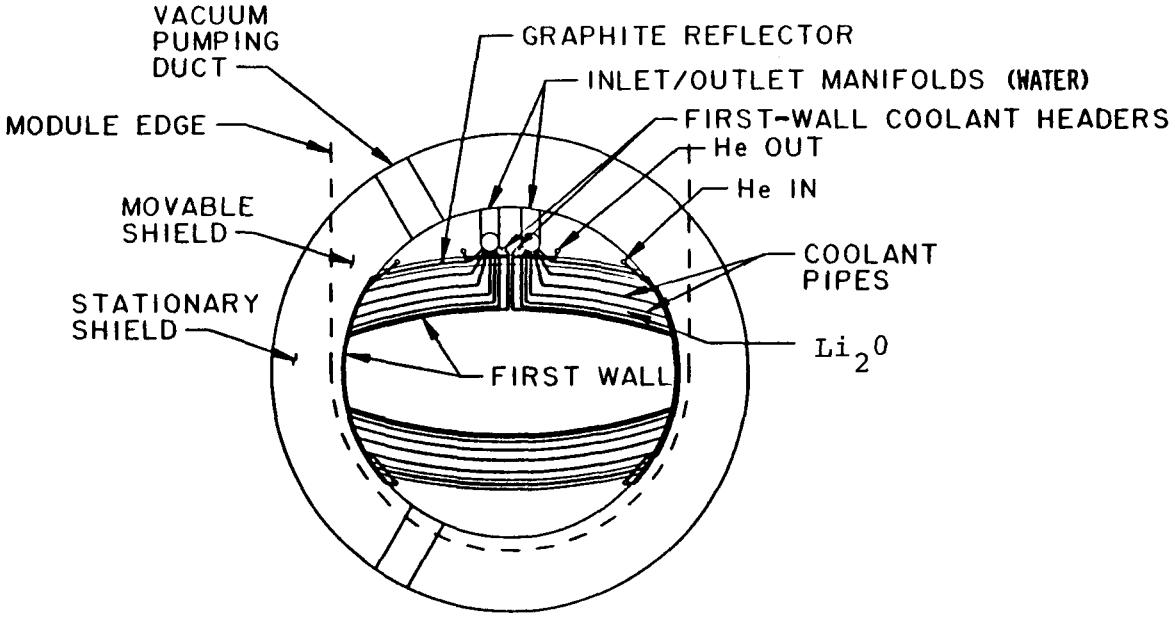

Fig. 1-3. MSR-IIB first-wall/blanket/shield (FW/B/S) cross section.

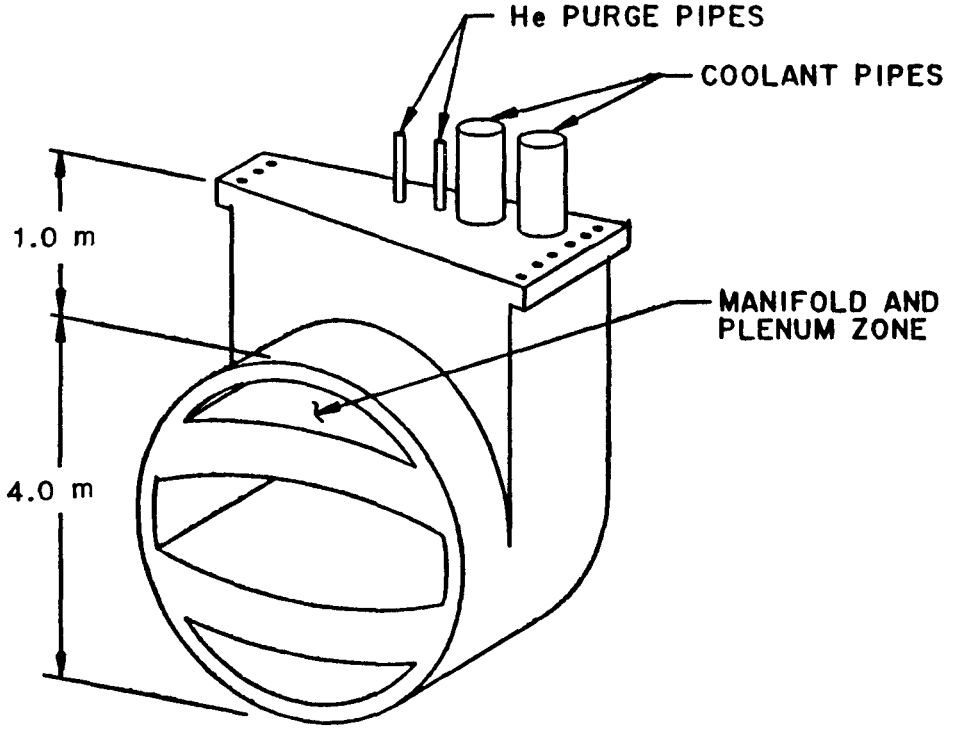

Fig. 1-4. Typical MSR-IIB center module incorporating pumped limiter, first wall, blanket, movable shield, vacuum flange, and duct access.

typical center module (1 of 3 per access port, 108 total) is illustrated in Fig. 1-4. The movable module mass is ~60 tonnes. A similar modularization scheme is compatible with the TR-B3 coil configuration. The pumped-limiter surface is subjected to ~2.5 MW/m^2 of average incident radiation and particle flux.

1.4. Technical/Economic Assessment

The larger aspect ratio of the S/T/H allows larger on-axis field strength for a common peak field limit when the S/T/H is compared with a tokamak. Net-current-free, steady-state operation allows a relaxed FW/B/S/C design, not requiring mitigation against disruptions and thermal cyclic fatigue. The S/T/H allows lower recirculating power fractions by eliminating current drive (as for STARFIRE) and relativistic-electron-ring drive (as for EBTR). Beta values approaching 10% appear feasible, but they must be confirmed. Coil design, fabrication, and support appear tractable for the MSR. Credible approaches to remote maintenance can be proposed.

Several unresolved technology issues (Sec. 6.) remain. Startup trajectories that minimize power requirements must be identified in conjunction with unresolved transport theory. The magnetics performance of modular coils is inferior to that of continuous helical coils, but modular coils reduce the financial risk and technical problems of on-site winding of monolithic helical coils whose integrity for the life of the plant cannot be guaranteed.

Preliminary cost estimates (Sec. 7.) have been made for the MSR-IIB and TR-B3 design points following DOE/OFE guidelines.[14] For the present effort, homogenized unit-cost averages were applied to the FW/B/S/C subsystems. The assumed unit costs are displayed in Table 1-3 with comparable numbers derived from the STARFIRE and EBTR design efforts.

TABLE 1-3

FPC HOMOGENIZED UNIT COSTS ($/kg)

	STARFIRE[9]	EBTR[10]	S/T/H
First-Wall/Blanket	54.3	41.2	42.0
Shield	13.9	14.6	15.0
Coils	20.8	21.3	25.0
Total FPC	19.0	19.0	22-24

Mass utilization (i.e., FPC mass, M, divided by total thermal power, P_{TH}) was used in Ref. 8 as an indication of MSR economic performance. Target values of $M/P_{TH} \simeq 5$ tonnes/MWt were established for $\langle\beta\rangle = 0.08$ to anticipate competitive performance. The shielding of the circular-bore MSR-IIB coils requires a stand-off distance between the coil inner bore and the plasma semi-major axis that precludes reduction of the MSR-IIB coil radius and, hence, mass, as was accomplished for the TR-B3. In the latter case, the plasma can bulge radially outward in the directions along the plasma semimajor axis as the helical-coil bore is reduced. The TR-B3 design, therefore, achieves the lower cost and M/P_{TH} values.

Summarized in Table 1-4 are the masses and costs of the MSR-IIB and TR-B3 compared with the STARFIRE and EBTR. Also tabulated are several cost figures of merit: fractional cost of the FPC relative to Reactor Plant Equipment (RPE) and fractional cost of FPC relative to Total Direct Cost (TDC). The dominance of the FPC in the costs of these superconducting magnetic fusion systems is apparent. The low recirculating power of the stellarators offsets the impact of a conservatively assumed longer construction time on interest and escalation costs to give comparable estimates for Cost of Electricity (COE). All of these systems assume a ~76% plant availability and a 30-yr plant life.

The following conclusions are drawn from the present study:

- Overall S/T/H reactor performance is critically coupled through beta to the magnetics performance of the coil set. The available (limited) physics data base supports the design choices made here for the S/T/H, which are generally conservative and subject to improvement.
- Engineering choices/options implemented for the MSR conceptual design provide a credible, maintainable preliminary design.
- The S/T/H is technologically and economically competitive with other mainline fusion approaches if $\langle\beta\rangle \gtrsim 0.08$.
- The modular-coil configuration sacrifices magnetics performance relative to the continuous-helical-coil configuration in return for fabrication/maintenance advantages and lower stored magnetic energy. If life-of-plant (LOP) coils cannot be postulated, the MSR is the preferred reactor configuration.

TABLE 1-4

FUSION POWER CORE (FPC) COMPARISON [a]

	STARFIRE[9]	EBTR[10]	MSR-IIB	TR-B3
Mass (tonne):				
First wall/blanket (FW/B)	1517	4116	2060	1699
Shield (S)	13360	13110	10275	5859
Coils (C)	8240	26150	14149	12037
Total FPC mass, M	23117	43376	26484	19595
Mass utilization, M/P_{TH} (tonne/MWt)	5.7	10.8	6.6	4.9
Cost (M$):				
First wall/blanket (FW/B)	82.4	174.5	91.1	74.5
Shield (S)	186.1	191.5	154.1	87.9
Coils (C)	171.6	556.9	353.7	300.9
Total FPC cost (FW/B/S/C)	440.1	922.9	598.9	463.3
Total RPE cost	968.6	1425.7	967.6	792.9
Total direct cost (TDC)	1726.5	2108.8	1647.0	1467.8
Total cost	2400.3(3197.9)	2871.9(3647.7)	2473.6(4015.2)	2204.5(3578.4)
Construction time (yr)	6	5	10	10
Cost Figures of Merit:				
FPC/RPE	0.45	0.65	0.62	0.58
RPE/TDC	0.56	0.68	0.59	0.54
UDC ($/kWe)	1439	1737	1265	1127
COE (mills/kWeh)	35.1(67.1)	38.9(7.17)	33.7(77.6)	30.1(69.3)
Net power output, P_E (MWe)	1275	1200	1302	1302
Recirculating power fraction, ε	0.167(0.06)[b]	0.15(0.07)[b]	0.07[b]	0.07[b]
Average beta, $\langle\beta\rangle$	0.067	0.17	0.08	0.08

[a] Paired entries indicate constant (1980) and then-current (at end of construction) costs.

[b] Auxiliary power requirement for cryogenics and other BOP systems.

REFERENCES

1. L. Spitzer, Jr., "The Stellarator Concept," Phys. Fluids 1, 253-264 (July - August 1958).

2. L. Spitzer, Jr., D. Grove, W. Johnson, L. Tonks, and W. Westendorp, "Problems of the Stellarator as a Useful Power Source," US Atomic Energy Commission report NYO-6047 (1954).

3. J. L. Johnson, "The Stellarator Approach to Toroidal Plasma Confinement," Nucl. Tech./Fusion 2, 340-361 (July 1982).

4. S. Rehker and H. Wobig, "A Stellarator Field Produced by Twisted Coils," Proc. 6th Eur. Conf. on Contr. Fusion and Plasma Phys. 1, 117-120 (July 30— August 4, 1973).

5. T. K. Chu, H. P. Furth, J. L. Johnson, C. Ludescher, and K. E. Weimer, "Optimization Techniques for Modular Stellarator Coils," Nucl. Fusion 22, 871-881 (1982) [also Princeton Plasma Physics Laboratory report PPPL-1873 (February 1982)].

6. R. L. Miller and R. A. Krakowski, "The Modular Stellarator Fusion Reactor Concept," Los Alamos National Laboratory report LA-8978-MS, (August 1981).

7. R. L. Miller, R. A. Krakowski, and C. G. Bathke, "Parametric Systems Analysis of the Modular Stellarator Reactor," Nucl.. Fusion 23, 467-479 (1983). [also Los Alamos National Laboratory document LA-UR-82-116 (Rev.) (October 1982)].

8. R. L. Miller, R. A. Krakowski, and C. G. Bathke, "Parametric Systems Analysis of the Modular Stellarator Reactor (MSR)," Los Alamos National Laboratory report LA-9344-MS (May 1982).

9. C. C. Baker, M. A. Abdou, D. A. DeFreece, C. A. Trachsel, D. W. Graumann, et al., "STARFIRE - A Commercial Tokamak Fusion Power Plant Study," Argonne National Laboratory report ANL/FPP-80-1 (September 1980).

10. C. G. Bathke, D. J. Dudziak, R. A. Krakowski, W. B. Ard, D. A. Bowers, J. W. Davis, et al., "ELMO Bumpy Torus Reactor and Power Plant Conceptual Design Study," Los Alamos National Laboratory report LA-8882-MS (August 1981).

11. G. Anania, J. L. Johnson, and K. E. Weimer, "Use of the Stellarator Expansion to Investigate Plasma Equilibrium in Modular Stellarators," Princeton Plasma Physics Laboratory report PPPL-1945 (November 1982).

12. O. B. Adams, R. L. Brown, W. D. Cain, B. A. Carreras, L. A. Charlton, et al., "Proposal to Build ATF-1," Oak Ridge National Laboratory report (October 1982).

13. B. Badger, I. N. Sviatoslavsky, S. W. Van Sciver, G. L. Kulcinski, G. A. Emmert, D. T. Anderson, et al., "UWTOR-M: A Conceptual Modular Stellarator Power Plant," University of Wisconsin report UWFDM-550 (October 1982).

14. S. C. Schulte, W. E. Bickford, C. E. Willingham, S. K. Ghose, and M. G. Walker, "Fusion Reactor Design Studies - Standard Unit Costs and Cost Scaling Rules," Pacific Northwest Laboratory report PNL-2987 (September 1979).

2. INTRODUCTION AND BACKGROUND

2.1. Overview

As a generic class, the stellarator[1] represents one of the earliest approaches to toroidal magnetic confinement. Unlike the tokamak, the nonaxisymmetric stellarator achieves the rotational transform required for equilibrium/stability by means of external windings alone, rather than by means of internal plasma currents. The stellarator class includes the torsatron,[2] heliotron,[3] and several non-planar-axis variations,[4-6] as illustrated in Fig. 2.1-1. It is beyond the scope and purpose of this report to review the broad range of theoretical and experimental stellarator research activity. Fortunately, a number of excellent reviews have recently addressed this task.[7-12] It is sufficient to note here that there has been a recently renewed interest in the stellarator after a period of relative de-emphasis, particularly in the US, lasting for about a dozen years following the ascendancy of the tokamak approach. This renewed interest results from a more highly developed theoretical base, encouraging experimental successes in the low-net-current regime, and innovative new coil configurations. This renewed interest has again prompted consideration of the reactor potential of the stellarator.

Qualitative advantages that in general can be invoked for the stellarator/torsatron/heliotron (S/T/H) reactor concept include

- steady-state magnetic fields and thermonuclear burn.
- operation at ignition or with a high Q-value for low recirculating power.
- plasma startup on existing magnetic surfaces with predictable particle and energy confinement at all times.
- optional impurity and ash removal by means of a magnetic limiter (i.e., helical poloidal divertor) that occur as natural consequences of the magnetic confinement topology or by a pumped limiter.
- net-current-free operation without major plasma disruptions that could lead to an intense, local energy deposition on the first wall or in the blanket, shield, or coil regions.

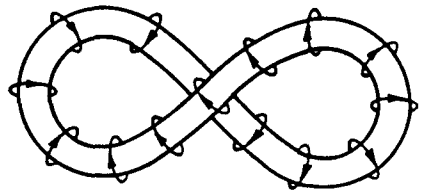

FIGURE-8 STELLARATOR

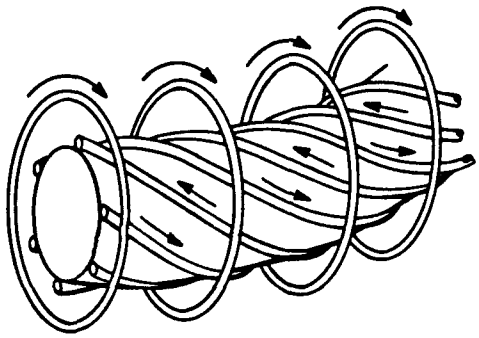

STELLARATOR ($\ell = 3$)

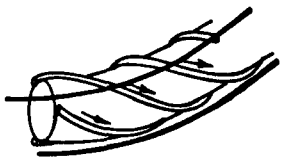

TORSATRON ($\ell = 3$) WITH VERTICAL - FIELD COILS

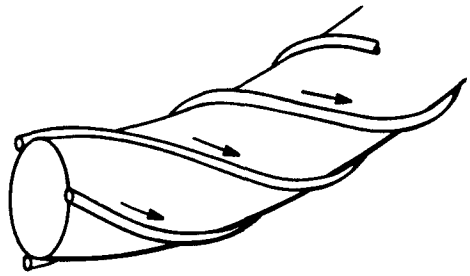

TORSATRON ($\ell = 3$)

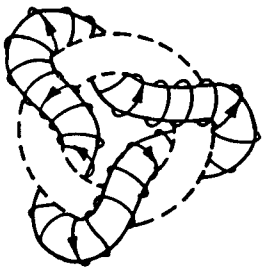

NON-PLANAR-AXIS STELLARATOR (n = 3)

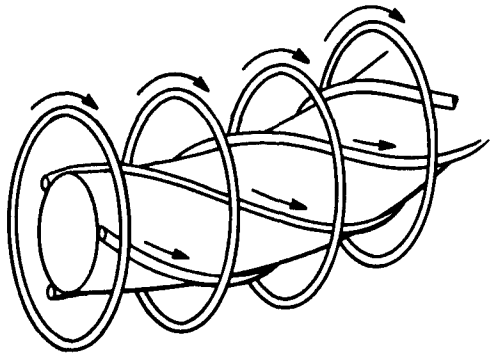

HELIOTRON ($\ell = 3$)

Fig. 2.1-1 Nonplanar figure-8 stellarator, classical stellarator, torsatron, heliotron, and a typical non-planar-axis toroidal configuration illustrating the range of the stellarator class of magnetic-confinement configurations.

Verification and quantification of these claims within the limits of computation and extrapolation are the central task of reactor studies. Where possible, reactor studies should emphasize the implications of reactor design choices and constraints on near-term experimental and theoretical priorities.

Of particular interest in the reactor context is the application of modular-coil configurations as pioneered by Rehker and Wobig.[13-15] A rudimentary coil of this type consists of a simple, out-of-plane sinusoidal deformation, as illustrated in Fig. 2.1-2. Variations on this basic coil configuration can improve its performance (Sec. 4.). Such configurations ease the severe fabrication and maintenance concerns inherent in continuous helical coil systems at the risk of degraded magnetics performance. Quantification of this tradeoff within the context of a self-consistent conceptual design of the stellarator Fusion Power Core (FPC) is the principal purpose of this study. The objectives, scope, and approach of this study are discussed below.

The present stellarator reactor study builds upon previous activity (Phase I) involving collaborative work between Los Alamos and the Princeton Plasma Physics Laboratory (PPPL). Phase I results have been reported in Refs. 10 and 16. These results were sufficiently encouraging to justify the present study (Phase II) in greater depth (see Sec. 2.3.) and involving industrial partners (IP) selected by Los Alamos in competitive response to a Request for Quotation (RFQ) in August 1981. The successful bidder was a team composed of Westinghouse Electric Corporation, Stone & Webster Engineering Corporation, and CVI, Incorporated. Pending implementation of the formal contract governing the present study, Los Alamos engaged in parametric studies[17] (Phase IA) leading to the identification of candidate design points for use in the present effort. The objectives and scope of the present study (Phase II) are discussed in the following subsections of this chapter.

2.2. Study Objectives

The objective of this study is to develop, on the basis of available physics understanding, conceptual designs for the FPC of a commercial fusion power plant based on the stellarator confinement scheme. A goal of the present study is to answer two fundamental questions regarding stellarator reactors

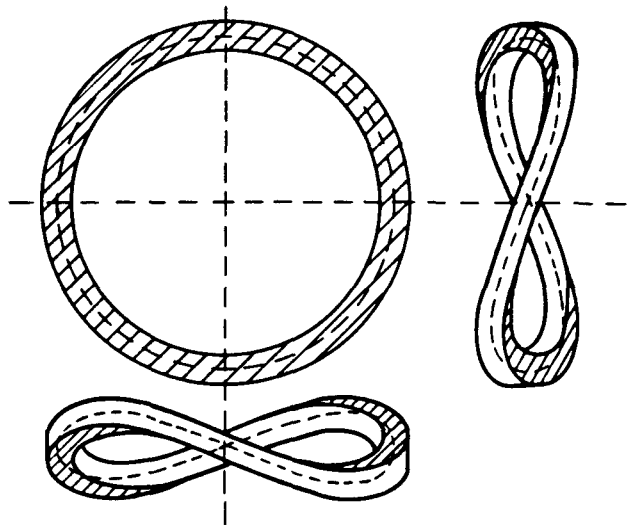

(A) ℓ=2 REHKER-WOBIG COIL

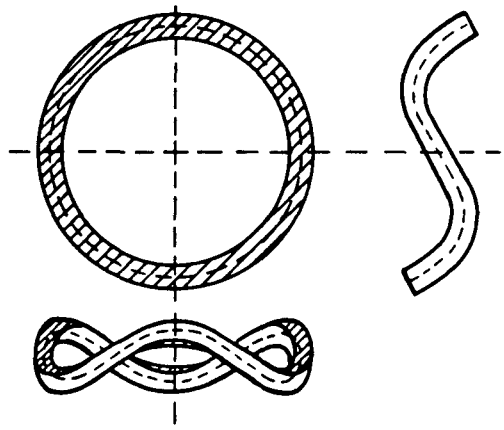

(B) ℓ=3 REHKER-WOBIG COIL

Fig. 2.1-2. Views of typical ℓ = 2 and ℓ = 3 Rehker-Wobig modular coils with circular bore and moderate lateral distortion.[15]

- What is the influence of key physics parameters and assumptions (e.g., magnetics, beta, and transport) on size and performance?

- What are the comparative advantages and disadvantages of continuous-coil and modular-coil configurations?

The data base developed to address these questions includes parametric studies and related tradeoff and optimization efforts; preliminary conceptual designs of key FPC subsystems; and a technical assessment of stellarator physics, engineering, and economics. A parallel study, emphasizing engineering and maintenance issues for modular stellarators, has been completed at the University of Wisconsin.[18]

To focus the present study on those features distinctive (if not unique) to stellarator concepts, the design of Balance-of-Plant (BOP) systems is de-emphasized. Some attention is paid, however, to making the present study compatible with the essentially common features of a number of other recent fusion reactor designs using the deuterium/tritium/lithium fuel cycle and producing 1000-1300 MWe(net). These other systems include the STARFIRE tokamak,[19] the MARS tandem mirror,[20] the Elmo Bumpy Torus Reactor (EBTR),[21] and the Reversed-Field Pinch Reactor (RFPR).[22,23] Such commonalty facilitates more meaningful technical and economic comparisons that serve as a primary purpose of any systems study.

2.3. Study Scope

As part of an overall program for assessing the reactor potential of alternative magnetic fusion concepts (AFCs), the Office of Fusion Energy of the US Department of Energy has funded systems studies according to a three-tier structure. These studies are categorized in order of decreasing level of effort and detail as Level I, Level II, and Level III. The highest level of study (Level I) includes, in a multi-man-year effort, considerable conceptual design and economic analysis in addition to sophisticated, state-of-the-art physics and operating-point analyses. The lowest level of study (Level III) would characterize less understood and developed confinement schemes by means of relatively simplified physics models and parametric analyses of potential reactor operating points. The present stellarator reactor study can be characterized as a Level II study. Although building on

a previous Level III study,[16] the present effort did not allow for either the breadth or depth characteristic of other recent Level I fusion reactor studies (e.g., STARFIRE[19] and MARS[20]). The parametric models of the previous Level III study were adapted for present use (Sec. 3.) together with extensive use of three-dimensional magnetics computations (Sec. 4.), to identify candidate design points for elaboration by the design effort (Sec. 5.).

2.4. Study Approach

This Phase II stellarator reactor study was divided into the four major tasks identified in Table 2.4-1. Subtask IA was a relatively low-level activity incorporating the Phase IA parametric codes, previous Los Alamos

TABLE 2.4-1

STUDY TASK IDENTIFICATION/ALLOCATION/STATUS[a]

TASK/SUBTASK	Los Alamos	Westinghouse	Stone & Webster	CVI
I. Flagship Design Point Identification/Optimization				
A. COE-based systems code	J	J	-	-
B. Plasma models	P	-	-	-
C. Magnetics	P	-	-	-
II. Preliminary Subsystem Design				
A. First-wall/blanket/shield	J	J	-	-
B. Magnets	S	J	J	-
C. Impurity/ash control (divertor, limiter)	J	J	S	-
D. Plasma heaters	D	D	D	D
E. Refueling	D	D	D	D
F. Vacuum system	-	-	-	T
G. Primary containment and support structure	S	J	J	-
H. Tritium handling systems	D	D	D	D
I. Primary coolant systems	D	D	D	-
J. Maintenance scheme	S	J	J	-
K. Balance-of-plant systems	D	D	D	D
III. Systems Integration and Plant Layout	J T	J T	J T	- -
IV. Reactor Assessment				
A. Physics	J	J	-	-
B. Technology	J	J	J	-
C. Economics	J	J	S	-

[a] J ≡ Joint Responsibility, P ≡ Primary Responsibility, S ≡ Major Support, D ≡ De-emphasized, and T ≡ Truncated by Contract Termination.

cost-code activities, and Westinghouse COAST code[24] data. Results are used in the Task IV economic assessment. The ongoing review and adaptation of plasma models (Subtask IB) were the primary responsibility of Los Alamos. These activities included the definition and use of beta scaling relationships, the upgrading of transport models, and the adaptation of other plasma engineering models. These activities were relatively low level, but they provide the interface for important input from the stellarator physics community. Magnetics (Subtask IC) was identified as the critical Los Alamos activity. This subtask included the TORSIDO code development and computations and the consequent magnet subsystem design and structural analysis by Westinghouse and Stone & Webster.

Task II subsystem design activities emphasized the coil configurations and related aspects of accommodating the first-wall/blanket/shield (FW/B/S) and impurity-control systems as well as preliminary Task III activity that was under way when the DOE/OFE reached a decision to truncate the study as a result of national budgetary constraints for FY 1983. This report summarizes the work completed by October 13, 1982, and the assessment of stellarator reactor potential based thereon.

To facilitate a comparison between modular-coil configurations and continuous-helical-coil systems, and at the same time explore the potential for higher beta operation, four "flagship" design points were identified. These flagships are characterized in Table 2.4-2.

TABLE 2.4-2

FLAGSHIP DESIGN-POINT CHARACTERISTICS

Designation	Coil Configuration	$\langle\beta\rangle$
MSR-IIA	modular coil, $\ell = 2$	0.04
TR-A	torsatron, $\ell = 2$	0.04
MSR-IIB	modular coil, $\ell = 2$	0.08
TR-B	torsatron, $\ell = 2$	0.08

The "A" design points retain the conservative assumption that $\langle\beta\rangle = 0.04$ as was imposed in Ref. 16, whereas the "B" design points assume a higher value ($\langle\beta\rangle = 0.08$) identified in Ref. 17 as a prerequisite for operation competitive with other conventional fusion reactor conceptual designs. Discussion of the beta-limit issue is presented in Sec. 3.2.2. The ground rules adopted by the

STARFIRE[19] and EBTR[21] design studies were used as the preliminary basis for this study, to facilitate comparison of the designs. These ground rules are summarized as follows:

- power plant design for an electric utility.
- deuterium/tritium/lithium fuel cycle.
- nominal 1200-MWe output.
- conventional steam turbine/generator power conversion.
- mature fusion industrial base.
- based on a 10th-of-a-kind plant.
- a 30-yr design life.
- a single plant at a site.
- midwestern US location.
- cooling towers required.
- use of STARFIRE/EBTR design features where applicable.
  - Buildings except reactor and electrical equipment
  - Turbine and electric plant equipment
  - Tritium handling equipment
  - Basic design concept for blanket/shield
  - Basic design concept for pumped-limiter impurity control and vacuum systems.
- total remote reactor maintenance scheme.
- minimum vacuum volume.
- use of pressurized-water-reactor (PWR) heat-transport system.

The adoption of a common BOP with the similar STARFIRE and EBTR studies allowed a focusing of the limited resources of this study on the crucial FPC analysis. Such subsystem design work as contributes to the comparison of the several coil configurations in terms of their relative compatibility with other reactor subsystems (e.g., FW/B/S, impurity control, heating) was performed.

Key notation used in this study is summarized in Table 2.4-3 and generally follows the usage established in Ref. 16.

TABLE 2.4-3

DEFINITION OF KEY PARAMETERS USED IN THIS STUDY

PARAMETER	SYMBOL
Number of poloidal-field periods	ℓ
Number of toroidal-field periods	m
Average rotational transform ($\tau \equiv \iota/2\pi$)	τ
Shear parameter ($d\tau/dr$)	τ'
Magnetic-well (hill) magnitude [$\delta\langle B(r)\rangle/\langle B(0)\rangle$]	V''
Radial profile index [e.g. $p/p_o = 1 - (r/r_p)^{\nu}$]	ν
Alpha-particle energy-trapping fraction	f_α
Alpha-particle fractional pressure	p_α/p
Average plasma density (m^{-3})	$\langle n\rangle$
Average plasma temperature (keV)	$\langle T\rangle$
Average plasma beta	$\langle\beta\rangle$
Equilibrium beta limit	β(EQ)
Stability beta limit	β(ST)
Plasma major toroidal radius (m)	R_T
Average plasma minor radius (m)	r_p
Plasma aspect ratio, R_T/r_p	A
First-wall radius (m)	r_w
Radial filling factor, r_p/r_w	x
Combined first-wall blanket/shield thickness (m)	Δb
Blanket neutron-energy multiplication factor	M_N
Maximum minor radius of separatrix (m)	r_s
Minor radius to coil current center (m)	r_c
Helical-field pitch parameter ($mr_c/\ell R_T$)	α
Maximum lateral deformation of modular coil (m)	d
Ultimate torsatron coil-winding pitch parameter	γ
Square-cross-section conductor dimension (m)	δ_c
Average coil current density (MA/m^2)	j
Coil current (MA)	I
Number of coils	N
Collision frequency (s^{-1})	ν

TABLE 2.4-3 (cont)

PARAMETER	SYMBOL
Connection length (m)	R_T/τ
Ion gyroradius (m)	ρ_i
Electron gyroradius (m)	ρ_e
Ion thermal speed (m/s)	v_{Ti}
Electron thermal speed (m/s)	v_{Te}
Ion cyclotron frequency (s^{-1})	ω_{ci}
Electron cyclotron frequency (s^{-1})	ω_{ce}
Particle diffusion coefficient (m^2/s)	D
Energy diffusion coefficient (m^2/s)	χ_E
Radial profile integral (see Table 3.2-1)	I_x
Energy confinement time (s)	τ_E
Coil force (N)	f
Coil stress (Pa)	σ
Coil strain (%)	ε
Stored magnetic energy (GJ)	E_M
On-axis magnetic field (T)	B_o
Peak magnetic field at coil (T)	B_{CM}
Magnetic field ripple (%)	ε
Total thermal power output (MWt)	P_{TH}
Gross electrical power output (MWe)	P_{ET}
Net electrical power output (MWe)	P_E
Thermal conversion efficiency	η_{TH}
Fusion-neutron first-wall loading (MW/m^2)	I_w
Fusion power core (FPC) mass (tonnes)	M
FPC mass utilization (tonnes/MWt)	M/P_{TH}
Recirculating power fraction, $(P_{ET} - P_E)/P_{ET}$	ε
Auxiliary systems power fraction	f_{AUX}

REFERENCES

1. L. Spitzer, Jr., "The Stellarator Concept," Phys. Fluids 1, 253-264 (July - August 1958).

2. C. Gourdon, D. Marty, E. K. Maschke, and J. Touche, "The Torsatron without Toroidal Field Coils as a Solution of the Divertor Problem," Nucl. Fusion 11, 161-166 (1971).

3. K. Uo, "The Helical Heliotron Field for Plasma Confinement," Plasma Phys. 13, 243-255 (1971).

4. H. P. Furth, J. Killeen, M. N. Rosenbluth, and B. Coppi, "Stabilization by Shear and Negative V''," Proc. 2nd Int. Conf. on Plasma Physics and Contr. Nucl. Fusion Research, IAEA-CN-21/106, I, 103-126 (1966).

5. A. E. Bazhanova, V. M. Glagolev, and V. D. Shafranov, "Toroidal Plasma Traps with Three-Dimensional Axes," Sov. Phys. - Tech. Phys., 11, 1177-1182 (March 1967).

6. A. Boozer, T. K. Chu, R. L. Dewar, H. P. Furth, J. A. Goree, et al., "Two Optimized Toroidal Configurations: A High-Beta Stellarator and a Tokamak - Torsatron Hybrid," Proc. 9th Inter. Conf. on Plasma Phys. and Contr. Nucl. Fusion Research, Baltimore, MD, IAEA-CN-41/Q-4 (September 1-8, 1982).

7. K. Miyamoto, "Recent Stellarator Research," Nucl. Fusion 18, 243-284 (1978).

8. V. D. Shafranov, "Stellarators," Nucl. Fusion 20, 1078-1083 (1980).

9. J. L. Shohet, "Stellarators," in Fusion, E. Teller, Ed. (Academic Press, New York) Vol. 1, Part A, 243-289 (1981).

10. Joint US-EURATOM Steering Committee on Stellarators, "Stellarators-Status and Future Directions," Max Planck Institut für Plasmaphysik report IPP 2/254 (also DE81026572) (July 1981).

11. J. L. Johnson, G. Grieger, D. J. Lees, M. S. Rabinovich, J. L. Shohet, and K. Uo, "The Stellarator Program," IEEE Trans. Plasma Sci. PS-9, 142-149 (December 1981).

12. J. L. Johnson, "The Stellarator Approach to Toroidal Plasma Confinement," Nucl. Tech./Fusion 2, 340-361 (July 1982).

13. H. Wobig and S. Rehker, "A Stellarator Coil System without Helical Windings," Proc. 7th Symp. on Fusion Tech., EURATOM report EUR 4938e, 345-357 (October 24-27, 1972).

14. S. Rehker and H. Wobig, "A Stellarator Field Produced by Twisted Coils," Proc. 6th Eur. Conf. on Contr. Fusion and Plasma Phys. 1, 117-120 (July 30 - August 4, 1973).

15. S. Rehker and H. Wobig, "Stellarator Fields with Twisted Coils," Max Planck Institut fur Plasmaphysik report IPP 2/215 (August 1973).

16. R. L. Miller and R. A. Krakowski, "The Modular Stellarator Fusion Reactor Concept," Los Alamos National Laboratory report LA-8978-MS (August 1981).

17. R. L. Miller, R. A. Krakowski, and C. G. Bathke, "Parametric Systems Analysis of the Modular Stellarator Reactor (MSR)," Los Alamos National Laboratory report LA-9344-MS (May 1982).

18. B. Badger, I. N. Sviatoslavsky, S. W. Van Sciver, G. L. Kulcinski, G. A. Emmert, D. T. Anderson, et al., "UWTOR-M: A Conceptual Modular Stellarator Power Plant," University of Wisconsin report UWFDM-550 (October 1982).

19. C. C. Baker, M. A. Abdou, D. A. DeFreece, C. A. Trachsel, D. W. Graumann, et al., "STARFIRE - A Commercial Tokamak Fusion Power Plant Study," Argonne National Laboratory report ANL/FPP-80-1 (September 1980).

20. B. G. Logan, C. D. Henning, G. A. Carlson, W. L. Barr, B. M. Boghosian, R. S. Devoto, et al., "Mirror Advanced Reactor Study-Interim Design Report," Lawrence Livermore National Laboratory report UCRL-53333 (April 1982).

21. C. G. Bathke, D. J. Dudziak, R. A. Krakowski, W. B. Ard, D. A. Bowers, J. W. Davis, et al., "ELMO Bumpy Torus Reactor and Power Plant Conceptual Design Study," Los Alamos National Laboratory report LA-8882-MS (August 1981).

22. R. L. Hagenson, R. A. Krakowski, and G. E. Cort, "The Reversed-Field Pinch Reactor (RFPR) Concept," Los Alamos Scientific Laboratory report LA-7973-MS (August 1979).

23. R. L. Hagenson and R. A. Krakowski, "Compact Reversed-Field Pinch Reactors (CRFPR): Sensitivity Study and Design-Point Determination," Los Alamos National Laboratory report LA-9389-MS (July 1982).

24. D. A. Sink and E. M. Iwinski, "User's Manual for COAST-4, A Code for Costing and Sizing Tokamaks," Westinghouse Electric Corporation report WFPS: TME-79-023 (September 1979).

3. DESIGN POINT SELECTION

3.1. Historical Background

3.1.1. Overview. The stellarator represents one of the earliest magnetic confinement concepts to receive attention as a commercial magnetic fusion power reactor.[1,2] In its classical embodiment, however, the stellarator faced problems associated with conservatively anticipated low values of plasma beta and technologically difficult coil configurations, leading about a dozen years ago to a general de-emphasis of stellarator reactor work in favor of the tokamak and other concepts. Fortunately, a moribund stellarator reactor design effort did not preclude ongoing clever theory and successful experiments, leading to recently renewed interest in and re-emphasis of the potential of the stellarator as a power source.

It is beyond the scope and purpose of this section to consider the broad range of stellarator research activity. A number of excellent reviews have recently addressed this task.[3-8] Rather, this section will more narrowly summarize and update recent international stellarator reactor design activity. Such activity has been sufficiently vigorous in the last few years that a considerable portion of the reactor information in even the more recent general reviews is often obsolete. This section will review the results of recent or ongoing reactor design studies. The term "stellarator" is used in this section as a generic classification to embrace the classical stellarator itself, the torsatron,[9,10] heliotron,[11] modular configurations,[12] and non-planar-axis systems[13,14] (e.g., heliac[15]).

Reactor studies tend to fall into two categories: broad parametric surveys and conceptual designs of specific configurations. Both categories are useful in defining a concept and assessing its merits and shortcomings relative to other systems. Examples of both approaches are available for stellarators and will be summarized here. Early stellarator parametric surveys[16-19] contributed, together with disappointing experimental results on the Princeton Model C, to the de-emphasis of stellarator reactor studies about a dozen years ago by calling attention to low power density (i.e., low beta), large power output, configurational complexity, severe coil forces, and uncompetitive economic performance. More recent surveys[20-23] have tended to brighten this early picture by allowing higher beta limits and technologically more suitable coil configurations.

Available stellarator reactor point designs in the pre-1980 period were collected and summarized in Table IV-I of Ref. 22. These included the Model-D design[2] (for historical purposes), several representative but unelaborated classical stellarator design points from the early survey period,[18,19] and three more modern torsatron reactor embodiments.[24,25] Design work relating to the latter three systems has continued to date. The Kyoto University heliotron[26] has evolved into the Heliotron-H conceptual reactor design.[27-30] The Kharkov torsatron has apparently been updated,[31] although a detailed description was not available for this review. The $\ell = 3$ T-1 torsatron design[25] proposed by the MIT group has been subjected to continued elaboration[32-34] and ongoing related work[35] leading to the $\ell = 2$ T-2 torsatron design.[36]

New reactor design activities have been initiated incorporating modular-coil configurations. These include the $\ell = 3$ UWTOR-M design[37-40] of the University of Wisconsin group and the present $\ell = 2$ Modular Stellarator Reactor (MSR) design.[40,41] Interim parameter summaries of these modular systems have appeared in Refs. 6, 8, 27, and 42. Those UWTOR-M and MSR parameters in conflict with Ref. 37 or this review should be considered obsolete. A report[43] of recent parametric work[44] at the UKAEA Culham Laboratory on an $\ell = 2$ modular reactor has also been issued. Some preliminary work on modular stellarator reactors has also been conducted at the Oak Ridge National Laboratory.[45]

The most recent available parameters of the active stellarator reactor designs are summarized for comparative purposes in Table 3.1-1. Of the six designs listed, the first three are continuous-helical-coil configurations, and the last three are modular-coil configurations. The two representative MSR design points, respectively emphasizing traditional performance (MSR-IIA, $\langle\beta\rangle = 0.04$) and optimistic performance (MSR-IIB, $\langle\beta\rangle = 0.08$), have been identified by means of the comprehensive parametric approach described in Ref. 23.

The remainder of this section will summarize the three active stellarator reactor design studies other than the present MSR study. All of the reactors burn DT fuel and are ignited.

TABLE 3.1-1

SUMMARY OF RECENT S/T/H FUSION REACTOR CONCEPTUAL DESIGNS

	MIT T-1 $\ell = 3$ $m = 20$	MIT T-2 $\ell = 2$ $m = 19$	KHARKOV $\ell = 3$ --	KYOTO U. HELIOTRON-H $\ell = 2$ $m = 15$	UW UWTOR-M $\ell = 3$ $m = 6$ $N = 18$	CULHAM $\ell = 2$ $m = 3$ $N = 15$	ORNI ATF-R $\ell = 2$ $m = 12$ $N = 24$	LA MSR-IIA $\ell = 2$ $m = 4$ $N = 36$	LA TR-A $\ell = 2$ $m = 16$	LA MSR-IIB $\ell = 2$ $m = 4$ $N = 36$	LA TR-B3 $\ell = 2$ $m = 25$
Reference	25	36	31	28-30	37	43	45				
Edge rotational transform	~2	1.9	--	2.2	1.13	0.5	0.7	0.43	1.47	0.80	1.85
Plasma radius (m)	2.3	1.5	2.0	1.7	1.72	1.97	1.8	2.25	2.25	0.81	0.57
Coil radius (m)	4.0	4.0	4.0	3.2	4.8	~5.5	3.5	5.0	5.0	3.3	2.3
Major radius (m)	29.2	24.0	50.0	21.0	24.1	15.8	12.25	27.9	27.9	23.0	23.0
Plasma volume (m^3)	3049	1070	3950	1200	1410	1210	785	2788	2788	298	149
Average density ($10^{20}/m^3$)	1.33	2.5	3.5	1.17	1.46	1.4	--	1.38	1.38	3.64	4.32
Temperature (keV)	7.3	15	5.5	10.3	9.8	~10	--	8.0	8.0	8.0	8.0
Lawson parameter (10^{20} s/m^3)	3.0	--	28	3.0	5.4	--	--	3.74	3.74	3.43	3.43
Average beta	0.035	0.065	0.04	0.06	0.06	0.039	0.08	0.04	0.04	0.08	0.08
DT plasma power density (MW/m^3)	1.2	--	0.9	2.4	3.0	3.2	4.7	1.7	1.7	12.4	24.9
Magnetic field (T)	5.0	5.0	6.0	4.0	4.5	6.6	6.0	5.72	5.71	6.56	7.64
Peak field at coil (T)	8.7	~9	--	9	11.6	10.0	12.0	11.2	12.5	11.6	12.14
Stored magnetic energy (GJ)	460+	--	--	120	171	--	--	230	609	109	252
Neutron current (MW/m^2)	1.4	2.2	1.0	1.3	1.41	2.0	2.7	1.0	1.0	2.0	3.0
Thermal power (MWt)	4340	3600	4000	3400	4820	4000	4000	5100	5100	4000	4000
Net power (MWe)	(1413)	(1170)	1300	1200	1836	1340	1302	1660	1660	1302	1302
System power density (MWt/m^3)	0.35	(0.35)	0.25	0.41	0.34	--	1.5	0.30	0.30	0.60	1.13
Mass utilization (tonne/MWt)	(9)	--	--	9	11.4	--	2.5	8.4	9.6	6.6	4.9
Recirculating power fraction	(0.07)	(0.07)	0.07	(0)	0.033	0.07	0.07	0.07	0.07	0.07	0.07
Net plant efficiency ($\eta_{TH} = 0.35$)	(0.33)	(0.33)	0.33	(0.31)	0.38[a]	0.33[b]	0.33	0.33	0.33	0.33	0.33
Unit direct cost[c] ($/kWe)	--	--	--	--	(1175)	1562	~1200	1482	1610	1265	1127

[a] Here, $\eta_{TH} = 0.39$.

[b] Here, $\eta_{TH} = 0.36$.

[c] 1980 dollars.

3.1.2. Kharkov Physico-Technical Institute. The Kharkov Physico-Technical Institute of the USSR has pursued the parametric study of $\ell = 3$ torsatron reactor systems.[20,21,25] The configuration is moderate-to-high aspect ratio and optimizes somewhat differently, depending on whether plateau[24] or helical-ripple[21] transport scaling is assumed. The basic layout of the system is indicated in Fig. 3.1-1. Gaps between three helical-coil windings (H) accommodate the divertor channels. Collector plates are attached to outboard coil structural members. Blanket/shield sectors (B) either are placed between the trefoil plasma and the windings or are displaced radially outward to accommodate the divertor channels and still provide adequate coverage.

At risk of drawing conclusions on the basis of incomplete information, the level of effort on this reactor study appears to be low, giving little engineering detail. Specific mechanical features and maintenance approaches of the MIT T-1 torsatron reactor[25] could be adapted, however. The physics parametric survey is comprehensive and thorough.

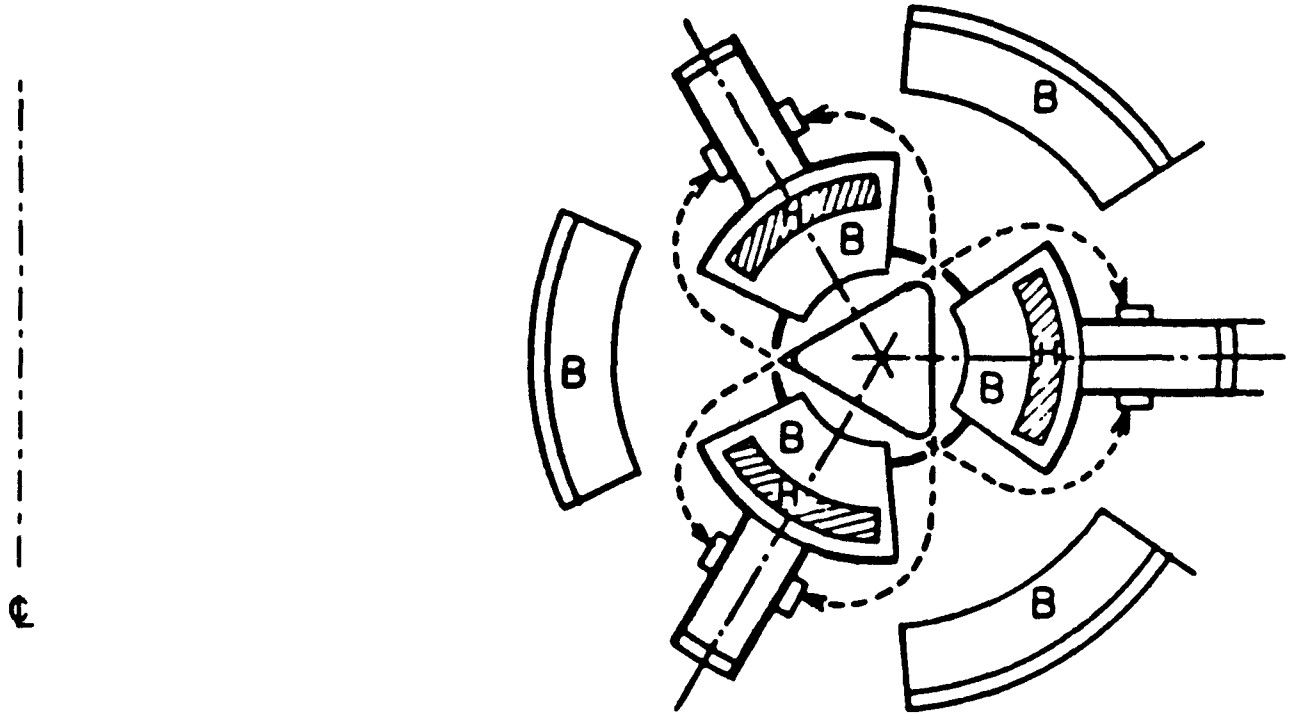

Fig. 3.1-1. Typical $\ell = 3$ torsatron reactor schematic cross section showing helical windings (H), blanket/shield sectors (B), and divertor topology (Ref. 3).

3.1.3. Kyoto University. The Heliotron group at Kyoto University and other Japanese institutions have evolved the Heliotron-H reactor design.[28,46] Minor internal inconsistency in the Heliotron-H parameters exists. The reported[45] net power output, P_E = 1200 MWe, leaves no allowance for recirculating power if the total thermal power output, P_{TH} = 3400 MWt, and the nominal thermal conversion efficiency, η_{TH} = 0.35, are used. The configuration is fundamentally similar to that of an ℓ = 2 torsatron, as depicted in Fig. 3.1-2. Sufficient mechanical design effort has been applied to refine the concept, as shown in Fig. 3.1-3. Blanket/shield components are modularized (~3 tonne) and can be installed/replaced without disturbing the continuous-helical windings, which are assumed to operate with life-of-plant (LOP) reliability (i.e., 30-40 yr). Coil support rings are provided at every half-pitch length to react the outward radial force of ~40 MN/m. The comparable force on the MIT T-1 winding is ~30 MN/m. Impurity control is provided by a helical divertor. Extensive blanket nucleonics computations have been performed[29,30] to verify adequate tritium breeding and protection of the superconducting coil. The blanket breeding material is Li_2O (natural

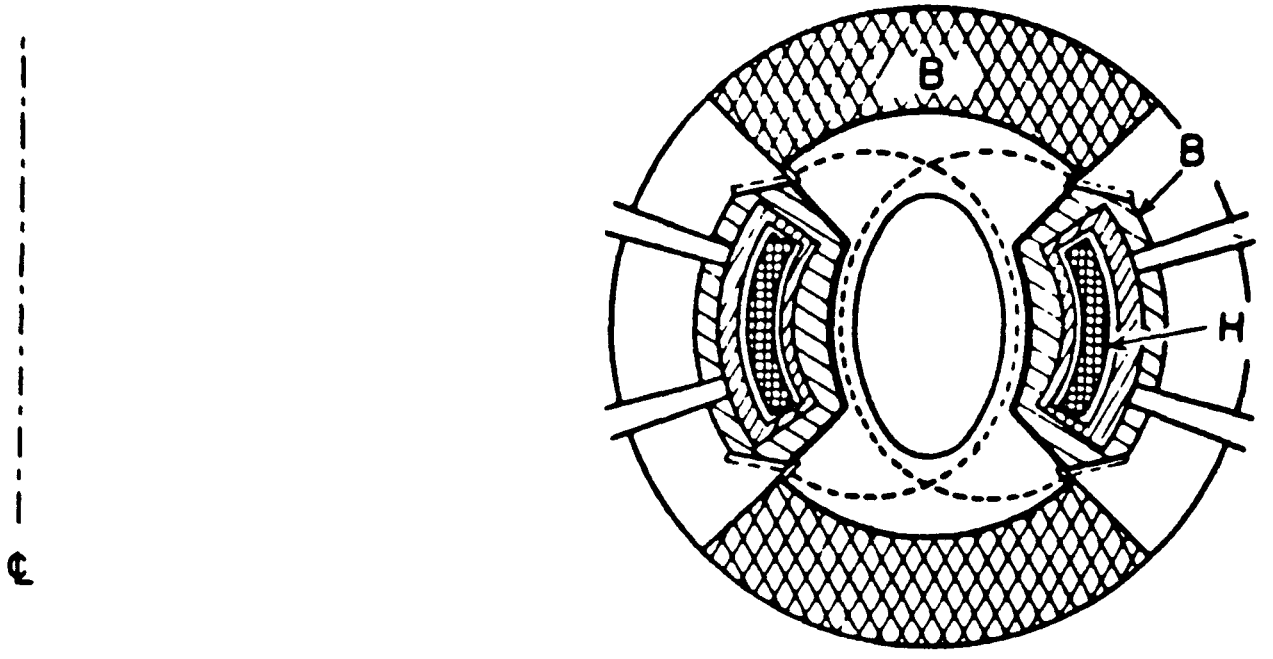

Fig. 3.1-2. Typical ℓ = 2 torsatron reactor schematic cross section showing helical windings (H), blanket/shield sectors (B), and divertor topology (Ref. 3). Heliotron-H is an advanced example of this basic configuration.

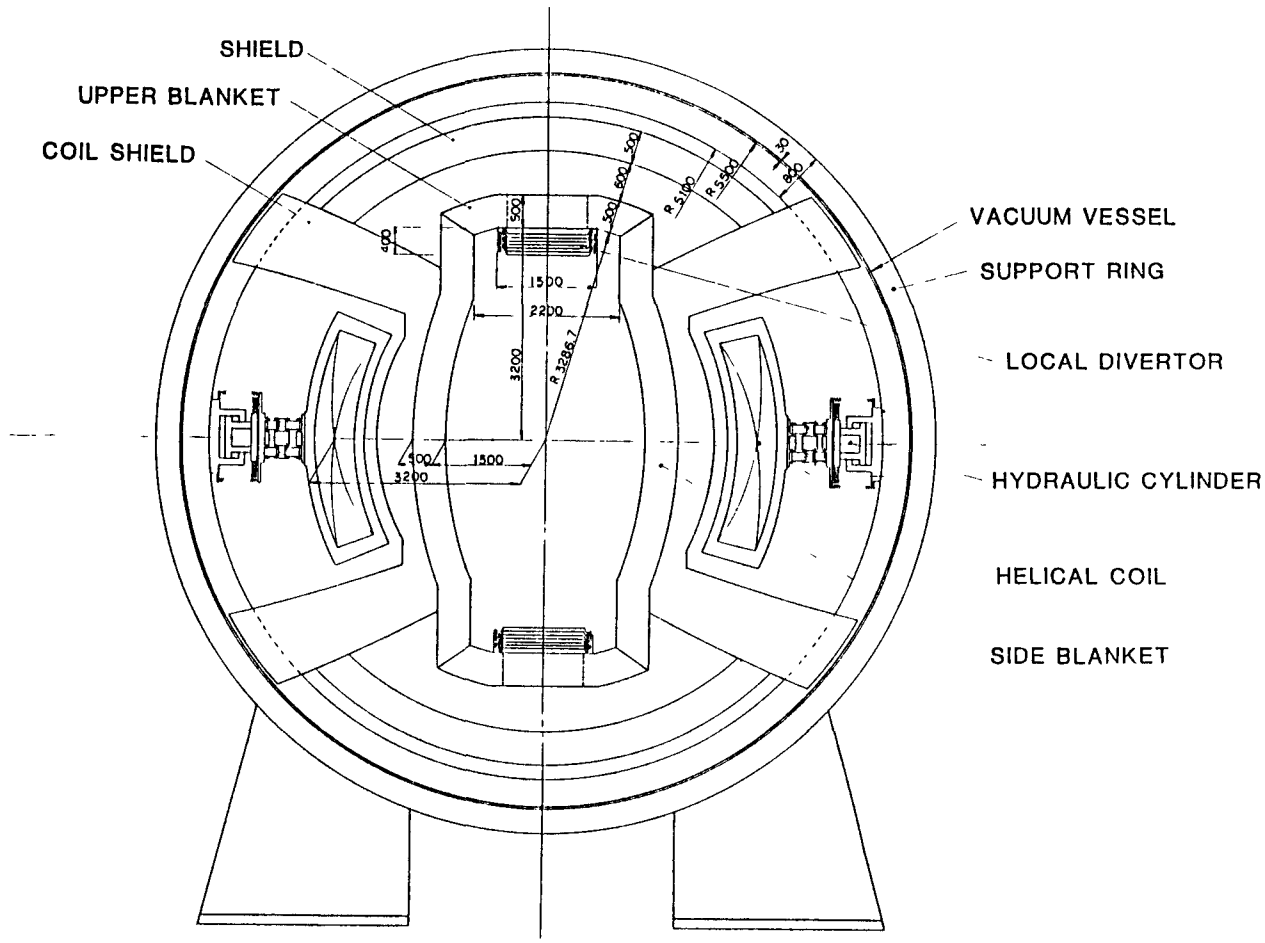

Fig. 3.1-3. Elevation view of the $\ell = 2$ Heliotron-H reactor. The required vertical field coils are not shown (Ref. 45).

lithium). Economics studies are anticipated but have not yet been reported. The physics basis is characterized as being conservative, assuming $\langle\beta\rangle = 0.06$, consistent with large transform and shear.

3.1.4. University of Wisconsin. The University of Wisconsin group has been conducting studies[37-40] of a stellarator reactor using modified Rehker-Wobig modular coils.[12] The study has emphasized engineering aspects and has concentrated on establishing a credible coil design and overall system integration. Poloidal stepping of the successive modules accommodates the helical precession of the plasma column without helical mechanical components.

The coil configuration consists of N = 18 wedged coils with ℓ = 3 and $d/r_c \simeq$ 0.5, as shown in Fig. 3.1-4. The physics basis of the design includes detailed one-dimensional radial transport computations and an assumed $\langle\beta\rangle$ = 0.06. Engineering aspects of the design are concluded to be within reasonable extrapolation of present technology. Radial coil forces (~70 MN/m) are reacted by structural rings at the coil midplanes. Lateral coil forces (~80 MN/m) are supported by contacting the neighboring coils at the points of maximum coil lateral deformation. Impurity control is provided by magnetic

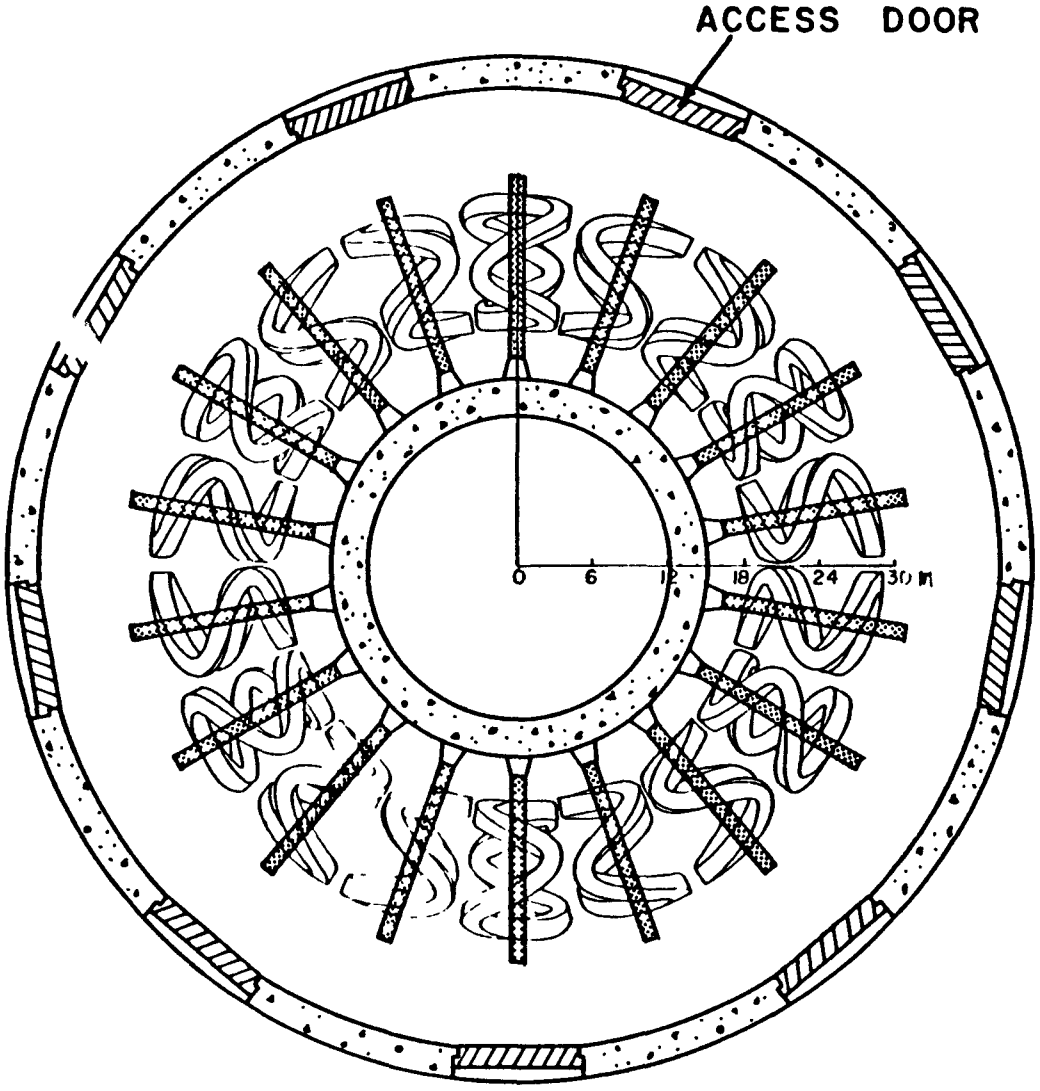

Fig. 3.1-4. Plan view of UWTOR-M ℓ = 3, m = 6 modular stellarator reactor coil set showing N = 18 coils and structural support rings (Ref. 37). Routine maintenance involves removal of reactor modules (i.e., coil and underlying blanket/shield) through the access doors.

divertors, that take advantage of discrete, localized flux bundles emerging between the bends of the coils.[47] Divertor targets, consisting of rotating graphite-coated cylinders, are located outside the shield.

Because access is diminished by the coil support rings, the routine maintenance scheme requires radially outward translation without lifting of a decoupled coil/blanket/shield module (~900 tonnes). To avoid vacuum seals between modules, the entire reactor torus is housed in a vacuum enclosure, as shown in Fig. 3.1-5. The blanket uses a static LiPb eutectic as the breeder material with embedded steam tubes for heat removal, as shown in Fig. 3.1-6. Cost estimates indicate a unit direct cost (UDC) of 1175 $/kWe, corrected to 1980 dollars.

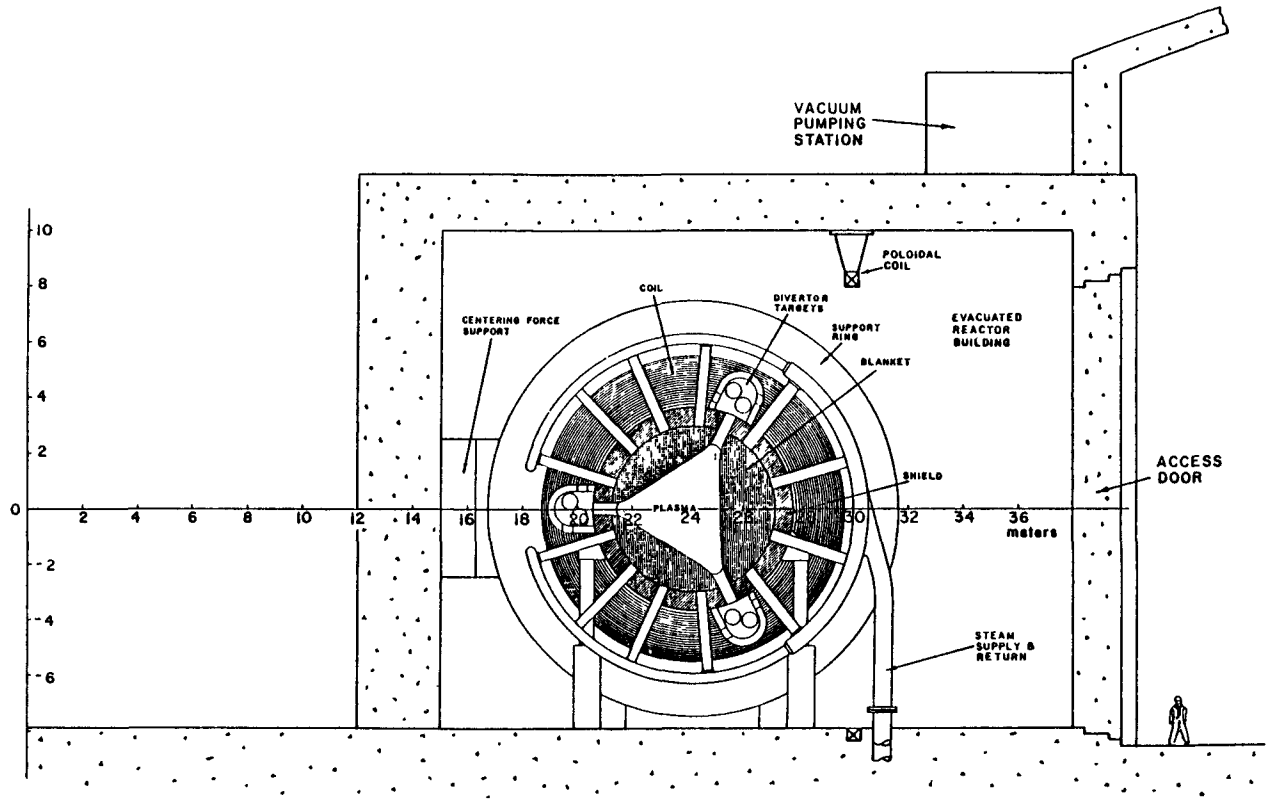

Fig. 3.1-5. Elevation of UWTOR-M modular stellarator reactor showing evacuated reactor containment (Ref. 37).

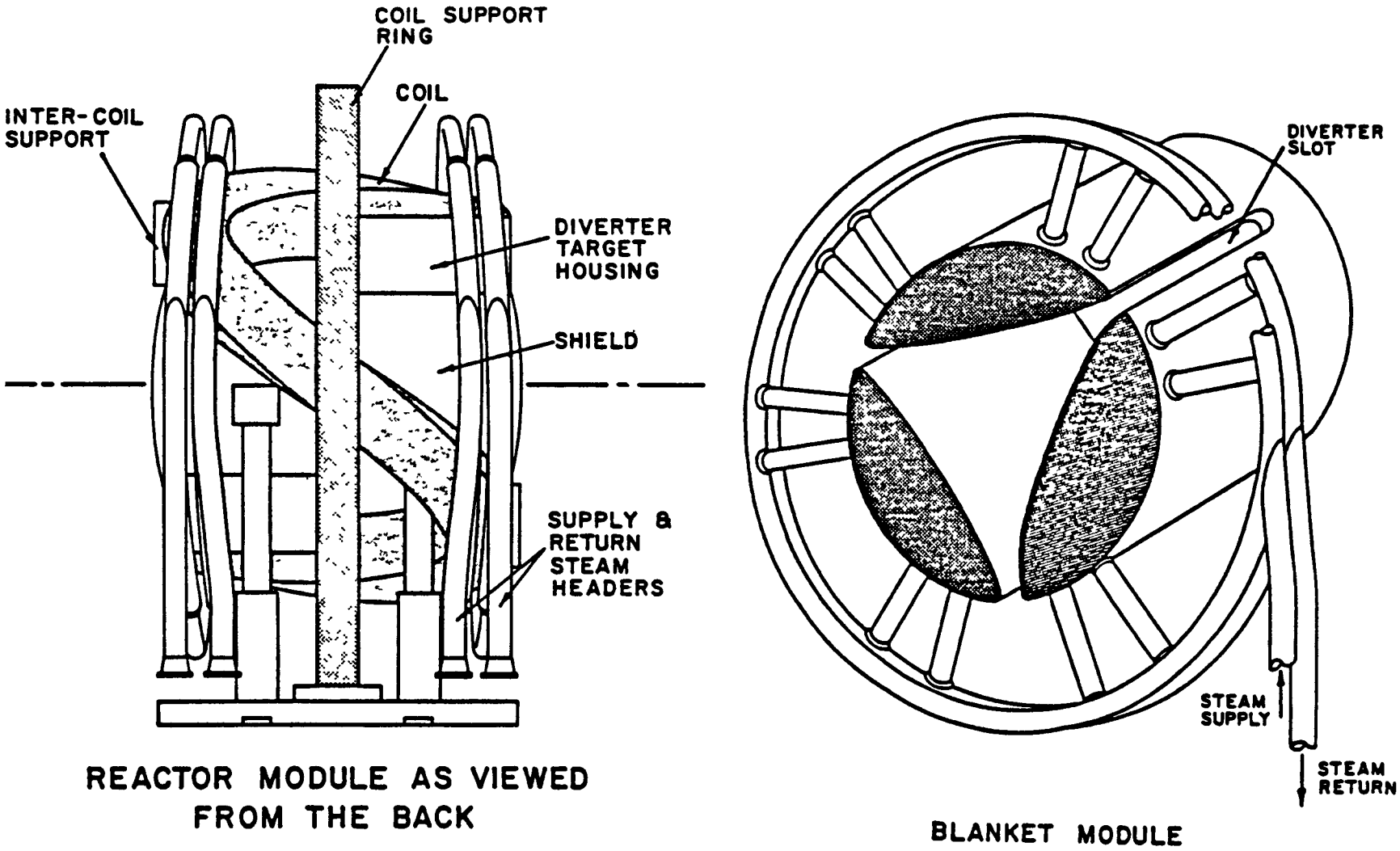

Fig. 3.1-6. Views of the UWTOR-M ℓ = 3 coil/blanket/shield/divertor-slot module (Ref. 37).

The following conclusions[37] have emerged from the UWTOR-M study:

- "The most critical engineering issue of modular stellarators is related to the coils. Apart from being physically large and heavy, no fundamental problems have been identified that cannot be solved with minor extrapolations of present technology.
- "The need for a high rotational transform drives modular stellarators to a large number of periods and a high aspect ratio resulting in rather large devices.
- "A modular divertor can be well integrated into a modular stellarator at the expense of a minor complication in the blanket geometry.
- "The magnetic volume utilization in a modular stellarator is similar to tokamaks with poloidal divertors and slightly lower than tokamaks without poloidal divertors. However, the low recirculating power fraction in stellarators seems to make up for this deficiency from the economic standpoint.
- "Maintainability for the whole reactor can be achieved with radial extraction of modular coils.
- "Modular stellarators of $\langle\beta\rangle \simeq 6\%$ and power output in the range of 4000-5000 MWt are economically competitive with tokamaks and other magnetic fusion reactor concepts."

3.2. Physics Basis

The stellarator reactor design effort rests on a physics basis representing a broad theoretical and experimental effort in several countries over a long historical period. This effort has been reviewed and summarized in Refs. 3-8 at a level beyond the scope of this section. However, in the remainder of this section is summarized the impact of key physics issues and assumptions on the selection of modular stellarator and torsatron design points developed in the course of the present study.[22,23,48] Of particular concern are the vacuum magnetics, stability/equilibrium beta limits, transport, and requirements for ignited, steady-state burn. These issues are considered in the following subsections.

3.2.1. Vacuum Magnetics. Detailed vacuum magnetics computations for this study are performed using the TORSIDO code, as discussed in depth in Sec. 4. In this subsection the usual stellarator model fields are discussed as an approach to motivate the constraints on the reactor design as provided by

magnetics considerations. Idealized stellarator magnetics models forming the basis of this discussion have been developed in Refs. 3, 49-52.

A plasma cannot be stably confined in a pure toroidal magnetic field of finite aspect ratio because a $\vec{B} \times \vec{\nabla B}$ drift force acts on the plasma ions and electrons, leading to a spatial charge separation and a resultant electric field; the $\vec{E} \times \vec{B}$ drift causes loss of both ions and electrons from the toroidal plasma column. If, however, when additional helical-field components are used, the magnetic field lines can be made to execute excursions around the minor circumference of the torus while trajectory is traced around the major circumference of the torus, particles moving along the magnetic field lines will tend to experience alternating $\vec{B} \times \vec{\nabla B}$ drifts, which ideally average to zero so that charge separation and toroidal drifts do not occur. The locus of intersections of a given magnetic field line with a plane cutting the minor diameter of the torus will trace out in an average sense a closed magnetic surface. The average incremental poloidal angle, ι, between two successive intersections, normalized by the one-turn toroidal angle, 2π, is defined to be the rotational transform angle, $\tau = \iota/2\pi$. The average rotational transform is a function of minor radius, r, and the geometry of the external current windings that produce the toroidal and the helical magnetic field components. The magnetic shear is given by the first derivative of the rotational transform, $d\tau/dr$. A given magnetic field line will close upon itself after traversing around the torus n times if $\tau = 1/n$. A shearless rotational transform may be induced by torsion of the magnetic axis into the nonplanar "figure-8" configuration used in early stellarator experiments.[1]

The magnetic field strength near the magnetic axis is approximately given by

$$B \sim B_o[1 - \varepsilon_t \cos \theta - \varepsilon_h \cos (\ell\theta - m\phi)] \quad , \tag{3.2-1}$$

where B_o is the on-axis magnetic-field strength, ϕ is the toroidal angle, θ is the poloidal angle, and the perturbations in the field strength caused by the toroidal effect and the helical-field component are given, respectively, by ε_t and ε_h. The torsatron configuration has ℓ helical conductors with unidirectional current flow. A separate set of vertical-field windings is required. The classical stellarator as shown in Fig. 3.2-1, on the other

hand, has ℓ pairs of conductors with alternately antiparallel current flow such that the net toroidal field is nulled on the magnetic axis and a separate set of toroidal coils is required. The pitch length, $1/\alpha = \ell R_T/m$, of the helical coils is defined by the pitch angle, α', such that

$$\tan \alpha' = \frac{m r_c}{\ell R_T} \equiv \alpha r_c \quad , \tag{3.2-2}$$

where m is the number of field periods around the major circumference of the torus, r_c is the minor radius of the helical coil, and R_T is the major toroidal radius of the device. On the basis of simplified expansions for straight systems (i.e., infinite aspect ratio) and certain simplified winding laws (i.e., the relationship between θ and ϕ as a conductor is traced around the torus), analytic expressions can be derived that relate $\iota(r)$ to other quantities of interest. Those quantities in turn can be related to plasma size and shape and to the magnet coil parameters. These relationships are discussed in Sec. 4. and serve as the magnetics basis of the present reactor study. Generally, the analytic magnetics models used in Ref. 22 have been found to provide an inadequate picture of the relationships between plasma cross-sectional area, shape, and rotational-transform behavior, necessitating a reliance on computational vacuum magnetics.

The performance of the stellarator depends crucially upon the ability of the coil configuration to produce the magnetic topology required for plasma confinement, under the constraints imposed by subsystems integration and structural mechanics. Attention has been given in this study to the development of the computational tools required to perform the following calculations and to address related vacuum magnetic issues:

- magnetic forces on the coils,
- mod-|B| surfaces, and
- field-line tracing in the context of
  - field ripple
  - magnetic surfaces
  - rotational transform and shear
  - magnetic-well (or hill) magnitude.

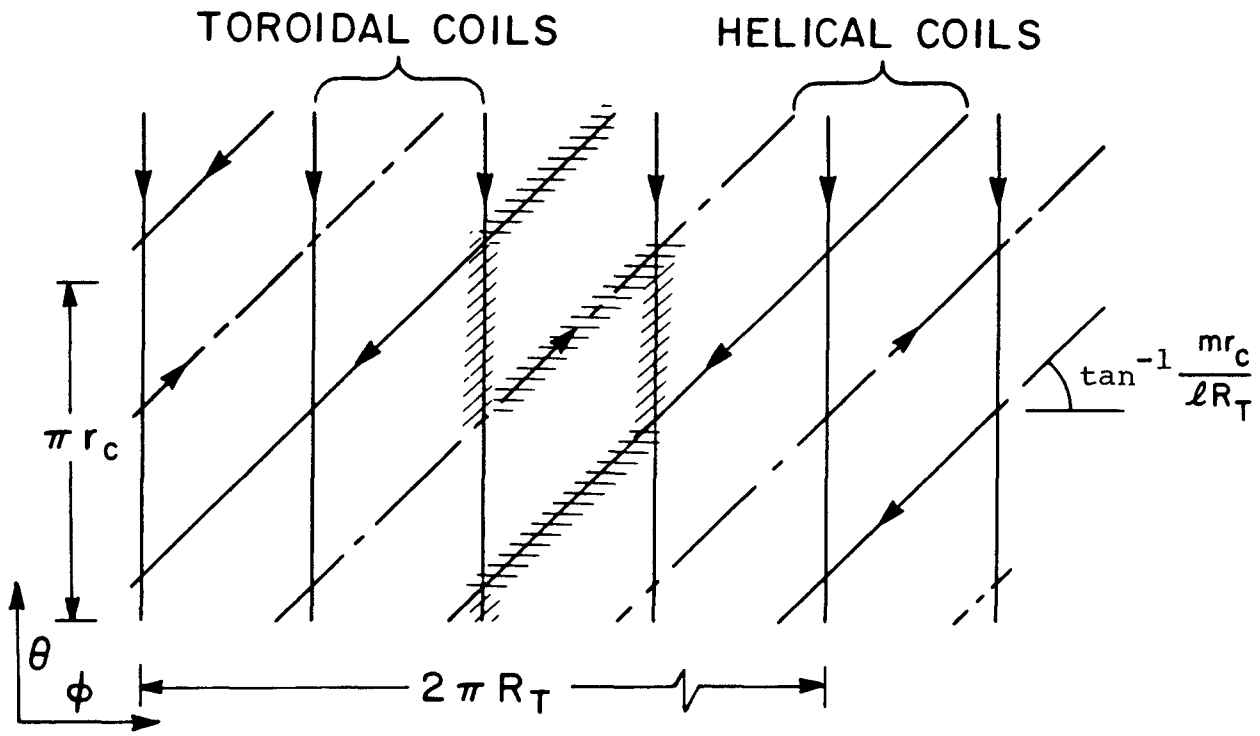

Fig. 3.2-1. Classical stellarator windings, assumed to lie, ideally, at a common radius. The cross-hatched coil reconnection leads to an essentially equivalent modular-coil configuration.

The detailed and relatively expensive magnetics computations are decoupled, where possible, from the reactor survey calculations reported in Sec. 3.4. Instead, model-field approximations are used when possible with calibration to the TORSIDO code results.

The present study focuses on the circular-bore, modular-coil configuration (Fig. 3.2-2) and its comparison with the continuous-helical-coil (torsatron) configuration. It is possible to envisage an elliptical-bore coil for the $\ell = 2$ case and a trefoil-bore coil for the $\ell = 3$ case in order to improve the utilization of magnetic volume and to obtain higher rotational transform for a given lateral coil distortion (see Sec. 4.4.). Such coil modifications imply correspondingly noncircular cross sections for the blanket and shield components and the first wall. Although not precluding the option for performance improvement using these modifications, this study has focused on the simpler, circular-bore configuration. The numerical tools developed for this study can readily be extended to the more complicated configuration

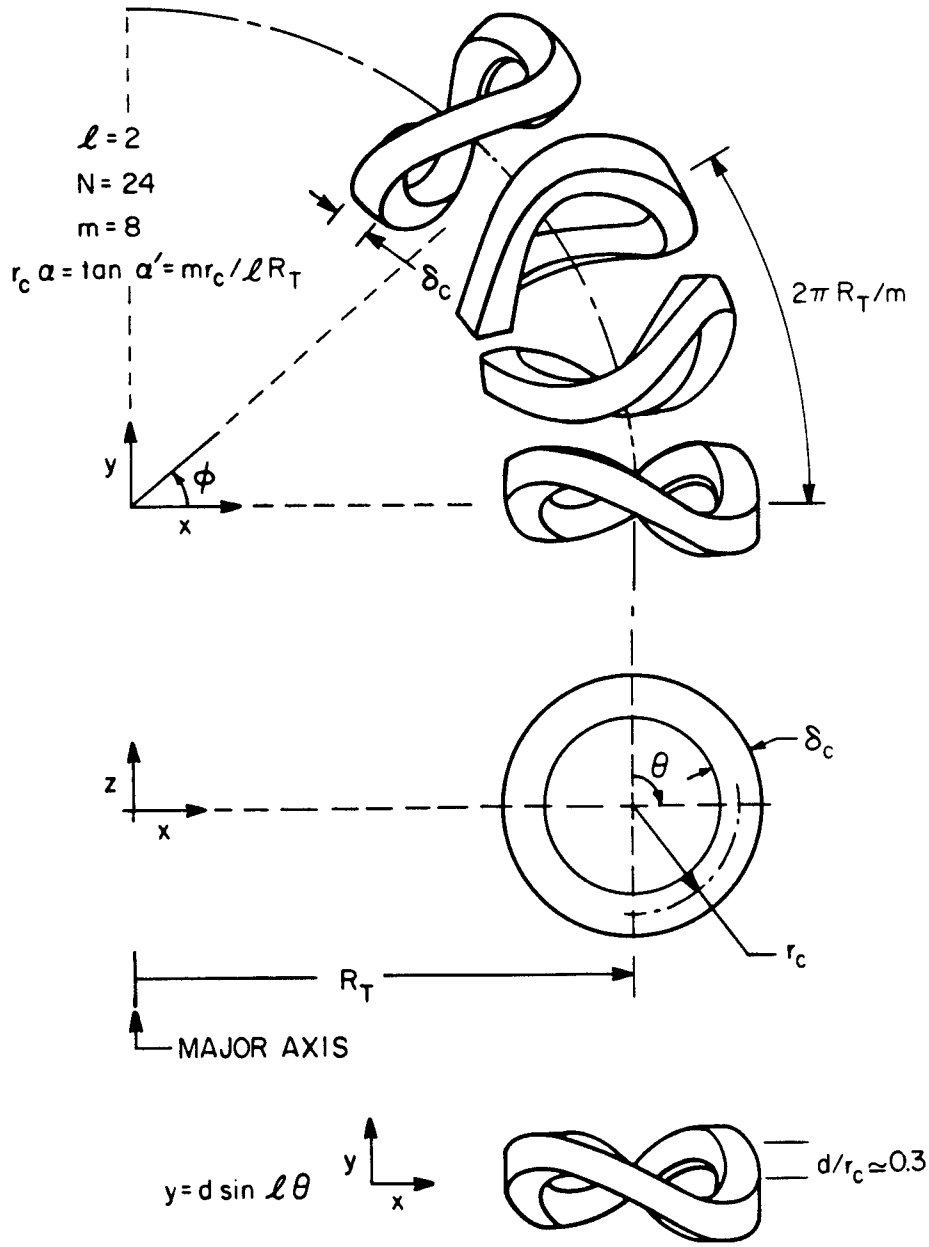

Fig. 3.2-2. Magnetic geometry used in MSR analysis and graphical definition of key variables. In this example there are N/m = 3 coils per field period.

should this refinement and the increased design complexity be deemed desirable or necessary.

3.2.2. Stability/Equilibrium Beta Limits. Establishment of stellarator beta limits is one of the crucial goals of the present theoretical and experimental effort and is a key driver of the eventual reactor extrapolation. Some, but not all, of the uncertainty and ambiguity surrounding this issue has

been dispelled in the interval since the Ref. 6 assessment.[53] No formal theorem for the existence of finite-beta equilibria in the nonaxisymmetric configurations characteristic of stellarators has been proved,[3,5] although within the limits of analytic and numerical approaches, such equilibria have been identified. Numerical codes are being benchmarked against experimental devices[54] and against each other,[55,56,57] with generally encouraging results. A simplified, macroscopic treatment of stellarator equilibrium begins with the stationary magnetohydrodynamic (MHD) approximation[8,49] and yields the usual equilibrium vector relation,

$$\vec{J} \times \vec{B} = \nabla p \quad , \tag{3.2-3}$$

between the plasma current density, $\vec{J}$; magnetic field strength, $\vec{B}$; and scalar plasma kinetic pressure, p, if electric fields are neglected. Maxwell's equations further require

$$\nabla \times \vec{B} = \mu_o \vec{J} \tag{3.2-4}$$

and

$$\nabla \cdot \vec{B} = 0 \quad . \tag{3.2-5}$$

It follows from Eqs. (3.2-3) through (3.2-5) that[58]

$$\vec{B} \cdot \nabla p = 0 \tag{3.2-6}$$

and

$$\vec{J} \cdot \nabla p = 0 \quad , \tag{3.2-7}$$

indicating the orthogonality of $\vec{B}$ and ∇p, so that toroidally nested constant-pressure surfaces coincide with magnetic surfaces and the $\vec{J}$-vector is everywhere parallel to the constant-pressure surfaces. Substitution of Eq. (3.2-4) into Eq. (3.2-3) yields

$$\nabla\left(p + \frac{B^2}{2\mu_o}\right) = (\vec{B} \cdot \nabla) \frac{\vec{B}}{\mu_o} \quad , \tag{3.2-8}$$

where B is the magnitude of the magnetic field embedded in the plasma. For the usual assumption that the radius of curvature of the lines of magnetic force is larger than the gradient length of B (i.e., taken as the plasma minor radius) and that the variation of $\vec{B}$ along field lines is much smaller than the perpendicular variation of $\vec{B}$, Eq. (3.2-8) reduces, by neglecting its right-hand side, to the usual pressure-balance relationship

$$p + \frac{B^2}{2\mu_o} \simeq \frac{B_o{}^2}{2\mu_o} \quad , \tag{3.2-9}$$

and the usual definition of beta, $\beta \equiv p/(B_o{}^2/2\mu_o)$.

Currents flow along the field lines to cancel the charge separation arising from particle drifts in the curved field. Secondary Pfirsch-Schlüter currents then arise to produce a vertical field and shift the magnetic surfaces outward toroidally and produce an average magnetic well to provide plasma stability. At the same time a separatrix approaches the plasma from the inside of the torus to limit the extent of outward plasma shift at a modest upper limit on plasma beta.[8]

The Pfirsch-Schlüter current is approximately given by[49]

$$j_{\parallel} = \frac{2}{\pm B_o} \frac{\partial p}{\partial r} \cos\theta \quad . \tag{3.2-10}$$

For a generalized plasma pressure profile given by

$$p(r) = p_o\left[1 - (r/r_p)^{\nu}\right] \quad , \tag{3.2-11}$$

where p_o is the on-axis pressure, and r_p is the average plasma radius, and for a rotational transform profile assumed to be given by

$$\iota(r) = \iota_o(r/r_p)^{2\ell-4} \quad , \tag{3.2-12}$$

where $\iota_o = \iota(0)$ is the on-axis rotational transform, Eq. (3.2-10) becomes

$$j_\parallel = -\frac{2\nu p_o}{\iota_o B_o r_p}\left(\frac{r}{r_p}\right)^{(\nu - 2\ell + 3)} \cos\theta \quad . \tag{3.2-13}$$

This current yields a vertical magnetic field, B_v, so that

$$B_v/B_o = \frac{(\nu - 2\ell + 6)\nu}{2[(\nu - 2\ell + 5)^2 - 1]\iota_o} \quad , \tag{3.2-14}$$

and an outward shift of the core plasma relative to its edge given by

$$\Delta = -\frac{2R_T}{\iota(\Delta)}\frac{B_v}{B_o} \quad . \tag{3.2-15}$$

Constraining the upper bound of the outward shift so that $\Delta < r_p/2$ provides an upper limit on beta from equilibrium considerations of the form

$$\beta(EQ) < \frac{1}{2}\iota^2/A \tag{3.2-16}$$

or

$$\langle\beta\rangle \lesssim \iota^2/A \tag{3.2-17}$$

for typical pressure profiles at the level of approximation used in this derivation. Equation (3.2-17) has been applied in the parametric search for candidate stellarator design points described in Sec. 3.4.

A numerical treatment of stellarator plasma equilibrium has recently been performed[59] for a particular case of $\ell = 2$, $m = 4$, $N = 36$, $R_T/r_c = 6.2854$, $d/r_c = 0.3354$, $d_2/r_c = 0.05$, $d_3/r_c = 0.0354$, and $r_p/r_c = 0.4875$, using the notation defined in Fig. 3.2-2. For an on-axis rotational transform, $\iota(0) = 1.11$, an equilibrium was identified with $\beta_o \simeq 0.15$, $\langle\beta\rangle \simeq 0.05$, and $\Delta/r_p \simeq 0.48$. This case is close to the MSR-IIB parameters. Studies supporting the ATF-1 experimental design[56] have identified equilibria with $\beta_o = 0.2$, $\langle\beta\rangle = 0.08$, and $\Delta/r_p \simeq 0.5$ using several numerical codes.

Stability analyses are performed by computing the change in potential energy, δW, resulting from an arbitrary fluid perturbation, ξ, from an initial equilibrium.[8] Stability is obtained by providing some average magnetic well and reasonable connection length, R_T/ι, or large shear, ι, to control pressure-driven modes. A simple analysis equates the plasma expansion energy, $2\xi^2 p \langle B_\delta{}^2\rangle / r_p{}^2 B^2$, where $\langle B_\delta\rangle^2$ is the average helical field, to the shear energy $\iota^2(r - r_o)^2 B^2 \xi'^2 \simeq \iota'^2 B^2 \xi^2/4$ resulting from the twisting of field lines in order to obtain an estimate of the stability beta limit of the form

$$\beta(ST) < \iota'^2 r_p{}^2 B^2 / 4\langle B_\delta{}^2\rangle \quad . \tag{3.2-18}$$

If the outward equilibrium shift of the plasma core is sufficient to dig a magnetic well, Eq. (3.2-18) leads to

$$\beta(ST) \lesssim \iota^2/A \quad , \tag{3.2-19}$$

which is similar to the equilibrium limit of Eq. (3.2-16). Numerical stability codes as apply to the ATF-1 studies have generally confirmed the projected levels of beta assumed for the present stellarator reactor design points. As illustrated in Fig. 3.1.9 of Ref. 56, for $\Delta/r_p \simeq 0.4$-0.5, approximately $\beta_o \simeq (0.9 \text{ to } 1.4)\iota(r_p)/A$, with the numerical codes predicting higher values of beta than does the stellarator expansion for a fixed plasma shift.

3.2.3. Transport. In the absence of internal sources and sinks (or when they just balance), the diffusion of particles from a plasma is governed by

$$\nabla\left(D\nabla n(\vec{r},t)\right) = \frac{\partial n}{\partial t}(\vec{r},t) \quad , \tag{3.2-20}$$

where $D(m^2/s)$ is the diffusion coefficient. Under the usual simplifying assumptions that D is constant and the plasma is a cylindrical column of radius, r_p, the solution of Eq. (3.2-20) is

$$n(r) = n_o J_o\left(\frac{2.405r}{r_p}\right) \exp\left(\frac{-t}{\tau}\right) \quad , \tag{3.2-21}$$

with the relaxation time constant

$$\tau \equiv \frac{r_p^2}{(2.405)^2 D} = \frac{r_p^2}{5.78D} \quad , \tag{3.2-22}$$

and $J_o(x)$ is the zeroth order Bessel function with argument x. An analogous relation exists between the energy diffusion coefficient, $\chi_E(m^2/s)$, and the confinement time, τ_E, of the internal plasma energy, $3nk_BT$.

Radial transport of energy in a nonaxisymmetric stellarator/torsatron plasma is a complicated subject that is receiving theoretical attention.[6,8] At this level of study, it was judged imprudent to incorporate at the outset a detailed, state-of-the-art model of particle and energy transport. Instead, the reactor-survey calculations are performed using simplified empirical or theoretical models in order that sensitive variables can be more directly identified. The resulting groundwork can be extended to more sophisticated models as the design progresses. For purposes of this study, therefore, transport is modeled using the Alcator (empirical) scaling relationship

$$\langle n_e\rangle \tau_{E(\text{Alcator})} = 3.0(10)^{-21} \langle n_e\rangle^2 r_p^2 \tag{3.2-23A}$$

$$= 4.613(10)^{21} \left[\frac{(I_{1/2}^2/I_1)\, f_{Z1}^{1/2}}{f_{Z2}}\right]^2 \left[\frac{\langle\beta\rangle B_o^2 r_p}{\langle T\rangle}\right]^2 \quad , \tag{3.2-23B}$$

where f_{Z2} and I_x are, respectively, Z_{eff} and profile corrections as defined in Sec. 3.2.4. The value of the numerical coefficient used in Eq. (3.2-23) was set deliberately lower than the $5.0(10)^{-21}$ value usually used in tokamak scaling to calibrate the present work with the work of Refs. 22 and 25.

It is instructive to review and update here the Ref. 22 discussion of the neoclassical treatment[60] of stellarator transport[61] to calibrate the use of the Alcator relationship. The usual presentation of neoclassical transport scaling in toroidal magnetic confinement devices is summarized schematically in Fig. 3.2-3. Different transport rates are encountered as a function of collision frequency, ν, giving rise to distinct transport scaling relationships. Like most steady-state, magnetic fusion devices, the stellarator reactor is anticipated to operate in the collisionless regime. As ν decreases, the rightmost region of Fig. 3.2-3 indicates that $D_{PS} \propto \nu$

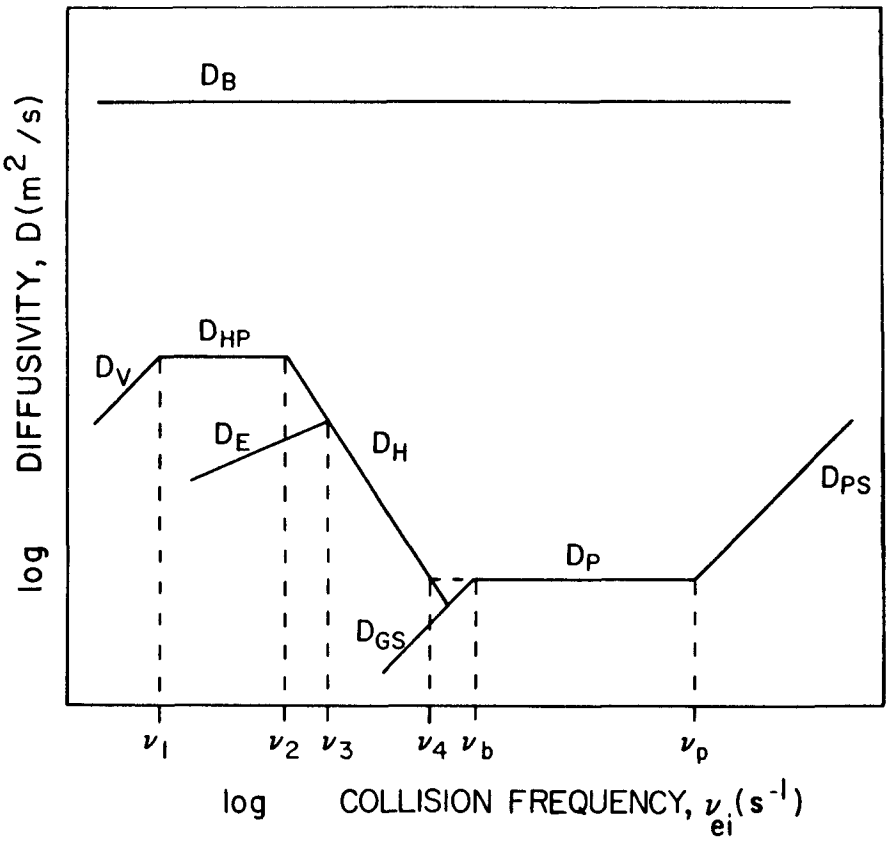

Fig. 3.2-3. Dependence of the diffusion coefficient, D, on electron-ion collision frequency, ν_{ei}, following Ref. 61. $D_{PS} \equiv$ Pfirsch-Schluter, $D_P \equiv$ plateau, $D_H \equiv$ helical ripple, $D_{HP} \equiv$ helical plateau, $D_V \equiv$ trapped superbanana, $D_E \equiv$ nonzero electric field, $D_{GS} \equiv$ Galeev-Sagdeev, and $D_B \equiv$ Bohm diffusion.

(Pfirsch-Schlüter) until $\nu < \nu_p$ and the plateau regime (D_P, independent of ν) is encountered. Continued application of tokamak axisymmetric theory would suggest that for $\nu < \nu_b$ the diffusion would resume the $D_{GS} \propto \nu$ (Galeev-Sagdeev) scaling. However, in nonaxisymmetric stellarators ($\nu_3 < \nu_b$) and torsatrons ($\nu_3 > \nu_b$), helical-ripple diffusion dominates for $\nu < \nu_4$ to give $D_H \propto \nu^{-1}$. If ν is less than the helical-banana precession frequency, $\nu_2 = \varepsilon_h{}^2\omega_o$, where $\omega_o = -T/eB_o r^2$, vertical drifts are compensated, and a helical plateau regime (D_{HP} independent of ν) is encountered. Finally, when ν is less than the superbanana bounce frequency, ν_1, trapped superbananas allow $D_V \propto \nu$. In the presence of radial electric fields, helical bananas may become untrapped for $\nu < \nu_e < \nu_3 \equiv \varepsilon_h\omega_E$ ($\omega_E = E_r/B_o r$), such that $D_E \propto \nu^{1/2}$. In the limit of infinite plasma aspect ratio ($\varepsilon_t \to 0$), axisymmetric theory would continue to apply for $\nu < \nu_b$ such that $D_{GS} \propto \nu$. Bohm diffusion D_B is formally independent of ν and is much more rapid than are the various neoclassical diffusion regimes discussed above.

The various quantities indicated in Fig. 3.2-3 can be defined in terms of reactor parameters. The collision frequency may be expressed as either the electron-ion or ion-ion collision frequency, assuming the average DT-ion mass is 2.5 amu, as follows:

$$\nu_{ei}(s^{-1}) = 5.397(10)^{-17}\ Z_{eff}^2 \ell n\Lambda\ \frac{\langle n_i\rangle}{\langle T\rangle^{3/2}} \qquad (3.2\text{-}24A)$$

$$\nu_{ii}(s^{-1}) = 1.399(10)^{-18}\ Z_{eff}^2 \ell n\Lambda\ \frac{\langle n_i\rangle}{\langle T\rangle^{3/2}} \approx \nu_{ei}/39 \ . \qquad (3.2\text{-}24B)$$

When the pressure-balance relationship is applied while neglecting the alpha-particle pressure contribution to $\langle\beta\rangle$ (i.e., $Z_{eff} = f_{Z2} = 1$), Eqs: (3.2-24) can be recast as follows:

$$\nu_{ei} = 6.69(10)^4\ \ell n\Lambda\ (I_{1/2}^2/I_1)\ \langle\beta\rangle\ \frac{B_o{}^2}{\langle T\rangle^{5/2}} \qquad (3.2\text{-}25A)$$

$$\nu_{ii} = 1.1(10)^3 \ell n\Lambda \, (I_{1/2}^2/I_1) \langle\beta\rangle \frac{B_o^2}{\langle T\rangle^{5/2}} \quad . \tag{3.2-25B}$$

As auxiliary variables it is useful to have the ion (m_i = 2.5 amu for 50-50 DT plasma) thermal speed,

$$v_{Ti}(m/s) = (2k_B T/m_i)^{1/2} = 2.77(10)^5 \, T^{1/2} \quad , \tag{3.2-26}$$

and the gyroradii for ions,

$$\rho_i(m) = v_{Ti}/\omega_{ci} = 7.198(10)^{-3} \frac{T^{1/2}}{B} \quad , \tag{3.2-27}$$

and electrons,

$$\rho_e(m) = v_{Te}/\omega_{ce} = 3.162(10)^{-5} \frac{T^{1/2}}{B} \quad , \tag{3.2-28}$$

evaluated here in the local magnetic field.

The classical diffusion coefficient for electrons moving in a random walk with a step length, ρ_e, is

$$D_{CL} = \rho_e{}^2 \nu_{ei} \quad . \tag{3.2-29}$$

In the MHD limit where the collision mean free path is short compared with the connection length, R_T/ι, in a toroidal plasma column (i.e., $v_{Te}/\nu_{ei} < R_T/\iota$), one obtains the Pfirsch-Schlüter diffusion coefficient

$$D_{PS} = D_{CL}\left(1 + \frac{T_i}{T_e}\right)\left(1 + \frac{1}{\iota^2}\right) \quad . \tag{3.2-30}$$

For collision frequencies dropping below $\nu_b \equiv V_{Te}\tau/R_T$, the plateau regime is encountered such that

$$D_P = \rho_e^2 \nu_p / \tau^2 \quad , \tag{3.2-31}$$

where $\nu_p \equiv \varepsilon_t^{3/2}\nu_b$ and $\nu_p < \nu_{ei} < \nu_b$. For even less collisional tokamak plasma such that $\nu_{ei} < \nu_p$, the Galeev-Sagdeev regime is reached such that

$$D_{GS} = \rho_e^2 \nu_{ei}\ \varepsilon_t^{-3/2}/\tau^2, \tag{3.2-32}$$

under the condition that electrons can complete a circuit of a banana orbit.

The picture for stellarators in the low-collisionality regime is different. Particles may be trapped in the inhomogeneous field ripples introduced by the rightmost term in Eq. (3.2-1) and may drift across the magnetic surface to contribute to the radial diffusion given by

$$D_H = \varepsilon_h^{3/2}\ \varepsilon_t^2\ \frac{\omega_o}{\nu_{ei}}\ \frac{T}{eB} \quad . \tag{3.2-33}$$

This process occurs for $\nu_{ei} < \nu_4 \equiv (\varepsilon_h/\varepsilon_t)^{3/2}\nu_b$. An upper limit on D_H is reached when $\nu_{ei} < \nu_2 \equiv \varepsilon_h^2\omega_{oi}$, where $\omega_o \equiv T/eBr^2$, and vertical drifts are compensated, such that

$$D_{HP} = \frac{\varepsilon_t^{3/2}}{\varepsilon_n^{1/2}}\ \frac{T}{eB} \quad . \tag{3.2-34}$$

For $\nu_{ei} < \nu_i \equiv (\varepsilon_t/\varepsilon_h)^{3/2}\ \varepsilon_h^2\omega_o$, the superbanana bounce frequency, trapped helical superbananas again reduce the diffusion coefficient to

$$D_V = \varepsilon_t^{1/2} \frac{r^2}{\varepsilon_h} \nu_{ei} \quad . \tag{3.2-35}$$

Untrapping of helical bananas by radial electric fields, E_r, can terminate the growth of D_H for $\nu_{ei} < \nu_3 \equiv \varepsilon_h \omega_E$, where $\omega_E \equiv E_r/B_o r$, to yield

$$D_E = \varepsilon_t^2 \left(\frac{\nu_{ei}}{\omega_E}\right)^{1/2} \frac{T}{eE_r} \frac{T}{eB} \quad . \tag{3.2-36}$$

For completeness, Bohm diffusion is governed by

$$D_B = \frac{1}{16} \frac{T}{eB} = 62.5 \frac{T}{B} \tag{3.2-37}$$

and is worse than the neoclassical terms considered. The corresponding thermal diffusion coefficients, $\chi_E(m^2/s)$, have the same functional dependencies as D; however, like-particle collisions rather than electron-ion collisions provide the mechanism for thermal diffusion.

The ion particle diffusion rate is reduced to the electron rate by the ambipolar electric field,

$$e\phi' = -\frac{}{T_i} \left[\frac{n'}{n} + 3.37 \frac{T_i'}{T_i}\right] \quad , \tag{3.2-38}$$

where $x' \equiv dx/dr$, to give a common ambipolar particle diffusion coefficient,[62]

$$D_{AMB} = 4.34(10)^6 \frac{\varepsilon_h^{3/2}}{\nu_{ei}} \left(\frac{T}{BR_T}\right)^2 \quad , \tag{3.2-39}$$

$$= 1.09 \ \varepsilon_h^{3/2} \ \rho_e^2 \ v_{Te}^2/\nu_{ei} \ R_T^2 \quad , \tag{3.2-40}$$

in the helical-ripple transport regime, $\nu_2 < \nu_{ei} < \nu_4$. Under the conditions of ambipolar diffusion, the ions dominate the heat loss so that

$$\chi_{EH} = 46.5(10)^6 \frac{\varepsilon_h^{3/2}}{\nu_{ii}} \left(\frac{T}{BR_T}\right)^2 \tag{3.2-41}$$

$$= 11.7\ \varepsilon_h^{3/2}\ \rho_i^2 v_{Ti}^2/\nu_{ii}R_T^2 \tag{3.2-42}$$

and $\chi_E/D_{AMB} \simeq 419$. The transition between the helical-ripple regime and the plateau regime at $\nu_{ii} = \nu_4$ requires that $x_{EH}(\nu_4) = x_{EP}(\nu_4)$, such that

$$\chi_{EP} = 11.7\ \varepsilon_t^{3/2}\ \rho_i^2\ v_{Ti}/\text{+}R_T \quad . \tag{3.2-43}$$

In terms of fundamental units, these thermal diffusion coefficients can be written using Eqs. (3.2-25) through (3.2-27) as

$$\chi_{EH} = \frac{1.06(10)^3 \langle T\rangle^{9/2}\ \varepsilon_h^{3/2}}{(I_{1/2}^2/I_1)\ \langle\beta\rangle B_o^4 R_T^2} \tag{3.2-44}$$

and

$$\chi_{EP} = \frac{83.9\ \langle T\rangle\ \varepsilon_t^{3/2}}{(I_{1/2}^2/I_1)B_o^2\text{+}R_T} \quad , \tag{3.2-45}$$

where $\ell n\Lambda = 20$, $B \simeq B_o$, and $T \simeq \langle T\rangle$, to provide a global estimate of energy confinement. When Eqs. (3.2-22) and (3.2-23) are used, the Alcator diffusion coefficient can be expressed similarly as

$$\chi_{EA} = \frac{4.65(10)^{-2}}{(I_{l/2}^2/I_l)} \frac{\langle T \rangle}{\langle \beta \rangle B_o^2} \quad . \tag{3.2-46}$$

Monte Carlo transport computations[63] using realistic fields have failed to reproduce the $1/\nu$ behavior of Eq. (3.2-41) and thus give more favorable reactor projections. Other recent work[64-66] using model fields, such as that given by Eq. (3.2-1), tends to support the analytic theory somewhat but is also more favorable. Crucial experimental investigation of transport scaling is a major goal of the proposed ATF-1 device.[56]

The general conclusions from the studies of ion thermal transport are 1) earlier estimates based on oversimplified models of transport in a rippled tokamak are not valid; 2) transport may not increase markedly in the low-collisionality regime, but remains at most a few times the "plateau" value; 3) optimization of the magnetic configuration from a transport viewpoint appears possible and may serve to distinguish between good and bad configurations; 4) the principal present limitation is insufficient research on a complete range of configurations.

3.2.4. Ignited Thermonuclear Burn. The stellarator reactor is characterized here by a point plasma model that determines the self-consistent parameters of an ignited, steady-state, DT thermonuclear burn. Ignition is defined when the self-heating power density, $p_\alpha(W/m^3)$, of alpha-particle fusion product energy that is trapped in the plasma with an efficiency, f_α, just offsets the combined Bremsstrahlung loss, $p_{BR}(W/m^3)$, and radial transport loss, $p_\ell(W/m^3)$. That is,

$$f_\alpha p_\alpha = p_{BR} + p_\ell \quad . \tag{3.2-47}$$

Bremsstrahlung is the dominant radiation loss in the temperature range of interest to DT fusion reactor applications. The terms in Eq. (3.2-47) can be expressed as follows, using SI units, with the exception of temperature expressed in keV units:

$$p_\alpha(W/m^3) = 1.41(10)^{-13}\, n_i^2 \langle \sigma v \rangle \quad , \tag{3.2-48}$$

$$P_{BR}(W/m^3) = 5.35(10)^{-37}\ n_e^2 Z_{eff}\ T^{1/2} \quad , \tag{3.2-49}$$

and

$$P_{\ell}(W/m^3) = \frac{4.806(10)^{-16}\ n_e^2 T}{n_e \tau_E} \quad . \tag{3.2-50}$$

The expression for the Bremsstrahlung term uses a Gaunt factor of 1.1; $n_i(m^{-3})$ is the plasma ion density; $n_e(m^{-3})$ is the plasma electron density ($n_e = n_i + 2n_\alpha$); T(keV) is the plasma temperature ($T_i = T_e = T$); and the energy confinement time is $\tau_E(s)$. For no impurities other than the alpha-particle fusion products, the effective charge of the plasma, Z_{eff}, is given by

$$Z_{eff} = \frac{n_i + 4n_\alpha}{n_i + 2n_\alpha} \tag{3.2-51A}$$

and

$$\frac{n_\alpha}{n_i} = \frac{Z_{eff} - 1}{2(2 - Z_{eff})} \quad . \tag{3.2-51B}$$

The DT fusion reactivity, $\langle\sigma v\rangle(m^3/s)$, can be approximated as a function of T to within 10% of nominal values[67] by

$$\langle\sigma v\rangle = 1.1(10)^{-24}\ T^2 \quad , \tag{3.2-52}$$

in the range $8 < T < 20$ keV. A number of scalings for the energy confinement time are considered in Sec. 3.2.3. The alpha-particle heating efficiency, f_α, can be varied parametrically in the range $0 < f_\alpha < 1$, pending the development of suitable scaling relationships obtained from numerical simulation studies of transport and orbit tracking.

A peaked radial pressure profile reduces the confinement required for ignition. To assess parametrically the influence of radial density and temperature profiles, the following profile functions are assumed, using a plasma of average radius, $r_p(m)$, so that

$$n(r) = n_o\ [1-(r/r_p)^\nu]^{1/2} \tag{3.2-53A}$$

and

$$T(r) = T_o \left[1-(r/r_p)^{\nu}\right]^{1/2} \quad . \tag{3.2-53B}$$

The corresponding radial pressure profile is given by

$$p(r) = p_o \left[1-(r/r_p)^{\nu}\right] \tag{3.2-54A}$$

$$= 2n_o k_B T_o \left[1-(r/r_p)^{\nu}\right] \quad , \tag{3.2-54B}$$

where $k_B = 1.602(10)^{-16}$ J/keV. The subscript "o" refers to on-axis (r = 0) quantities, and ν ($\nu = 1,2,3,\ldots,\infty$) is a parametric radial-profile index. Low values of ν represent sharply peaked profiles, and larger values of ν give increasingly flatter profiles.

The radially averaged value of the density (or analogous temperature) profile is defined by

$$\langle n \rangle = \frac{\int_o^{r_p} n(r)2\pi r dr}{\int_o^{r_p} 2\pi r dr} = \frac{2}{r_p^2}\int_o^{r_p} n(r) r dr \quad . \tag{3.2-55}$$

Substitution of Eqs. (3.2-52) and (3.2-53) into Eqs. (3.2-48) and (3.2-49) gives expressions for profile-averaged power densities related to alpha-particle heating and Bremsstrahlung losses. An accurate estimate of the alpha-particle heating power density, therefore, is restricted to the same temperature range ($8 < T < 20$ keV) as was used in Eq. (3.2-52). If this convenient approximation proves inaccurate, the profile averages can be calculated numerically for the general case. The volume-averaged density, temperature, and pressure are related to the on-axis values by

$$\langle n \rangle = n_o \frac{2}{r_p^2}\int_o^{r_p} \left[1-(r/r_p)^{\nu}\right]^{1/2} r dr = n_o I_{1/2} \quad , \tag{3.2-56A}$$

$$\langle T \rangle = T_o \frac{2}{r_p^2} \int_o^{r_p} [1-(r/r_p)^\nu]^{1/2} \, rdr = T_o I_{1/2} \quad , \tag{3.2-56B}$$

and

$$\langle p \rangle = p_o \frac{2}{r_p^2} \int_o^{r_p} [1-(r/r_p)^\nu] \, rdr = p_o I_1 \quad , \tag{3.2-56C}$$

where the following simplifying notation for radial-profile integrals is introduced:

$$I_x \equiv \frac{2}{r_p^2} \int_o^{r_p} [1-(r/r_p)^\nu]^x \, rdr \quad . \tag{3.2-57}$$

The profile-averaged power densities related to alpha-particle heating and Bremsstrahlung can be written as

$$\langle p_\alpha \rangle = p_\alpha \, I_{1/2}^{-4} \frac{2}{r_p^2} \int_o^{r_p} [1-(r/r_p)^\nu]^2 \, rdr = p_\alpha I_{1/2}^{-4} \, I_2 \tag{3.2-58A}$$

and

$$\langle p_{BR} \rangle = p_{BR} \, I_{1/2}^{5/2} \frac{2}{r_p^2} \int_o^{r_p} [1-(r/r_p)^\nu]^{5/4} \, rdr = p_{BR} I_{1/2}^{5/2} \, I_{5/4} \quad . \tag{3.2-58B}$$

In Eqs. (3.2-58A) and (3.2-58B), p_α and p_{BR} are obtained by substituting the profile-averaged values of Eq. (3.2-57) into Eqs. (3.2-48) and (3.2-49). Values of the profile integrals $I_{1/2}$, I_1, $I_{5/4}$, and I_2, as functions of the profile index, ν, are summarized in Table 3.2-1. For an on-axis vacuum magnetic field, $B_o(T)$, the on-axis beta is given by

$$\beta_o = \frac{\sum_{j=i,e,\alpha} n_{oj} k_B T_{oj}}{B_o^2/2\mu_o} = \frac{p_o}{B_o^2/2\mu_o} \quad , \tag{3.2-59}$$

where μ_o is the permeability of free space [$4\pi(10)^{-7}$ h/m]. A pressure-balance relationship can be written in consistent units as

$$\sum_{j=i,e,\alpha} n_{oj}T_{oj} = 2.48(10)^{21}\ \beta_o B_o^2 \quad , \tag{3.2-60A}$$

which, upon substitution of the profile-averaged parameters, becomes

$$\sum_{j=i,e,\alpha} \langle n_j\rangle\langle T_j\rangle = 2.48(10)^{21}\ (I_{1/2}^2/I_1)\ \langle\beta\rangle B_o^2 \quad . \tag{3.2-60B}$$

It is noted that $\langle\beta\rangle = \beta_o I_1 = \beta_o\nu/(\nu + 2)$. The remainder of this discussion is presented on the basis of homogeneous profile-averaged parameters.

The accumulation of impurities and alpha-particle ash is neglected for the purposes of this study. If alpha particles are allowed to build up to an

TABLE 3.2-1

RADIAL PROFILE INTEGRALS [EQ. (3.2-57)]

ν	$I_{1/2}$	I_1	$I_{5/4}$	I_2
1	0.5332	0.3333	0.2735	0.1667
2	0.6667	0.5000	0.4444	0.3333
3	0.7390	0.6000	0.5515	0.4500
4	0.7851	0.6667	0.6243	0.5333
5	0.8173	0.7143	0.6769	0.5952
6	0.8410	0.7500	0.7166	0.6429
7	0.8592	0.7773	0.7476	0.6806
8	0.8737	0.8000	0.7725	0.7111
9	0.8854	0.8182	0.7930	0.7364
10	0.8951	0.8333	0.8101	0.7576
•				
•				
•				
∞	1.0	1.0	1.0	1.0

equilibrium level characterized by Z_{eff}, Eqs. (3.2-51), (3.2-49), (3.2-50), and (3.2-60) can be recast as follows:

$$\langle p_\alpha \rangle = 1.41(10)^{-13}\langle n_i \rangle^2 \langle \sigma v \rangle (I_2/I_{1/2}^4) \quad , \tag{3.2-61A}$$

$$\langle p_{BR} \rangle = 5.35(10)^{-37}\langle n_i \rangle^2 \left[1 + \frac{Z_{eff} - 1}{2 - Z_{eff}}\right]^2 Z_{eff} \langle T \rangle^{1/2} (I_{5/4}/I_{1/2}^{5/2}) \quad , \tag{3.2-61B}$$

$$\langle p_\ell \rangle = \frac{4.806(10^{-16}\langle n_i \rangle^2 \left[1 + \frac{Z_{eff} - 1}{2 - Z_{eff}}\right]^2 \langle T \rangle}{\langle n_e \rangle \tau_E} \quad , \tag{3.2-61C}$$

and

$$\langle n_i \rangle \langle T \rangle \left[1 + \frac{(Z_{eff} - 1)}{2(2 - Z_{eff})} (1 + \tfrac{1}{2} T_\alpha / \langle T \rangle)\right] = 1.24(10)^{21} (I_{1/2}^2/I_1) \langle \beta \rangle B_o^2 . \tag{3.2-61D}$$

These relationships eliminate the explicit use of the electron and alpha-particle densities in favor of the ion densities. The ratio $T_\alpha/\langle T \rangle$ is taken to be ~10 based on Fokker-Planck computations of burning DT plasma in other systems. The following variables are defined to simplify the notation:

$$f_{Z1} = \left[1 + \frac{Z_{eff} - 1}{2 - Z_{eff}}\right]^2 \tag{3.2-62A}$$

and

$$f_{Z2} = 1 + \frac{(Z_{eff} - 1)}{2(2 - Z_{eff})} (1 + \frac{1}{2} T_\alpha / \langle T \rangle) \tag{3.2-62B}$$

such that $\langle n_e \rangle = \langle n_i \rangle f_{Z1}^{1/2}$. The presence of suprathermal alpha particles may be interpreted as a reduction in the productive $\langle \beta \rangle$ of the fusion plasma when the confining magnetic field strength is fixed. Figure 3.2-4 displays $1/f_{Z2}$ as a function of Z_{eff} for several ratios of $T_\alpha/\langle T \rangle$. The quantity $1/f_{Z2}$ may be seen from Eq. (3.2-61D) to be the ratio of $\langle \beta \rangle$ for $Z_{eff} > 1.0$ to the value of $\langle \beta \rangle$ when the pressure contribution, p_α/p, of alpha particles is neglected

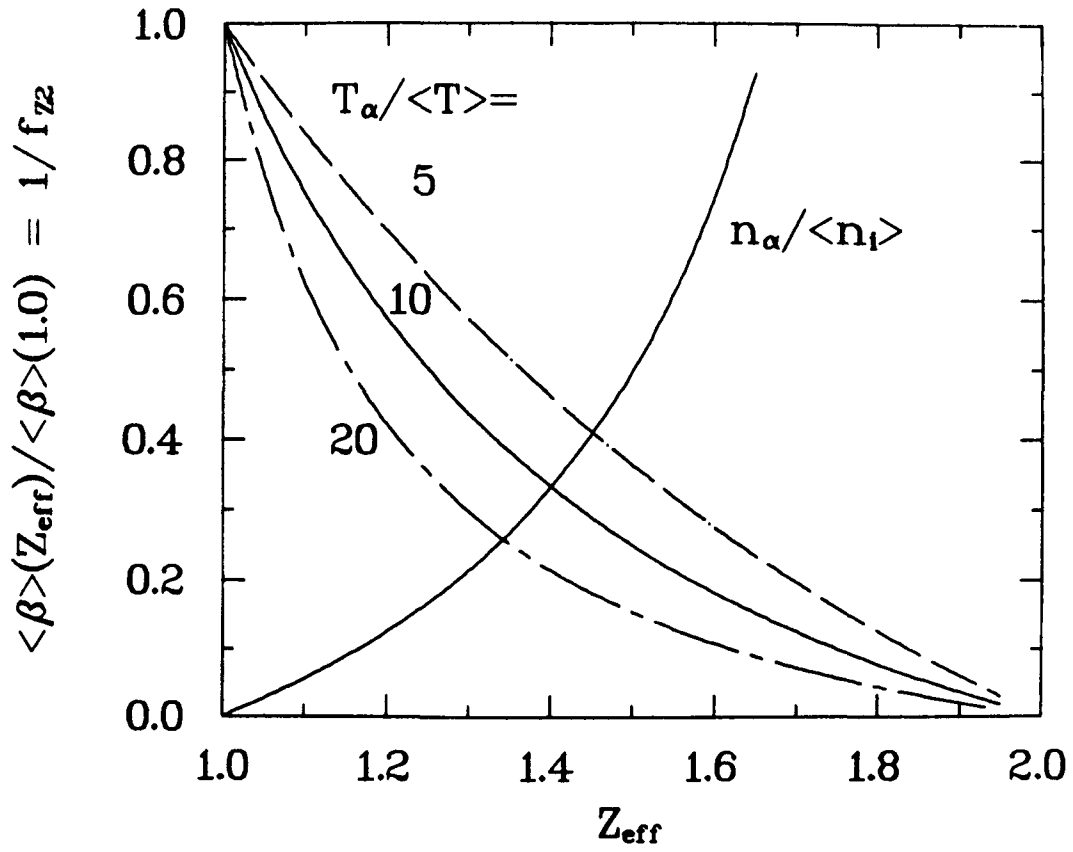

Fig. 3.2-4. Dependence of f_{Z2} and n_α/n_i on Z_{eff} in the Z_{eff} range of 1-2.

(i.e., $Z_{eff} = 1.0$). Equations (3.2-61) reduce to the following set of working relationships:

$$<p_\alpha> = 1.41(10)^{-13} <n_i>^2 <\sigma v>(I_2/I_{1/2}^4) \quad , \tag{3.2-63A}$$

$$<p_{BR}> = 5.35(10)^{-37} <n_i>^2 f_{Z1} Z_{eff} <T>^{1/2}(I_{5/4}/I_{1/2}^{5/2}) \quad , \tag{3.2-63B}$$

$$<p_\ell> = \frac{4.806(10)^{-16} <n_i>^2 f_{Z1} <T>}{<n_e>\tau_E} \quad , \tag{3.2-63C}$$

and

$$<n_i><T> f_{Z2} = 1.24(10)^{21}(I_{1/2}^2/I_1)<\beta>B_o^2 \quad . \tag{3.2-63D}$$

Once a specific radial transport scaling for $\langle n_e \rangle \tau_E$ or τ_E is adopted and a pressure balance is enforced, Eqs. (3.2-63) can be used in the ignition condition [Eq. (3.2-47)] to give $\langle n_e \rangle \tau_E$ as a function of $\langle T \rangle$.

When Eqs. (3.2-47) and (3.2-63) are combined, once the $\langle n_i \rangle^2$ terms have been cancelled, the ignition condition can be written in the form of the Lawson criterion as

$$\langle n_e \rangle \tau_E = \frac{4.806(10)^{-16} f_{Z1} \langle T \rangle}{\left[f_\alpha 1.41(10)^{-13} \langle \sigma v \rangle (I_2/I_{1/2}^4) - 5.35(10)^{-37} f_{Z1} Z_{eff} \langle T \rangle^{1/2} (I_{5/4}/I_{1/2}^{5/2})\right]} . \quad (3.2\text{-}64)$$

The alpha-particle energy-trapping efficiency, f_α, can be selected parametrically or, as will be seen below, can be modeled directly. If Z_{eff} is known, the quantity f_{Z1} on the right-hand side of Eq. (3.2-64) is determined by Eq. (3.2-62A). Also, if the profile index, ν, is known, the various I_x profile integrals are determined (Table 3.2-1). The right-hand side of Eq. (3.2-64) is, therefore, a pure function of $\langle T \rangle$ once these auxiliary parameters are known. Equation (3.2-64) is plotted in Fig. 3.2-5 as the dashed curve. The dashed curve reflects the approximations contained in Eqs. (3.2-52) and (3.2-58A) that are built into the reactor-survey model. The solid curve in Fig. 3.2-5 is the result of a numerical integration, which does not depend on these approximations, of the first term (representing alpha-particle heating) in the denominator of Eq. (3.2-64). The agreement between the two results is considered good and justifies the use of the approximate model. The stellarator design point at $\langle T \rangle$ = 8 keV is also shown in Fig. 3.2-5. The $\langle n_e \rangle \tau_E$ curves in Fig. 3.2-5 exhibit a shallow minimum in the vicinity of $\langle T \rangle$ = 20 keV. The design point is not selected to minimize the required Lawson parameter. If the Alcator transport scaling expression is substituted for the left-hand side of Eq. (3.2-64), the following "engineering Lawson criterion" results:

$$[\langle\beta\rangle B_o^2 r_p]^2 =$$

$$\frac{f_{Z2}^2 \langle T\rangle^3}{1.35(10)^{24} f_\alpha \langle\sigma v\rangle (I_2/I_1^2) - 5.13\, f_{Z1}\, Z_{eff}[I_{5/4}/(I_{1/2}^{3/2}\, I_1^2)]\langle T\rangle^{1/2}} \cdot \tag{3.2-65}$$

This expression can be plotted as a function of $\langle T\rangle$ as in Fig. 3.2-6. The stellarator design point at $\langle T\rangle$ = 8 keV is near the minimum of this parameter, reflecting low-field and compact reactor performance for a given value of $\langle\beta\rangle$.

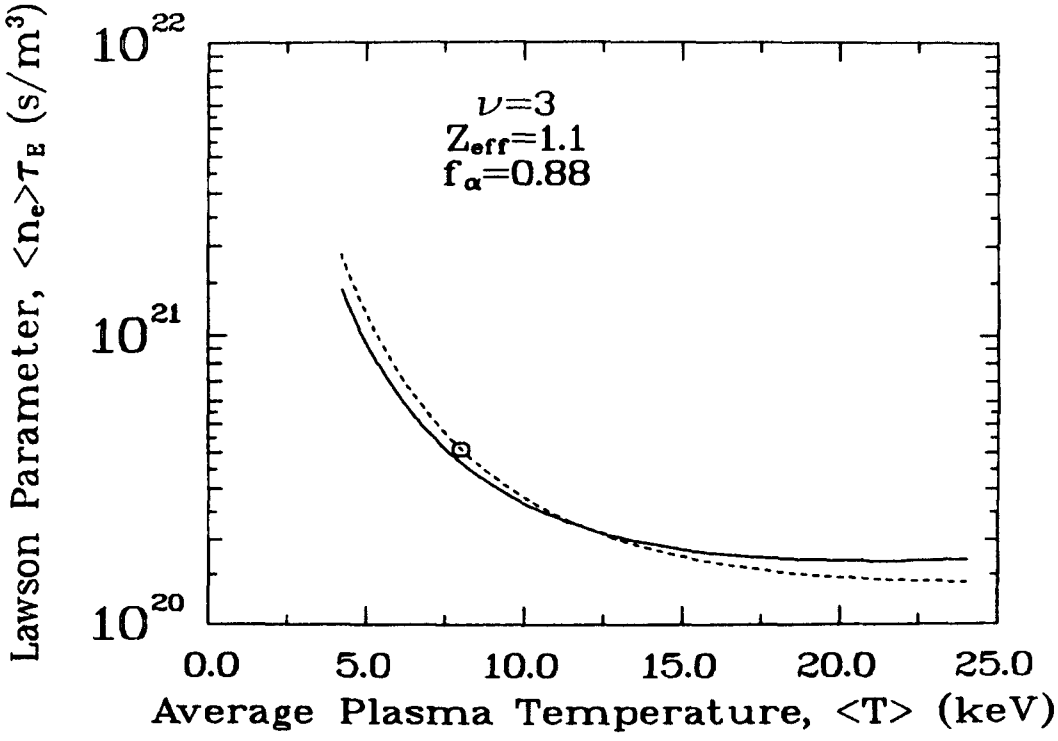

Fig. 3.2-5. Lawson parameter, $\langle n_e\rangle\tau_E$, required for ignition as a function of average plasma temperature, $\langle T\rangle$, for ν = 3, Z_{eff} = 1.1, and f_α = 0.88. The design point at $\langle T\rangle$ = 8 keV is shown. The dashed curve is a plot of Eq. (3.2-64) that reflects the approximations contained in Eqs. (3.2-52) and (3.2-58A). The solid curve is the result of a numerical integration of the alpha-particle power density without these approximations.

The alpha-particle energy-trapping efficiency, f_α, has been estimated[68] to be a function of plasma aspect ratio, $A = R_T/r_p$. This dependence is approximated here by the expression

$$f_\alpha \sim 1 - e^{-A/5.22} \quad , \tag{3.2-66}$$

which is shown graphically in Fig. 3.2-7. If f_α is too small, the denominator on the right-hand sides of Eqs. (3.2-64) and (3.2-65) will become negative, and physical solutions to the ignition condition will not exist. This condition corresponds to the ideal ignition condition (i.e., trapped alpha-particle power just balances Bremsstrahlung losses) and defines an ideal ignition threshold, $\langle T \rangle^*$, as a function of f_α; this condition is also shown in Fig. 3.2-7.

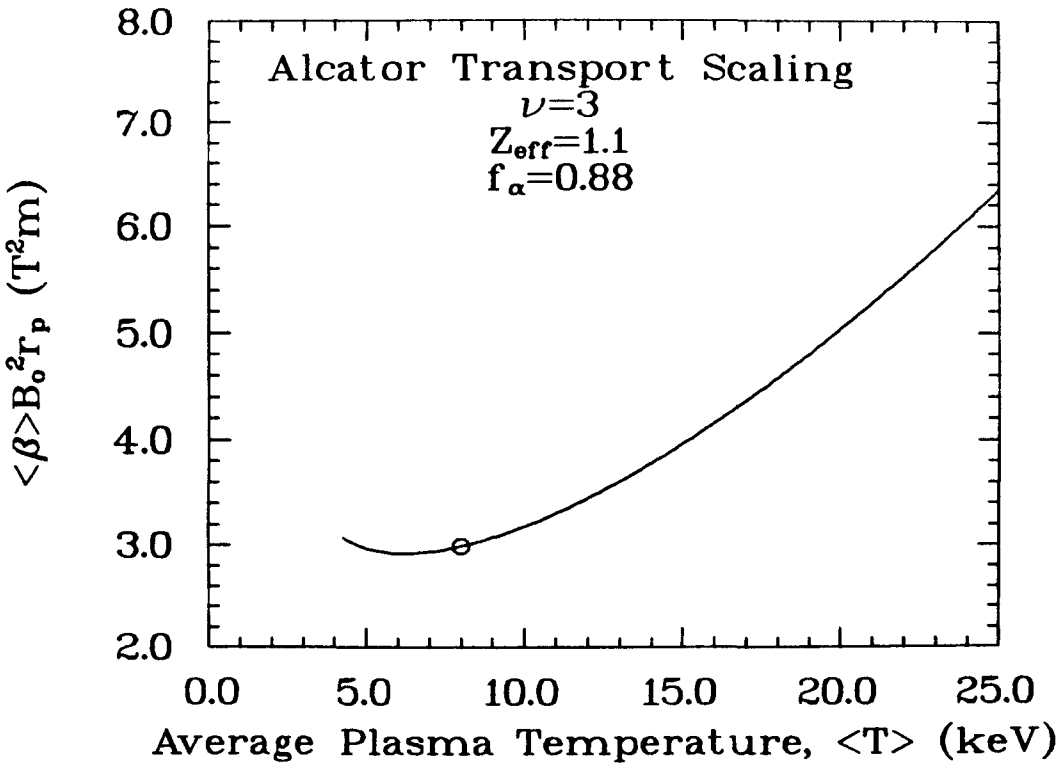

Fig. 3.2-6. Dependence of the parameter $\langle\beta\rangle B_o^2 r_p$ required for ignition, assuming Alcator transport scaling, as a function of average plasma temperature, $\langle T \rangle$, for $\nu = 3$, $Z_{eff} = 1.1$, and $f_\alpha = 0.88$. The design point at $\langle T \rangle = 8$ keV is shown.

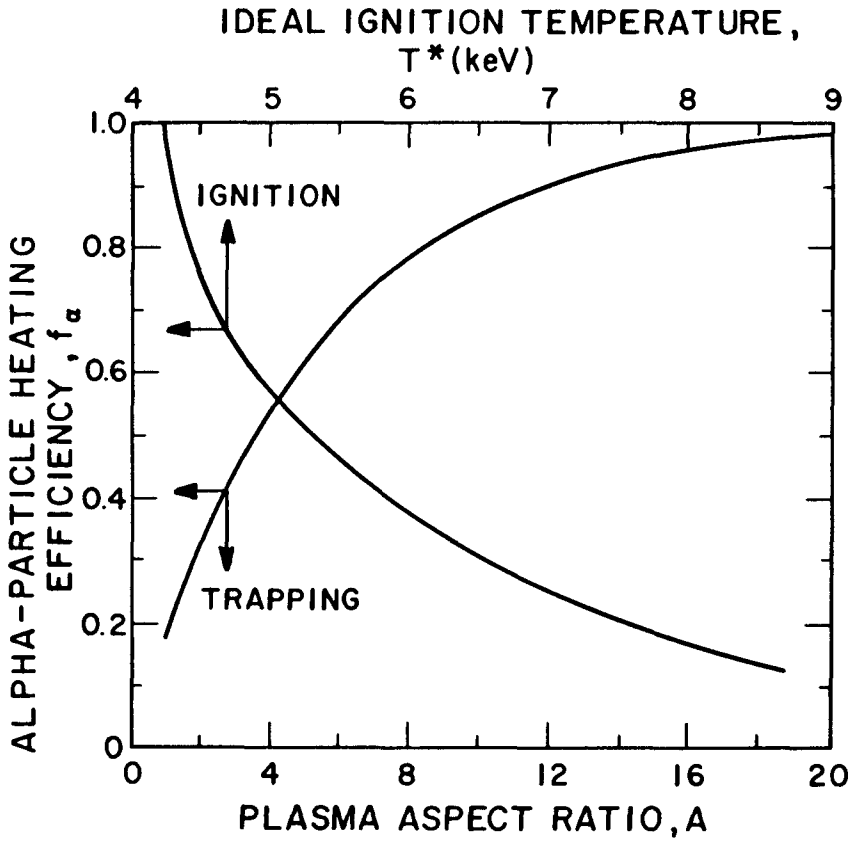

Fig. 3.2-7. Approximate dependence[68] of the alpha-particle heating efficiency, f_α, on the plasma aspect ratio, $A = R_T/r_p$, and the ideal ignition temperature, T*, on f_α.

The total thermal power output of the ignited reactor, $P_{TH}(Wt)$, is given by

$$P_{TH} = \langle P_\ell \rangle + \langle P_{BR} \rangle + \langle P_N \rangle M_N + (1 - f_\alpha)\langle P_\alpha \rangle = \langle P_N \rangle M_N + \langle P_\alpha \rangle \quad . \qquad (3.2\text{-}67)$$

Each component of P_{TH} is related to its corresponding power density, $\langle p \rangle$, by $P_j = \langle p_j \rangle V_p = \langle p_j \rangle (2\pi^2 R_T r_p^2)$, where the subscript "j" $\equiv$ "α," "BR," or "ℓ." The average neutron power density, $\langle p_N \rangle (W/m^3)$, is related to the alpha-particle power expression [Eq. (3.2-63A)] by

$$\langle p_N \rangle = \frac{14.06}{3.52} \langle p_\alpha \rangle \qquad (3.2\text{-}68A)$$

$$= 5.63(10)^{-13} \langle n_i \rangle^2 \langle \sigma v \rangle (I_2/I_{1/2}^4) \quad . \tag{3.2-68B}$$

If the neutron energy multiplication in the blanket is modeled by the factor, M_N (typically $M_N \sim 1.1$), the total thermal power, $P_{TH}(Wt)$, can be written as

$$P_{TH} = 5.63(10)^{-13} \langle n_i \rangle^2 \langle \sigma v \rangle (M_N + 0.25)(I_2/I_{1/2}^4)V_p \quad . \tag{3.2-69}$$

An additional constraint of engineering and economic interest is the average neutron first-wall loading, $I_w(W/m^2)$, which takes the following form:

$$I_w = \frac{P_{TH}}{(2\pi)^2 R_T r_w (M_N + 0.25)} \tag{3.2-70A}$$

$$= \frac{P_{TH} x}{(2\pi)^2 A r_p^2 (M_N + 0.25)} \quad . \tag{3.2-70B}$$

If the value of $x = r_p/r_w$ is sufficiently large, the poloidal deviations of the local neutron wall loading can be expected to be small, particularly for large-aspect-ratio systems and an outward-shifted core plasma equilibrium.

3.3. Configuration Options: General Considerations

Several modern coil configurations[6] are available for use in the present reactor study. Of particular present interest are the modular stellarator[12] using higher harmonic winding laws[69] and the "ultimate" torsatron without separate vertical-field coils.[10] Other continuous-coil systems, including the traditional $\ell = 3$ torsatron[25] and the $\ell = 2$ heliotron,[28] have been or are being subjected to reactor studies. A parallel study of an $\ell = 3$ modular stellarator reactor has been completed,[37] drawing directly on the design effort of the first modular stellarator experiment,[70] which is just now commencing operation. The present reactor study continues exploration of the $\ell = 2$ modular stellarator[22] and adds a comparison with an $\ell = 2$ ultimate torsatron. Potentially attractive configurations remain that have yet to be subjected to a detailed reactor study: the modular torsatron,[34] heliac,[13] the

advanced modular configuration anticipated for the Wendelstein VIII-AS experiment,[71] and the "symmotron" configuration.[56]

The stellarator embodies the steady-state, ignited operation of a DT thermonuclear plasma in a toroidal device of moderate aspect ratio. Except for startup power requirements, therefore, an ignited burn implies operation with low recirculating power beyond that required for major power users, such as the cryogenic refrigeration of the superconducting coils. Steady-state operation without plasma disruptions can be expected to minimize thermal cyclic fatigue of reactor components. Modularity of the coil set allows exoreactor testing of components to improve reliability and to assure more rapid change-out in the event of coil failure. No obstacles to plasma fueling by means of pellet injection and to impurity and ash removal by means of either a magnetic divertor[47] or a pumped limiter[72,73] have been identified in this study. A marginal value for the average plasma beta can be offset by a higher on-axis confining magnetic field in a device of moderate aspect ratio without exceeding peak magnetic field limitations at the inboard side of the coils. Coil forces appear manageable in both magnitude and orientation. Operation of the stellarator coil at a peak field of ~12 T will require Nb_3Sn superconducting magnet technology or the supercooling of a NbTi conductor.

Modularity for the modular stellarator may imply the ability to remove and to replace efficiently a single coil with minimal disturbance to the neighboring coils. An additional, desirable feature in promoting high plant availability would be the ability to replace blanket and shield modules without moving or disturbing the coils in either the modular-coil or continuous-coil case.[33] In the worst case the unit module would consist of a toroidal sector of the reactor together with the underlying blanket and shield modules.

An electric generating plant with a total thermal power output, P_{TH} = 4.0 GWt, will produce a gross electric power output, P_{ET} = 1.4 GWe, for a nominal thermal conversion efficiency, η_{TH} = 0.35. A fraction, f_{AUX}, of the gross electric power must be recirculated within the plant to drive auxiliary systems such as coil refrigeration, vacuum systems, and coolant pumps. An allowance[74,75] of f_{AUX} = 0.07 for these purposes in an ignited stellarator system leaves a net power output of $P_E \simeq 1.3$ GWe. No unique requirements for the BOP are anticipated, although, again, more detailed conceptual design of key stellarator systems is required.

The question of an operational mode for any magnetically confined fusion reactor is centered around the following issues: pulsed versus steady-state plasma, driven high-Q versus ignited operation, refueling mechanism, impurity-control scheme, and plasma startup and shutdown procedure. Each of these issues will strongly affect the reactor design and cost of electricity (COE), and each is determined by physical phenomena that to date are computed or extrapolated from experimental observation. The uniqueness of the stellarator approach in this respect rests with the generation of the full magnetic field topology solely by external electrical conductors. Even the ELMO Bumpy Torus approach[75] relies on significant, local perturbations of the field topology by plasma processes (i.e., the energetic electron rings). Furthermore, because the stellarator/torsatron reactor may be an inherently low-beta device, the vacuum field topology is expected to be left relatively unperturbed by the presence of plasma. These factors affect the reactor mode of operation by suggesting a steady-state plasma that would more than likely be achieved through a low-density startup on existing, relatively unperturbed field lines.

The nature and level of the external power requirement needed to achieve a desirable steady state are determined primarily by the particle and energy transport scaling, which also determines the thermal stability of that steady state. Neoclassical transport theories in certain collisionality regimes can lead to a positive temperature coefficient, thermal instability, and perhaps the need to operate the plasma in a subignited but high-Q- (where Q is the ratio of fusion power output to driver input power) driven mode. The nature of the transport scaling during the low-density initiation and subsequent density buildup to an ignited or high-Q-driven mode will also affect the operating mode in that the delivery systems for the startup power can affect the reactor design while not necessarily affecting the steady-state energy balance itself.

When combined with a goal to generate electricity at power levels of approximately 1 GWe with a fusion-neutron first-wall loading of $\gtrsim$1-2 MW/m^2, the stability and equilibrium scaling of beta and plasma aspect ratio used for stellarator reactors generally lead to plasma densities of $\gtrsim 1(10^{20})$ m^{-3}, moderate temperatures (8-15 keV), and large minor radii ($\gtrsim$2 m). For these conditions, total edge refueling is not possible and supplementary high-velocity (>10^4 m/s) pellet injectors may be needed.[2,76-78]

The issue of transport in plasmas with these parameters also affects the method by which impurity and helium-ash levels will be controlled. Impurity and ash control at the plasma edge in stellarator reactors can be achieved by either pumped limiters or magnetic divertors. Although the latter approach can be a natural consequence of the stellarator magnetic field topology, the engineering convenience and feasibility of extracting open field lines to an adequately engineered divertor plate and vacuum region depend crucially on the coil configuration. Furthermore, location of the separatrix at or near the coil, rather than within the vacuum first wall, may offer some advantage in maximizing the plasma volume utilization within the first wall and minimizing the complexity of the blanket and shield design. Hence, the use of pumped limiters *versus* (natural) magnetic divertors appears strongly dependent upon the specific stellarator configuration and remains to be fully quantified.

In summary, those unique characteristics of the stellarator approach that are related to low-beta plasma confined within an externally produced field topology almost certainly will lead to a steady-state operating mode for the reactor. The issue of high-Q-driven *versus* ignited operation depends crucially upon the energy transport scaling, the related thermal stability of the burn, and the ability to refuel and control impurity levels by external means. As for most approaches to magnetic fusion, the latter issue remains to be understood and quantified fully in the reactor context, although the choice between (natural) magnetic divertors (i.e., separatrix near the first wall) *versus* pumped limiters (i.e., separatrix near the coils) represents an option for the stellarator.

3.4. Parametric Survey Results

3.4.1. Plasma Model. The plasma model adopted for Phase IA of this study[23,48] follows closely that of that Phase I effort described in Ref. 22, with the exception of not explicitly stating the stability/equilibrium beta limits as functions of aspect ratio, magnetics, coil, and other parameters. The MSR geometry and notation are defined in Fig. 3.4-1. For present purposes, beta is specified parametrically, thereby decoupling the plasma performance from specific magnetics requirements. As assumed in Ref. 25, the particle/energy confinement time, $\tau_E(s)$, is described by empirical Alcator transport (Sec. 3.2.3.),

$$\tau_E = 3.0(10)^{-21} \langle n \rangle r_p^2 \quad , \tag{3.4-1}$$

where $\langle n \rangle (m^{-3})$ is the average ion density, $r_p(m)$ is an average plasma radius, and mks units are used. This expression for τ_E is a factor of ~3/5 less than that usually assumed for tokamak reactor scaling.[74] If $\langle \beta \rangle \equiv \langle p \rangle / (B_o^2/2\mu_o)$ is the average plasma beta, where $\langle p \rangle$ is the average plasma pressure and B_o designates the average confining toroidal field strength measured at the magnetic axis, plasma pressure balance dictates

$$\langle n \rangle \langle T \rangle f_{Z1} = 1.24(10)^{21} (I_{1/2}^2/I_1) \langle \beta \rangle B_o^2 \quad , \tag{3.4-2}$$

where $\langle T \rangle$(keV) is the average ion and electron temperature, assumed here to be equal. The Z_{eff} correction and profile factors, I_x, have been defined in Sec. 3.2. In this simplified formalism, the temperature and density profiles are assumed equal. Application of Eqs. (3.4-1) and (3.4-2) to a global energy balance that requires alpha-particle heating to equal radiation and transport losses gives the Eq. (3.2-65) ignition condition. The ratio of alpha-particle temperature, T_α, to plasma temperature is taken to be ~10. The alpha-particle energy trapping fraction, f_α, has been estimated[68] to be a function of the plasma aspect ratio, $A = R_T/r_p$, where R_T is the plasma major radius. The energy trapping fraction used in Eq. (3.2-65) is approximated here by the following expression.

$$f_\alpha \simeq 1 - e^{-A/5.22} \quad . \tag{3.4-3}$$

In a sense, the parameter $\langle \beta \rangle B_o^2 r_p$ represents an "engineering Lawson criterion" for ignition and is based on pressure balance and a specific form (i.e., Alcator scaling) for plasma transport.

The ignition condition, Eq. (3.2-65), is displayed in Fig. 3.4-2 as a function of $\langle T \rangle$ for a range of aspect ratios (or f_α values), pressure profiles, and Z_{eff} values. In addition to a flat pressure profile ($\nu \to \infty$), a cubic pressure profile ($\nu = 3$) corresponding to the Ref. 22 design point ($f_\alpha = 0.88$, $A \simeq 11$) is shown. Specific points for a number of reactor designs are also shown. It should be noted that the EBTR point in Fig. 3.4-2 has been

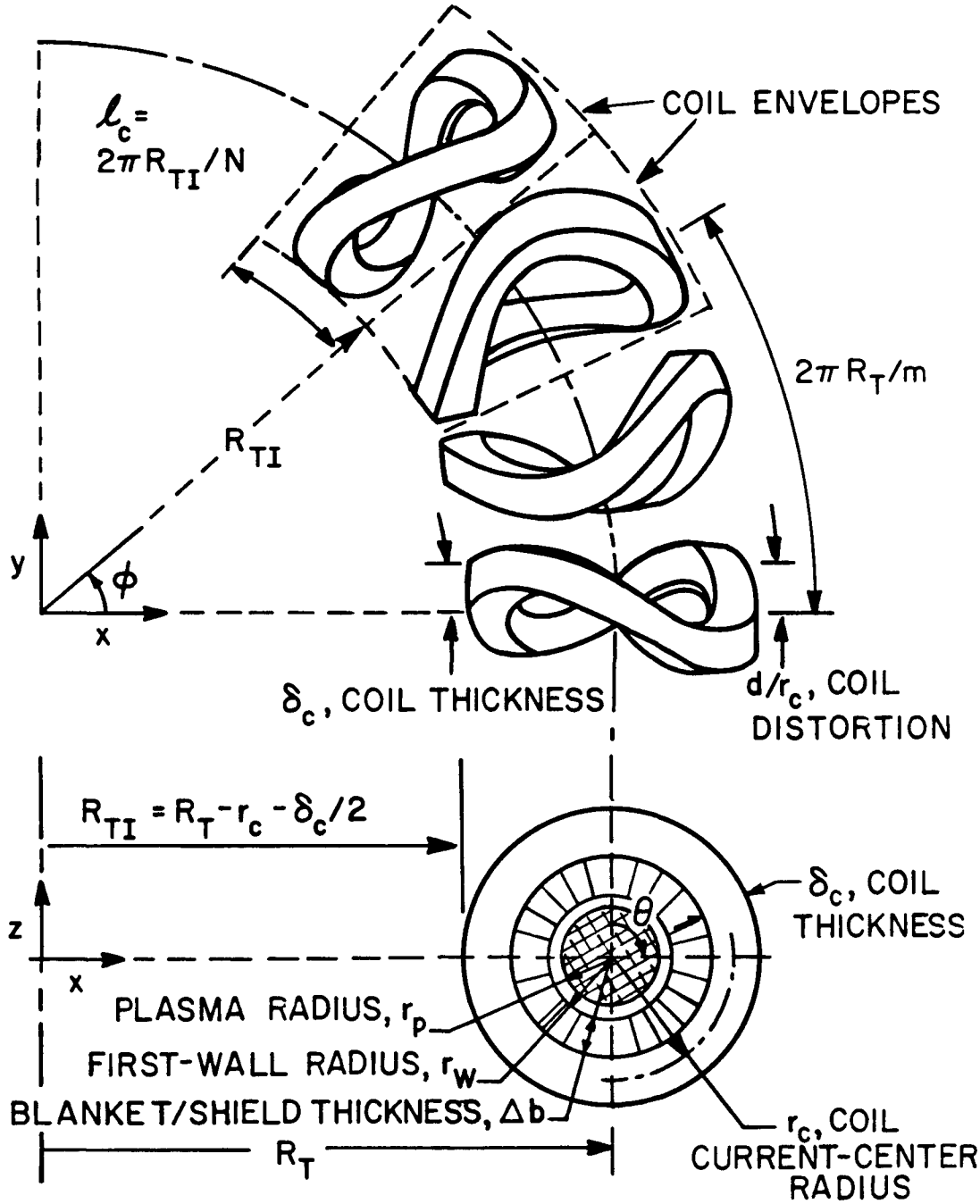

EXAMPLE SHOWN CORRESPONDS TO $\ell = 2$, $m = 8$, $N = 24$, $d/r_c = 0.3$ WITH $N/m = 3$ COILS PER FIELD PERIOD. INBOARD COIL FILLING FRACTION, $f_c = \delta_c/\ell_c$.

Fig. 3.4-1. Summary of coil geometry, notation, and essential elements and interrelationships of the MSR parametric systems analysis.

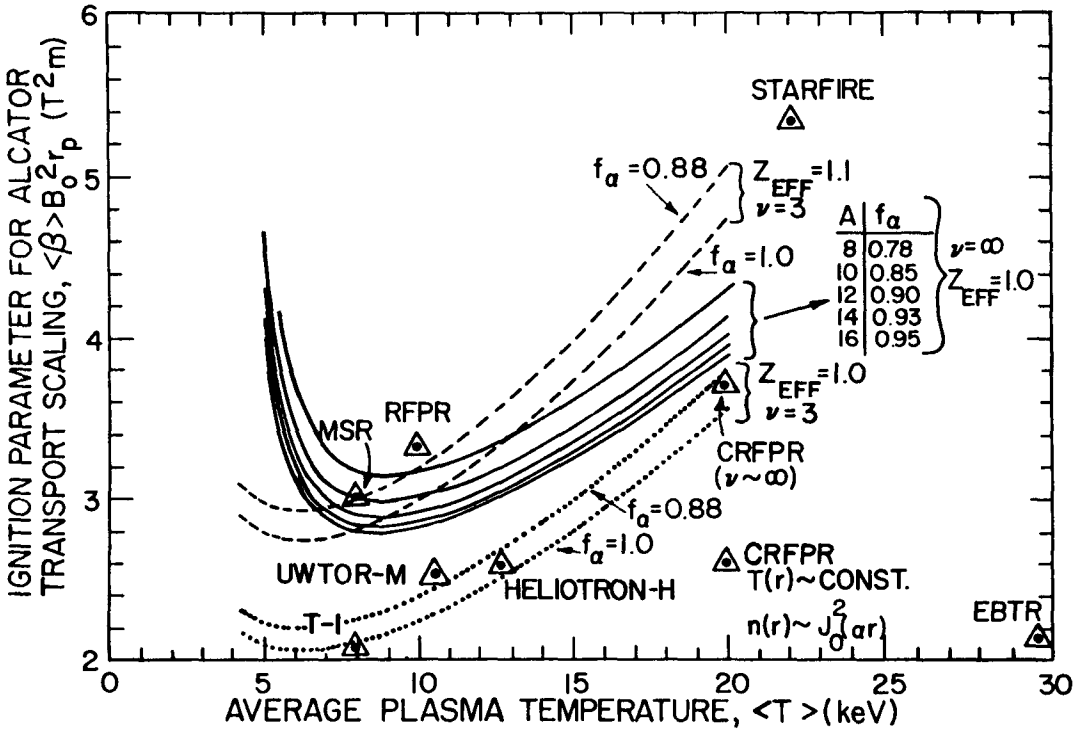

Fig. 3.4-2. Combined ignition and pressure balance conditions as a function of average plasma temperature for a $\nu = 3$ (dashed line) and a $\nu \to \infty$ (solid line) pressure profile for the Z_{eff} values indicated. Typical points used for the range of reactor design points are also shown, reflecting a certain degree of optimism for the T-1, Heliotron-H, and UWTOR-M designs, relative to the interim MSR design.[22] The EBTR[75] point is included only for completeness and to compare the implication of bumpy-torus neoclassical theory with empirical Alcator scaling. The STARFIRE[74] point corresponds to a fairly high-Z_{eff}, driven plasma, whereas all other designs have assumed ignition.

included only for comparison, the neoclassical, bumpy-torus transport ($\langle n\rangle\tau_E \propto A^2T^{3/2}$) having no relationship to the empirical transport [$\langle n\rangle\tau_E \propto (\langle n\rangle r_p)^2$] used for most of the reactor designs cited in Fig. 3.4-2. It is seen that minimum values of $\langle\beta\rangle B_o^2 r_p$ occur in the plasma temperature range 7-10 keV, this ignition parameter equaling 2.0-3.0 T^2 m for a wide range of aspect ratios, Z_{eff} values, and assumed pressure profiles. A nominal value of $\langle\beta\rangle B_o^2 r_p \simeq 3.0\ T^2$ m is selected for the remainder of this study and depends primarily on the assumed transport (i.e., the value of $\tau_E/\langle n\rangle r_p^2$). It is noted that optimism in the assumed ignition condition for any given design is reflected by lower values of $\langle\beta\rangle B_o^2 r_p$.

The majority of the physics subelements given in Fig. 3.4-1 are either treated parametrically (i.e., $\langle\beta\rangle$) or are left unspecified. An alternative to a purely parametric treatment of $\langle\beta\rangle$ would vary the rotational transform, ι, with $\langle\beta\rangle$, for example, being given (Sec. 3.2.2.) by a relationship of form,

$$\langle\beta\rangle \simeq \iota^2/A \quad . \tag{3.4-4}$$

Such an assumption, however, would lead the present analysis toward the more restrictive beta-coupled approach used in Ref. 22, and for this reason is not emphasized here. A few results are given, however, where ι instead of $\langle\beta\rangle$ is specified parametrically and Eq. (3.4-4) is used to determine $\langle\beta\rangle$ for a given reactor geometry. It is noted that ι in Eq. (3.4-4) corresponds to the total rotational transform (i.e., vacuum plus finite-beta components within the plasma column that, in a vaccum treatment, is conveniently evaluated at the plasma edge).

3.4.2. Overall Plant Performance Model. One measure of the overall plant performance is the total thermal power, P_{TH}(Wt), generated by a reactor operating with a blanket neutron-energy multiplication, M_N, given by

$$P_{TH} = 1.11(10)^{-11}\,(I_2/f_{Z2}^2 I_{1/2}^4)\langle n\rangle^2\,\langle\sigma v\rangle(M_N + 1/4)\,R_T\,r_p^2 \tag{3.4-5A}$$

$$= 1.71(10)^{31}\,(I_2/f_{Z2}^2 I_1^2)(\langle\sigma v\rangle/\langle T\rangle^2)(M_N + 1/4)(\langle\beta\rangle B_o^2 r_p)^2\,R_T \tag{3.4-5B}$$

$$\simeq 1.65(10)^7(M_N + 1/4)(\langle\beta\rangle B_o^2 r_p)^2\,R_T \quad . \tag{3.4-5C}$$

In developing Eq. (3.4-5C), pressure balance [Eq. (3.4-2)] and the approximation that $\langle\sigma v\rangle/\langle T\rangle^2 \simeq 1.1(10)^{-24}$ m^3/s keV^2, which is accurate to within 10% in the temperature range $8 < T < 20$ keV, could be used. To calibrate the present approach more carefully against past work,[22] however, the actual value at 8 keV [$\langle\sigma v\rangle/\langle T\rangle^2 = 9.64(10)^{-25}$ m^3/s keV^2] was used. The latter expression for P_{TH} sets $(I_2/f_{Z2}^2 I_1^2)$ to unity, which corresponds to a flat pressure profile with $Z_{eff} = 1.0$ or a cubic profile with $Z_{eff} \simeq 1.05$; either assumption is consistent with $\langle\beta\rangle B_o^2 r_p \simeq 3.0\ T^2$ m at 8 keV (Fig. 3.4-2).

With a typical value of $M_N = 1.1$ and the ignition condition as $\langle\beta\rangle B_o^2 r_p = 3.0\ T^2\ m$, Eq. (3.4-5) reduces to the following expression:

$$P_{TH}(MWt) = 200.5\ R_T \quad . \tag{3.4-6}$$

This highly condensed relationship represents the first of three key "working equations" used in the Phase IA parametric study to cast the overall plant characterization in terms of geometry.

The recirculating power fraction, ε, for ignited operation is expected to be below 0.1, which for a thermal conversion efficiency of $\eta_{TH} \simeq 0.35$ gives a net plant efficiency of $(1-\varepsilon)\eta_{TH} \simeq 0.32$. For the purposes of this parametric systems analysis, however, only the total thermal power, P_{TH}, is monitored. The net electrical output, $P_E(MWe)$, is given by $(1-\varepsilon)\eta_{TH}P_{TH} \simeq P_{TH}/3$.

Additional parameters can be identified as "figures of merit" in evaluating overall power plant performance without performing a detailed cost analysis. If V_c is defined as the total engineered toroidal volume enclosed by and including the magnet-coil annulus, the engineering or system power density, $P_{TH}/V_c(MWt/m^3)$, can serve as one such figure of merit.

$$P_{TH}/V_c \equiv \frac{P_{TH}}{2\pi^2 R_T (r_c + \delta/2)^2} \tag{3.4-7A}$$

$$= \frac{7.51(M_N + 1/4)}{(r_p/x + \Delta b + \delta)^2} \quad . \tag{3.4-7B}$$

In Eq. (3.4-7) $r_c = r_p/x + \Delta b + \delta/2$ is the coil current-center radius, Δb is the FW/B/S thickness, $r_w = r_p/x$ is a nominal first-wall radius, and δ is the overall coil thickness, including a square cross-section conductor with thickness, δ_c, and a surrounding structural/cryogenic shell.

A more direct economic measure of overall plant performance is the total Fusion-Power-Core (FPC) mass, taken here to be the combined mass of FW/B/S, $M_{B/S}$, and coils, M_c, divided by the total thermal power, P_{TH}. A strong correlation between the unit direct costs, UDC($/kWe), and this "mass-

utilization" (i.e., inverse specific power) factor, $(M_{B/S} + M_c)/P_{TH}$, is identified in Sec. 7.1. Given an average FW/B/S density, $\rho_{B/S}$ (typically 5-6 tonne/m^3), and an average coil density, ρ_c (typically 6-8 tonne/m^3), the mass-utilization factor can be expressed as follows, where $M \equiv M_{B/S} + M_c$.

$$\frac{M}{P_{TH}} = \left(\frac{\pi}{10}\right)^2 \left[\rho_{B/S}\Delta b^2(1 + 2r_w/\Delta b) + \rho_c(N/\pi)\delta^2 r_c g_c/R_T\right] \quad . \tag{3.4-8}$$

Equation (3.4-6) has been used, and N is the total number of modular coils. The coil form factor, g_c, is the ratio of the current-center circumference of a deformed coil, with lateral deformation (Fig. 3.4-1) given by

$$y = d \sin \ell\Theta \quad , \tag{3.4-9}$$

to the circumference at the current center of an undeformed toroidal coil (i.e., $2\pi r_c$). If k is defined by the expression

$$k^2 = \frac{(\ell d)^2}{(\ell d)^2 + r_c^2} \quad , \tag{3.4-10}$$

then g_c is given by

$$g_c = \frac{(2/\pi)E(k,\pi/2)}{(1 - k^2)^{1/2}} \tag{3.4-11A}$$

$$\simeq 1 + 0.21\,\frac{\ell d}{r_c} \quad , \tag{3.4-11B}$$

where $E(k,\pi/2)$ is the complete elliptic integral of the second kind and the approximation to g_c is accurate to within a few percent over the practical range of $\ell d/r_c$ values. It is noted from Eqs. (3.4-8) and (3.4-11) that MSRs with higher polarity (i.e., ℓ values) will operate with poorer (higher) mass

utilization and greater cost. Equation (3.4-8) is used to monitor an important aspect of system performance. Typically, most of the conventional fusion reactor designs predict mass utilizations in the 5-10 tonne/MWt range, compared to values of 0.2-0.4 tonne/MWt for a Light Water (fission) Reactor (LWR). For the purposes of this study, a goal of $M/P_{TH} \lesssim 5$ tonne/MWt is established for the MSR, to give a MSR performance that is comparable with the best tokamak projections.[74] Detailed design and cost estimates, however, must be performed to substantiate the desirability and magnitude of this constraint.

3.4.3. First-Wall/Blanket/Shield Model. A simplified FW/B/S model is used for this parametric systems analysis. Specifically, the blanket/shield thickness for systems using superconducting coils is specified to have a nominal thickness $\Delta b \simeq 1.3$ m, and the blanket energy multiplication is specified to be $M_N \simeq 1.1$. These values of Δb and M_N are considered typical for most DT fusion systems.[22] Introducing the 14.1-MeV neutron first-wall loading, $I_w(MW/m^2)$, leads to a second "working equation" used in this parametric model.

$$I_w(r_p/x) = \frac{P_{TH}/(M_N + 1/4)}{(2\pi)^2 R_T} \tag{3.4-12A}$$

$$\simeq 3.76 \quad , \tag{3.4-12B}$$

where the first expression is simply a definition and the last expression results from use of Eq. (3.4-6). Although the plasma filling fraction, $x = r_p/r_w$, can be estimated from the magnetics, x is optimistically fixed to 0.7 for this study. The scaling of x considered in Ref. 22 gives $x = 0.66(m/A)^{1/3}$, where m is the number of toroidal field periods and $A = R_T/r_p$ is the plasma aspect ratio for elliptic plasma cross sections with $\ell = 2$. Indeed, this scaling could be a handicap for systems with higher beta values and/or low values of m (i.e., $m \lesssim 5$) with adequately high values of rotational transform, ι. This scaling applies to plasmas filling the last closed flux surface ($r_s \simeq r_w$) consistent with divertor impurity control. Larger values of x by a factor $(1 - \Delta b/r_c)^{-2/3}$ are expected if a limiter is used to define the plasma boundary ($r_s \simeq r_c$) as noted in Ref. 22. In addition, use of noncircular first-wall configurations, which could place the first wall into the plasma surface, and which are molded to whatever shape the plasma might

have, could reduce the adverse impact of the present modelistic assumption of circular first-wall cross section. Effective x values as high as 0.7 could result.

It is interesting to note that by specifying the ignition condition, transport scaling, and reactor geometry (r_p, R_T), both P_{TH} and I_w are determined. Because the ignition condition combines with pressure balance to give $\langle\beta\rangle B_o^2 r_p \simeq 3.0\ T^2\ m$ for a plasma described by Alcator transport, and because $\langle\beta\rangle$ is either specified parametrically or related to ι through geometry [e.g., Eq. (3.4-4)], the ignition condition can also be expressed conveniently in a geometric "r_p-R_T space" once the on-axis field, B_o, is related to a limiting coil condition (field, current density, or stress limits) through an appropriate geometric relationship. This missing link, as described in terms of the coil-set model in the next section, completes the parametric systems model, which becomes dependent only on geometry once a specific ignition condition and $\langle\beta\rangle$ are specified. Although $\langle\beta\rangle$ is treated parametrically in this study, in principle by relating $\langle\beta\rangle$ to ι, ι', or V" through a given coil (magnetics) configuration, $\langle\beta\rangle$ also becomes a function of geometry. Reactor design studies of S/T/H configurations would benefit immensely by the availability of such a relationship, particularly if the relationship shared more acceptance than the one originally evaluated in the course of the Phase I study.[22]

3.4.4. Coil-Set Model. The "beta-decoupled" parametric systems model described thus far can in principle be applied to any ignited toroidal system that is characterized by Alcator transport scaling. Features that are unique to the modular stellarator configuration are injected into this analysis primarily through the models and constraints applied to the magnetics topology ($\langle\beta\rangle$, x) and coil design (δ, δ_c, d, r_c, R_T). The third "working equation" that completes this parametric systems model uses the pressure-balance/transport/ignition relationship [i.e., Eq. (3.4-4), $T \simeq 8$ keV, $\langle\beta\rangle B_o^2 r_p \simeq 3.0\ T^2\ m$] and relates the on-axis toroidal magnetic field, B_o, to an estimate of the peak (inboard) field at the coil winding, B_{CM}, through the following approximate expression (characterizing only the toroidal field):[79]

$$B_{CM}/B_o = \frac{R_T}{R_T - r_c + \delta_c/2}\left\{1 + \frac{1}{\left[1 + \frac{\delta_c}{2(R_T - r_c)}\right]^N - 1}\right\} . \qquad (3.4\text{-}13)$$

Figure 3.4-1 depicts the geometry used, and B_{CM} is evaluated at the inboard side of the torus at the conductor surface. By specifying B_{CM}, the on-axis field, B_o, can be eliminated from the ignition condition, yielding a set of relationships that depend solely on geometry, once $\langle\beta\rangle$ is specified.

Equation (3.4-15) along with the ignition condition, $\langle\beta\rangle B_o^2 r_p \simeq 3.0\ T^2\ m$, provides a means by which a trajectory in r_p-R_T space can be traced if δ_c, N, B_{CM}, and $\langle\beta\rangle$ [or ι, Eq. (3.4-6)] are specified. In the spirit of a "best case" parametric systems study, variables are chosen to exhibit physical upper limits. Although $\langle\beta\rangle$ and B_{CM} can be so specified, N and δ_c are not as conveniently posed. For this reason, the (maximum) allowable current density in the coil conductor, j_c; the linear inboard coil "filling fraction," f_c (Fig. 3.4-1); and the coil interference parameter, f_c^*, are introduced. In this way, variations of N and δ_c can be recast in terms of variation in j_c, f_c, and f_c^*. The following expression is used to relate δ_c and N to j_c:

$$\delta_c^2 = \frac{2\pi R_T B_o}{\mu_o N j_c g_I} , \qquad (3.4\text{-}14)$$

where the current form factor, g_I, is the ratio of effective poloidal current to total current in a coil with conductor cross-sectional area, δ_c^2, and (maximum) lateral distortion d. For a modular coil described by Eq. (3.4-9) and by using k as defined in Eq. (3.4-10), the current form factor is given by

$$g_I = \frac{2/\pi}{(1 - k^2)^{1/2}} K(k,\pi/2) , \qquad (3.4\text{-}15)$$

where $K(k,\pi/2)$ is the complete elliptic integral of the first kind. In effect, $g_I \lesssim 1$ gives the increased coil cross section needed for a limiting

current density to provide for a given on-axis toroidal field. The actual rotational transform produced for a given winding law [i.e., Eq. (3.4-9)]; distortion, d/r_c; and number of poloidal-field periods, ℓ, must be determined by a three-dimensional vacuum magnetics calculation. Nevertheless, for this model incorporation of the stellarator-like character into the otherwise purely toroidal-field coil model through g_I is adequate.

The linear inboard filling fraction is given by

$$f_c = \frac{N\delta}{2\pi(R_T - r_c + \delta/2)} \quad , \tag{3.4-16}$$

where $\delta > \delta_c$ is the radial thickness of the coil, δ_c being the conductor thickness. The space required around the inboard torus circumference for a coil with toroidal distortion, d/r_c, can be introduced into the parametric systems analysis through the parameter f_c. Separate, more detailed magnetics calculations again relate f_c (i.e., d/r_c, R_T, etc.) to the desired magnetics parameters (i.e., ι, $d\iota/dr$, V", etc.), which in turn must be related to $\langle\beta\rangle$ by a yet-to-be-specified stability/equilibrium condition. Experience derived from detailed magnetics models indicates that f_c values much above ~ 0.3 will not be allowed if rotational transforms above ~ 0.7 are desired from realistically distorted (i.e., $d/r_c \lesssim 0.5$) coils operating with supportable forces.

An approximate coil interference constraint can be generated that specifies the condition, $f_c^* = 1$, where a coil set with distortion d/r_c will require intersecting coil envelopes, as indicated by the dashed lines in Fig. 3.4-1. This condition is given by the following expression:[22]

$$f_c^* \equiv \frac{\delta + 2d}{2(R_T - r - \delta/2)\tan(\pi/N)} \lesssim 1 \tag{3.4-17A}$$

$$= \left[\frac{\pi/N}{\tan(\pi/N)}\right](1 + 2d/\delta)\, f_c \quad , \tag{3.4-17B}$$

where Eq. (3.4-16) is used to express the basic noninterference constraint, $f_c^* \lesssim 1$, in terms of the linear, inboard filling fraction, f_c. It is noted

that if f_c^* exceeds unity, then a given coil may not be removed from the torus by a simple horizontal (outward-radial) translation. Generally, for $d/r_c \lesssim 0.5$, f_c^* as high as ~1.2 may be allowed before in-place coils physically interfere; this situation, however, will require more complex maneuvering to extricate a given coil from the torus.

Equation (3.4-8) can be evaluated to give the mass utilization, M/P_{TH}, for the $f_c^* = 1$ condition; this condition represents the best mass usage and least accessibility, although still requiring only simple horizontal (outward-radial) coil movement for replacement. A case where actual coil interference is expected to occur ($f_c^* \lesssim 1.2$) is also examined. In the spirit of the "best case" parameter search, $f_c^* = 1$ is used in Eq. (3.4-17) to relate N and δ to the r_p-R_T geometry space.

3.4.5. Summary of Systems Model. Figure 3.4-3 gives a logic diagram for the MSR parametric systems model. Three working equations have been evolved that relate three systems quantities (P_{TH}, I_w, ignition condition) solely in terms of geometric quantities (r_p, r_w, Δb, r_c, d, R_T, δ, δ_c, ℓ, f_c^*) and a minimum number of physics and physical constraints ($\langle\beta\rangle B_o^2 r_p$, $\langle\beta\rangle$, x, B_{CM}, j). These quantities and constraints can be expressed as curves or surfaces in r_p-R_T space and are summarized below.

SYSTEMS QUANTITIES:

- Total thermal power, P_{TH} [Eq. (3.4-5) or (3.4-6)].
- Neutron wall loading, I_w [Eq. (3.4-12)].
- Pressure balance/transport/ignition, $\langle\beta\rangle B_{CM}^2 r_p$ [Eqs. (3.2-65) and (3.4-13) with $\langle\beta\rangle B_o^2 r_p \simeq 3.0\ T^2\ m$].

PHYSICS AND PHYSICAL CONSTRAINTS (parametrically varied):

- Average plasma beta, $\langle\beta\rangle$ (0.04-0.12).
- Coil filling fraction, f_c ($\gtrsim$0.3-0.4), $f_c^* \lesssim 1$ (coil envelope interference) for a given d/r_c, or $f_c^* \simeq 1.2$ (coil interference).
- System power density [Eq. (3.4-7)] and mass utilization [Eq. (3.4-8)].

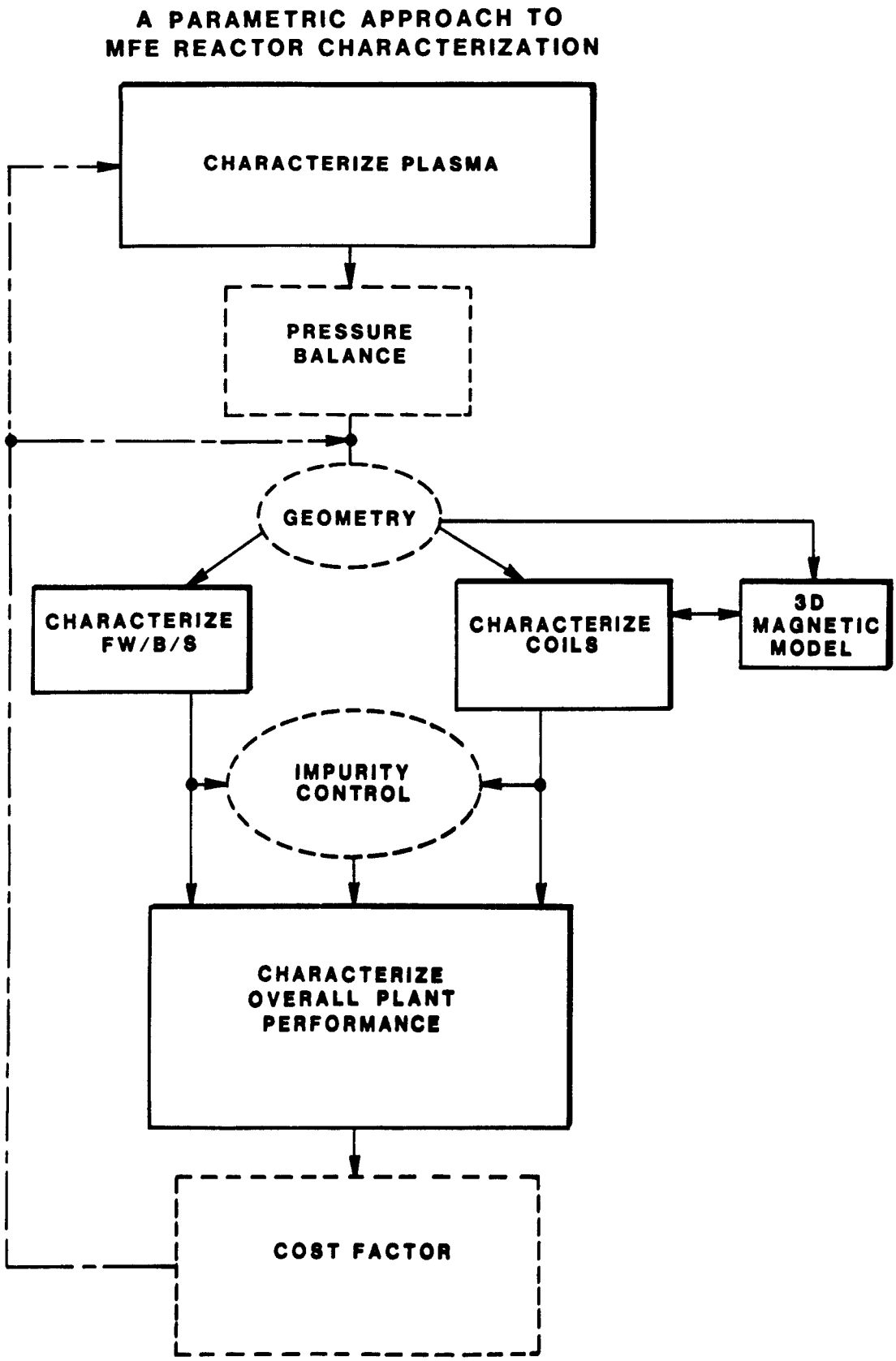

Fig. 3.4-3. Logic diagram for parametric systems analysis model.

Quantities that are generally held fixed throughout this analysis are summarized below.

- Peak field at coil conductor, B_{CM} (12 T).
- Conductor current density, j_c (usually ~20 MA/m^2), equal to the overall coil current density, j(~13 MA/m^2), when $\delta_c \; \delta$.
- Blanket/shield thickness, Δb = 1.3 m.
- Blanket neutron-energy multiplication, M_N = 1.1.
- Alcator transport scaling, $\tau_E/\langle n \rangle r_p^2 = 3(10)^{-21}$ s m.
- Ignition condition, $\langle \beta \rangle B_o^2 r_p$ = 3.0 T^2 m at $\langle T \rangle \simeq$ 8 keV.
- Plasma-to-wall radius ratio, $x = r_p/r_w$ = 0.7.
- Average mass densities of FW/B/S and coils, $\rho_{B/S}$ = 5.5 tonne/m^3 and ρ_c = 7.0 tonne/m^3.

The results given in the following section define ignited, DT reactors in terms of a range of $\langle \beta \rangle$ and $d/r_c(f_c^* = 1)$ values for otherwise optimally (maximum) selected parameters (i.e., j_c, j, B_{CM}, minimum ignition conditions, maximum $x = r_p/r_w$, tight coil packing $f_c^* = 1$, etc.). In a sense, these results depict the "best" reactor performance for the assumed transport. It remains for more detailed support computation to relate the desired (prescribed) parameters [$\langle \beta \rangle$ and $d/r_c(f_c^* = 1)$] to required magnetics (ι, $d\iota/dr$, V", etc.), coil (d/r_c, R_T, forces, etc.), and stability/equilibrium (i.e., $\langle \beta \rangle$ versus ι, $d\iota/dr$, V", etc.) parameters and/or constraints. In a sense, these results dictate the minimum range of $\langle \beta \rangle$ or the magnitude of a $\langle \beta \rangle \simeq \iota^2/A$ scaling needed to achieve the optimally specified performance. Furthermore, the continual monitoring of the mass utilization, M/P_{TH}, should give a fairly accurate indication of expected UDCs. It is recognized that the best-case reactors presented here can in fact be made "better" for a given $\langle \beta \rangle$ primary by reducing the ignition value for $\langle \beta \rangle B_o^2 r_p$ [Fig. 3.4-2], although the value of 3 T^2 m was shown to encompass a range of assumed plasma conditions and is considered "typical."

3.4.6. General Parametric Results. All parametric results are expressed as curves in r_p-R_T space. As indicated by Eq. (3.4-6), the total power, P_{TH}, is related to the major radius by a scaling parameter ($P_{TH}/R_T \simeq$ 200 MWt/m), and the neutron wall loading is related to the minor radius by Eq. (3.4-12).

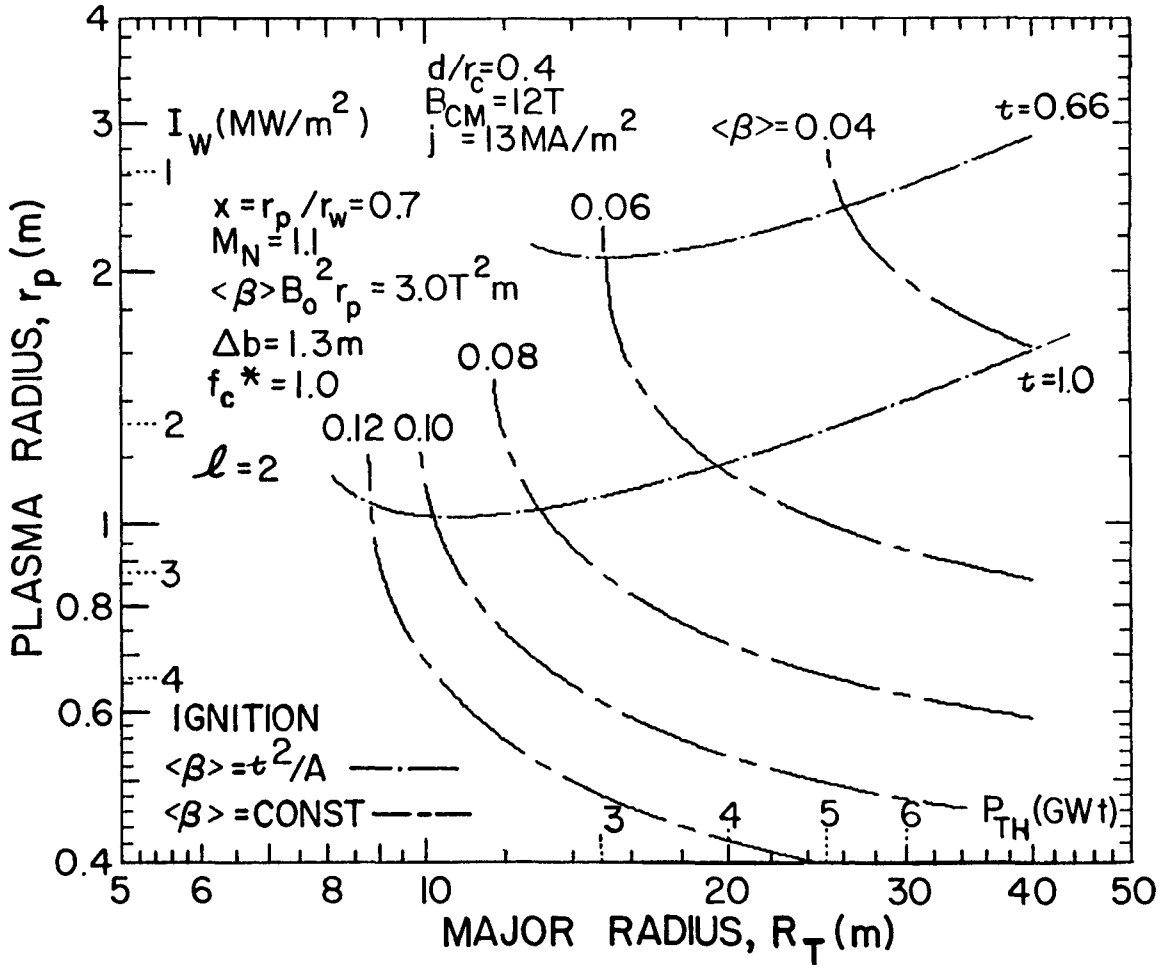

Fig. 3.4-4. Sample ignition curves for the $\langle\beta\rangle$ = constant and $\langle\beta\rangle = \iota^2/A$ cases for the $d/r_c = 0.4$ case.

Figure 3.4-4 shows the ignition curves in r_p-R_T space for $d/r_c = 0.4$ and a range of $\langle\beta\rangle$ values. For each value of $\langle\beta\rangle$, the constraints that $x = 0.7$, $B_{CM} = 12$ T, $j_c = j = 13$ MA/m^2, $\delta = \delta_c$, etc., are enforced. Generally, increasing R_T for a toroidal array of coils will allow higher on-axis fields, B_o, for a given limit imposed on the peak coil field, B_{CM}. The ignition condition, $\langle\beta\rangle B_o^2 r_p$ = constant, then allows r_p to decrease with increasing R_T. Also, as expected from Eq. (3.4-7), increasing $\langle\beta\rangle$ allows higher system power density for a given total power. Figure 3.4-4 also gives the ignition curves for the case where $\langle\beta\rangle \simeq \iota^2/A$ and a range of fixed values of rotational transform. In this case the behavior of these system-constrained ignition curves is somewhat more complex. The ignition condition now requires $\langle\beta\rangle B_o^2 r_p = (\iota B_o r_p)^2/R_T$ to be constant. As before, increasing R_T generally allows higher on-axis fields for a given field constraint at the coil, B_{CM}, and r_p decreases initially as R_T is

increased. A point is reached, however, where further increases in R_T must require r_p to increase again to maintain the ignition condition. The minimum shown in Fig. 3.4-4 for the $\langle\beta\rangle = \iota^2/A$ curves results from this interplay between R_T, r_p, and B_o for constant $\langle\beta\rangle B_o^2 r_p$. For both the $\langle\beta\rangle$ = constant and $\langle\beta\rangle = \iota^2/A$ ignition curves displayed in Fig. 3.4-4, the dependence of f_α on A, and hence that of $\langle\beta\rangle B_o^2 r_p$ on A, has been ignored (Fig. 3.4-2). A more consistent application of Eqs. (3.2-65) and (3.4-3) would give curves that rise more rapidly at lower values of R_T ($A \lesssim 11$) and fall more rapidly at higher values of R_T ($A \gtrsim 11$).

The ignition curves shown in Fig. 3.4-4 depend on d/r_c. Generally, decreasing d/r_c will allow higher system power densities, as measured by decreased r_p or increased $I_w(MW/m^2)$ for the same total power. Decreasing d/r_c simply allows a higher on-axis field for a given R_T (and P_{TH}), and the ignition condition for a given $\langle\beta\rangle$ allows r_p to decrease and I_w [Eq. (3.4-12)] to increase. Decreasing d/r_c, however, will lead to reduced rotational transform, an effect that ultimately must be reconciled with the specified value of $\langle\beta\rangle$ through detailed magnetics and stability/equilibrium computations.

Figures 3.4-5 through 3.4-7 depict three sets of ignition curves in r_p-R_T space for d/r_c = 0.3, 0.4, and 0.5. In addition to the I_w and P_{TH} values, lines of constant number of coils, N, and mass utilization, M/P_{TH}, are shown. Generally, as d/r_c is increased from 0.3 to 0.5 in Figs. 3.4-5 through 3.4-7, the values of r_p required for ignition, using either beta-scaling relationship, shift upward. The interpretation of this behavior is that for a fixed r_p-R_T geometric configuration, as d/r_c increases and the on-axis field strength decreases relative to the fixed peak field at the coil as a result of the Eq. (3.4-17) correction, the required value of $\langle\beta\rangle$ needed to satisfy the ignition condition must increase. The constant-N curves, which are shown in Figs. 3.4-5 through 3.4-7, simultaneously shift to the right as fewer coils fit into a fixed r_p-R_T coil array as d/r_c increases. A slight shift downward in the lines of constant M/P_{TH}, which are also shown in Figs. 3.4-5 through 3.4-7, also occurs as d/r_c increases. This behavior is a result of the increase in coil mass required to retrieve a given B_o because of the distortion [Eq. (3.4-17)] correction for a given combination of r_p and $\langle\beta\rangle$ satisfying the ignition condition. Within the limits of this model, this adverse effect is expected to be greater for $\ell = 3$ than for the $\ell = 2$ case

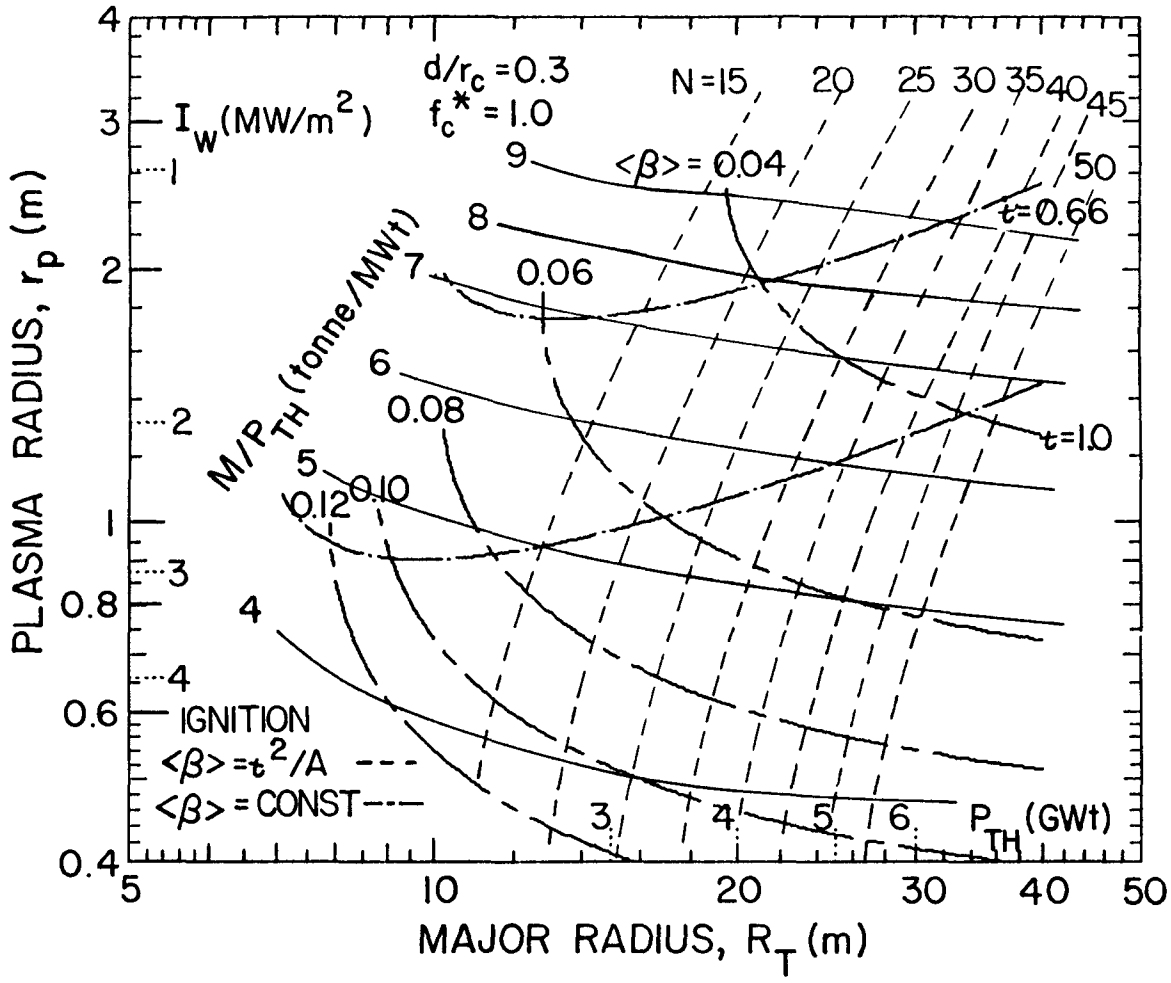

Fig. 3.4-5. Ignition curves for the $d/r_c = 0.3$ case, superposed onto a grid of constant N and M/P_{TH} lines with other fixed parameters as given in Fig. 3.4-4.

examined here. Systems with mass utilization below ~5 tonne/MWt will require $\langle\beta\rangle$ above ~0.06 if d/r_c can be held at or below 0.3, or $\langle\beta\rangle$ in excess of ~0.08 will be needed if the more likely values of d/r_c in the 0.4-0.5 range prove necessary to achieve the t values suggested for stable, higher beta operation.

In Fig. 3.4-8, f_c^* is set equal to 1.2 for the $d/r_c = 0.4$ case with other parameters being held consistent with the Figs. 3.4-5 through 3.4-7 results. As noted previously, this $f_c^* = 1.2$ case corresponds to a tight packing of the modular-coil set, which would be expected to reduce the toroidal-field ripple but could complicate maintenance and access. Compared with Fig. 3.4-6, the ignition curves shift upward, because $f_c^* > 1$ is consistent with greater coil distortion (all other parameters/constraints are equal). The constant-N

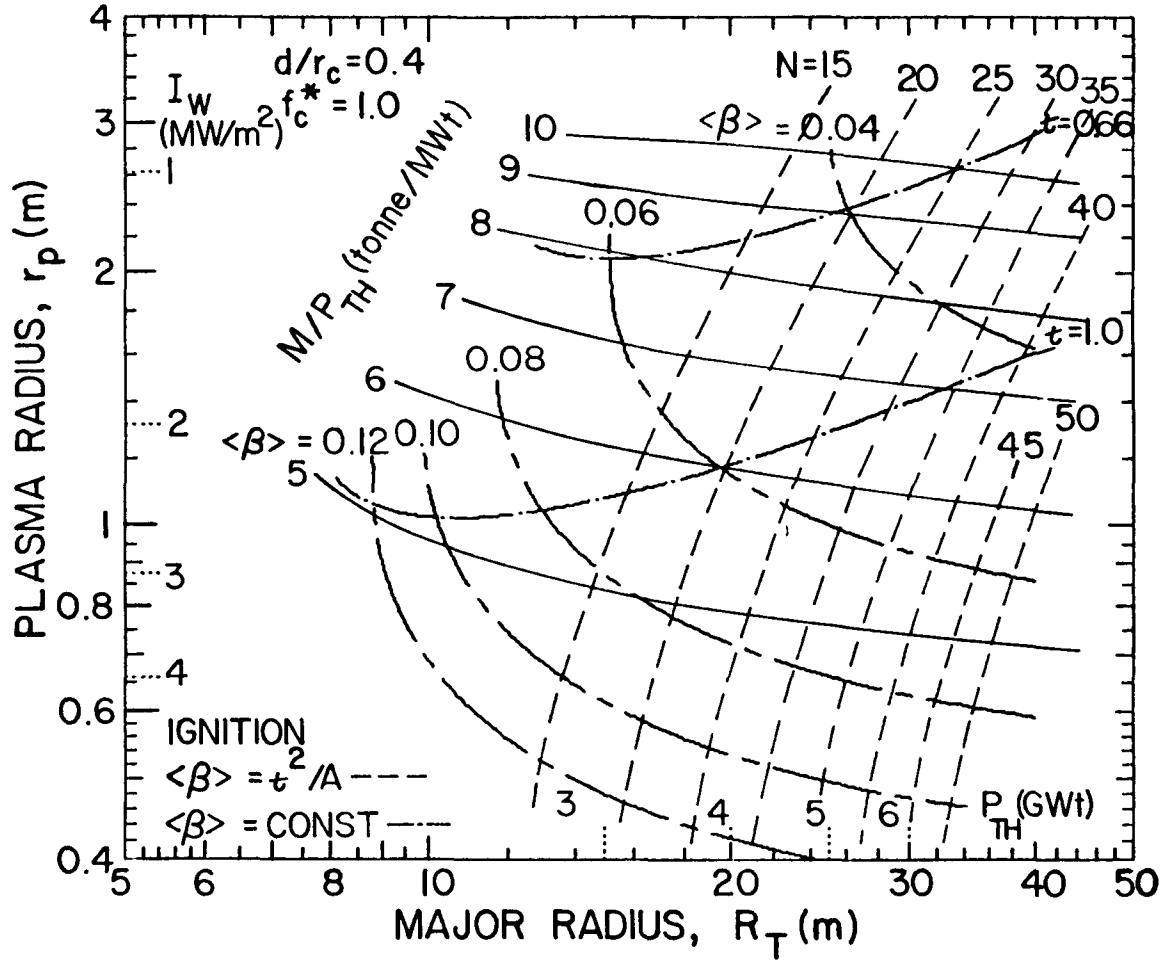

Fig. 3.4-6. Ignition curves for the d/r_c = 0.4 case, superposed onto a grid of constant N and M/P_{TH} lines with other fixed parameters as given in Fig. 3.4-4.

curves, however, shift to the left, allowing more coils to be accommodated in the same r_p-R_T configuration. The curves of constant M/P_{TH} shift upward, allowing equivalent or better (lower) mass utilization in a more tightly packed configuration with somewhat lower $\langle\beta\rangle$ for a given r_p-R_T configuration.

3.4.7. Focused Parametric Results. The benefits of higher beta performance are shown in Figs. 3.4-5 through 3.4-7. For a nominal total power output of P_{TH} = 4.0 GWt, corresponding to $R_T \simeq 20$ m, the mass utilization figure of merit, M/P_{TH}, plotted in Fig. 3.4-9, is a function of $\langle\beta\rangle$ for various values of the modular-coil distortion parameter, d/r_c. For low values of $\langle\beta\rangle$, M/P_{TH} (and cost) can become unattractively large. As $\langle\beta\rangle$ increases, however, M/P_{TH} decreases to an asymptotic value near ~4-5 tonne/MWt. The incremental improvement in M/P_{TH} as $\langle\beta\rangle$ exceeds ~0.08 is small. Systems with

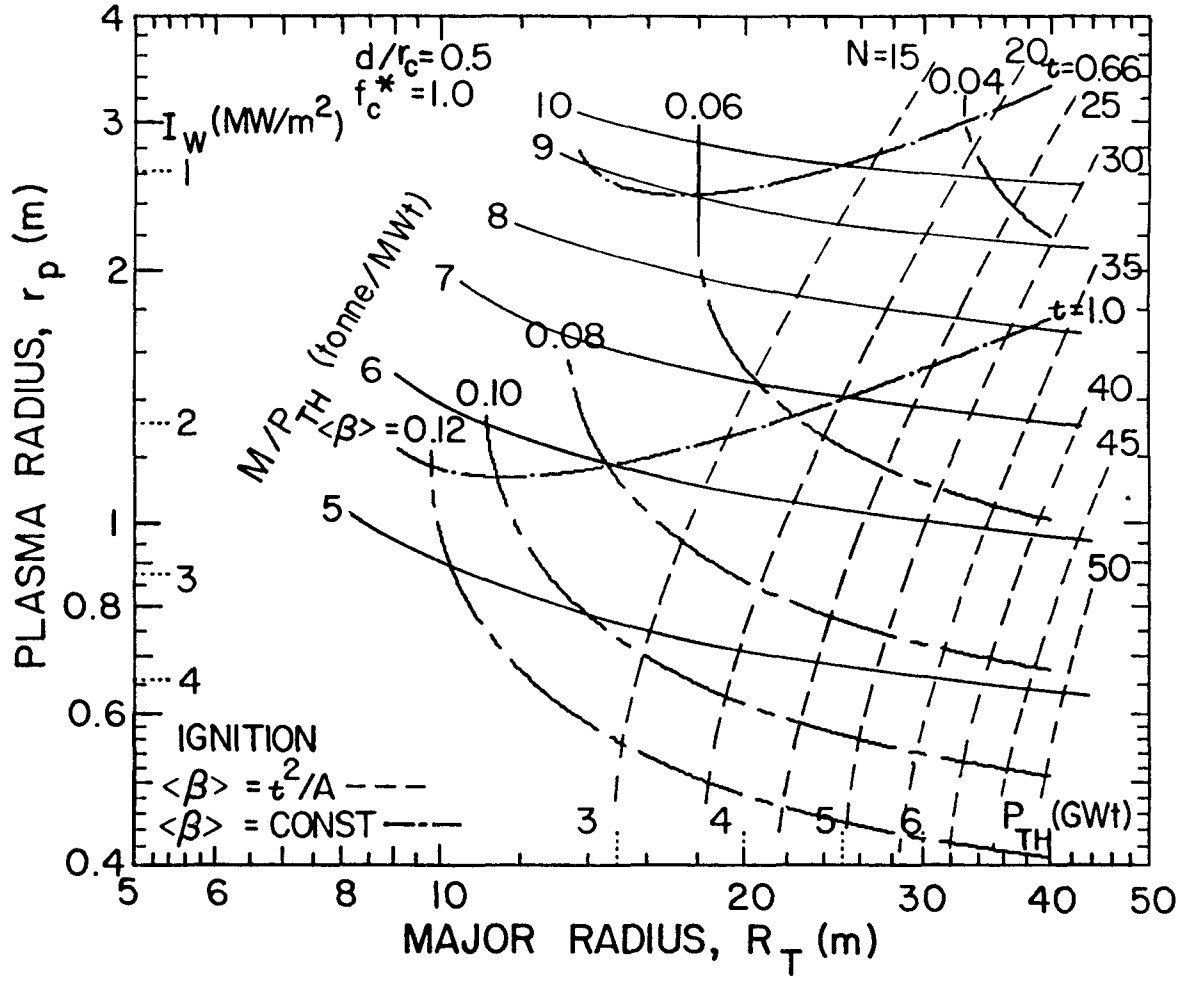

Fig. 3.4-7. Ignition curves for the d/r_c = 0.5 case, superposed onto a grid of constant N and M/P_{TH} lines with other fixed parameters as given in Fig. 3.4-4.

lower values of d/r_c are capable of achieving the required on-axis field with lower values of M/P_{TH} because less current is used to generate poloidal or radial fields [i.e., g_I in Eq. (3.4-14) approaches unity]. As will be seen below, however, these cases with lower d/r_c may not provide the levels of rotational transform expected to be required by the assumed beta values. Again, the incremental benefit of $\langle\beta\rangle$ values in excess of 0.08 is small. The advantage of higher beta operation is magnified by the inclusion of time-related costs and the potential for mass-related construction times. Again, the incremental improvement of pushing $\langle\beta\rangle$ beyond 0.08-0.10 is small for $P_{TH} \simeq 4.0$ GWt. Higher beta, however, will be required for power plants of lower capacity.

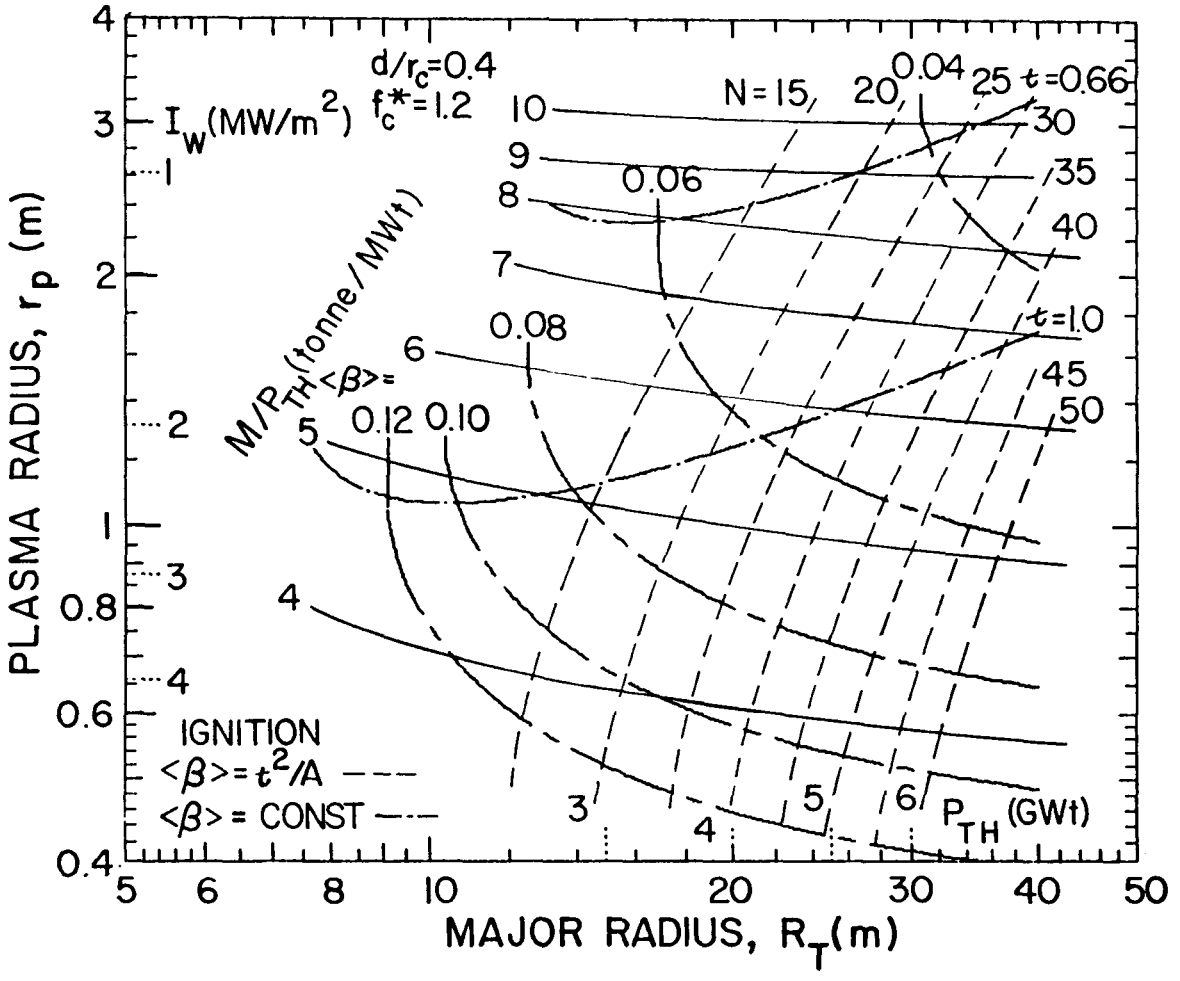

Fig. 3.4-8. Ignition curves for the $d/r_c = 0.4$ case, superposed onto a grid of constant N and M/P_{TH} lines with a tightly packed ($f_c^* = 1.2$ modular-coil set). These results should be compared to the results given in Fig. 3.4-6 ($d/r_c = 0.4$, but $f_c^* = 1.0$).

A missing link in the discussion thus far is the relation between the modular-coil configuration as characterized by coil aspect ratio, $A_c = R_T/r_c$; coil number, N; number of toroidal-field periods, m; and lateral coil distortion, d/r_c, on the one hand and resultant rotational transform, ι, on the other. Detailed resolution of this issue is the subject of magnetics computations and optimization (Sec. 4.). A simplified, analytic picture is available for parametric use, however, using the models of Refs. 22. The dependence of on-axis rotational transform, $\iota(0)$, as a function of lateral coil distortion, d/r_c, for various plasma aspect ratios, $A = R_T/r_p$, in the range 10-30 is shown in Fig. 3.4-10 for an MSR with the indicated fixed parameters. A plasma aspect ratio of $A \simeq 10$ is consistent with $P_{TH} = 4.0$ GWt

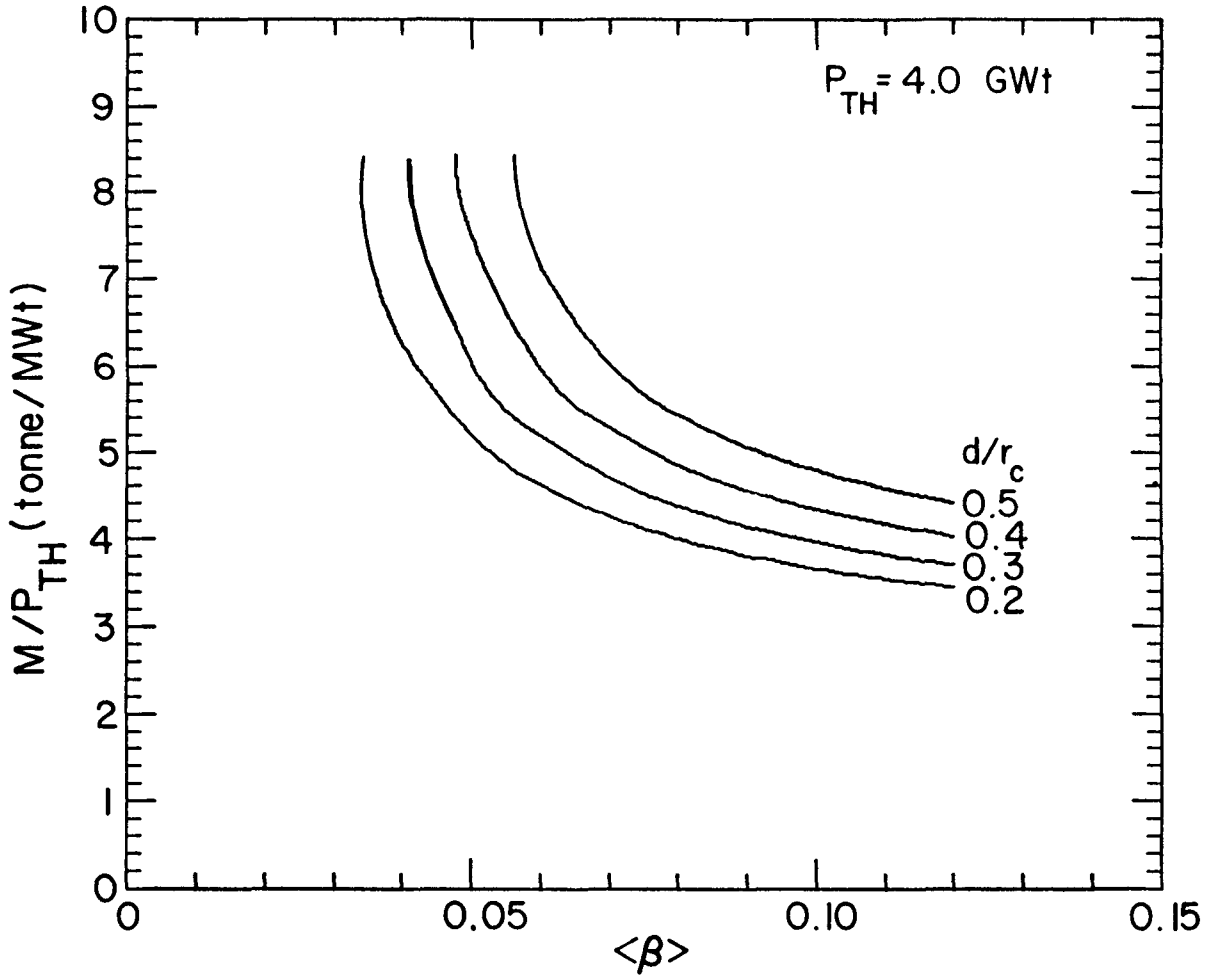

Fig. 3.4-9. Dependence of mass utilization, M/P_{TH}, on average beta, $\langle\beta\rangle$, for a fixed thermal output power, P_{TH} = 4.0 GWt, corresponding to $R_T \simeq 20$ m for various values of modular-coil distortion, d/r_c.

and $\langle\beta\rangle \simeq 0.04$; $A \simeq 30$ would be required for $P_{TH} \simeq 4.0$ GWt at $\langle\beta\rangle \simeq 0.08$, as can be seen from Fig. 3.4-6. For the nominally fixed number of coils, N = 24, only those coil configurations to the left of the dashed curves representing the coil-interference constraint of Eq. (3.4-17) are allowed. The tighter packed constraint ($f_c^* = 1.2$) allows more coil distortion than the envelope constraint ($f_c^* = 1.0$) and hence allows higher on-axis transform values. The larger values of plasma aspect ratio allow the system to achieve the higher values of rotational transform required of the $\langle\beta\rangle = \iota^2/A$ scaling. Generally, however, the coil configuration is always pushing the f_c^* geometric constraint, and more sophisticated coil winding laws than the sinusoidal deformations considered here may be required to make the overall design of the MSR fully self-consistent. In the spirit of the goals of the parametric systems model,

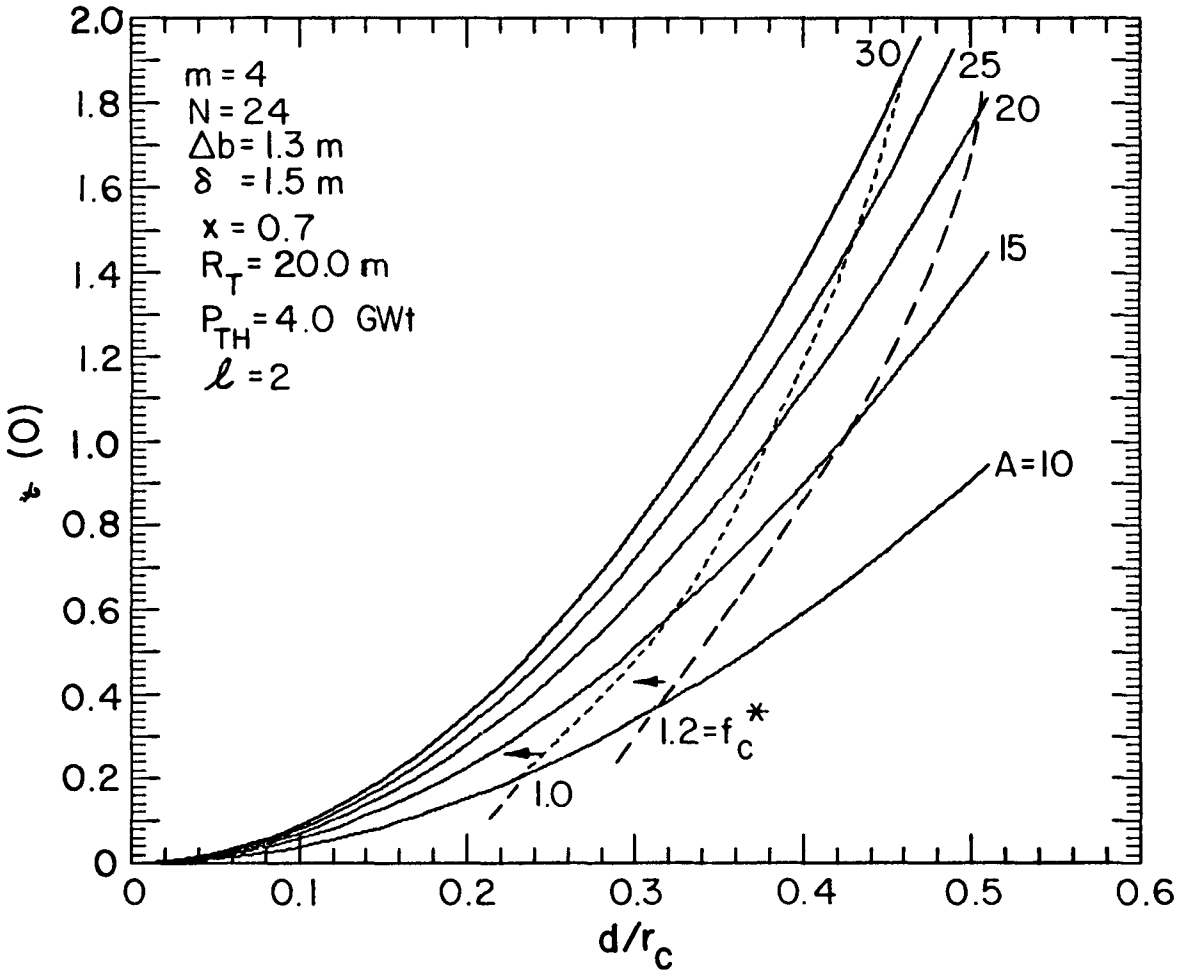

Fig. 3.4-10. Approximate dependence of the on-axis rotational transform, $\iota(0)$, on the modular-coil lateral distortion, d/r_c, for various plasma aspect ratios, $A = R_T/r_p$, and the indicated fixed parameters. Geometric coil interference constraints using Eq. (3.4-17) for the base case ($f_c^* = 1.0$) and the tighter packed case ($f_c^* = 1.2$) are indicated.

therefore, guidance is provided to assure that the more time-consuming magnetics calculations are considering reactor-relevant regions of parameter space.

The results of the previous parametric studies can be further condensed into a useful set of comprehensive design curves for purposes of identifying self-consistent MSR design points. For a nominal total thermal output power P_{TH} = 4.0 GWt and the conservative coil envelope interference condition, $f_c^* = 1.0$, Fig. 3.4-11 displays the dependence of plasma aspect ratio, $A = R_T/r_p$; number of coils, N; coil radius, r_c; and conductor thickness, δ_c,

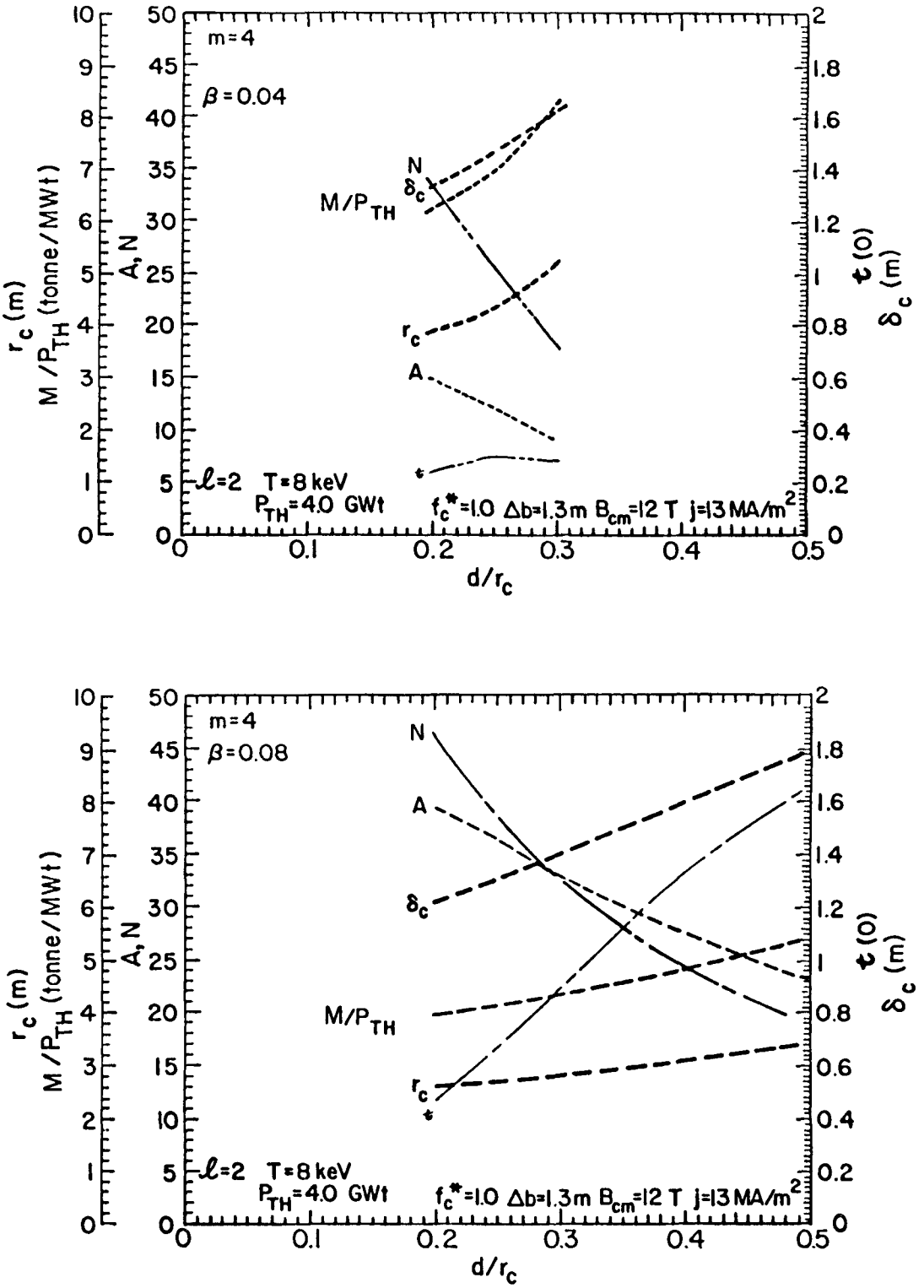

Fig. 3.4-11. MSR design-point prescription using the parametric results of Figs. 3.4-5 through 3.4-7 for $\langle\beta\rangle$ = 0.04 (top) and $\langle\beta\rangle$ = 0.08 (bottom) as a function of coil distortion, d/r_c, and the indicated fixed parameters. Rotational transforms are calculated assuming m = 4 toroidal-field periods.

on the modular-coil distortion parameter, d/r_c. Recall that fixing P_{TH} determines R_T by Eq. (3.4-6) to be ~20 m. Results for a low-beta ($\langle\beta\rangle = 0.04$) and a high-beta ($\langle\beta\rangle = 0.08$) MSR are presented in Figs. 3.4-11A and 3.4-11B, respectively. As indicated by Figs. 3.4-5 through 3.4-7, MSR reactors with $\langle\beta\rangle = 0.04$ and $P_{TH} = 4.0$ GWt are inaccessible for $d/r_c \gtrsim 0.3$. The on-axis rotational transform, $\iota(0)$, is also plotted for the assumed number of toroidal field periods, m = 4. Higher values of m would tend to result in lower values of $\iota(0)$ performance. Only integer values of N/m greater than or equal to 3 would be allowed in candidate design points. Selection of a candidate design point with $\langle\beta\rangle = 0.08$ and $M/P_{TH} \lesssim 5.0$ tonne/MWt leads directly to the choice of N = 24 for which N/m = 6 and $d/r_c = 0.41$. All other parameters follow by

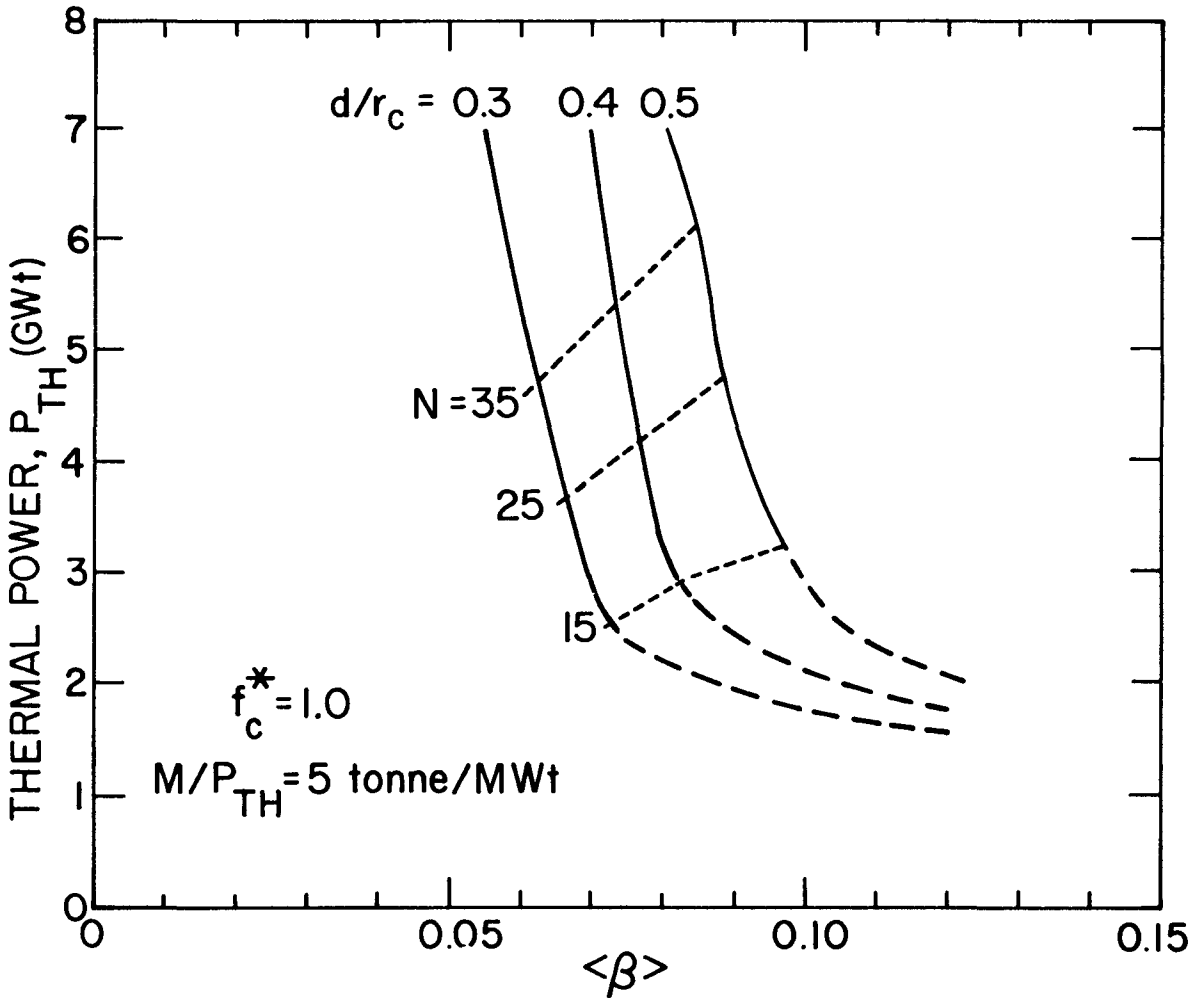

Fig. 3.4-12. Thermal power output, P_{TH}, as a function of $\langle\beta\rangle$ for fixed mass utilization, $M/P_{TH} = 5$ tonne/MWt and various values of coil distortion, d/r_c, and coil number, N, assuming $f_c^* = 1.0$. Systems with $N \lesssim 15$ are probably inaccessible.

TABLE 3.4-1

INTERIM (Ref. 23) LOW-BETA AND HIGH-BETA MSR DESIGNS

PARAMETER	$\langle\beta\rangle = 0.04$ Ref. 22[a]	$\langle\beta\rangle = 0.04$ (0.0067, 0.012)[b]	$\langle\beta\rangle = 0.08$ (0.067, 0.108)[b]
Number of poloidal-field periods, ℓ	2	2	2
Number of coils, N	24	24	24
On-axis rotational transform, $\iota(0)$	0.28(m = 4) ~0.15	1.36(m = 4) 0.38(m = 3)	1.72(m = 3)
Major toroidal radius, R_T (m)	21.35	20.0	20.0
Coil aspect ratio, $A_c = R_T/r_c$	4.65	4.49	6.45
Coil minor radius, r_c (m)	4.6	4.45	3.1
Plasma aspect ratio, $A = R_T/r_p$	11.0	11.6	27.5
Plasma minor radius, r_p (m)	1.94	1.72	0.73
Lateral coil distortion, d/r_c	0.30	0.26	0.408
Coil thickness, δ (m)	1.51	1.51	1.62
Blanket/shield thickness, Δb (m)	1.5	1.3	1.3
Interference parameter, f_c^*	1.0	1.0	1.0
Inboard filling fraction, f_c	0.36	0.39	0.38
Mass utilization, M/P_{TH} (tonne/MWt)	~9	7.2	4.9
Plasma power density, P_{TH}/V_p (MWt/m^3)	2.5	3.42	19.0
System power density, P_{TH}/V_c (MWt/m^3)	0.33	0.37	0.66
Total thermal power, P_{TH} (GWt)	4.0	4.0	4.0
First-wall neutron loading, I_w (MW/m^2)	1.5	1.53	3.61
Radial plasma filling fraction, x	0.83	0.7(0.61)[c]	0.7(0.54)[c]
On-axis field, B_o (T)	6.37	6.60	7.17
Peak field at coil, B_{CM} (T)	~11.5	12.0	12.0
Coil current density, j (MA/m^2)	12.5	13.0	13.0
Total coil current, I (MA)	28.5	29.64	34.12

[a] Number of toroidal-field periods, m = 8; ignition condition, $\langle\beta\rangle B_o^2 r_p = 3.15\ T^2\ m$.

[b] Beta values obtained from expression $\langle\beta\rangle = \iota^2(0)/A$ for number of toroidal-field periods m = 4 and 3, respectively.

[c] Obtained from the $x = 0.66(m/A)^{1/3}(1 - \Delta b/r_c)^{-2/3}$ formalism described in Ref. 22 for m = 4 and $r_s \simeq r_c$, consistent with limiter impurity control.

inspection of Fig. 3.4-11 or by straightforward calculation. The parameter list of Table 3.4-1 results. A similar process for the low-beta case leads to the selection of a design point with the rotational-transform performance that may be too low as noted in Ref. 22. Table 3.4-1 also includes the Ref. 22 design point with $\langle\beta\rangle = 0.04$ for comparison. The relatively low value of coil distortion (i.e., $d/r_c = 0.25\text{-}0.30$) and low coil aspect ratio (i.e., $A_c \simeq 4.5$) allowed in the low-beta case (i.e., $\langle\beta\rangle = 0.04$) with $N = 24$ leads to poor rotational-transform performance (i.e., $\iota(0) < 0.5$) in contrast to the high-beta (i.e., $\langle\beta\rangle = 0.08$) case. Figure 3.4-11 can be used to determine quickly the sensitivity of design-point performance to changes in parameter choices and to guide the application of more elaborate computations.

The results in Figs. 3.4-7 through 3.4-11 have focused on MSR systems with $P_{TH} = 4.0$ GWt at $R_T \simeq 20$ m. Such systems lead to total unit cost estimates of 3000-4000 \$/kWe for $\langle\beta\rangle = 0.08$, depending on the degree of optimism used in the cost data base. For a nominal net output power $P_E = 1250$ MWe, these unit costs would imply total capital costs of 3.8-5.4 billion dollars. The ability of utilities to raise such vast sums in today's financial markets may force consideration of smaller plants to keep the total capital cost at more manageable levels, despite a penalty incurred by sacrificing the unit-cost economies of scale of the larger plant. The consequences of such a strategy can be seen from Fig. 3.4-6 for the $\langle\beta\rangle = 0.08$ case of Table 3.4-1. Lower power (smaller plant) systems are achieved at lower values of R_T. The plasma radius, r_p, and hence the first-wall loading, I_w, may be held fixed as R_T is decreased. In this case, the mass utilization decreases slowly, but this decrease occurs at the expense of higher required values of $\langle\beta\rangle$ (e.g., $\langle\beta\rangle \simeq 0.12$ for $R_T \simeq 10$ m and $P_{TH} \simeq 2.0$ GWt). A smaller reactor system or a demonstration device, therefore, would require even more favorable physics performance in terms of $\langle\beta\rangle$ and ι. Alternatively, for a fixed $\langle\beta\rangle = 0.08$ and $d/r_c = 0.4$, as $R_T \to 10$ m for $P_{TH} \to 2.0$ GWt, the plasma radius, r_p, and the mass utilization, M/P_{TH}, can grow to unacceptable levels at the asymptotic limit, necessitating a lower value of coil distortion (Fig. 3.4-5). A third approach is to fix the mass utilization and examine the tradeoff between P_{TH} and $\langle\beta\rangle$. Figure 3.4-12 depicts the tradeoff for coil distortion values in the range 0.3-0.5, consistent with Figs. 3.4-5 through 3.4-7, for $M/P_{TH} = 5$ tonne/MWt. The thermal power is a strong function of beta for systems with more than 15 coils. Below 15 coils, the curves in

Fig. 3.4-12 change behavior reflecting the crowding of the constant-$\langle\beta\rangle$ curves at the leftward asymptotic limits shown in Figs. 3.4-5 through 3.4-7 and so that values of P_{TH} less than ~1.5 GWt are generally inaccessible. Lower values of d/r_c give insufficient rotational transform. However, as N falls below 15, the toroidal-field ripple increases and the magnetics requirement that $N/m \gtrsim 3$ can be met only for very low m values. The curves in Fig. 3.4-12 for $N < 15$ are therefore dashed to indicate that this attractive low-power regime is probably not accessible.

3.4.8. Parametric Survey Conclusions. On the basis of optimistic (i.e., "best case") assumptions and constraints, a plasma beta of 0.08 or greater appears to be necessary if the MSR is to be competitive with other approaches to magnetic fusion of the $P_{TH} = 4.0$ GWt class; higher beta values will be required for lower values of P_{TH}. To achieve this goal of mass utilization, M/P_{TH}, near or below 5 tonne/MWt, the desired value of $\langle\beta\rangle$ must be achieved with a magnetics topology that can be created by a modular-coil set of distortion $d/r_c \lesssim 0.4$. If a $\langle\beta\rangle \simeq \iota^2/A$ scaling applies, this constraint (i.e., $\langle\beta\rangle \gtrsim 0.08$, $M/P_{TH} \lesssim 5$ tonne/MWt) implies that rotational transforms on the order of unity must be obtained for $d/r_c \simeq 0.4$. Additional optimism needed to alleviate these conditions can be injected into these results by

- increasing the assumed Alcator transport coefficient (i.e., $\tau_E/\langle n\rangle r_p^2 > 3(10)^{-21}$ s m) or otherwise "fine tuning" other plasma parameters (i.e., profiles, f_α, Z_{eff}, etc.) to reduce the $\langle\beta\rangle B_o^2 r_p$ value needed for ignition;
- increasing f_c^* beyond unity, with the attendant complexity of "interlocked" coils and reduced torus access;
- accounting for differences between vacuum and beta-related rotational transforms in the $\langle\beta\rangle \simeq \iota^2/A$ scaling; and
- decreasing the nominal thickness of blanket/shield, Δb.

It is recalled, however, that the level of optimism built into the constraints that $B_{CM} = 12$ T, $j = 13$ MA/m^2, $x = 0.7$, $\Delta b = 1.3$ m, $\ell = 2$, etc., is unlikely to be fully attained by a detailed engineering design and that the parametric results presented here are judged to be close to a "best case". These findings, however, must be tested against more exact analyses, although they can be considered indicative of the requirement that the MSR should provide $\langle\beta\rangle$ values in the range 0.08-0.10 if a truly interesting alternative fusion

system is ultimately to emerge from this approach. The analytic rotational transform results displayed in Fig. 3.4-10 must be verified by three-dimensional magnetics computations before a self-consistent MSR design point can be selected.

These conclusions, however, must be moderated by obvious modelistic shortcomings. This parametric survey does not treat accurately several important but subtle influences on the ultimate reactor desirability of the MSR. For example, systems with attractively low values of M/P_{TH} and higher values of $\langle\beta\rangle$ also must operate at higher values of first-wall loading; therefore, for a fixed first-wall life (10-20 MWyr/m^2), these higher power density systems may operate with higher rate of FW/B change out, lower plant availability, and higher operating costs. Second, the dependence of plasma filling fraction, $x = r_p/r_w$, on the number of toroidal-field periods, m, and plasma aspect ratio, $A = R_T/r_p$, has been ignored for present purposes, as was noted previously. Inclusion of this dependence may make it difficult to achieve the desired values of lower mass utilization in systems with high beta values and correspondingly large values of A, particularly if m must be sufficiently low to yield appropriately high values of rotational transform, ι. The desire to maximize x suggests that pumped-limiter impurity control may be preferable to divertor impurity control, in the absence of overriding technical considerations including heat removal and maintenance.

Lower output power than the nominal $P_{TH} = 4.0$ GWt for a fixed mass utilization requires higher beta values but offers the prospect of reduced total cost. Clearly, an optimum power density, mass utilization, and cost exists for the MSR. This optimum probably lies in the $\langle\beta\rangle \simeq 0.08$-$0.10$, $I_w = 3$-4 MW/m^2 range rather than the $\langle\beta\rangle = 0.04$-$0.05$, $I_w = 1$-2 MW/m^2 range projected by past MSR studies.[22]

3.5. Candidate Design Point Selection

Interim candidate design points identified by means of the Phase IA parametric survey[23] described in the previous subsection have been iterated with the vacuum magnetics computations described in Sec. 4. In addition, the coil was recharacterized by a stepped-conductor model to accommodate peak-coil-field operation near 12 T. The evolution of the candidate modular stellarator design points [i.e., MSR-IIA ($\langle\beta\rangle = 0.04$) and MSR-IIB ($\langle\beta\rangle = 0.08$)] is shown in Table 3.5-1 and elaborated in Tables 3.5-2 and 3.5-3. Parameters for the analogous torsatron reactors are summarized in Tables 3.5-4

TABLE 3.5-1

EVOLUTION AND COMPARISON OF $\ell = 2$ MSR DESIGN POINTS

PARAMETER	$\langle\beta\rangle = 0.04$ MSR-IA	$\langle\beta\rangle = 0.04$ (0.067, 0.012)[b]	$\langle\beta\rangle = 0.08$ (0.067, 0.108)[b]	$\langle\beta\rangle = 0.04$ MSR-IIA[d]	$\langle\beta\rangle = 0.08$ MSR-IIB[d]
Number of coils, N	24	24	24	36	36
On-axis rotational transform, $\iota(0)$	~0.15	0.28(m = 4) 0.38(m = 3)	1.36(m = 4) 1.72(m = 3)	0.48(0.43)[e]	0.69(0.80)[e]
Major toroidal radius, R_T (m)	21.35	20.0	20.0	27.9	23.0
Coil aspect ratio, $A_c = R_T/r_c$	4.65	4.49	6.45	5.58	6.95
Coil minor radius, r_c (m)	4.6	4.45	3.1	5.0	3.31
Plasma aspect ratio, $A = R_T/r_p$	11.0	11.6	27.5	12.4	29.9
Plasma minor radius, r_p (m)	1.94	1.72	0.73	2.24	0.77
Lateral coil distortion, d/r_c	0.30	0.26	0.408	0.235	0.28
Coil thickness, δ (m)	1.51	1.51	1.62	1.08[f]	1.05[f]
Blanket/shield thickness, Δb (m)	1.5	1.3	1.3	0.83-2.59[g]	1.02-2.07[g]
Interference parameter, f_c^*	1.0	1.0	1.0	1.0	1.0
Inboard filling fraction, f_c	0.36	0.39	0.38	0.35	0.40
Mass utilization, M/P_{TH} (tonne/MWt)	~9	7.2	4.9	8.4	6.1
Plasma power density, P_{TH}/V_p (MWt/m^3)	2.5	3.42	19.0	1.7	12.4
System power density, P_{TH}/V_c (MWt/m^3)	0.33	0.37	0.66	0.30	0.60
Total thermal power, P_{TH} (GWt)	4.0	4.0	4.0	5.1	4.0
First-wall neutron loading, I_w (MW/m^2)	1.5	1.53	3.61	1.0	1.9
Radial plasma filling fraction, x	0.83	0.7(0.61)[c]	0.7(0.54)[c]	0.64	0.47
On-axis field, B_o (T)	6.37	6.60	7.17	5.72	6.56
Peak field at coil, B_{CM} (T)	~11.5	12.0	12.0	10.9	~12
Coil current density, j (MA/m^2)	12.5	13.0	13.0	10.3[h]	10.1[h]
Total coil current, I (MA)	28.5	29.64	34.12	22.3	21.0

[a] Number of toroidal-field periods, m = 8; ignition condition, $\langle\beta\rangle B_o^2 r_p = 3.15$ T^2 m, (Ref. 22).

[b] Beta values from $\langle\beta\rangle = \iota^2(0)/A$ for m = 4 and 3 (Ref. 23).

[c] Obtained from the $x = 0.66(m/A)^{1/3}(1 - \Delta b/r_c)^{-2/3}$ formalism described in Ref. 22 for m = 4 and $r_s \simeq r_c$, consistent with limiter impurity control.

[d] Number of toroidal field periods, m = 4.

[e] Edge value of transform obtained from vacuum magnetics calculations.

[f] Thickness of the square cross-section conductor.

[g] First wall conforms approximately to plasma shape.

[h] Value averaged over all the coil structure which no longer has a square cross section.

TABLE 3.5-2

MSR-IIA MAGNETICS RESULTS

PARAMETER	UNIFORM j_c[a]
Design $\langle\beta\rangle$	0.04
Coil type	Modular
Pitch parameter, γ	NA
Normalized distortion, d/r_c	0.235
Distortion coefficients:	
a_1	0.2350
a_2	0.0
a_3	0.0
a_4	0.0
a_5	0.0
a_6	0.0
Conductor major radius, R_T (m)	27.9
Conductor minor radius, r_c (m)	5.0
Conductor aspect ratio, $A_c = R_T/r_c$	5.58
Total coil current, I (MA)	22.23
Conductor cross section (m × m)	1.082 × 1.082
Conductor length, L_c (m)	33.085
Number of poloidal field periods, ℓ	2
Number of toroidal field periods, m	4
Number of coils, N	36
Plasma major radius (m)	27.90
Plasma minor radius, r_p (m)	2.18
Plasma volume, V_p (m^3)	2613.15
Magnetic axis (m)	27.977
Semiminor radius[b] (m)	1.477(1.484)
Semimajor radius[b] (m)	3.089(3.331)
Limiter radius (m)	3.435
On-axis field, B_o (T)	5.72
Well depth (%)	-0.054
Peak field at coil, B_{CM} (T)	11.24[d]
On-axis ripple, $\varepsilon(0)$%	<1.73
Edge ripple, $\varepsilon(r_p)$%	25.08
On-axis transform, $\iota(0)$	0.488
Edge transform, $\iota(r_p)$	0.448
Stored magnetic energy, E_M (GJ)	230.26
Peak radial force, f_r (MN/m)	79.78[d](76.42)[c]
Peak lateral force, f_ℓ (MN/m)	29.46[d](29.10)[c]

[a] $j_c = 19$ MA/m^2.

[b] Under a key coil and half a field period away.

[c] Results for key coil.

[d] Results for the worst case, coil 7.

TABLE 3.5-3

MSR-IIB MAGNETICS RESULTS

PARAMETER	UNIFORM j_c[a]	STEPPED j_c[b]
Design <β>	0.08	0.08
Coil type	Modular	Modular
Pitch parameter, γ	NA	NA
Normalized distortion, d/r_c	0.28	0.28
Distortion coefficients:		
a_1	0.2111	0.2111
a_2	0.0955	0.0955
a_3	0.0534	0.0534
a_4	0.0304	0.0304
a_5	0.0160	0.0160
a_6	0.0066	0.0066
Conductor major radius, R_T (m)	23.0	23.0
Conductor minor radius, r_c (m)	3.31	3.31
Conductor aspect ratio, $A_c = R_T/r_c$	6.95	6.95
Total coil current, I (MA)	21.0	21.0
Conductor cross section (m × m)	1.051 × 1.051	1.051 × 1.051
Conductor length, L_c (m)	22.916	22.916
Number of poloidal field periods, ℓ	2	2
Number of toroidal field periods, m	4	4
Number of coils, N	36	36
Plasma major radius (m)	23.025	23.02
Plasma minor radius, r_p (m)	0.630	0.81
Plasma volume, V_p (m^3)	180.62	298.76
Magnetic axis (m)	23.039	23.04
Semiminor radius[c] (m)	0.362(0.377)	0.479(0.500)
Semimajor radius[c] (m)	1.115(1.180)	1.406(1.425)
Limiter radius (m)	1.260	1.526
On-axis field, B_o (T)	6.55	6.47
Well depth (%)	-0.052	-0.049
Peak field at coil, B_{CM} (T)	11.75[e](11.45)[d]	11.59[d]
On-axis ripple, ε(0)%	<3.15	<2.89
Edge ripple, $\varepsilon(r_p)$%	9.72	11.32
On-axis transform, ι(0)	0.729	0.626
Edge transform, $\iota(r_p)$	0.880	0.804
Stored magnetic energy, E_M (GJ)	108.35	108.35
Peak radial force, f_r (MN/m)	79.20[e](78.95)[d]	78.36[d]
Peak lateral force, f_ℓ (MN/m)	39.61[e](39.31)[d]	38.21[d]

[a] j_c = 19 MA/m^2.

[b] j_c = 12.04 MA/m^2 for $0 < t < 0.519$; j_c = 22.43 MA/m^2, $0.519 < t < 0.811$; and j_c = 32.83 MA/m^2, $0.811 < t < 1.0$; where the fraction t is measured radially through the conductor cross section.

[c] Under a key coil and half a field period away.

[d] Results for a key coil.

[e] Results for the worst case, coil 5.

TABLE 3.5-4

TR-A MAGNETICS RESULTS

PARAMETER	UNIFORM j_c[a]
Design $\langle\beta\rangle$	0.04
Coil type	Torsatron
Pitch parameter, γ	0.57
Normalized distortion, d/r_c	NA
Distortion coefficients:	
a_1	NA
a_2	NA
a_3	NA
a_4	NA
a_5	NA
a_6	NA
Conductor major radius, R_T (m)	27.9
Conductor minor radius, r_c (m)	5.0
Conductor aspect ratio, $A_c = R_T/r_c$	5.58
Total coil current, I (MA)	50.018
Conductor cross section (m × m)	1.082 × 2.434
Conductor length, L_c (m)	304.224
Number of poloidal field periods, ℓ	2
Number of toroidal field periods, m	16
Number of coils, N	2
Plasma major radius (m)	27.87
Plasma minor radius, r_p (m)	2.30
Plasma volume, V_p (m^3)	2909.74
Magnetic axis (m)	27.891
Semiminor radius[b] (m)	1.685(2.302)
Semimajor radius[b] (m)	2.936(2.401)
Limiter radius (m)	3.160
On-axis field, B_o (T)	5.71
Well depth (%)	-2.11
Peak field at coil, B_{CM} (T)	12.47
On-axis ripple, $\varepsilon(0)$%	<9.73
Edge ripple, $\varepsilon(r_p)$%	25.61
On-axis transform, $\iota(0)$	0.569
Edge transform, $\iota(r_p)$	1.469
Stored magnetic energy, E_M (GJ)	609.64
Peak radial force, f_r (MN/m)	151.04
Peak lateral force, f_ℓ (MN/m)	18.90

[a] j_c = 19 MA/m^2.

[b] Under a key coil and half a field period away.

TABLE 3.5-5

TR-B3 MAGNETICS RESULTS

PARAMETER	UNIFORM j_c [a]	STEPPED j_c [b]	STEPPED j_c [b]
Design <β>	0.08	0.08	0.08
Coil type	Torsatron	Torsatron	Torsatron
Pitch parameter, γ	0.365	0.365	0.388
Normalized distortion, d/r_c	NA	NA	NA
Distortion coefficients:			
a_1	NA	NA	NA
a_2	NA	NA	NA
a_3	NA	NA	NA
a_4	NA	NA	NA
a_5	NA	NA	NA
a_6	NA	NA	NA
Conductor major radius, R_T (m)	23.0	23.0	23.0
Conductor minor radius, r_c (m)	2.3	2.3	2.3
Conductor aspect ratio, $A_c = R_T/r_c$	10.0	10.0	10.0
Total coil current, I (MA)	35.7	35.7	35.7
Conductor cross section (m × m)	0.994 × 1.889	0.994 × 1.889	0.994 × 1.889
Conductor length, L_c (m)	461.405	461.405	461.57
Number of poloidal field periods, ℓ	2	2	2
Number of toroidal field periods, m	25	25	25
Number of coils, N	1	1	1
Plasma major radius (m)	22.990	23.271	22.989
Plasma minor radius, r_p (m)	0.574	0.572	0.573
Plasma Volume, V_p (m^3)	149.47	150.08	148.89
Magnetic axis (m)	23.002	23.303	23.001
Semiminor radius[c] (m)	0.448(0.533)	0.433(0.572)	0.446(0.559)
Semimajor radius[c] (m)	0.717(0.641)	0.721(0.615)	0.721(0.612)
Limiter radius (m)	0.758	1.01	0.762
On-axis field, B_o (T)	7.72	7.50	7.64
Well depth (%)	-0.46	0.019	-0.16
Peak field at coil, B_{CM} (T)	12.01	12.09	12.14
On-axis ripple, ε(0)%	<4.65	<10.23	<4.62
Edge ripple, $\varepsilon(r_p)$%	10.90	15.40	10.23
On-axis transform, ι(0)	1.861	1.872	1.479
Edge transform, $\iota(r_p)$	2.357	2.034	1.847
Stored magnetic energy, E_M (GJ)	252.03	252.03	252.03
Peak radial force, f_r (MN/m)	107.16	110.57	112.25
Peak lateral force, f_ℓ (MN/m)	12.35	13.51	11.82

[a] $j_c = 19$ MA/m^2.

[b] $j_c = 12.04$ MA/m^2 for $0 < t < 0.519$; $j_c = 22.43$ MA/m^2, $0.519 < t < 0.811$; and $j_c = 32.83$ MA/m^2, $0.811 < t < 1.0$; where the fraction t is measured radially through the conductor cross section.

[c] Under a key coil and half a field period away.

and 3.5-5. These flagship design points were to serve as the framework for a detailed intercomparison of modular versus continuous-coil and low- versus high- beta operation on the basis of four relatively well-characterized designs. Only the MSR-IIB design point has been defined well enough to be reported in Sec. 4., although the features of the other flagships would be similar. Key magnetics parameters (Sec. 4.) are summarized here in Tables 3.5-2 through 3.5-5. The use of higher harmonic winding-law components results in B_{CM}/B_o values which are locally higher than values predicted by Eq. (3.4-13). A self-consistent iteration of the present models would therefore require an adjustment on this point.

Torsatron coils have lower peak lateral forces than the MSR cases (i.e., 9-12 MW/m versus 25-33 MW/m) and hence require less structural support between coils, but the fabrication and maintenance questions are more difficult, unless life-of-plant coils can be postulated. Relatively few MSR toroidal-field periods (m = 4) allow radial rotational transform profiles, $\iota(r)$, in the ranges 0.5-0.4 (MSR-IIA) and 0.7-0.9 (MSR-IIB), providing significant non-zero transform on-axis, avoiding rational surfaces within the plasma, and with the addition of appropriate higher harmonics into the coil winding law,[69] providing significant positive shear at the plasma edge (MSR-IIB). Except for the out-of-plane winding, the internal coil technology is comparable to other recent superconducting fusion reactor system designs (Sec. 5.2.).

Radial energy transport in both MSR systems is assumed conservatively to scale as $\tau_E = 3.0(10)^{-21} \langle n \rangle r_p^2$ (i.e., 40% reduced Alcator scaling). This results in similar confinement to that of UWTOR-M.[37] Use of the Alcator scaling relation allows convenient minimization of the $\langle \beta \rangle B_o^2 r_p$ ignition parameter, which is 2.94 T^2 m and 2.79 T^2 m at $\langle T \rangle$ = 8 keV for the respective design points, reflecting a higher trapping of fusion-product alpha-particle energy in the higher aspect ratio MSR-IIB case. The higher beta of the MSR-IIB case is reflected directly in a lower plasma radius, r_p, for a $\langle \beta \rangle B_o^2 r_p$ value fixed by ignition and nr_p^2 scaling.

The lower plasma radius for MSR-IIB allows the concentric annuli of blanket/shield/coil to be reduced in minor radius, giving higher system power density, P_{TH}/V_c, and lower fusion-power-core mass, M. Impurity control is assumed to be provided by a pumped limiter,[73,74] although divertors are also generally compatible with the design. Routine MSR maintenance and replacement of limiter/first-wall/blanket components would be accomplished without moving

modular coils to promote high plant availability. The coils in the MSR-IIA and MSR-IIB configurations cover 35% and 41%, respectively, of the outer blanket/shield surface area, compared to 34% and 41% for torsatron systems designed to similar constraints (i.e., same, P_{TH}, R_T, B_o).

The MSR-IIB design point has been subjected to more detailed engineering design analysis with particular emphasis on the FPC. This effort is described in Sec. 5. The Appendix contains a detailed parameter list for the MSR-IIB design point.

REFERENCES

1. L. Spitzer, Jr., "A Proposed Stellarator," Project Matterhorn report NYO-993 (May 1951).

2. L. Spitzer Jr., D. Grove, W. Johnson, L. Tonks, and W. Westendorp, "Problems of the Stellarator as a Useful Power Source," US Atomic Energy Commission report NYO-6047 (1954).

3. K. Miyamoto, "Recent Stellarator Research," Nucl. Fusion 18, 243-284 (1978).

4. V. D. Shafranov, "Stellarators," Nucl. Fusion 20, 1075-1083 (1980).

5. J. L. Shohet, "Stellarators," in Fusion, E. Teller, Ed. (Academic Press, New York) Vol. 1, Part A, 243-289 (1981).

6. Joint US-EURATOM Steering Committee on Stellarators, "Stellarators-Status and Future Directions," Max Planck Institut für Plasmaphysik report IPP 2/254 (also DE81026572) (July 1981).

7. J. L. Johnson, G. Grieger, D. J. Lees, M. S. Rabinovich, J. L. Shohet, and K. Uo, "The Stellarator Program," IEEE Trans. Plasma Sci. PS-9, 142-149 (December 1981).

8. J. L. Johnson, "The Stellarator Approach to Toroidal Plasma Confinement," Nucl. Tech./Fusion 2, 340-361 (July 1982).

9. C. Gourdon, D. Marty, E. K. Maschke, and J. Touche, "The Torsatron without Toroidal Field Coils as a Solution of the Divertor Problem," Nucl. Fusion 11, 161-166 (1971).

10. T. W. Krukewitt and J. L. Shohet, "Magnetic Properties of Ultimate Torsatrons," Nucl. Fusion 20, 1375-1380 (1980).

11. K. Uo, "The Helical Heliotron Field for Plasma Confinement," Plasma Phys. 13, 243-255 (1971).

12. H. Wobig and S. Rehker, "A Stellarator Coil System without Helical Windings," Proc. 7th Symp. on Fusion Tech., EURATOM report EUR 4938e, 345-357 (October 24-27, 1972).

13. H. P. Furth, J. Killeen, M. N. Rosenbluth, and B. Coppi, "Stabilization by Shear and Negative V''," Proc. 2nd Int. Conf. on Plasma Physics and Contr. Nucl. Fusion Research, Culham, IAEA-CN-21/106, I, 103-126 (1966).

14. A. E. Bazhanova, V. M. Glagolev, and V. D. Shafranov, "Toroidal Plasma Traps with Three-Dimensional Axes," Sov. Phys. - Tech. Phys. 11, 1177-1182 (March 1967).

15. A. Boozer, T. K. Chu, R. L. Dewar, H. P. Furth, J. A. Goree, J. L. Johnson, et al., "Two High-Beta Toroidal Configurations: A High-Beta Stellarator and a Tokamak - Torsatron Hybrid," 9th Inter. Conf. on Plasma Phys. and Contr. Nucl. Fusion Research, Baltimore, MD, IAEA-CN-41/Q-4, (September 1-8, 1982).

16. R. G. Mills, "Economic Prospects for Thermonuclear Reactors," Princeton Plasma Physics Laboratory report MATT-60 (February 1961).

17. R. G. Mills, "Thermonuclear Power and Superconductivity," Engineering Aspects of Magnetohydrodynamics, (Columbia University Press, NY) 514-520 (1962).

18. A. Gibson, "Permissible Parameters for Economic Stellarator and Tokamak Reactors," Proc. BNES Nucl. Fusion Reactor Conf. at Culham Laboratory, 233-241 (September 1969).

19. A. Gibson, R. Hancox, and R. J. Bickerton, "Economic Feasibility of Stellarator and Tokamak Fusion Reactors," Proc. 4th Inter. Conf. on Plasma Phys. and Contr. Nucl. Fusion Research, IAEA-CN-28/K-4, III, 275-392 (June 17-23, 1971).

20. Yu. M. Loktionov, "Numerical Modelling of Torsatron Fusion Reactors," Kharkov Physico-Technical Institute report KhFTI-79-58 (1979).

21. Yu. M. Loktionov, "The Mutual Connection among the Fundamental Characteristics of a Torsatron Thermonuclear Reactor," Kharkov Physico-Technical Institute report KhFTI-82-24 (1982).

22. R. L. Miller and R. A. Krakowski, "The Modular Stellarator Fusion Reactor Concept," Los Alamos National Laboratory report LA-8978-MS (August 1981).

23. R. L. Miller, R. A. Krakowski, and C. G. Bathke, "Parametric Systems Analysis of the Modular Stellarator Reactor (MSR)," Los Alamos National Laboratory report LA-9344-MS (May 1982).

24. A. V. Georgievskii, Yu. M. Loktionov, and V. A. Suprunenko, "Characteristics of a Hypothetical Thermonuclear Stellarator Reactor in the 'Plateau' Regime," Kharkov Physico-Technical Institute report KhFTI-76-38 (1976) [English Translation in UKAEA Culham Laboratory report CTO/1299 (November 1976)].

25. P. A. Politzer, L. M. Lidsky, and D. B. Montgomery, "Torsatrons and TOREX Proof of Principle Experiment," Massachusetts Institute of Technology report PFC/TR-79-1 (March 1979).

26. A. Iiyoshi and K. Uo, "Heliotron as a Steady Fusion Reactor," Proc. 5th Inter. Conf. on Plasma Phys. and Contr. Nucl. Fusion Research, IAEA-CN-33/G4, III, 619-640 (1975).

27. Y. Iso, W. M. Stacey, Jr., G. L. Kulcinski, R. A. Krakowski, G. A. Carlson, C. Yamanaka, et al., "Fusion Reactor Design-III: Report on the 3rd IAEA Technical Committee Meeting and Workshop, Tokyo, October 5-16, 1981," Nucl. Fusion 22, 671-719 (1982).

28. O. Motojima, A. Iiyoshi, and K. Uo, "The Design of Heliotron Steady Reactor," 9th International Conf. on Plasma Physics and Contr. Nucl. Fusion Research, IAEA-CN-41/L-3, Baltimore, MD (September 1-8, 1982).

29. H. Nakashima and M. Ohta, "Nuclear Design of Heliotron Fusion Reactor Blankets (II)," Proc. 9th Symp. on Eng. Problems of Fusion Research, Chicago, IEEE Pub. No. 81CH1715 NPS, II, 1805-1808 (1981).

30. H. Nakashima, M. Ohta, and A. Iiyoshi, "Tritium Breeding Capability of Heliotron-H Fusion Reactor Blankets," J. Nucl. Sci. and Tech. 19, 762-764 (September 1982).

31. "World Survey of Major Activities in Contr. Fusion Research," Nucl. Fusion Special Supplement, p. 234 (1982).

32. R. E. Potok, P. A. Politzer, and L. M. Lidsky, "Ion Thermal Conductivity in a Helical Toroid," Phys. Rev. Lett. 45, 1328-1331 (20 October 1980).

33. T. Uchikawa, "Design Study of Torsatron Power Reactors on the Basis of Maintenance Requirements," Massachusetts Institute of Technology report PFC/RR-80-20 (1980).

34. D. T. Anderson, F. S. B. Anderson, R. L. Bonomo, K. A. Buckle, J. D. Callen, et al., "Recent Progress in Torsatron/Stellarator Research in the United States of America," Proc. 8th International Conf. on Plasma Physics and Contr. Nucl. Fusion Research, IAEA-CN-38/BB-1, I, 793-805 (1981).

35. L. M. Lidsky, R. E. Potok, and D. Cohn, "Transport and Design Features of a Continuously Wound Torsatron Reactor," Amer. Physical Soc. Div. of Plasma Physics Twenty-Fourth Annual Mtg., New Orleans (November 1-5, 1982).

36. R. E. Potok, D. R. Cohn, and L. M. Lidsky, "Design Features of T-2, A Torsatron Reactor with Continuous, Demountable Coils," Massachusetts Institute of Technology report PFC/RR-82-35 (December 1982).

37. B. Badger, I. N. Sviatoslavsky, S. W. Van Sciver, G. L. Kulcinski, G. A. Emmert, D. T. Anderson, et al., "UWTOR-M: A Conceptual Modular Stellarator Power Plant," University of Wisconsin report UWFDM-550 (October 1982).

38. I. N. Sviatoslavsky, S. W. Van Sciver, G. L. Kulcinski, D. T. Anderson, A. W. Bailey, et al., "UWTOR-M: A Conceptual Design of a Modular Stellarator Power Reactor," IEEE Trans. Plasma Sci., PS-9, 163-172 (December 1981).

39. I. N. Sviatoslavsky, S. W. Van Sciver, G. L. Kulcinski, A. W. Bailey, J. D. Callen, et al., UWTOR-M : A Conceptual Design of a Modular Stellarator Power Reactor," Proc. 9th Symp. on Eng. Problems of Fusion Research, Chicago, IEEE Pub. No. 81CH1715 NPS, II, 1894-1897 (1981).

40. I. N. Sviatoslavsky, S. W. Van Sciver, G. L. Kulcinski, G. A. Emmert, D. T. Anderson, et al., "Progress in Modular Stellarator Fusion Power Reactor Conceptual Designs," Proc. 9th International Conf. on Plasma Physics and Contr. Nucl. Fusion Research, Baltimore, MD, IAEA-CN-41/E-3, I, 387-398 (September 1-8, 1982).

41. R. L. Miller and R. A. Krakowski, "Conceptual Design Studies of the Modular Stellarator Reactor (MSR)," Proc. 9th Symp. on Eng. Problems of Fusion Research, Chicago, IEEE Pub. No. 81CH1715 NPS, II, 1863-1866 (1981).

42. C. C. Baker, G. A. Carlson, and R. A. Krakowski, "Trends and Developments in Magnetic Confinement Fusion Reactor Concepts," Nucl. Tech./Fusion 1, 5-78 (January 1981).

43. W. N. G. Hitchon, P. C. Johnson, and C. J. H. Watson, "Parameter and Cost Optimizations for a Modular Stellarator Reactor," UKAEA Culham Laboratory report CLM-P628 (September 1982) [to be published, J. of Fusion Energy, 1983].

44. W. N. G. Hitchon, P. C. Johnson, and C. J. H. Watson, "Parameter and Cost Optimizations for a Modular Stellarator Reactor," Proc. 4th Int. Stellarator Workshop, Cape May, NJ, II, 362-377 (September 12-15, 1982).

45. R. A. Dory and J. Sheffield, "Optimization of Stellarator Reactors," Proc. US/JAPAN Workshop on Stellarator/Torsatron/Heliotron Reactors, Los Alamos (February 14-15, 1983).

46. O. Motojima, "Heliotron Reactor," Proc. US/JAPAN Workshop on Stellarator/Torsatron/Heliotron Reactors, Los Alamos (February 14-15, 1983).

47. J. A. Derr and J. L. Shohet, "A Modular Stellarator Divertor," IEEE Trans. Plasma Sci. PS-9, 234-239 (December 1981).

48. R. L. Miller, C. G. Bathke, and R. A. Krakowski, "Parametric Systems Analysis of the Modular Stellarator Reactor," Nucl. Fusion 23, 467-479 (1983).

49. K. Miyamoto, Plasma Physics for Nuclear Fusion, (the MIT Press, Cambridge, MA) p. 29ff. (1980).

50. A. I. Morozov and L. S. Solov'ev, "The Structure of Magnetic Fields," Reviews of Plasma Physics, M. A. Leontovich, Ed., (Consultants Bureau, New York) 2, 1-101 (1966).

51. K. Ohasa and K. Miyamoto, "Rotational Transform Angle of the Stellarator Field with Twisted Coils," Japanese Jour. of Applied Physics 16, 813-816 (May 1977).

52. A. H. Boozer, "Establishment of Magnetic Coordinates for a Given Magnetic Field," Phys. Fluids 25, 520-521 (March 1982) [also Princeton Plasma Physics Laboratory report PPPL-1775 (April 1981)].

53. V. D. Shafranov, "The MHD Theory of Plasma Equilibrium and Stability in Stellarators: Survey of Results," Proc. 4th Int. Stellarator Workshop I, 269-297, Cape May, NJ (September 12-15, 1982) [also Phys. Fluids 26, 357-364 (February 1983)].

54. P. Garabedian, "Equilibrium and Stability Calculations on Heliotron E, ATF-1, and Heliac," ibid., p. 329-336.

55. J. Nührenberg, "Application of Two Three-Dimensional Codes to Stellarators," ibid., p. 298-328.

56. O. B. Adams, R. L. Brown, W. D. Cain, B. A. Carreras, L. A. Charlton, et al., "Proposal to Build ATF-1," Oak Ridge National Laboratory document (October 1982).

57. J. F. Lyon, B. A. Carreras, J. H. Harris, J. A. Rome, L. A. Charlton, et al., "Stellarator Physics Evaluation Studies," Proc. 9th Int. Conf. on Plasma Physics and Contr. Nucl. Fusion Research, Baltimore, MD, IAEA-CN-41/Q3 (September 1-8, 1982) [also Oak Ridge National Laboratory report ORNL/TM-8496 (February 1983)].

58. M. D. Kruskal and R. M. Kulsrud, "Equilibrium of a Magnetically Confined Plasma in a Toroid," Phys. Fluids 1, 265-274 (July - August 1958).

59. G. Anania, J. L. Johnson, and K. E. Weimer, "Use of the Stellarator Expansion to Investigate Plasma Equilibrium in Modular Stellarators," Princeton Plasma Physics Laboratory report PPPL-1945 (November 1982).

60. F. L. Hinton and R. D. Hazeltine, "Theory of Plasma Transport in Toroidal Confinement Systems," Rev. Mod. Phys. 48, 239-308 (April 1976).

61. J. L. Shohet, "Transport in Toroidal Stellarators and Torsatrons," Comments Plasma Phys. 5, 55-68 (1979).

62. J. W. Connor and R. J. Hastie, "Neoclassical Diffusion in an $\ell = 3$ Stellarator," Phys. Fluids 17, 114-123 (January 1974).

63. R. E. Potok, P. A. Politzer, and L. M. Lidsky, "Ion Thermal Conductivity in a Helical Toroid," Phys. Rev. Letts. 45, 1328-1331 (20 October 1980).

64. A. Pytte and A. H. Boozer, "Neoclassical Transport in Helically Symmetric Plasmas," Phys. Fluids 24, 88-92 (January 1981).

65. A. H. Boozer and G. Kuo-Petravic, "Monte Carlo Evaluation of Transport Coefficients," Phys. Fluids 24, 851-859 (May 1981).

66. H. E. Mynick, "Verification of the Classical Theory of Helical Transport in Stellarators," Phys. Fluids 25, 325-329 (February 1982).

67. S. L. Greene, "Maxwell Averaged Cross Sections for Some Thermonuclear Reactions on Light Isotopes," Lawrence Livermore Laboratory report UCRL-70522 (May 1967).

68. R. E. Potok, "Particle Orbits and Diffusion in Torsatrons," Ph.D. diss. Massachusetts Institute of Technology (May 1980).

69. T. K. Chu, H. P. Furth, J. L. Johnson, C. Ludescher, and K. E. Weimer, "Optimization Techniques for Modular Stellarator Coils," Nucl. Fusion 22, 871-881 (1982) [also Princeton Plasma Physics Laboratory report PPPL-1873 (February 1982)].

70. D. T. Anderson, J. A. Derr, and J. L. Shohet, "The Interchangeable Modular Stellarator," IEEE Trans. on Plasma Sci. PS-9, 212-220 (December 1981).

71. U. Brossmann, W. Dommaschk, F. Herrnegger, G. Greiger, J. Kisslinger, W. Lotz, et al., "Concept of an Advanced Stellarator," Proc. 9th Int. Conf. on Plasma Physics and Contr. Nucl. Fusion Research, Baltimore, MD, IAEA-CN-41/Q5 (September 1-8, 1982).

72. J. F. Schivell, "Method of Plasma Impurity Control Without Magnetic Divertor," Princeton Plasma Physics Laboratory report PPPL-1342 (April 1977).

73. R. W. Conn, I. N. Sviatoslavsky, and D. K. Sze, "Limiter-Pumping for Divertorless Tokamaks," Proc. 8th Symp. on Eng. Problems of Fusion Research I, 568-573 (1979).

74. C. C. Baker, M. A. Abdou, D. A. DeFreece, C. A. Trachsel, D. W. Graumann, et al., "STARFIRE - A Commercial Tokamak Fusion Power Plant Study," Argonne National Laboratory report ANL/FPP-80-1 (September 1980).

75. C. G. Bathke, D. J. Dudziak, R. A. Krakowski, W. B. Ard, D. A. Bowers, J. W. Davis, et al., "ELMO Bumpy Torus Reactor and Power Plant Conceptual Design Study," Los Alamos National Laboratory report LA-8882-MS (August 1981).

76. P. B. Parks and R. J. Turnbull, "Effect of Transonic Flow in the Ablation Cloud on the Lifetime of a Solid Hydrogen Pellet in a Plasma," Phys. Fluids 21, 1735-1741 (1978).

77. R. P. Gilliard and K. Kim, "Significance of Magnetic Shielding in the Ablation of a Solid Hydrogen Pellet in a Plasma," IEEE Trans. on Plasma Sci. PS-8, 477-484 (December 1980).

78. S. L. Milora, "Review of Pellet Fueling," J. Fusion Energy I, 15-48 (1981).

79. H. Gorenflo and M. Soll, "STELLA- A Computer Program System for Calculating Magnetic Fields, Forces, and Mechanical Stresses for Twisted Stellarator Coil Systems," Max-Planck-Institut fur Plasmaphysik Interner Bericht No. 27 (July 1981).

4. VACUUM MAGNETICS

An integral element of this stellarator reactor study is the capability to determine the rotational transform resulting from a given coil configuration. Such a capability existed at the beginning of this study in the form of the computer codes EFFI[1] and BARC.[2] Both of these codes were thought to be impractical for performing the kinds of parametric studies and design point iterations/refinements envisaged for this study because of the prohibitive amount of computer time required to trace a field line far enough to generate a flux surface (~1/2 Cray hour per surface using EFFI). The problem created by requiring coils to be constructed from "rectangular" blocks, which is common to both codes, dictates that stellarator coils be composed of many ($\gtrsim$90) such blocks for the sake of accuracy, thereby contributing to the long execution time. In addition, the more widely known and used EFFI code requires a preprocessor to provide the coil geometry and a postprocessor to deduce the average rotational transform from a field-line tracing. Consequently, the development of a single "fast" code that performs all aspects of the rotational transform calculations was necessary. The end product of that effort is the TORSIDO code. A discussion of this code and the techniques employed to enhance both its speed and accuracy are presented in Sec. 4.1. The accuracy of TORSIDO can be gauged by the results presented in Sec. 4.2. on code verification and benchmarking. The bulk of the magnetics effort associated with this study used TORSIDO to iterate upon and refine the four flagship design points. These flagships are a high- and low-beta version of the Modular Stellarator Reactor (MSR) and a high- and low-beta version of a torsatron; both are described in Sec. 4.3. Finally, a discussion of ways to improve the coil performance of the MSR concept using parametric studies is presented in Sec. 4.4. for the benefit of future studies. Sections 4.1. and 4.2. can be by passed if a direct continuation of the MSR reactor-design study per se is desired.

4.1. TORSIDO Code Methodology

4.1.1. Magnetic Field and Vector Potential Calculations. In developing an algorithm for calculating the vacuum magnetic field in a stellarator, the most difficult task is to provide the capability to handle the broad range of stellarator coil shapes while ensuring a reasonably high degree of accuracy. To accommodate arbitrary coil shapes, the coil geometry must be correctly specified. The prescription adopted for the TORSIDO code is that the winding

laws for all the coils are provided in the form of user-coded formulae of a single dependent variable, s. The only stipulation upon s is that it monotonically trace the current path of a coil. A winding law consists of a vector function, $\vec{P}(s)$, that defines a coil centroid; the tangent, $\vec{T}(s) \equiv d\vec{P}(s)/ds$; and a vector function, $\vec{N}(s)$, that denotes the radial direction for winding the coil and is orthogonal to $\vec{T}(s)$. A unit normal, $\hat{N}(s)$, is constructed from the normal, $\vec{N}(s)$, by the definition of a unit vector, $\hat{N}(s) \equiv \vec{N}(s)/|\vec{N}(s)|$. By restricting coil cross sections to a rectangular shape, the coil geometry is completely specified with the addition of a unit binormal, $\hat{b}(s)$, defined as

$$\hat{b}(s) \equiv \frac{\vec{T}(s) \times \hat{N}(s)}{|\vec{T}(s) \times \hat{N}(s)|} \quad . \tag{4.1-1}$$

Then, an arbitrary location, $\vec{u}$, within a coil is given by

$$\vec{u} = \vec{P}(s) + w\hat{N}(s) + \ell\hat{b}(s) \quad , \tag{4.1-2}$$

where the scalars w and ℓ denote the distances from the coil centroid measured along the normal and binormal, respectively. Note that for a coil with a cross section of dimensions δ_w by δ_ℓ, a trace of the coil edges is obtained by setting $w = \pm\delta_w/2$ and $\ell = \pm\delta_\ell/2$ in Eq. (4.1-2).

The magnetic field, $\vec{B}$, at a point $\vec{x}$ is given by the following generalization of the Biot-Savart law.[3]

$$\vec{B}(\vec{x}) = \frac{\mu_o}{4\pi} \int \frac{\vec{J}_c(\vec{u}) \times (\vec{x} - \vec{u})}{|\vec{x} - \vec{u}|^3} \, d^3u \quad , \tag{4.1-3}$$

where $\vec{J}_c(\vec{u})$ is the local conductor current density in a coil. Assumming that the current-density variations occur only through the cross section (i.e., $\vec{J}_c$ is independent of s) and the current at any point in the cross section flows

in the direction of the local tangent, $d\vec{u}/ds$, which is parallel to $\vec{T}(s)$, the vector current density is given by

$$\vec{j}_c(\vec{u}) = j_c(\ell,w) \frac{d\vec{u}/ds}{|d\vec{u}/ds|} \quad . \tag{4.1-4}$$

Using Eq. (4.1-2) and the definition of $\vec{T}(s)$, the local tangent is

$$\frac{d\vec{u}}{ds} = \vec{T}(s) + w \frac{d\hat{N}(s)}{ds} + \ell \frac{d\hat{b}(s)}{ds} \quad . \tag{4.1-5}$$

The calculation of $d\hat{N}(s)/ds$ and $d\hat{b}(s)/ds$ can be obtained numerically by a cubic spline fit[4] to $\hat{N}(s)$ and $\hat{b}(s)$. The magnetic field resulting from a single coil can be expressed as the following double integral over the cross section and a single integral along the current path

$$\vec{B}(\vec{x}) = \frac{\mu_o}{4\pi} \int d\ell \int dw \; j_c(\ell,w) \int ds \; \frac{d\vec{u}}{ds} \times \frac{(\vec{x} - \vec{u})}{|\vec{x} - \vec{u}|^3} \quad , \tag{4.1-6}$$

where the infinitesimal volume element, d^3u, has been taken to be

$$d^3u = \left|\frac{d\vec{u}}{ds}\right| ds \; d\ell \; dw \quad . \tag{4.1-7}$$

The factor $|d\vec{u}/ds|$ in Eq. (4.1-7) accounts for the variation that occurs in an infinitesimal element of arc length, measured along the local path of the current, when either ℓ or w in Eq. (4.1-2) is varied for fixed s. If a coil has no cross section [i.e., a line current with $j_c(\ell,w) = I\,\delta(\ell)\,\delta(w)$, where $\delta(\ell)$ is the Dirac delta function and I is the current flowing in the filament], then the magnetic field resulting from this single coil is given by the single integral equation

$$\vec{B}(\vec{x}) = \frac{\mu_o I}{4\pi} \int ds\ \vec{T}(s) \times \frac{(\vec{x} - \vec{u})}{|\vec{x} - \vec{u}|^3} \quad . \tag{4.1-8}$$

The total magnetic field resulting from all coils is obtained by summing the magnetic-field vectors from individual coils.

All the integrals in Eqs. (4.1-6) and (4.1-8) are performed numerically by the TORSIDO code. The vector capability of modern computers can be utilized by writing the integral of an arbitrary function, f(t), as the following dot product.

$$\int dt\ f(t) = \sum_{i=1}^{n} f(t_i)\ g_i = \vec{f} \cdot \vec{g} \quad , \tag{4.1-9}$$

where g_i and t_i are the appropriate weights and abscissas for a given quadrature integration technique and n is the number of integrand samples. Performing integrations according to Eq. (4.1-9) also permits the tabulation of the integrand, f, in vector format. The integration methods used in TORSIDO are 4th-order closed-type Newton-Cotes[5] method for the integration over s in Eqs. (4.1-6) and (4.1-8) and Gaussian quadrature[5] for the integrations over ℓ and w in Eq. (4.1-6).

The accuracy of the integration in Eq. (4.1-9) is determined by the smoothness of the integrand and by the step size, $t_{i+1} - t_i$, and hence n. Because the smoothness of the integrand in Eq. (4.1-6) is potentially a strong function of the distance between the point where the field is to be evaluated and the coil (i.e., $|\vec{x} - \vec{u}|$), the n for each of the integrations can be made a function of the distance $|\vec{x} - \vec{u}|$ without sacrificing accuracy. The monitoring of $|\vec{x} - \vec{u}|$ requires the definition of a coordinate system.

TORSIDO employs two coordinate systems: a standard Cartesian (i.e., x, y, and z) and a left-handed cylindrical (i.e., R, ϕ, and z) coordinate system. Both systems share a common origin that coincides with the center of the array of magnets to be simulated and a common z axis. The Cartesian coordinate system facilitates the writing of the winding laws [e.g., $\vec{P}(s) = P_x(s)\hat{i} + P_y(s)\hat{j} + P_z(s)\hat{k}$, using standard Cartesian notation]. The cylindrical coordinate system is a natural consequence of the assumption that

all coils are arrayed toroidally. The equatorial plane of the coil set is the $z = 0$ plane in either coordinate system. The major radius, R_T, of the coil set is then measured along the R coordinate. The toroidal angle, ϕ, is measured clockwise from the y-axis, as shown in Fig. 4.1-1. The beginning of the first field period coincides with the $\phi = 0$ plane and the end of the period with the $\phi = 2\pi/m$ plane, where m is the number of field periods. The winding laws need only be given for those coils within a field period, thereby reducing computer storage requirements. Furthermore, TORSIDO requires the winding laws be written as if the coil plane for each coil in a field period coincided with the $\phi = 0$ plane. When TORSIDO calculates the contribution to the field at the point $\vec{x}$ from a coil at a particular location around the torus, the point $\vec{x}$ is rotated by the appropriate integer multiple of $2\pi/N$, where N is the total number of coils, to simulate the same relative position of $\vec{x}$ and the coil. Deviations from equal coil spacing must be factored into the winding laws.

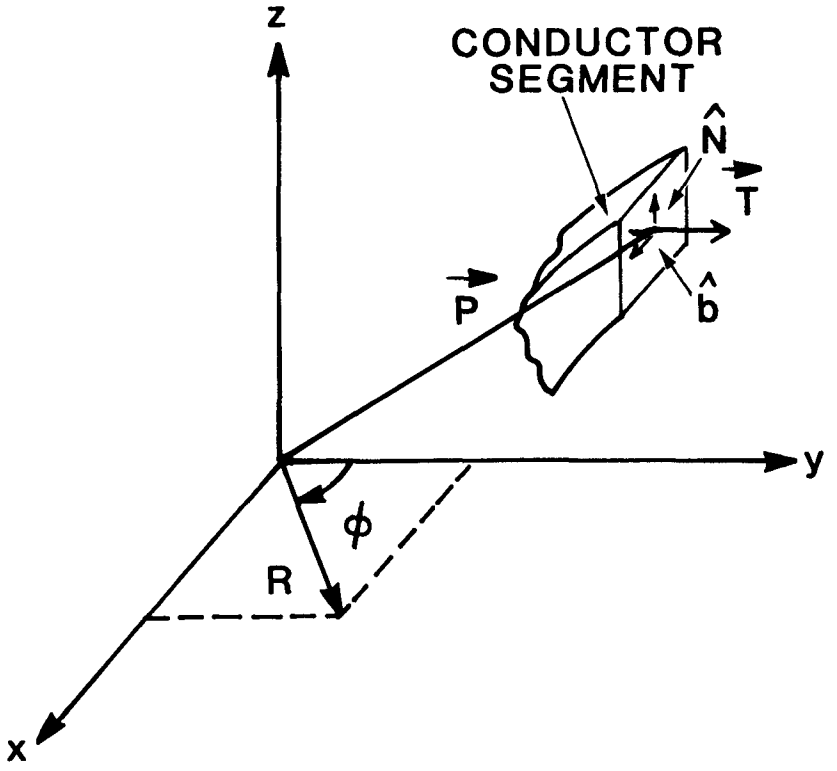

Fig. 4.1-1. The Cartesian and cylindrical coordinate systems employed by the TORSIDO vacuum magnetics code. Also shown are the vectors $\vec{P}$, $\hat{T}$, $\hat{N}$, and $\hat{b}$ for a segment of an arbitrary coil.

The cylindrical coordinate system is used for monitoring the quantity $|\vec{x} - \vec{u}|$. The point $\vec{x}$ is associated with the toroidal location of the closest toroidal-field (TF) coil, expressed as an integer multiple of $2\pi/N$. Similarily, $\vec{u}$ is assigned a toroidal location. Then $|\vec{x} - \vec{u}|$ is expressed as an integer multiple of $2\pi/N$ ranging from zero to N/2. TORSIDO requires a user-specified a set of n's for both the Gaussian quadrature and the Newton-Cotes method plus corresponding sets of integers indicating the range over which the n's are applicable, expressed as multiples of $2\pi/N$. For example, the first element of the Gaussian set of n's may be a 12 and the second element a 6, whereas the corresponding set of integers has a 0 and a 2 for the first and second elements, respectively. These sets indicate that in the calculation of the field at the location, $\vec{u}$, resulting from the coil closest to $\vec{u}$, a 12-point Gaussian quadrature is used to evaluate the integrals over ℓ and w in Eqs. (4.1-6). Then for the calculation of the field at $\vec{u}$ resulting from the next two coils on either side toroidally of the coil closest to $\vec{u}$, a 6-point Gaussian quadrature is used for the same integrals in Eq. (4.1-6). The number of elements in the sets must also be specified by the user. If the last element in the set of integers corresponding to the Gaussian set of n's is less than N/2, then Eq. (4.1-8) is used to calculate the contributions to the field at $\vec{u}$ from the remaining coils not covered by the two sets. The notation for depicting these sets is {0,2|2,6}.

In addition to the calculation of the magnetic field, the vector potential is also calculated. The general definition of the vector potential, $\vec{A}$, at the point $\vec{x}$ is given by[3]

$$\vec{A}(\vec{x}) = \frac{\mu_o}{4\pi} \int \frac{\vec{j}_c(\vec{u})}{|\vec{x} - \vec{u}|} d^3u \quad . \tag{4.1-10}$$

From the same assumptions used in deriving Eq. (4.1-6) for the magnetic field from a coil of finite cross section Eq. (4.1-10) is modified as follows

$$\vec{A}(\vec{x}) = \frac{\mu_o}{4\pi} \int d\ell \int dw \; j_c(\ell,w) \int ds \; \frac{d\vec{u}/ds}{|\vec{x} - \vec{u}|} \quad . \tag{4.1-11}$$

The vector potential resulting from a line current coil with current I is then analogously written as

$$\vec{A}(\vec{x}) = \frac{\mu_o I}{4\pi} \int ds \, \frac{\vec{T}(s)}{|\vec{x} - \vec{u}|} \quad . \tag{4.1-12}$$

All of the aforementioned techniques for evaluating the magnetic field according to Eqs. (4.1-6) and (4.1-8) apply to the vector field calculations of Eqs. (4.1-11) and (4.1-12). As with the magnetic field calculations, the total vector potential from all coils is obtained by summing the vector potential from individual coils.

4.1.2. Coil Calculations. Several calculations to aid in the design of a coil set are possible based on the capability to calculate vacuum magnetic fields and vector potentials. The following calculations are incorporated into TORSIDO: the length of the conductor, L_C; the forces acting on each coil; the peak field at the conductor, B_{CM}; and the stored energy in the entire coil set, E_M. The length of the conductor measured along the conductor's center, $\vec{P}(s)$, is given by

$$L_C = \int |d\vec{P}(s)/ds| \, ds = \int |\vec{T}(s)| ds \quad . \tag{4.1-13}$$

The electromagnetic forces calculated by TORSIDO are limited to the force per unit length resolved into its components along the tangent, normal, and binormal vectors of each coil; the net force acting on a coil resolved into its Cartesian components; and the average force along the tangent, normal, and binormal vectors. The prescription for calculating the forces is based upon the following expression for the differential force, $d\vec{F}$, acting on an infinitesimal element of volume, d^3u, located at $\vec{u}$ within the coil:[3]

$$d\vec{F}(\vec{u}) = \vec{J}_c(\vec{u}) \times \vec{B}(\vec{u}) \, d^3u \quad , \tag{4.1-14}$$

where $\vec{B}(\vec{u})$ is the magnetic field resulting from all coils. To avoid a singularity in the integrand of Eq. (4.1-6) when evaluating $\vec{B}$ within a coil

for the above equation, $|\vec{x} - \vec{u}|$ in the denominator of Eq. (4.1-6) is not permitted to be smaller than the finest spacing used for evaluating the integral along s. If the volume element is resolved into its components (i.e., $d^3u = |d\vec{u}/ds|\ ds\ d\ell\ dw$) and Eq. (4.1-4) is used for the current density, Eq. (4.1-14) becomes

$$d\vec{F}(\vec{u}) = j_c(\ell,w)\ \left\{\frac{d\vec{u}}{ds} \times \vec{B}(\vec{u})\right\} ds\ d\ell\ dw \quad . \tag{4.1-15}$$

Integrating Eq. (4.1-15) across the cross section yields

$$d\vec{F}(s) = ds \int d\ell \int dw\ j_c(\ell,w)\ \left\{\frac{d\vec{u}}{ds} \times \vec{B}(\vec{u})\right\} \quad . \tag{4.1-16}$$

Then the force per unit value of the dependent variable s is given by

$$\frac{d\vec{F}(s)}{ds} = \int d\ell \int dw\ j_c(\ell,w)\ \left\{\frac{d\vec{u}}{ds} \times \vec{B}(\vec{u})\right\} \quad . \tag{4.1-17}$$

The force per unit length, $\vec{f}$, is obtained by dividing Eq. (4.1-17) by the infinitesimal length of the conductor, $|\vec{T}(s)|$. That is,

$$\vec{f} = |\vec{T}(s)|^{-1} \int d\ell \int dw\ j_c(\ell,w)\ \left\{\frac{d\vec{u}}{ds} \times \vec{B}(\vec{u})\right\} \quad . \tag{4.1-18}$$

The components of the force per unit length along the tangent, normal, and binormal are given by

$$f_t = \vec{f} \cdot \frac{\vec{T}(s)}{|\vec{T}(s)|} \quad , \tag{4.1-19}$$

$$f_r = \vec{f} \cdot \hat{N}(s) \quad , \quad \text{and} \tag{4.1-20}$$

$$f_\ell = \vec{f} \cdot \hat{b}(s) \quad , \tag{4.1-21}$$

respectively. The Cartesian components of the net body force are given by integrating the Cartesian components of $d\vec{F}(s)/ds$ along s; i.e.,

$$F_x = \int ds \, \frac{d\vec{F}(s)}{ds} \cdot \hat{i} \quad , \tag{4.1-22}$$

$$F_y = \int ds \, \frac{d\vec{F}(s)}{ds} \cdot \hat{j} \quad , \quad \text{and} \tag{4.1-23}$$

$$F_z = \int ds \, \frac{d\vec{F}(s)}{ds} \cdot \hat{k} \quad . \tag{4.1-24}$$

Similarly, the average force along the tangent, normal, and binormal directions are given by

$$\langle F_t \rangle = \int ds \, \frac{d\vec{F}(s)}{ds} \cdot \frac{\vec{T}(s)}{|\vec{T}(s)|} \quad , \tag{4.1-25}$$

$$\langle F_r \rangle = \int ds \, \frac{d\vec{F}(s)}{ds} \cdot \hat{N}(s) \quad , \quad \text{and} \tag{4.1-26}$$

$$\langle F_\ell \rangle = \int ds \, \frac{d\vec{F}(s)}{ds} \cdot \hat{b}(s) \quad , \tag{4.1-27}$$

respectively. The convention adopted in this study is to take the normal vector to be radial, then $\langle F_r \rangle$ is analogous to the average radial force for a circular coil and $\langle F_\ell \rangle$ measures the average force acting to distort the coil away from the coil plane.

The numerical methods used for evaluating the integrals over the cross section in Eqs. (4.1-17) and (4.1-18) and along s in Eqs. (4.1-22) through (4.1-27) are the same methods employed for evaluating similar integrals over the cross section and along s appearing in the magnetic field and vector potential calculations of Eqs. (4.1-6) and (4.1-11), respectively. The number of integrand samples, n, for the cross-sectional integral and for the integral along s is taken to be the first element in the set of n for the Gaussian quadrature and Newton-Cotes methods, respectively. Hence, the calculation of the magnetic field from the coil for which the forces are to be calculated is necessarily as accurate as the resulting force calculation because there is no difference in the number of integrand samples used in calculating either the magnetic field using Eq. (4.1-6) or the force from Eq. (4.1-18).

The peak field at the conductor, B_{CM}, is calculated using Eq. (4.1-6) evaluated along the conductor surface, S, as defined by

$$\vec{S}(s,\ell) = \vec{P}(s) - \delta_w \hat{N}(s) + \ell \hat{b}(s) \quad , \tag{4.1-28}$$

where ℓ is limited to the range $-\frac{3}{8}\delta_\ell \lesssim \ell \lesssim \frac{3}{8}\delta_\ell$. The same scheme is used for choosing the locations for s and for choosing the locations for sampling the integrand of Eq. (4.1-6) along s. Only the second element of the set of n for the Newton-Cotes method is used, whereas the scheme for ℓ takes the locations corresponding to a Gaussian quadrature with twice the number of points indicated by the first element in the set of n for the Gaussian quadrature along ℓ and w in Eq. (4.1-6). The singular nature of the integrand of Eq. (4.1-6) introduces oscillations in $\vec{B}$ as the conductor surface is traversed. These oscillations are an artifact of the numerical evaluation of Eq. (4.1-6) and are most pronounced in the ℓ direction on the surface. Then, the proceedure for calculating B_{CM} is to spline fit $\vec{B}$ along s for a given ℓ and determine the maximum in the spline fit to $\vec{B}$. Because the maxima for adjacent values of ℓ may not be connected by a ridge of maxima if ℓ were permitted to vary continuously between two adjacent discrete values of ℓ, a fit to these maxima in ℓ is of no use. Consequently, B_{CM} is taken to be the largest maximum with the accuracy of B_{CM} ensured by choosing a large number of samples in ℓ.

Treating the coils as line currents to calculate the stored magnetic energy is sufficient for the purposes of this study. The stored energy in the i^{th} line-current coil is given by[3]

$$E_i = \frac{1}{2} I_i \int \vec{A}(\vec{v}) \cdot d\vec{v} \quad , \tag{4.1-29}$$

where $\vec{v}$ is the vector along the current and the vector potential, $\vec{A}(\vec{v})$, is calculated from all of the coils. Upon centering all of the current in a coil of finite cross section at the coil center, the scalar v can be replaced by s in the notation adopted for the winding law and

$$d\vec{v} = d\vec{P}(s) = \frac{d\vec{P}(s)}{ds} ds = \vec{T}(s)ds \quad . \tag{4.1-30}$$

Then, Eq. (4.1-29) becomes

$$E_i = \frac{1}{2} I_i \int \{\vec{A}(\vec{P}(s)) \cdot \vec{T}(s)\} ds \quad . \tag{4.1-31}$$

The same constraint on $|\vec{x} - \vec{u}|$ used in the calculation of $\vec{B}$ for the force calculations is used here for evaluating $\vec{A}$ within the coil. The stored energy in the entire coil set is

$$E_M = \sum_{i=1}^{N} E_i \quad , \tag{4.1-32}$$

where N is the total number of coils in the coil set. The integral in Eq. (4.1-31) is evaluated using the second element of the set of n for the Newton-Cotes method.

4.1.3. Flux Surface Calculations. The flux surface calculations include the tracing of a field line for a distance sufficient to generate a surface plus those calculations which characterize the physical and magnetic attributes of the surface. Also calculated by TORSIDO are: the volume of the flux surface; its centroid; its semimajor and semiminor radii measured under the key coil, which determines the beginning or end of a field period, and in the center of a field period; and the radius of the largest circle centered on the coil axis, which is tangent to a point on the surface without intersecting the surface elsewhere and corresponds to a poloidal limiter radius. In addition, TORSIDO calculates the following magnetics parameters for each surface: the rotational transform, ι; the magnitude of the field as measured by $\langle B \rangle^2$; and the ripple in the magnetic field, ε.

The field lines are generated from the following conditions,[6] expressed in the cylindrical coordinate system used by TORSIDO.

$$\frac{dR}{B_R} = \frac{Rd\phi}{B_\phi} \quad \text{and} \tag{4.1-33}$$

$$\frac{dz}{B_z} = \frac{Rd\phi}{B_\phi} \quad . \tag{4.1-34}$$

Equations (4.1-33) and (4.1-34) are solved simultaneously for $R(\phi)$ and $z(\phi)$ by a 4th order Adams predictor-corrector algorithm[7] with a scheme for halving or doubling the step size based upon a user-specified error tolerance band. A 4th order Runge-Kutta method[7] is used as a starter. The user also has the option of using a modified Adams method[7] (also known as the Adams-Moulton method) in place of the Adams method. However, the modified Adams method does not ensure numerical stability of the solution and was consequently not used in this study. The halving of the step size is bounded by requiring the user to specify the maximum number of uniformly spaced toroidal grid points that the code may use in solving Eqs. (4.1-33) and (4.1-34) in a toroidal range of $2\pi/N$, (i.e., between two adjacent TF coils). Similarly, the doubling of the step size is bounded by requiring the user to specify the minimum number of uniformly spaced toroidal grid points between adjacent coil planes within a field period that are to be retained in computer memory for constructing the

flux surfaces. The integer number of field periods over which Eqs. (4.1-33) and (4.1-34) are to be integrated is also user specified.

The volume, V, of a flux surface is calculated by integrating an infinitesimal volume element, d^3v, over the volume of a flux surface. Upon introducing a third, polar coordinate system (i.e., r and θ) for the cross section of a flux surface intersecting a constant ϕ plane, then

$$d^3v = rd\theta\, dr\, Rd\phi \quad . \tag{4.1-35}$$

An estimate of a local cross-sectional centroid, R_o, can be made by averaging the radial locations of the field lines in a cross section; then

$$R = R_o + r \cos \theta \quad . \tag{4.1-36}$$

Integrating Eq. (4.1-35) for the volume yields

$$V = \int d\phi \int d\theta\, r^2(\theta,\phi) \left\{\frac{R_o(\phi)}{2} + \frac{r(\theta,\phi)}{3} \cos \theta\right\} \quad , \tag{4.1-37}$$

where the dependencies of r and R_o upon θ and ϕ have been expressed explicitly and the integral over r has been performed analytically. The integral over θ is done numerically by TORSIDO using the trapezoidal rule[5] in case the cross section has a irregular shape. The user has the option of invoking top-bottom symmetry about the middle of a field period that is applicable for some winding laws to double the number of integrand samples for the θ integration. The integration over ϕ is performed by integrating a cubic spline fit[4] to the results of the θ integrations as a function of ϕ.

The centroid, $\langle R \rangle$, is obtained by averaging R over the volume in accordance with

$$\langle R \rangle = V^{-1} \int R d^3v \quad . \tag{4.1-38}$$

If Eq. (4.1-36) is used, analytical integration over r modifies Eq. (4.1-38) to the form

$$\langle R \rangle = V^{-1} \int d\phi \int d\theta \; r^2(\theta,\phi)$$

$$\left\{ \frac{R_o^2(\phi)}{2} + \frac{2}{3} r(\theta,\phi) R_o(\phi) \cos\theta + \frac{r^2(\theta,\phi)}{4} \cos^2\theta \right\}. \qquad (4.1\text{-}39)$$

The same numerical techniques for integrating Eq. (4.1-37) are used by TORSIDO for integrating Eq. (4.1-39).

An average plasma minor radius, r_p, can be obtained from V and $\langle R \rangle$ by

$$r_p = \left[\frac{V}{2\pi^2 \langle R \rangle} \right]^{1/2} , \qquad (4.1\text{-}40)$$

which is consistent with the reactor modeling assumption for Sec. 3.4. for a plasma torus of circular cross section. The semimajor and semiminor radii are calculated under the key coil and in the center of a field period by searching for the R and z extrema of the field-line locations previously stored for the appropriate constant ϕ planes. The limiter radius is calculated by searching for the r extremum of the field line locations previously stored for all the constant ϕ planes using the major radius of the coil set as the polar coordinate origin.

The rotational transform, ι, is obtained by calculating the ϕ-θ history of a field line only from its intersections with the coil plane under the key coil. A cubic spline fit[4] is then made of ϕ as a function of θ. Because the cubic spline fit is least accurate near the end points of the θ range, the last two points in θ are discarded for the ι calculation. The integer number, I_{pr}, of poloidal revolutions of the field line in the shorter, more accurate θ range is calculated. Then the rotational transform is calculated as

$$\iota = \frac{2\pi I_{pr}}{\phi(2\pi I_{pr} + \theta_o) - \phi(\theta_o)} , \qquad (4,1\text{-}41)$$

where θ_o is the first θ point in the ϕ-θ history. A second calculation of ι is performed for purposes of checking the accuracy of the above calculation. The second calculation drops the first two points in θ in addition to the last two. Then, a second number, I'_{pr}, of poloidal revolutions is calculated and the transform is calculated as

$$\iota = \frac{2\pi I'_{pr}}{\phi(2\pi I'_{pr} + \theta_1) - \phi(\theta_1)} , \qquad (4.1\text{-}42)$$

where θ_1, is the third θ point in the ϕ-θ history. A comparison of the results of Eqs. (4.1-41) and (4.1-42) will reveal as a minimum (i.e., $I_{pr} = I'_{pr}$) the effect of staggering the starting location in the ι measurement and as a maximum (i.e., $I_{pr} = I'_{pr} + 1$) the effect of changing the field line length over which ι is measured.

A number of methods exist for measuring the magnitude of the magnetic field on a flux surface. The method[8] adopted here is

$$\langle B \rangle^2 = \frac{\int B d\ell}{\int d\ell / B} . \qquad (4.1\text{-}43)$$

The expressions for $\int B d\ell$ and $\int d\ell/B$ are obtained by integrating the following equations along a field line trajectory simultaneously with Eqs. (4.1-33) and (4.1-34):

$$\frac{d\ell}{B} = \frac{R d\phi}{B_\phi} \quad \text{and} \qquad (4.1\text{-}44)$$

$$B d\ell = \frac{B^2 R d\phi}{B_\phi} . \qquad (4.1\text{-}45)$$

The integrals over the field line length, ℓ, in Eq. (4.1-43) are performed over the same toroidal range as that used in the calculation of ι by Eq. (4.1-41). Obtaining the same toroidal range is accomplished by fitting a

cubic spline[4] to the integration results of $\int Bd\ell$ and $\int d\ell/B$ parameterized as functions of the length of integration expressed in increments of $2\pi/m$. The above method insulates the results for Eq. (4.1-43) from variations in $\int Bd\ell$ and $\int d\ell/B$ that occur within a field period.[9] The <B> profile is often distilled into a single parameter termed "well depth," which is calculated here as $\left(<B(r = 0)>/<B(r = r_p)>\right) - 1$.

The ripple, ε, on a magnetic surface is found by keeping track of the extrema in the local magnetic field along its entire trajectory. The definition of the ripple adopted here is computed[10] as

$$\varepsilon = \frac{B_{MAX} - B_{MIN}}{B_{MAX} + B_{MIN}} \quad , \tag{4.1-46}$$

where the subscripts "MAX" and "MIN" denote the maximum and minimum values of B encountered along the field line.

4.2. TORSIDO Code Verification/Benchmarking

Among the best methods for verifying a code is the comparison of code-generated results with a separate analytic calculation. An applicable analytic problem for benchmarking TORSIDO is the calculation of the magnetic field along the coil axis resulting from a planar, circular hoop current. The corresponding analytic expression is given by[3]

$$B(z) = \frac{\mu_o I r_c^2}{2(r_c^2 + z^2)^{3/2}} \quad , \tag{4.2-1}$$

where r_c is the radius of the hoop, I is the current in the hoop, and z is the distance from the coil plane. To exercise fully the capabilities of TORSIDO, the code should simulate a coil that has been rotated 45^o about the y-axis, corresponding to a laterally distorted coil with a poloidal periodicity, $\ell = 1$. The winding law for such a coil is given by the Cartesian components of $\vec{P}(\theta)$:

$$P_x(\theta) = 2^{-1/2}\, r_c \sin\theta \quad , \tag{4.2-2A}$$

$$P_y(\theta) = R_T - r_c \cos\theta \quad , \quad \text{and} \tag{4.2-2B}$$

$$P_z(\theta) = 2^{-1/2}\, r_c \sin\theta \quad . \tag{4.2-2C}$$

The components of $\vec{T}(\theta)$ are

$$T_x(\theta) = 2^{-1/2}\, r_c \cos\theta \quad , \tag{4.2-2D}$$

$$T_y(\theta) = r_c \sin\theta \quad , \quad \text{and} \tag{4.2-2E}$$

$$T_z(\theta) = 2^{-1/2}\, r_c \cos\theta \quad ; \tag{4.2-2F}$$

and the components of $\vec{N}(\theta)$ are

$$N_x(\theta) = P_x(\theta) \quad , \tag{4.2-2G}$$

$$N_y(\theta) = -\, 2^{1/2}\, T_z(\theta) \quad , \quad \text{and} \tag{4.2-2H}$$

$$N_z(\theta) = P_z(\theta) \quad . \tag{4.2-2I}$$

In Eq. (4.2-2) the poloidal angle, θ, is measured clockwise from the equatorial plane on the inboard side of the coil. The introduction of a coil-center major radius, R_T, into Eq. (4.2-2) does not affect the calculation. The field is then calculated for I = 4.42 MA, r_c = 5.4 m, and R_T = 23.24 at $z = r_c$ in Eq. (4.2-1) and at $z = 2^{-1/2} r_c$ and $x = 2^{-1/2} r_c$ in TORSIDO; and the results are presented in Table 4.2-1 for two values of the number, n, of integrand samples used in evaluating Eq. (4.1-8). Excellent agreement between TORSIDO and the analytic expression is found for the hoop current problem.

An analytic expression can be generated for the same problem but for a coil of finite cross section. Replacing the current in Eq. (4.2-1) with $I = j_c dz dr$ and integrating over the coil cross section yield

$$B(z) = \frac{\mu_o j_c}{2}\left\{(z + \ell/2)\ell n\left[\frac{r_c + \ell/2 + [(r_c + \ell/2)^2 + (z + \ell/2)^2]^{1/2}}{r_c - \ell/2 + [(r_c - \ell/2)^2 + (z + \ell/2)^2]^{1/2}}\right]\right.$$

$$\left.+(z - \ell/2)\ell n\left[\frac{r_c - \ell/2 + [(r_c - \ell/2)^2 + (z - \ell/2)^2]^{1/2}}{r_c + \ell/2 + [(r_c + \ell/2)^2 + (z - \ell/2)^2]^{1/2}}\right]\right\} , \quad (4.2\text{-}3)$$

where the coil cross section is $\ell \times \ell$ and the current density is $j_c = I/\ell^2$. The results for the same case as in Table 4.2-1, but for a finite cross-section coil are presented in Table 4.2-2 for various values of the numbers, n_N and n_G, of integrand samples used by the Newton-Cotes and Gaussian quadrature methods, respectively, in evaluating Eq. (4.1-6). Although the agreement between TORSIDO and the analytic expression for the coil of finite cross section is not as good as that for the hoop current case, the agreement

TABLE 4.2-1

BENCHMARKING TORSIDO AGAINST THE ANALYTIC RESULT FOR A PLANAR, CIRCULAR HOOP CURRENT

	B(T)	
n	TORSIDO	ANALYTIC
33	1.81829098024634	1.81829098024630
65	1.81829098024632	

TABLE 4.2-2

BENCHMARKING TORSIDO AGAINST THE ANALYTIC RESULT FOR A PLANAR, CIRCULAR COIL OF FINITE CROSS SECTION

		B(T)	
n_N	n_G	TORSIDO	ANALYTIC
65	3	1.8208498806419	1.8205220555514
65	6	1.8208498760041	
65	12	1.8208498760039	

is more than sufficient for the calculations TORSIDO was designed to perform. The major source of the discrepancy is that $d\hat{N}/ds$ and $d\hat{b}/ds$ in Eq. (4.1-5) are calculated numerically.

In addition to comparing TORSIDO with analytic calculations, TORSIDO was benchmarked against EFFI[1] and the EBT magnetics code.[11] The results for the magnetic field in a coil plane of a set of 18 planar, circular TF coils with minor radius, r_c = 5.4 m; major radius, R_T = 23.24 m; current density, j_c = 12.9 MA/m^2; and current, I = 44.2 MA, are presented in Table 4.2-3. The winding law used by TORSIDO for this calculation is given by

$$P_x(\theta) = 0 \quad , \tag{4.2-4A}$$

$$P_y(\theta) = R_T - r_c \cos\theta \quad , \tag{4.2-4B}$$

$$P_z(\theta) = r_c \sin\theta \quad , \tag{4.2-4C}$$

$$T_x(\theta) = 0 \quad , \tag{4.2-4D}$$

$$T_y(\theta) = r_c \sin\theta \quad , \tag{4.2-4E}$$

$$T_z(\theta) = r_c \cos\theta \quad , \tag{4.2-4F}$$

$$N_x(\theta) = 0 \quad , \tag{4.2-4G}$$

$$N_y(\theta) = - T_z(\theta) \quad , \text{ and} \tag{4.2-4H}$$

$$N_z(\theta) = T_y(\theta) \quad . \tag{4.2-4I}$$

The poloidal coordinate system of Eq. (4.2-2) is used in Eq. (4.2-4). The Gaussian set of n has been taken to be {1|3} and for the Newton-Cotes set, {1,2,9|65,33,17}. The coils are constructed of 45 rectilinear blocks for the EFFI results. The EBT code used a 6 × 6 hoop current grid for the calculation.

The differences between the EBT and TORSIDO results are very small and result from numerical methods of essentially different order for integrating over the cross section; the EBT code uses a less accurate method. The differences between EFFI and TORSIDO results are ~1.5%, and are acceptable. These differences arise from the EFFI requirement that all coils be

TABLE 4.2-3

A CODE COMPARISON OF FIELDS IN A TF COIL SET

R	B(T)		
(m)	EFFI	TORSIDO	EBT
19.50	10.922	10.766	10.753
21.00	8.524	8.432	8.438
22.50	7.700	7.623	7.628
23.25	7.511	7.433	7.438
24.00	7.446	7.361	7.366
25.50	7.848	7.721	7.726
27.00	10.122	9.842	9.824

constructed from blocks of current that may overlap each other and represent a linear approximation to a curve.

A second code comparison was made betwen EFFI and TORSIDO for a laterally distorted TF coil set. The results for the magnetic field under a key coil are presented in Table 4.2-4 for a set of N = 18 Rehker-Wobig[12] coils configured with a poloidal periodicity, ℓ = 2; a toroidal periodicity, m = 6; a sinusoidal lateral distortion, $d = 0.4r_c$; R_T = 23.24 m; r_c = 5.4 m; j_c = 12.9 MA/m^2; and I = 44.2 MA. The winding law used by TORSIDO is

$$P_x(\theta) = d \sin(\ell\theta + 2\pi mi/N) \quad , \tag{4.2-5A}$$

$$P_y(\theta) = R_T - r_c \cos\theta \quad , \tag{4.2-5B}$$

$$P_z(\theta) = r_c \sin\theta \quad , \tag{4.4-5C}$$

$$T_x(\theta) = \ell d \cos(\ell\theta + 2\pi mi/N) \quad , \tag{4.2-5D}$$

$$T_y(\theta) = r_c \sin\theta \quad , \tag{4.2-5E}$$

$$T_z(\theta) = r_c \cos\theta \quad , \tag{4.2-5F}$$

$$N_x(\theta) = 0 \quad , \tag{4.2-5G}$$

$$N_y(\theta) = -T_z(\theta) \quad , \quad \text{and} \tag{4.2-5H}$$

$$N_z(\theta) = T_y(\theta) \quad , \tag{4.2-5I}$$

where i denotes the number of the coil within a toroidal field period and $1 \leq i \leq N/m$. The key coil corresponds to i = 0 or i = N/m. The Gaussian and Newton-Cotes sets of n for this calculation are {1|3} and {1,2,9|65,33,17}, respectively. For the EFFI results, the coils are constructed of 91 blocks. The differences between EFFI and TORSIDO results for this case are ~1%, reflecting an increased resolution of the coils used by EFFI compared to the resolution used for generating Table 4.2-3.

TABLE 4.2-4

A CODE COMPARISON OF FIELDS IN A LATERALLY DISTORTED TF COIL SET

R	B_ϕ(T)		B_z(T)	
(m)	EFFI	TORSIDO	EFFI	TORSIDO
21.64	7.5314	7.5537	-1.2493	-1.2637
21.84	7.4663	7.4788	-1.0797	-1.0946
22.04	7.4068	7.4094	-0.9153	-0.9309
22.24	7.3519	7.3450	-0.7551	-0.7714
22.44	7.3011	7.2850	-0.5980	-0.6153
22.64	7.2540	7.2291	-0.4433	-0.4618
22.84	7.2102	7.1771	-0.2903	-0.3101
23.04	7.1697	7.1288	-0.1382	-0.1597
23.24	7.1326	7.0844	0.0134	-0.0100
23.44	7.0988	7.0439	0.1654	0.1398
23.64	7.0689	7.0074	0.3181	0.2900
23.84	7.0431	6.9755	0.4724	0.4414
24.04	7.0220	6.9484	0.6288	0.5946
24.24	7.0064	6.9268	0.7881	0.7502
24.44	6.9970	6.9115	0.9511	0.9090
24.64	6.9951	6.9033	1.1186	1.0719
24.84	7.0018	6.9034	1.2919	1.2399
25.04	7.0187	6.9132	1.4721	1.4141
25.24	7.0479	6.9345	1.6607	1.5961
25.44	7.0918	6.9695	1.8598	1.7874
25.64	7.1532	7.0209	2.0716	1.9903

The results of radial force per unit length calculations are presented in Table 4.2-5 for the same case as that in Table 4.2-4. The differences between the EFFI and TORSIDO results are ~4%. The force per unit length along the current, f_t, was calculated by TORSIDO to be <0.01 MN/m. Because f_t should equal zero, then 0.01 MN/m represents a lower bound on the accuracy of the f_r and f_ℓ calculations performed by TORSIDO. The reason f_t is not zero is that $d\hat{N}/ds$ and $d\hat{b}/ds$ in Eq. (4.1-5) are calculated numerically.

The rotational transform calculations were verified first for the special case of a rational surface where ι is known. Agreement to five significant digits was observed. In the course of this study, several chance computational encounters of rational surfaces occurred. They all displayed five significant digit accuracy. However, this result should not be regarded as a general accuracy test because the results of ι in both Eqs. (4.1-42) and (4.1-43) agree to five significant digits only for these special surfaces. For the input parameters used in this study, the two calculations generally agree to three significant digits. Consequently, TORSIDO was benchmarked against the EFFI result for the interim MSR design point of Ref. 13 and reproduced the numerical result of $\iota = 0.15$ to the two significant digits reported there. In addition, every MSR case run by TORSIDO includes an analytic calculation of ι.[13] These results are presented as part of the TORSIDO calculations in Sec. 4.3.2.1. and 4.4. Agreement with the analytic calculation becomes poorer as ι increases, which is caused by breakdown of the approximations made in the analytic formulation. Consequently, the analytic formula for ι is not a good benchmark.

TABLE 4.2-5

A CODE COMPARISON OF FORCES IN A LATERALLY DEFORMED TF COIL SET

Poloidal Angle (Radians)	f_r (MN/m)	
	EFFI	TORSIDO
0	169.80	164.46
$\pi/2$	144.29	148.77
π	135.90	132.80
$3\pi/2$	144.23	148.76
2π	169.80	164.46

The calculation of the magnetic field strength, $\langle B \rangle$, on a surface could only be benchmarked against the magnetic field calculated at various points on or near the surface. Agreement to within the ripple, ε, on the surface was found, thereby crudely verifying both $\langle B \rangle$ and ε calculations.

4.3. Design Point Selection

4.3.1. Ground Rules/Philosophy. The selection of design points should be made ideally upon the basis of orbit and equilibrium/stability calculations. Because both types of calculations are beyond the resources of this study, the design points must be selected upon the basis of vacuum-magnetics calculations and whatever guidance can be obtained from experimental and theoretical efforts. The sources of the guidance followed here included published literature,[14] private communications from the Advanced Toroidal Facility (ATF) group at Oak Ridge National Laboratory, and the US-EURATOM survey report.[15] The guidance so accumulated has resulted in a set of ground rules discussed below.

The existence of closed magnetic surfaces free of magnetic islands is essential to both energy and particle confinement. The introduction of plasma cannot be expected to improve flux surface quality. Consequently, the vacuum magnetics should display closed magnetic surfaces free of islands. The presence of rational-q surfaces ($q \equiv \iota^{-1}$) within the plasma volume can adversely affect stability and transport. Two approaches circumvent this problem as evidenced[15] by the Wendelstein VII-A and Heliotron-E experiments. The former possesses a flat transform profile and a magnetic well, whereas the latter has strong positive shear (i.e., $d\iota/dr > 0$) in the vicinity of rational surfaces and a magnetic hill. This study adheres to a philosophy based on a desire for the strong positive shear, but it also makes every attempt to avoid the major rational-q surfaces by seeking the following ranges for ι:

$$1 < \iota \quad , \tag{4.3-1A}$$

$$1/2 < \iota < 1 \quad , \quad \text{and} \tag{4.3-1B}$$

$$1/3 < \iota < 1/2 \quad . \tag{4.3-1C}$$

The value of the vacuum transform sought from a coil set can be related to the

average plasma beta, $\langle\beta\rangle$, at which a plasma of major radius, R_T, and minor radius, r_p, is expected to operate by (see Sec. 3.2.)

$$\iota \simeq \left(\frac{R_T \langle\beta\rangle}{r_p}\right)^{1/2} \quad . \tag{4.3-2}$$

Because Eq. (4.3-2) is viewed as accurate to within a factor of 2, it is imposed here as a goal which need not be met strictly.

In addition to the above physics considerations, several general engineering ground rules need to be imposed. The assumption of a 4-K, pool boiling, He-cooled, superconducting Nb_3Sn technology precludes a peak field, B_{CM}, anywhere in the conductor in excess of 12 T. The conductor designs reported in Sec. 5.2. limit the average conductor current density, $j_c \leq 19$ MA/m^2. The shielding requirements of the coils necessitate a clearance between the plasma and the conductor of at least 0.9 m. Cost, construction, and maintenance considerations led to the adoption of a design philosophy that emphasizes simplicity, which in turn prohibits the use of auxiliary coils for either torsatron or MSR designs. In addition, the coils have a circular bore and are "identical." Finally, the winding laws must be realistic; that is, the radius of curvature in any bend of a coil must be greater than half of the coil thickness.

4.3.2. Modular Stellarators. One winding law for modular stellarators that complies with the above design philosophy is given by

$$P_x(\theta) = r_c \sum_{i=1}^{6} a_i \sin\{i(\ell\theta + 2\pi mj/N)\} \quad , \tag{4.3-3A}$$

$$P_y(\theta) = R_T - r_c \cos\theta \quad , \tag{4.3-3B}$$

$$P_z(\theta) = r_c \sin\theta \quad , \tag{4.3-3C}$$

$$T_x(\theta) = r_c \sum_{i=1}^{6} i\ell a_i \cos\{i(\ell\theta + 2\pi mj/N)\} \quad , \tag{4.3-3D}$$

$$T_y(\theta) = r_c \sin\theta \quad , \tag{4.3-3E}$$

$$T_z(\theta) = r_c \cos\theta \quad , \tag{4.3-3F}$$

$$N_x(\theta) = 0 \quad , \tag{4.3-3G}$$

$$N_y(\theta) = - T_z(\theta) \quad , \quad \text{and} \tag{4.3-3H}$$

$$N_z(\theta) = T_y(\theta) \quad . \tag{4.3-3I}$$

In Eqs. (4.3-3), ℓ is the number of poloidal field periods, m is the number of toroidal field periods, R_T is the major radius, r_c is the coil minor radius, N is the number of coils, a_i are the harmonic coefficients of the lateral distortion, and j denotes a coil position within a field period. All that remains is choosing ℓ, m, R_T, r_c, N, and the a_i coefficients on the basis of a design rationale.

4.3.2.1. Modular Stellarator Sensitivity Studies. A series of sensitivity studies were performed to aid in the selection of the magnetics design parameters. These sensitivity studies were performed about the base case presented in Table 4.3-1. This base case possesses no particular significance other than representing an early iteration with $\langle\beta\rangle = 0.04$ at $P_{TH} = 4$ GWt. Because it is close in parameter space to the MSR performance goal, the trends displayed about the base case should be applicable for the final reactor designs.

TABLE 4.3-1

MSR BASE-CASE DESIGN PARAMETERS FOR SENSITIVITY STUDIES

PARAMETER	VALUE
Number of poloidal field periods, ℓ	2
Number of toroidal field periods, m	4
Major toroidal radius, R_T (m)	25
Coil minor radius, r_c (m)	4.42
Number of coils, N	36
Lateral distortion coefficients:	
a_1	0.22
$a_i (i = 2, 3 \ldots, 6)$	0
Current per coil, I (MA)	21.35
Conductor current density, j_c (MA/m^2)	19.0
Conductor cross section shape	square

The first parameter investigated for selection is ℓ. The results of changing ℓ from two to three are presented in Figs. 4.3-1 through 4.3-3. A comparison of the $\ell = 2$ flux surfaces in Fig. 4.3-1 with those for $\ell = 3$ in Fig. 4.3-2 reveals the $\ell = 3$ case better utilizes the volume within the coil bore. The lateral forces, f_ℓ, and the conductor peak field, B_{CM}, depicted in Fig. 4.3-3 are larger, however for the $\ell = 3$ case because of a decreased half-width of an individual (lateral) distortion peak and a decreased distance between distortion peaks. However, the critical factor in choosing ℓ is the rotational transform, ι, profile. For $\ell \geq 3$, the on-axis value of ι is nearly zero, resulting in an ι profile which passes through one or more of the major rational q surfaces [see (Eq. 4.3-1)], depending on the value of $\langle\beta\rangle$ [Eq. (4.3-2)] chosen. Consequently, the selection of an $\ell = 2$ design is required by the ground rules of this study, following the work of Ref. 13.

The effects of varying m are displayed in Figs. 4.3-4 through 4.3-6. One of the most striking effects in changing from $m = 3$ to $m = 9$ is the change in the shape of the flux surfaces, as seen in Figs. 4.3-4 and 4.3-5, respectively. The outer flux surfaces for $m = 3$ are highly elongated and of an irregular shape, suggesting that the corresponding $m = 2$ case may have islands. In sharp contrast, the flux surfaces for $m = 9$ display very little elongation, being very nearly circular; a better utilization of the volume within the coil results. The only other major differences resulting from changing m are in the ε and ι profiles in Fig. 4.3-6. Changing the value of m appears to be a very effective method of obtaining a desired level of ι. The consequences upon ε and the implications for orbit calculations are a concern, but this issue has not precipitated a constraint on ε in this study. However, the correlation between high ε and high B_{CM} provides an implied constraint on ε through the condition that $B_{CM} \lesssim 12$ T.

Parameterizations intended to illustrate the effects of varying the coil aspect ratio can be obscured by toroidal effects on the field or changes in coil spacing. This effect has been avoided in the coil-aspect-ratio variations presented in Figs. 4.3-7 through 4.3-9 by requiring that N/R_T be held constant. The flux surfaces for $R_T = 30.555$ m in Fig. 4.3-7 are more elongated than those for $R_T = 11.111$ m in Fig. 4.3-8, reflecting a higher rotational transform. This pronounced correlation between high transform and highly elongated flux surfaces pervades the MSR results, including the many unreported cases examined in the course of this study. It should be noted

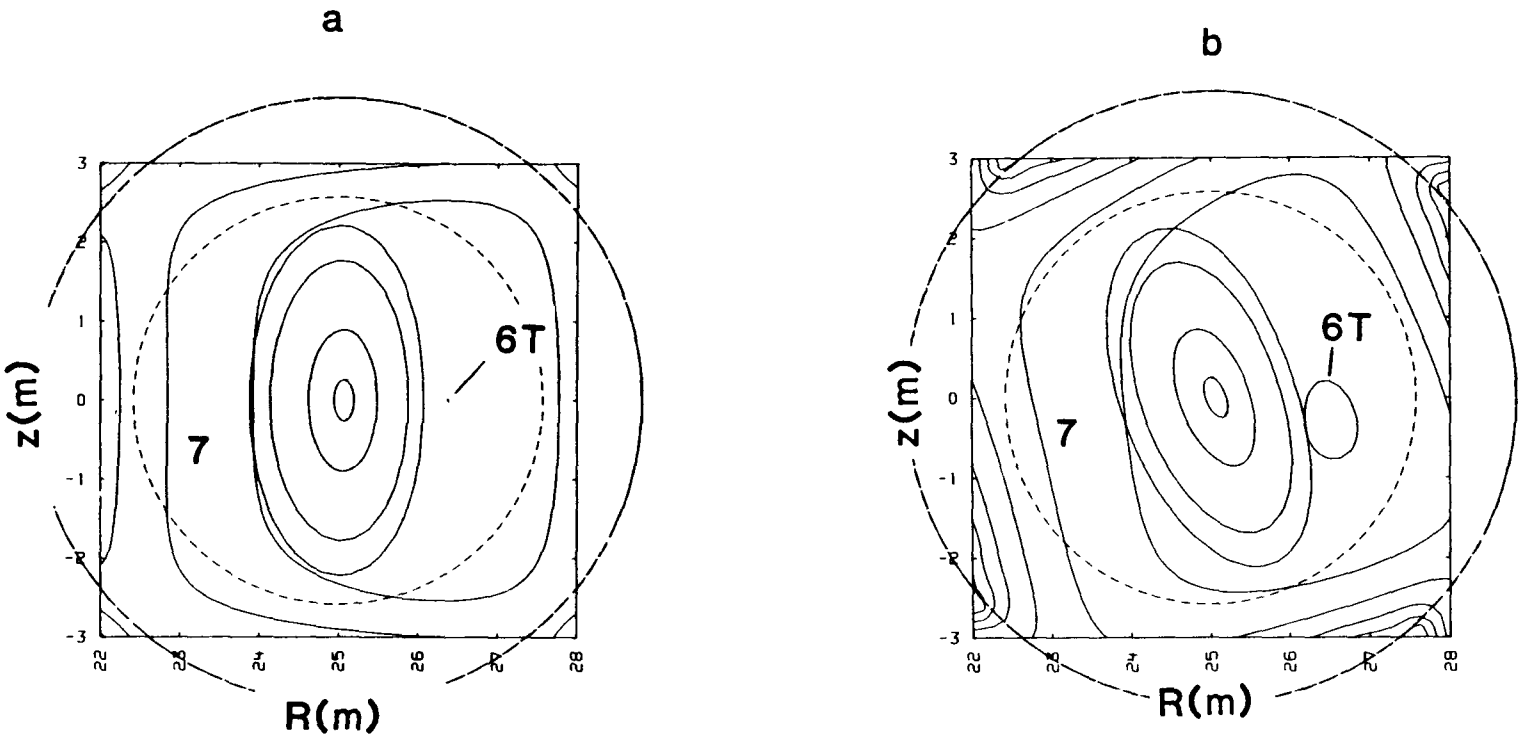

Fig. 4.3-1. The flux surfaces for $\ell = 2$ as viewed in constant-ϕ cross sections (frames a-g) and from above the equatorial plane. The outer and inner bores of the FW/B/S appear as dashed lines in cross sections and as solid lines in the equatorial-plane view. The outer bore of the FW/B/S is determined by using an engineering current density, $j_c = 15.2$ MA/m^2, which includes a small ($\lesssim$ 0.1 m) provision for a coil casing. The FW/B/S thickness is nominally 1.25 m. The flux surfaces appear as solid lines in the cross sections and as dashed lines in the equatorial-plane view. Mod-B contours in increments of 0.5 T are included in all the frames. The portions of the corners of a coil above the equatorial plane are drawn as solid lines in the equatorial plane and those below, as dotted lines. Frame a corresponds to $\phi = 0$; b, to $\pi/18$; c, to $\pi/9$; d, to $\pi/6$; e, to $2\pi/9$; f, to $\pi/4$; and g, to $5\pi/18$.

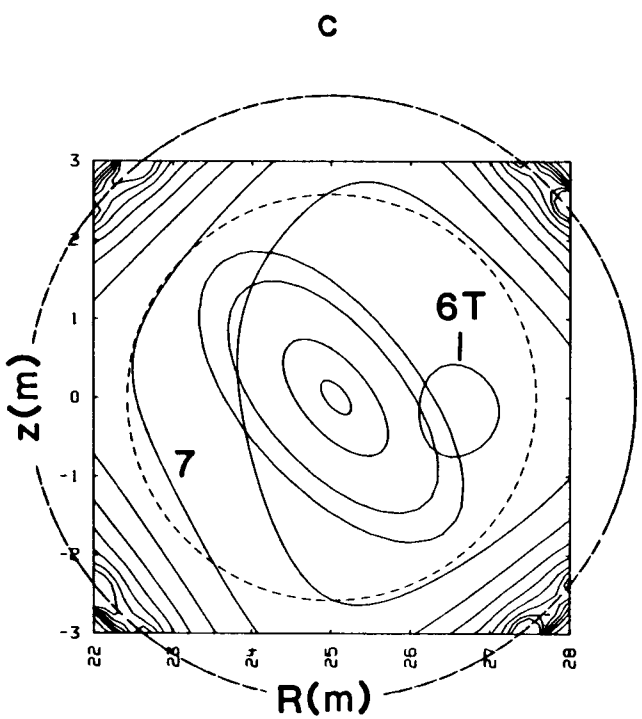

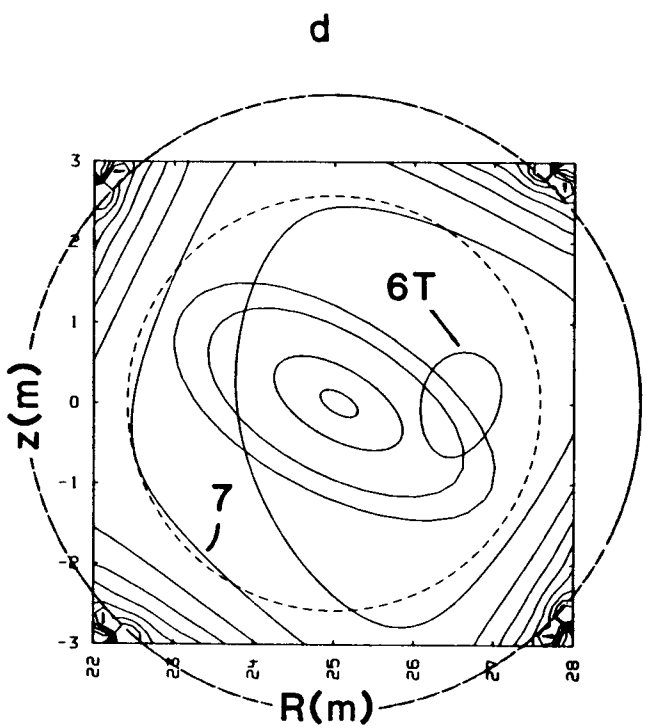

Fig. 4.3-1. (contd)

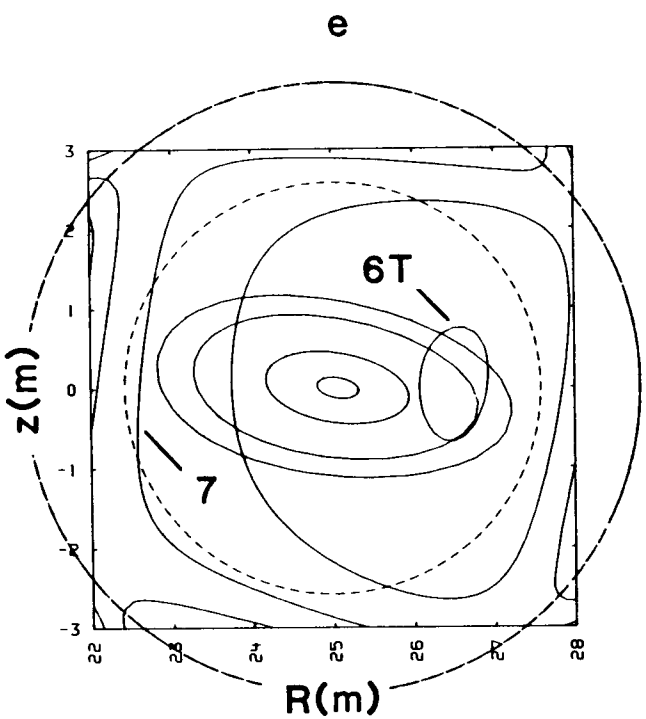

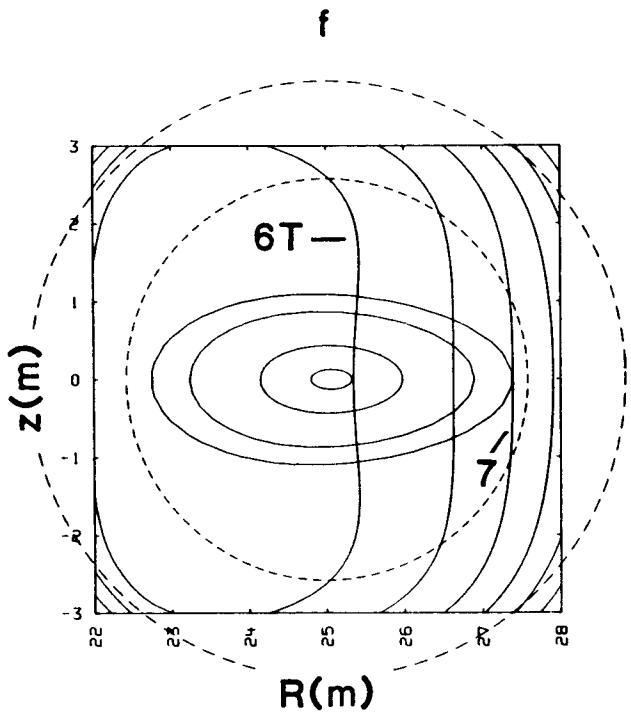

Fig. 4.3-1. (contd)

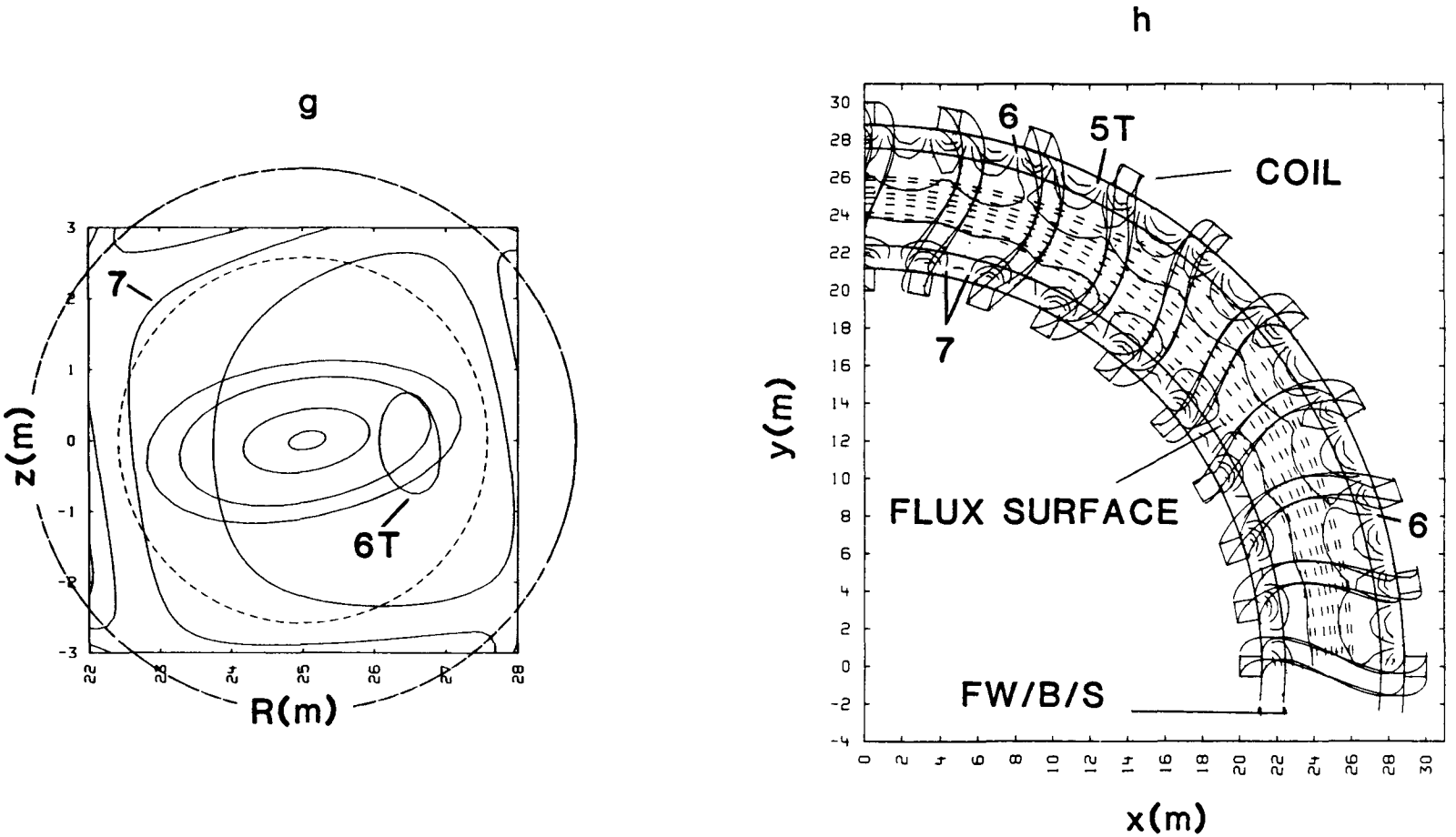

Fig. 4.3-1. (contd)

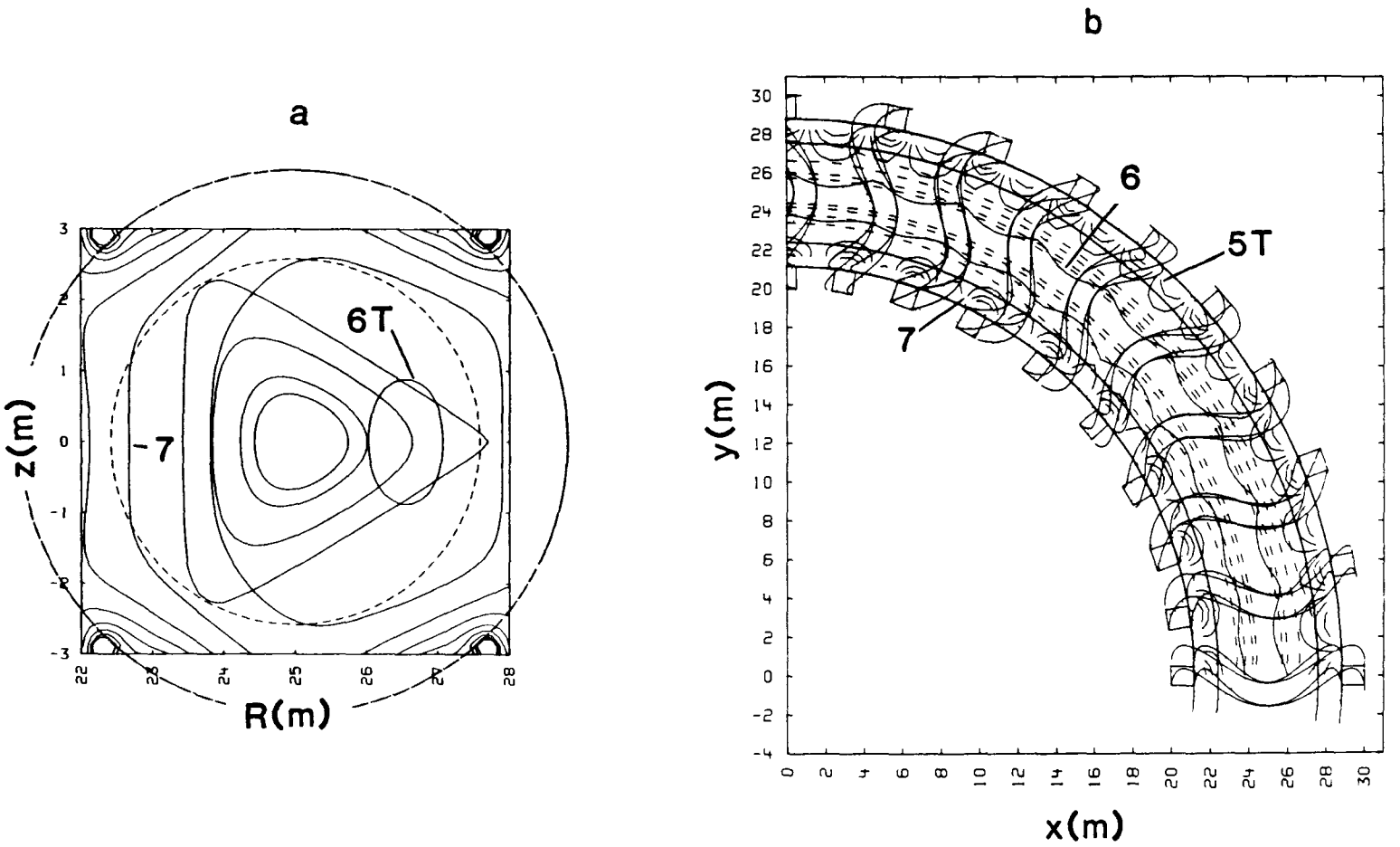

Fig. 4.3-2. The flux surfaces for $\ell = 3$ as viewed in the cross section under the key coil (frame a), corresponding to $\phi = 0$, and from above the equatorial plane (frame b). The same plotting conventions used in Fig. 4.3-1 are used here.

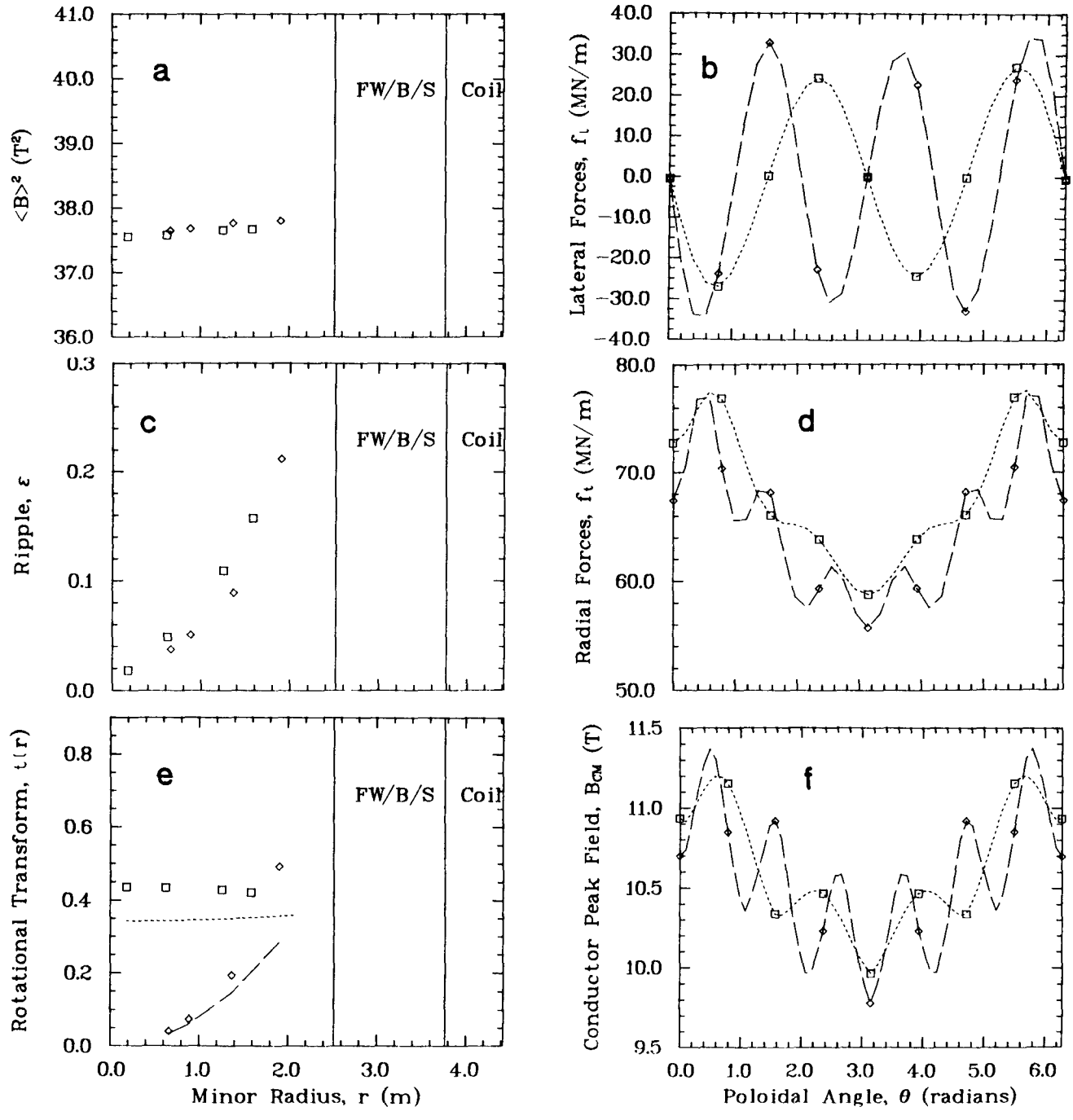

Fig. 4.3-3. A comparison of parameters measuring plasma and coil performance for ℓ = 2 (squares and dashed lines) and ℓ = 3 (diamonds and chain-dotted lines). A 1.25-m-thick FW/B/S, a 0.125-m-thick coil casing, and half of the conductor are included in frames a, c, and e for scaling purposes. The results of analytic calculations of $\iota^{1/3}$ are included in frame e as a dashed line for ℓ = 2 and a chain-dotted line for ℓ = 3. The poloidal angle in frames b, d, and f is measured clockwise along the coil beginning at the inboard side of the coil at the equatorial plane. Only the results for the key coil [j = 0 or j = N/m in (Eq. 4.3-3)] are presented in frames b, d, and f.

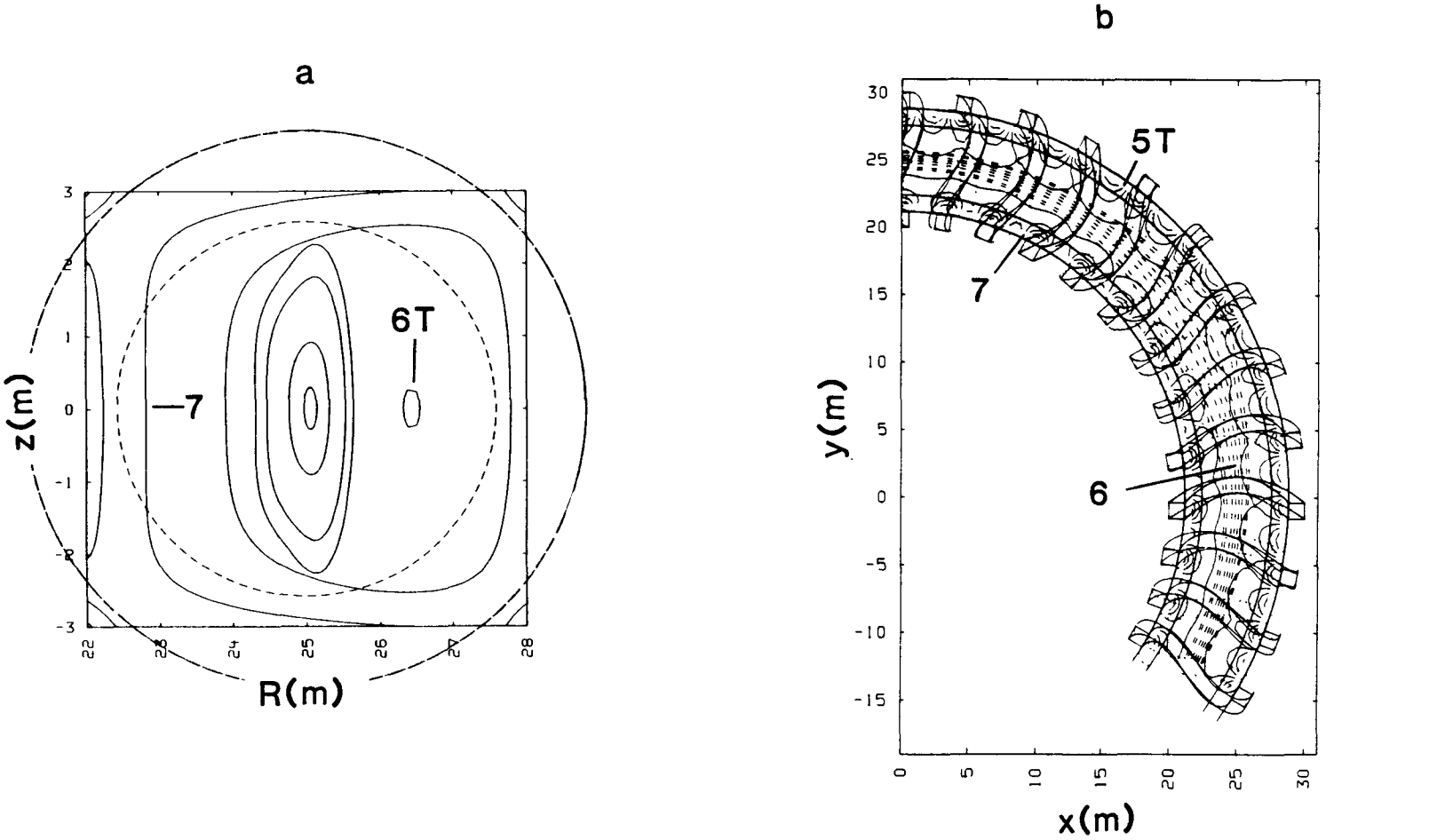

Fig. 4.3-4. The flux surfaces for m = 3 as viewed in the cross section under the key coil (frame a), corrrsponding to ϕ = 0, and from above the equatorial plane (frame b). The same plotting conventions used in Fig. 4.3-1 are used here.

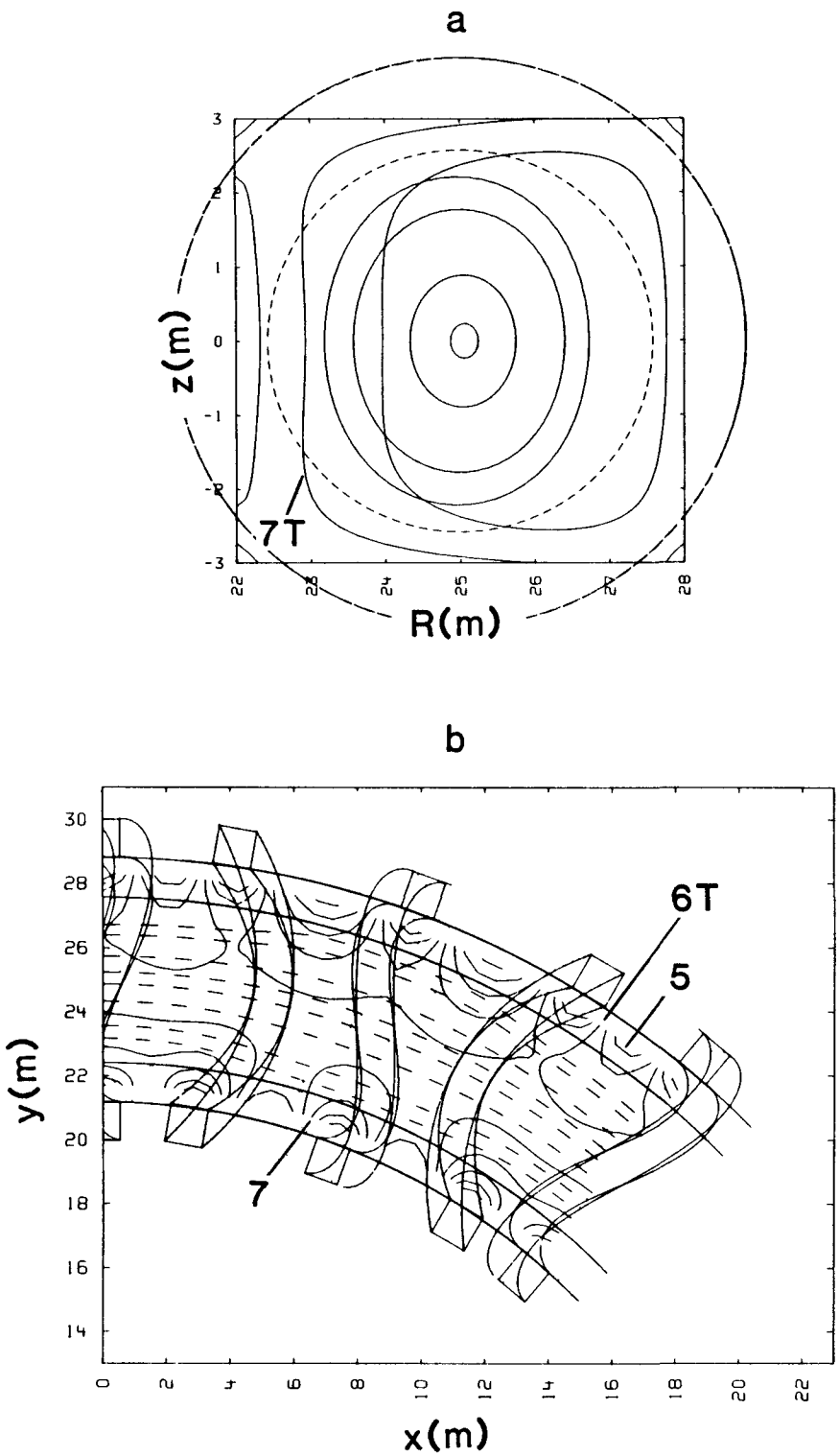

Fig. 4.3-5. The flux surfaces for m = 9 as viewed in the cross section under the key coil (frame a), corresponding to $\phi = 0$, and from above the equatorial plane (frame b). The same plotting conventions used in Fig. 4.3-1 are used here.

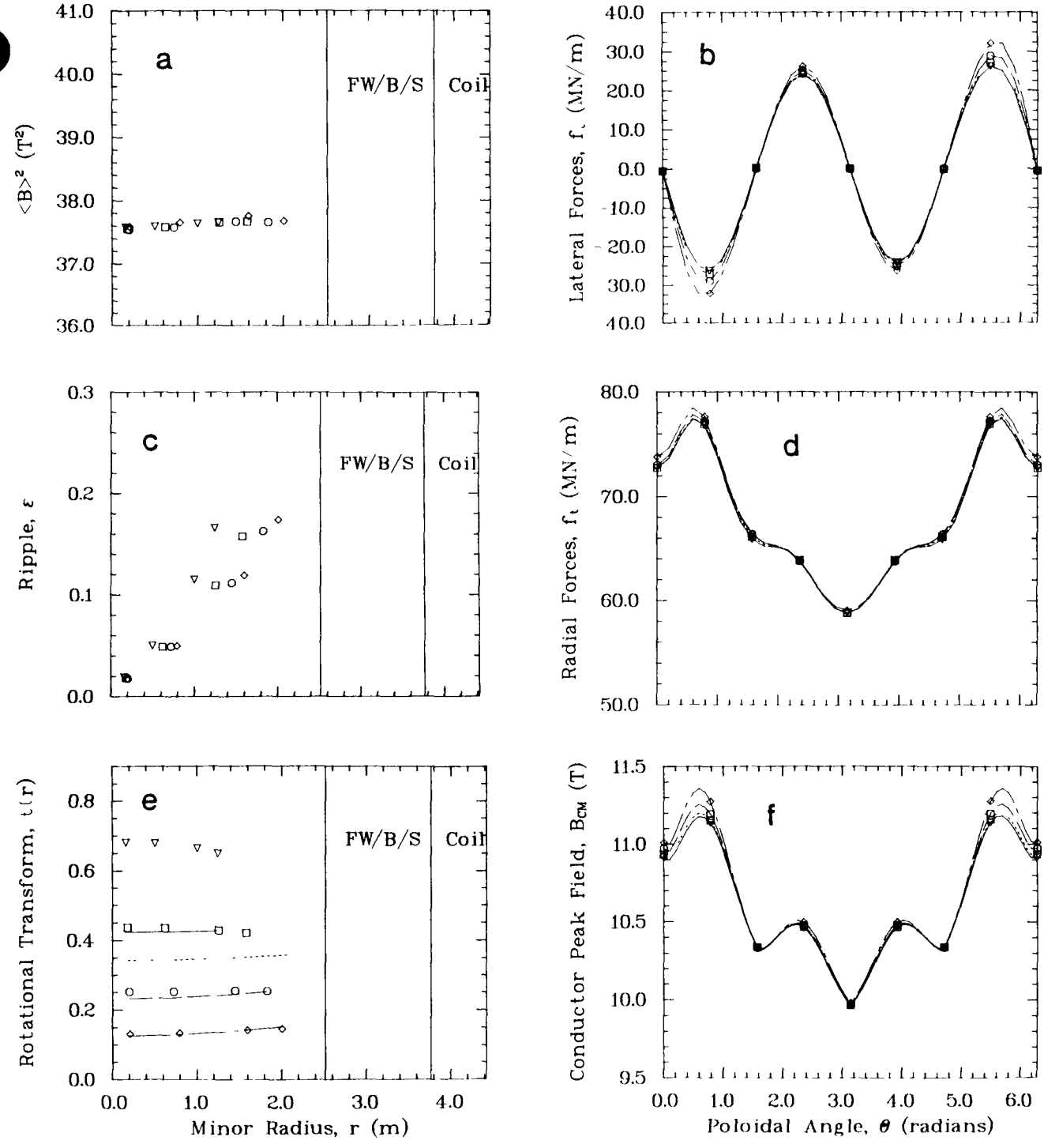

Fig. 4.3-6. A comparison of parameters measuring plasma and coil performance for m = 3 (triangles and solid lines), m = 4 (squares and dashed lines), m = 6 (circles and chain-dotted lines), and m = 9 (diamonds and chain-dashed lines). See the caption for Fig. 4.3-3 for an explanation of other plot features.

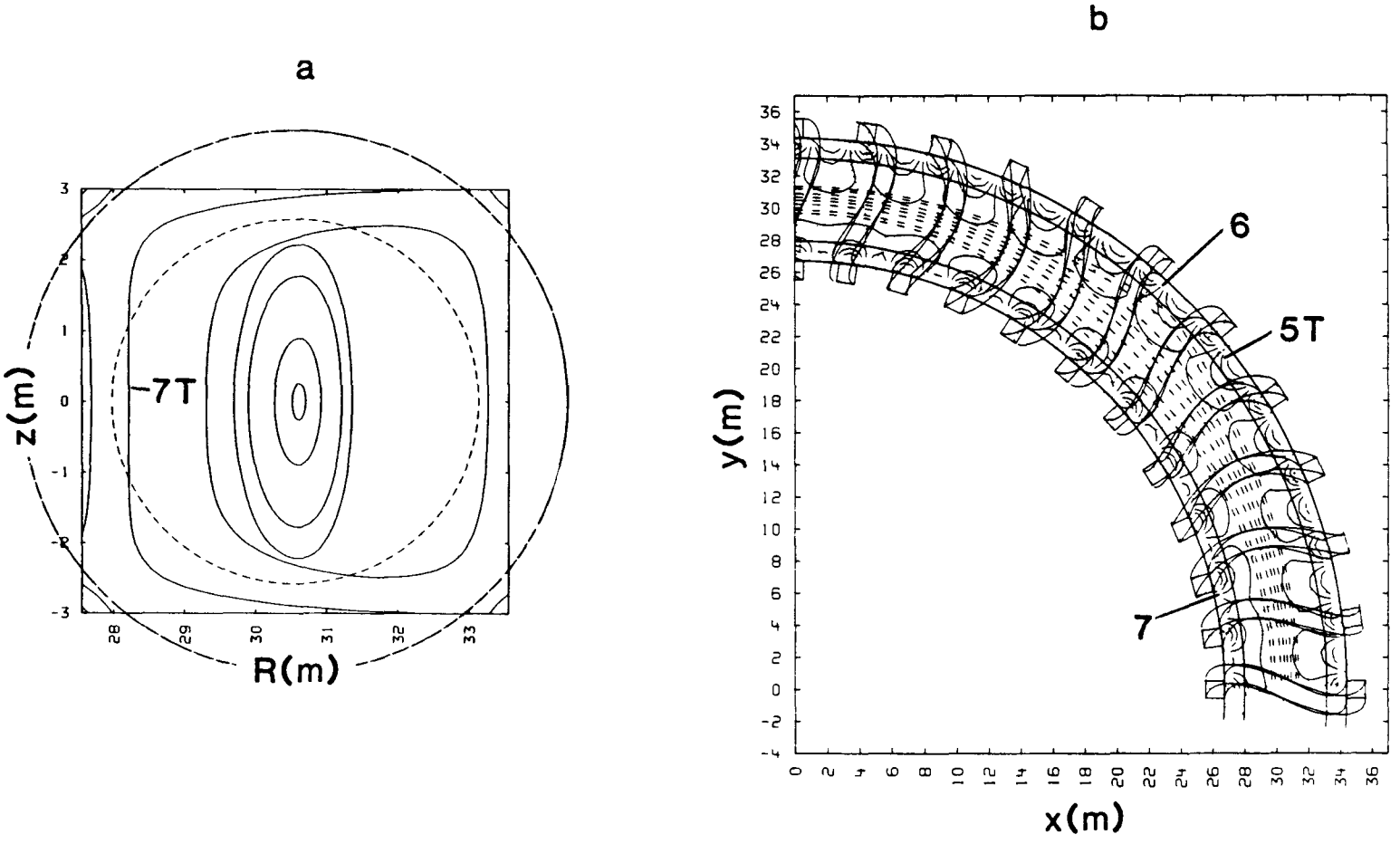

Fig. 4.3-7. The flux surfaces for R_T = 30.555 m and N = 44 as viewed in the cross section under the key coil (frame a), corresponding to ϕ = 0, and from above the equatorial plane (frame b). The same plotting conventions used in Fig. 4.3-1 are used here.

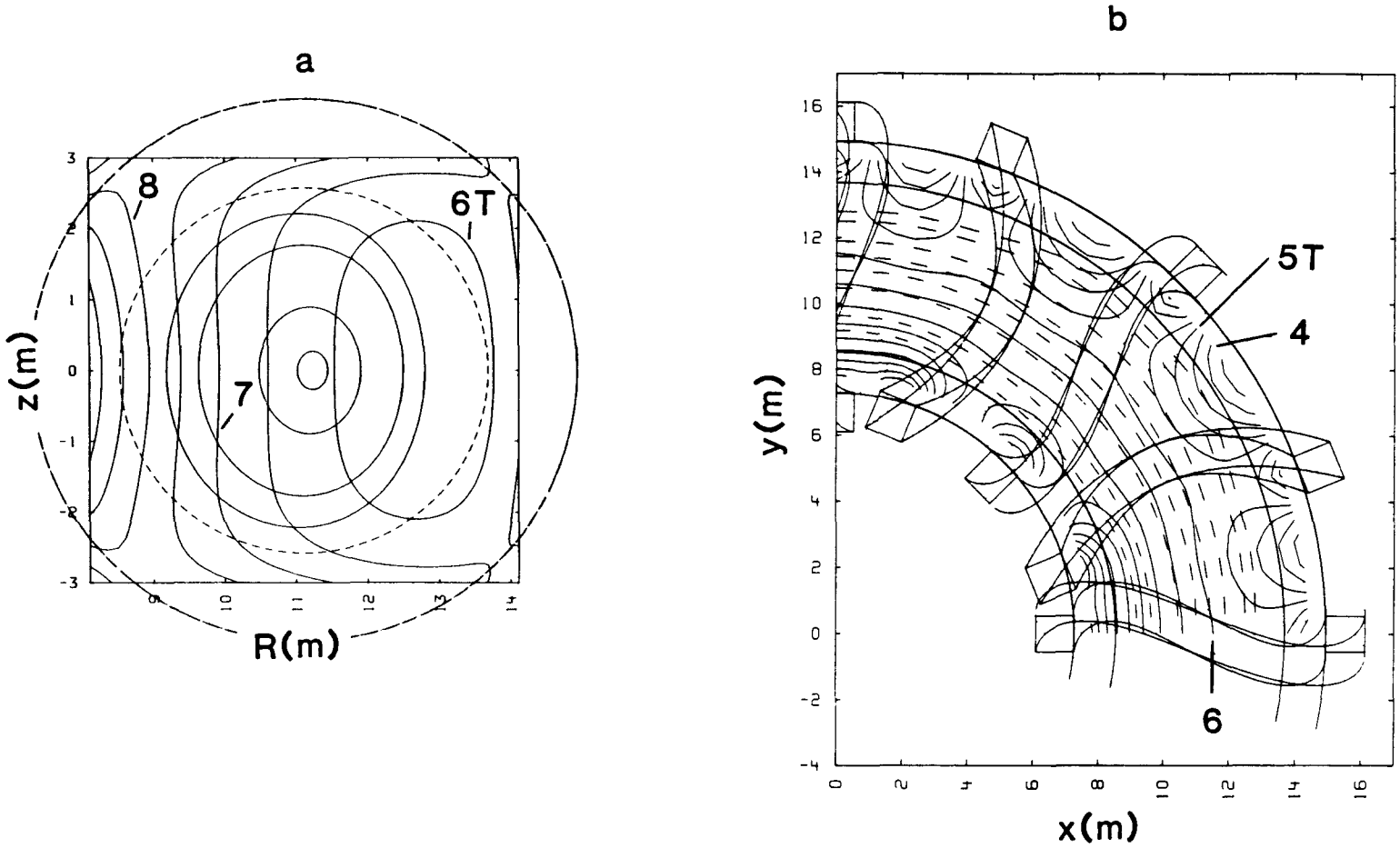

Fig. 4.3-8. The flux surfaces for R_T = 11.111 m and N = 16 as viewed in the cross section under the key coil (frame a), corresponding to ϕ = 0, and from above the equatorial plane (frame b). The same plotting conventions used in Fig. 4.3-1 are used here.

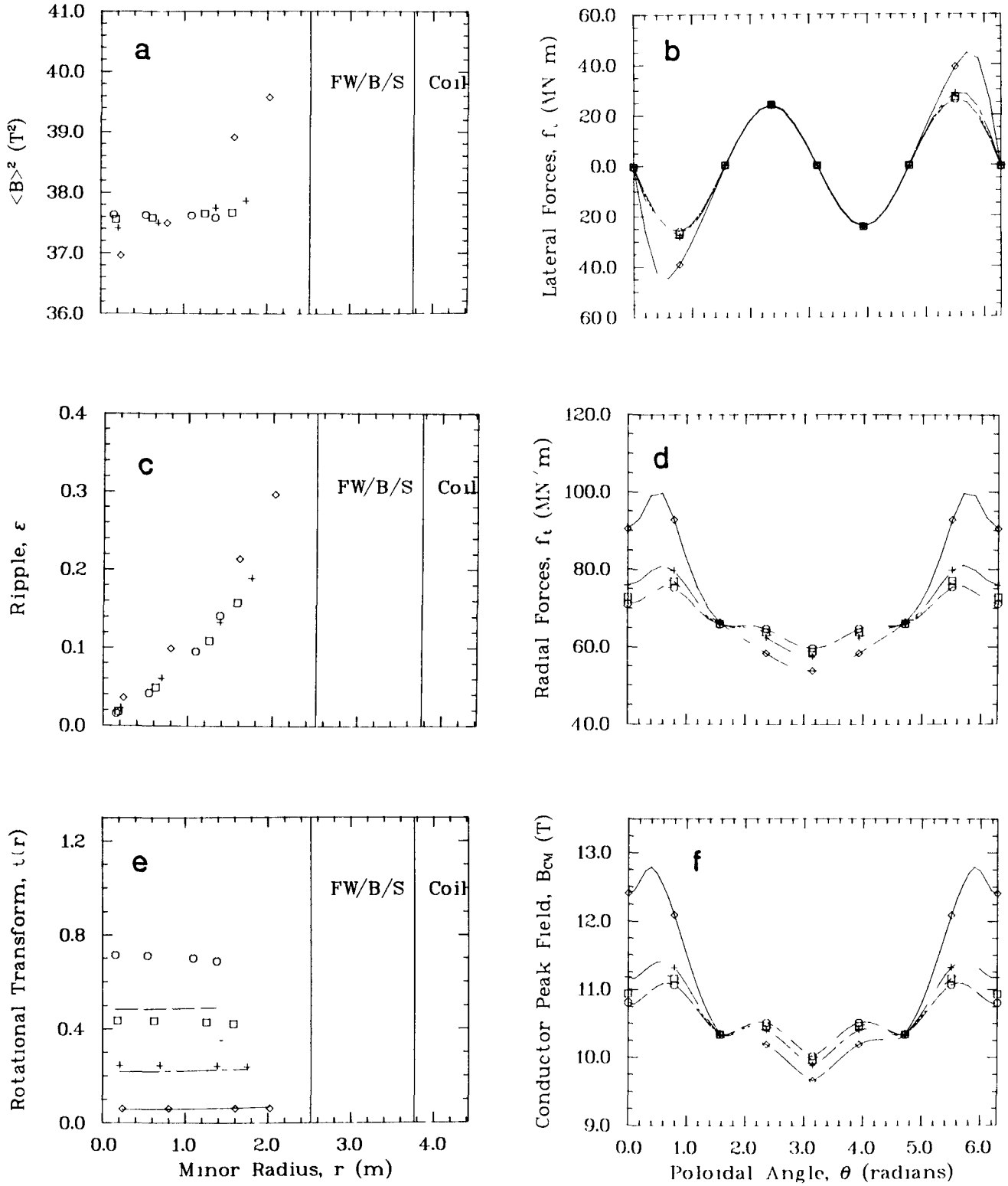

Fig. 4.3-9. A comparison of parameters measuring plasma and coil performances for R_T = 30.555 m and N = 44 (circles and chain-dotted lines), R_T = 25 m and N = 36 (squares and dashed lines), R_T = 19.444 m and N = 28 (pluses and chain-dashed lines), and R_T = 11.111 m and N = 16 (diamonds and solid lines). See the caption for Fig. 4.3-3 for an explanation of other plot features.

that other parameterizations[16] have demonstrated the existence of an optimum rotational transform as a function of aspect ratio, albeit for $\ell = 3$. Somewhat disconcerting is the observation that the well depth as seen in Fig. 4.3-9 can be enhanced by lowering the aspect ratio. The forces and B_{CM} are larger for the lower aspect ratio cases because the increment in poloidal phase between adjacent coils [Eq. (4.3-3A)] is increasing, resulting in shorter distances between the peaks in the lateral distortion of adjacent coils, which in turn enhances the field at these locations. Although the plasma aspect ratio is determined by the gross thermal power and the transport scaling (Sec. 3.4.), sufficient benefit exists in imposing the highest coil aspect ratio afforded by the minimum FW/B/S possible.

Similar to the coil aspect ratio, parameterizations investigating changes in the amplitude of the lateral distortion can be obscured by changes in coil spacing and magnetic field. To avoid this situation, the lateral distortion variations in Figs. 4.3-10 through 4.3-12 maintain both of the products of NI and $a_1 N$ constant. The most pronounced effect of increasing the lateral distortion upon the flux surfaces is the increased elongation. When the flux surfaces are highly elongated, they also display substantial deviations from an elliptical cross section, as seen in Fig. 4.3-10, which in turn raises questions regarding the possible existence of islands. Coincident with the increased elongation of the flux surfaces, the transform has increased and the volume utilization decreased. The increased distortion has also resulted undesirably in the conversion of a magnetic well into a hill and in a substantial increase in ripple. The increased ripple results in increases in B_{CM} and the forces on the coils. Had the number of coils not been adjusted between cases, the ripple effects would have been even larger. Consequently, a high N and a low lateral distortion reduces the deleterious effects of ripple.

The final parameterizations performed for the MSR concept before arriving at a design focused on varying the a_i's of Eq. (4.3-3A) without changing the peak amplitude, d, of the lateral distortion. To limit the number of possible combinations of a_i's investigated while ensuring a representative sampling, the prescription for choosing the a_i's is based on the Fourier representations of a "square wave" and a "saw-tooth wave" shown in Fig. 4.3-13. Upon the introduction of a factor of 1/i raised to a power for the purposes of damping the Gibbs phenomenon[17], the expressions for the a_i's are

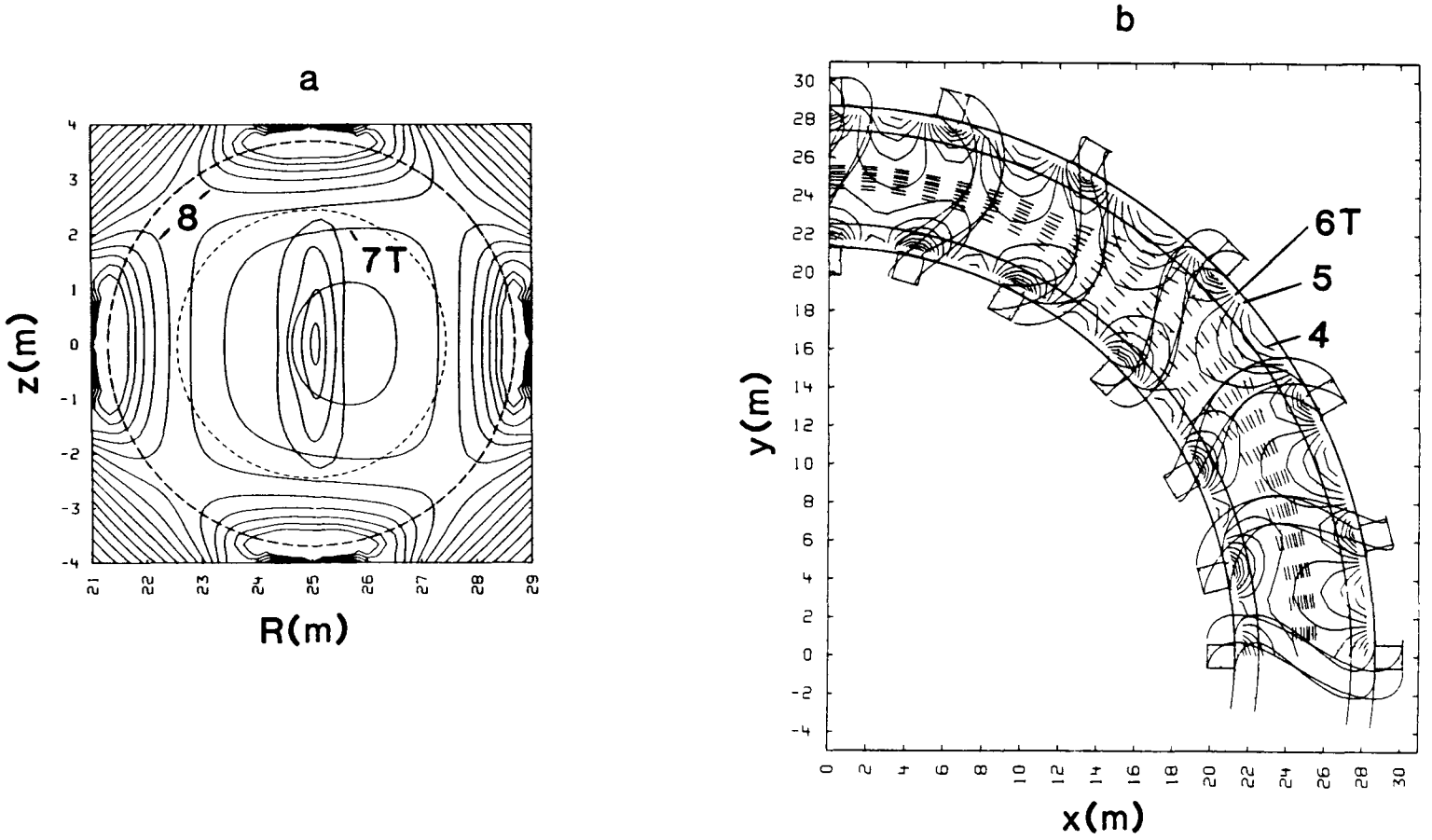

Fig. 4.3-10. The flux surfaces for a_1 = 0.33, N = 24, and I = 32.025 MA as viewed in the cross section under the key coil (frame a), corresponding to ϕ = 0, and from above the equatorial plane (frame b). The same plotting conventions used in Fig. 4.3-1 are used here.

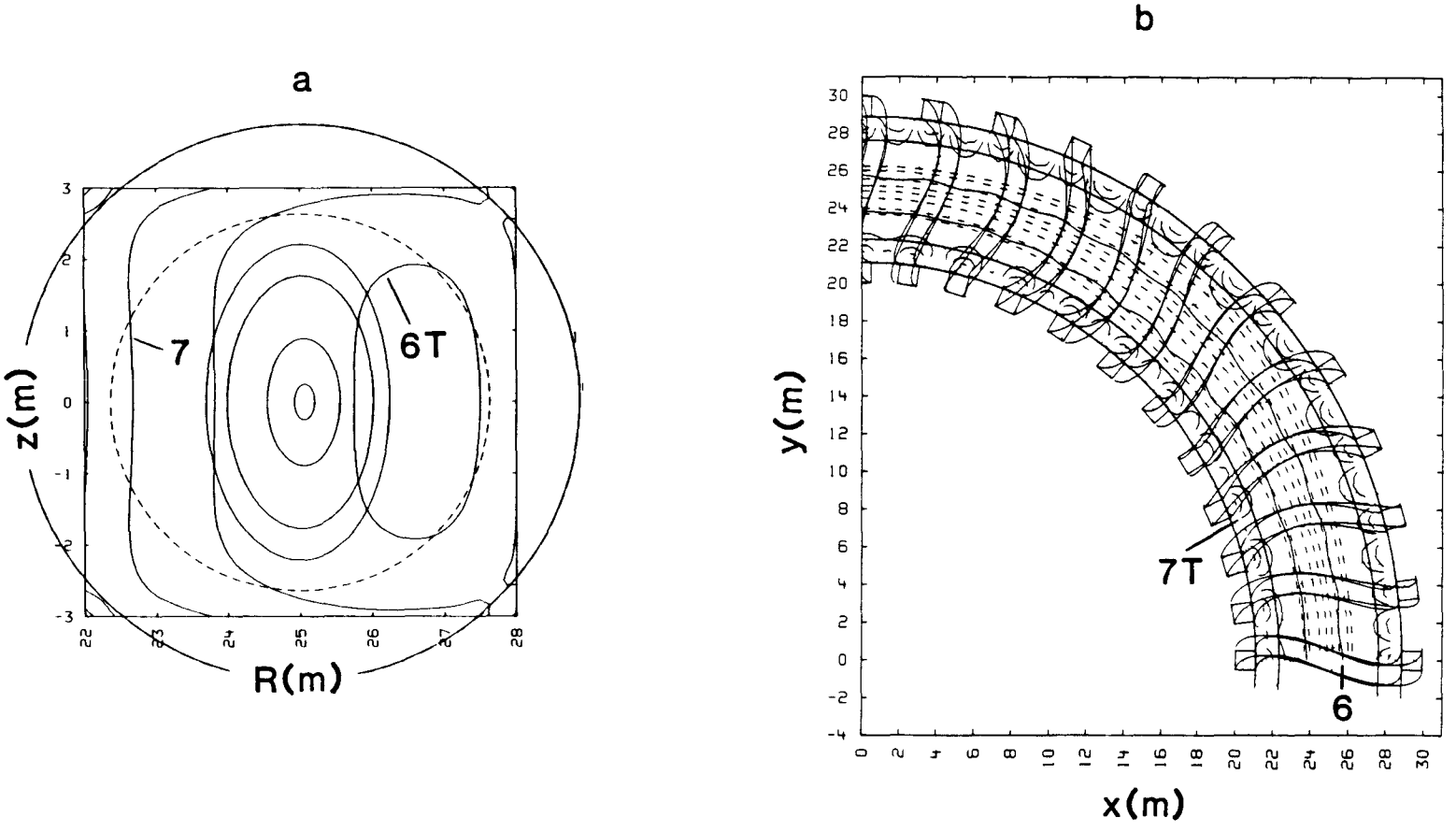

Fig. 4.3-11. The flux surfaces for a_1 = 0.18, N = 44, and I = 17.468 MA as viewed in the cross section under the key coil (frame a), corresponding to ϕ = 0, and from above the equatorial plane (frame b). The same plotting conventions used in Fig. 4.3-1 are used here.

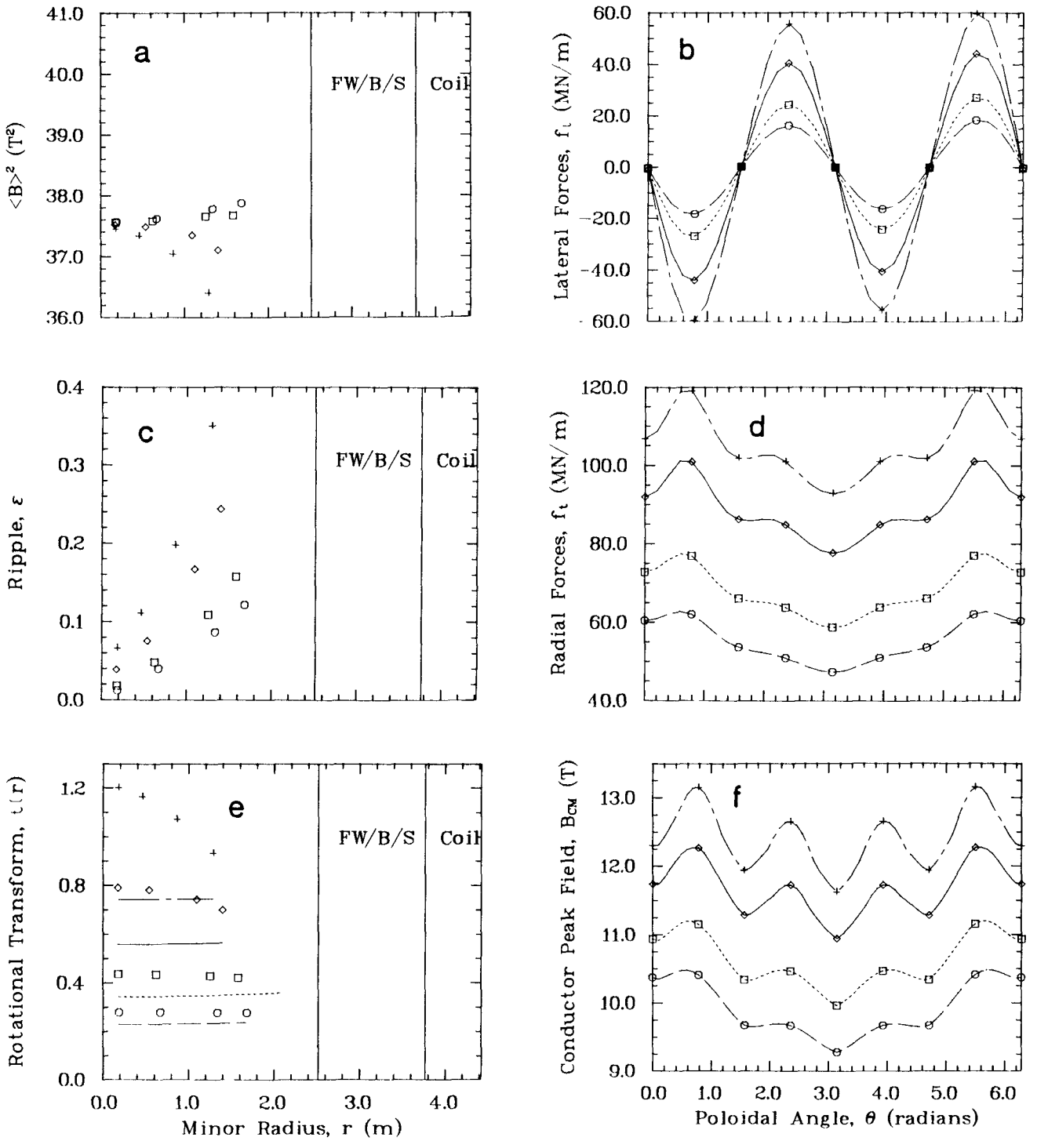

Fig. 4.3-12. A comparison of parameters measuring plasma and coil performance a_1/r_c = 0.33, N = 24, and I = 32.025 MA (pluses and chain-dashed lines); a_1/r_c = 0.2829, N = 28, and I = 27.45 MA (diamonds and solid lines); a_1/r_c = 0.22, N = 36, and I = 21.35 MA (square and dashed lines; a_1/r_c = 0.18, N = 44, and I = 17.468 MA (circles and chain-dotted lines). See the caption for Fig. 4.3-3 for an explanation of other plot features.

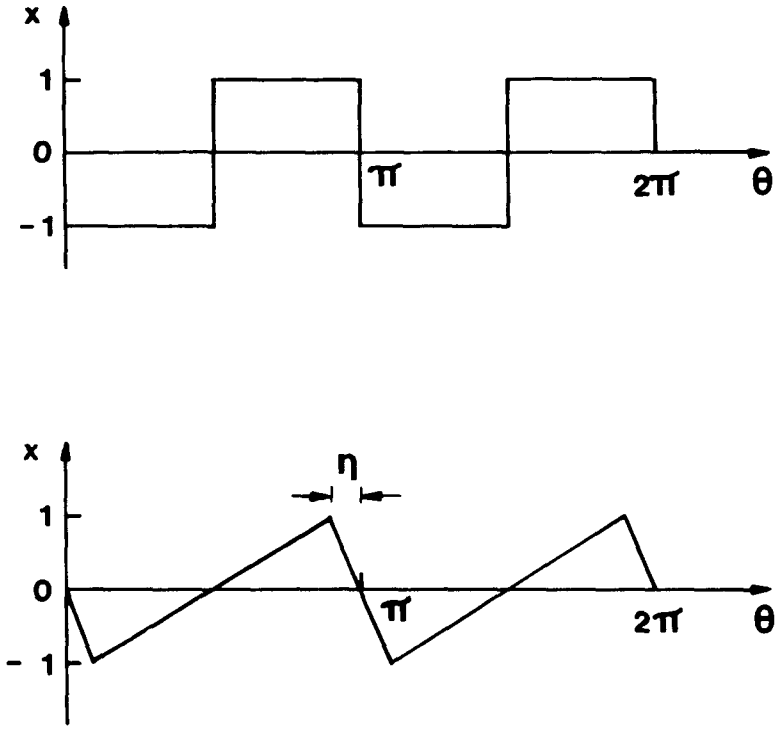

Fig. 4.3-13. The periodic functions upon which the models for determining the a_i's of Eq. (4.3-3A) are based. The square wave is above and the saw-tooth below.

$$a_i = \frac{C_1}{i^{\nu}} \quad \text{and} \tag{4.3-4}$$

$$a_i = \frac{C_2 \sin i\pi\eta}{i^2} \quad , \tag{4.3-5}$$

respectively. In this equation C_j is a normalization constant such that the amplitude of the lateral distortion, $|x(\theta)| \lesssim d/r_c$; ν is a variable that not only controls the damping of the Gibbs phenomenon but also how "square" the distortion is; and η is a variable controlling the location of the maximum distortion. Equation (4.3-4) yields lateral distortions that are symmetric

about the maximum distortion, whereas Eq. (4.3-5) yields a symmetric distortion only when $\eta = 0.5$.

The first parameterization of the a_i's that was performed varies the half-width of the symmetric distortion. In addition to the simple sinusoidal distortion of the base case, the distortions for the case with a fuller distortion, obtained by setting $\nu = 2.5$ in Eq. 4.3-4, and for the case with a thinner distortion, with $\eta = 0.5$ in Eq. 4.3-5, are presented in Fig. 4.3-14. The Gibbs phenomenon becomes a problem for values of ν below 2.5, whereas values above 2.5 show little distinction from the base case. The results of varying the half-width of the symmetric distortion are presented in Figs. 4.3-15 and 4.3-16. Changing the fullness of the distortion has a noticeable effect only on ι, shifting the entire profile by an additive constant. The flux surfaces in Fig. 4.3-16 are elongated, elliptical cross sections consistent with higher transforms. The sharper distortion peak predictably results in slightly higher f_ℓ and B_{CM}.

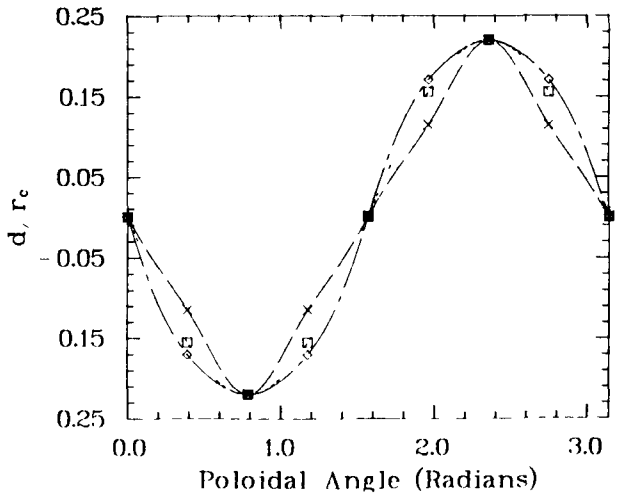

Fig. 4.3-14. The lateral distortion of the key coil as a function of poloidal angle for the symmetric distortion parameterization. The lateral distortion coefficients for the fuller distortion case are $a_1 = 0.2306$, $a_2 = 0$, $a_3 = 0.0147$, $a_4 = 0$, $a_5 = 0.0041$, and $a_6 = 0$ (diamonds); for the base case, $a_1 = 0.2200$ and $a_2 = a_3 = a_4 = a_5 = a_6 = 0$ (squares); and for the thinner distortion, $a_1 = 0.1911$, $a_2 = 0$, $a_3 = -0.0212$, $a_4 = 0$, $a_5 = 0.0076$, and $a_6 = 0$ (x's).

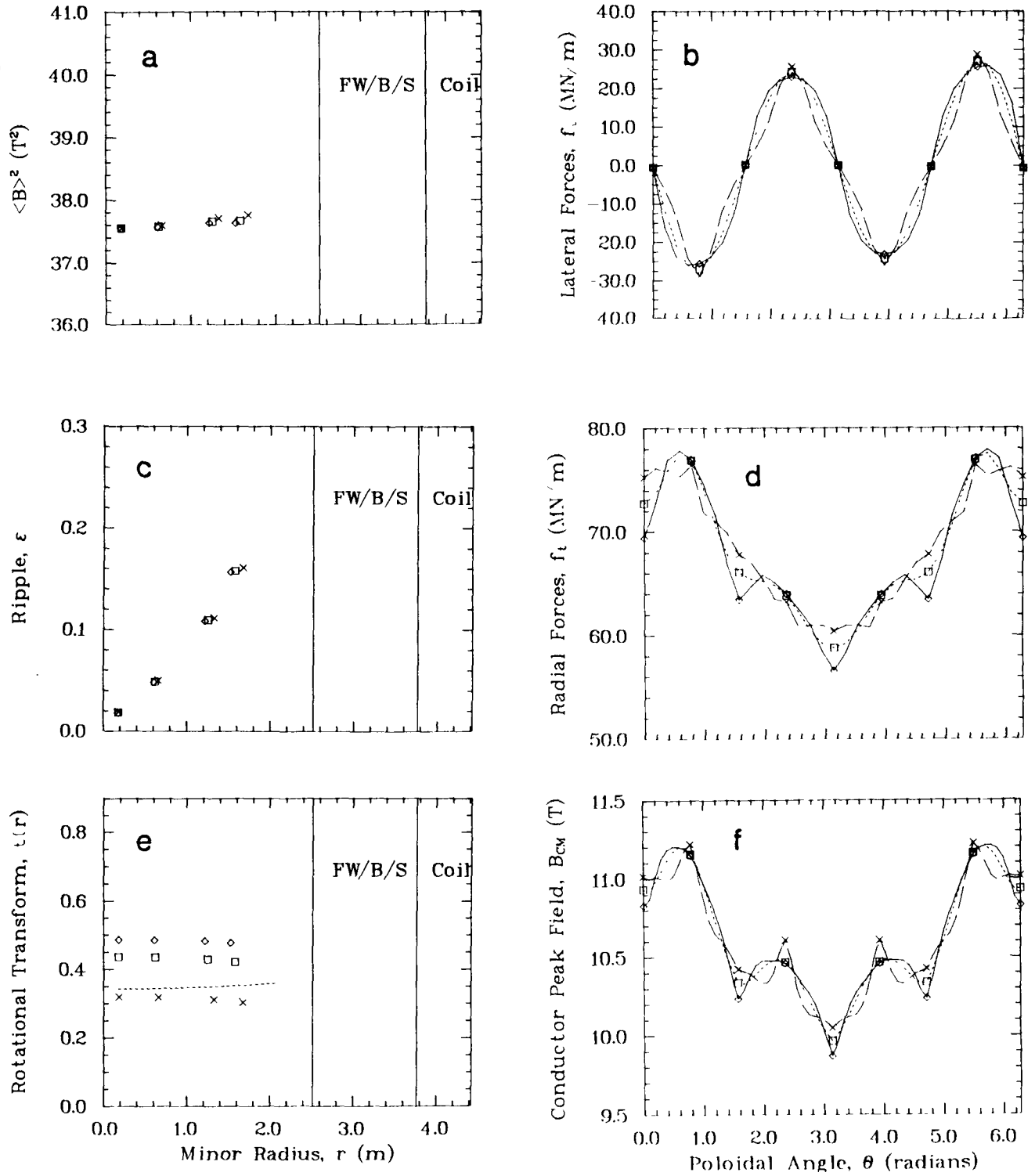

Fig. 4.3-15. A comparison of parameters measuring plasma and coil performance for $a_1 = 0.2306$, $a_2 = 0$, $a_3 = 0.0147$, $a_4 = 0$, $a_5 = 0.0041$, and $a_6 = 0$ (diamonds); $a_1 = 0.2200$ and $a_2 = a_3 = a_4 = a_5 = a_6 = 0$ (squares); and $a_1 = 0.1911$, $a_2 = 0$, $a_3 = -0.0212$, $a_4 = 0$, $a_5 = 0.0076$, and $a_6 = 0$ (x's). See the caption for Fig. 4.3-3 for an explanation of other plot features.

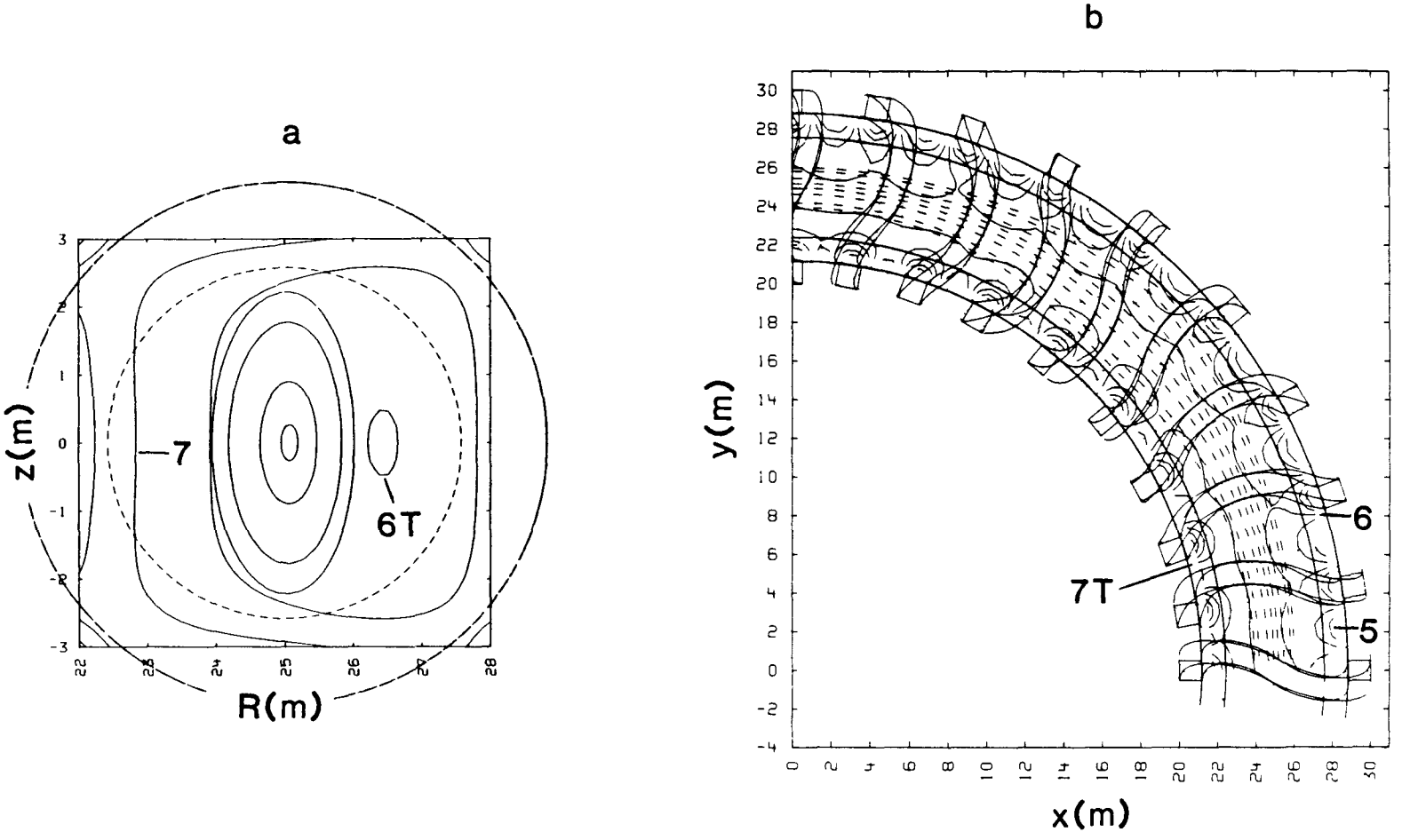

Fig. 4.3-16. The flux surfaces for $a_1 = 0.2306$, $a_2 = 0$, $a_3 = 0.0147$, $a_4 = 0$, $a_5 = 0.0041$ and $a_6 = 0$ as viewed in the cross section under the key coil (frame a), corresponding to $\phi = 0$, and from above the equatorial plane (frame b). The same plotting conventions used in Fig. 4.3-1 are used here.

The second parameterization of the a_i's that was performed is an asymmetric distortion presented in Fig. 4.3-17. The a_i's corresponding to the lateral distortions presented in Fig. 4.3-17 were obtained by setting η = 0.15, 0.25, 0.35, and 0.5 in Eq. 4.3-5, which results in the cases with a_1 = 0.1690, a_1 = 0.1770, a_1 = 0.1869, and a_1 = 0.1911, respectively. The results of varying the location of the peak of the asymmetric distortion are presented in Figs. 4.3-18 and 4.3-19. Of the plasma parameters monitored in Fig. 4.3-18, decreasing η produces a noticeable effect only on the transform, lowering ι at the center more than at the edge by emphasizing the helical component of the winding over the antihelix component. This shaping of the ι profile primarily resulted in an increase in the lateral forces acting on the key coil that is partially obscured by the resolution of the plot. The radial forces displayed only a minor increase with decreasing η. The peak field on the key coil actually decreased. The peak field in the entire coil set was larger, however, because of the poloidal displacement of the location of the

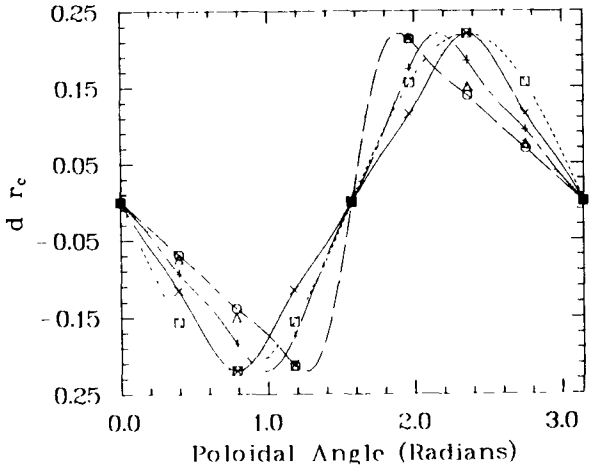

Fig. 4.3-17. The lateral distortion of the key coil as a function of poloidal angle for the asymmeteric distortion parameterization. The lateral distortion coefficients used are a_1 = 0.1690, a_2 = 0.0753, a_3 = 0.0408, a_4 = 0.0221, a_5 = 0.0105, and a_6 = 0.0032 (circles and chain-dotted line); a_1 = 0.1770, a_2 = 0.0626, a_3 = 0.0197, a_4 = 0, a_5 = -0.0071, and a_6 = -0.0069 (triangles and dotted lines); a_1 = 0.1869, a_2 = 0.0424, a_3 = -0.0036, a_4 = -0.0125, a_5 = -0.0059, and a_6 = 0.0018 (pluses and chain-dashed lines); a_1 = 0.1911, a_2 = 0, a_3 = -0.0212, a_4 = 0, a_5 = 0.0076, and a_6 = 0 (x's and solid lines); and a_1 = 0.2200, a_2 = a_3 = a_4 = a_5 = a_6 = 0 (squares and dashed lines).

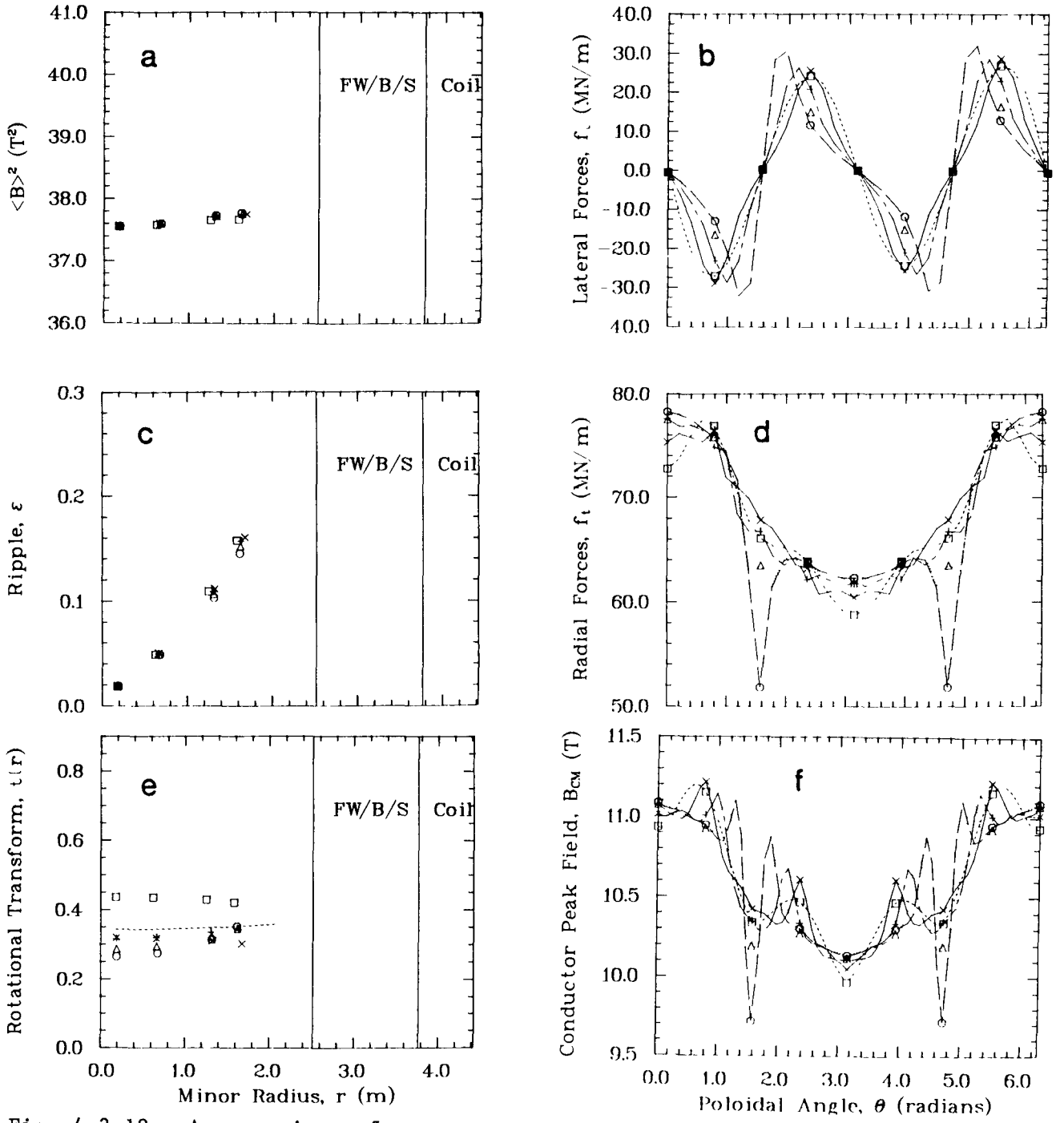

Fig. 4.3-18. A comparison of parameters measuring plasma and coil performance for a_1 = 0.1690, a_2 = 0.0753, a_3 = 0.0408, a_4 = 0.0221, a_5 = 0.0105, and a_6 = 0.0032 (circles and chain-dotted line); a_1 = 0.1770, a_2 = 0.0626, a_3 = 0.0197, a_4 = 0, a_5 = -0.0071, and a_6 = -0.0069 (triangles and dotted lines); a_1 = 0.1869, a_2 = 0.0424, a_3 = -0.0036, a_4 = -0.0125, a_5 = -0.0059, and a_6 = 0.0018 (pluses and chain-dashed lines); a_1 = 0.1911, a_2 = 0, a_3 = -0.0212, a_4 = 0, a_5 = 0.0076, and a_6 = 0 (x's and solid lines); and a_1 = 0.2200, $a_2 = a_3 = a_4 = a_5 = a_6 = 0$ (squares and dashed lines). See the caption for Fig. 4.3-3 for an explanation of other plot features.

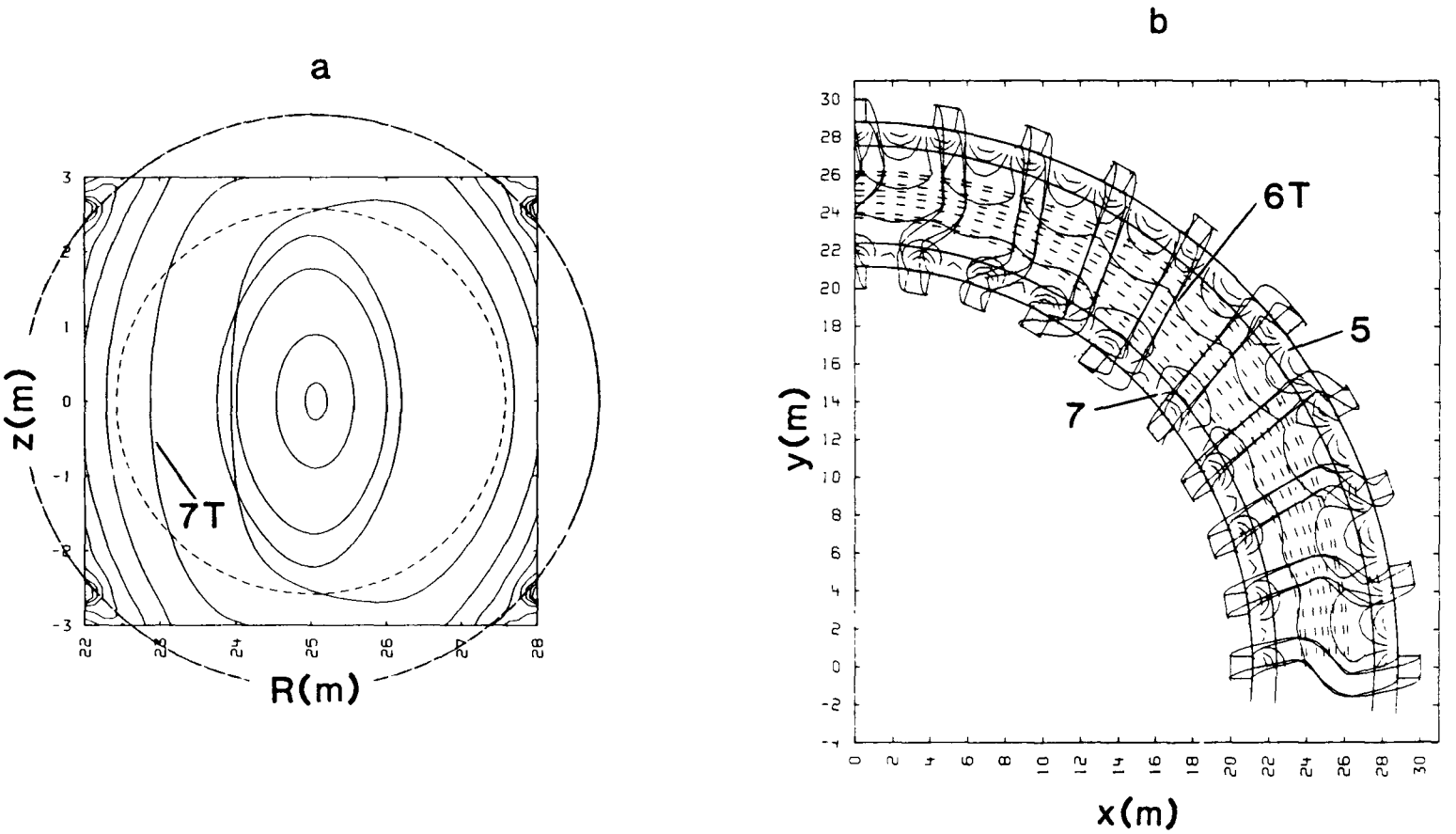

Fig. 4.3-19. The flux surfaces for $a_1 = 0.1690$, $a_2 = 0.0753$, $a_3 = 0.0408$, $a_4 = 0.0221$, $a_5 = 0.0105$, and $a_6 = 0.0032$ as viewed in the cross section under the key coil (frame a), corresponding to $\phi = 0$, and from above the equatorial plane (frame b). The same plotting conventions used in Fig. 4.3-1 are used here.

maximum distortion. The flux surfaces for $\eta = 0.15$ in Fig. 4.3-19 display a subtle deviation from the elliptical shape found in Fig. 4.3-16. The outer surfaces have sharper corners on top and bottom and are slightly fuller on the inboard side, suggestive of a weak introduction of an $\ell = 3$ component to the field. Because of the ability to shape the ι profile to introduce positive shear, lateral distortions of the asymmetric type with low values of η [see Eq. 4.3-5)] are preferred.

To summarize the results of the single variable parameterizations, the MSR designs should strive for the following design parameters where possible. The design should be $\ell = 2$ to avoid the major rational q surfaces. The m should be determined by the desired value of ι as determined by Eq. (4.3-2). Although little latitude exists for in choosing R_T amd r_c, the use of the minimum-sized FW/B/S, and hence r_c, is desirable. A design with a high N and low lateral distortion appears best to avoid the consequences of large ripple. An asymmetric distortion of the type in Eq. (4.3-5) with low values of η is preferred because of the positive shear introduced into the ι profile.

4.3.2.2. Modular Stellarator Design Points. The process of selecting MSR design points involved iterating between the survey code of Sec. 3.4. and TORSIDO. The survey code determines R_T, r_c, N, I_{TF}, and the amplitude of the lateral distortion, d/r_c, based upon estimates of the volume ulitization as measured by $x = r_p/r_w$ and the ratio of the on-axis field to the peak field at the conductor, B_o/B_{CM}. Then TORSIDO is used to calculate x and B_o/B_{CM} for the values of R_T, r_c, N, I_{TF}, and d/r_c produced by the survey code; m is chosen to produce the appropriate ι for an assumed $\langle\beta\rangle$ and the a_i's are suitably chosen to yield the desired ι profile. This iteration process continued until the two codes converged on x and B_o/B_{CM}.

Two MSR designs were generated: a high-beta case, $\langle\beta\rangle = 0.08$, and a low-beta case, $\langle\beta\rangle = 0.04$. The survey code indicated that the high-beta case should have $R_T = 23$ m and $r_p = 0.81$ m to produce 4 GWt of recoverable thermal power. By Eq. (4.3-2), the high-beta design, designated MSR-IIB, should have $\iota = 1.5$. However, no design could be found with $r_p \simeq 0.8$ m that had $\iota \gtrsim 1$ and was free of islands. Consequently, a design with $0.5 < \iota < 1$ as a goal was considered.

The MSR-IIB design that finally emerged is summarized in Table 4.3-2. The two entries appearing in the table represent a uniform-current-density case used in the survey code/TORSIDO iteration process and a stepped-current-

TABLE 4.3-2

MSR-IIB MAGNETICS RESULTS

PARAMETER	UNIFORM j_c[a]	STEPPED j_c[b]
Design <β>	0.08	0.08
Coil type	Modular	Modular
Pitch parameter, γ	NA	NA
Normalized distortion, d/r_c	0.28	0.28
Distortion coefficients:		
a_1	0.2111	0.2111
a_2	0.0955	0.0955
a_3	0.0534	0.0534
a_4	0.0304	0.0304
a_5	0.0160	0.0160
a_6	0.0066	0.0066
Conductor major radius, R_T (m)	23.0	23.0
Conductor minor radius, r_c (m)	3.31	3.31
Conductor aspect ratio, $A_c = R_T/r_c$	6.95	6.95
Total coil current, I (MA)	21.0	21.0
Conductor cross section (m × m)	1.051 × 1.051	1.051 × 1.051
Conductor length, L_c (m)	22.916	22.916
Number of poloidal field periods, ℓ	2	2
Number of toroidal field periods, m	4	4
Number of coils, N	36	36
Plasma major radius (m)	23.025	23.02
Plasma minor radius, r_p (m)	0.630	0.81
Plasma volume, V_p (m^3)	180.62	298.76
Magnetic axis (m)	23.039	23.04
Semiminor radius[c] (m)	0.362(0.377)	0.479(0.500)
Semimajor radius[c] (m)	1.115(1.180)	1.406(1.425)
Limiter radius (m)	1.260	1.526
On-axis field, B_o (T)	6.55	6.47
Well depth (%)	-0.052	-0.049
Peak field at coil, B_{CM} (T)	11.75[e](11.45)[d]	11.59[d]
On-axis ripple, ε(0)%	<3.15	<2.89
Edge ripple, $\varepsilon(r_p)$%	9.72	11.32
On-axis transform, ι(0)	0.729	0.626
Edge transform, $\iota(r_p)$	0.880	0.804
Stored magnetic energy, E_M (GJ)	108.35	108.35
Peak radial force, f_r (MN/m)	79.20[e](78.95)[d]	78.36[d]
Peak lateral force, f_ℓ (MN/m)	39.61[e](39.31)[d]	38.21[d]

[a] j_c = 19 MA/m^2.

[b] j_c = 12.04 MA/m^2 for $0 < t < 0.519$; j_c = 22.43 MA/m^2, $0.519 < t < 0.811$; and j_c = 32.83 MA/m^2, $0.811 < t < 1.0$; where the fraction t is measured radially through the conductor cross section.

[c] Under a key coil and half a field period away.

[d] Results for a key coil.

[e] Results for the worst case, coil 5.

density case that reflects the more realistic conductor design of Sec. 5.2. The stepped current density effectively increases r_c resulting in a slightly lower transform, as seen in Fig. 4.3-20. The lower transform results in less elongation and moves the separatrix radially outward as seen from Figs. 4.3-21 and 4.3-22. The outermost flux surface in each case is near the separatrix. The apparent anomalies in the flux surfaces in these two figures result from not obtaining a uniform sampling of a surface (i.e., some of the surfaces are near minor rational-q surfaces) and from numerical errors of the field-line integration algorithm; these errors accumulated as the integration was performed for a long distance along the field line in an attempt to get a uniform sampling. The minimum clearance between the outermost flux surface and the conductor for stepped j_c is 1.26 m, which must accommodate a plasma scrapeoff layer, a FW/B/S, and a coil casing. Only minor differences exist in the other parameters for the two cases.

Transport and a net thermal power of ~5 GWt again determined r_c and R_T, respectively, for the low-beta design, MSR-IIA. Because the high-beta design achieved $0.626 \lesssim \iota \lesssim 0.804$, the MSR-IIA transform target was set lower at $1/3 < \iota < 1/2$. Because of the narrowness of the target range, no harmonic distortion coefficients beyond the first were used in arriving at the MSR-IIA design of Table 4.3-3. Without the profile-shaping ability of the higher harmonics, the ι profile is flat, as seen from Fig. 4.3-23. The smaller coil aspect ratio of MSR-IIA compared to MSR-IIB results in a shallow magnetic well near the axis that eventually turns into an overall magnetic hill. The ripple increased in MSR-IIA as a result of not maintaining the same N/R as in MSR-IIB. The increased ripple also resulted in decreased B_o/B_{CM} for MSR-IIA. The lateral forces are smaller for MSR-IIA because of the smaller amplitude of the lateral distortion compared to MSR-IIB. Although the volume utilization has increased as a result of the lower ι, the clearance between the plasma and the coil has decreased 1.024 m as a result of the required increase in plasma volume to accommodate the lower beta as seen in Fig. 4.3-24. The stored energy in the MSR-IIA coil set is more than double that for MSR-IIB because of the larger value of r_c.

4.3.3. Torsatrons. The design philosophy described in Sec. 4.3.1. can be met for torsatrons with the following winding law:

$$P_x(\theta) = (R_T - r_c \cos \theta) \sin \phi \ , \qquad (4.3\text{-}6A)$$

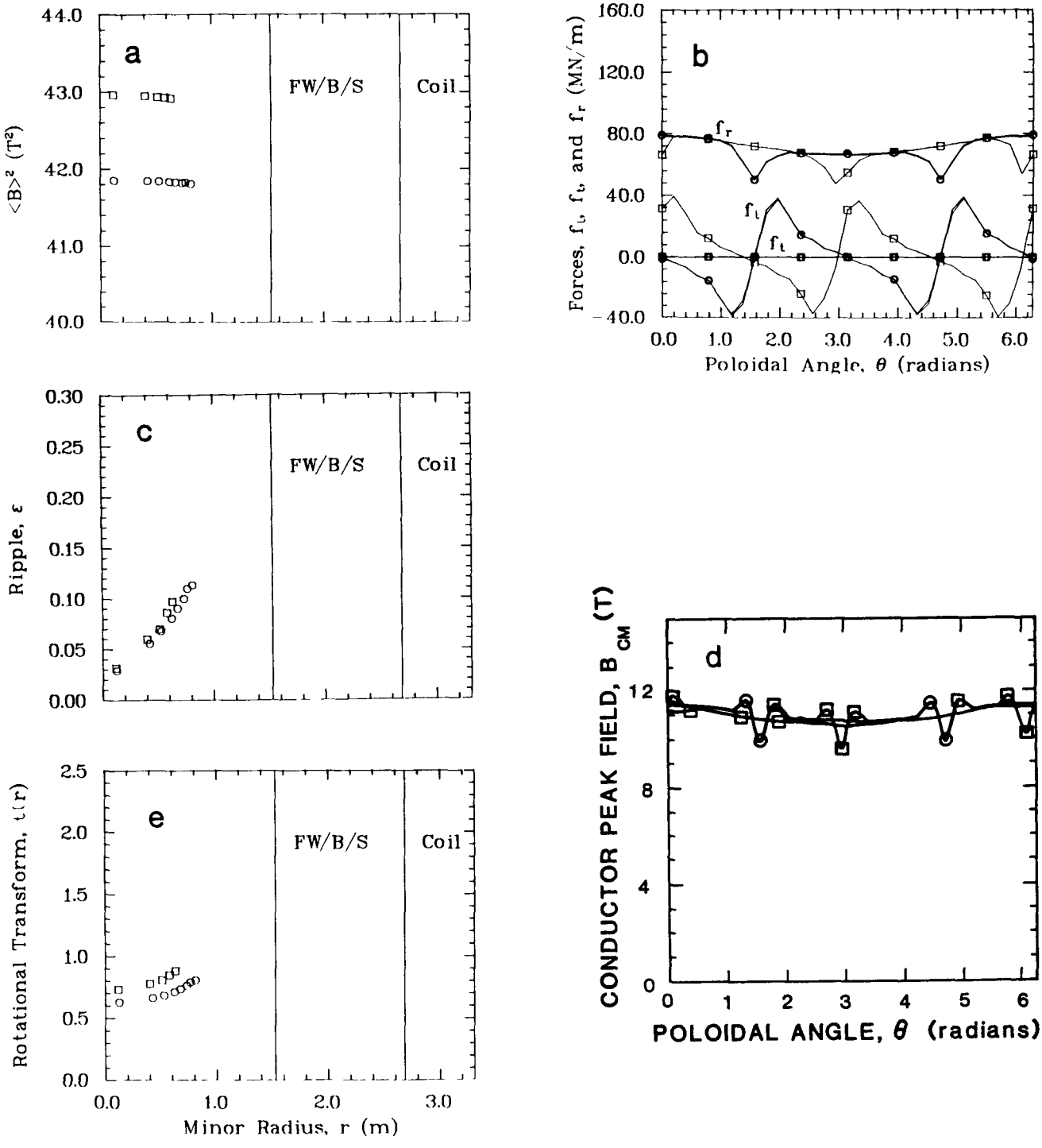

Fig. 4.3-20. A comparison of parameters measuring plasma and coil performance for MSR-IIB with uniform j_c (squares) and stepped j_c (circles). The plotting conventions of Fig. 4.3-3 are used here except the FW/B/S thickness is determined by the limiter radius and the coil casing is 0.1 m which are consistent with the final designs. The forces and fields are shown for the key coil and the worst-case coil in the case of uniform j_c.

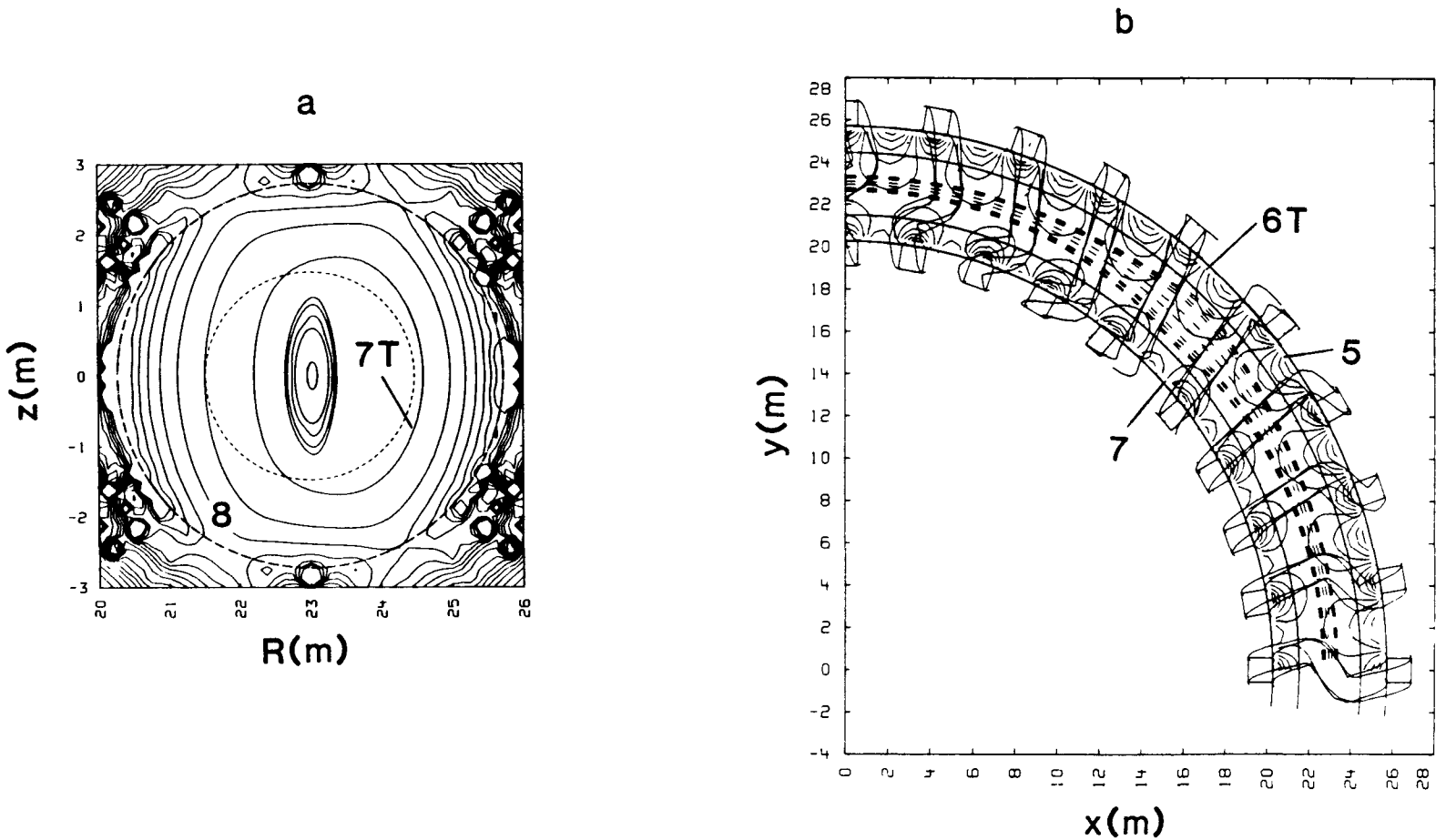

Fig. 4.3-21. The flux surfaces for MSR-IIB with uniform j_c as viewed in the cross section under the key coil (frame a), corresponding to $\phi = 0$, and from above the equatorial plane (frame b). The same plotting conventions used in Fig. 4.3-1 are used here.

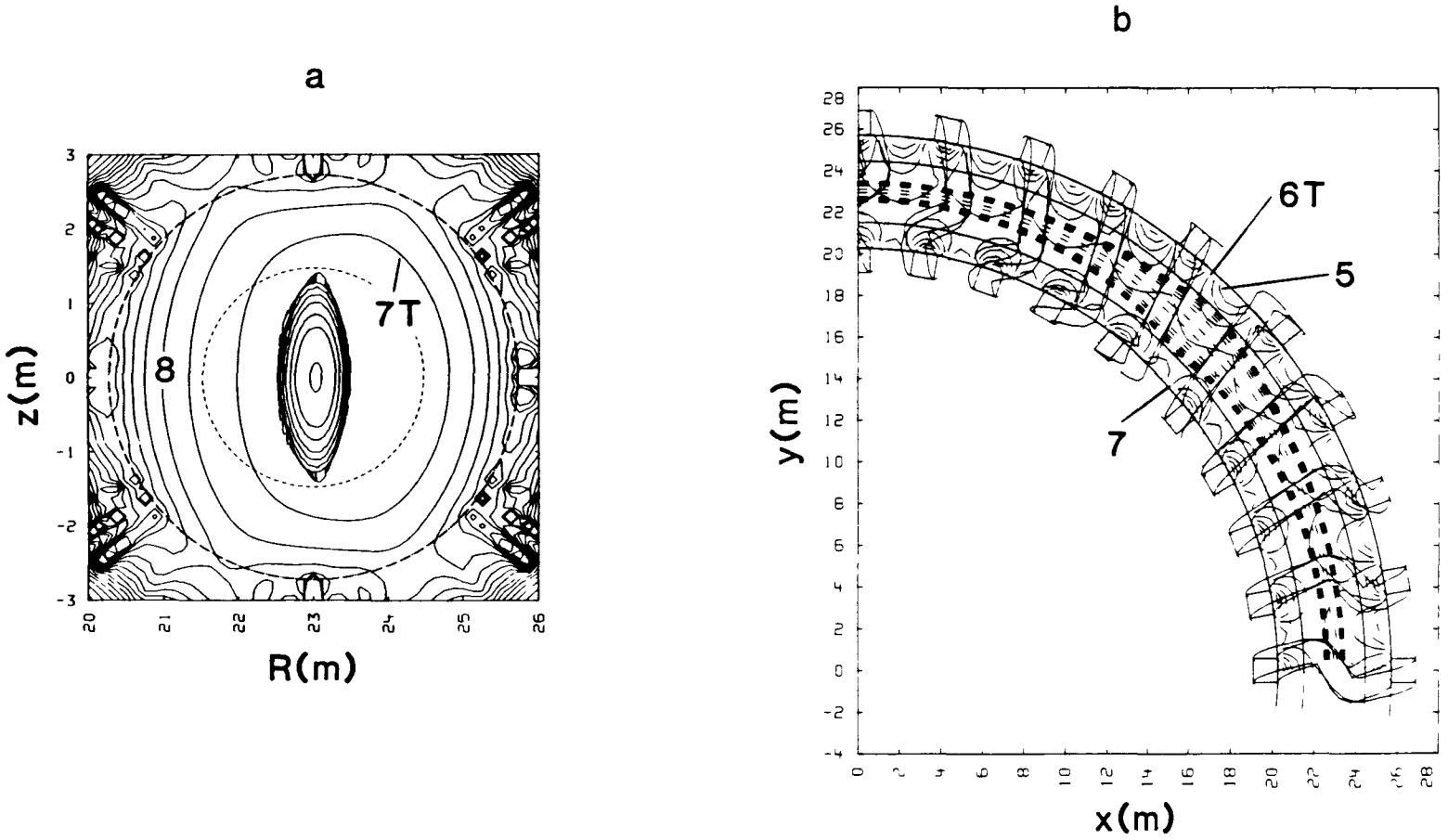

Fig. 4.3-22. The flux surfaces for MSR-IIB with stepped j_c as viewed in the cross section under the key coil (frame a), corresponding to $\phi = 0$, and from above the equatorial plane (frame b). The same plotting conventions used in Fig. 4.3-1 are used here.

TABLE 4.3-3

MSR-IIA MAGNETICS RESULTS

PARAMETER	UNIFORM j_c[a]
Design <β>	0.04
Coil type	Modular
Pitch parameter, γ	NA
Normalized distortion, d/r_c	0.235
Distortion coefficients:	
a_1	0.2350
a_2	0.0
a_3	0.0
a_4	0.0
a_5	0.0
a_6	0.0
Conductor major radius, R_T (m)	27.9
Conductor minor radius, r_c (m)	5.0
Conductor aspect ratio, $A_c = R_T/r_c$	5.58
Total coil current, I (MA)	22.23
Conductor cross section (m × m)	1.082 × 1.082
Conductor length, L_c (m)	33.085
Number of poloidal field periods, ℓ	2
Number of toroidal field periods, m	4
Number of coils, N	36
Plasma major radius (m)	27.90
Plasma minor radius, r_p (m)	2.18
Plasma volume, V_p (m^3)	2613.15
Magnetic axis (m)	27.977
Semiminor radius[b] (m)	1.477(1.484)
Semimajor radius[b] (m)	3.089(3.331)
Limiter radius (m)	3.435
On-axis field, B_o (T)	5.72
Well depth (%)	-0.054
Peak field at coil, B_{CM} (T)	11.24[d]
On-axis ripple, ε(0)%	<1.73
Edge ripple, $\varepsilon(r_p)$%	25.08
On-axis transform, ι(0)	0.488
Edge transform, $\iota(r_p)$	0.448
Stored magnetic energy, E_M (GJ)	230.26
Peak radial force, f_r (MN/m)	79.78[d](76.42)[c]
Peak lateral force, f_ℓ (MN/m)	29.46[d](29.10)[c]

[a] j_c = 19 MA/m^2.

[b] Under a key coil and half a field period away.

[c] Results for key coil.

[d] Results for the worst case, coil 7.

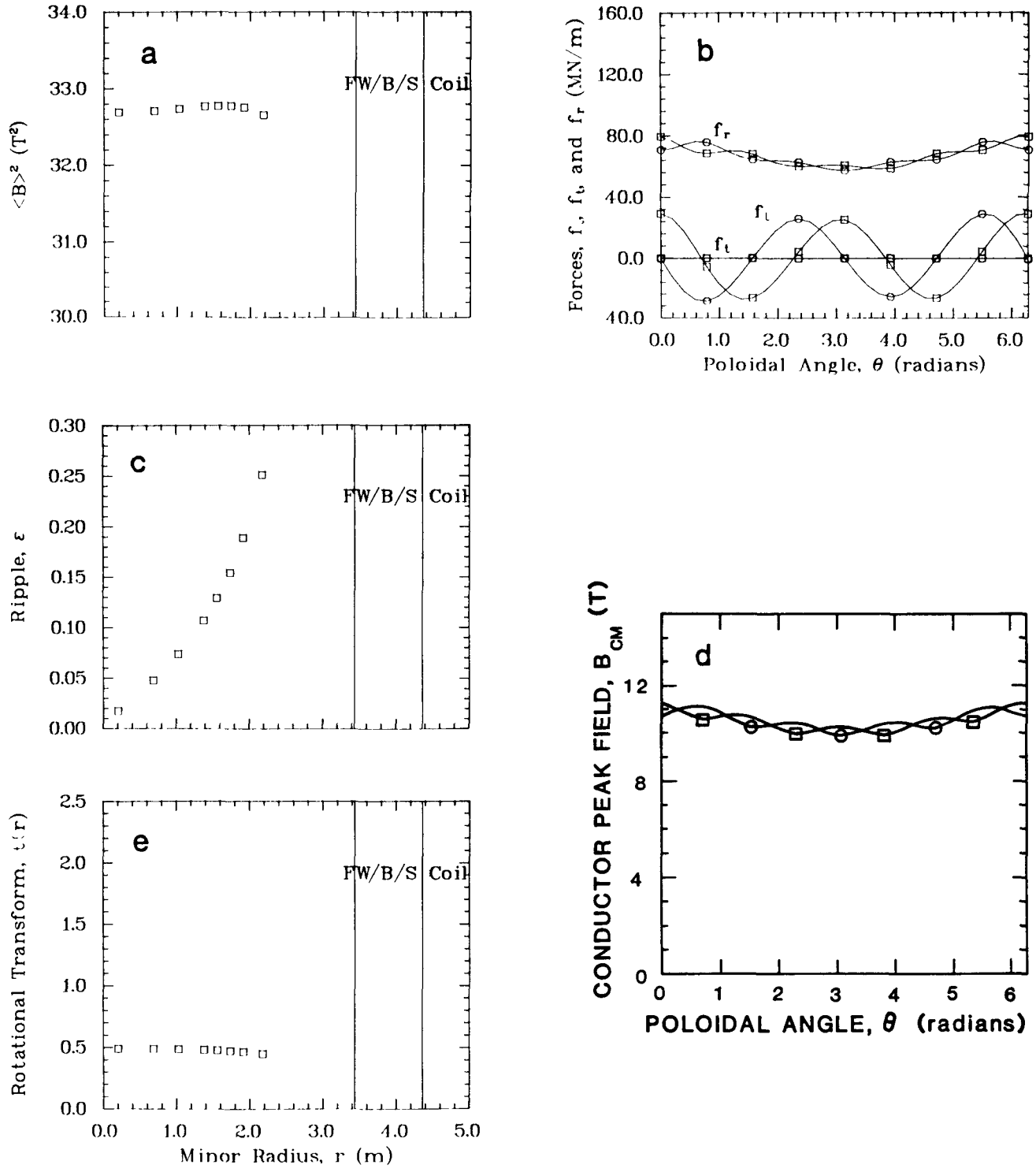

Fig. 4.3-23. The parameters measuring plasma and coil performance for MSR-IIA with uniform j_c. The plotting conventions of Fig. 4.3-3 with the exceptions noted in Fig. 4.3-20 are used here. The forces and fields are shown for the key coil (circles) and the worst-case coil (squares).

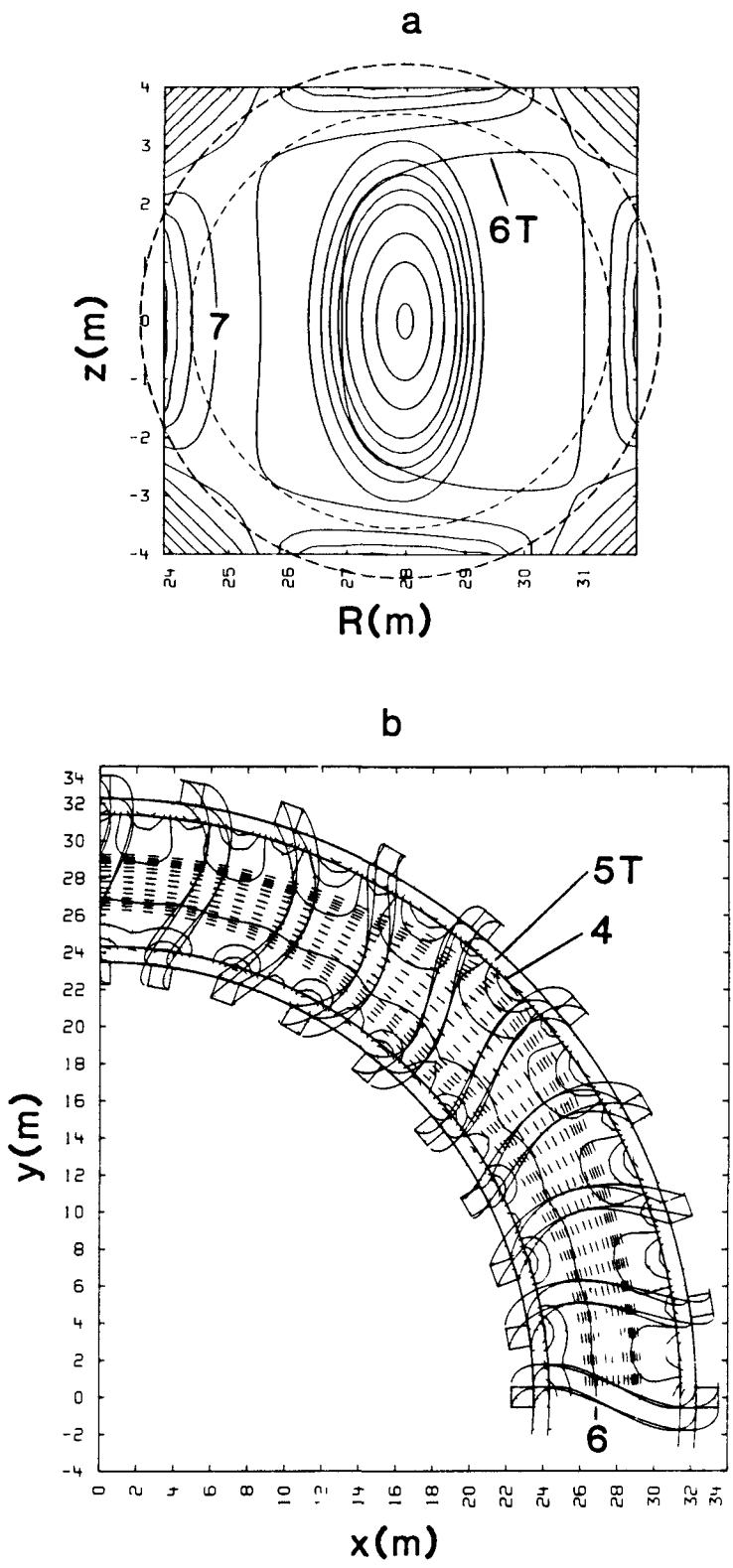

Fig. 4.3-24. The flux surfaces for MSR-IIA with uniform j_c as viewed in the cross section under the key coil (frame a), corresponding to ϕ = 0, and from above the equatorial plane (frame b). The same plotting conventions used in Fig. 4.3-1 are used here.

$$P_y(\theta) = (R_T - r_c \cos\theta)\cos\phi \ , \tag{4.3-6B}$$

$$P_z(\theta) = r_c \sin\theta \ , \tag{4.3-6C}$$

$$T_x(\theta) = r_c \sin\theta \sin\phi + (R_T - r_c \cos\theta)\frac{\ell}{m}(1+\gamma\cos\theta)\cos\phi \ , \tag{4.3-6D}$$

$$T_y(\theta) = r_c \sin\theta \cos\phi - (R_T - r_c \cos\theta)\frac{\ell}{m}(1+\gamma\cos\theta)\sin\phi \ , \tag{4.3-6E}$$

$$T_z(\theta) = r_c \cos\theta \ , \tag{4.3-6F}$$

$$N_x(\theta) = - r_c \cos\theta \sin\phi \ , \tag{4.3-6G}$$

$$N_y(\theta) = - r_c \cos\theta \cos\phi \ , \tag{4.3-6H}$$

$$N_z(\theta) = r_c \sin\theta \ , \qquad \text{and} \tag{4.3-6I}$$

$$\phi = \frac{\ell}{m}(\theta + \gamma \sin\theta) - \frac{\pi\ell}{m} \ , \tag{4.3-6J}$$

where θ is limited to the interval $0 \lesssim \theta \lesssim 2\pi$. In Eqs. (4.3-6), ϕ is the toroidal angle in TORSIDO's cylindrical coordinate system (see Fig. 4.1-1), and γ is a pitch parameter. All other notation is identical to that used in the MSR winding law of Eqs. (4.3-3). The section of the torsatron coil described in Eqs. (4.3-6) is all that is needed for TORSIDO to construct the complete coil set by means of toroidal rotation in the same manner as with MSR coils. The selection of ℓ, γ, m, R_T, and r_c, then, remains.

4.3.3.1. Torsatron Sensitivity Studies. As in the case of the MSR concept, a series of sensitivity studies were performed to aid in the selection of the torsatron design parameters. These sensitivity studies were performed about the base case presented in Table 4.3-4, which has the same design parameters (where applicable) as the MSR base case of Table 4.3-1, except for m. A value of m was chosen for the base case that yields an on-axis rotational transform, $1/2 < \iota < 1$. The pitch parameter, γ, replaces the lateral distortion coefficients. A value of γ was chosen that makes the magnetic axis coincide with R_T on average. The degree by which the magnetic axis oscillates about R_T can be seen from the base-case flux surfaces in Fig. 4.3-25. The outer flux surfaces display a pronounced triangularity in their

TABLE 4.3-4

TORSATRON BASE-CASE DESIGN PARAMETERS

FOR SENSITIVITY STUDIES

PARAMETER	VALUE
Number of poloidal field periods, ℓ	2
Number of toroidal field periods, m	16
Major toroidal radius, R_T (m)	25
Coil minor radius, r_c (m)	4.42
Number of coils, N	2
Pitch parameter, γ	0.5542
Current per coil, I (MA)	21.35
Conductor current density, f_c (MA/m^2)	19
Conductor cross section	square

shape that was not seen in the MSR surfaces. The triangular-shaped surfaces are the result of using the variable pitch winding law of Eq. (4.3-6J) to generate the appropriate vertical field to center the flux surfaces within the coil bore. Based on the MSR sensitivity studies, the ℓ number is fixed at two. The remaining parameters varied in the sensitivity study are γ, m, and the coil aspect ratio $A_c = R_T/r_c$. The shape of the cross section (as determined by its dimensions, δ_ℓ and δ_w) is also varied to investigate its potential for increasing the coil aspect ratio.

The pitch parameter is the first torsatron parameter investigated. The primary effect of varying γ, as seen from the plots of flux surfaces in Figs. 4.3-26 ($\gamma = 0.52$) and 4.3-27 ($\gamma = 0.60$), is to move the plasma along the major radius in the same manner as would result from the introduction of an external vertical field. Tuning γ led to the base case of Fig. 4.3-25 with its magnetic axis coincident with the coil axis on average. The remainder of the effects of varying γ are documented in Fig. 4.3-28. Moving the magnetic axis inward by increasing γ increases the field slightly but makes a larger magnetic hill. Of special concern is the fact that the on-axis field for a torsatron with the same current in the coils as in a MSR is smaller by a substantial amount, resulting in much heavier coils to produce the same field. In addition, the ripple is observed to vary inversely as the γ. Changing γ appreciably affects only the lateral forces, which are small compared to those for an MSR even when scaled up to the same field (see Eqs. 4.1-8 and 4.1-14).

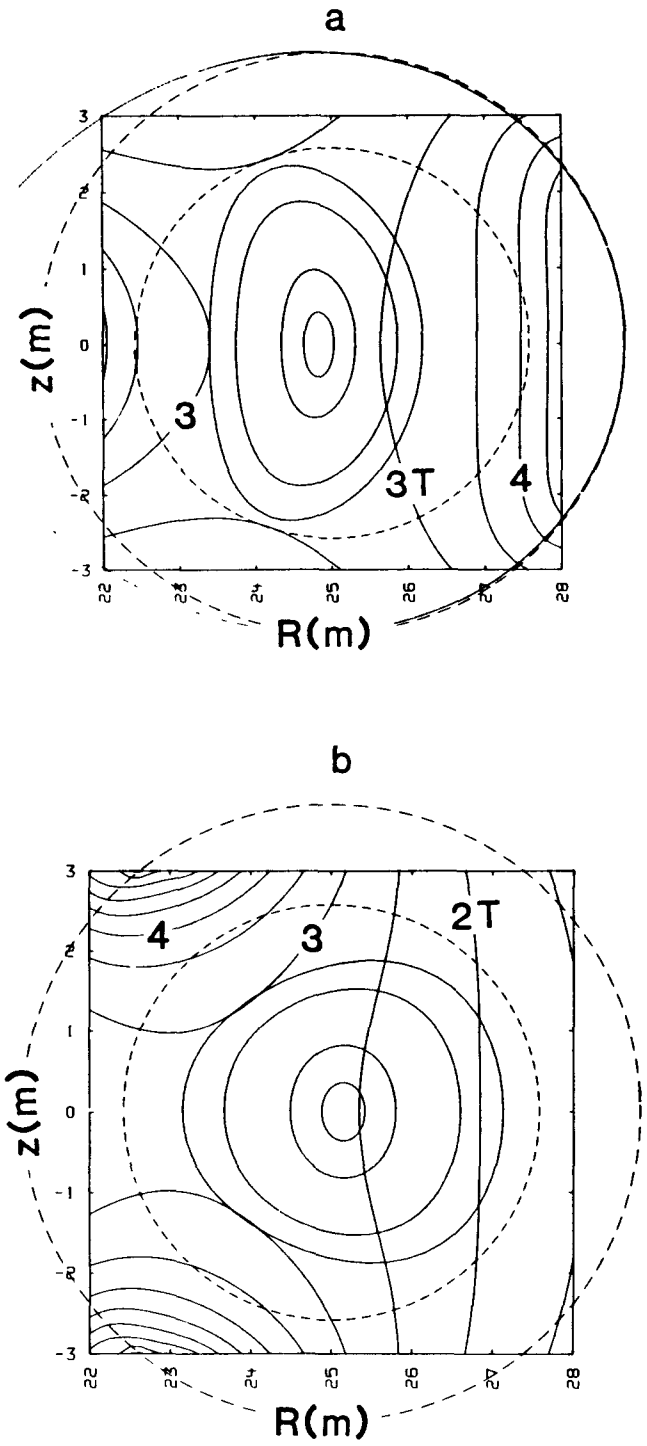

Fig. 4.3-25. The flux surfaces for the base case parameters of Table 4.3-4 as viewed in constant-ϕ cross sections (frames a and b) and from above the equatorial plane (frame c). Frame a corresponds to $\phi = 0$ and b, to $\pi/16$. The same plotting conventions used in Fig. 4.3-1 are used here.

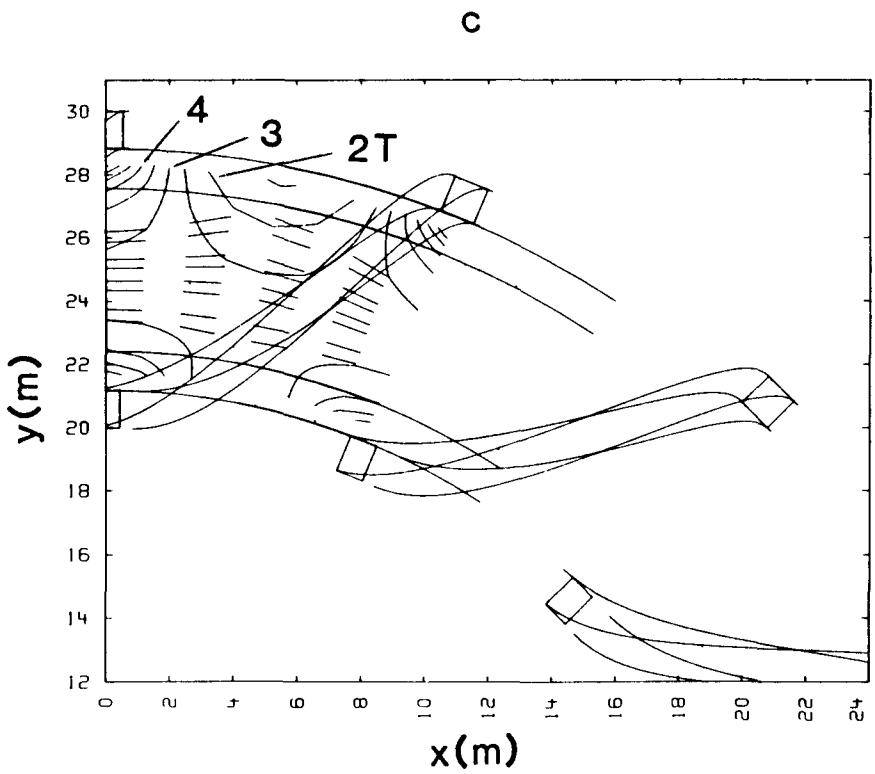

Fig. 4.3-25. (cont)

The radial forces and B_{CM} for a torsatron display a substantially different profile than for an MSR. Both f_r and B_{CM} are functions of the deviation of the current path from a constant-ϕ plane; the lower the deviation, the larger are f_r and B_{CM}. For the range of γ's considered here, the conductor intersects the equatorial plane closer to normal on the outboard side than on the inboard side, as is evident from the square coil cross sections on the outboard sides of Figs. 4.3-25 through 4.3-27. This difference is large enough to overcome the 1/R effects that dominate the MSR profiles of f_r amd B_{CM}.

The results of varying m are presented in Figs. 4.3-29 through 4.3-31. As with the MSR, varying m appears to be an effective means for attaining in the desired ι performance. From frame e of Fig. 4.3-29, ι is seen to be more sensitive to changes in m for the torsatron than for the MSR. However, the torsatron does not share the MSR flux quality problems observed at $\iota \gtrsim 1$ as is evident for the plots of the flux surfaces in Fig. 4.3-30. The better quality

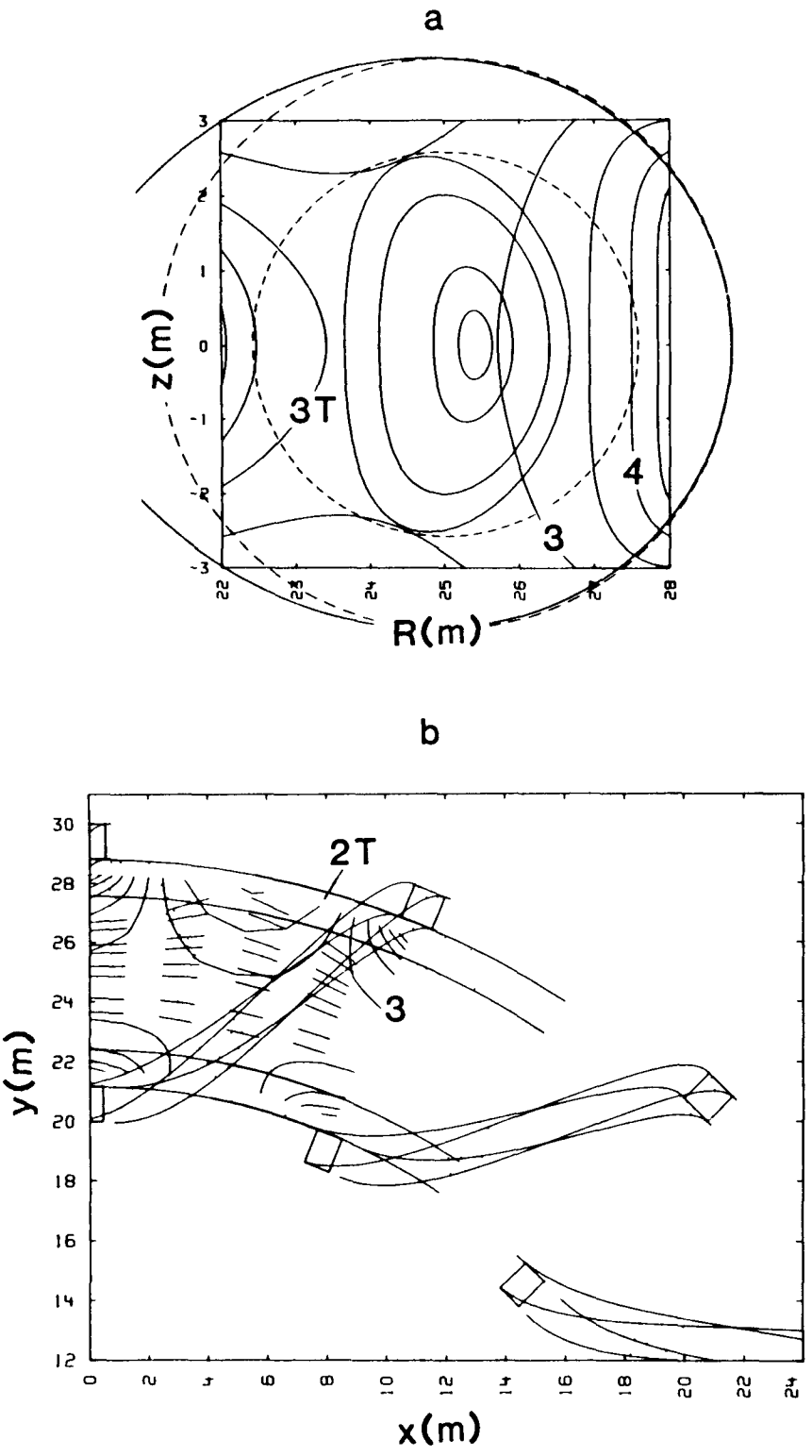

Fig. 4.3-26. The flux surfaces for $\gamma = 0.52$ as viewed in the constant-ϕ = 0 cross section (frame a), and from above the equatorial plane (frame b). The same plotting conventions used in Fig. 4.3-1 are used here.

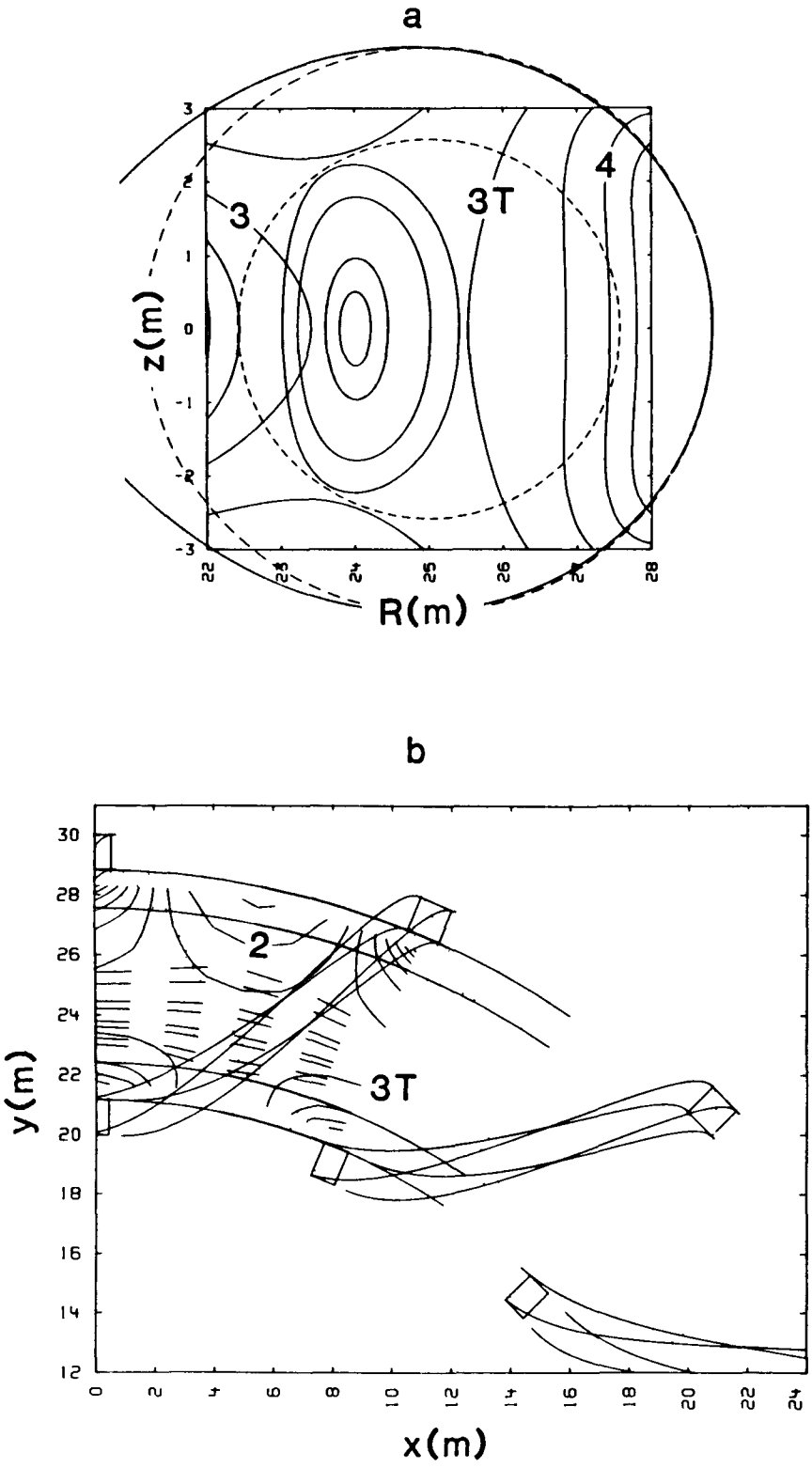

Fig. 4.3-27. The flux surfaces for $\gamma = 0.60$ as viewed in the cross section under the key coil (frame a), corresponding to $\phi = 0$, and from above the equatorial plane (frame b). The same plotting conventions used in Fig. 4.3-1 are used here.

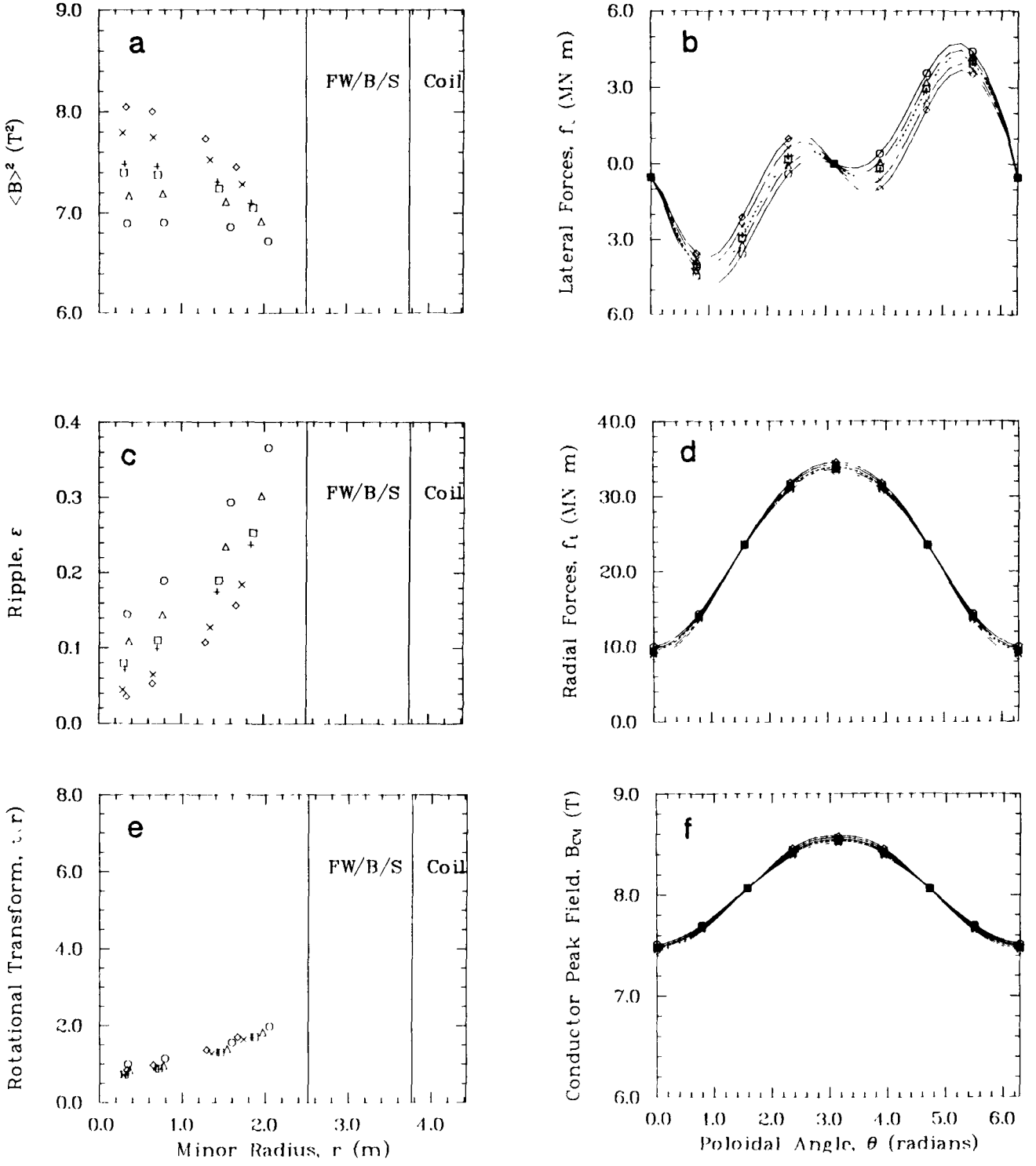

Fig. 4.3-28. A comparison of parameters measuring plasma and coil performance for $\gamma = 0.52$ (circles and solid lines), $\gamma = 0.54$ (triangles and chain-dotted lines), $\delta = 0.5542$ (squares and dashed lines), $\delta = 0.56$ (pluses and dotted lines), $\delta = 0.58$ (x's and chain-dashed lines), and $\delta = 0.60$ (diamonds and solid lines). See the caption for Fig. 4.3-1 for an explanation of the other plot features.

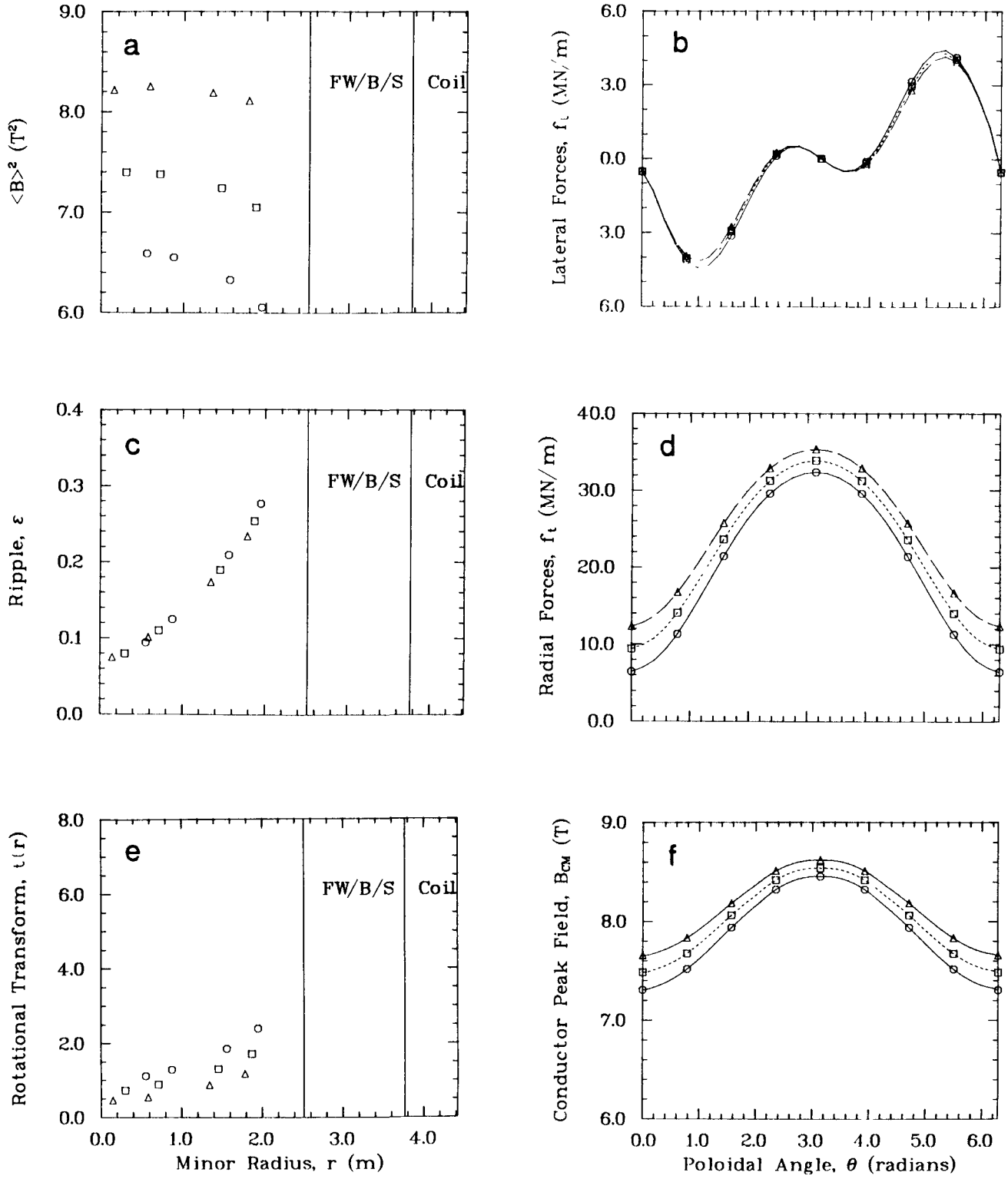

Fig. 4.3-29. A comparison of parameters measuring plasma and coil performance for m = 15 (circles), m = 16 (squares), and m = 17 (triangles). See the caption for Fig. 4.3-3 for an explanation of the other plot features.

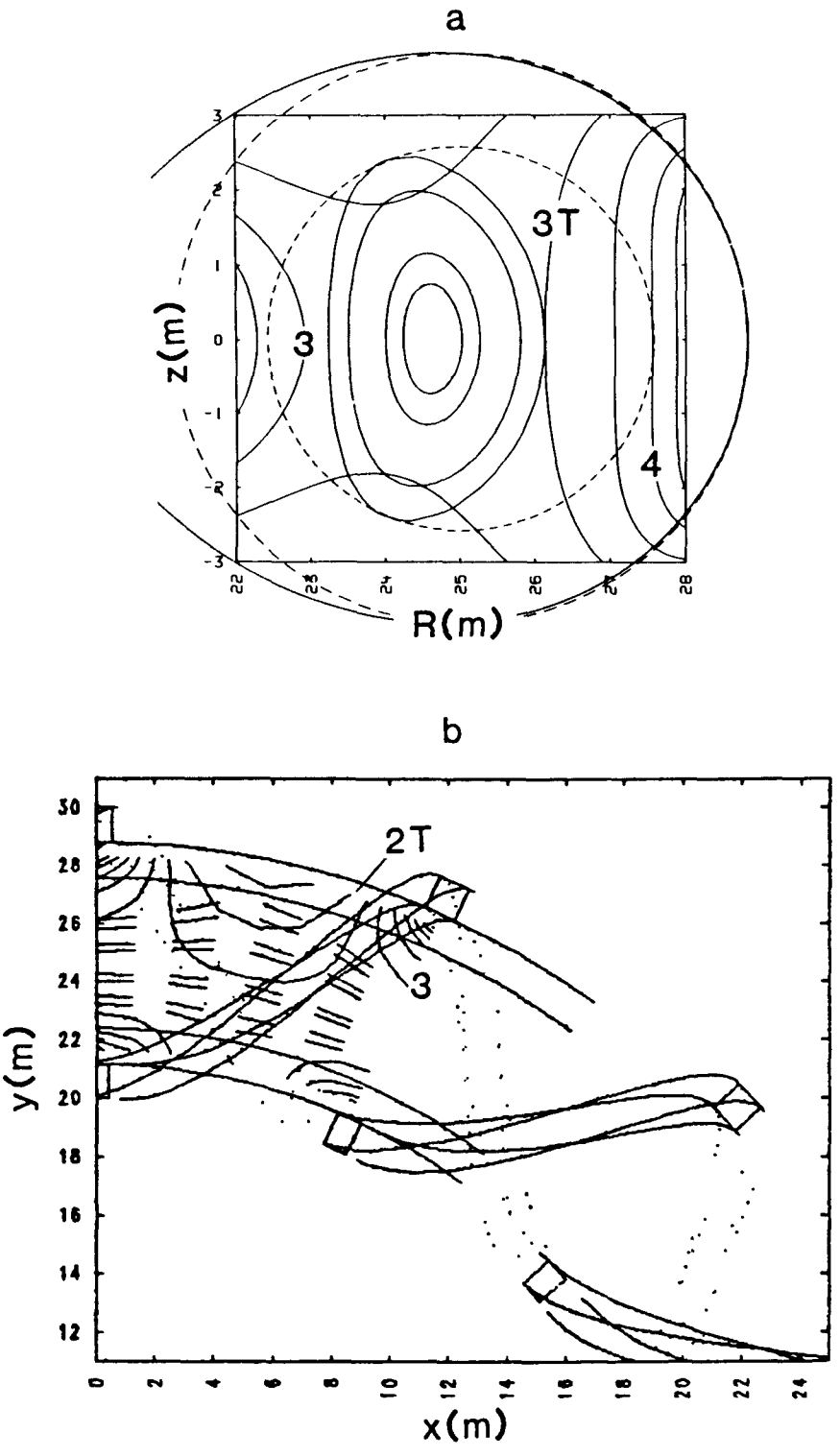

Fig. 4.3-30. The flux surfaces for m = 15 as viewed in the constant-ϕ cross section (frame a) and from above the equatorial plane (frame b). The same plotting conventions used in Fig. 4.3-1 are used here.

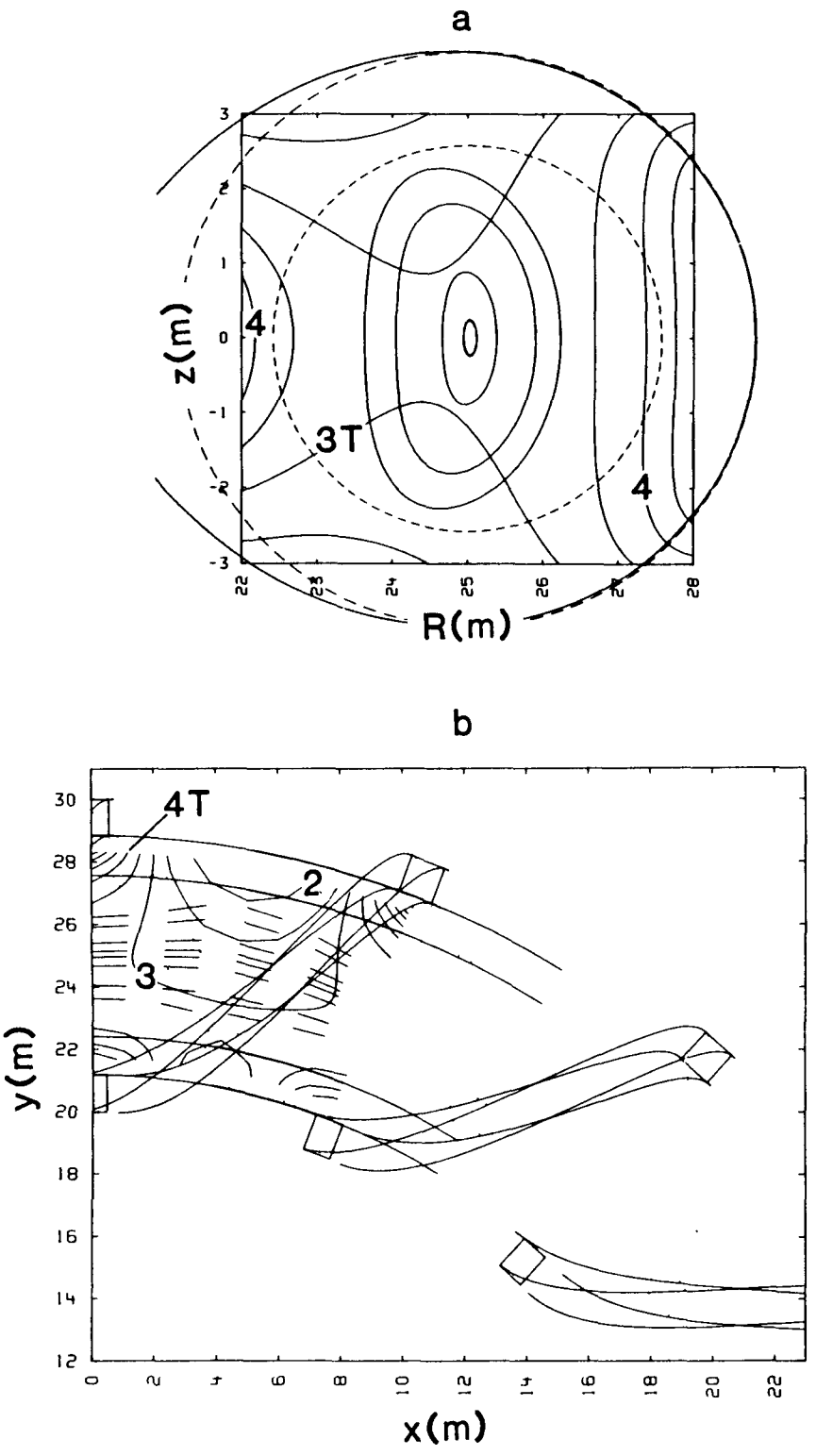

Fig. 4.3-31. The flux surfaces for m = 17 as viewed in the constant-ϕ cross section (frame a) and from above the equatorial plane (frame b). The same plotting conventions used in Fig. 4.3-1 are used here.

of the torsatron flux surfaces at $\iota \gtrsim 1$ could be attributed to the more circular shape of their flux surfaces compared with those for the MSR. Consequently, the torsatrons have a much higher volume utilization than MSR configurations with $\iota \gtrsim 1$. Increasing m also affects the <B> profile but not ε. The opposite behavior (i.e., m affected ε and not <B>) was observed for the MSR. This behavior in the torsatron can be explained by the shift of the magnetic axis, which could not be compensated without adjusting γ. The tighter winding of the higher m, resulting in more toroidal magnetic field, produced increases in the radial forces and B_{CM}.

The variations in coil aspect ratio were accomplished by changing r_c. The effect of changing r_c upon ι is the most dramatic of those presented in Figs. 4.3-32 and 4.3-33. The relative height of the magnetic hill and the ripple also change inversely as r_c. The higher aspect ratio also results in lower B_{CM} and f_r as a result of the ~1/R dependence of the field within the coil bore. The lateral forces are adversely affected by decreasing r_c, but they are still small compared to those for the MSR. Figure 4.3-33 reveals that the increased elongation of the flux surfaces as a result of the increased transform does not interfere with the clearance between the flux surfaces and the coils as was the case with the MSR. Consequently, the torsatron is better suited to take advantage of changes in the coil cross section made in an attempt to decrease r_c. The variations on the cross section shape (i.e., δ_ℓ/δ_w) produce only minor changes in all of the parameters presented in Fig. 4.3-34 except B_{CM}. Consequently, changing δ_ℓ/δ_w should be a viable means to change the coil aspect ratio in the torsatron that is not available to the MSR.

The results of the single-variable sensitivity studies for the torsatron indicate that the final designs should fine and impose the γ that centers the flux surfaces within the coils, yielding the optimum volume utilization. The m should be determined through the ι performance expected of the coil set. Because the clearance between the flux surfaces and the coils is not an issue 360° poloidially within a cross section as was the case for the MSR, r_c should be made as small as possible including reducing r_c by minimizing δ_w.

4.3.3.2. Torsatron Design Points. As for the MSR, high- and low-beta cases were generated for the torsatron approach. To permit a comparison of the two concepts, the torsatron designs were evolved from their MSR counterparts. The limited resources of this study permitted the pursuit of

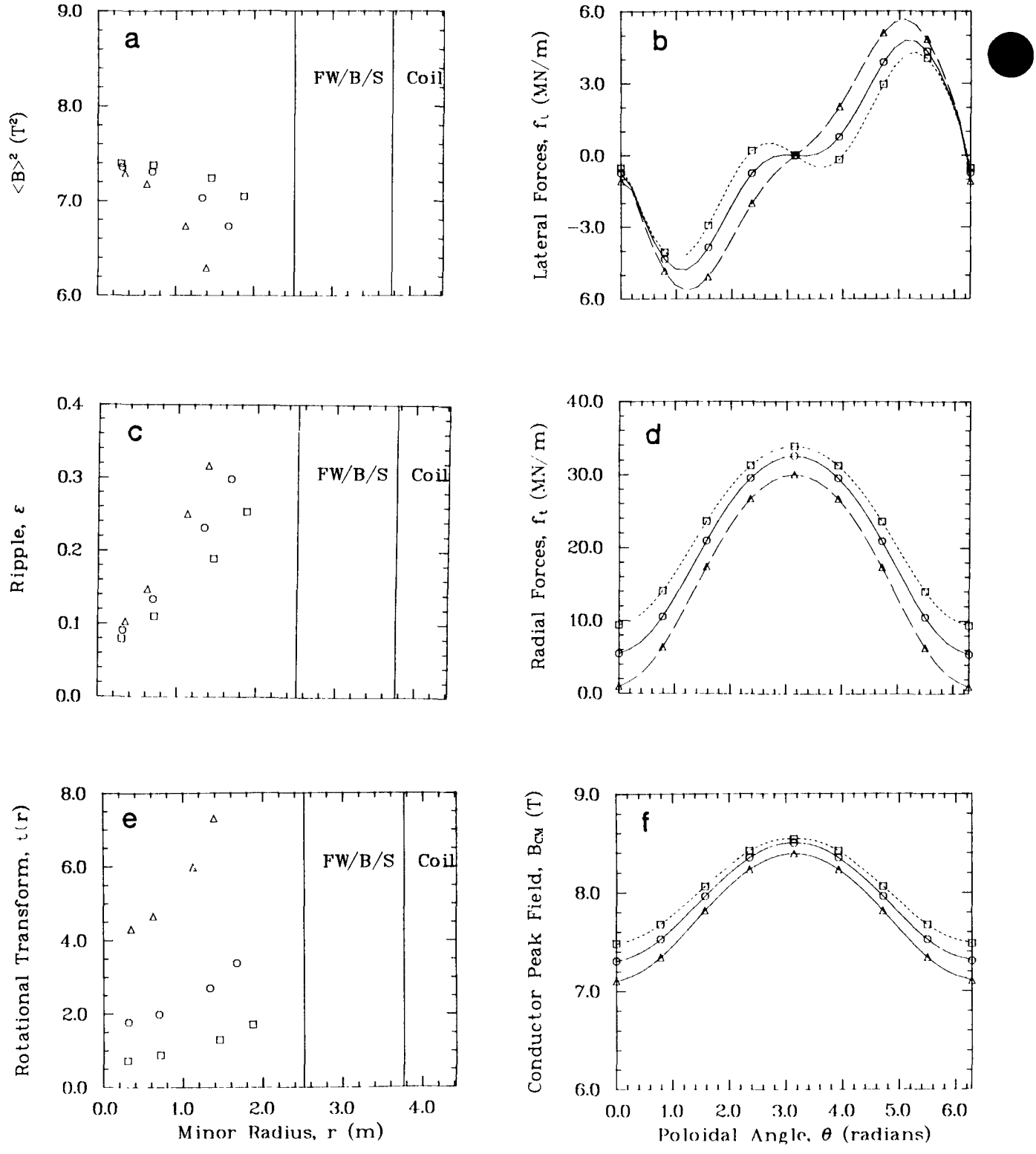

Fig. 4.3-32. A comparison of parameters measuring plasma and coil performance for r_c = 4.42 m (squares), r_c = 3.92 m (circles), and r_c = 3.42 m (triangles). See the caption for Fig. 4.3-3 for an explanation of the other plot features.

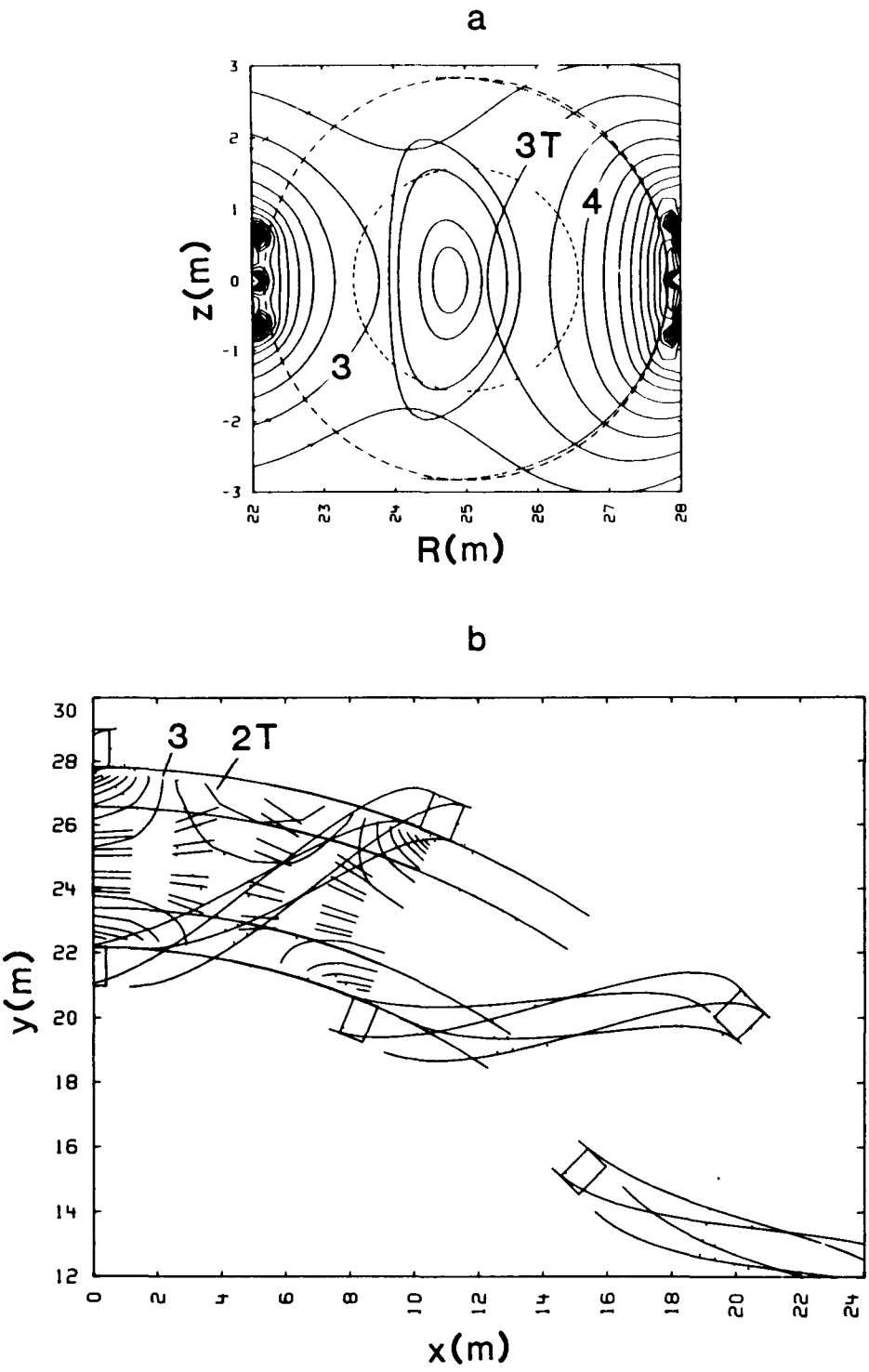

Fig. 4.3-33. The flux surfaces for r_c = 3.42 m as viewed in the constant-ϕ cross section (frame a) and from above the equatorial plane (frame b). The same plotting conventions used in Fig. 4.3-1 are used here.

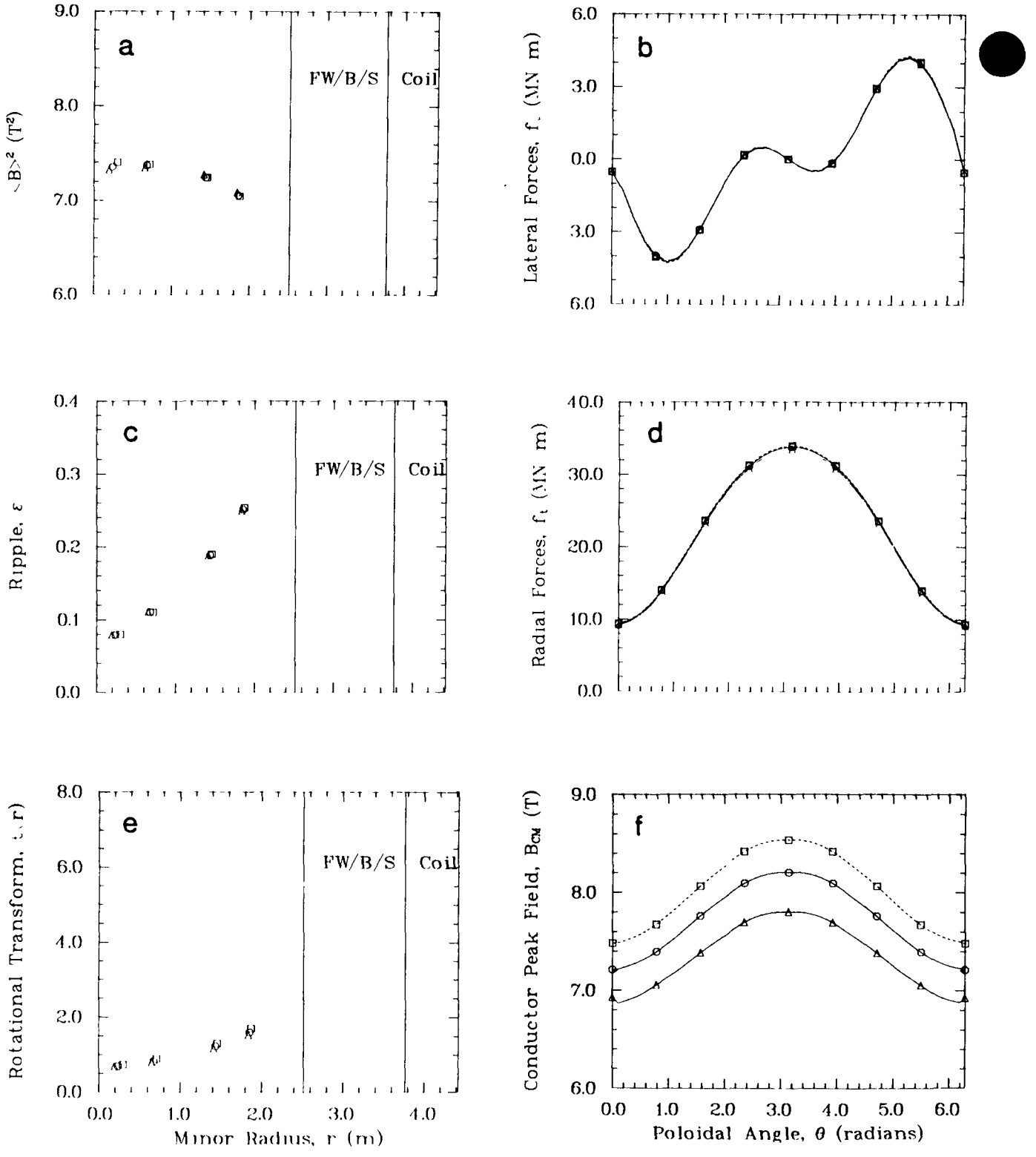

Fig. 4.3-34. A comparison of parameters measuring plasma and coil performance for $\delta_l/\delta_w = 1$ (squares), $\delta_\ell/\delta_w = 3/2$ (circles), and $\delta_\ell/\delta_w = 2$ (triangles). See the caption for Fig. 4.3-3 for an explanation of the other plot features.

the beneficial differences between the MSR and torsatron for only the high-beta torsatron design, TR-B3. The smaller coil radius, higher on-axis field, and rectangular coil cross section design presented in Table 4.3-5 resulted. As can be seen from the plots of the flux surfaces in Figs. 4.3-35 and 4.3-36, proceeding from a uniform-j_c simulation of the coil set to the stepped-j_c simulation, which reflects the conductor design in Sec. 5.2., results in an outward shift of the flux surfaces because of an effective change in the current center, r_c. The final design of Fig. 4.3-37 resulted from an adjustment of γ to center the flux surfaces. The better volume utilization of the torsatron has permitted a ~1-m-smaller r_c, while providing for approximately the same clearance between the coils and plasma. The higher ratio of B_o/B_{CM} for the torsatron permitted a reduction in r_p because of the constant-$<\beta>B_o^2 r_p$ ignition constraint used in this study; the reduced r_p contributed to the increased coil aspect ratio. The most striking difference, however, between MSR-IIB and TR-B3 is the rotational transform. The TR-B3 design obtained its goal of 1.8 [Eq. (4.3-2)] with $d\iota/dr > 0$ as seen in Fig. 4.3-38, whereas the MSR-IIB design could not meet its ι goal of ~1.5. In terms of the coils, the radial forces in the TR-B3 are 50% larger than those for the MSR-IIB, whereas the lateral forces are 25% of those for the MSR-IIB. A coil design for both systems is required to determine if the TR-B3 radial forces or the MSR-IIB lateral forces are more difficult to support. In addition, the stored energy of TR-B3 is 2.5 times larger than in the MSR-IIB because of the increased toroidal orientation of the current in the torsatron winding. The ripple values in both high-beta designs are comparable and both cases display slight magnetic hills.

Study resources permitted only a minimal effort in converting the low-beta MSR-IIA parameters into the TR-A design of Table 4.3-6. Consequently, none of the unique torsatron features, for example the volume utilization depicted in Fig. 4.3-39, could be used to advantage, as it was in the high-beta case. Again, the torsatron was able to meet its low-beta goal of ~0.7 as seen from Fig. 4.3-40. However, the strong shear inherent to torsatrons causes the ι profile to cross the rational $q = 1$ surface, but the shear at that surface should be stabilizing as in Heliotron-E.[15] Because the TR-A design has not been optimized, little more can be inferred from a comparison of TR-A and MSR-IIA. However, the TR-A design confirms the same trends exhibited by the TR-B3 design.

TABLE 4.3-5

TR-B3 MAGNETICS RESULTS

PARAMETER	UNIFORM j_c [a]	STEPPED j_c [b]	STEPPED j_c [b]
Design $\langle\beta\rangle$	0.08	0.08	0.08
Coil type	Torsatron	Torsatron	Torsatron
Pitch parameter, γ	0.365	0.365	0.388
Normalized distortion, d/r_c	NA	NA	NA
Distortion coefficients:			
a_1	NA	NA	NA
a_2	NA	NA	NA
a_3	NA	NA	NA
a_4	NA	NA	NA
a_5	NA	NA	NA
a_6	NA	NA	NA
Conductor major radius, R_T (m)	23.0	23.0	23.0
Conductor minor radius, r_c (m)	2.3	2.3	2.3
Conductor aspect ratio, $A_c = R_T/r_c$	10.0	10.0	10.0
Total coil current, I (MA)	35.7	35.7	35.7
Conductor cross section (m × m)	0.994 × 1.889	0.994 × 1.889	0.994 × 1.889
Conductor length, L_c (m)	461.405	461.405	461.57
Number of poloidal field periods, ℓ	2	2	2
Number of toroidal field periods, m	25	25	25
Number of coils, N	1	1	1
Plasma major radius (m)	22.990	23.271	22.989
Plasma minor radius, r_p (m)	0.574	0.572	0.573
Plasma Volume, V_p (m^3)	149.47	150.08	148.89
Magnetic axis (m)	23.002	23.303	23.001
Semiminor radius[c] (m)	0.448(0.533)	0.433(0.572)	0.446(0.559)
Semimajor radius[c] (m)	0.717(0.641)	0.721(0.615)	0.721(0.612)
Limiter radius (m)	0.758	1.01	0.762
On-axis field, B_o (T)	7.72	7.50	7.64
Well depth (%)	-0.46	0.019	-0.16
Peak field at coil, B_{CM} (T)	12.01	12.09	12.14
On-axis ripple, $\varepsilon(0)$%	<4.65	<10.23	<4.62
Edge ripple, $\varepsilon(r_p)$%	10.90	15.40	10.23
On-axis transform, $\iota(0)$	1.861	1.872	1.479
Edge transform, $\iota(r_p)$	2.357	2.034	1.847
Stored magnetic energy, E_M (GJ)	252.03	252.03	252.03
Peak radial force, f_r (MN/m)	107.16	110.57	112.25
Peak lateral force, f_ℓ (MN/m)	12.35	13.51	11.82

[a] $j_c = 19$ MA/m^2.

[b] $j_c = 12.04$ MA/m^2 for $0 < t < 0.519$; $j_c = 22.43$ MA/m^2, $0.519 < t < 0.811$; and $j_c = 32.83$ MA/m^2, $0.811 < t < 1.0$; where the fraction t is measured radially through the conductor cross section.

[c] Under a key coil and half a field period away.

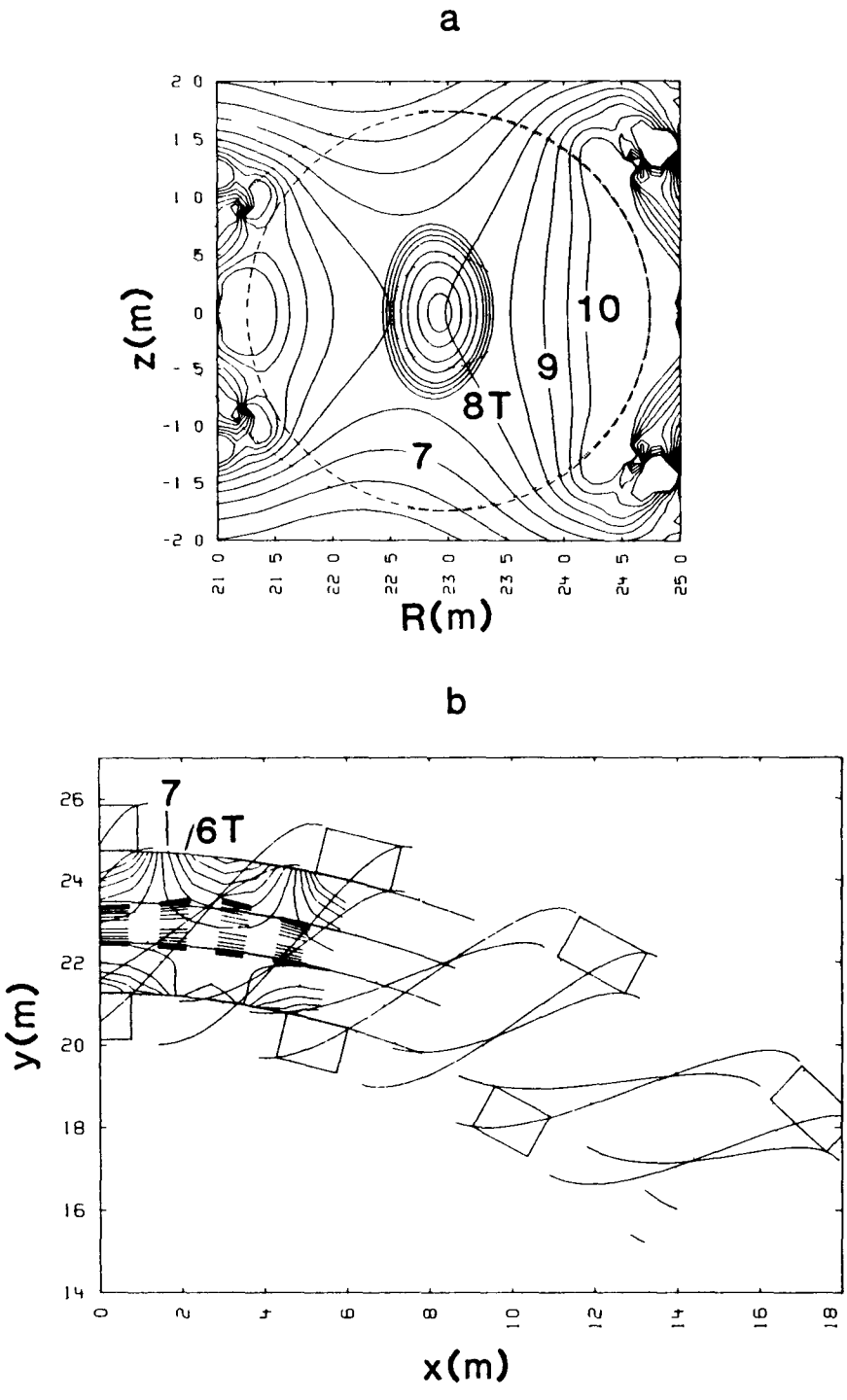

Fig. 4.3-35. The flux surfaces for TR-B3 with uniform j_c and $\gamma = 0.365$ as viewed in the constant-ϕ = 0 cross section (frame a) and from above the equatorial plane (frame b). The same plotting conventions used in Fig. 4.3-1 are used here. The next to the outermost surface traced defines the plasma volume of Table 4.3-5.

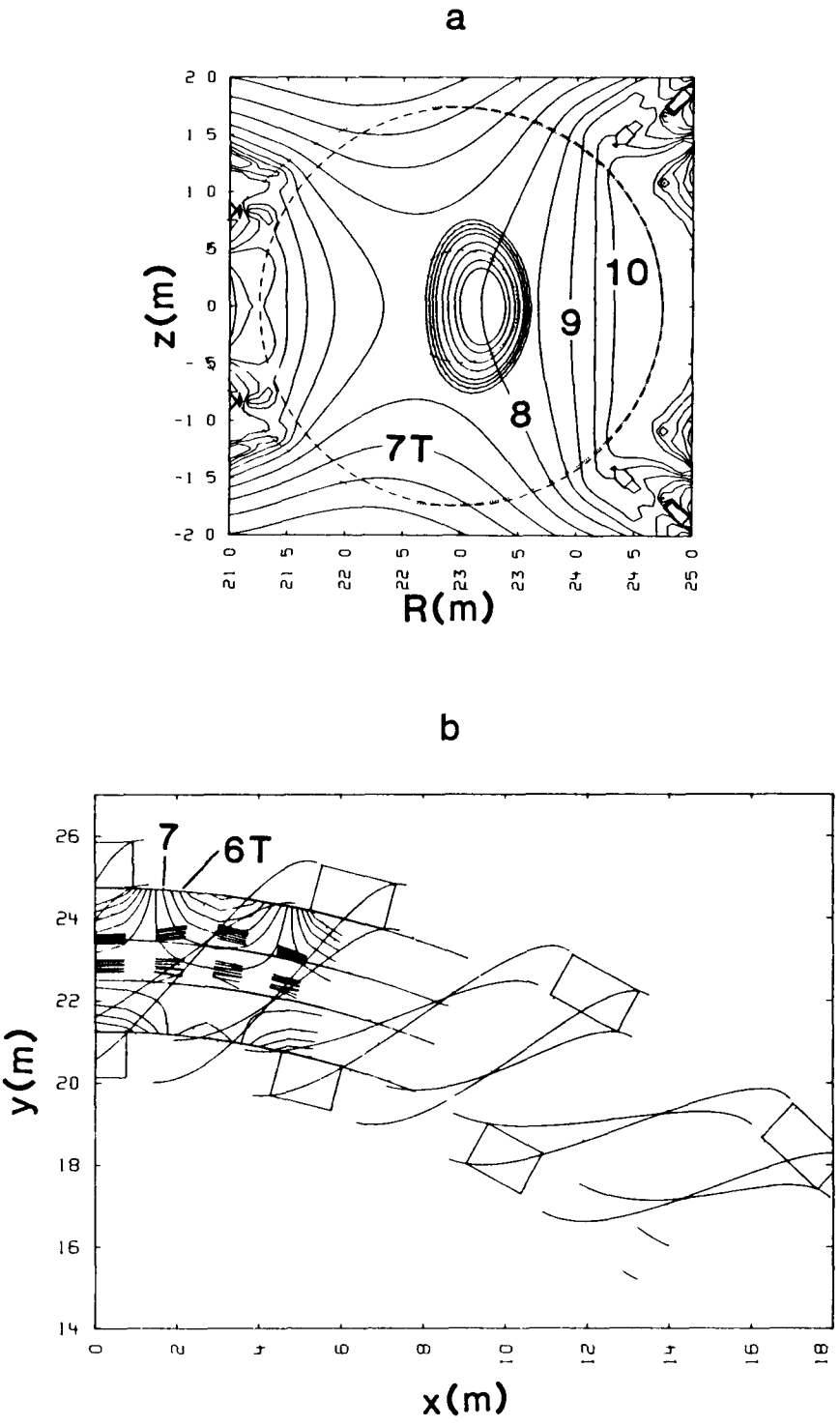

Fig. 4.3-36. The flux surfaces for TR-B3 with stepped j_c and $\gamma = 0.365$ as viewed in the constant-ϕ = 0 cross section (frame a) and from above the equatorial plane (frame b). The same plotting conventions used in Fig. 4.3-1 are used here. The next to the outermost surface traced defines the plasma volume of Table 4.3-5.

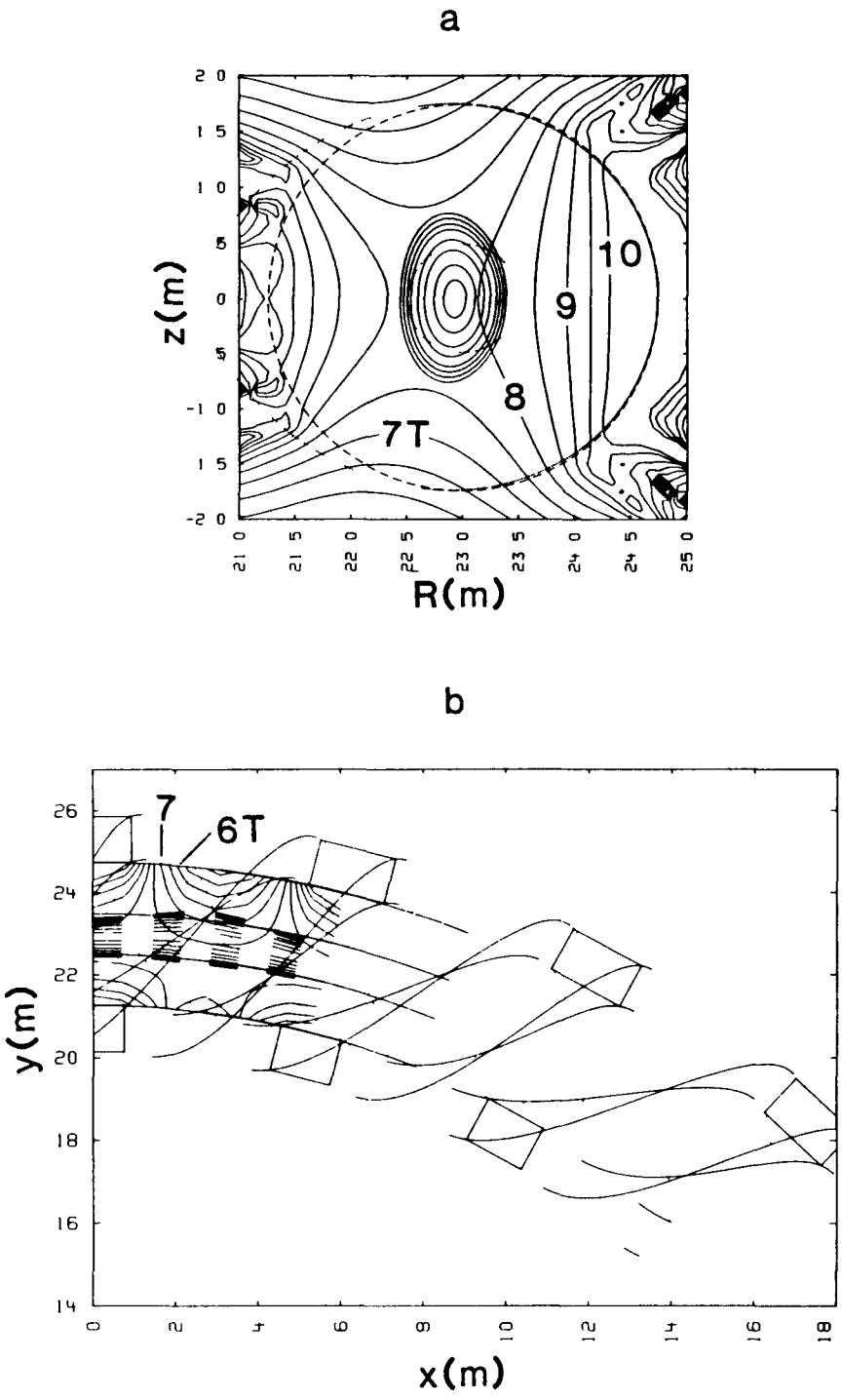

Fig. 4.3-37. The flux surfaces for TR-B3 with stepped j_c and γ = 0.388 as viewed in the constant-ϕ = 0 cross section (frame a) and from above the equatorial plane (frame b). The same plotting conventions used in Fig. 4.3-1 are used here. The next to the outermost surface traced defines the plasma volume of Table 4.3-5.

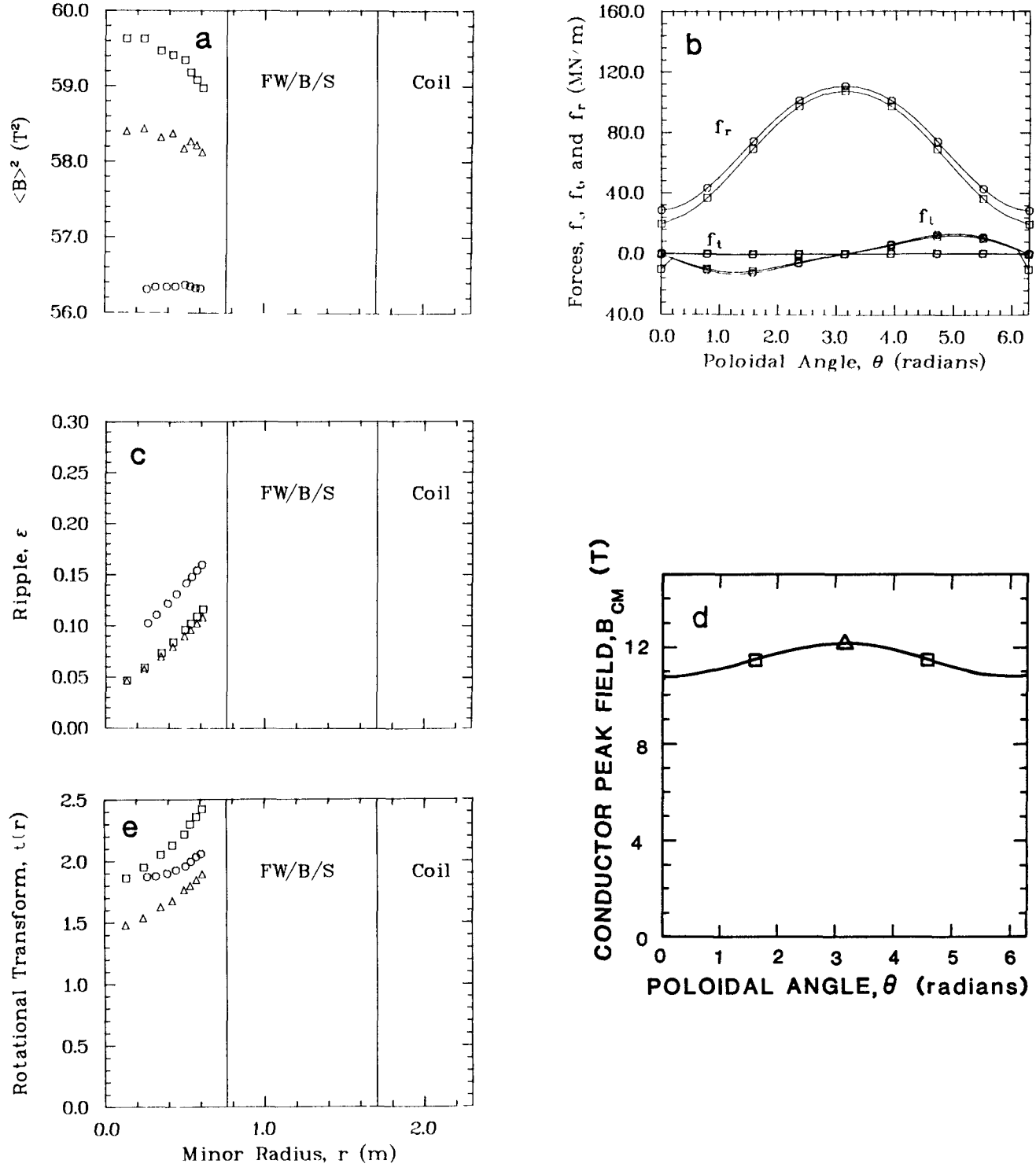

Fig. 4.3-38. A comparison of parameters measuring plasma and coil performance for TR-B3 with uniform j_c and $\gamma = 0.365$ (squares), with stepped j_c and $\gamma = 0.365$ (circles), and with stepped j_c and $\gamma = 0.388$ (triangles). The plotting conventions of Fig. 4.3-3 with the exception noted in Fig. 4.3-20 are used here.

TABLE 4.3-6

TR-A MAGNETICS RESULTS

PARAMETER	UNIFORM j_c (a)
Design $\langle\beta\rangle$	0.04
Coil type	Torsatron
Pitch parameter, γ	0.57
Normalized distortion, d/r_c	NA
Distortion coefficients:	
a_1	NA
a_2	NA
a_3	NA
a_4	NA
a_5	NA
a_6	NA
Conductor major radius, R_T (m)	27.9
Conductor minor radius, r_c (m)	5.0
Conductor aspect ratio, $A_c = R_T/r_c$	5.58
Total coil current, I (MA)	50.018
Conductor cross section (m × m)	1.082 × 2.434
Conductor length (m)	304.224
Number of poloidal field periods, ℓ	2
Number of toroidal field periods, m	16
Number of coils, N	2
Plasma major radius (m)	27.87
Plasma minor radius, r_p (m)	2.30
Plasma volume, V (m^3)	2909.74
Magnetic axis (m)	27.891
Semiminor radius(b) (m)	1.685(2.302)
Semimajor radius(b) (m)	2.936(2.401)
Limiter radius (m)	3.160
On-axis field, B_o (T)	5.71
Well depth (%)	-2.11
Peak field at coil, B_{CM} (T)	12.47
On-axis ripple, $\varepsilon(0)$%	<9.73
Edge ripple, $\varepsilon(r_p)$%	25.61
On-axis transform, $\iota(0)$	0.569
Edge transform, $\iota(r_p)$	1.469
Stored magnetic energy, E_M (GJ)	609.64
Peak radial force, f_r (MN/m)	151.04
Peak lateral force, f_ℓ (MN/m)	18.90

(a) $j = 19$ MA/m^2.

(b) Under a key coil and half a field period away.

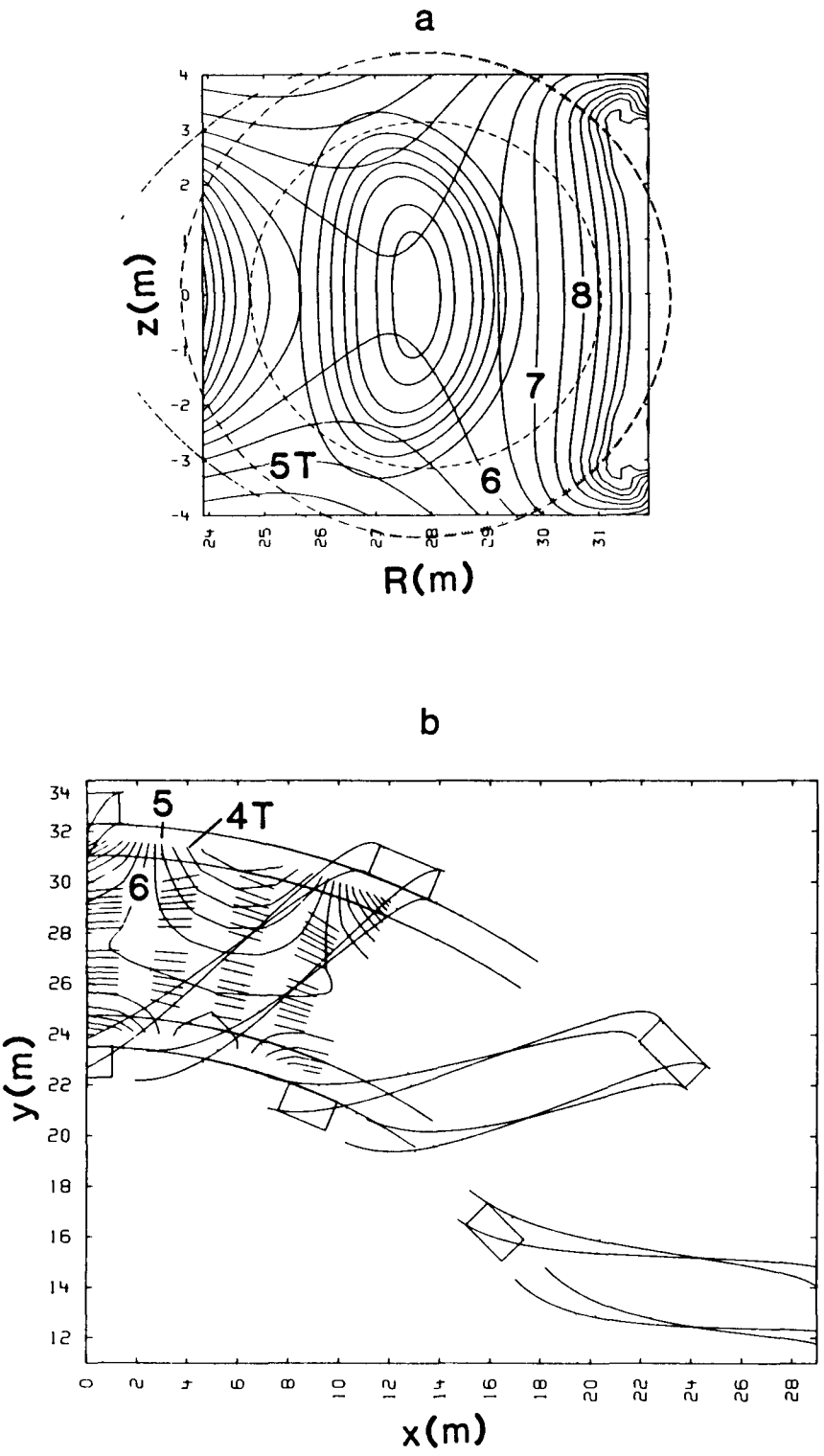

Fig. 4.3-39. The flux surfaces for TR-A as viewed in the constant-ϕ = 0 cross section (frame a) and from above the equatorial plane (frame b). The same plotting conventions used in Fig. 4.3-1 are used here.

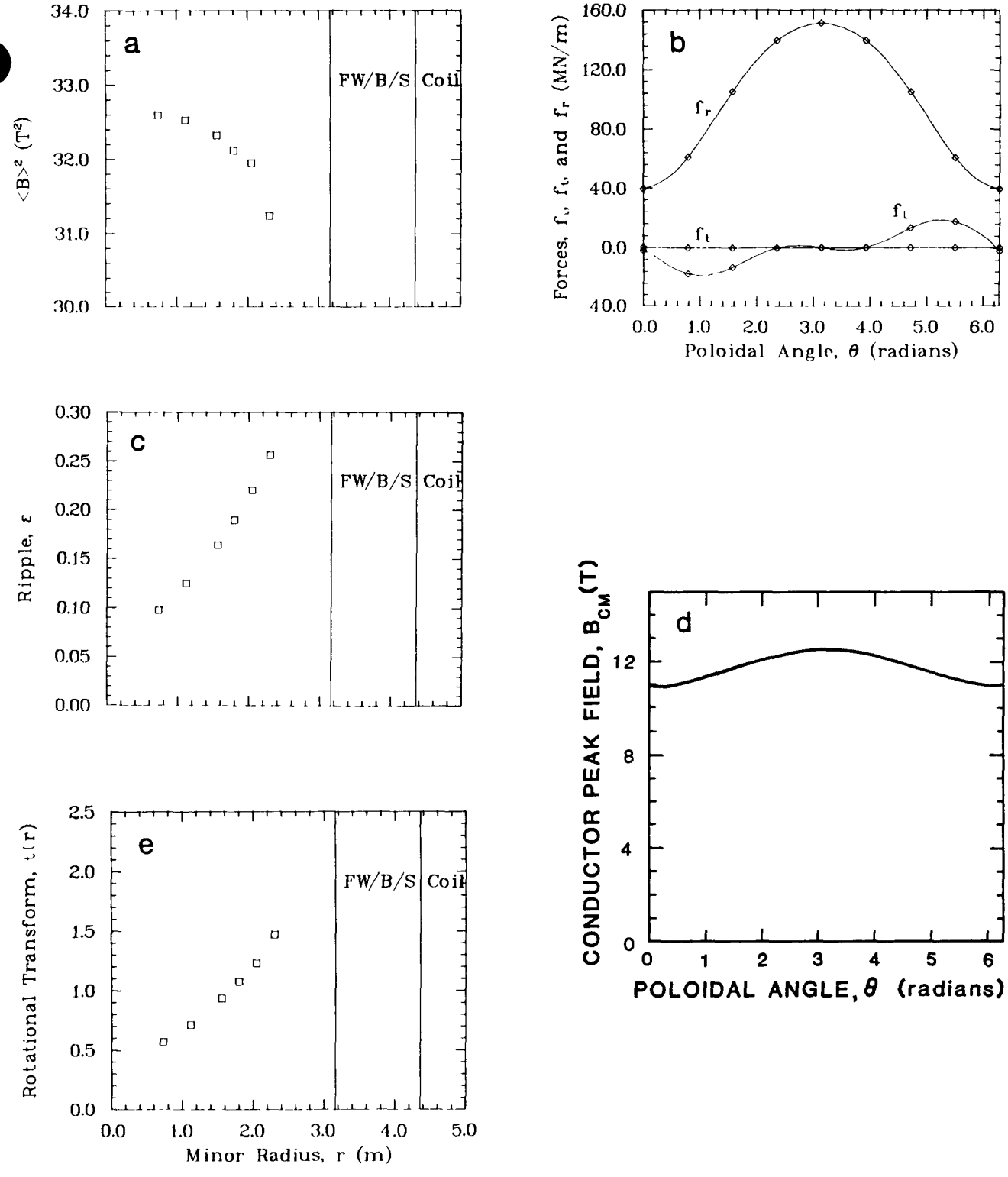

Fig. 4.3-40. The results of parameters measuring plasma and coil performance for TR-A. The plotting conventions of Fig. 4.3-3 with the exceptions noted in Fig. 4.3-20 are used here.

4.4. Advanced Configurations/Future Directions

An ideal reactor embodiment was not found for either of the stellarator concepts considered in this study: the modular stellarator and the torsatron. The inherent modularity of the MSR results in designs with excellent engineering properties (i.e., ease of fabrication, assembly, and maintenance). However, the physics properties (principally, the rotational transform and shear) of the MSR were inferior to the corresponding torsatrons. The torsatron, on the other hand, is capable of producing nearly any level of physics performance desired (as measured by transform and shear); but without breakable superconducting joints, the nature of the torsatron winding poses severe problems for the fabrication, assembly, and maintenance of the coils. The heliac[18] is similar to the torsatron in that it promises good physics performance and high beta[19], but the heliac has interlocking coils. The Meyer-Schmidt (M&S) approach[9,15] also promises both good physics performance and high beta, and good engineering properties because of its modularity. The M&S approach minimizes the variance of $\int d\ell/B$ over a field period, S. In the course of this study, only the torsatron was found to minimize S to the levels needed by the M&S approach, as seen by the representative results of Fig. 4.4-1, by virtue of a higher m compared to the MSR. The limited resources of this study did not permit the study of this approach in addition to the MSR and torsatron.

Attempts were made to improve the physics performance of the MSR. However, the truncation of this study prevented the application of the results of sensitivity studies that extended those of Sec. 4.3.2.1. These studies are presented in this section in order to document recommendations concerning the future directions in which MSR design studies should proceed.

The problem of lower overall transform profile associated with the introduction of the asymmetric lateral distortion of Eq. (4.3-5) can be overcome by a Fourier representation of a flat-top, saw-tooth wave shown in Fig. 4.4-2. If a factor is introduced to damp the Gibbs phenomenon, the expression for the a_i's is

$$a_i = \frac{C}{i^2}\left\{1 + \frac{\sin i\pi\rho}{i\pi(1-\rho)}\right\} \quad , \tag{4.4-1}$$

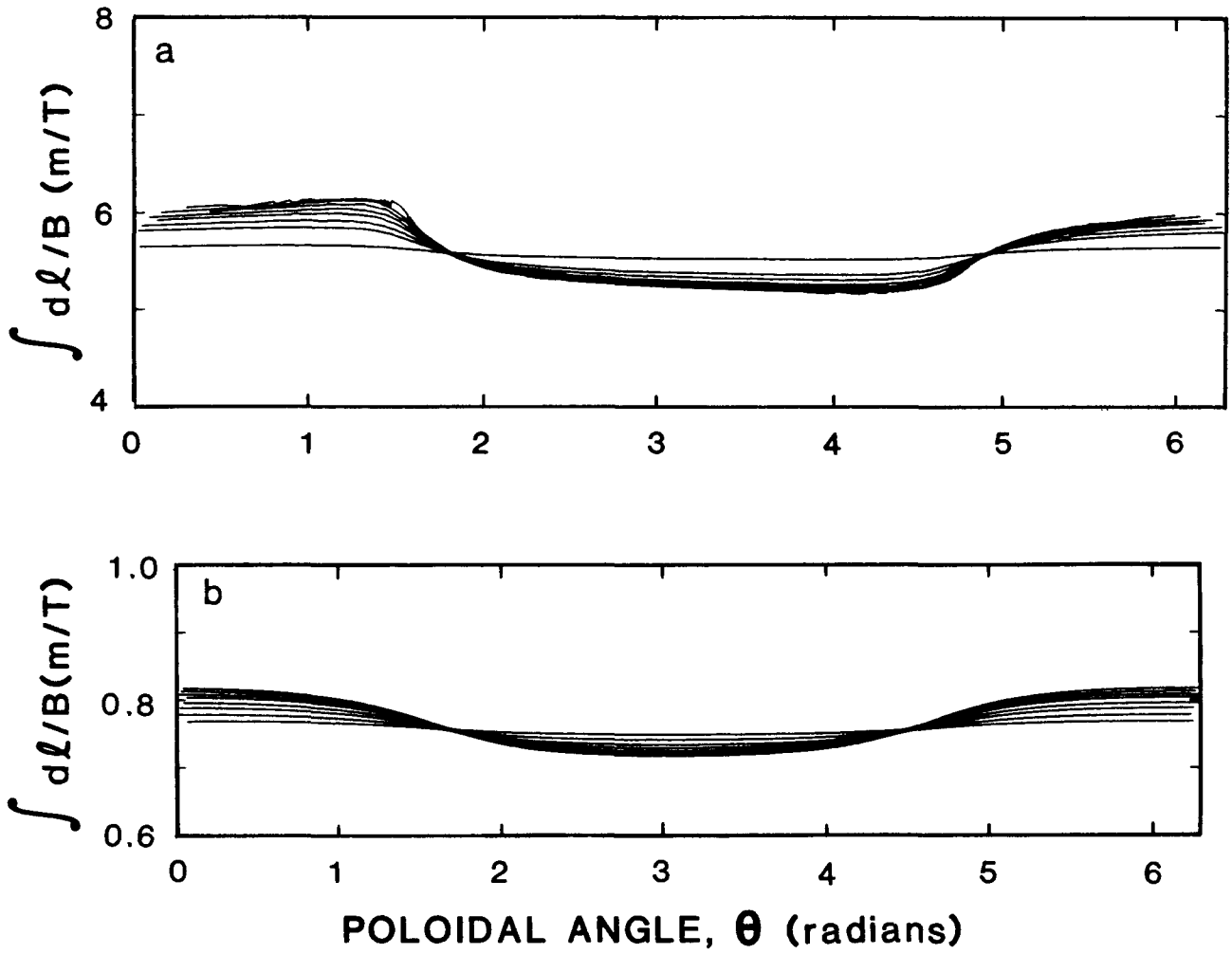

Fig. 4.4-1. The poloidal variation under the key coil (ϕ = 0) of $\int d\ell/B$, where the integration is over one field period only. Frame a is for MSR-IIB and frame b, TR-B3.

where C is a normalization constant determining the maximum distortion and ρ controls the angular extent of the flat top as well as indirectly due to the the Gibbs phenomenon. Letting ρ = 0.04 in Eq. (4.4-1) results in the distortion pattern shown in Fig. 4.4-3 with a_1 = 0.2200, a_2 = 0.0550, a_3 = 0.0244, a_4 = 0.0137, a_5 = 0.0088, and a_6 = 0.0061 for a maximum distortion, d = $0.22r_c$. The results of letting ρ = 0.04 in Eq. (4.4-1) are presented in Figs. 4.4-4 and 4.4-5. The most noticeable effect is the attainment of positive shear (i.e., $d\iota/dr > 0$) without sacrificing transform, as was the case with the asymmetric distortion. In addition the forces and B_{CM} are

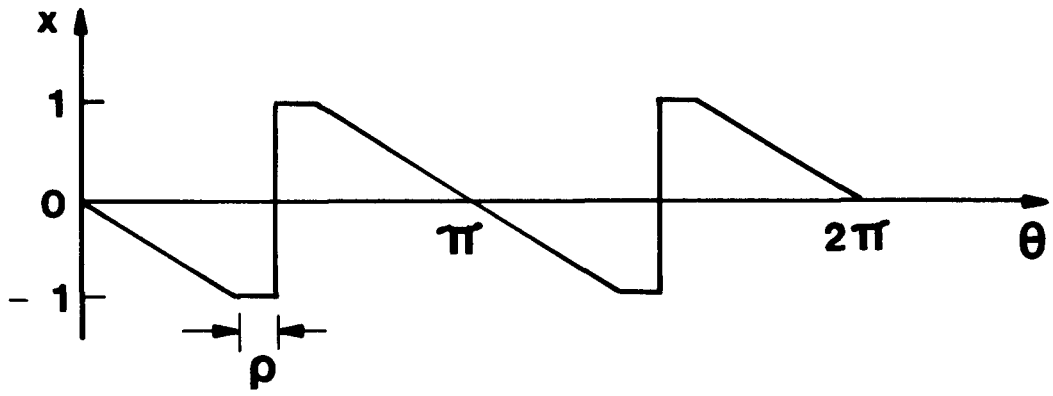

Fig. 4.4-2. The periodic function upon which the model for determining the a_i's of Eq. (4.4-1) is based.

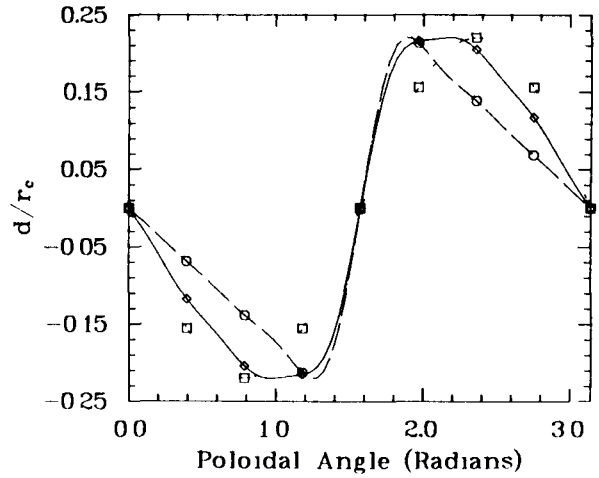

Fig. 4.4-3. The lateral distortion of the key coil as a function of poloidal angle for $\rho = 0.04$ in Eq. (4.4-1) (diamonds) relative to the asymmetric distortion with $\delta = 0.15$ in Eq. (4.3-5) (circles) and the base case with $a_1 = 0.22$ and $a_2 = a_3 = a_4 = a_5 = a_6 = 0$ (squares).

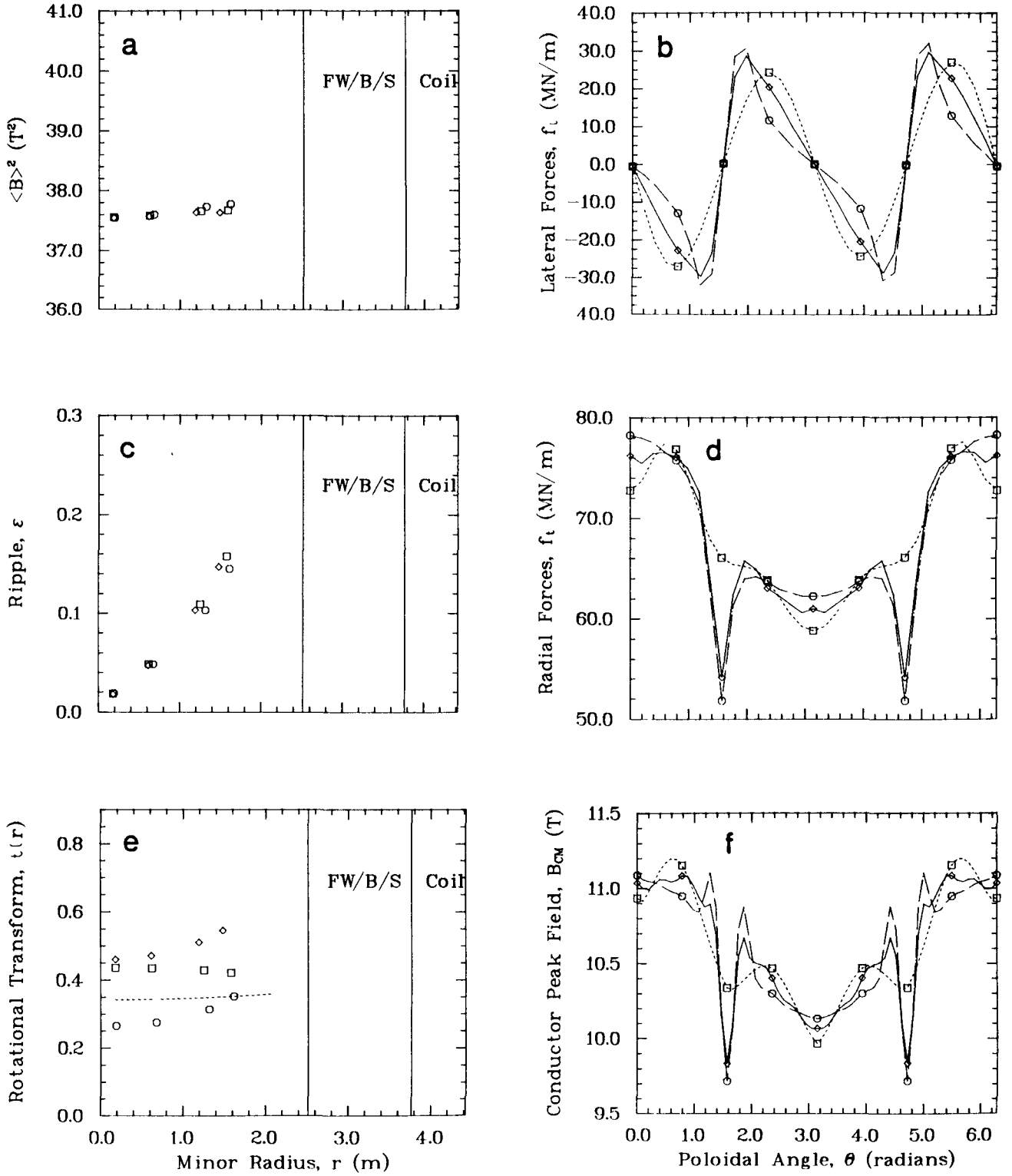

Fig. 4.4-4. A comparison of parameters measuring plasma and coil performance for $\rho = 0.04$ in Eq. (4.4-1) (diamonds), $\delta = 0.15$ in Eq. (4.3-5) (circles), and base case with $a_1 = 0.22$ and $a_2 = a_3 = a_4 = a_6 = 0$ (squares). See the caption for Fig. 4.3-3 for an explanation of other plot features.

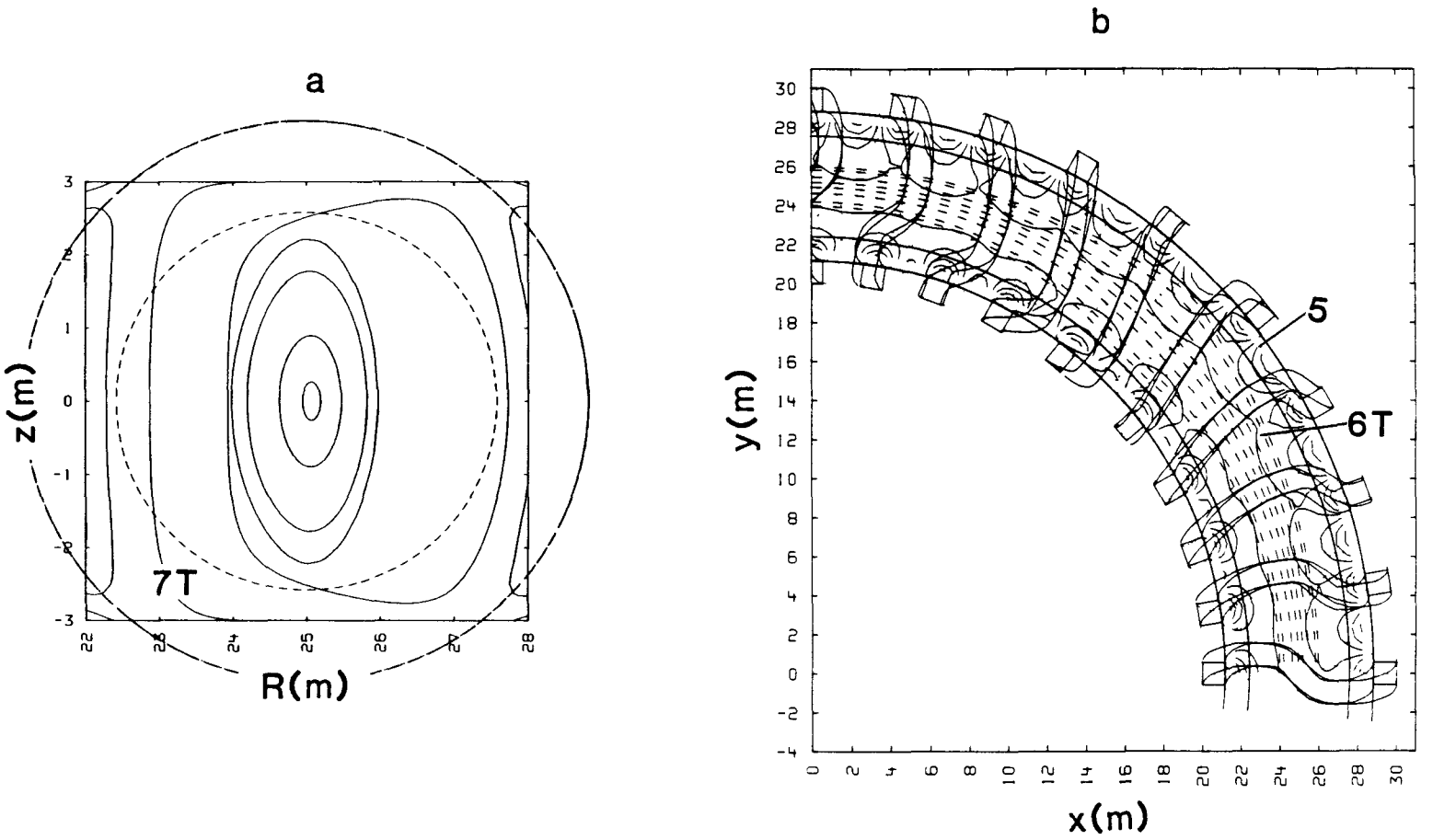

Fig. 4.4-5. The flux surfaces for $\rho = 0.04$ as viewed in the cross section under the key coil (frame a), corresponding to $\phi = 0$, and from above the equatorial plane (frame b). The same plotting conventions used in Fig. 4.3-1 are used here.

slightly smaller than those for Eq. (4.3-5) because of the more rounded peak in the distortion produced by Eq. (4.4-1). The flux surfaces in Fig. 4.4-4 display no peculiarities.

The non-zero on-axis transform and positive shear produced by Eq. (4.4-1) would seem to be attainable by merely mixing $\ell = 2$ and $\ell = 3$ winding laws. Two possible ways of mixing them are to use a combination of $\ell = 2$ and $\ell = 3$ harmonic distortions in Eq. (4.3-3A) or to alternate between $\ell = 2$ and $\ell = 3$ coils in a field period. The results for alternating coils are presented in Figs. 4.4-6 through 4.4-8 with and without a $\pi/2$ phase change on the $\ell = 2$ coils for an $m = 3$ variation on the base case of Table 4.3-1. The poor transform performance of alternating coils is indicative of the results of combining harmonics. The flux surfaces are limited to a small volume by a separatrix that is close to the last surface traced in Figs. 4.4-7 and 4.4-8. The flux surfaces do display an elliptical shape near the magnetic axis and a triangular shape near the separatrix.

The poor volume utilization exhibited by highly elliptical flux surfaces resulting from high transforms suggests shaping the coil bore to match the flux surface shape. The first coil of noncircular bore investigated was the elliptical-bore coil whose winding law is given by

$$P_x(\theta) = r_c \sum_{i=1}^{6} a_i \sin\left(i(\ell\theta + 2\pi mj/N)\right) \quad , \tag{4.4-2A}$$

$$P_y(\theta) = R_T - A \cos\left(\theta + \frac{2\pi mj}{\ell N}\right) \cos\left(\frac{2\pi mj}{\ell N}\right)$$

$$- B \sin\left(\theta + \frac{2\pi mj}{\ell N}\right) \sin\left(\frac{2\pi mj}{\ell N}\right) \quad , \tag{4.4-2B}$$

$$P_z(\theta) = - A \cos\left(\theta + \frac{2\pi mj}{\ell N}\right) \sin\left(\frac{2\pi mj}{\ell N}\right)$$

$$+ B \sin\left(\theta + \frac{2\pi mj}{\ell N}\right) \cos\left(\frac{2\pi mj}{\ell N}\right) \quad , \tag{4.4-2C}$$

$$T_x(\theta) = r_c \sum_{i=1}^{6} i\ell a_i \cos\left(i(\ell\theta + 2\pi mj/N)\right) \quad , \tag{4.4-2D}$$

$$T_y(\theta) = A \sin\left(\theta + \frac{2\pi mj}{\ell N}\right) \cos\left(\frac{2\pi mj}{\ell N}\right)$$

$$- B \cos\left(\theta + \frac{2\pi mj}{\ell N}\right) \sin\left(\frac{2\pi mj}{\ell N}\right) \quad , \tag{4.4-2E}$$

$$T_z(\theta) = A \sin\left(\theta + \frac{2\pi mj}{\ell N}\right) \sin\left(\frac{2\pi mj}{\ell N}\right)$$

$$+ B \cos\left(\frac{\theta + 2\pi mj}{\ell N}\right) \cos\left(\frac{2\pi mj}{\ell N}\right) \quad , \tag{4.4-2F}$$

$$N_x(\theta) = 0 \quad , \tag{4.4-2G}$$

$$N_y(\theta) = - T_z(\theta) \quad , \text{ and} \tag{4.4-2H}$$

$$N_z(\theta) = T_y(\theta) \quad . \tag{4.4-2I}$$

In Eqs. (4.4-2), A is the half-width of the key coil in the equatorial plane, B is the height of the key coil above the equatorial plane, and all other notation is the same as in Eq. (4.3-3). The incremental poloidal rotation between adjacent coils is ℓ times faster for the lateral distortion in Eq. (4.4-2A) than it is for the elliptical bore in Eqs. (4.4-2B) and (4.4-2C), which rotates with the elongation of the flux surfaces. Consequently, each coil in a field period is unique and mass production techniques are less applicable. The results of varying the ellipticity of the bore are presented in Figs. 4.4-9 through 4.4-11. The most pronounced effect of increasing the ellipticity is to raise substantially the rotational transform. The introduction of ellipticity does convert the base-case magnetic well into a small hill but leaves the ripple essentially unperturbed. The forces and B_{CM} for the key coil, which is elongated vertically, are smaller but are larger overall when the elongation is horizontal. The flux surfaces for the intermediate ellipticity in Fig. 4.4-10 are of good quality. However, the flux surfaces for the extreme ellipticity of Fig. 4.4-11 are of poor quality, which is more of a function of the transform achieved than of the coil ellipticity.

The sensitivity to the actual shape of the coil bore can be investigated with the following winding law

$$P_x(\theta) = r_c \sum_{i=1}^{6} a_i \sin\left(i(\ell\theta + 2\pi mj/N)\right) \quad , \tag{4.4-3A}$$

$$P_y(\theta) = R_T - \left[r_c - \zeta \cos\left(\lambda\left(\theta + \frac{2\pi mj}{\ell N}\right)\right)\right] \cos\theta \quad , \tag{4.4-3B}$$

$$P_z(\theta) = \left[r_c - \zeta \cos\left(\lambda\left(\theta + \frac{2\pi mj}{\ell N}\right)\right)\right] \sin\theta \quad , \tag{4.4-3C}$$

$$T_x(\theta) = r_c \sum_{i=1}^{6} i\ell a_i \cos\left(i(\ell\theta + 2\pi mj/N)\right) \quad , \tag{4.4-3D}$$

$$T_y(\theta) = -\lambda\zeta \sin\left(\lambda\left(\theta + \frac{2\pi mj}{\ell N}\right)\right) \cos\theta + \left[r_c - \zeta \cos\left(\lambda\left(\theta + \frac{2\pi mj}{\ell N}\right)\right)\right] \sin\theta \quad , \tag{4.4-3E}$$

$$T_z(\theta) = \lambda\zeta \sin\left(\lambda\left(\theta + \frac{2\pi mj}{\ell N}\right)\right) \sin\theta + \left[r_c - \zeta \cos\left(\lambda\left(\theta + \frac{2\pi mj}{\ell N}\right)\right)\right] \cos\theta \quad , \tag{4.4-3F}$$

$$N_x(\theta) = 0 \quad , \tag{4.4-3G}$$

$$N_y(\theta) = -T_z(\theta) \quad , \text{ and} \tag{4.4-3H}$$

$$N_z(\theta) = T_y(\theta) \quad . \tag{4.4-3I}$$

In Eqs. (4.4-3), ζ controls the amplitude of the deviation from a circular bore, the integer λ determines the shape of the bore, and all other notation is the same as in Eq. (4.3-3). The poloidal periodicity of the bore, λ, must be an integer multiple of the poloidal periodicity of the lateral deformation, ℓ, if the coil bore is to follow in phase with the flux surface rotation and not alter the toroidal periodicity. Experimentation with the relative rate of rotation of the bore indicated the highest transforms were obtained when the coil bore rotated in phase with the flux surfaces. As with the elliptical coils, the winding law of Eq. (4.4-3) results in the fraction ℓ/λ of the coils within a field period being unique. The results of varying the bore shape are presented in Figs. 4.4-12 through 4.4-16. The results for the elliptic-like case with $\lambda = 2$ display little difference from the elliptical case with the same amplitude of deviation from a circular bore. Figure 4.4-12 suggests the existence of an optimum in ι as a function of the shape of the coil bore. Furthermore, the $\lambda = 4$ case has a substantially higher B_{CM}, which results in

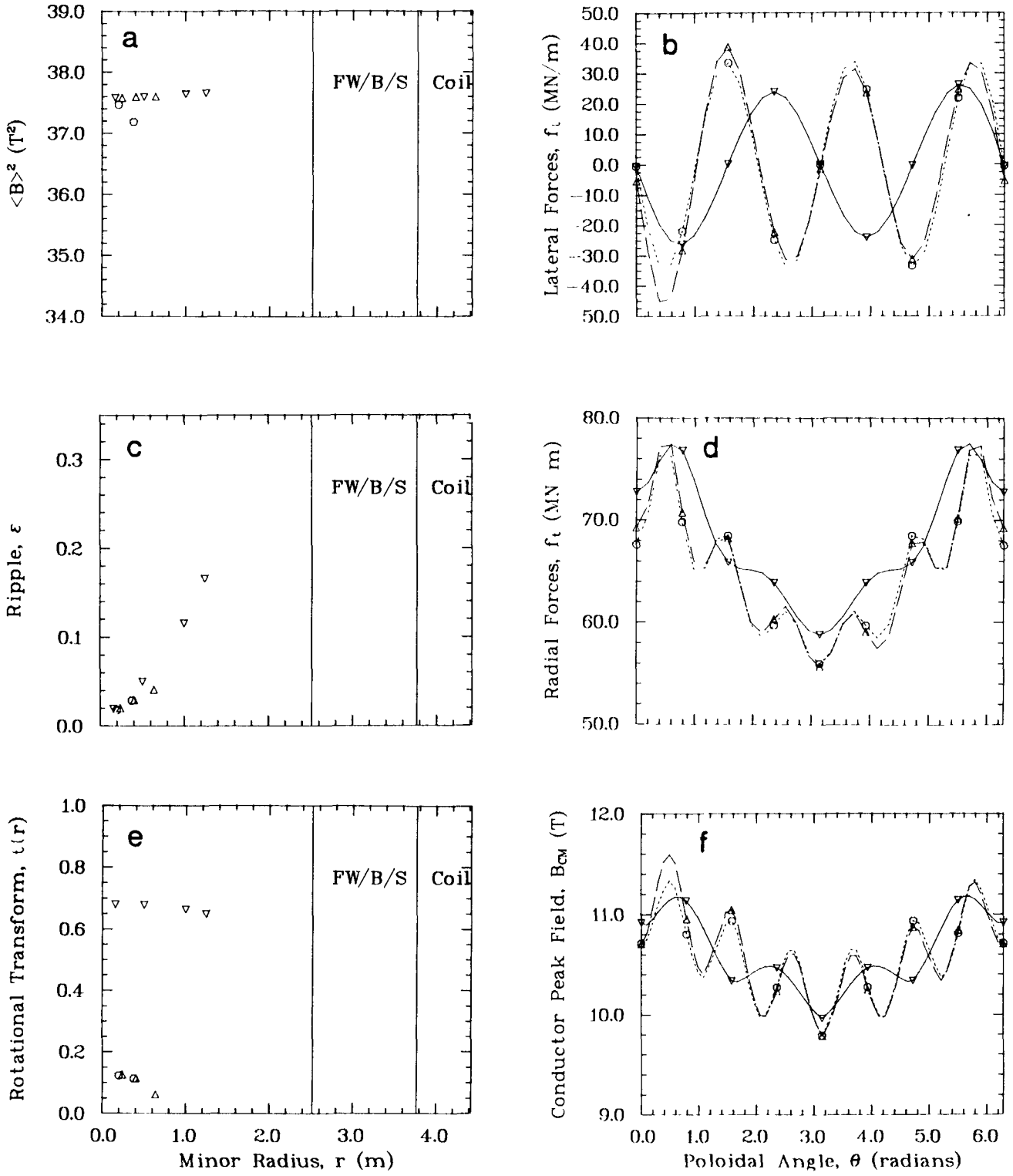

Fig. 4.4-6. A comparison of parameters measuring plasma and coil performance for a mix of ℓ = 2 and 3 coils with (triangles) and without (circles) a $\pi/2$ phase change on the ℓ = 2 coils and for pure ℓ = 2 coils (inverted triangles). The base-case parameters of Table 4.3-1 are used with the single exception of ℓ = 3. See the caption for Fig. 4.3-3 for an explanation of other plot features.

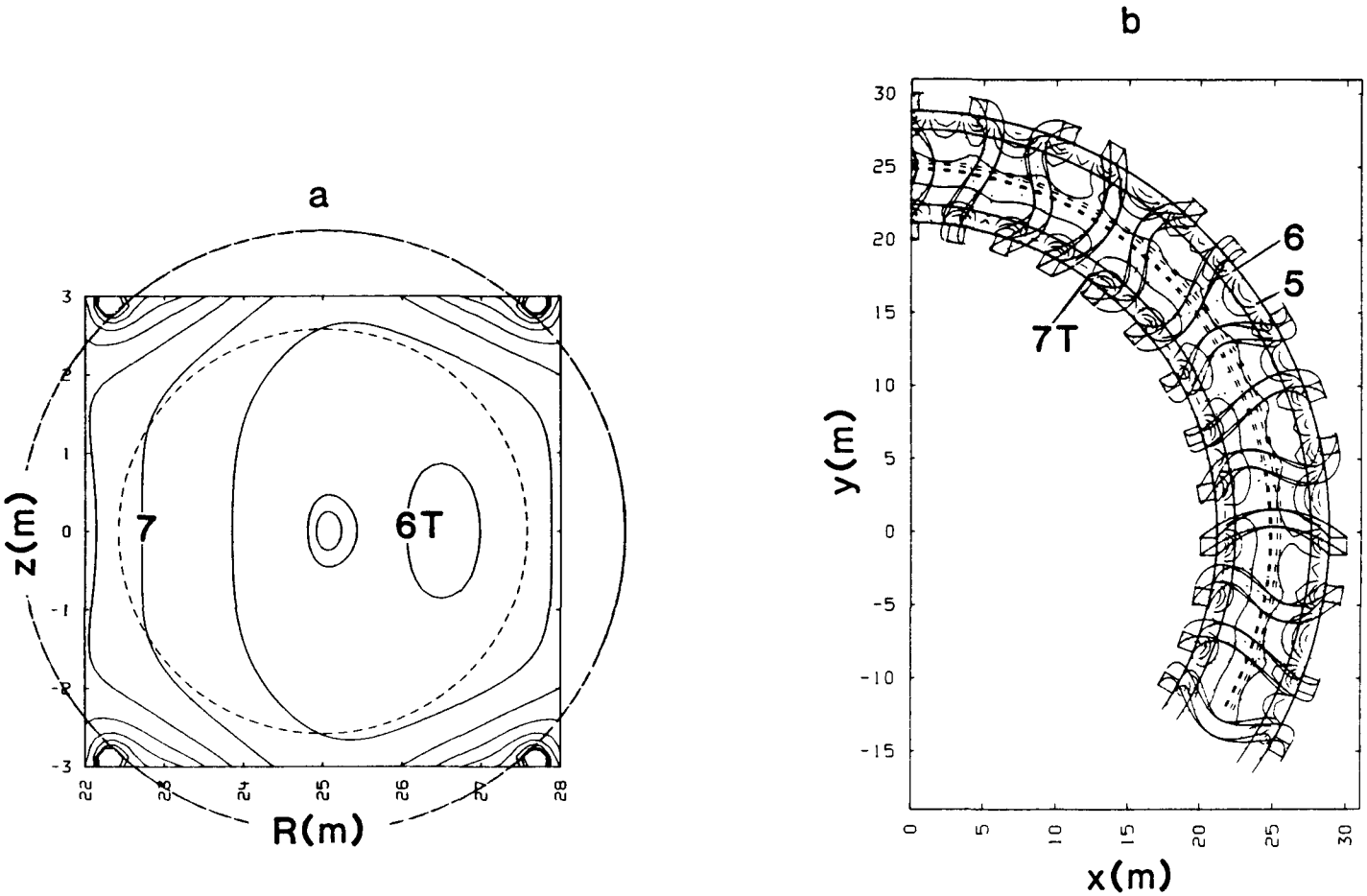

Fig. 4.4-7. The flux surfaces for a mix of ℓ = 2 and 3 coils as viewed in the cross section under the key coil (frame a), corresponding to ϕ = 0, and from above the equatorial plane (frame b). The same plotting conventions used in Fig. 4.3-1 are used here.

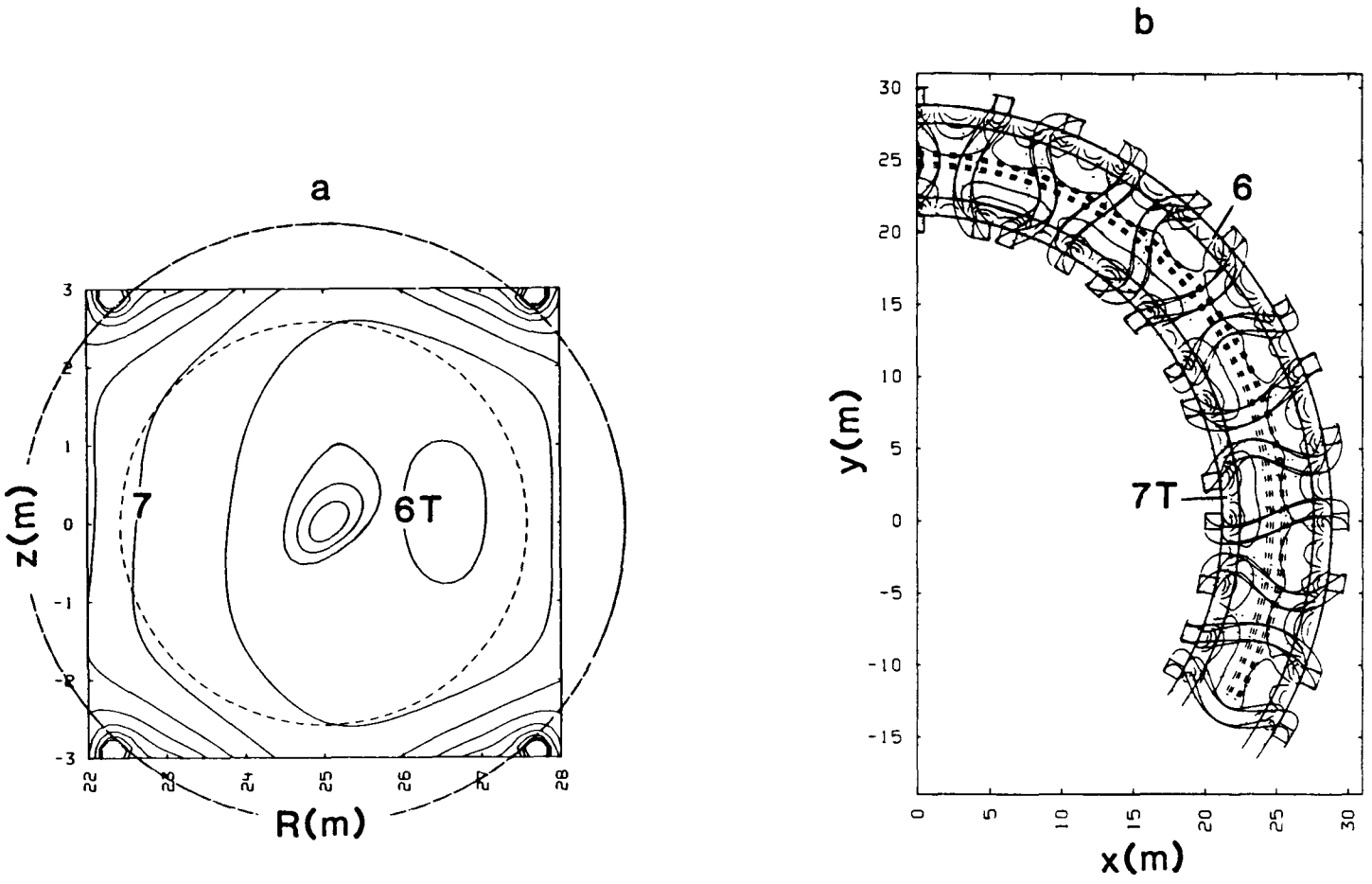

Fig. 4.4-8. The flux surfaces for a mix of $\ell = 2$ and 3 coils with $\pi/2$ phase change on the $\ell = 2$ coils as viewed in the cross section under the key coil (frame a), corresponding to $\phi = 0$, and from above the equatorial plane (frame b). The same plotting conventions used in Fig. 4.3-1 are used here.

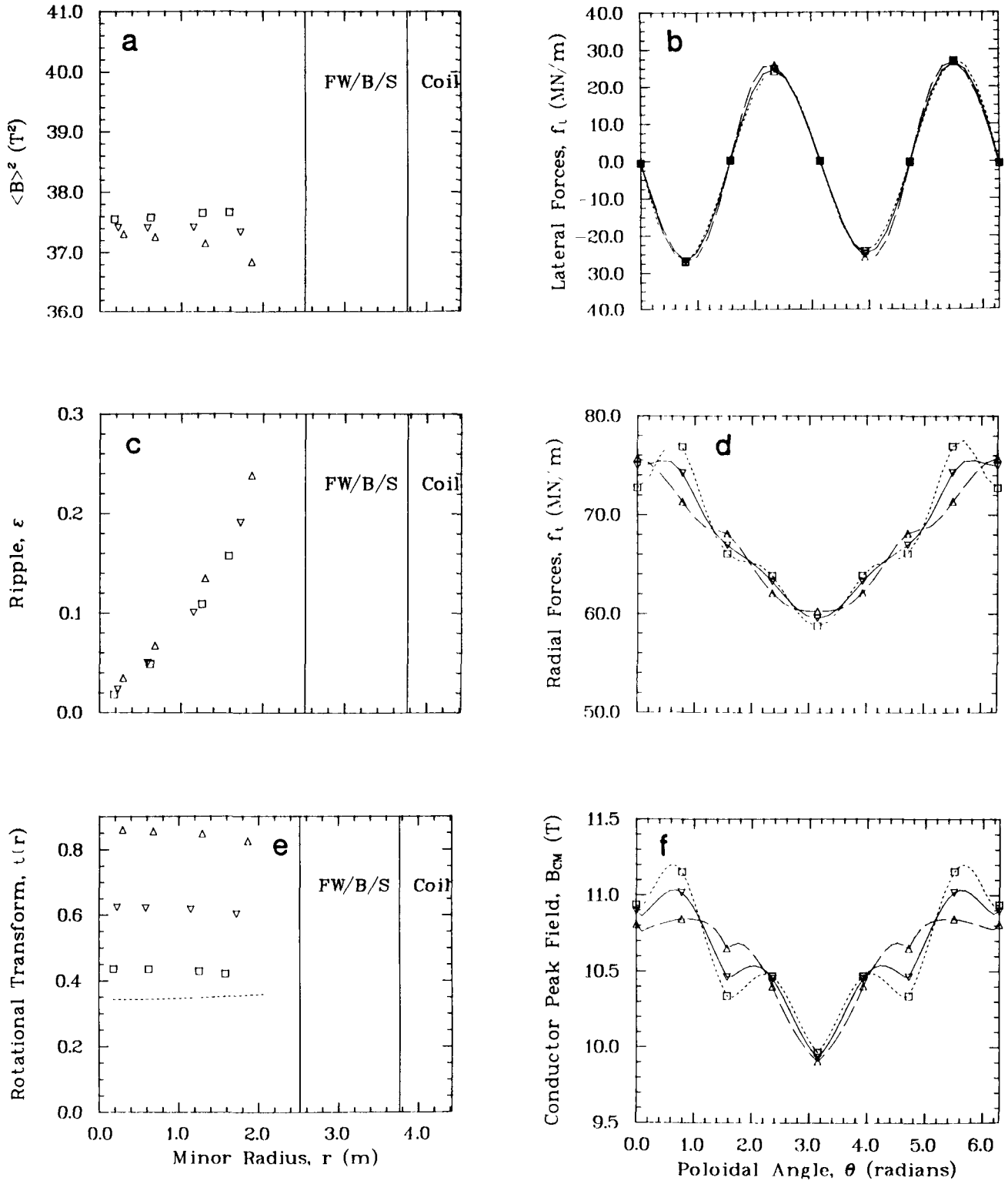

Fig. 4.4-9. A comparison of parameters measuring plasma and coil performance for A = $0.8r_c$ and B = $r_c/0.8$ (triangles) A = $0.9r_c$ and B = $r_c/0.9$ (inverted triangles), and A = B = r_c (squares). See the caption for Fig. 4.3-3 for an explanation of other plot features.

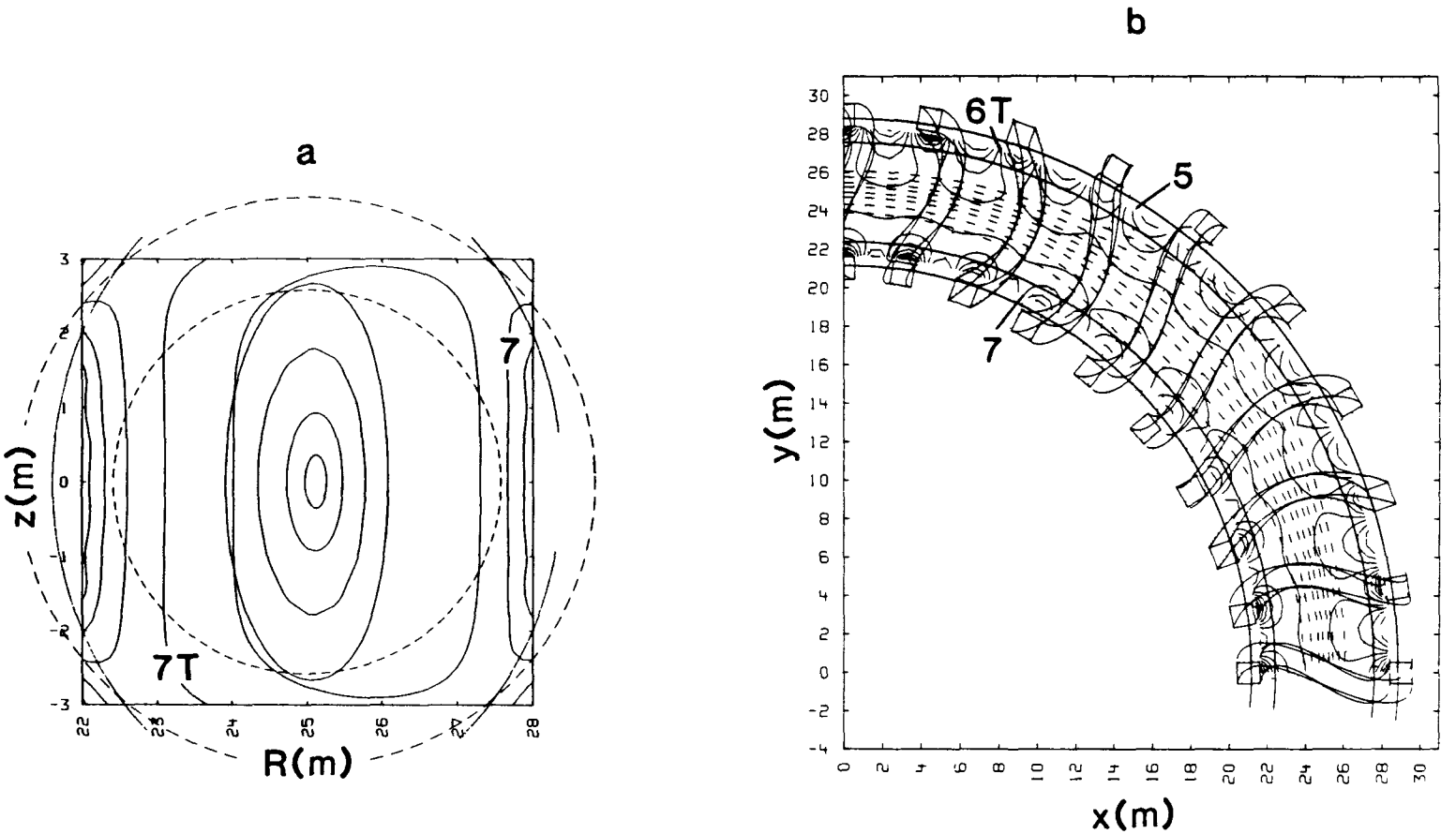

Fig. 4.4-10. The flux surfaces for A = $0.10r_c$ and B = $r_c/0.10$ as viewed in the cross section under the key coil (frame a), corresponding to $\phi = 0$, and from above the equatorial plane (frame b). The same plotting conventions used in Fig. 4.3-1 are used here. The FW/B/S has been drawn with a circular bore.

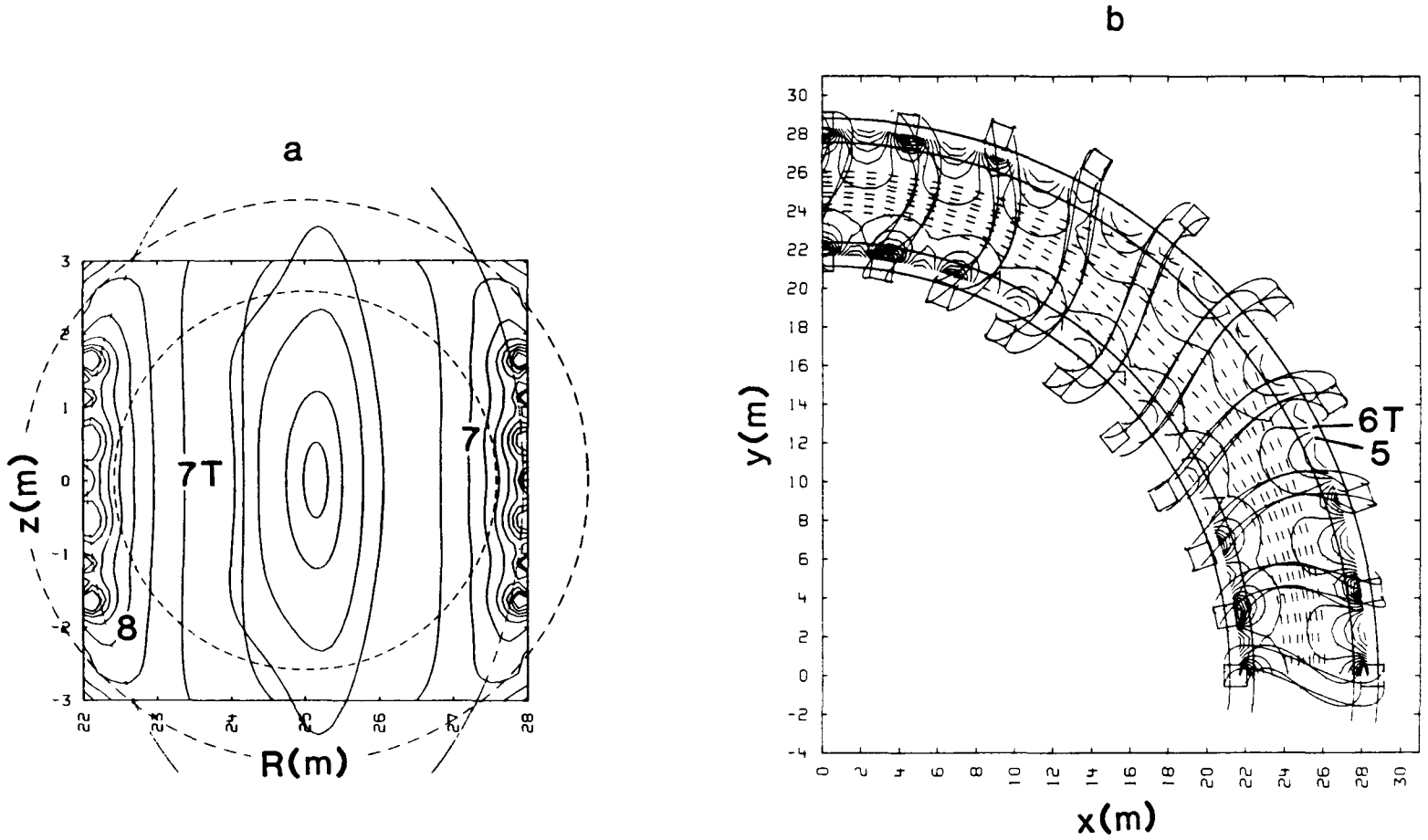

Fig. 4.4-11. The flux surfaces for A = $0.8r_c$ and B = $r_c/0.8$ as viewed in the cross section under the key coil (frame a), corresponding to $\phi = 0$, and from above the equatorial plane (frame b). The same plotting conventions used in Fig. 4.3-1 are used here. The FW/B/S has been drawn with a circular bore.

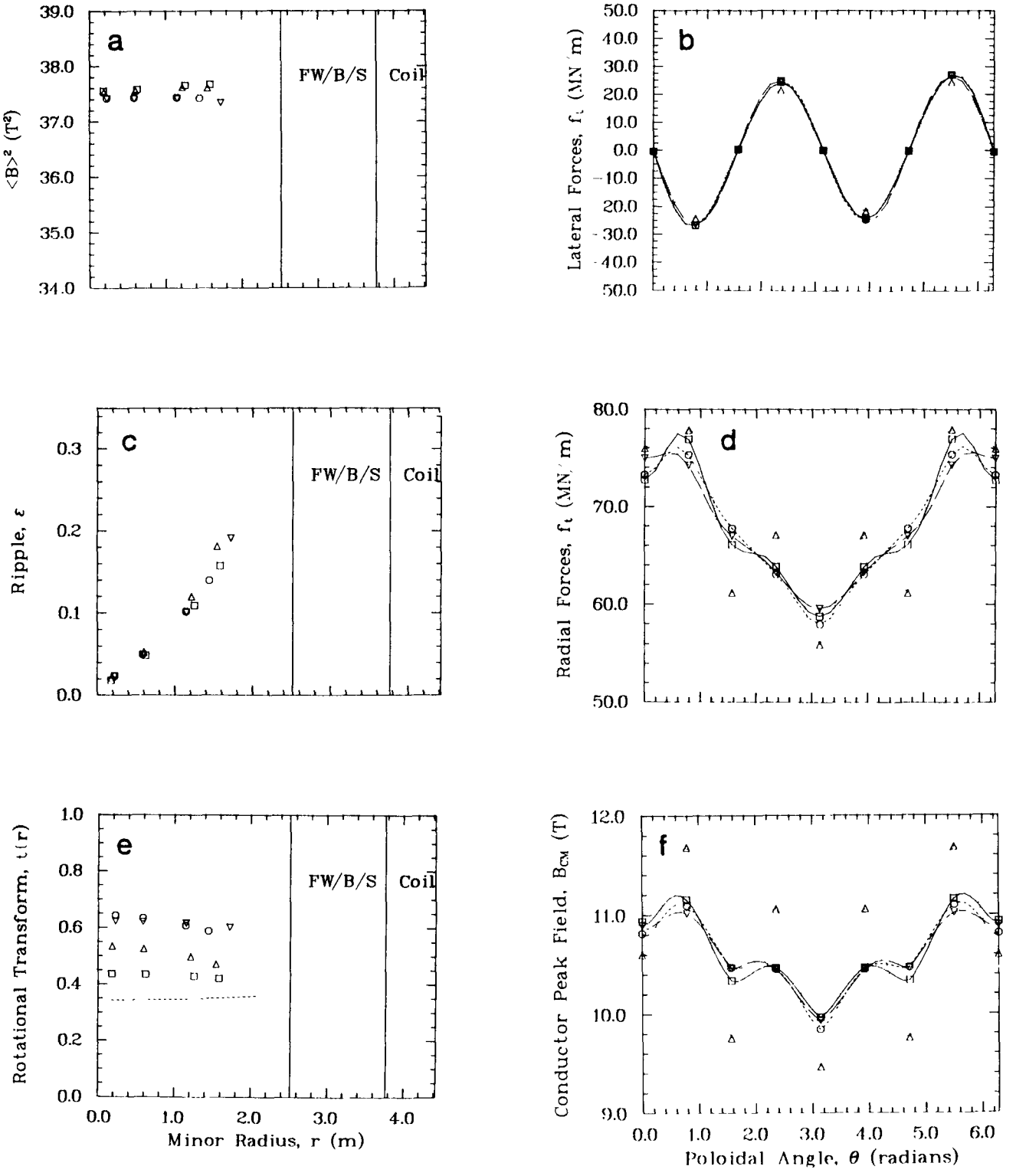

Fig. 4.4-12. A comparison of parameters measuring plasma and coil performance for $\zeta = 0.9$ and $\lambda = 2$ (circles), $\zeta = 0.9$ and $\lambda = 4$ (triangles), $A = 0.9r_c$ and $B = r_c/0.9$ (inverted triangles), and the base case of Table 4.3-1 (squares). See the caption for Fig. 4.3-3 for an explanation of other plot features.

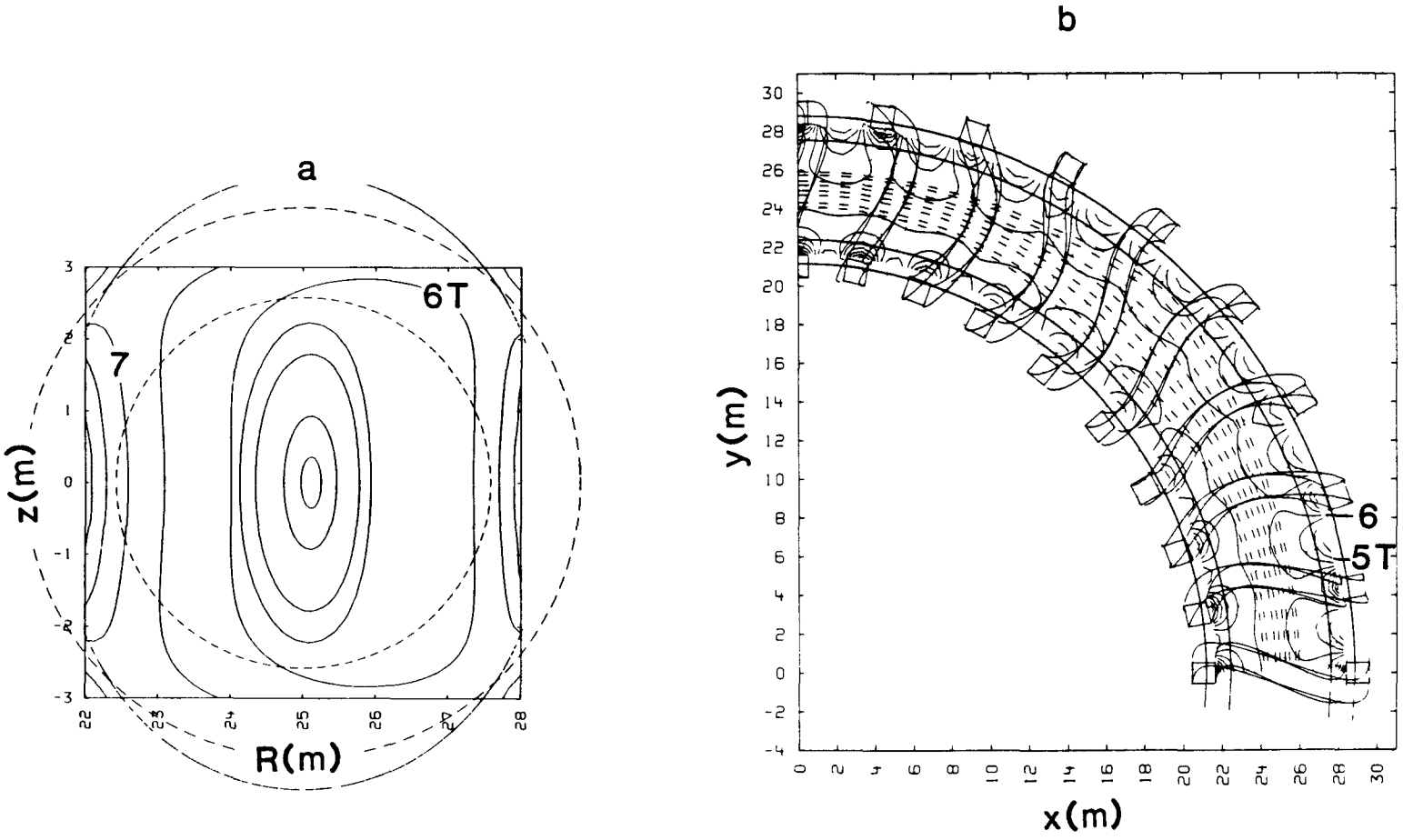

Fig. 4.4-13. The flux surfaces for $\zeta = 0.9$ and $\lambda = 2$ as viewed in the cross section under the key coil (frame a), corresponding to $\phi = 0$, and from above the equatorial plane (frame b). The same plotting conventions used in Fig. 4.3-1 are used here.

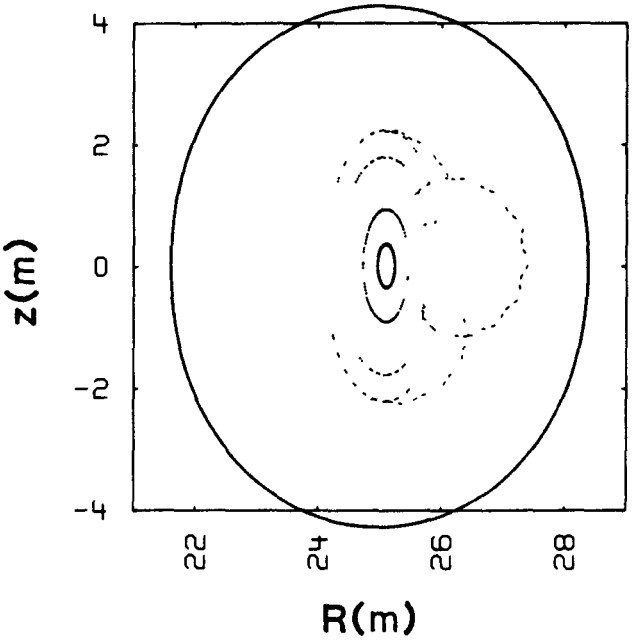

Fig. 4.4-14. A plot of the intersections of the field lines with the constant-ϕ cross section under the key coil for $\zeta = 0.9$ and $\lambda = 2$. The inner bore of the coil is also shown as is the projection of a field line tracing for three field periods.

higher forces on the coil which is closest to being rotated poloidally by $\pi/4$ from the orientation of the key coil.

The aforementioned attempts at raising ι appear to be limited by flux surface quality to $\iota \lesssim 1$. The torsatron results of Sec. 4.3.3.1. suggest the introduction of poloidal field (PF) coils to improve flux surface quality. Two candidates for introducing PF coils are the m = 3 case of Fig. 4.3-4 and the elliptical case of Fig. 4.4-11, both having irregularly shaped outer flux surfaces which may contain magnetic islands. The results of introducing PF coils for these cases are presented in Figs. 4.4-17 and 4.4-18 and Figs. 4.4-19 and 4.4-20, respectively. The PF coils have reduced the degree of irregularity displayed by the flux surfaces. The flux surfaces are, however, even more elongated with PF coils, in addition to being shifted radially outward. The shift of the magnetic axis is the cause for the change in the $\langle B \rangle^2$ profile. The remainder of the parameters of Figs. 4.4-18 and 4.4-20 are not appreciably affected by the PF coils. However, the stored energy in the coil sets has approximately doubled with the introduction of PF coils. Even though the PF coils in these cases may not be positioned at the

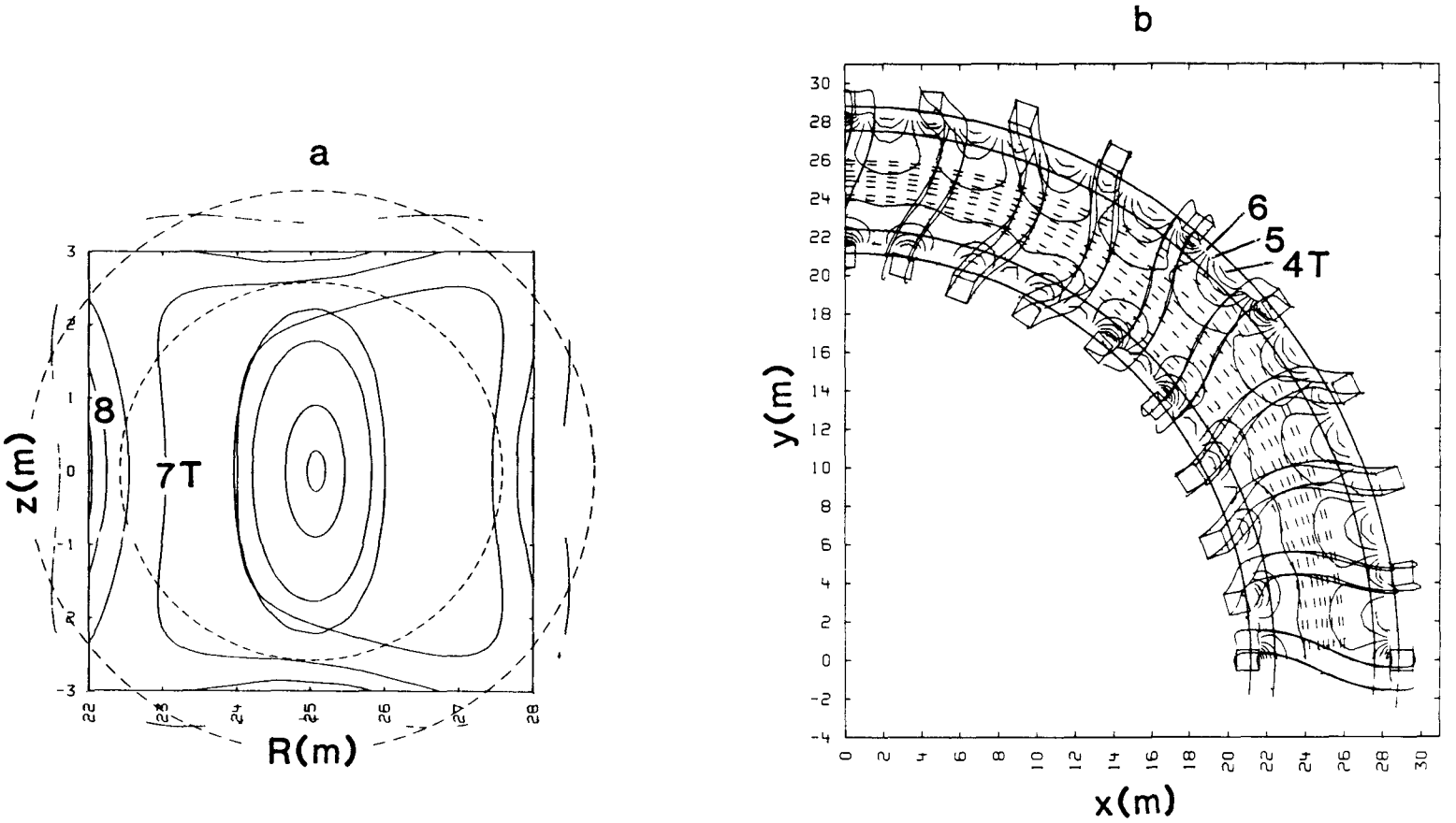

Fig. 4.4-15. The flux surfaces for $\zeta = 0.9$ and $\lambda = 4$ as viewed in the cross section under the key coil (frame a), corresponding to $\phi = 0$, and from above the equatorial plane (frame b). The same plotting conventions used in Fig. 4.3-1 are used here.

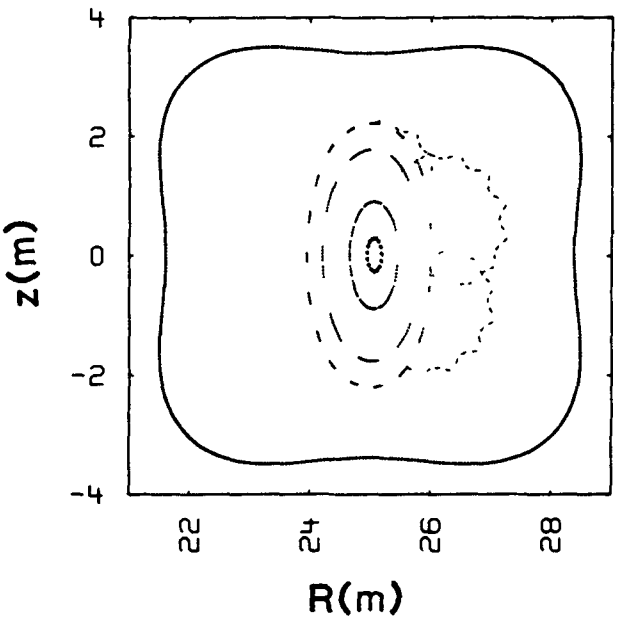

Fig. 4.4-16. A plot of the intersections of the field lines with the constant-ϕ cross section under the key coil for $\zeta = 0.9$ and $\lambda = 4$. The inner bore of the coil is also shown as is the projection of a field-line tracing for three field periods.

optimum locations nor have the optimum relative current distribution, their results indicate the shapes of the flux surfaces of an MSR design can be manipulated. The wish is that the flux surface quality (and perhaps volume utilization) can be improved with auxiliary coils, permitting $\iota > 1$ in MSR designs.

Although experimental evidence with which to determine whether a magnetic well is necessary does not exist, the means by which a magnetic well can be generated, nevertheless, is of interest. One method is to introduce a vertical field which moves the magnetic axis radially inward. This adjustment can be accomplished without auxiliary coils by tilting the TF coil set. The effects of tilting can be simulated by the following winding law:

$$P_x(\theta) = r_c \sum_{i=1}^{6} a_i \sin\left(i(\ell\theta + 2\pi mj/N)\right) + r_c \tau \sin\theta \quad , \tag{4.4-4A}$$

$$P_y(\theta) = R_T - r_c \cos\theta \quad , \tag{4.4-4B}$$

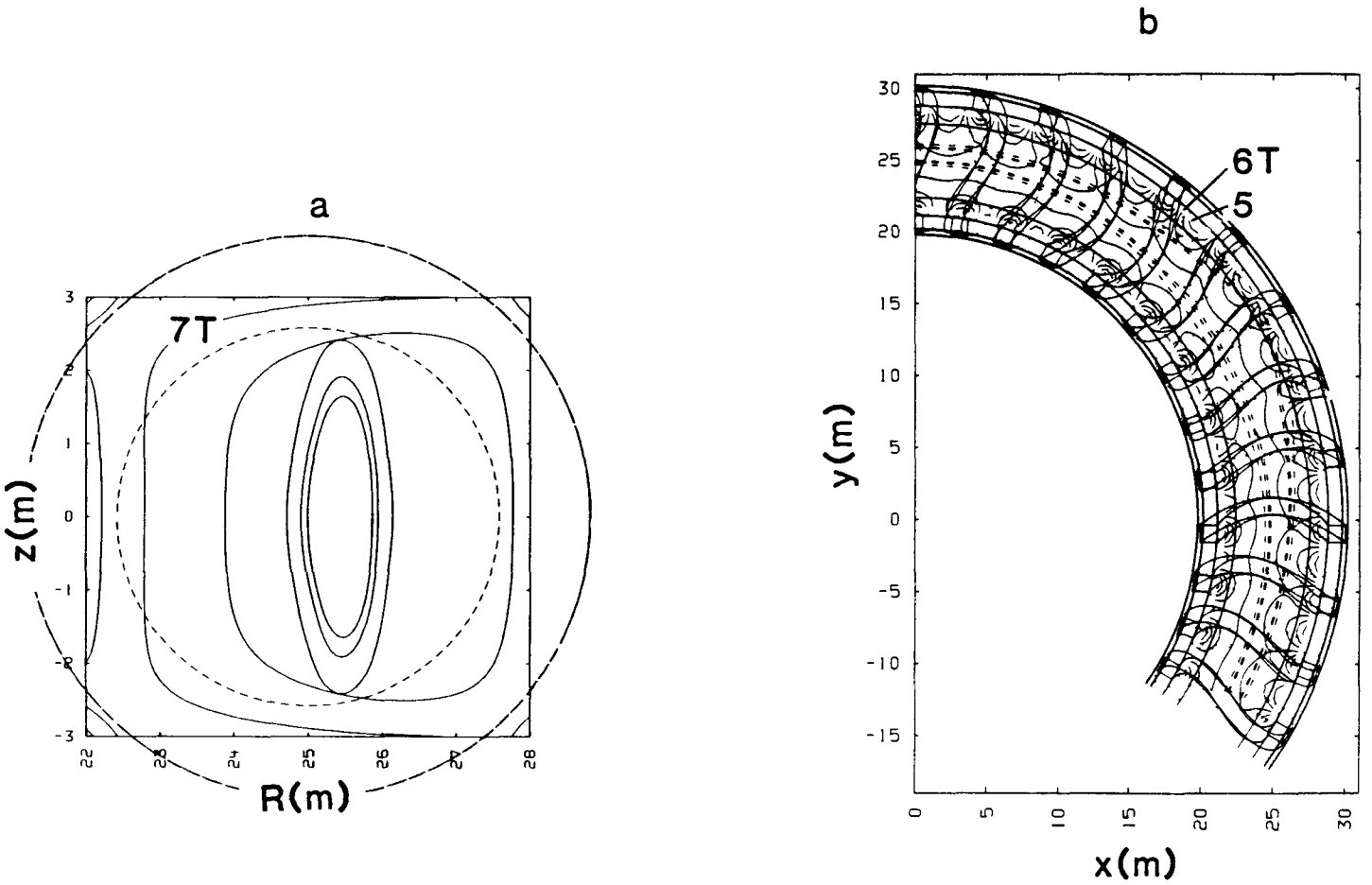

Fig. 4.4-17. The flux surfaces for m = 3 with four poloidal field coils each operated at a current equal to 10% of that in a main coil as viewed in the cross section under the key coil (frame a), corresponding to ϕ = 0, and from above the equatorial plane (frame b). The same plotting conventions used in Fig. 4.3-1 are used here. The poloidal field coils positioned at R = 25 ± 5 m and z = ±5 m have also been added to frame b.

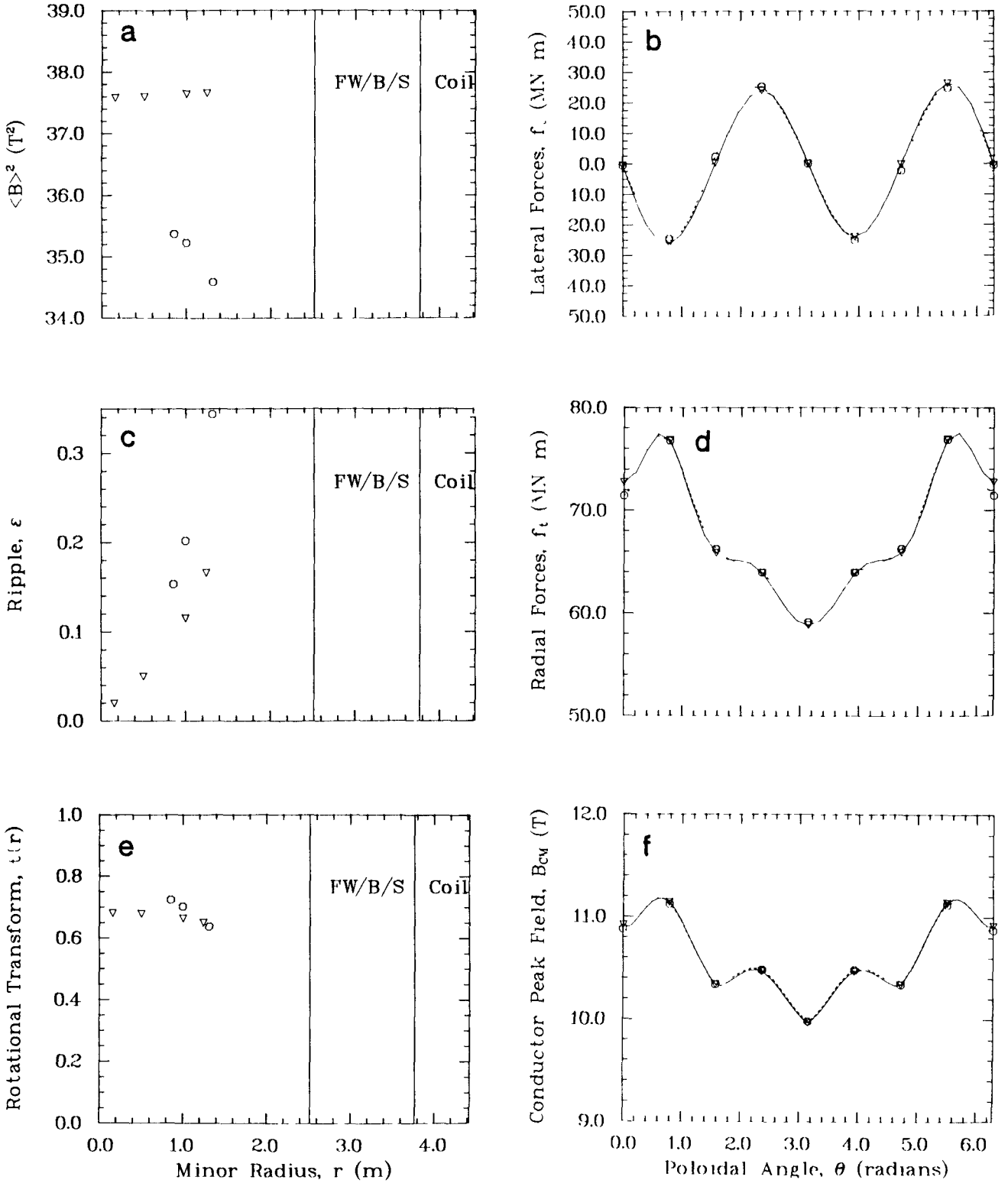

Fig. 4.4-18. A comparison of parameters measuring plasma and coil performance for m = 3 with (circles) and without (inverted triangles) poloidal field coils. See the caption of Fig. 4.3-3 for an explanation of other plot features.

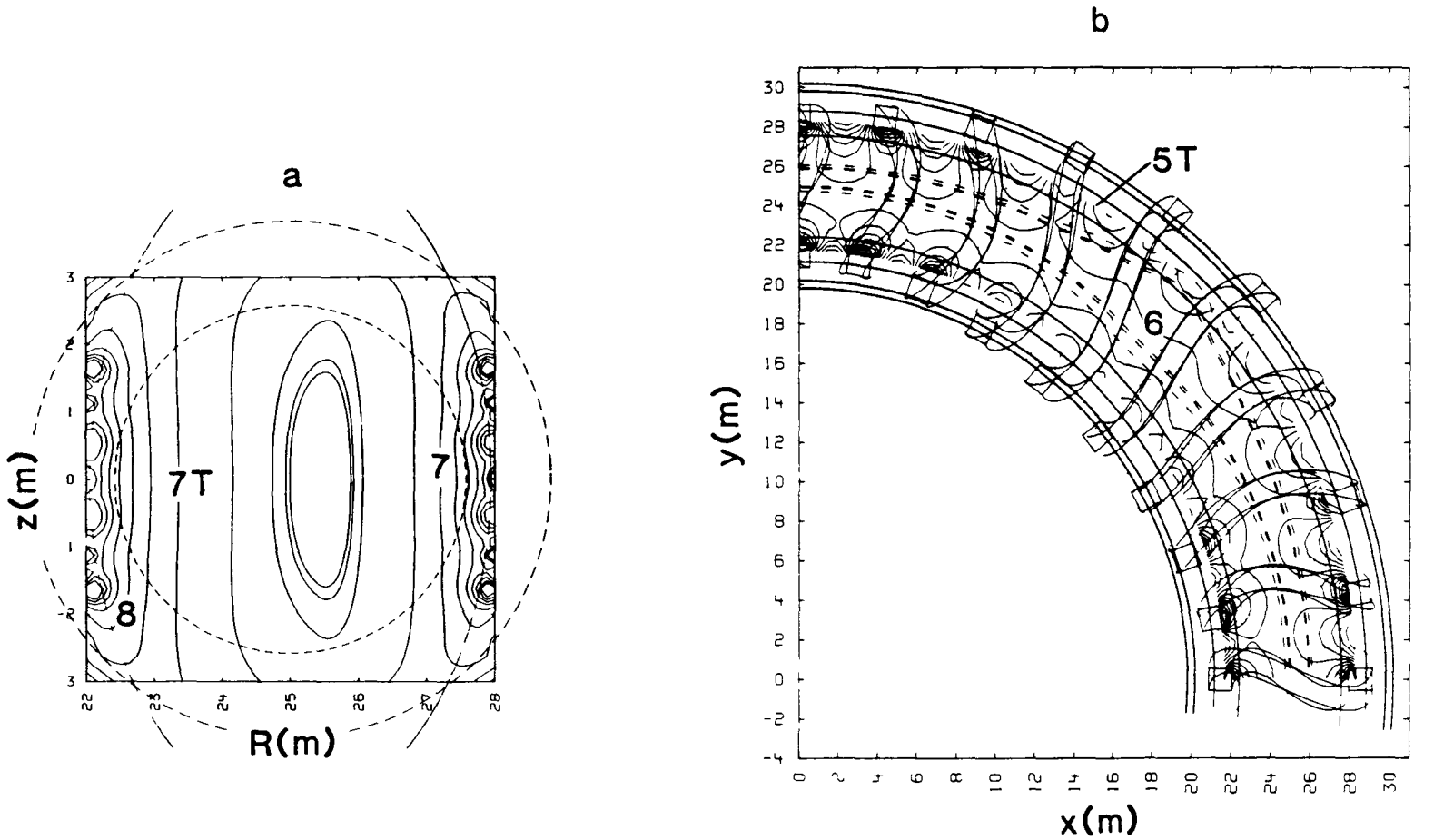

Fig. 4.4-19. The flux surfaces for $A = 0.8r_c$ and $B = r_c/0.8$ with four poloidal field coils each operated at a current equal to 10% of that in a main coil as viewed in the cross section under the key coil (frame a), corresponding to $\phi = 0$, and from above the equatorial plane (frame b). The same plotting conventions used in Fig. 4.3-1 are used here. The poloidal field coils positioned at R = 25 ± 5 m and z = ±5 m have also been added to frame b. The inner bore of the elliptical key coil is shown in frame a.

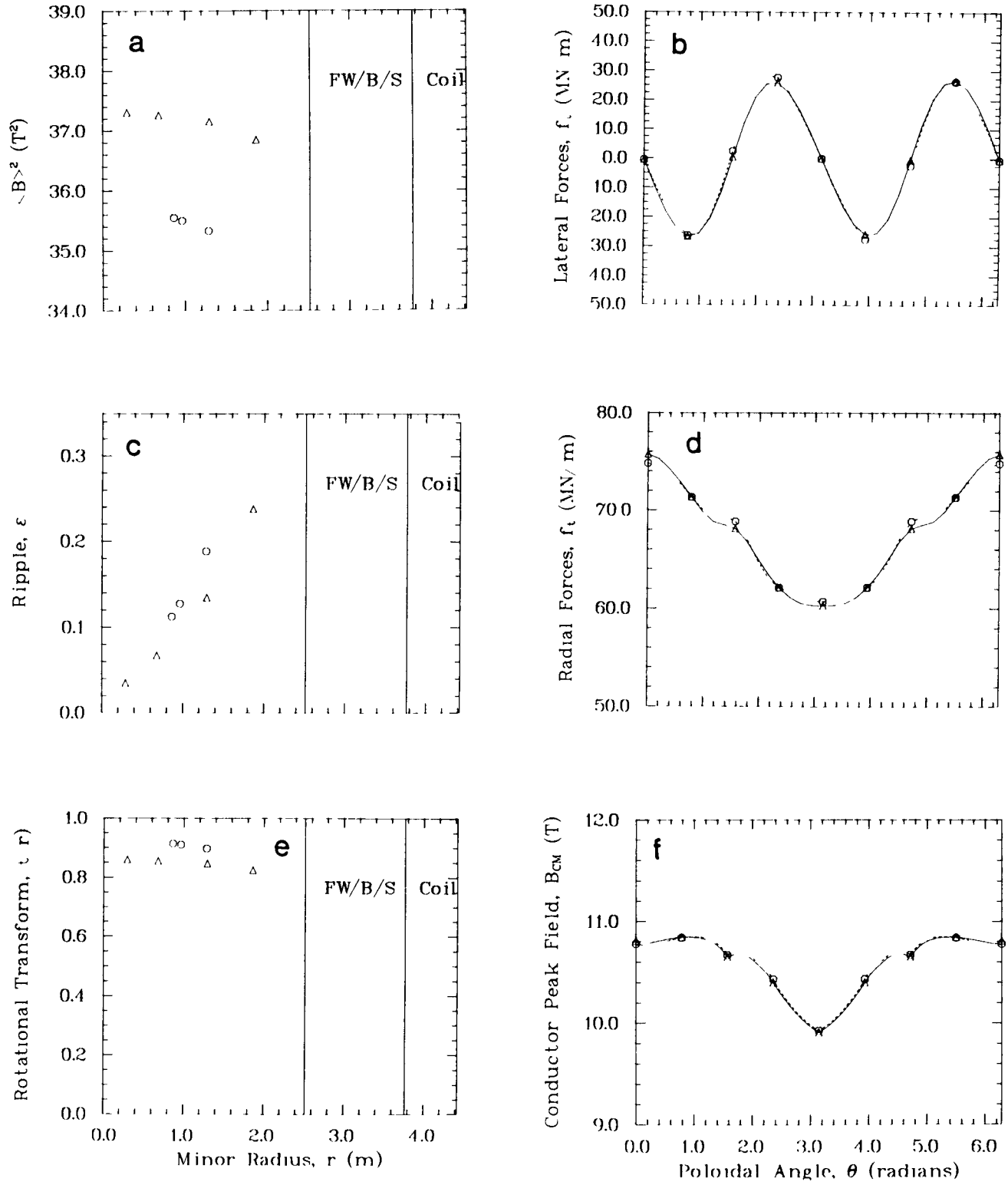

Fig. 4.4-20. A comparison of parameters measuring plasma and coil performance for A = $0.8r_c$ and B = $r_c/0.8$ with (circles) and without (triangles) poloidal field coils. See the caption for Fig. 4.3-3 for an explanation of other plot features.

$$P_z(\theta) = r_c \sin\theta \quad , \tag{4.4-4C}$$

$$T_x(\theta) = r_c \sum_{i=1}^{6} i\ell a_i \sin\big(i(\ell\theta + 2\pi mj/N)\big)$$

$$+ r_c \tau \cos\theta \quad , \tag{4.4-4D}$$

$$T_y(\theta) = r_c \sin\theta \quad , \tag{4.4-4E}$$

$$T_z(\theta) = r_c \cos\theta \quad , \tag{4.4-4F}$$

$$N_x(\theta) = 0 \quad , \tag{4.4-4G}$$

$$N_y(\theta) = -T_z(\theta) \quad , \quad \text{and} \tag{4.4-4H}$$

$$N_z(\theta) = T_y(\theta) \quad . \tag{4.4-4I}$$

In Eqs. (4.4-4) τ is the amplitude of the tilt and all other notation is the same as for Eqs. (4.3-3). The effects of tilting are presented in Figs. 4.4-21 and 4.4-22. The increase in well depth due to tilting is small. In addition, the volume utilization has decreased significantly as evidenced by Fig. 4.4-22. With the exception of a small decrease in τ, the remaining parameters are not affected by changing τ.

Another method to affect well depth is to modulate the amplitude of the distortion to yield wedge-shaped coils. The winding law used to examine this effect is given by

$$P_x(\theta) = \Big(1 - \frac{r_c}{R_T}\cos\theta\Big)^{\xi} r_c \sum_{i=1}^{6} a_i \sin\big(i(\ell\theta + 2\pi mj/N)\big) \quad , \tag{4.4-5A}$$

$$P_y(\theta) = R_T - r_c \cos\theta \quad , \tag{4.4-5B}$$

$$P_z(\theta) = r_c \sin\theta \quad , \tag{4.4-5C}$$

$$T_x(\theta) = \Big(1 - \frac{r_c}{R_T}\cos\theta\Big)^{\xi} r_c \sum_{i=1}^{6} i\ell a_i \cos\big(i(\ell\theta + 2\pi mj/N)\big)$$

$$+ \xi\Big(1 - \frac{r_c}{R_T}\cos\theta\Big)^{\xi-1} \frac{r_c^2}{R_T} \sin\theta \sum_{i=1}^{6} a_i \sin\big(i\ell\theta + 2\pi mj/N\big) \quad , \tag{4.4-5D}$$

$$T_y(\theta) = r_c \sin\theta \quad , \tag{4.4-5E}$$

$$T_z(\theta) = r_c \cos\theta \quad , \tag{4.4-5F}$$

$$N_x(\theta) = 0 \quad , \tag{4.4-5G}$$

$$N_y(\theta) = - T_z(\theta) \quad , \text{ and} \tag{4.4-5H}$$

$$N_z(\theta) = T_y(\theta) \quad . \tag{4.4-5I}$$

In Eqs. (4.4-5), ξ is used to control the degree of modulation and all other notation is the same as in Eqs. (4.3-3). The results of varying ξ for the base-case parameters of Table 4.3-1 are presented in Figs. 4.4-23 through 4.4-25. The most pronounced effect of increasing ξ is to increase the well depth dramatically. The increase in well depth was obtained with only a small radially inward shift of the magnetic axis compared with the results for tilting the TF coil set. The penalty for increasing ξ is a lower ι and higher lateral forces. The radial forces and B_{CM} also increase but not for the key coil. The ripple remains, surprisingly, unaffected.

One last parameterization investigated was the modulation of the major radius of the TF coil set as is done for the M&S configurations.[9,15] A planar modulation of the coil axis was performed using the winding law of Eq. (4.3-3) with the modification

$$P_y(\theta) = R_T - r_c \cos\theta + r_o \cos\left(\frac{2\pi m j}{\ell N}\right) \quad , \tag{4.4-6}$$

where r_o is the amplitude of the modulation and all the other notation is the same as in Eqs. (4.3-3). A helical modulation was also performed using the winding law of Eqs. (4.3-3) with the modifications

$$P_y(\theta) = R_T - r_c \cos\theta + r_h \cos\left(\frac{2\pi m j}{\ell N}\right) \quad , \text{ and} \tag{4.4-7A}$$

$$P_z(\theta) = r_c \sin\theta + r_h \sin\left(\frac{2\pi m j}{\ell N}\right) \quad , \tag{4.4-7B}$$

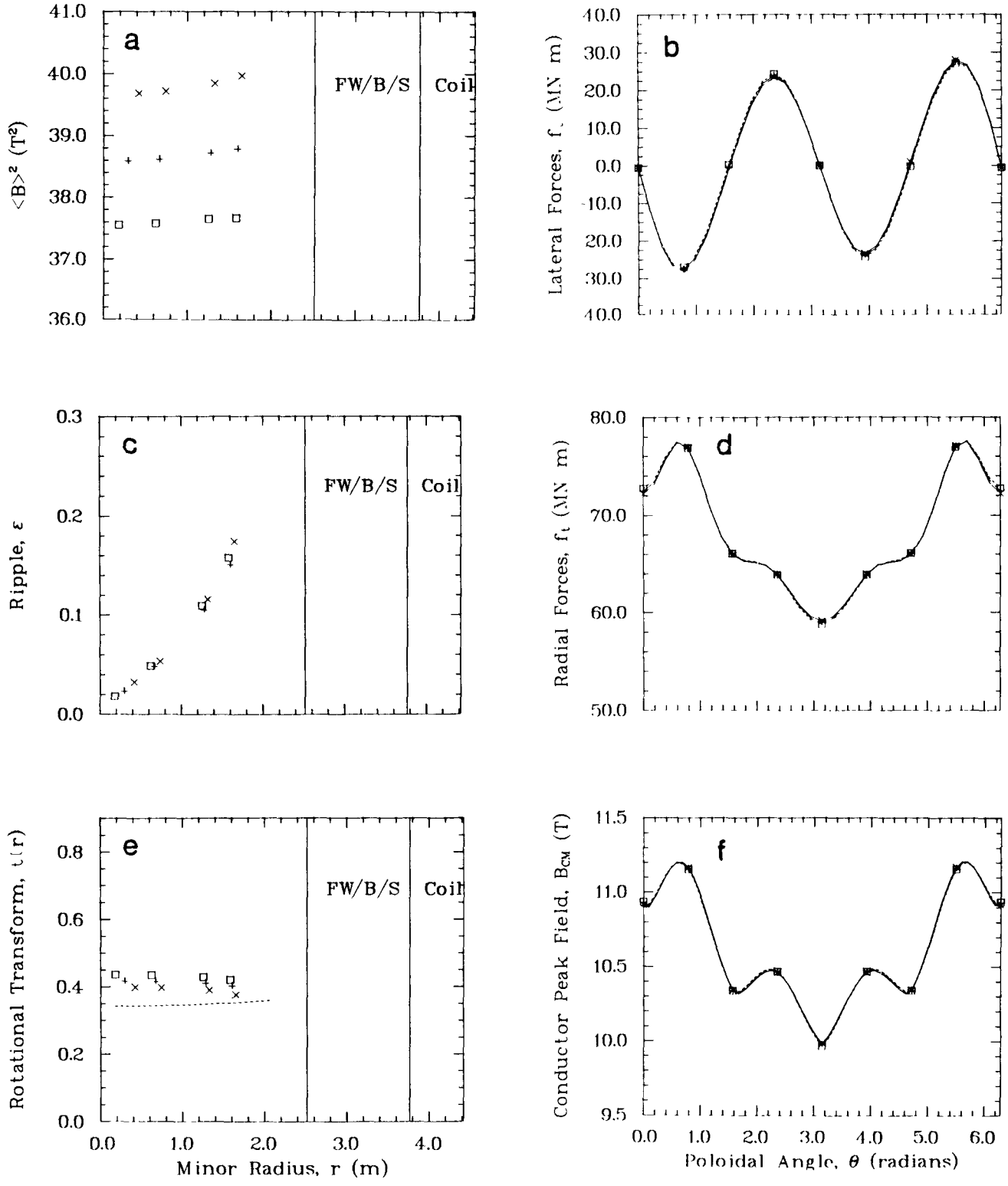

Fig. 4.4-21. A comparison of parameters measuring plasma and coil performance for $\tau = 0.02$ (x's), $\tau = 0.01$ (pluses), $\tau = 0$ (squares). See the caption for Fig. 4.3-3 for an explanation of other plot features.

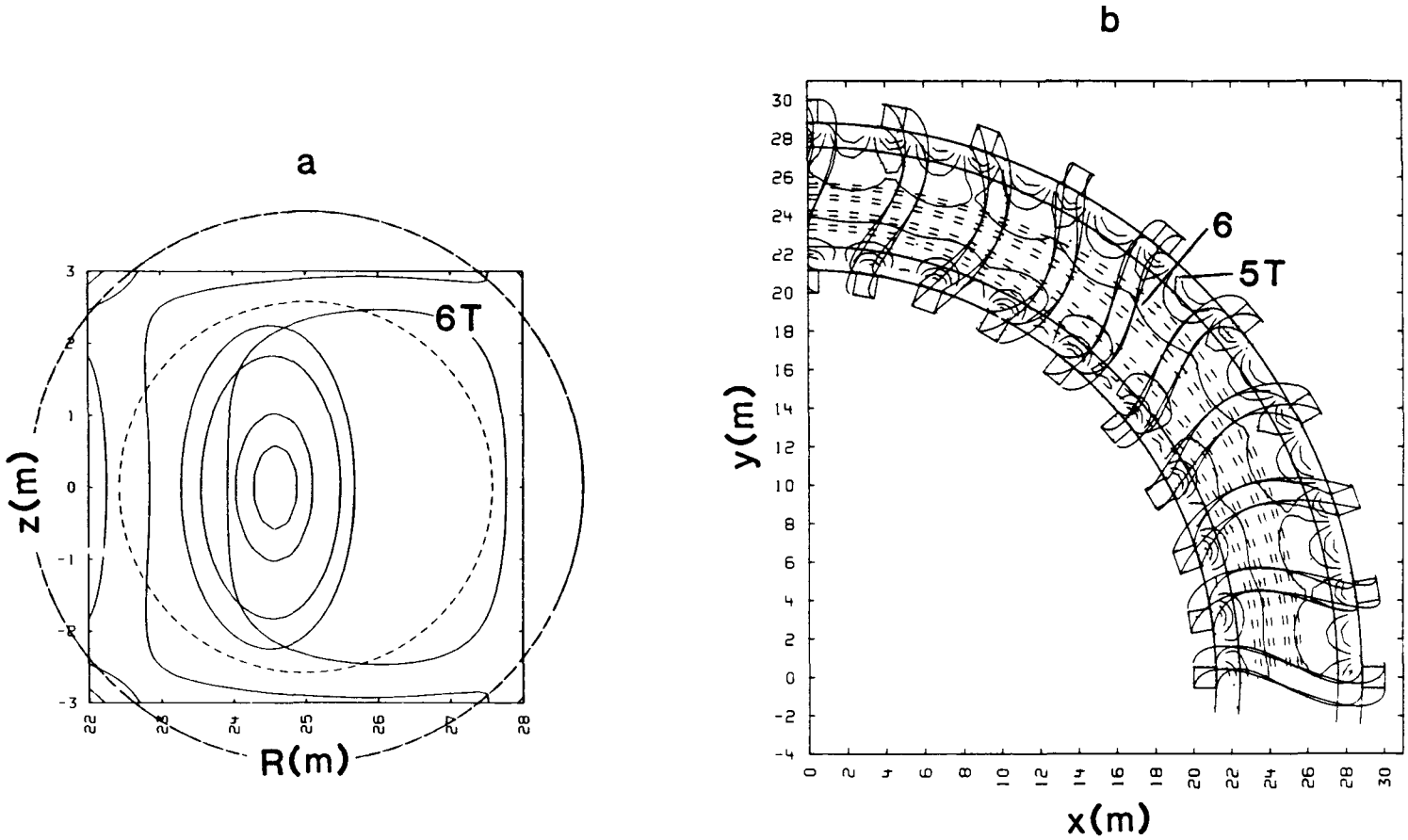

Fig. 4.4-22. The flux surfaces for $\tau = 0.02$ as viewed in the cross section under the key coil (frame a), corresponding to $\phi = 0$, and from above the equatorial plane (frame b). The same plotting conventions used in Fig. 4.3-1 are used here.

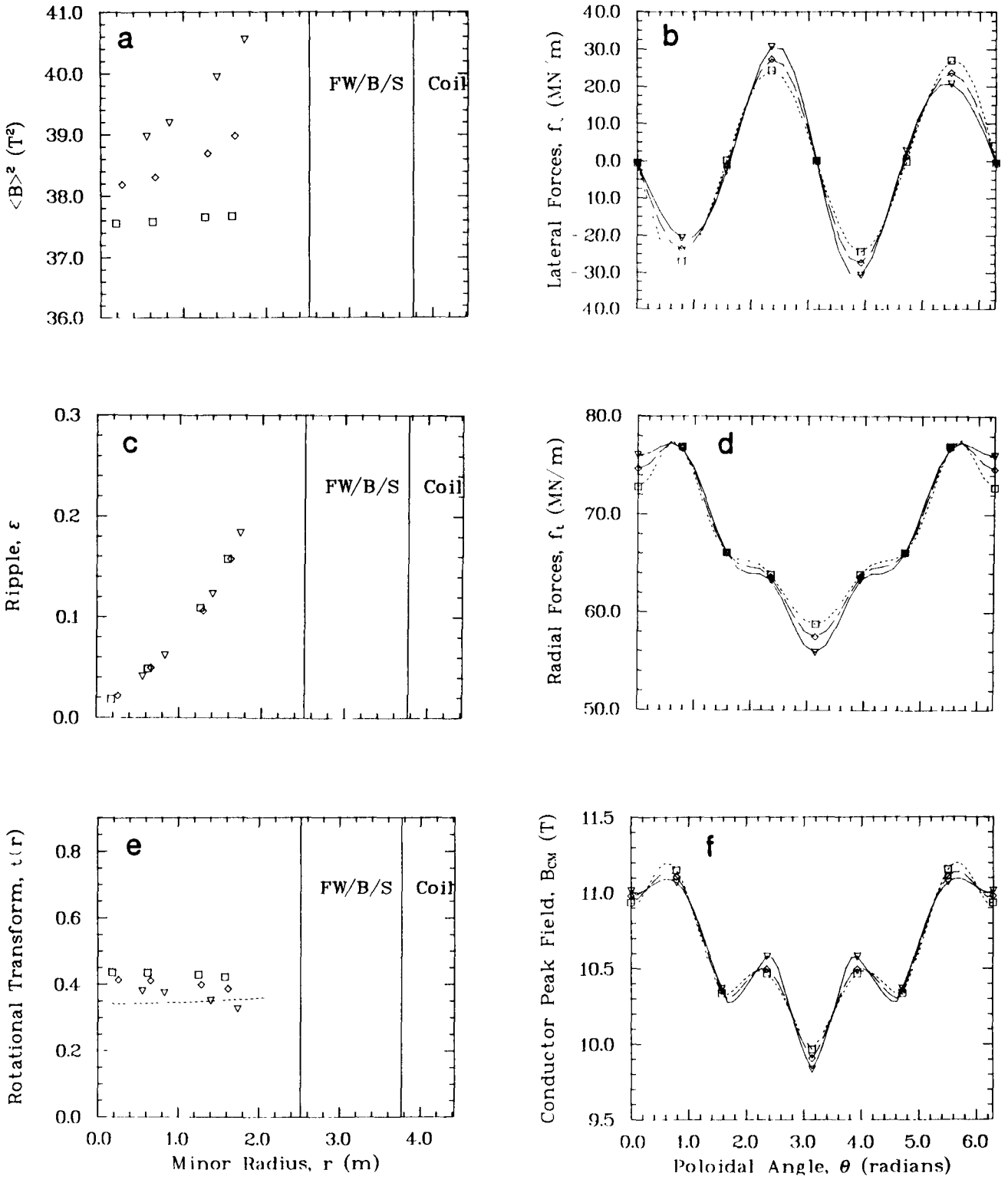

Fig. 4.4-23. A comparison of parameters measuring plasma and coil performance for ξ = 2 (inverted triangles), ξ = 1 (diamonds) and ξ = 0 (squares). See the caption of Fig. 4.3-3 for an explanation of other plot features.

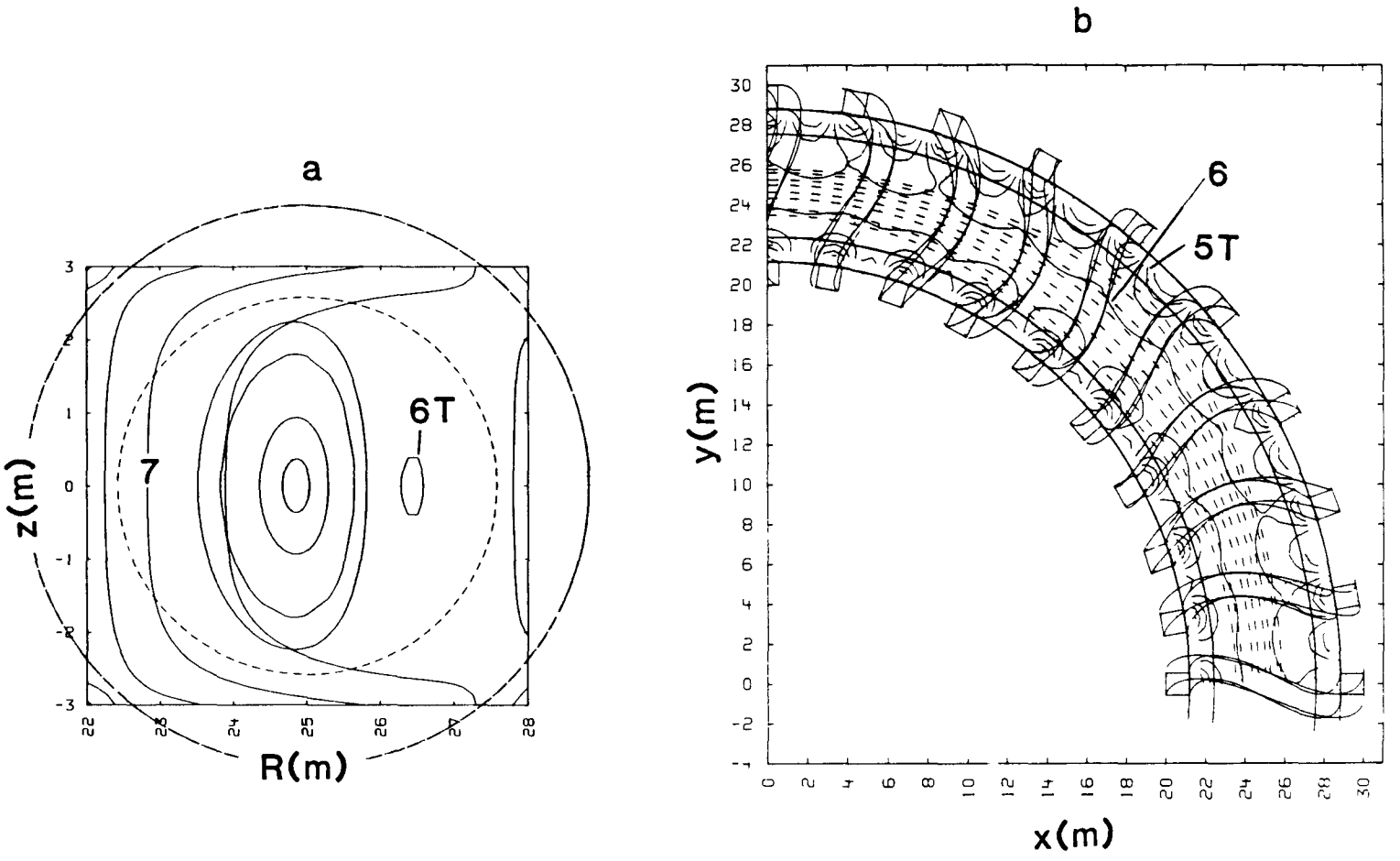

Fig. 4.4-24. The flux surfaces for $\xi = 1$ as viewed in the cross section under the key coil (frame a), corresponding to $\phi = 0$, and from above the equatorial plane (frame b). The same plotting conventions used in Fig. 4.3-1 are used here.

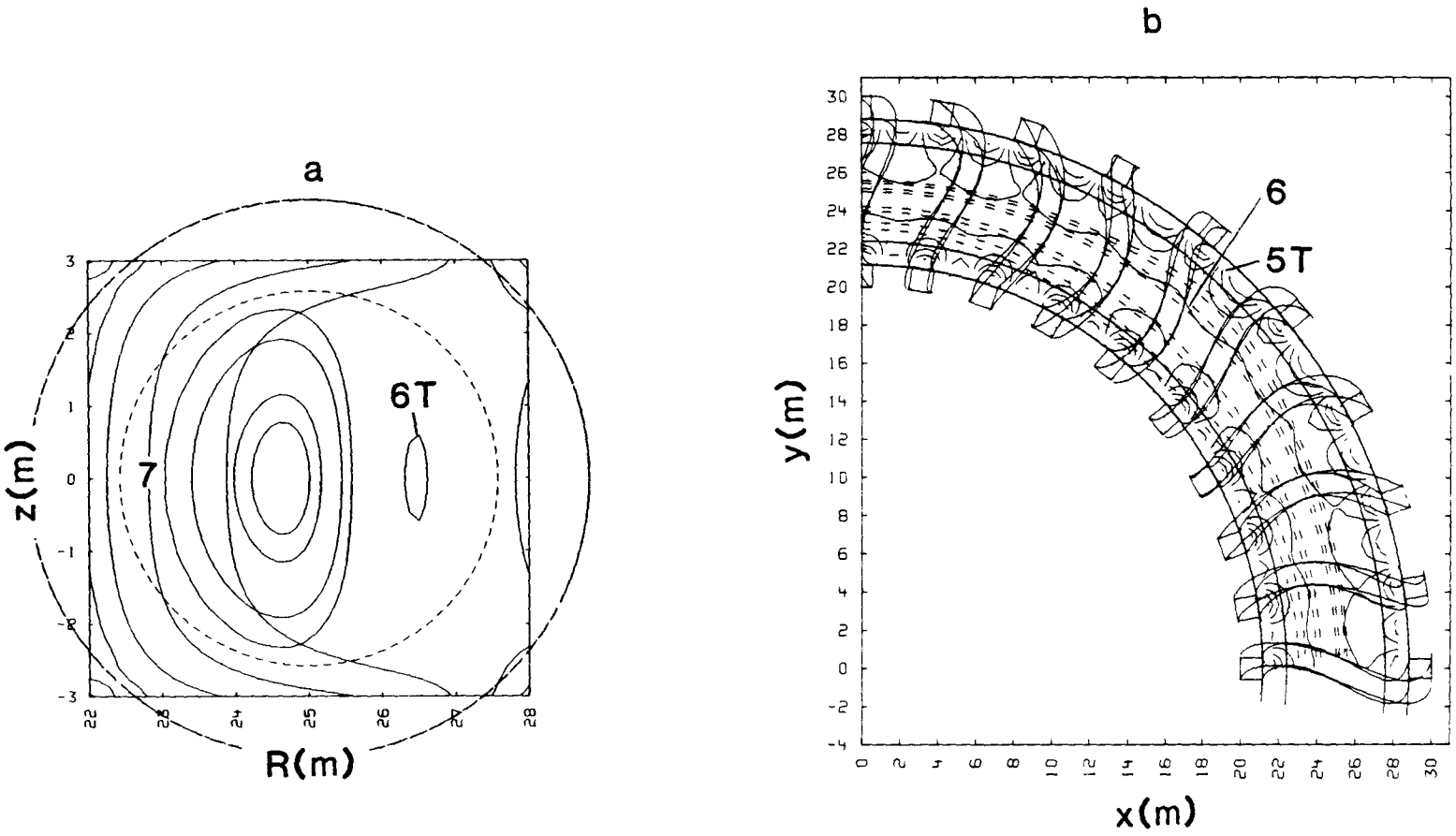

Fig. 4.4-25. The flux surfaces for $\xi = 2$ as viewed in the cross section under the key coil (frame a), corresponding to $\phi = 0$, and from above the equatorial plane (frame b). The same plotting conventions used in Fig. 4.3-1 are used here.

where r_h is the amplitude of the modulation and all the other notation is the same as in Eqs. (4.3-3). The phase of the modulation was chosen to attempt to align the outboard edge of the flux surfaces at a constant major radius. The results of varying both r_o and r_h are displayed in Figs. 4.4-26 through 4.4-28. One effect of increasing r_o and r_h is to increase the magnetic field, on axis and at the coil, which will result in higher forces, especially on those coils with centers farthest inboard. The transform has also decreased but could be made to increase with the appropriate choice of the phase and sense of the modulation. The most dramatic effect, however, is to decrease the volume utilization as seen from Figs. 4.4-27 and 4.4-28, which is undesirable.

The sensitivity studies of this section as well as those of Sec. 4.3. indicate a direction for future studies. An optimum MSR (the MSR is preferred for engineering reasons discussed in Sec. 5.) should have $\ell = 2$. An ι profile with positive shear is possible with higher harmonic distortion coefficients of the type in Eq. (4.4-1). A large number of coils with small distortion are preferred to reduce B_{CM} and the forces and to avoid possible adverse ripple effects on orbits. A ripple criterion needs to be established based upon orbit and transport calculations. Also, equilibrium and stability calculations are needed to confirm a correlation between $\langle\beta\rangle$ and ι. In the absence of such computations and assuming high beta requires high transform, low m numbers and noncircular coils [preferably elliptical bores using either Eqs. (4.4-2) or Eqs. (4.4-3) with $\lambda = 2$ in the latter case] should be used with auxiliary coils to ensure good flux surface quality. Should a magnetic hill be required, modulating the distortion amplitude as in Eqs. (4.4-5) is suggested. Even though coils with noncircular bores and "wedge" shapes sacrifice some of the favorable MSR engineering properties, such configurations may be required to attain the desired physics performance (e.g., beta). Considerably more effort should be devoted to coupling the kinds of magnetics calculations performed in this study with orbit and equilibrium/stability calculational efforts to realize the full potential of the modular stellarator concept. Many of the recommendations presented here are consistent with the symmotron approach.[20]

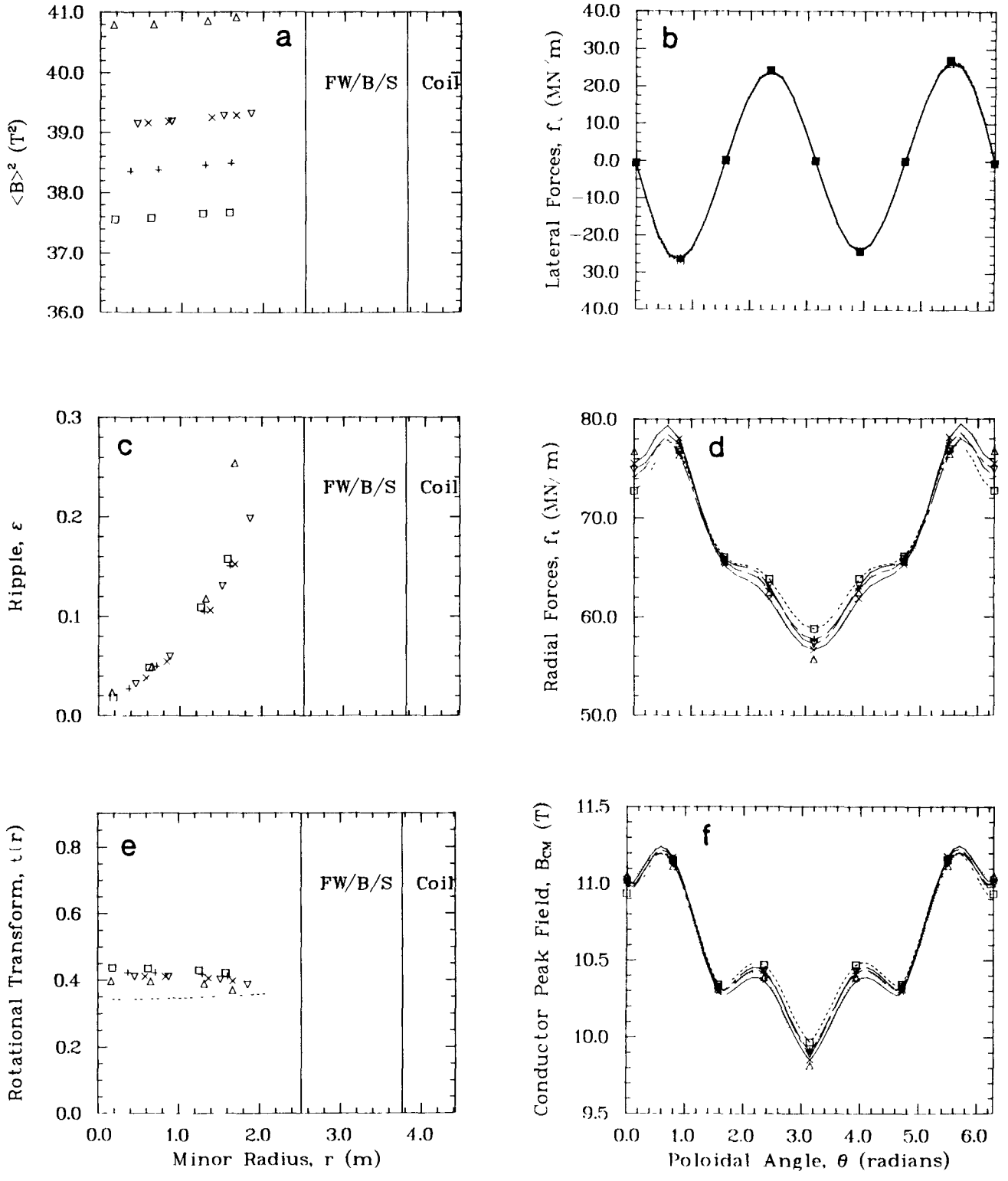

Fig. 4.4-26. A comparison of parameters measuring plasma and coil performance for r_h = 0.5 m (triangles), r_h = 0.25 m (x's), r_o = 0.5 m (inverted triangles), r_o = 0.25 m (pluses), and r_h = 0 m (squares). See the caption of Fig. 4.3-3 for an explanation of other plot features.

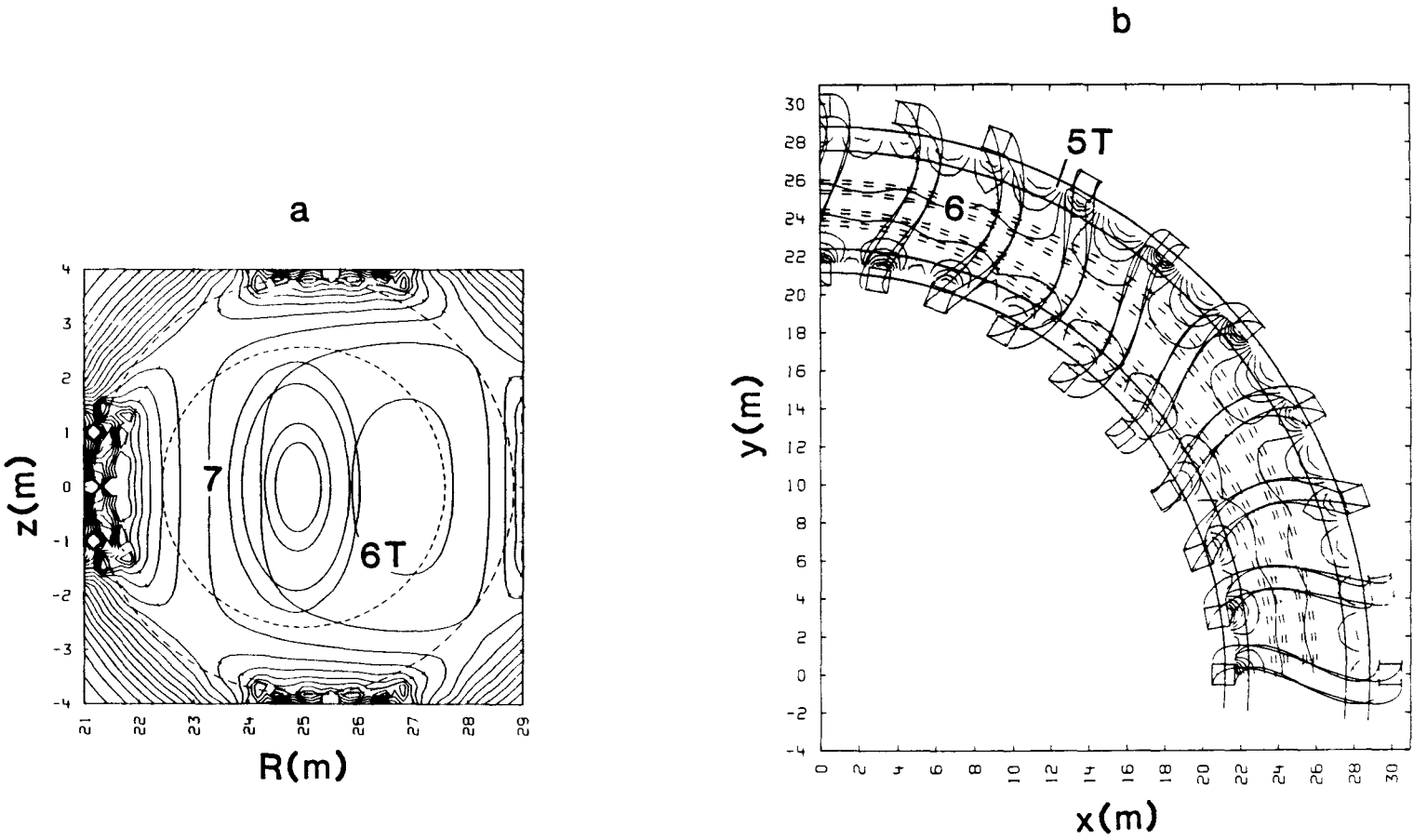

Fig. 4.4-27. The flux surfaces for r_o = 0.5 m as viewed in the cross section under the key coil (frame a), corresponding to ϕ = 0, and from above the equatorial plane (frame b). The same plotting conventions used in Fig. 4.3-1 are used here. The FW/B/S remains centered at R_T. The bore of the key coil is drawn as a dotted line in frame a.

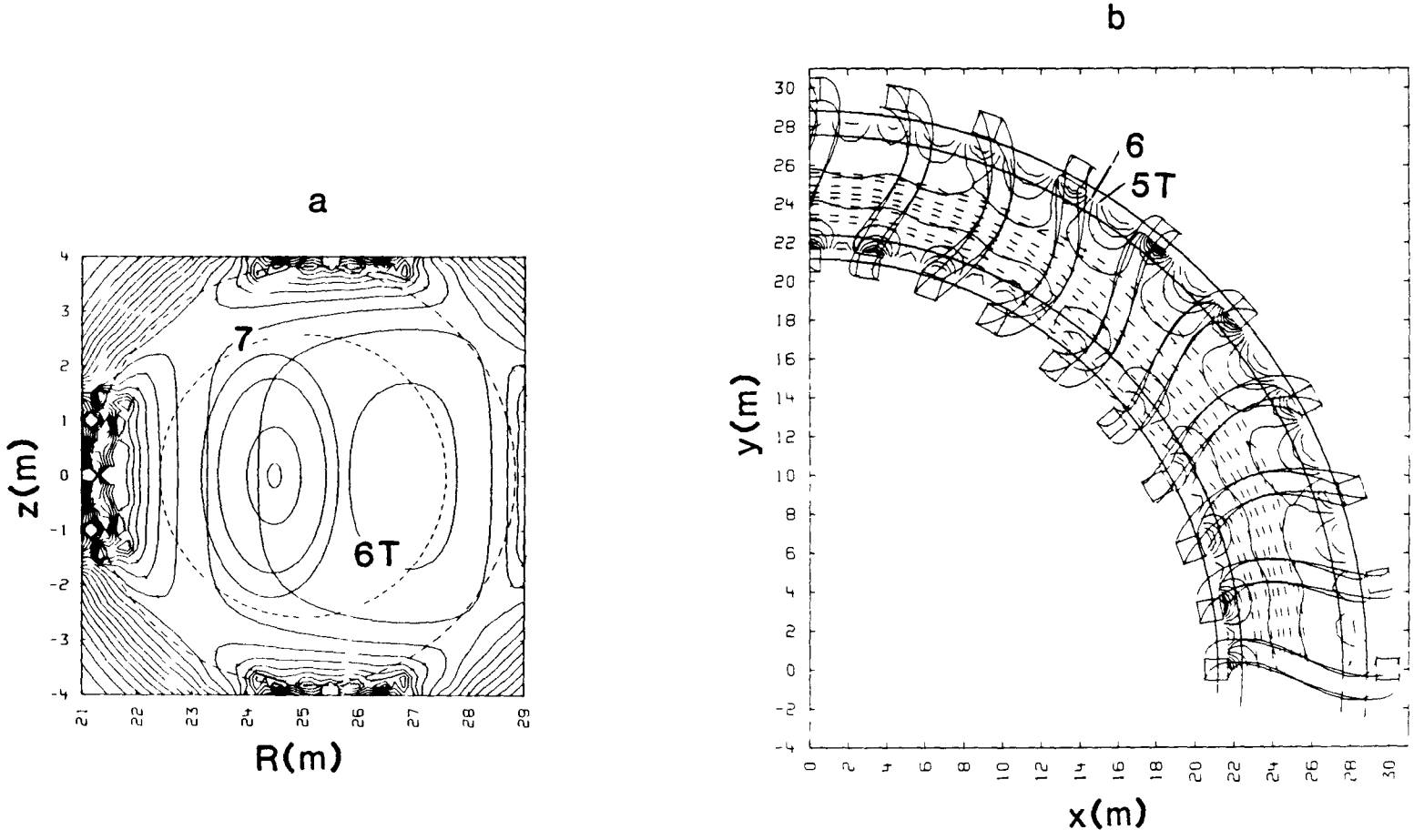

Fig. 4.4-28. The flux surfaces for r_h = 0.5 m as viewed in the cross section under the key coil (frame a), corresponding to ϕ = 0, and from above the equatorial plane (frame b). The same plotting conventions used in Fig. 4.3-1 are used here. The FW/B/S remains centered at R_T. The bore of the key coil is drawn as a dotted line in frame a.

REFERENCES

1. S. J. Sackett, "EFFI - A Code for Calculating the Electromagnetic Field, Force and Inductance in Coil Systems of Arbitrary Geometry - User's Manual," Lawrence Livermore National Laboratory report UCID-17621 (1977).

2. O. B. Adams, R. L. Brown, W. D. Cain, B. A. Carreras, L. A. Charlton, et al., "Proposal to Build ATF-1," Oak Ridge National Laboratory document, p. 3-103, Ref. 2 (October 1982).

3. D. R. Corson and P. Lorrain, Introduction to Electromagnetic Fields and Waves (W. H. Freeman and Co. San Francisco, CA, 1962).

4. G. E. Forsythe, M. A. Malcolm, and C. B. Moler, Computer Methods for Mathematical Computations (Prentice-Hall, Inc., Englewood Cliffs, NJ, 1977).

5. M. Abramowitz and I. A. Stegun, Handbook of Mathematical Functions (Dover Pub., Inc., NY, 1965).

6. W. R. Smythe, Static and Dynamic Electricity (McGraw-Hill Book Co., Inc., NY, 1939).

7. R. W. Hamming, Introduction to Applied Numerical Analysis (McGraw-Hill Book Co., NY, 1971).

8. K. Uo, "The Helical Heliotron Field for Plasma Confinement," Plasma Physics 13, 243-255 (1971).

9. U. Brossmann, W. Dommaschk, F. Herrnegger, G. Grieger, J. Kisslinger, W. Lotz, H. Nührenberg, F. Rau, H. Renner, H. Ringler, J. Sapper, A. Schlüter, and H. Wobig, "Concept of an Advanced Stellarator," 9th Inter. Conf. on Plasma Physics and Controlled Nucl. Fus. Research, IAEA-CN-41/Q5, Baltimore, MD (September 1-8, 1982).

10. D. T. Anderson, J. A. Derr, and J. L. Shohet, "The Interchangeable Modular Stellarator," IEEE Trans. on Plasma Sci. PS-9, 212-220 (December 1981).

11. C. G. Bathke, D. J. Dudziak, R. A. Krakowski, W. B. Ard, D. A. Bowers, J. W. Davis, et al., "ELMO Bumpy Torus Reactor and Power Plant," Los Alamos National Laboratory report LA-8882-MS (August 1981).

12. S. Rehker and H. Wobig, "A Stellarator Field Produced by Twisted Coils," 7th European Conf. on Controlled Fus. and Plasma Physics, 1, 117-120 (July 30 - August 4, 1973).

13. R. L. Miller and R. A. Krakowski, "The Modular Stellarator Fusion Reactor Concept," Los Alamos National Laboratory report LA-8978-MS (August 1981).

14. T. K. Chu, H. P. Furth, J. L. Johnson, C. Ludescher, and K. E. Weimer, "Optimization Techniques for Modular Stellarator Coils," Nucl. Fusion 22, 871-881 (1982).

15. "STELLARATORS; Status and Future Directions," Joint US/EURATOM Stellarator Steering Committee Report IPP-2/254 (DE81026572) (July 1981).

16. J. A. Derr and J. L. Shohet, "A Modular Stellarator Divertor," IEEE Trans. on Plasma Sci. PS-9, 234-239 (December 1981).

17. F. S. Acton, Numerical Methods that Work (Harper & Row, NY, 1970).

18. H. P. Furth, J. Killeen, M. N. Rosenbluth, and B. Coppi, "Stabilization by Shear and Negative V''," Proc. 2nd Int. Conf. on Plasma Physics and Contr. Nucl. Fusion Research, IAEA-CN-21/106, I, 103-126 (1966).

19. A. H. Boozer, T. K. Chu, R. L. Dewar, H. P. Furth, J. A. Goree, J. L. Johnson, et al., "Two High-Beta Toroidal Configurations: A Stellarator and a Tokamak-Torsatron Hybrid," 9th Inter. Conf. on Plasma Physics and Controlled Nucl. Fus. Research, IAEA-CN-41/Q4, Baltimore, MD (September 1-8, 1982)

20. J. F. Lyon, B. A. Carreras, J. H. Harris, J. A. Rome, L. A. Charlton, R. A. Dory, et al., "Stellarator Physics Evaluation Studies," 9th Inter. Conf. on Plasma Physics and Controlled Nucl. Fus. Research, IAEA-CN-41/Q3, Baltimore, MD (September 1-8, 1982).

5. MACHINE DESIGN

5.1. MSR Overview

This section summarizes the features of the Modular Stellarator Reactor (MSR) with particular reference to the MSR-IIB ($\langle\beta\rangle = 0.08$) design point (see Tables 3.5-1 and 3.5-3). Termination of the study precluded parallel development of the other flagship design points and also inhibited iteration to a self-consistent magnetics/engineering configuration. The specific objectives of the design effort are summarized in Table 5.1-1 subject to the overall goal of sufficiently characterizing the MSR fusion power core (FPC) to assess its potential as a commercial fusion power plant. Features of the design are summarized in Table 5.1-2. Figure 5.1-1 shows a plan view of the MSR-IIB coil layout, consisting of N = 36 modular coils. The MSR elevation is shown schematically in Fig. 5.1-2. The coil set is essentially fixed under routine conditions allowing access through a permanent vacuum shell to the underlying first wall/blanket/shield (FW/B/S) systems for routine maintenance, as shown Fig. 5.1-3. Provision for coil removal/replacement is made in the rare event of coil failure, consistent with the philosophy adopted for the STARFIRE tokamak conceptual design.[1] This fixed-coil configuration contrasts with the approach taken in the UWTOR-M modular stellarator reactor study,[2]

TABLE 5.1-1

ENGINEERING DESIGN OBJECTIVES

- Provide for regular first-wall replacement.
- Provide for regular blanket replacement.
- Provide for regular limiter replacement.
- Provide for a permanent vacuum vessel.
- Provide for a fixed-coil configuration.

TABLE 5.1-2

SUMMARY OF ENGINEERING FEATURES

- First-wall, blanket, and limited shielding in removable modules.
- Three modules per coil allow insertion and removal without moving coils.
- One module of three is placed on center between coils.
- Coils centering forces are reacted by 4-K steel bucking rings.
- Modules are inserted and removed above midplane.
- Pumped limiters, vacuum pumping, and RF ports in central modules.

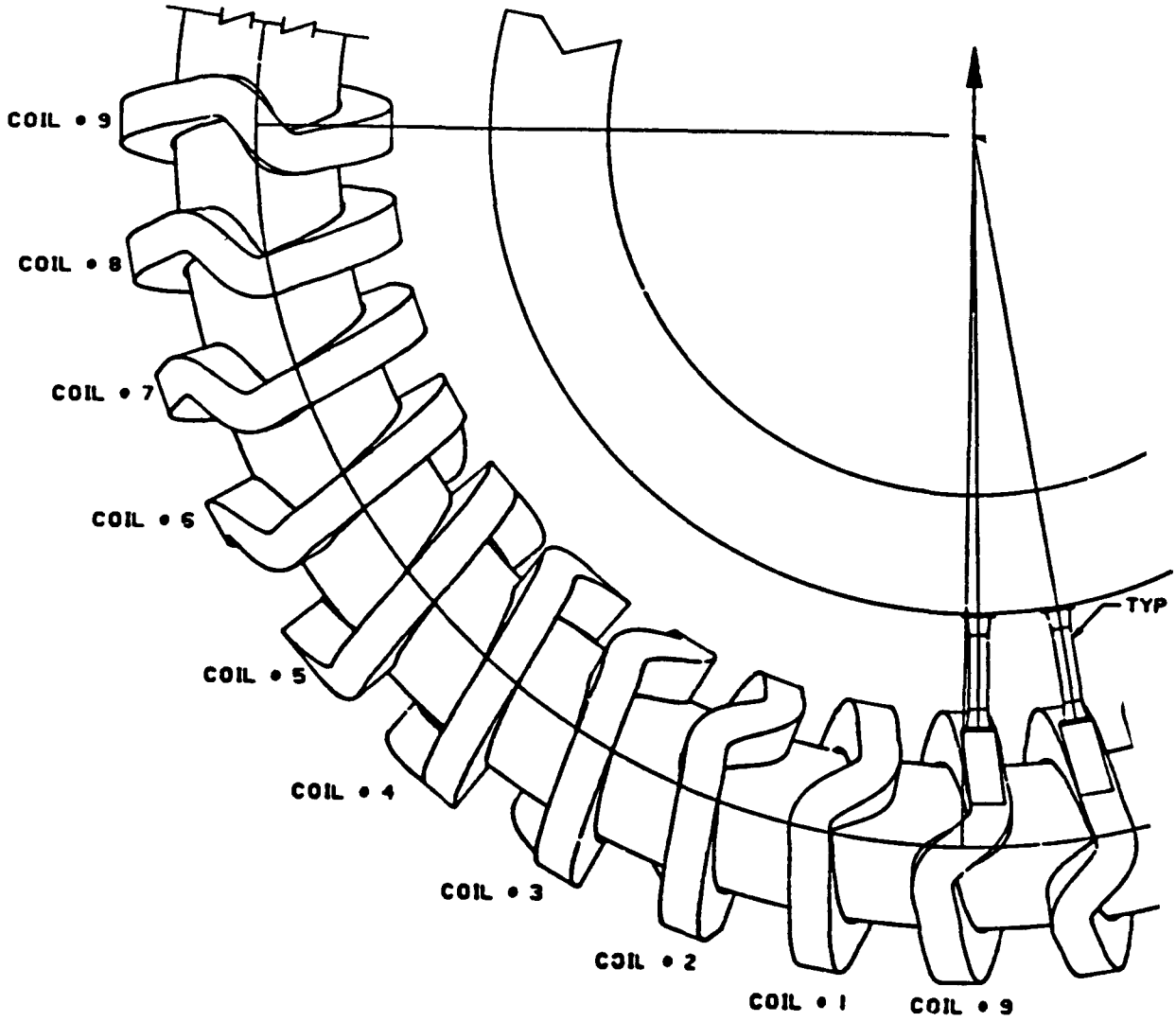

Fig. 5.1-1. Plan view of a toroidal sector of the MSR-IIB coil layout.

which envisages routine movement (i.e., extraction along the major radius without lifting) of a module consisting of a single modular coil (1 of 18) and its underlying FW/B/S components. Reasons for choosing the fixed-coil option in the present study are summarized in Table 5.1-3. However, should it prove superior, a movable-coil version of the MSR is certainly possible. A conductor configuration, distribution of coil winding, and coil cross-section configuration were developed by as a basis for design of both the modular (MSR-IIB) and continuous-helical-coil (TR-B3) cases. The reference configuration is shown in Fig. 5.1-4 and was based on the magnetic requirements given in Sec. 4.3.2.2. A square superconductor cross section was selected to minimize winding and lateral bending stresses caused by the

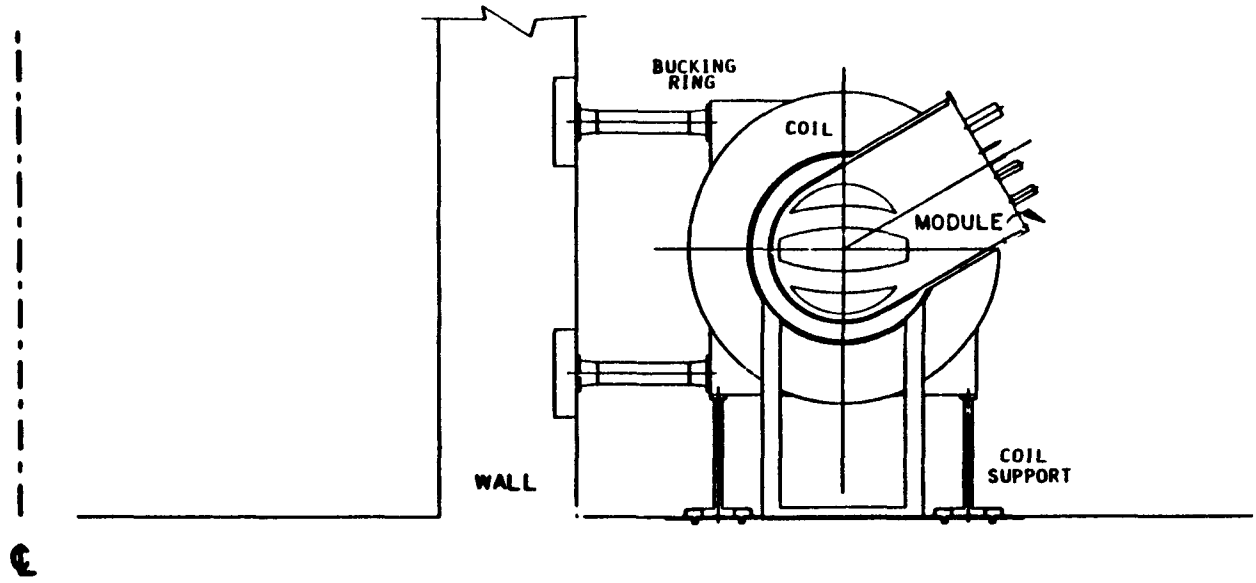

Fig. 5.1-2. Elevation view of the MSR-IIB coil layout.

laterally distorted MSR coil shape. The coil cross section was divided into three subsections, each having approximately the same number of turns. Because a constant current (~5 kA) was assumed for all conductors, each section of the coil also has approximately the same number of Ampere-turns. To achieve 12 T at the inboard region of the coil, Nb_3Sn was selected for operation at 4.2 K. The middle and outboard subcoil sections were limited in field to 8 and 4 T, respectively. Because of the lower field in these regions, Nb_3Ti conductor was used. The conductor sizes in the high, medium and low field regions are approximately 0.015 × 0.015 m, 0.013 × 0.013 m, and 0.011 × 0.011 m square, respectively. The preliminary coil size was based on using internal structure on which the conductor was wound as well as external structure consisting of the inner and outer structural rings and the side walls of the coil case. The conductor and structure were assumed to share the Lorentz forces. The amount of internal structure was determined by that required to limit the conductor strain to 0.35% without the additional support of the external structure of the coil case.

The square conductor configuration, similar to that used in the Mirror Fusion Test Facility (MFTF),[3] was selected for the reference design because the square cross section bends well in two perpendicular directions. The configuration provides space for coolant passages, structural support, and

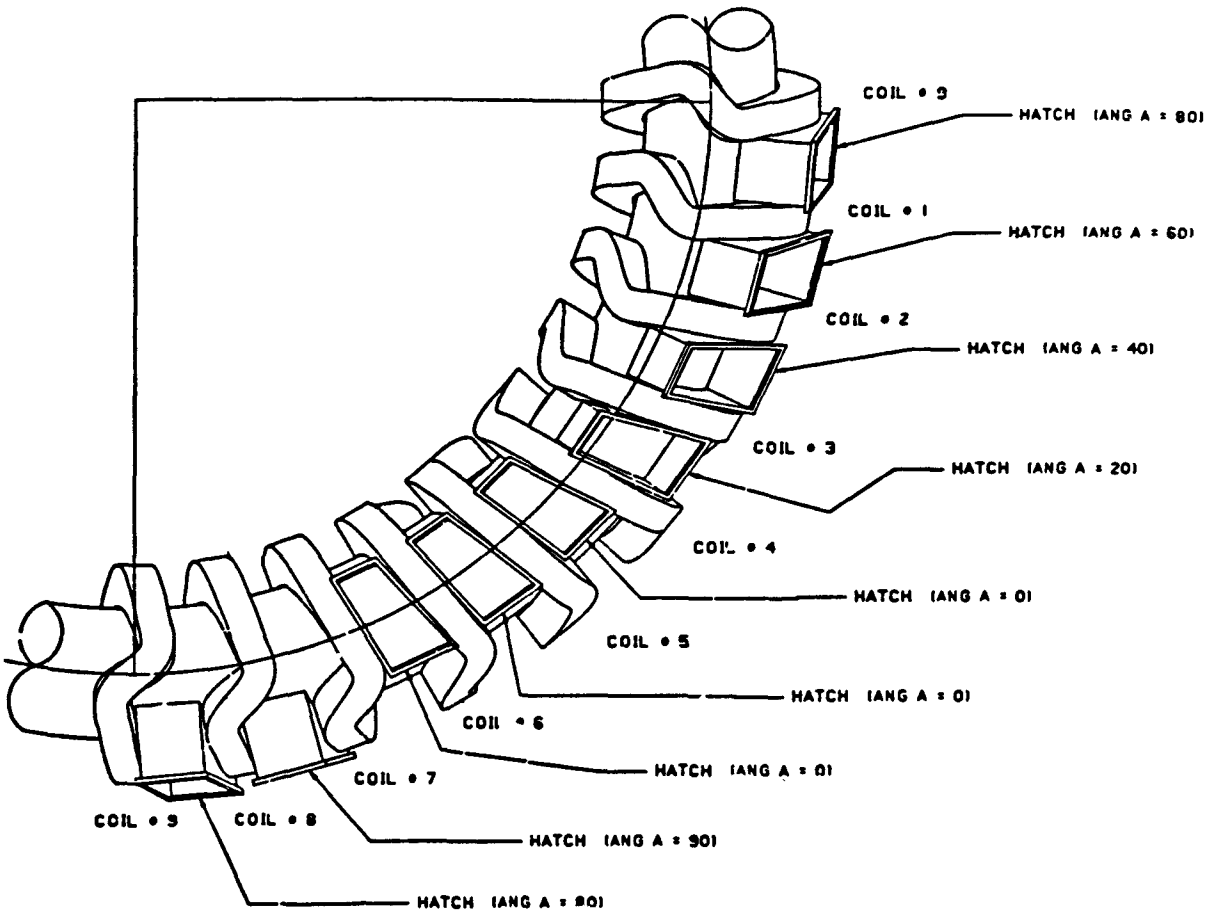

Fig. 5.1-3. MSR-IIB blanket/shield module access ports. The polodial orientation with respect to the vertical is designated by "ANG A" as measured in degrees.

TABLE 5.1-3

ENGINEERING ASPECTS OF MOVABLE COIL ASSEMBLIES

- Experience with large transformers indicates moving reduces reliability, shortens life.
- Moving causes unusual loads, strains, shocks.
- Alternately, movable coils can be more conservative designs with reduction in current density.
- Coil system must be realigned after moving.
- Mechanical connections must be remade and tested after moving as warping may occur.
- Before dewar vacuum space is brought up to air, coils must be warmed to room temperature and later cooled.

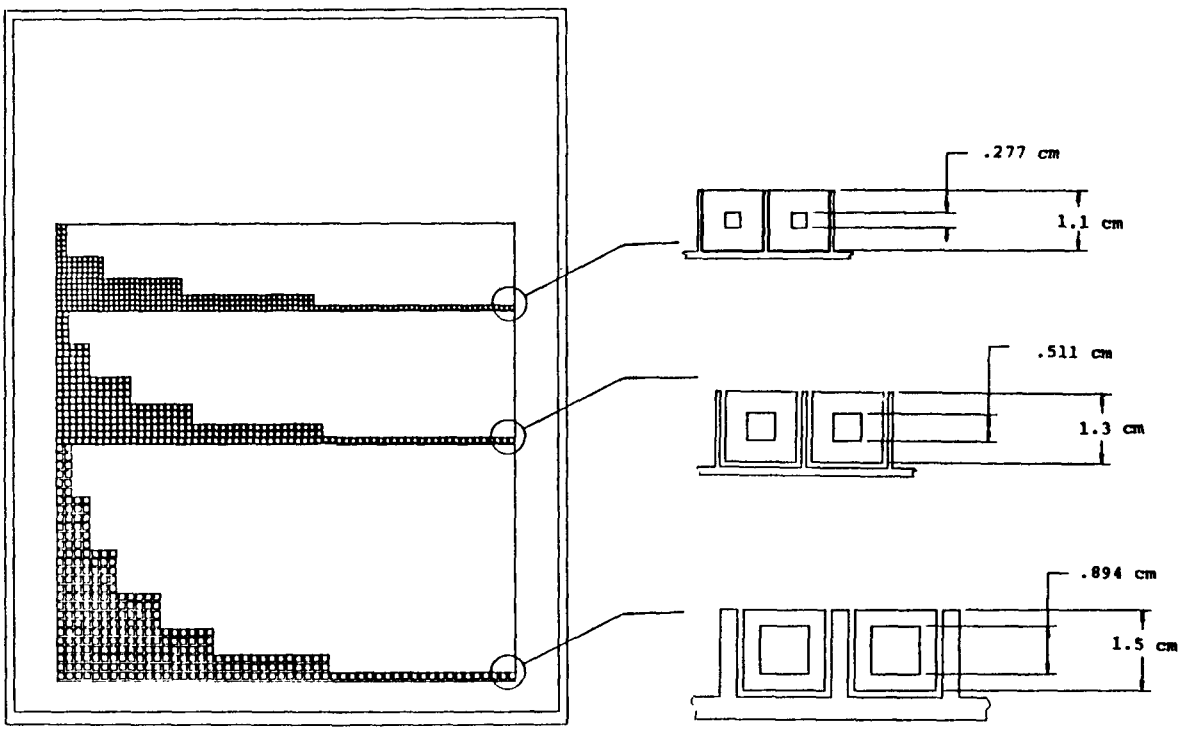

Fig. 5.1-4. MSR superconducting coil cross section. The inboard direction is down.

insulation. Two conductor cooling methods were investigated: a) bath cooling with helium at atmospheric pressure (He I), and b) cooling with superfluid helium (He II). The He-I method was selected for the reference concept because of reliability and lower operating cost. The second cooling option showed that the coil cross section required was only about 2/3 that of the reference design. However, a detailed study of the life-cycle costs would be required to have a better understanding of the cost/benefit relationship to justify the increased refrigeration requirement of a superfluid cooled coil. This level of optimization was beyond the scope of the study, but should be considered for later study. In addition, if the coil size became more restrictive, the alternate He-II cooling method could also be considered.

Because the coil design was sized by early scoping analysis (Sec. 3.4.), the coil envelope varies slightly from the dimensions finally calculated by the detailed structural analysis (Sec. 5.4.). Although the outer ring of the coil case is 0.47 m in both cases, the coil structural side walls were increased to 0.20 m, except near the blanket ports, as a result of the

structural analysis. Additionally, detailing of a dewar (not yet designed) around the coils would change the overall shape.

A finite element (FE) structural analysis was performed on a typical MSR-IIB modular coil. The coil was within acceptable stress limits with the external backing ring of 0.47-m thickness sized to sustain the radial forces generated by the energized windings. The analysis showed that the side walls of the coil case required a structural thickness of 0.20 m in order to withstand the twisting and side loads imposed by the four lateral supports assumed in the analysis. The inner ring of the coil was sized at 0.10 m. Although the stresses in the coil are adequate, it is possible with further iterations to optimize the side wall stresses and thickness by moving the support points. Details of this analysis are discussed in Sec. 5.4.

Lithium and lithium compounds were considered as breeding media, and coolant options consisted of H_2O (water or steam), helium, or the liquid breeding material itself. The reference concept consists of a first wall similar to the STARFIRE-DEMO,[4] which has the corrugations connected to, but located behind, the first wall. Pressurized water flowing in the passages between the first wall and the corrugation cools the first-wall structure. The blanket material, Li_2O, was selected as the breeder material because of its high breeding rate and the extensive engineering performed as part of STARFIRE-DEMO study.[4] An array of pressurized-water coolant tubes is dispersed throughout the solid breeder region to remove the heat. Headers supply the coolant to both the tube array and the first-wall corrugation coolant channels. Tritium removal is accomplished by slowly purging the blanket with helium and extracting the tritium-containing purge gas from the module for tritium removal.

The MSR-IIB reactor design point contains N = 36 modular coils, each with ℓ = 2 poloidal field periods. The coil arrangement provides for m = 4 toroidal field periods, each containing nine modular coils. The coils are fixed, and a combined shield/vacuum vessel assembly is constructed within the inner bore of the magnets. Ports are located between the magnets for insertion and removal of the blanket assemblies (or modules) with pumped limiters. Each module contains its associated blanket coolant piping and manifolds. Because of the space limitation provided by the ports, the blanket modules are inserted in three sections. The first section is inserted into the fixed shield/vessel assembly through the port and moved under a magnet.

The second section is similarly inserted and moved under the adjacent magnet. The third or center module is lastly inserted to fill the space between the two modules that were previously inserted. The modules are fitted with flanges and seals and are bolted to the flange of the port that extends beyond the outer radius of the magnet. The flange is located outboard of the magnet to maximize the access opening of the port. Because of the distorted coil shape and rotation (change in angular orientation) of the coils around the torus, the angular location of the port varies around the torus. Because of the coil shape, orientation, and access limitation, nine different port and module group configurations are required.

The elliptical (ℓ = 2) plasma cross-sectional shape is fitted by a quasi-rectangular first-wall/blanket (FW/B) structure built into the modules. The first wall is separated from the core-plasma surface by a scrapeoff layer of thickness $\delta_s \simeq 0.20$ m, this thickness being determined by the height of the pumped-limiter blades above the first-wall surface. The longitudinal apertures through the adjacent modules are stacked toroidally to form the plasma chamber. The aperture through a given module does not adapt directly to the helical precession of the plasma, but is designed as a straight-through opening for ease of fabrication. The poloidal rotation of the plasma cross section is tracked by offsetting the orientation of adjacent modules by $\Delta\theta = 6.67^{\circ}$ for the MSR-IIB configuration. Clockwise progression around the torus as viewed from above requires counter-clockwise stepping of the modules, as illustrated in Fig. 5.1-5.

Substantial relative movement is expected to occur between the vessel assembly (containing blanket and shield) and the cryogenic coils as the temperature swings between room temperature and that of reactor operation. The vessel assembly and coils therefore are supported separately. The weight of the coil is supported by a pair of vertical radial columns. The thermal plus elastic radial deflection of the coils can be ~0.05 m toward the center of the reactor. The bases of the columns, therefore, are equipped with oil-pad bearings, as shown in Fig. 5.1-6, to permit the coil to move freely during cooldown. Movement of the coils is not anticipated for routine maintenance, however. The centering force of each coil is transmitted to a pair of steel bucking rings through a pair of columns arranged like spokes in a wheel. The spokes extend from the coils to the steel bucking rings. The bucking rings are in turn backed up by a thick concrete reinforcing cylinder.

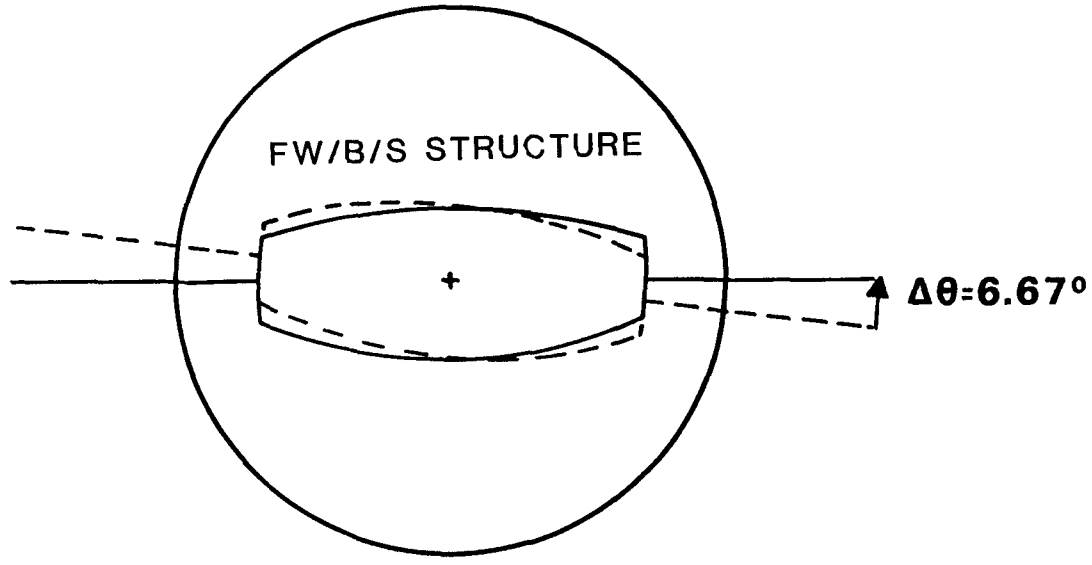

Fig. 5.1-5. Clockwise progression (i.e., from dashed orientation to solid orientation) around the MSR torus of the poloidal orientation of adjacent first-wall/blanket modules to track the helically symmetric plasma cross section. With its major axis oriented horizontally in this view.

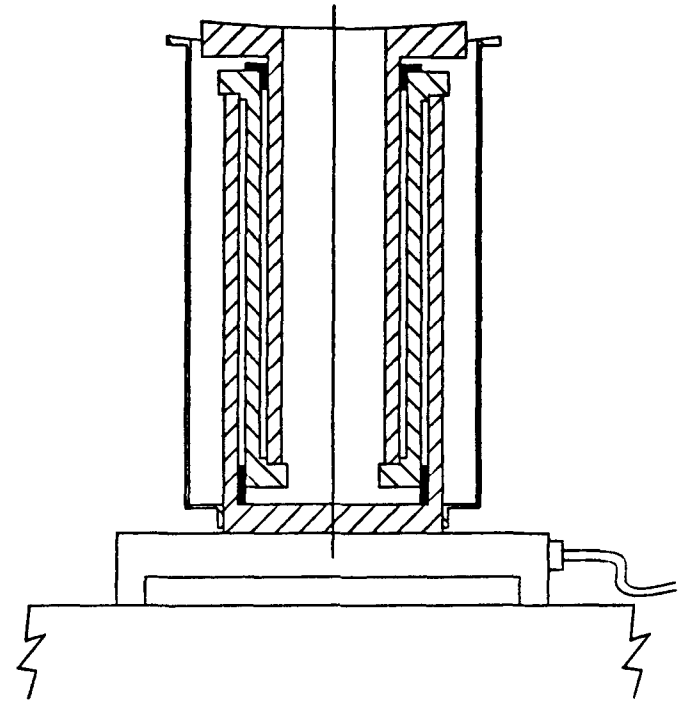

Fig. 5.1-6. Detail of the MSR coil-support column equipped with oil-pad bearings to facilitate coil movement during cooldown and heatup.

Horizontal and radial support columns will have to be designed and insulated to accommodate the temperature gradient from the 4-K coil to the room-temperature concrete foundation.

The remainder of this chapter summarizes the available engineering design detail of the MSR-IIB design point. The preliminary nature and potential for design inconsistency that is a result of the truncation of the study are again noted. Were this study completed, the results contained herein would be considered interim.

5.2. Coil Internals

5.2.1. Overview. This subsection summarizes the design effort applied to the MSR modular-coil internal arrangement.[5] Figure 5.2-1 schematically illustrates some of the major geometrical characteristics of MSR under present consideration. Each coil is identical in shape, but the coils assume different orientations around the torus.

This subsection develops current profiles within the proposed coil envelopes for use in the MSR scoping study. The analyses presented herein, therefore, are based upon analytic approximations that should lead to current profiles which can form the basis of a more complete conceptual design. Because the MSR magnets are distorted toroidal-field (TF) coils, the conductor configurations must have two orthogonal axes around which the coils are easily bent. This mechanical requirement suggests that the conductors should be square rather than rectangular in cross section. Because the outflow of helium from the conductor must be nearly independent of conductor orientation, the conductor cooling channels should be symmetrically arranged. Furthermore, to get a high surface-to-volume ratio required for good cooling, the cooling channels should be made integral with the interior of the conductor. All of these requirements lead to conductor configurations generically similar to the MFTF conductor[3] illustrated in Fig. 5.2-2.

The MSR coils under consideration could be described as solenoids that have been distorted so that the windings have a sinusoidal axial displacement from the centerline. To analyze the coil cross-sections, these coils have been approximated as segments of infinite solenoids. The coil cross section is then divided into three sections, each with an equal number of ampere-turns. If the peak field in these stellarator coils is 12 T, the above approximation divides the coils into subcoils with peak fields of 4, 8, and 12 T. In the 4- and 8-T subcoils, the superconductor can be NbTi. However,

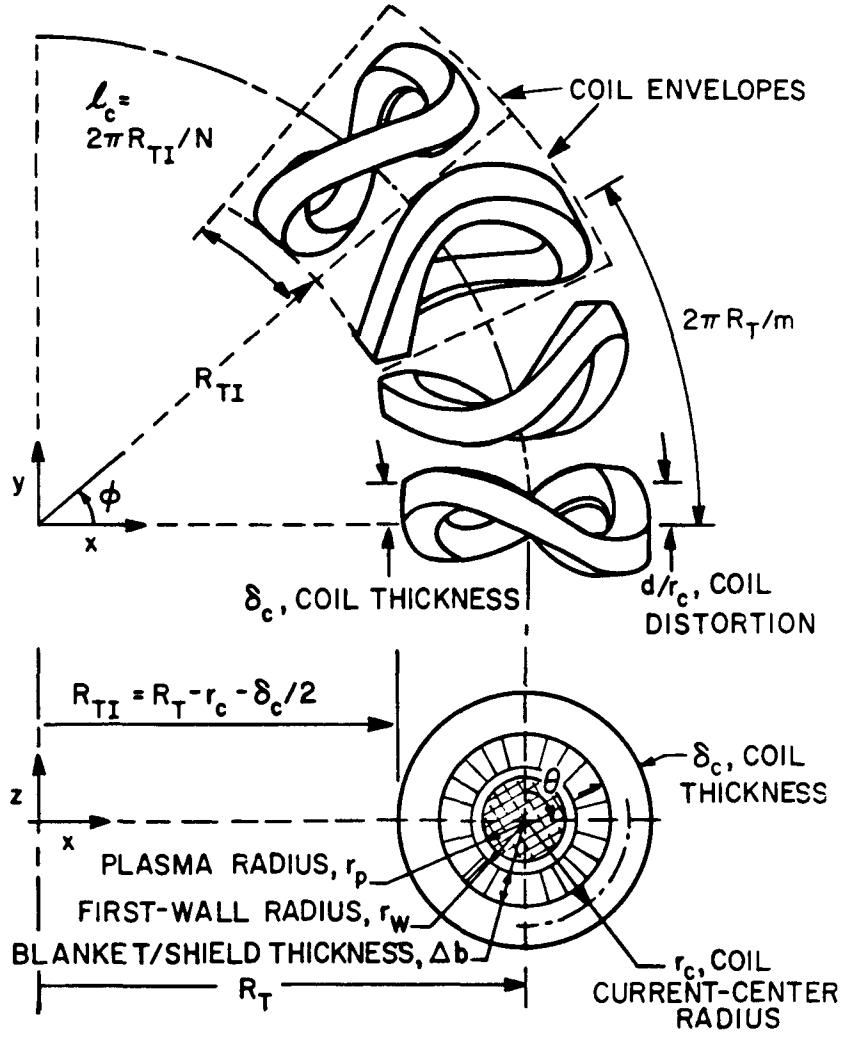

Fig. 5.2-1. Schematic diagram of a toroidal sector of a typical MSR coil set.

the 12-T subcoil should be made of Nb_3Sn for operation at temperatures between 1.8 and 4.6 K.

5.2.2. He-I Cooled Magnet Design. There are a number of alternative methods for cooling the superconducting MSR magnets. These methods include a) bath cooling with atmospheric pressure liquid helium (He I), b) bath cooling with subatmospheric pressure normal liquid helium (He I), c) bath cooling with superfluid helium (He II), d) forced cooling with subcritical liquid helium (He I), and e) forced cooling with supercritical gaseous helium. The selection of the cooling method is often based upon achieving the most

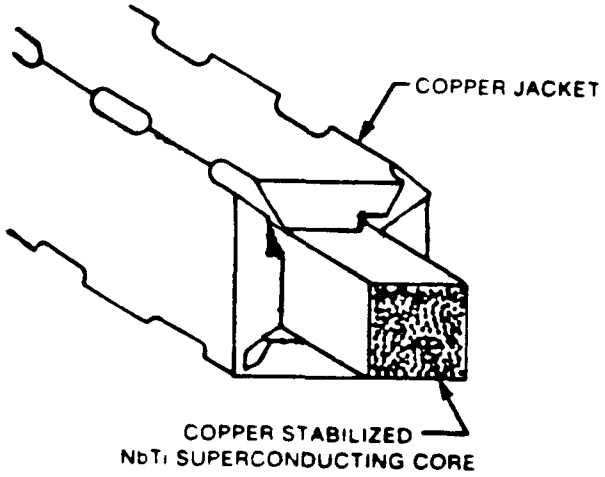

Fig. 5.2-2. MFTF conductor[3] configuration adapted for the MSR.

reliable design at the lowest operating cost. The highest operational reliability is found in refrigeration systems based upon atmospheric and higher pressure operation. The lowest operating costs are found in systems utilizing bath cooling instead of forced cooling. In the absence of a detailed study of the magnet life-cycle costs as a function of the cooling modes, the selection of the cooling mode should be based on the criterion of achieving the highest reliability at the lowest operating cost; hence, bath cooling with atmospheric pressure liquid helium is highly preferred.

The following sections present a preliminary analysis of an atmospheric pressure He-I bath cooled superconducting magnet system. The details of the conductor, insulation, coolant passages, and structural support remain to be developed; however, space factors have been defined to allow for these elements in the superconducting magnets.

To size the envelope of the conductors for each subcoil, a square cryostable conductor with 50% of the external surface exposed to helium cooling is assumed. In this analysis, the conductor is considered to be cryostable if the surface heat flux is below 3000 W/m^2 when all of the current is carried by the copper stabilizer. For a representative conductor design, the conductor current was nominally set to 5 kA. This current level was selected to minimize the bending requirements for winding the conductor of the 12-T subcoil. Higher operating currents are possible at the proposed

operating current densities, and, therefore, this current should not be considered invariant.

Listed in Table 5.2-1 are the characteristics of the conductor envelope derived in sizing the reference conductors for the stellarator. This analysis concludes that the envelope of the conductor cross section should be 0.011 × 0.011 m^2 for the 4-T subcoil, 0.013 × 0.013 m^2 for the 8-T subcoil, and 0.015 × 0.015 m^2 for the 12-T subcoil.

The actual conductors are internally cooled, similar to the MFTF conductor. For the same average current density, internal cooling of the conductors reduces the amount of copper stabilizer in the conductor cross section, requiring a larger wetted perimeter.

The conductor consists of two parts: a square conductor core that is wrapped in a grooved and punched copper sheath. This conductor promises low cost, as demonstrated by the MFTF. The NbTi conductor core should be made of a square multifilamentary superconductor with a copper-to-superconductor ratio of 2:1. The Nb_3Sn conductor core could be made of a compacted cable of

TABLE 5.2-1

CONDUCTOR SIZING ANALYSIS FOR A He-I COOLED CONDUCTOR

Subcoil fields (T)	0 - 4	4 - 8	8 - 12
Material	NbTi	NbTi	Nb_3Sn
j_c [(4K, B_{MAX}) (MA/m^2)]	2300	675	245*
j/j_c	0.85	0.85	0.85
j (MA/m^2)	1955	574	208
Superconductor area (m^2)	$2.56(10)^{-2}$	$8.71(10)^{-2}$	$2.404(10)^{-1}$ (a)
Average copper resistivity (Ω m)	$3(10)^{-10}$	$5(10)^{-10}$	$7(10)^{-10}$
Heat flux, q/A (W/m^2)	2878	2999	2900
Copper area (m^2)	$1.1844(10)^{-4}$	$1.6029(10)^{-4}$	$2.0096(10)^{-4}$
Total conductor area (m^2)	$1.21(10)^{-4}$	$1.69(10)^{-4}$	$2.25(10)^{-4}$
j_{Cu} (MA/m^2)	42.22	31.19	24.88
Conductor cross section dimensions (m × m)	0.011 × 0.011	0.013 × 0.013	0.015 × 0.015
j_{COND} (MA/m^2)	41.32	29.59	22.22

(a)These quantities are measured over the Nb_3Sn and CuSn cross-sectional area.

multifilamentary superconductors, each having a ratio of copper-to-superconductor of 2:1, embedded in a solder matrix which represents approximately 10% of the conductor core cross section.

In the designs presented in Table 5.2-2, the conductors have been redesigned for 20 to 30% of the conductor volume filled with helium. The channel size and number have been selected to provide a wetted perimeter that is sufficient for the surface heat removal rate to be below 0.003 MW/m^2. As when rough-sizing the conductor envelope, only 50% of the total surface area is assumed to be available for cooling the conductor. The current of 5077 A produces 21.0 MA in a 1.50-m-wide and 1.65-m-deep (dimensions to warm walls) coils. The coil structure can be divided into two parts: an internal structure and an external structure. The amount of internal structure required will be based upon limiting the Nb_3Sn strain associated with radial loads to below 0.35% without the aid of the external structural members. In this estimation, the structure and conductor both contribute to restraining the coil deflection. The amount of external structure required is initially based upon limiting the stress resulting from the radial loads below 2/3 of the yield stress of 310 stainless steel (717 MPa). In the latter calculation, the external structure is doubled in thickness to account for the lateral loads.

To limit the strain in the internal structure and conductor below 0.35%, approximately 35% of the total cross-sectional area must be structure. Because the Lorentz forces vary with the peak magnetic field, the structure should be graded to keep the peak force per unit volume nearly a constant. Accordingly, it was assumed in the 0 to 4-T subcoil that 20% of the volume should be structure, in the 4- to 8-T subcoil that 30% of the volume should be structure, and in the 8- to 12-T subcoil 45% of the volume should be structure. Under these assumptions, the 0 to 4-T subcoil represents approximately 18.9% of the available volume; the 4- to 8-T subcoil represents approximately 30.1% of the available volume, and the 8- to 12-T subcoil represents approximately 51% of the available volume.

Table 5.2-3 lists the estimated stresses and strains in the internal structure and conductor in the absence of an external structure and any application of lateral loads. The maximum and minimum Lorentz forces are estimated in the infinite solenoid model. The elastic modulus is determined from the law of mixtures assuming that it is $2.068(10)^5$ MPa for stainless

TABLE 5.2-2

He-I COOLED CONDUCTOR CHARACTERISTICS

Subcoil field range (T)	0 - 4	4 - 8	8 - 12
Conductor core			
Cross section (mm × mm)	2.77 × 2.77	5.11 × 5.11	8.94 × 8.94
Superconductor	NbTi	NbTi	Nb_3Sn
Stabilizer	Cu	Cu	Cu
Ratio of stabilizer to nonstabilizer	2:1	2:1	2:1
Average resistivity of stabilizer (Ω m)	$3(10)^{-10}$	$5(10)^{-10}$	$7(10)^{-10}$
Solder (%)	--	--	10
j_c (MA/m^2)	2300	675	245[a]
j/j_c	0.865	0.865	0.865
Current, I (kA)	5.077	5.077	5.077
Conductor			
Cross section (m × m)	0.011 × 0.011	0.013 × 0.013	0.015 × 0.015
Stabilizer sheath	Cu	Cu	Cu
Total ratio of stabilizer to nonstabilizer	32	14	3.8
Average resistivity of stabilizer (Ω m)	$3(10)^{-10}$	$5(10)^{-10}$	$7(10)^{-10}$
Size of channels (mm × mm)	3 × 3	3 × 3	1.5 × 1.5
Number of channels	4	4	24
Average conductor j (MA/m^2)	41.96	30.05	22.56
Percentage helium (%)	29.8	21.0	24.0
Average copper j (MA/m^2)	61.58	40.85	55.79
P_{wetted} (m)	0.034	0.038	0.066
q/A (W/m^2)	2760	2730	3000

[a] This j_c is measured over the Nb_3Sn and CuSn cross sectional area.

steel and $6.894(10)^4$ MPa for the conductor: the latter assumption is very conservative. As shown in Table 5.2-3, the maximum strain in the Nb_3Sn windings will be below 0.35% as originally proposed.

However, the internal structure has too high a stress relative to the proposed structural yield stress: therefore, additional external structure is required. The addition of the needed structure internally would lead to a very low current density winding and would require a greater number of ampere-turns to produce the required field topology at the plasma. Therefore, the needed structure is added externally. To reduce the average stress to approximately 2/3 of the yield stress for stainless steel, a 0.47-m-thick "ring" on the outside of the coil cross section will be required. The average

TABLE 5.2-3

SIZING OF THE INTERNAL STRUCTURE FOR A He-I COOLED COIL

Subcoil field range (T)	0 - 4	4 - 8	8 - 12
Lorentz force density (MN/m^3)			
Maximum radial	134.3	168.3	148.9
Minimum radial	0.0	84.1	99.3
Average stress (MPa)	249	436	375
Average elastic modulus (10^4 MPa)	8.01	10.02	12.19
Average strain (%)	0.311	0.435	0.308

strain in the coil, ignoring the contribution from the conductor, is approximately 0.23%, which is an acceptable strain level for operation of the superconductors within 14% of their unstrained critical current level. Figure 5.2-3 schematically illustrates the coil configuration analyzed for MSR coils. The overall area needed to produce 21.0 MA, including the area required to handle lateral loading, is 1.50-m-wide by 1.65-m-deep. The warm bore of these coils is 5.3 m, and the outside diameter is 8.6 m.

5.2.3. He-II Cooled Magnet Design. The current density achievable in a superconducting magnet is strongly dependent upon the cooling mode selected. In the reference design, bath cooling with atmospheric helium has been selected to achieve the highest reliability at the lowest cost. However, in the event that the current density is insufficient to achieve the required design objectives, the cooling mode could be changed to bath cooling with superfluid helium to increase the magnet current density.

A preliminary analysis of the use of superfluid cooling to increase the current density is presented here. This analysis has been restricted to identifying an approximate value for the level of average current density within the magnets. Hence, details of the conductor, insulation, coolant passages, and structural support remain to be fully defined.

The method used to analyze the conductor in a He-II (superfluid) cooled system is similar to that used with the He-I cooled system. Thermal conduction along the conductor in addition to surface heat removal is included

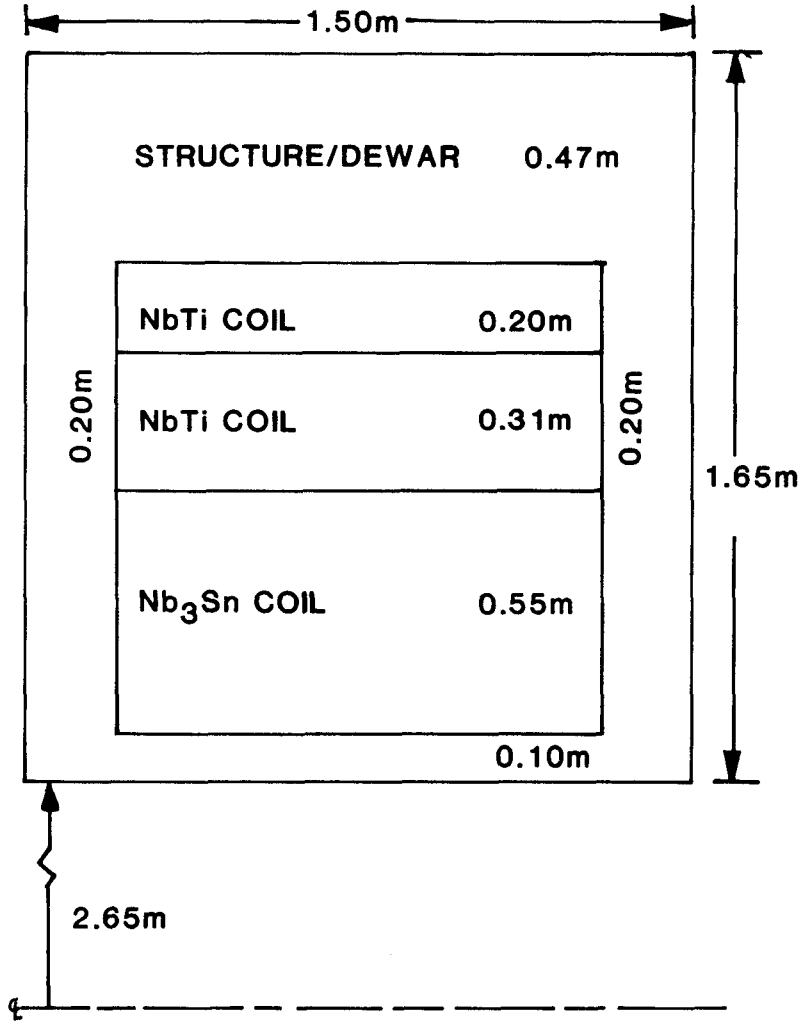

Fig. 5.2-3. He-I cooled MSR-IIB coil cross section.

in this design. This technique[6] leads to the so-called "equal-area" criterion:

$$\int_{T_b}^{T_f} [Q(T) - G(T)]\, dT = 0 \quad , \tag{5.2-1}$$

when the conductor's thermal conductivity is a constant. Here, T_b(K) is the bulk temperature of the coolant; T_f(K) is the film boiling temperature at the conductor hot spot; Q(T) is the surface heat removal rate (W/m^2); and G(T) is the heat generation rate per unit surface area (W/m^2).

For He-II cooling, the surface heat removal rate can be divided into three regions. In the low heat-flux region, Kapitza conductance dominates and

$$Q(T) \simeq 0.0486 \left(T^{2.8} - T_b^{2.8}\right) \quad . \tag{5.2-2}$$

In the heat-flux-limited region, an insulating barrier of He-I and/or vapor limits the heat flux such that

$$Q(T) \simeq 4.64 \frac{nfw}{PL^{1/3}} \left[7.3 - 20.3(T_b - 1.6)^2 - 1.25(2.17 - T_b)^{1/4}\right] \quad , \tag{5.2-3}$$

where n is the number of channels, f is the fraction of channel area of flow, w(m) is the width of cooling channels, P(m) is the wetted perimeter, and L(m) is the channel length. In the highest heat-flux region, He-II, like He-I, exhibits a film boiling behavior and

$$Q(T) \simeq 0.06 \left(T - T_b\right) \quad . \tag{5.2-4}$$

The heat generation rate used is a simple approximate form based upon the critical-state model of superconductivity and is given by

$$G(T) = \begin{cases} 0 & , T < T_{cs} \\ \\ \dfrac{10^4 \rho_m I^2}{A_m P} & , T > T_{cs} \quad , \end{cases} \tag{5.2-5}$$

where $A_m(m^2)$ is the matrix cross sectional area, I(A) is the conductor current, ρ_m is the matrix resistivity, and $T_{cs}(K)$ is the temperature at which the critical current equals the conductor current. Using this approximate form for G(T) gives conservative results within 10% of the results obtained using the more complete current sharing model.

For most conductors, the temperature at which the conductor normalizes, T_{cs}, can be determined from the linear relationship

$$\frac{j}{j_c(H, T_b)} = \frac{T_c(H) - T_{cs}}{T_c(H) - Tb} \quad , \tag{5.2-6}$$

where $T_c(H)$ is the lowest temperature satisfying

$$j_c\left(H, T_c(H)\right) = 0 \quad . \tag{5.2-7}$$

The results of parametric analyses of the superfluid-cooled conductors are illustrated in Figs. 5.2-4 through 5.2-6. These curves illustrate the impact of the cooling channel dimensions on the conductor current density when operating near $T_c(H)$; the highest current densities tend to occur for low values of operating current relative to critical current.

Based upon this analysis, Table 5.2-4 summarizes the characteristics of the superfluid-cooled conductors. Obviously, superfluid cooling has allowed the conductor current densities to be increased. Material savings are now possible. A 39% reduction in core material cost is possible for the NbTi conductors, when superfluid cooling is considered. A 32% reduction in core material cost is possible for the Nb_3Sn case. The greatest volumetric savings is an 80% reduction in copper required to cryostabilize the conductors. Overall these savings should result in approximately a 40% reduction in the conductor costs.

These material savings are offset to some degree by an increased refrigeration requirement, which from the refrigerator efficiency should approach 2.5 times the refrigeration power required in the He-I reference design. To better appreciate the cost/benefit relationship, a more detailed examination of the life-cycle costs of a superfluid-cooled stellarator with a normal-fluid-cooled stellarator must be made. This kind of study is beyond the scope of the present work.

The structure for the superfluid-cooled coil design differs significantly from the He-I cooled coil design. Less superconductor is available to support the loads in the former case. However, the methodology of determining the

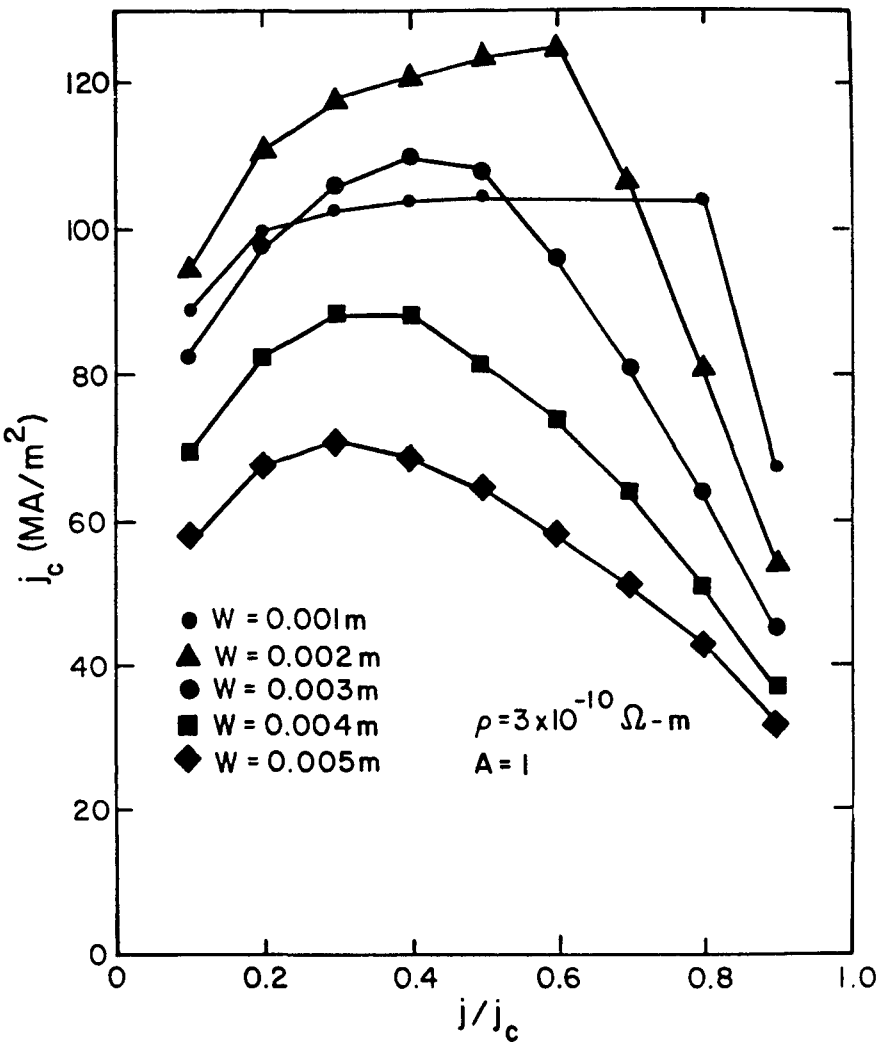

Fig. 5.2-4. Effect of j/j_c and channel width, w, on the 4-T subcoil 5-kA NbTi conductor.

structural requirements remains the same. In this analysis, the structural distribution was selected to give nearly the same strain distribution as in the He-I coil design. Accordingly, it was found in the 0 to 4-T subcoil that 55% of the volume should be structure, in the 4- to 8-T subcoil that 60% of the volume should be structure, and in the 8- to 12-T subcoil that 70% of the volume should be structure. Under these conditions, the 0- to 4-T subcoil represents 15.5% of the available volume; the 4- to 8-T subcoil represents 27.5% of the available volume; and the 8- to 12-T subcoil represents 57% of the available volume.

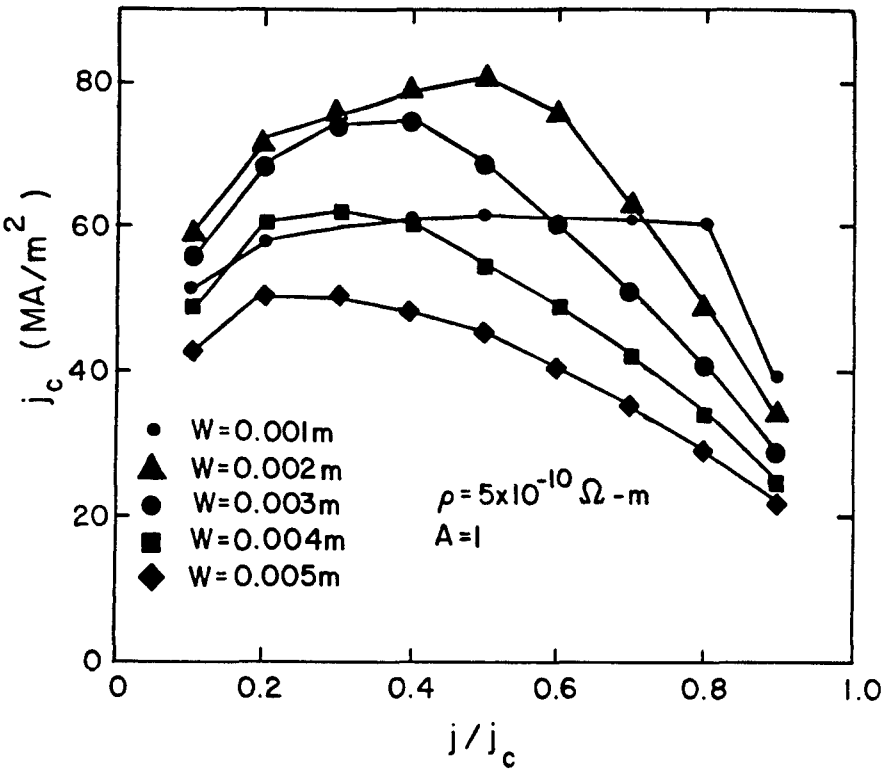

Fig. 5.2-5. Effect of j/j_c and channel width, w, on the 8-T subcoil 5-kA NbTi conductor.

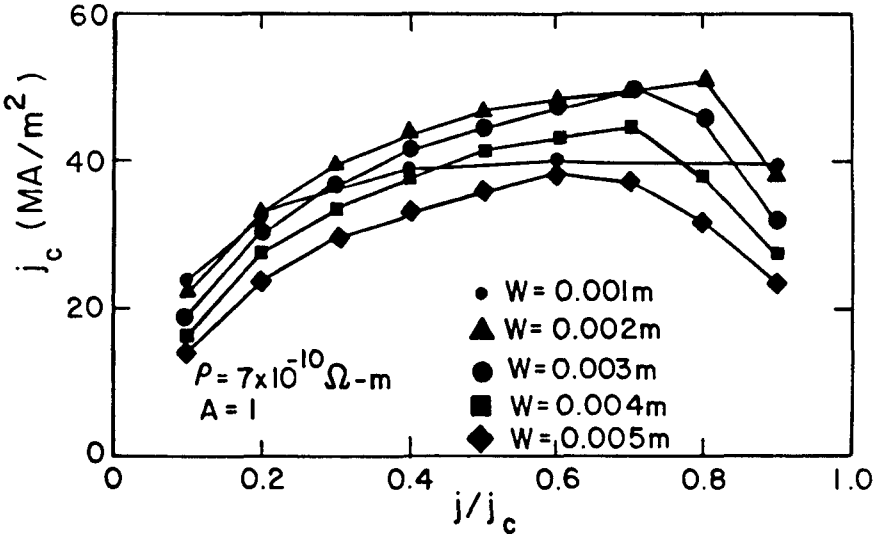

Fig. 5.2-6. Effect of j/j_c and channel width, w, on the 12-T subcoil 5-kA NbTi conductor.

TABLE 5.2-4

He-II COOLED CONDUCTOR CHARACTERISTICS

Subcoil field range (T)	0 - 4	4 - 8	8 - 12
Conductor core			
Cross section (mm × mm)	2.37 × 2.37	3.56 × 3.56	7.35 × 7.35
Superconductor	NbTi	NbTi	Nb_3Sn
Cu:non-Cu ratio	2:1	2:1	2:1
Cu resistivity, (Ω m)	$3(10)^{-10}$	$5(10)^{-10}$	$7(10)^{-10}$
Solder (%)	--	--	10
$T_c[B_{MAX}]$ (K)	7.4	5.6	9.4
j_c[1.8 K, B_{MAX}] (MA/m^2)	4500	2400	388[a]
j/j_c	0.6	0.5	0.8
I (kA)	5.077	5.077	5.077
Conductor			
Cross section (m × m)	0.0064 × 0.0064	0.008 × 0.008	0.01 × 0.01
Total Cu:non-Cu ratio	9.3	7.5	2.9
Sheath resistivity (Ω m)	$3(10)^{-10}$	$5(10)^{-10}$	$7(10)^{-10}$
f, flow area fraction	0.5	0.5	0.5
w, channel width (m)	0.002	0.002	0.002
L, channel length (m)	0.0085	0.00129	0.0139
n, number of channels	8	8	8
j_{COND}, average conductor current density (MA/m^2)	123.95	79.43	50.77
Percentage helium (%)	53	44	36
A_m, copper area (m^2)	$0.1748(10)^{-4}$	$0.3177(10)^{-4}$	$0.4764(10)^{-4}$
P, wetted perimeter (m)	0.0087	0.0118	0.0159
$(q/A)_{MAX}$ (W/m^2)	$5.52(10)^4$	$3.74(10)^4$	$2.57(10)^4$

[a]This j_c is measured over the Nb_3Sn and CuSn cross-sectional area.

Table 5.2-5 lists the estimated stresses and strains in the internal structure in the absence of the external structure and lateral loads. The methodology of calculating these results is the same as used in the He-I coil design. In addition to the internal structure, a 0.47-m-thick ring on the outside of the coil should be added to handle the lateral loading and to reduce the average strain in the superconducting winding. The resulting cross section is schematically illustrated in Fig. 5.2-7.

5.2.4. Magnet Summary. Two coil configurations have been investigated. The major differences between these two configurations are the cooling mode and the current density. To achieve a high reliability at a low operating cost, the He-I bath cooled option is recommended. To achieve higher current

TABLE 5.2-5

SIZING OF THE INTERNAL STRUCTURE FOR A

He-II COOLED COIL

Subcoil field range (T)	0 - 4	4 - 8	8 - 12
Lorentz force density (MN/m^3)			
Maximum radial	223.1	254.2	182.8
Minimum radial	0.0	127.1	121.8
Average stress (MPa)	396	641	464
Average elastic modulus (10^4 MPa)	13.36	13.96	15.46
Average strain (%)	0.296	0.459	0.300

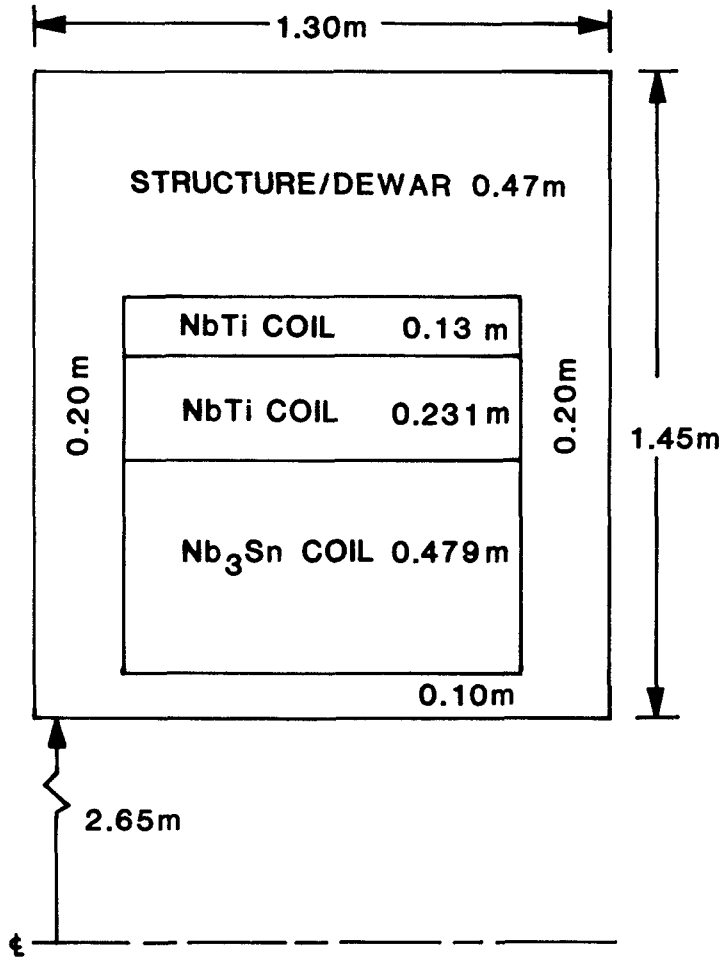

Fig. 5.2-7. He-II cooled stellarator coil cross section.

densities at the cost of lower reliability and higher operating costs, the superfluid-cooled (He-II) option is available.

Because the MSR coils are distorted TF coils, generically similar in shape to the yin-yang coils of mirror reactors, using the stellarator conductor designs based on the MFTF coil concept is recommended. Because the superconducting coils are only moderately distorted solenoidal coils and the lateral loading can be handled by external structure, the present analysis is based upon solenoid models subdivided into three sections. The peak fields in these three subcoils are assumed to be 4, 8, and 12 T.

All conductors should be designed to be cryostable. NbTi superconductors are recommended for fields below 8 T and a Nb_3Sn superconductor is recommended for fields above 8 T. Table 5.2-6 lists the key characteristics of the recommended conductors. For the He-I conductors the current and cross section proposed are only nominal values; the conductor current density quoted should be valid for currents up to 8 to 10 kA.

TABLE 5.2-6
SUMMARY OF STELLARATOR CONDUCTOR DESIGNS

COOLING MODE	He-I COOLING			He-II COOLING		
Peak field (T)	8	4	12	4	8	12
Superconductor	NbTi	NbTi	Nb_3Sn	NbTi	NbTi	Nb_3Sn
Stabilizer	Cu	Cu	Cu	Cu	Cu	Cu
Current (A)	5077	5077	5077	5077	5077	5077
Current density (MA/m^2)	41.96	30.05	22.56	123.95	79.43	50.77
Cross section (m × m)	0.011 × 0.011	0.013 × 0.013	0.015 × 0.015	0.0064 × 0.0064	0.008 × 0.008	0.01 × 0.01

The proposed stellarator coil structure is divided into two parts: internal and external structure. The internal structure is designed, independent of lateral loading and external structure, for a maximum strain in the Nb_3Sn of 0.35%. Table 5.2-7 summarizes the structural distribution within the superconducting coil. To keep the stresses in the structure below 2/3 of the yield stress and to restrain the lateral loading, an additional 30% of the total coil cross section must be provided for external structure.

TABLE 5.2-7

SUMMARY OF STELLARATOR COIL STRUCTURAL DISTRIBUTION WITHIN THE WINDING CAVITY OF THE COIL

COOLING MODE	He-I COOLING			He-II COOLING		
Peak field (T)	4	8	12	4	8	12
Percentage of winding cavity	18.9	30.1	51.0	15.5	27.5	57.0
Percentage of structural content	20	30	45	55	60	70

Comparing the He-I and He-II coil geometries, it is concluded that the average overall current density in the He-I coil is 8.48 MA/m^2 and that the average current density in the He-II coil is 11.14 MA/m^2. Hence, a 30% increase in the overall coil current density can be achieved by cooling with superfluid He.

5.3. First-Wall/Blanket/Shield Design

5.3.1. Overview. This subsection summarizes the features of the MSR first-wall/blanket/shield (FW/B/S) design effort.[7] The FW/B/S of a fusion reactor performs four vital functions:

- provides a suitable vacuum containment for the reacting plasma,
- breeds tritium to replace burned and lost fuel,
- converts the fusion energy to sensible heat for power generation, and
- provides shielding of the superconducting magnet components against radiation damage and nuclear heating.

Although these functions are separate and distinct, they are closely interrelated. For example, the first-wall design strongly impacts the tritium-breeding potential of the blanket, whereas the shield requirements are

affected by the radiation transport properties of the blanket. Therefore, the FW/B/S must be designed as an integrated, self-consistent system. Within the framework of the above functions, Table 5.3-1 lists generic requirements that must be satisfied by the the FW/B/S components.

In meeting the conditions listed in Table 5.3-1, the variables under control fall into two broad categories: geometry and materials. Within these categories, numerous combinations exist that, with data currently available, can be shown to satisfy the necessary requirements for a given fusion driver. Figure 5.3-1 shows schematically the arrangement of the FW/B/S, along with material options considered in recent near-term reactor studies, as well as the range of dimensions. The actual dimensions depend upon the particular choice of materials and the fusion driver. For the MSR, a number of unique features drive the blanket configuration and material choices including

- an elongated plasma shape (1.65-m major radius, 0.45-m minor radius),
- a plasma center-to-coil-case distance of 2.60 m,
- a complex (non axisymmetric), magnetic-field topology,
- two poloidal field periods ($\ell = 2$),
- modularity (fixed-coil set),
- steady-state operation, and
- disruption-free operation.

The effect of the first two features provides a blanket/shield spatial envelope (assuming a 0.20-m scrapeoff zone) varying between 0.8 and 2.0 m. The minimum fast-neutron attenuation necessary to satisfy the magnet protection requirements in the range of wall loadings being considered here (2-4 MW/m^2) is about 10^{-5}. High-efficiency fast-neutron shielding (e.g., iron-based alloys, tungsten) can provide this attenuation for thicknesses around 0.80 m. Figure 5.3-2, shows[1] the calculated dose response in epoxy insulator for Fe 1422, an iron-based alloy having good neutron attenuation and activation properties. Nearly 0.8 m is needed for a five-decade dose reduction. These considerations indicate little space for blanket material along the direction of the plasma major axis in the present MSR-IIB design,

TABLE 5.3-1

GENERIC FIRST-WALL/BLANKET/SHIELD REQUIREMENTS

First Wall

- Removal of surface heat load
- Adequate radiation damage lifetime
- Acceptable sputtering and erosion properties
- Compatibility with first-wall coolant
- Limited neutron interactions

Blanket

- Tritium breeding ratio (global) ≈ 1.1
- Low-tritium inventory (<10 kg tritium)
- Absorption of ~99% of the available neutron energy
- Temperature distribution consistent with structural limits and tritium extraction requirements
- Low storage chemical energy
- Good energy multiplication
- Provisions for changeout/maintenance

Shield

- Limitation of nuclear energy deposition in the superconducting magnets to $\lesssim$20 kW.
- Limitation of radiation damage to organic insulators to $\lesssim 10^8$ Gy in 40 yr and stabilizer fluence to $\lesssim 10^{22}$ n/m^2 ($E_n \gtrsim 0.1$ MeV) in 10 yr
- Limitation of activation of critical components to permit "hands on" maintenance during shutdown
- Selection of constituents to minimize amount of long term activation products
- Provide first stage bulk and penetration shielding

all of the available space being required for shielding. Therefore, the blanket thickness must vary poloidally direction.

Complex magnetic field topology, represents the third MSR-specific feature that coupled with the high field magnitude (B_o = 6.6 T on axis, 10-12 T in the blanket region), to preclude the use of pumped, highly conducting fluids, (i.e., liquid lithium). Such a system would almost certainly be characterized by large MHD pressure drops, uncertain heat-transfer properties,

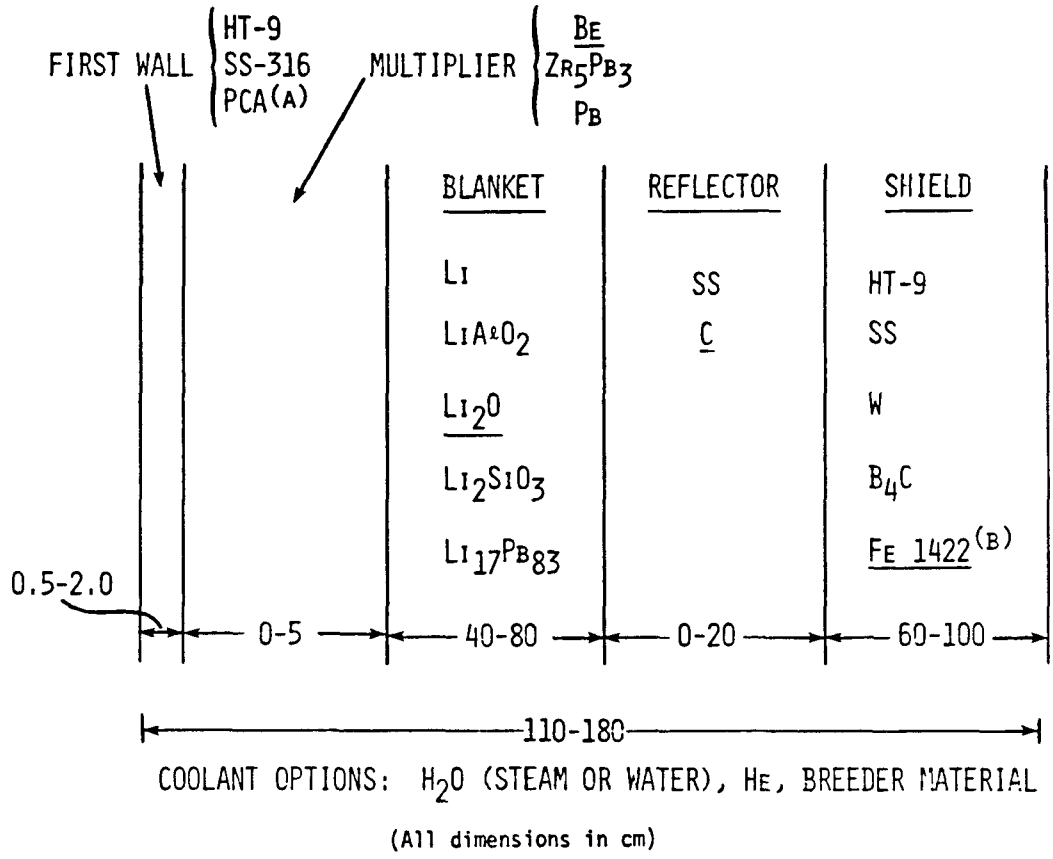

(A) Prime Candidate Alloy - A Titanium Modified Austenitic Stainless Steel

(B) FE14Mn2Ni2Cr

Fig. 5.3-1. FW/B/S arrangement and options.

and the presence of stagnation zones. Therefore, blanket breeder materials must be limited to the solids, or perhaps stagnant LiPb.

The third and fourth features suggest the use of a pumped limiter for impurity control and exhaust. For the present $\ell = 2$ field configuration, the natural magnetic separatrix occurs somewhere in the shield zone, along the direction of the plasma major axis. The shield thickness in this region is adequate only for magnet protection, leaving little space for a divertor impurity-control system. Moreover, the modular configuration in conjunction with a magnetic divertor would result in complex mechanical design. An added advantage of a pumped limiter is that better plasma volume utilization results. The pumped-limiter design is adapted from the STARFIRE design[1] and is discussed more fully in Sec. 5.3.2.

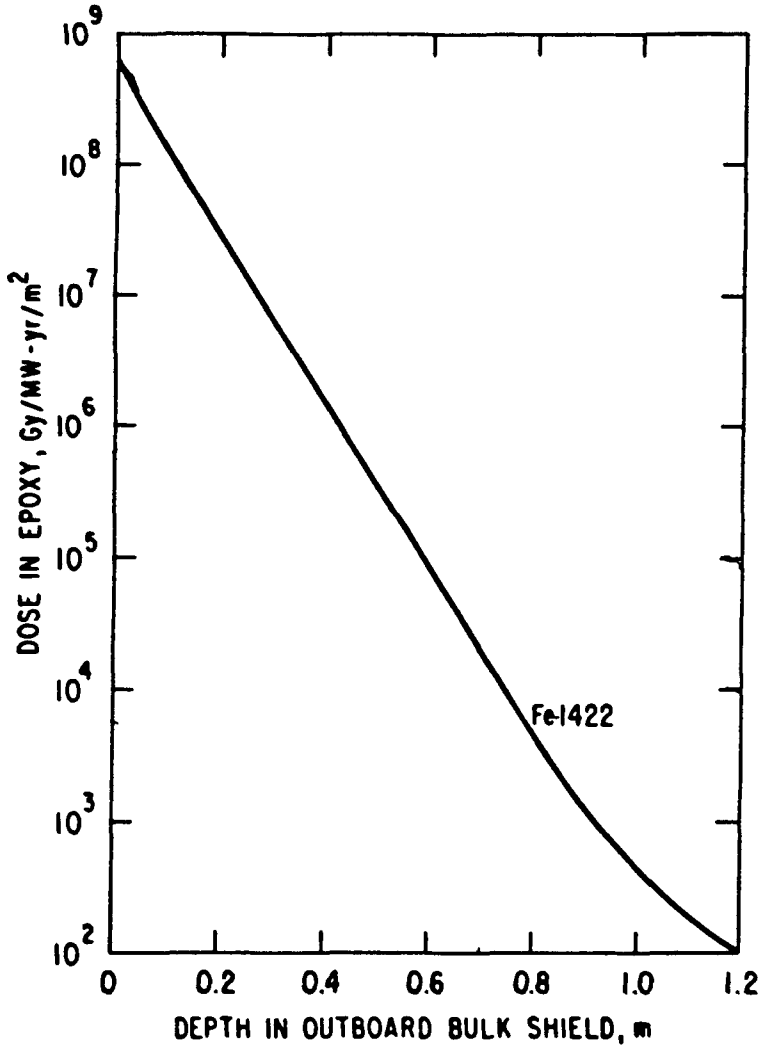

Fig. 5.3-2. Calculated[1] dose response in epoxy insulator for Fe 1422 shield material.

Steady state operation affects favorably material choices and design lifetime of the first-wall and blanket structure. In particular, both the austenitic and ferritic stainless steel alloys, which have poor cyclic stress performance, can be utilized and are expected to have radiation lifetimes in excess of 20 MWyr/m^2 at operating temperatures <500°C. A shorter lifetime (i.e., $I_w\tau$ = 16 MWyr/m^2) is assumed in the economic analysis of Sec. 7. This lifetime is consistent with solid breeder blanket changeout requirements related to ^{6}Li burnup, as well as being attractive from the points of view of maintenance, availability, and overall plant factor.

The last of the important MSR features affecting blanket design is disruption-free operation. This benefit lends considerable freedom to choose the limiter location. For tokamak applications, it is desirable to locate the limiter in a region unlikely to receive a large portion of the energy during a major plasma disruption. Hence, present designs usually locate it on the outer midplane. It will be seen later that this flexibility in limiter location permitted excess blanket/shield space to be used as a vacuum pumping plenum and coolant manifold region.

5.3.2. Reference First-Wall/Blanket/Shield Design. An adaptation of the STARFIRE design[1] to the MSR geometry is used to define the FW/B/S. A comparison of relevant reactor parameters is given in Table 5.3-2. Also listed are conditions for the STARFIRE/DEMO[4] and the UWTOR-M[2] designs. These parameters are similar for STARFIRE and the MSR, except for the choice of breeder material. A description of each of the FW/B/S components, a justification for the design choice, and the expected performance is described below.

The STARFIRE/DEMO first-wall design is adopted for the MSR and is shown schematically in Fig. 5.3-3. This FW design differs in several respects from that proposed for STARFIRE: the most significant differences are that the corrugated surface of the coolant panels faces away from the plasma and the beryllium coating has been increased from 1 to 10 mm. The first change does not adversely affect thermal hydraulic performance and does improve fabricability, whereas the coating thickness increase extends the first-wall

TABLE 5.3-2

COMPARISON OF REACTOR PARAMETERS

	STARFIRE[1]	DEMO[4]	UWTOR-M[2]	MSR
Fusion power P_F (MW)	3500	920	4247	3500
Neutron current, I_w (MW/m^2)	3.6	1.8	1.6	1.9
Thermal power, P_{TH} (MW)	4300	1050	4360	4200
Structural Material	PCASS	SS-316	HT-9	PCASS
Breeder Material	$LiAlO_2$	Li_2O	$Li_{17}Pb_{83}$	Li_2O
Coolant	Pressurized Water	Water	Steam	Pressurized water
Impurity control	Pumped limiter	Limiter or divertor	Divertor	Pumped limiter

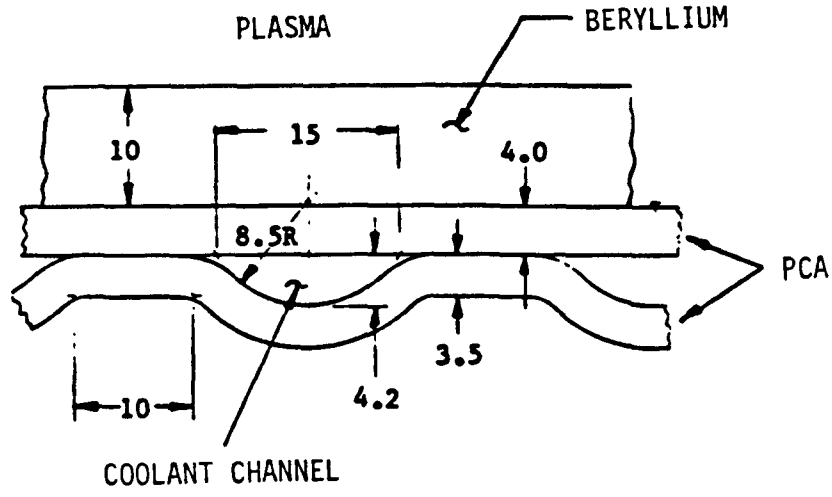

Note: All dimensions in mm.

Fig. 5.3-3. First wall design (from Ref. 4).

lifetime against sputtering erosion and improves tritium breeding. Neutronic calculations showed the tritium-breeding potential of the Li_2O blanket increased from about 1.2 to 1.4. The improvement is especially important here because of the limited blanket coverage for the MSR.

A cross section through the reference blanket design is shown in Fig. 5.3-4, and the important features are listed in Table 5.3-3. Additional structural details and dimensions are shown in Fig. 5.3-5. The FW/B/S materials chosen for the MSR are similar to those proposed for STARFIRE, except for the breeder material, which is Li_2O rather than $LiAlO_2$. The oxide was chosen because of its higher breeding potential (higher Li density). In addition, the concerns about tritium solubility and the consequent high tritium inventory in Li_2O have been relieved by more recent data. The primary disadvantage of the oxide is its more limited operating temperature range (410-660° C) and the presence of corrosive LiOT and LiOH.

It can be seen from Figs. 5.3-4 and 5.3-5 that the blanket is divided into two symmetrical sections, each located on either side of the plasma major axis. This configuration was necessary to maintain at least 0.75 m of high-density shielding between the plasma and the coil casing; the casing itself adds an additional 0.10 m of shielding. The two blanket sections are

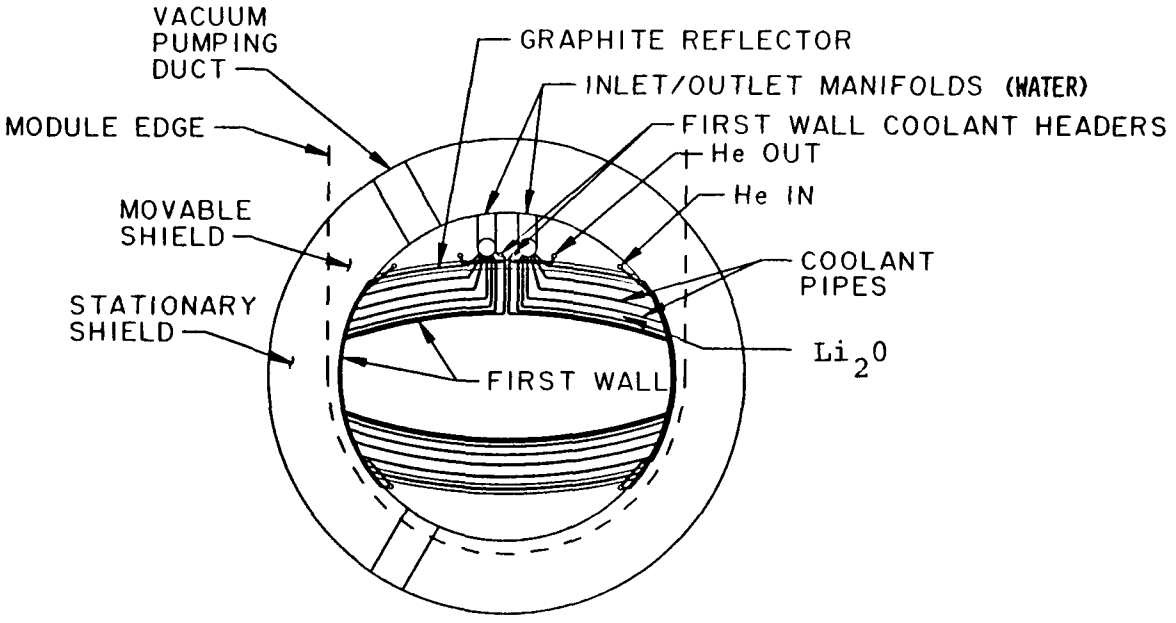

Fig. 5.3-4. Reference MSR conceptual blanket design.

TABLE 5.3-3

REFERENCE MSR BLANKET DESIGN FEATURES

Breeder material	Li_2O (70% dense)
Coolant	Pressurized water (15 MPa)
Structural material	PCASS
Neutron multiplier	Be (70% dense)
Breeder zone thickness (m)	0.45
Reflector material	Graphite
Reflector zone thickness (m)	0.15
Blanket solid angle fraction	0.75
Tritium recovery	Low Pressure (~0.1 MPa) He Purge
Blanket inlet temperature (K)	553
Blanket outlet temperature (K)	593

connected by coolant lines and tritium collection channels which run through the 0.20 m shield space between the first wall and the edge of the removable module. The resulting coolant flow path lengths through the two blanket

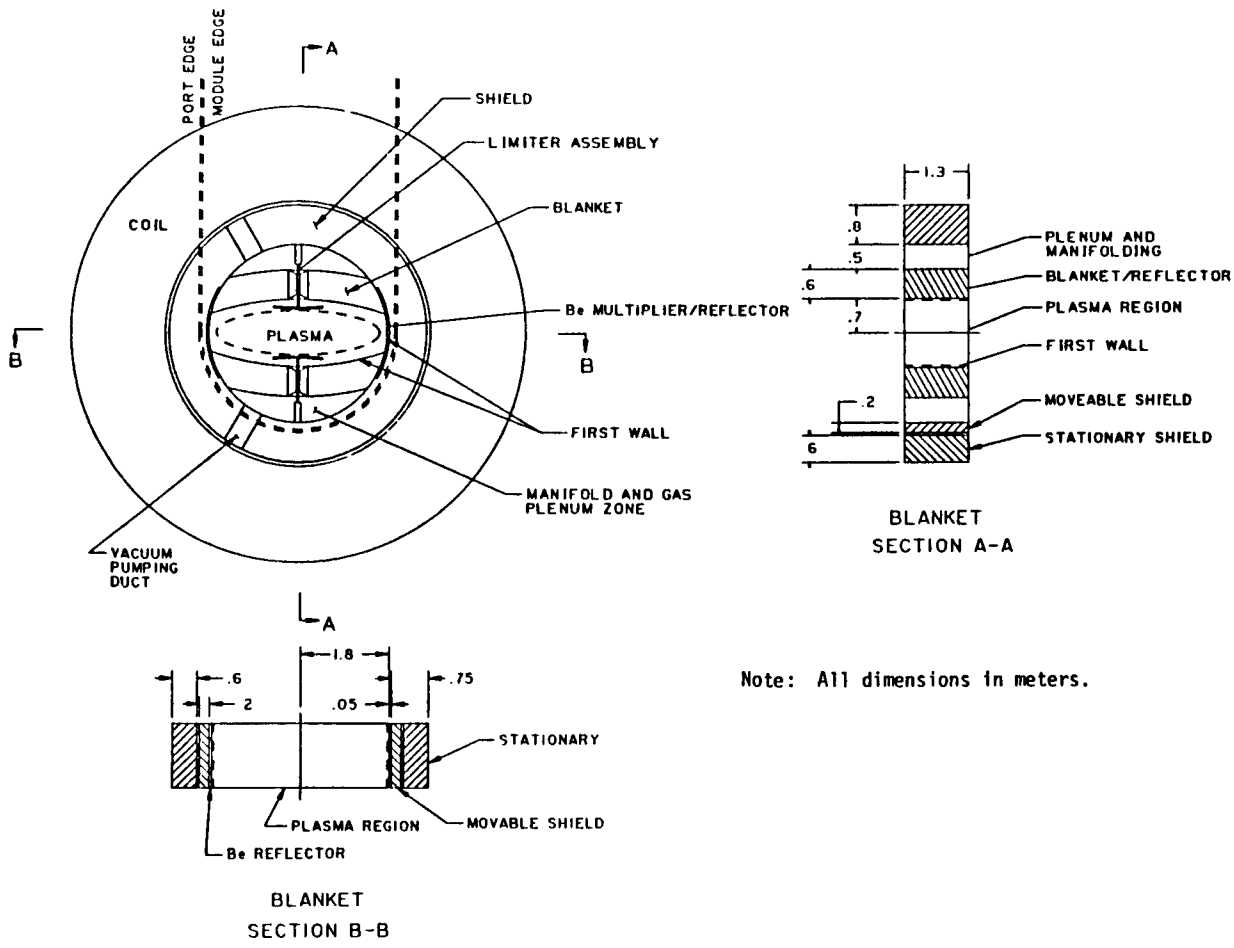

Fig. 5.3-5. MSR blanket/shield cross section.

sections and the movable shield regions is ~10 m, about twice as long as in STARFIRE, requiring that the pipe ID be increased from 0.01 to 0.012 m.

The tritium removal system consists of low pressure helium flowing in channels drilled through the Li_2O ceramic. These channels empty into thin gas plena connecting the two blanket sectors at either end. The tritium collection boundary is then formed by the walls of those plenum zones and the outer blanket structure.

The two options available for impurity control are the pumped limiter and the magnetic divertor. Divertor action is provided by the formation of a magnetic separatrix at a location suitable for the insertion of a particle collector and coolant system. For the MSR, with two poloidal field periods, the separatrix is formed along the plasma major axis and in the present design lies in the shield region. Conceptually, additional coils could be added to shift the separatrix, but the resulting engineering complexity in a modular arrangement would be very great. Moreover, as indicated above, shield thickness cannot be sacrificed because it is currently only marginal.

These considerations led to the choice of the pumped limiter for impurity removal and plasma exhaust for the MSR. The basic limiter design adopted is that of STARFIRE, a cross section of which is shown in Fig. 5.3-6 with relevant design parameters listed in Table 5.3-4. Of the total of 700 MWt of alpha power, only 90 MWt, (13%) appears as incident particle energy (both charged and neutral). This is in contrast to INTOR,[8] for which particle energy accounts for nearly 70% of the alpha power. This reduction in particle surface heat load on the limiter surface is accomplished by adding a high-Z poison (e.g., iodine) to the plasma edge. This enhances the plasma radiation loss, which is distributed uniformly over the entire first wall surface. The resultant average surface heat load on the limiter is ~2.5 MW/m^2.

A similar, preliminary analysis using common assumptions has been performed for the MSR-IIB case in order to verify the adaptability of the STARFIRE pumped-limiter design. The alpha-particle power, $P_\alpha \simeq 740$ MWt divides into a bulk-plasma Bremsstrahlung loss, $P_{BR} \simeq 79$ MWt, and a radial-transport loss, $P_\ell \simeq 661$ MWt, to the plasma edge region. Introduction of impurities into the plasma edge is assumed to result in a fraction, f_{RAD} ($\simeq$ 90%), of P_ℓ being radiated (P_R) to the first-wall surface area ($A_w \simeq 1480$ m^2) with the remaining 66 MWt being deposited on the limiter surfaces by charged particles. If the limiter surface area is taken to be a fraction, f_L, of the first-wall surface area, a simple balance equation using the above assumptions requires that the power to the limiter, P_L, be given by

$$P_L = (1-f_{RAD})P_\ell + (f_{RAD}P_\ell + P_{BR})f_L \qquad (5.3\text{-}1)$$

$$= I_{QL}A_w f_L \quad . \qquad (5.3\text{-}2)$$

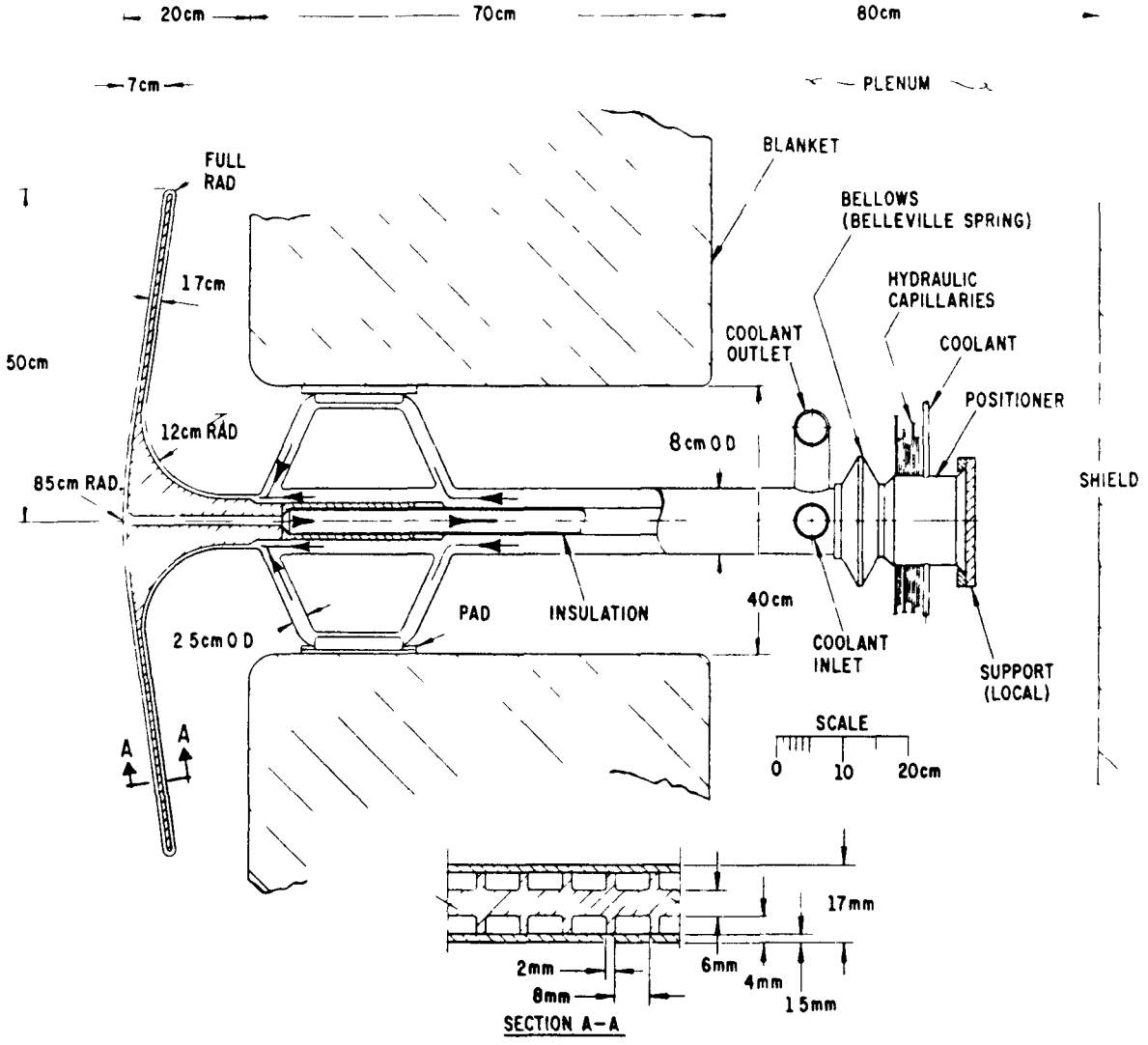

Fig. 5.3-6. Cross section of the STARFIRE limiter design[1] adapted for the MSR.

If $P_{BR}/P_{\ell} \ll 1$, then

$$f_L = \frac{1-f_{RAD}}{(4I_{QL}/I_w - f_{RAD})} \quad , \tag{5,3-3}$$

where $I_{QL}(MW/m^2)$ is the design value for the (uniform) limiter surface heat deposition, taken here to be 2.5 MW/m^2. Solving Eq. (5.3-1) for f_L yields 0.022, which is rounded to 0.025 for convenience to give $A_L = f_L A_w = 37\ m^2$ of required limiter surface area. This approach leads to a design choice of ~1 m^2 of limiter surface per each of the 36 center modules, or with 2 limiter panels per module, a (square) limiter panel measuring approximately 0.75 × 0.75 m results. Limiters could be incorporated into the end modules to reduce the surface heat-load constraint or to provide spares.

It can be seen from Fig. 5.3-5 that the excess space available between the blanket and shield forms the vacuum plenum zone for the limiters. This approach provides a simple, convenient, high-pumping-conductance arrangement. The plenum zone is also utilized for all of the manifolding for the blanket coolant and tritium removal systems. The welds and connections, which are

TABLE 5.3-4

STARFIRE PUMPED-LIMITER DESIGN[a] PARAMETERS

Coolant	Water			
Reference structural materials	Ta-5W, AMAX-MZC, FS-85, or V-20Ti			
Low-Z coating material	Beryllium			
Total heat removed from limiter (MW)				
(90 MW transport, 56 MW radiation plus neutrals, and 54 MW nuclear)	200			
Average surface heat load (MW/m^2)	2.3			
Peak surface heat load[a] (MW/m^2)	4			
Coolant inlet temperature (K)	388			
Coolant outlet temperature (2-pass) (K)	418			
Coolant pressure (MPa)	4.2			
Coolant channel size (mm × mm)	8 × 4			
Wall thickness (mm)	1.5			
Maximum temperature (K)	Ta-5W	AMAX-MZC	FS-85	V-20Ti
Water side	466	455	465	464
Coating side	563	469	677	722

[a] Includes transport load (3.4 MW/m^2) plus load from radiation and charge-exchange neutrals.

particularly sensitive to radiation damage and subsequent failure are thereby removed to a low-radiation region.

A view of a typical center modular (from a three-module sector), illustrating the appearance of the plenum and plasma regions, is shown in Fig. 5.3-7. The vacuum boundary is formed by the module walls and the plate that covers the sector hatch opening between magnets. The plenum and plasma regions line up between adjacent modules with a rotational step, $\Delta\theta = 6.67^{o}$, between adjacent modules, as illustrated in Fig. 5.1-5. Only the center module contains vacuum-pumping ducts.

A typical side module, with the round section that extends under the adjacent magnet, is shown in Fig. 5.3-8. Both end modules are also wedge shaped, as illustrated in the figure. The module mass is ~60 tonnes.

An isometric cross-section view, illustrating a center module and one side module positioned inside the stationary shield, is shown in Fig. 5.3-9. The modules are supported from the stationary shield by means of bolts passing through the module flange and into the shield step. The additional holes shown provide vacuum sealing of the hatch cover. A view through the hatch cover opening and between adjacent magnet coils is shown in Fig. 5.3-10.

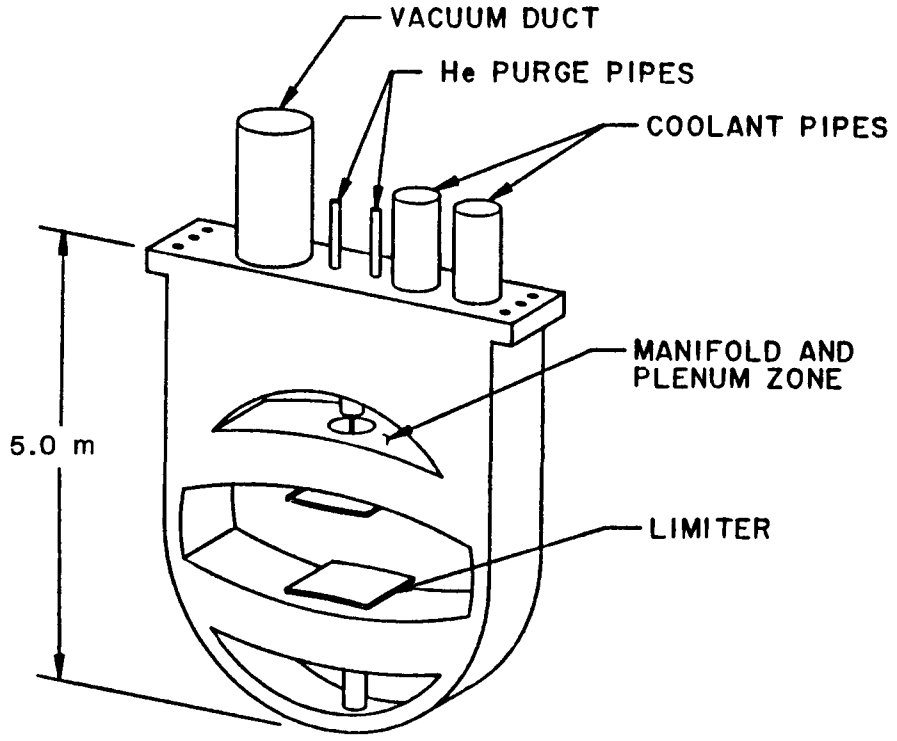

Fig. 5.3-7. MSR center module configuration.

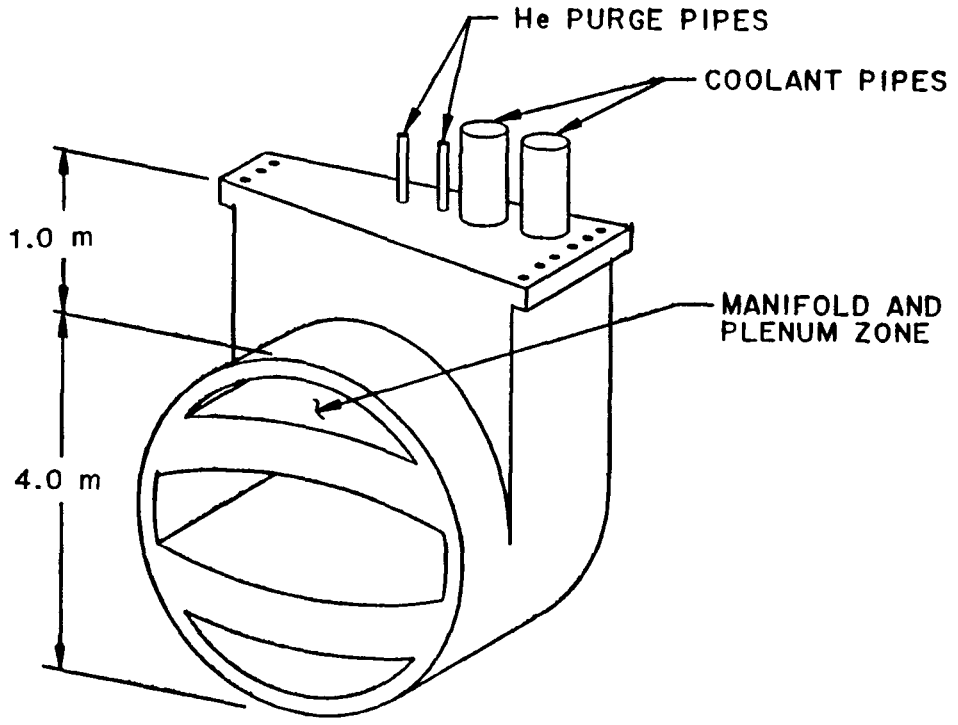

Fig. 5.3-8. MSR end module configuration (typical).

The solid angle fraction subtended at the plasma center by the blanket is 0.75. For an assumed poloidally uniform neutron distribution, the tritium-breeding-ratio potential, based upon STARFIRE/DEMO 1-D calculations, is 1.05. This result is probably insufficient when calculational uncertainty, penetrations, and other losses are taken into account. To enhance tritium production, a 0.05-m-thick beryllium-multiplier/reflector zone was placed immediately behind the first wall in the plasma major axis end regions. It is estimated that this will increase the tritium breeding ratio to approximately 1.2.

The shield material used throughout is Fe 1422, which is an iron alloy containing 12 w/o manganese, 2 w/o nickel, and 2 w/o chrome; this alloy has excellent shielding properties and good radioactive decay characteristics and is relatively inexpensive and not limited in resource. Except for the region behind the beryllium multiplier, the shield is cooled by low-pressure, low-temperature water containing 0.7 w/o dissolved boron. The movable portion of the shield behind the beryllium multiplier, as well as the multiplier itself, is cooled by the high-pressure, high-temperature water flowing between the blanket sections. The shield described is, of course, the bulk magnet

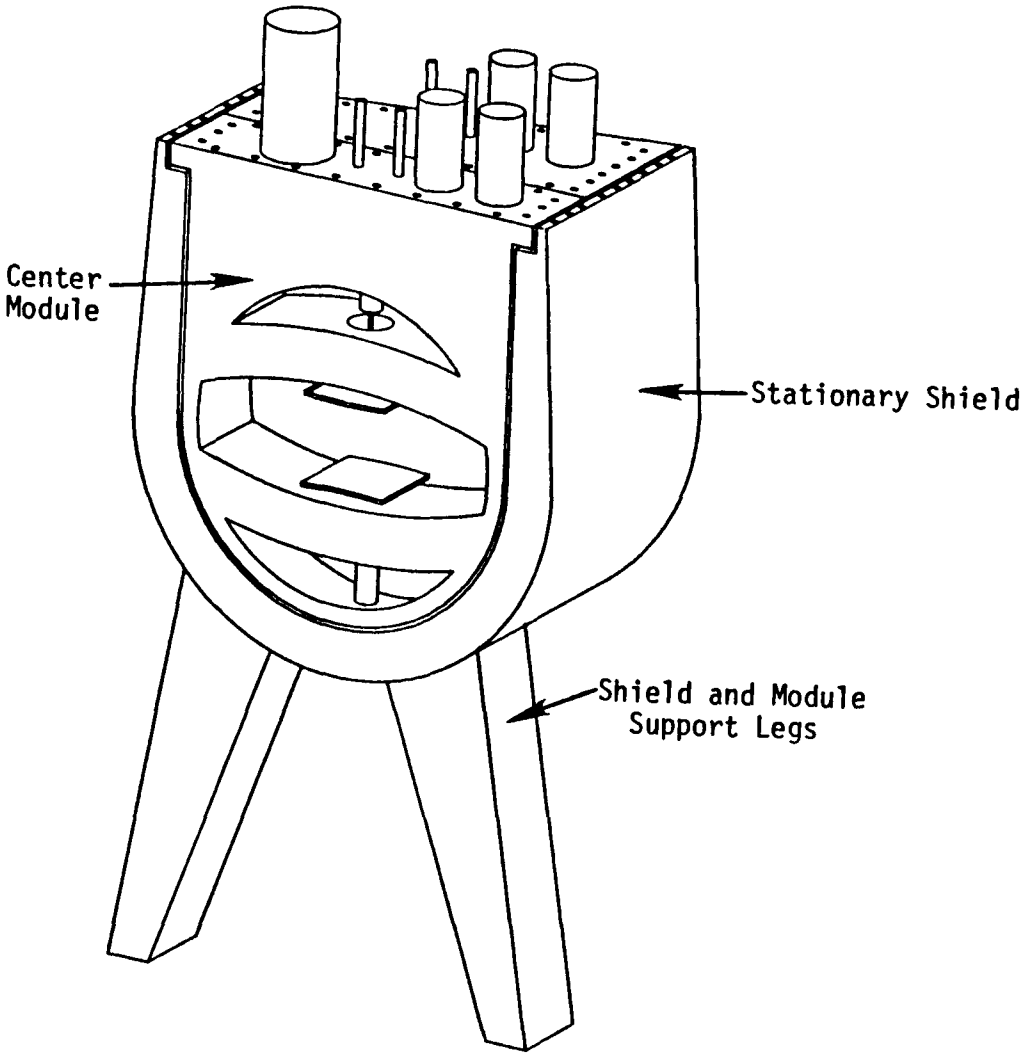

Fig. 5.3-9. Positioning of MSR modules inside stationary shield (typical).

shielding. Additional shielding around penetrations will be required, as well as the biological shield.

5.3.3. Neutronics. Detailed neutronics computations for the MSR FW/B/S/C system *per se* were not performed. Some preliminary scoping calculations, described here, were initiated to anticipate possible design modifications and iterations truncated by the study termination. The material densities and corresponding nuclear number densities of all of the FW/B/S constituents are listed in Table 5.3-5. As an aid in setting up neutronics calculations, Figs. 5.3-11 through 5.3-13 show the compositions and dimensions of the various material zones in the transport problem. Figure 5.3-11 is applicable to all of the first wall, whereas Figs. 5.3-12 and 5.3-13 apply

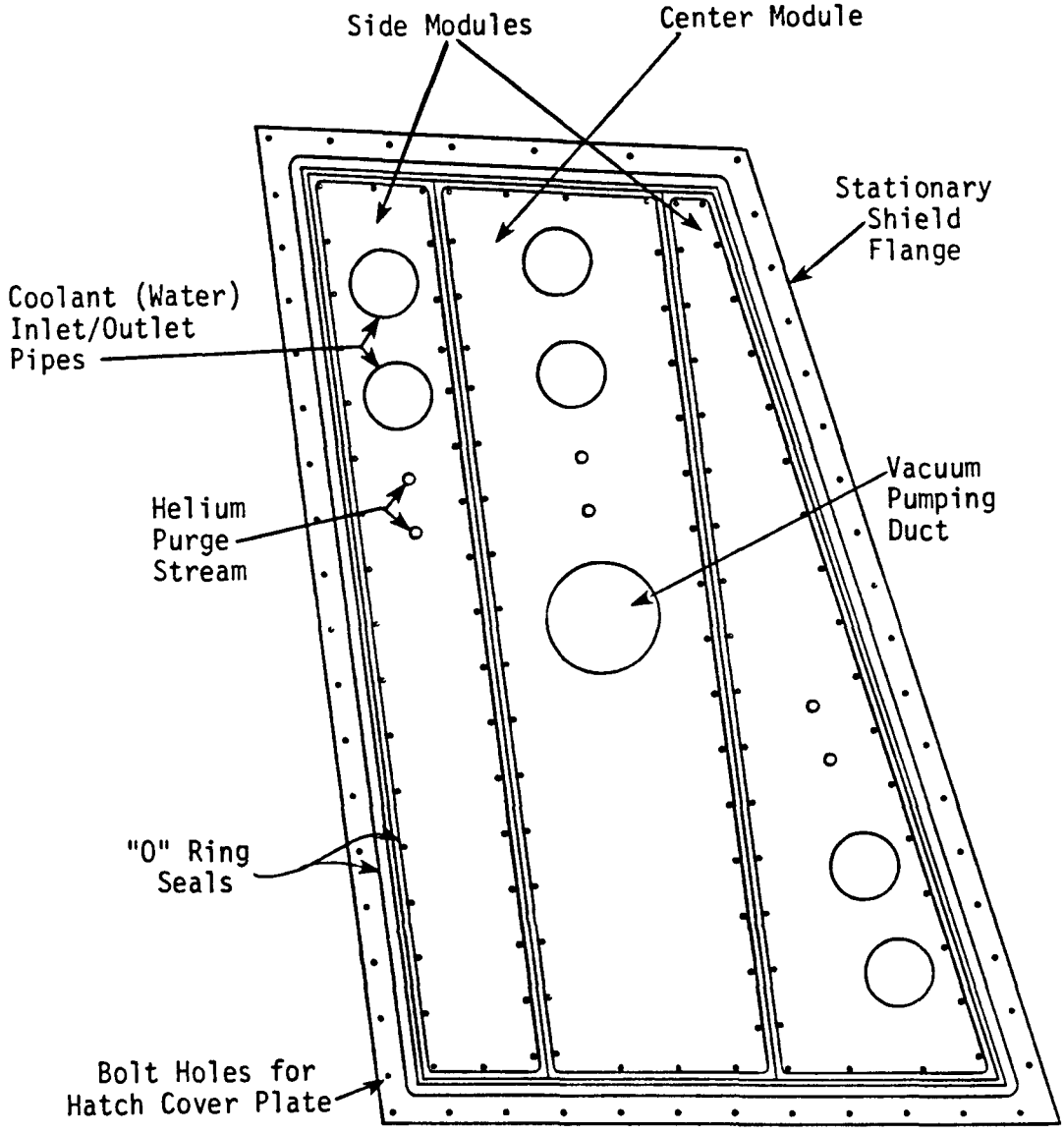

Fig. 5.3-10. View of MSR module tops through a hatch cover opening.

only to cuts along the plasma semimajor (i.e., from the plasma center, horizontally to the right in Fig. 5.3-4) and semiminor axes (i.e., up or down from the plasma center in Fig. 5.3-4), respectively. Although zone dimensions change in the poloidal direction, the zone constituents remain unchanged. Although a proper neutron/gamma transport analysis requires of a multidimensional code, one-dimensional neutronics calculations were performed[9] by Los Alamos Group T-2 using the ONEDANT discrete-ordinates transport code[10] in the S_8P_3 approximation. A multigroup, coupled cross section set (30 neutron + 12 gamma ray), XSLIBA, was used for the calculations. XSLIBA is a

TABLE 5.3-5

DENSITIES OF MATERIAL CONSTITUENTS (FW/B/S)

MATERIAL	DENSITY (100%)	NUMBER DENSITY (at/barn cm)[a]	
Li_2O	2.023	O	0.04078
		Li	0.08156
Be	1.85	Be	0.1236
Pressurized H_2O	0.73[b]	H	0.0489
		O	0.0245
Borated H_2O	1.0	H	0.0670
		O	0.0335
		^{10}B	$9.639(10)^{-5}$
		^{11}B	$3.954(10)^{-4}$
C	1.6	C	0.08023
Fe 1422	7.9	Fe	0.06953
		Mn	0.01219
		Ni	$1.580(10)^{-3}$
		Cr	$1.848(10)^{-3}$
		C	$2.309(10)^{-3}$
PCASS	7.86	Fe	0.05499
		Ni	0.01290
		Cr	0.01274
		Mn	$1.7237(10)^{-3}$
		Ti	$2.9657(10)^{-4}$
		Mo	$9.9868(10)^{-4}$
		C	$1.9718(10)^{-4}$

[a] 1 at/barn cm = $(10)^{30}$ at/m^3.

[b] Density of pressurized water at approximately 300° C and 15 MPa.

35-element (a few isotopes are included) library compiled by G. L. Woodruff at the University of Washington. Data for kerma factors, dpa, and H and He production were retrieved from the KERMA8 file compiled by D. J. Dudziak of Los Alamos Group T-1. These data are mainly derived from the ENDF/B-IV evaluated nuclear data file. An additional calculation was made in which ENDF/B-IV tritium production data for ^7Li was replaced with recent Los Alamos

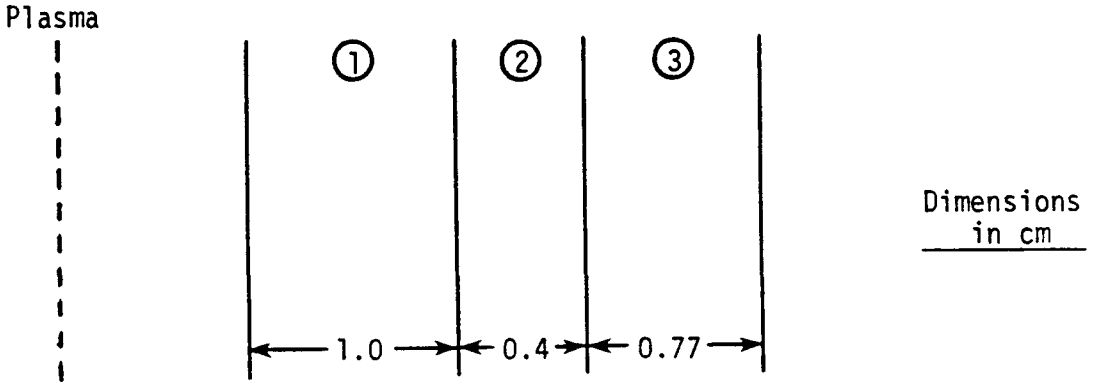

① 70% dense Be

② 100% dense PCA

③ 38.3% dense PCA
31.8% dense pressurized water

Fig. 5.3-11. MSR first wall dimensions and compositions.

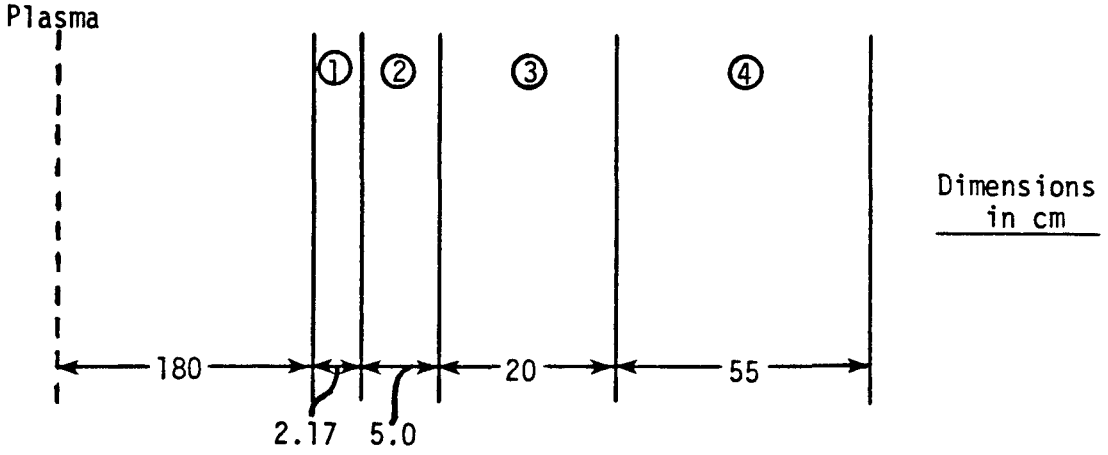

① First Wall (see above for composition)

② Be, 70% dense

③ Movable Shield 75% dense Fe 1422
25% dense Pressurized H_2O

④ Stationary Shield 95% dense Fe 1422
5% dense Borated H_2O

Fig. 5.3-12. Radial build along the MSR-IIB semimajor plasma axis.

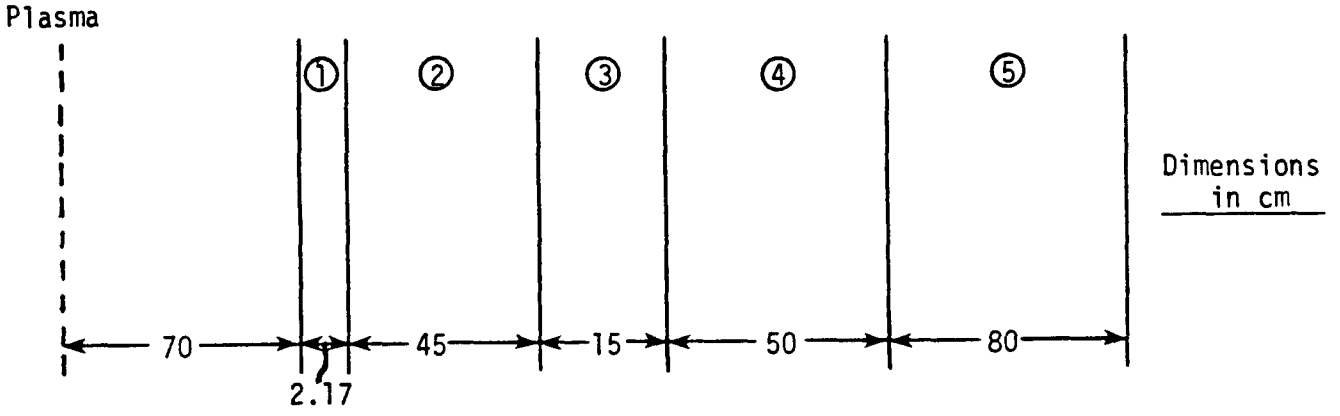

① First Wall

② Li_2O Blanket 90% V/O Li_2O at 70% density
5% dense PCA
5% dense pressurized water

③ Graphite Reflector 90 V/O at 70% density
5% dense PCA
5% dense pressurized water

④ Plenum Zone 5% dense PCA
5% dense pressurized water

⑤ Shield 95% dense Fe 1422
5% dense Borated water

Fig. 5.3-13. Radial build along the MSR-IIB semiminor plasma axis.

tritium production data for ^7Li.[11] Activation cross sections were prepared from data contained in the GAMMON activation library.[12]

Normalizations for the three models used in the calculations were different because of the different plasma radii and geometries used. For example, for the minor radius cylindrical problem, a wall loading, I_w, of 1 MW/m^2 at a radius of 0.7 m corresponds to 4.398 MW ($1.0 \times 2\pi \times 0.7$) per meter of height at the first wall, or 43.98 kW/cm of height. Converting to MeV/s, an energy current of $2.75(10)^{17}$ MeV/s is obtained.

Based on a value of 14.06 MeV/neutron, the source current at the first wall is $1.952(10)^{16}$ neutrons/s, which is the normalization factor input to ONEDANT. In a similar manner, a normalization factor of $5.201(10)^{16}$ neutrons/s was computed for the major-axis infinite cylinder model and a normalization factor of $3.11(10)^{14}$ neutrons/s was computed for the slab problem.

Because of the difficulties of applying these one-dimensional results to obtain meaningful conclusions about the actual three-dimensional system, only the limited results shown in Tables 5.3-6 and 5.3-7 are given. Most of the results are for the infinite cylinder calculations. Only the breeding ratio is given for the slab problem and only the breeding ratio is given for the problem using the new Los Alamos ^{7}Li data evaluation. Complete results for all three problems, however, are available. Heating, displacement, and gas production rates are higher along the semimajor because of the marginal shield thickness in this direction.

TABLE 5.3-6

MSR NEUTRONICS RESULTS (INFINITE CYLINDER)

NORMALIZED TO I_w = 1 MW/m^2

	Seminor	Semimajor
Breeding ratio (BR)	1.390[a](1.350)[b]	--
Power deposition MW/m:		
FW1	0.245	0.764
FW2	0.150	0.799
FW3	0.182	0.800
Blanket	4.599	
Cylinder reflector	4.554-02	
Plenum	2.554-02	
Fe shield	3.427-02	
Be reflector		2.697
Movable shield		13.493
Stationary shield		1.537
PCASS 1	9.150-07	2.170-03
Coil 1	3.356-07	9.314-04
Coil 2	2.280-09	7.354-06
Coil 3	9.642-11	3.239-07
PCASS 2	1.273-11	4.369-08
Incident on FW	4.398	11.310
TOTAL	5.282	20.094
Neutron multiplication, M_N	1.20	1.78
Blanket of efficiency, e_B	1.0	1.0

[a]BR for ∞ slab = 1.434.

[b]BR for Los Alamos National Laboratory ^{7}Ti data set.

TABLE 5.3-7

DISPLACEMENT AND GAS PRODUCTION RATES IN MSR COILS

	Semiminor	Semimajor
Max dpa/yr	9.97-08	3.04-04
Max appm He/yr	1.46-08	1.20-04
Max appm H/yr	2.14-09	2.26-05

5.3.4. Maintenance. The MSR design envisages routine maintenance of the FW/B/S components without requiring movement of the modular-coil set. Access between the coils to the underlying FW/B/S modules is provided through ports located above the reactor midplane, as illustrated in Fig. 5.3-14. MSR module features impacting the maintenance approach are summarized in Table 5.3-8.

As shown on Fig. 5.1-3, access ports in the vacuum vessel have different configurations and orientations around the torus. Module removal and replacement schemes will be complicated, because all modules cannot be inserted or withdrawn from the same poloidal angular location. Module insertion varies from vertical through a series of angles approaching the horizontal. As shown in Fig. 5.3-1, the module is stored on a support pedestal. For the series of figures, a center module is used. For module installation, a lifting fixture is bolted to the module that is vertically oriented in the support stand.

The procedure for module replacement is illustrated in Figs. 5.3-15 through 5.3-19. In Fig. 5.3-15 a typical central reactor module, tested out of the reactor, rests on its support pedestal with an overhead lifting fixture attached (step 1). The lifting fixture is designed to hold the module in roughly the appropriate orientation for subsequent insertion into the reactor torus itself, as typified by the sequence between Fig. 5.3-16 (step 2) and Fig. 5.3-17 (step 3). The module mass is ~60 tonnes.

A keyway in the slide is provided to mate with the alignment fixture keys so that the module is properly positioned for installation. The module is then slid into the vessel (by lowering the crane hook) until the module support flange contacts the vessel port support flange as shown in Fig. 5.3-19. With the module lowered into place, as shown in Fig. 5.3-19 (step 5), the lifting fixture can be decoupled and removed together with the alignment slide. With vacuum seals made and coolant connections re-established, the reactor is ready for operation. The module removal

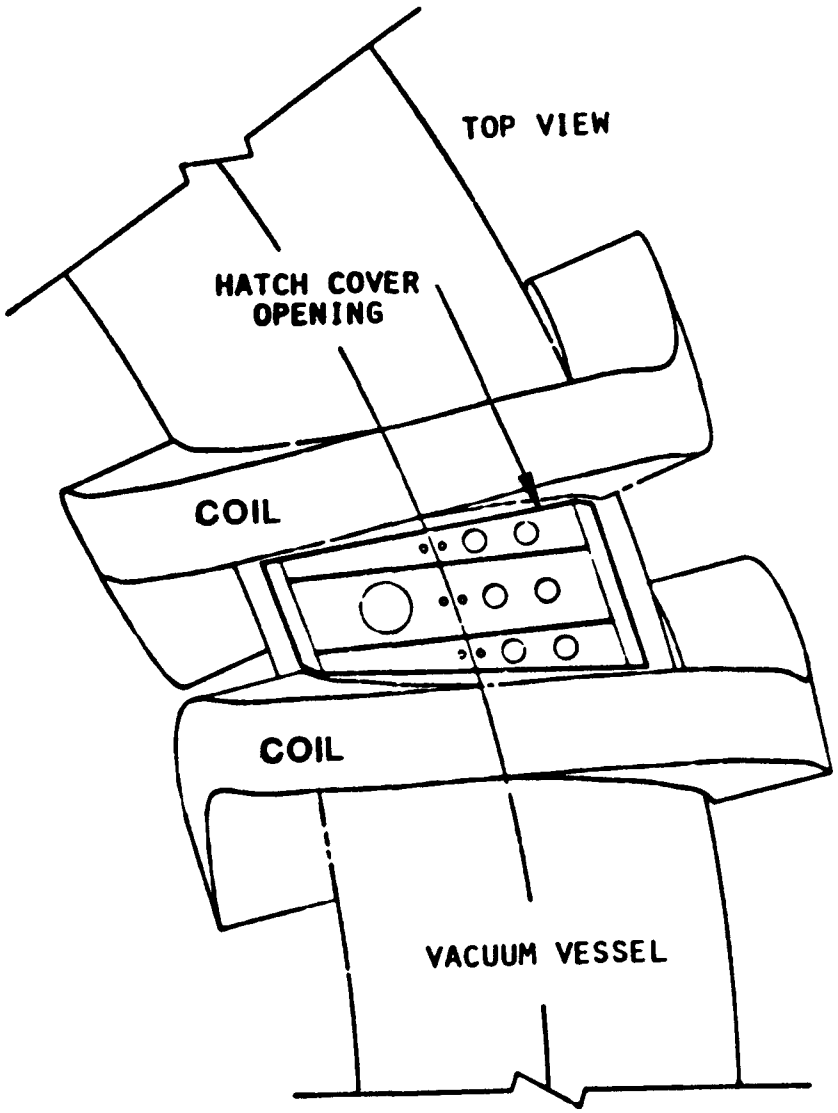

Fig. 5.3-14. Typical MSR maintenance access port at the top of the MSR torus.

sequence is accomplished by essentially reversing the steps described above. An alternate concept would use a special stiff leg overhead crane design to eliminate the multiple handling fixtures. This concept remains to be fully evaluated.

An integral neutron wall loading of 16 MWyr/m^2, a neutron wall load of 2 MW/m^2, and an overall plant availability of 76% yield a first-wall life of approximately 10.5 calendar years. The maintenance plan calls for replacing 12 of the 108 modules during each annual maintenance period in the last 9

TABLE 5.3-8

MSR REPLACEABLE MODULE FEATURES

- Three modules fit between coil centerlines.
- Central module of each three carries movable pumped limiters and RF posts/antennae for startup heating.
- Modules provide all tritium breeding.
- Modules provide vacuum vessel shielding.
- Module seals to vacuum vessel are in low temperature, low radiation area.
- All coolant, control, instrumentation lines are sealed within the modules.
- All connections are made in shielded zone above port.

years of a 10-yr cycle. Three such cycles comprise the assumed 30-yr plant life.

5.3.5. Summary and Conclusions. A preliminary conceptual design of the FW/B/S for the MSR, as derived from the STARFIRE/DEMO designs, has been presented. The design conforms to the unique geometry of the $\ell = 2$ modular, stationary magnet stellarator. Based upon present information, this design is likely to satisfy all of the FW/B/S requirements in terms of tritium production, shielding, heat removal, lifetime, and maintainability. The most limiting design feature appears to be the marginal shield space available along the direction of the plasma cross sectional major axis, resulting from the highly elongated plasma shape. Multidimensional neutron transport calculations to confirm expected performance should be performed before proceeding to the next level of design detail.

An additional area of uncertainty, common to all solid breeder blankets, is the question of tritium extraction, particularly under irradiation. Based upon present data, there does not appear to be a clear-cut advantage for either the solid breeder or the LiPb blanket concept in the present application and a choice will have to await the result of test programs currently in place.

Interim engineering conclusions, based on work up to the point of contract termination are summarized below.

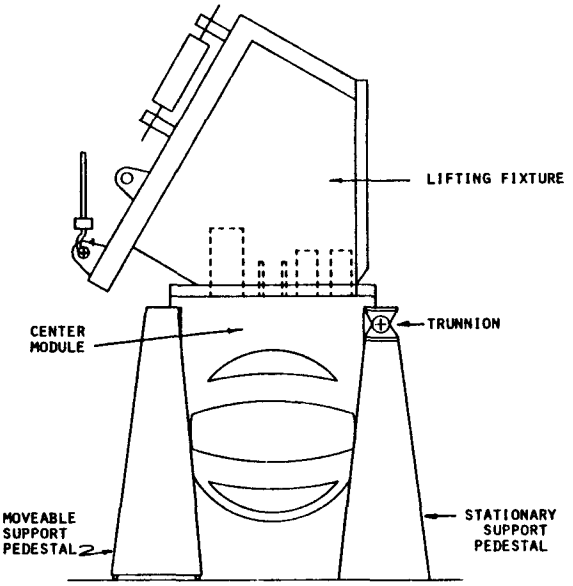

Fig. 5.3-15. MSR blanket module stored on support stand - step 1.

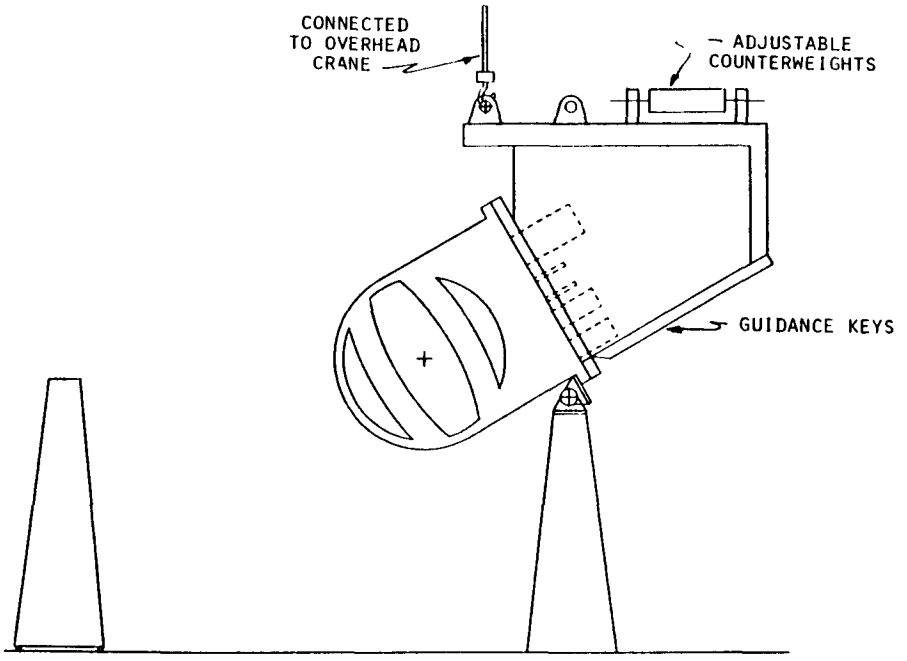

Fig. 5.3-16. MSR blanket module being lifted off support stand - step 2.

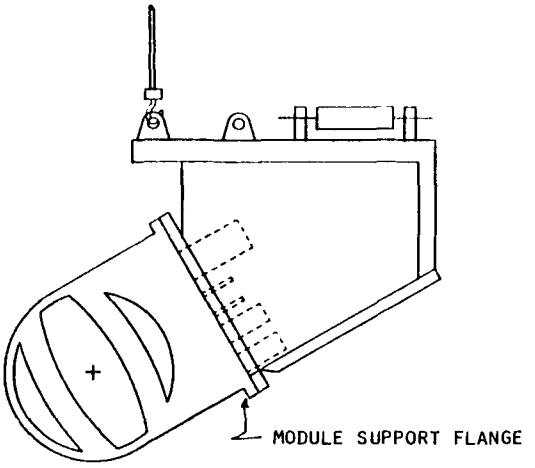

Fig. 5.3-17. MSR blanket module moving to reactor - step 3.

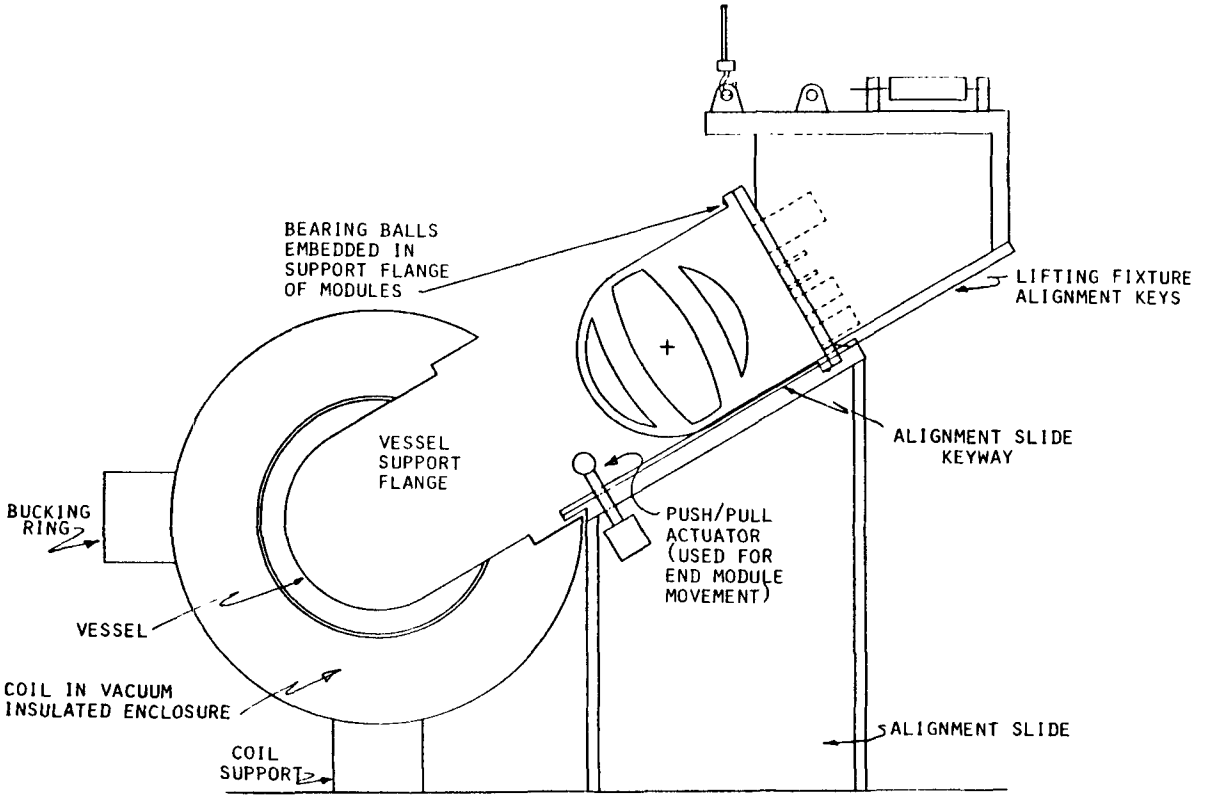

Fig. 5.3-18. MSR blanket module guided by alignment slide - step 4.

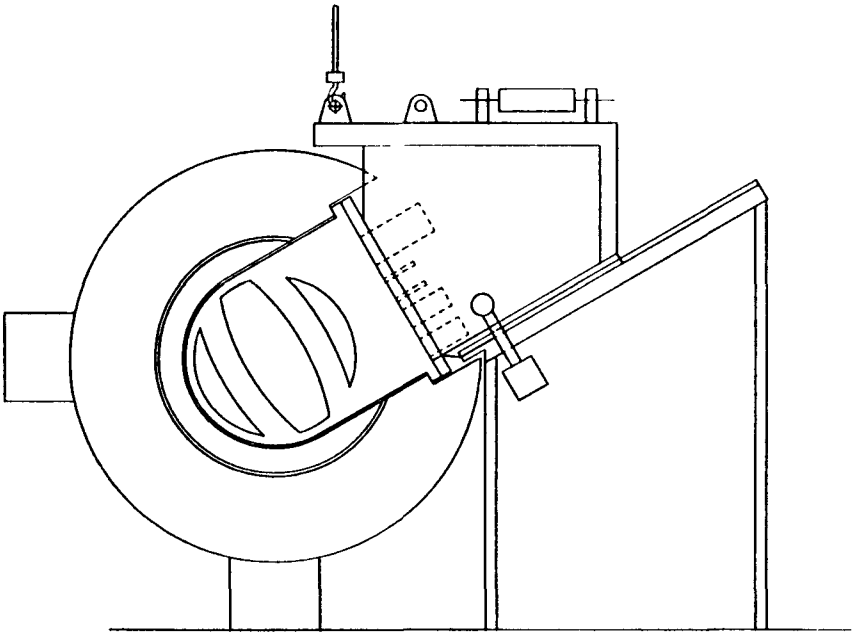

Fig. 5.3-19. MSR blanket module installed in vessel - step 5.

- permanent fixed coil arrays appear feasible,
- permanent fixed vacuum vessel and bulk shield appear feasible,
- vacuum seals can be made in low-temperature, low-radiation area,
- vacuum seals can be made either remotely or direct contact,
- vacuum seals can be soft metal, elastomer, or welds,
- routine maintenance can be partially direct contact,
- first wall, limiter, blanket, and primary shield can be combined in modular assemblies,
- relative to tokamaks, the coils
  - exhibit lower centering forces
  - have no overturning moment and
  - pose more difficult design problems resulting from lateral distortion.

5.4. Coil Structural Analysis

Preliminary structural analysis of a typical MSR-IIB modular coil was performed using the magnetics parameters of Sec. 4.3. as modified by the coil cross-sectional configuration proposed by Westinghouse for the He-I cooled case (Sec. 5.2.2.). Iteration to a final, self-consistent coil/structure design was interrupted by the contract termination. Hence, only preliminary analytic and numerical results using the three-dimensional ANSYS[13] FE computer code are presented here. The detailed discussion[14] will only be summarized here.

For purposes of the FE computation and computer graphics, the modular-coil structure/dewar casing illustrated in Fig. 5.2-3 was modeled by 29 nodes as illustrated in Fig. 5.4-1. A three-dimensional, 8-node isoparametric FE was used, as shown in Fig. 5.4-2. Pressure loads that simulated the electromagnetic forces that would be experienced by the coil casing were

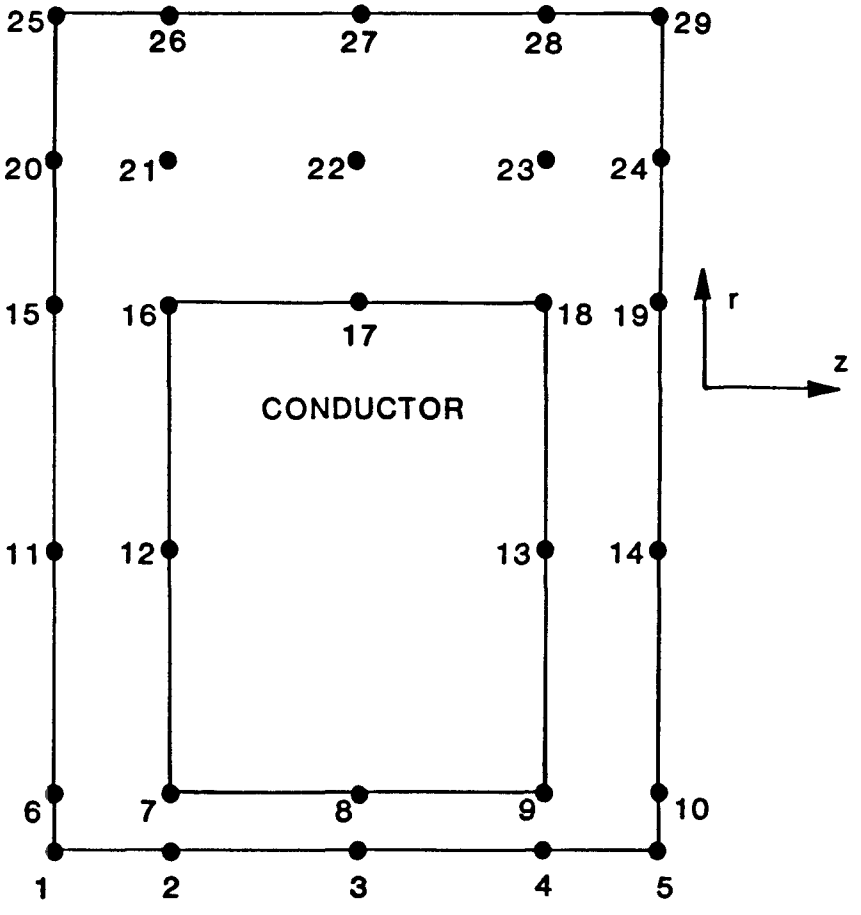

Fig. 5.4-1. Notation for spline numbering system used in computer graphic generation of the MSR-IIB coil cross section.

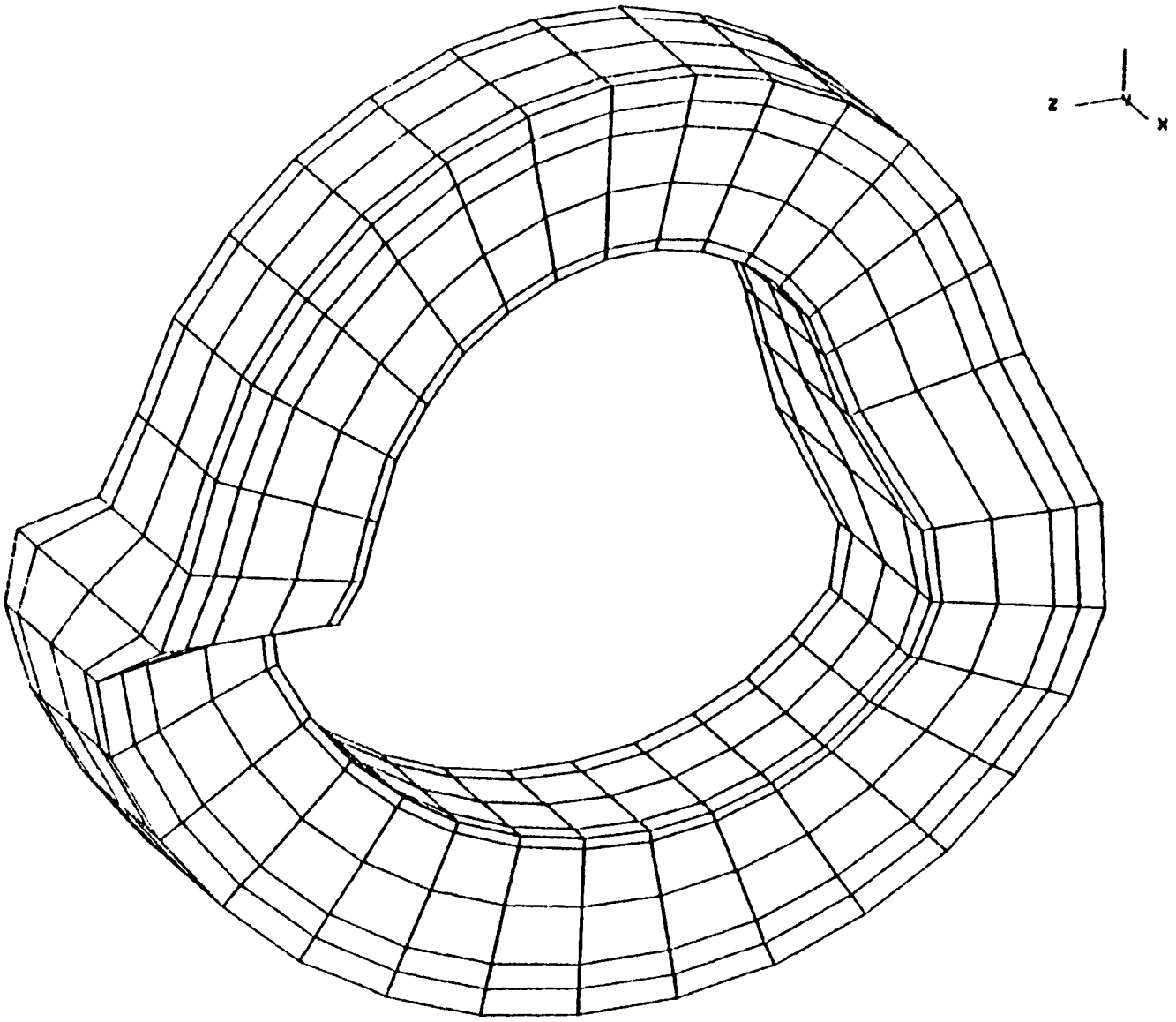

Fig. 5.4-2. An isometric plot of the generated modular-coil mesh with hidden lines removed.

provided by Los Alamos for MSR-IIB key coil (No. 9) and were subsequently adapted to the FE mesh as nodal-point pressures for input into the ANSYS code. An input file,[14] of the conductor on the inner surface of the casing (Fig. 5.1-2) was prepared for this mesh with electromagnetic pressure load, dead weight, and 3/radial supports, which simulated bucking ring and vertical supports. Initial analytic calculations indicated that 4/lateral (coil-to-coil) supports were sufficient. The location of these supports was

chosen to coincide with the position of the maximum lateral pressure, which occurs near the points of maximum lateral distortion of the coils. Two ANSYS static runs were made. In the first run, each lateral support was simulated as one row of nodes. In the second run, a more realistic simulation was used that resulted in lower levels of stress and strain. In this case, the supports were assumed to be one element thick.

The results of this preliminary study indicate that the present configuration for the coil casing could withstand the electromagnetic forces without excessive stresses and strains. The highest stress and strains occurred at $\theta = 78^{\circ}$ at the coil midplane and a combined torsion and bending and hoop stress were present. The strain levels in the vicinity of the superconductor were about 0.36%, while the stress for this portion was about 660 MPa. These results are preliminary, however, and more favorable levels of stress could have been obtained in subsequent iterations by changing lateral support positions and increasing wall thickness in high stress areas.

Two cases were studied before the project was halted. In the first case, the lateral supports were modeled by a single row of nodes fixed laterally. This unrealistic case was replaced by a second run in which an entire set of elements at four locations was fixed in lateral direction, this modification resulted in an average reduction of about 25% in the stress level. Other reductions could be obtained by changing the location of the lateral supports. In the second run, the supports were located at segments with maximum lateral pressure. For the key coil (No. 9), the modification was quite favorable, because a large access port was provided in the outside region of the magnet. However, to insure the same result for all of the coils, a complete study would be required in which the same accessibility in all nine coils in the field period would be assured. The results of FE stress analysis for the section with the highest stresses and strains are shown in Fig. 5.4-3.

The MSR-IIB coil was within acceptable stress limits with the external backing ring of 0.47-m thickness to sustain the radial forces. The analysis showed that the side walls of the coil case required a 0.20-m structural thickness to withstand the twisting and side loads imposed by the four lateral supports assumed in the analysis. The inner ring of the coil was sized at 0.10 m. Although the stresses in the coil are adequate, it is possible with further iterations to optimize the side wall stresses and thickness by moving the support points.

CROSS-SECION $\theta = 7\ (\frac{360}{32}) = 78.75^{\circ}$ CW

15 MPa 0.00020 2,175 psi	78 MPa 0.00036 11,310 psi	303.7 MPa 0.0014 44,037 psi	669 MPa 0.00310 97,000 psi
42.7 MPa 0.00035 6,192 psi	90.3 MPa 0.00053 13,090 psi	361 MPa 0.0015 52,345 psi	728 MPa 0.00340 105,560 psi
114 MPa 0.00066 16,530 psi	CONDUCTOR		487.4 MPa 0.0020 70,673 psi
45.5 MPa 0.00038 6,500 psi			423.4 MPa 0.0017 61,670 psi
18.7 MPa 0.00038 2,700 psi	238 MPa 0.00119 34,500 psi	475.4 MPa 0.0021 68,900 psi	863 MPa 0.00369 124,700 psi

Fig. 5.4-3. MSR-IIB key coil (No. 9) section exhibiting the highest stresses and strains.

REFERENCES

1. C. C. Baker, M. A. Abdou, D. A. DeFreece, C. A. Trachsel, D. W. Graumann, et al., "STARFIRE - A Commercial Tokamak Fusion Power Plant Study," Argonne National Laboratory report ANL/FPP-80-1 (September 1980).

2. B. Badger, I. N. Sviatoslavsky, S. W. Van Sciver, G. L. Kulcinski, G. A. Emmert, D. T. Anderson, et al., "UWTOR-M: A Conceptual Modular Stellarator Power Plant," University of Wisconsin report UWFDM-550 (October 1982).

3. C. D. Henning, A. J. Hodges, J. H. Van Sant, E. N. Dalder, R. E. Hinkle, J. A. Horvath, et al., "Mirror Fusion Test Facility Magnet System - Final Design Report," Lawrence Livermore National Laboratory report UCRL-52955 (September 3, 1980).

4. M. Abdou, C. Baker, J. Brooks, D. DeFreece, D. Ehst, R. Mattas, et al., "A Demonstration Tokamak Power Plant Study (DEMO)," Argonne National Laboratory report ANL/FPP/82-1 (September 1982).

5. J. H. Murphy, "Examination of Superconducting Magnets for a Modular Stellarator Reactor," Westinghouse Electric Corporation internal report 82-88C9-STELL-R2 (October 22, 1982).

6. B. J. Maddock, G. B. James, and W. T. Norris, "Superconducting Composites: Heat Transfer and Steady State Stabilization," Cryogenics 9, 261-273 (August 1969).

7. L. Green, "Stellarator/Torsatron Reactor First Wall, Blanket, and Shield," Westinghouse Electric Corporation report WARD-FE-TME-82-4 (October 1982).

8. INTOR Group, "INTOR-International Tokamak Reactor: Phase One," International Atomic Energy Agency report STI/PUB/819, Vienna (1982).

9. R. J. LaBauve and M. E. Battat, Los Alamos National Laboratory letter to R. L. Miller (September 22, 1982).

10. R. D. O'Dell, F. W. Brinkley, Jr., and D. R. Marr, "User's Manual for ONEDANT: A Code Package for One-Dimensional, Diffusion-Accelerated, Neutral-Particle Transport," Los Alamos National Laboratory report LA-9184-M (February 1982).

11. P. G. Young, "Evaluation of n+^{7}Li Reactions Using Variance-Covariance Techniques," Trans. Am. Nucl. Soc. 39, p. 272 (November 1981).

12. M. E. Battat, R. J. LaBauve, and D. W. Muir, "The GAMMON Activation Library," Los Alamos National Laboratory report LA-8040-MS (September 1979).

13. Swanson Analysis Systems, Inc., "ANSYS - Engineering Analysis System," Rev. 3, Update 67L1, CYBERNOS (June 1, 1979).

14. Stone & Webster Engineering Corporation, "Stellarator/Torsatron Fusion Reactor Study: Final Activity Report June, 1982 through October, 1982," unpublished internal report (January, 1983).

6. TECHNICAL ASSESSMENT

Reactor design studies have identified competitive fusion systems on the basis of generally conservative physics assumptions and engineering design constraints. This chapter summarizes the assessment of key physics and technology issues for the stellarator reactor approach.

6.1. Physics

Detailed magnetics computations have demonstrated several coil configurations with good rotational transform, positive shear, and adequate volume utilization (i.e., r_p/r_c). Equilibrium/stability computations indicate that beta values approaching 10% are credible for stellarators. Simulations show >90% retention of alpha-particle energy, which is adequate for ignited operation. The absence of net parallel current should make stellarators immune from Mirnov and sawtooth oscillations as well as major disruptions, thereby providing more assurance for projections of oscillation-free, steady-state operation.

The conclusions[1] from the studies of ion thermal transport are a) earlier estimates based on oversimplified models of transport in a rippled tokamak are not valid; b) transport does not increase markedly in the low-collisionality regime but remains at most a few times the "plateau" value; c) optimization of the magnetic configuration from a transport viewpoint appears possible and may serve to distinguish between good and bad configurations; and d) the principal present limitation is a lack of sufficient studies of a complete range of configurations. The neoclassical bootstrap current, which might otherwise act to limit the attainable beta value, is calculated to be much smaller than first predicted and has not been found in any experiment. In summary, the theoretical outlook now appears much more favorable than it did a few years ago; and for plasma aspect ratios of about 10 or more with electrostatic effects included, thermal transport in stellarators now appears manageable.

Critical information that is presently missing includes

- experiments in low-collisionality regimes,
- detailed theoretical studies of low-collisionality regimes, to match the relevant experiments, and
- a comparison of transport in various stellarator confinement configurations.

6.2. Engineering

Coil design and access/maintenance options remain critical issues. Recent reactor studies have made considerable progress in identifying viable solutions to these problem areas. A qualitative summary of coil features is given in Table 6.2-1. The construction of $\ell = 2$ modular coils is similar to that of yin-yang mirror coils, which have been successfully built and tested in moderate size. Except for the out-of-plane winding, the internal S/T/H coil technology is comparable to other recent superconducting fusion reactor system designs.

TABLE 6.2-1

QUALITATIVE COMPARISON OF MAGNETIC SYSTEMS FOR STELLARATOR REACTORS (Ref. 1)

	Continuous Helices (Torsatron)	Modular with Windbacks (Torsatron)	Twisted Rehker/Wobig (Stellarator)	Heliac High Beta
Magnetic field limit	High	Moderate	Moderate	High
Rotational transform production	High	High	High	High
Flux surface quality	Good	Good	Good	Good
Magnetic volume utilization	Moderate	Moderate	Moderate	Moderate
Modularity	No	Yes	Yes	---
Support/force restraint	Rel. Easy	Difficult	Difficult	---
Ease of construction	Moderate	Difficult	Difficult	---
Blanket maintainability	Difficult	Moderate	Rel. Easy	---
Magnet maintainability	Very Difficult	Moderate	Rel. Easy	---

For purposes of this study, design effort was concentrated on the modular embodiment of the stellarator. The generally superior (except for stored magnetic energy) magnetics performance of the continuous-helical-coil (torsatron) embodiment was established in Sec. 4.3. However, this

superiority may be overridden in practice by the engineering aspects of initial fabrication, including the following features

- coils are physically large (54-m across by 8-m high),
- because of size, site fabrication is required,
- fabrication time is ~2-3 yr,
- fabrication in place is not practical because of interference with other construction and clean conditions are impractical,
- size requirements for fabrication include
  - temporary clear span building ~250′ × 250′ × 50′
  - temporary concrete roadway ~180′ wide
  - temporary containment opening ~180′ × 30′ high
  - weight to be moved is 10,000 - 20,000 tonnes, and
- financial risk in fabrication exceeds $0.5(10)^9$ dollars.

In addition to allowing the stellarator to achieve the same or higher power density as a low-aspect-ratio tokamak when both systems are constrained by the same beta and same peak-coil-field limit, the moderate aspect ratio allows good access. Routine maintenance schemes, allowing for movable coils or fixed coils, are entirely consistent with those of other superconducting fusion systems. Coil design, fabrication, and support appear tractable for the MSR. Credible approaches to remote maintenance are available.

The engineering development needs for the stellarator have been compared to those of other systems.[2-4] The critical issues for stellarators are summarized in Table 6.2-2.

TABLE 6.2-2

FUTURE ENGINEERING/TECHNOLOGY NEEDS OF STELLARATORS (Ref. 2)

PLASMA ENGINEERING SYSTEMS

- Better resolve/understand the effects of magnetics on beta/transport/stability/equilibrium and crucial interdependence on FW/B/C engineering design and system economics.

- Minimum-power startup procedure that properly adjusts flux surfaces as beta increases to ignition.

- Maximize plasma filling fraction for noncircular shapes (toroidal ripple, limiter versus divertor).

- Understand role of ambipolar electric fields on transport and stability/equilibrium.

NUCLEAR SYSTEMS

- Stability/equilibrium/beta-dictated magnetics may require thin, sub-breeding B/S directly under coils, like bumpy tori.

- Engineer, support, install, maintain helically arrayed FW/B/S, divertor, and coil systems.

MAGNET SYSTEM

- Need for accurate coil alignment, as for the bumpy tori and for similar reasons.

- Effect of field fluctuations associated with high-powered RF startup on magnetic island formation, vertical field and confinement.

- The proximity of opposing current conductors and the associated forces not as serious as for bumpy tori but the problem nonetheless exists for S/T/H. Need arises for methods to achieve desired magnetics with less massive (costly) coil sets.

- Adjust/tune magnetics as plasma beta is increased during startup to maintain stability/equilibrium condition.

- Need better engineering understanding of β versus on-axis B tradeoff between bumpy tori and S/T/H. For same βB^2 (plasma power density), S/T/H has higher B for a given limit imposed on the coil field, and a lower β is possible, compared to bumpy tori.

- Nonplanar coil fabrication and winding required, cannot wind modular coils under tension, unlike yin-yang coils for tandem mirrors.

REMOTE MAINTENANCE SYSTEMS

- Maintenance scheme similar to bumpy tori wherein the more complex S/T/H coils (400-500 tonne each) remain fixed, but system is lower aspect ratio and perhaps more open and amenable for FW/B/S module extraction.

TABLE 6.2-2 (cont)

- Impact on maintenance scheme of realistically design coil-support and bucking-ring systems, as well as divertor/vacuum system, must be better resolved.
- Maintenance problems on a modular but helically arrayed system of FW/B/S segments need better resolution.
- The key issue of fixed modular coils versus fixed continuous-helical coils with respect to maintenance of a segmented/modular FW/B/S must be better resolved.

The larger aspect ratio of the S/T/H allows larger on-axis field strength for a common peak field limit when compared to a tokamak. Net-current-free, steady-state operation allows a relaxed FW/B/S/C design, not requiring mitigation against disruptions and thermal-cyclic fatigue. The S/T/H allows lower recirculating power fractions by eliminating current drive (as for STARFIRE and RFPR) and ring drive (as for EBTR). Beta values approaching 10% appear feasible but must be confirmed. Beta is the key driver of overall S/T/H reactor viability.

Certain advanced stellarator coil configurations (e.g., heliac) are projected, on the basis of preliminary investigations, to have a potential for reaching beta values of 15-20%. Improved beta values enhance any fusion reactor conceptual design. For beta above 15%, it even becomes possible to consider resistive copper-coil systems, thereby reducing the neutron shield and thus achieving compact high-power-density operation. Confirmation of the possibility of stable high-beta operation, and detailed engineering designs of the novel coil configurations required for these systems are not yet available but a strong incentive exists to pursue this possibility. The conventional superconducting version of this concept would tend to produce large power output unless the magnetic field was lowered below the usually applied engineering constraints. A general rationale for pursuing the high power density approach can be found in Ref. 5.

Several unresolved technology issues remain. Startup procedures that minimize power requirements must be identified in conjunction with unresolved transport theory. The magnetics performance of modular coils is inferior to that of continuous-helical coils, but modular coils reduce the financial risk and technical problems of on-site winding of monolithic helical coils, whose integrity for the life of plant cannot be guaranteed.

REFERENCES

1. P. H. Rutherford (Chairman), J. P. Freidberg, J. H. Harris, J. F. Lyon, R. L. Miller, J. L. Shohet, I. N. Sviatoslavsky, H. Weitzner, and S. Yoshikawa, "Stellarator: A Report of a Subpanel to the Panel PQ2 of the Magnetic Fusion Advisory Council," unpublished (July 1982).

2. R. A. Krakowski, "Identification of Future Engineering Development Needs of Alternative Concepts for Magnetic Fusion Energy," The Future Engineering Development Needs for Magnetic Fusion Workshop, Washington, DC (August 3-4, 1982), [also Los Alamos National Laboratory document LA-UR-82-1973].

3. W. M. Stacey, Jr., C. C. Baker, R. W. Conn, R. A. Krakowski, D. Steiner, and K. Thomassen, "Technology Development Needs for Magnetic Fusion," Georgia Institute of Technology report GTFR-38 (March 1983) [submitted to Nucl. Fusion].

4. R. K. Linford, Ed., "Report of the US/JAPAN STELLARATOR/TORSATRON/HELIOTRON (S/T/H) Fusion Reactor Workshop," Los Alamos, NM (February 14-15, 1983).

5. R. A. Krakowski and R. L. Hagenson, "Compact Fusion Reactors," 5th ANS Topical Meet. on the Tech. of Fusion Energy, Knoxville, TN (April 26-28, 1983) [also Los Alamos National Laboratory document LA-UR-83-930 (Rev.)].

7. ECONOMICS

7.1. Cost Basis

Although detailed conceptual point designs of the flagship stellarators are not available, preliminary cost estimates were made to assess the relative economic performance of these systems. In addition, because the economic data base used here is generally well calibrated to that used in the more detailed STARFIRE[1] and EBTR[2] studies, a broader set of comparisons is allowed.

The stellarator cost estimate is specific to this system and reflects the unique ground rules applied to this truncated study. It is expected, however, that many of the results can be used to assess economic trends for many other magnetic fusion concepts, and the data base has been calibrated by other recent studies. When comparing results with an estimated cost of an existing power plant, it should be emphasized that the stellarator design is preconceptual, with most subsystems not fully defined or developed. Cost estimates for poorly defined subsystems were determined with implicit design allowances to account for uncertainties. Fortunately, many of the balance-of-plant (BOP) and heat transport systems are similar to existing Pressurized Water Reactor (PWR) fission systems, and this similarity should enhance the cost credibility. The direct capital cost estimates associated with the reactor plant equipment (RPE), the BOP equipment, land, and all the related structures and site facilities, are based upon supplier quotes, historical data, and costs of analogous systems.[1-3] The indirect cost estimates related to construction are based upon DOE recommendations[3] with design-specific modifications being made. Time-related costs account for both interest and escalation during construction. The annual costs include the annualized capital cost, the operations and maintenance costs, the fuel costs, and any scheduled component replacement costs. Given these costs along with the plant capacity (i.e., net power) and the plant availability, the bus-bar energy cost estimate is determined. These costs are presented in both constant (1980) dollars and then-current (1990) dollars reflecting the assumed 10-yr construction time, which represents a nominal facility cost for the first year of operation.

This section defines the economic guidelines and assumptions used in the study and analyses. The key design, performance, and operational features and their impact on the economics of the overall system are discussed. The capital cost accounts summarized in Table 7.1-1 generally follow the DOE

guidelines[3] and provide a uniform evaluation/accounting tool by which possible comparisons can be made with other studies. The estimated costs for stellarators are discussed, with any significant influencing factors or components highlighted. Table 7.1-2 shows the total bus-bar energy cost components for fusion-generated energy. These values are higher than are currently being projected for new fission plants, but stellarator fusion power plants will become competitive as the cost of fissile fuel continues to escalate compared to the negligible cost of the fusion fuel.

TABLE 7.1-1

SUMMARY OF STANDARD CAPITAL COST ACCOUNTS (Ref. 3)

	Cost Account Title
Direct Costs:	
20.	Land and Land Rights
21.	Structures and Site Facilities
22.	Reactor Plant Equipment (RPE)
23.	Turbine Plant Equipment
24.	Electric Plant Equipment
25.	Miscellaneous Plant Equipment
26.	Special Materials
	Total Direct Cost (TDC)
	Unit Direct Cost (UDC) ($/kWe)
Indirect Costs:	
91.	Construction Facilities, Equipment, and Services
92.	Engineering and Construction Management Services
93.	Other Costs
	Total Base Cost
	Unit Base Cost ($/kWe)
94.	Interest During Construction (IDC)
95.	Escalation During Construction (EDC)
99.	Total Cost
	Total Unit Cost ($/kWe)

TABLE 7.1-1 (cont)

Annual Costs:

40. Annual Salaries of Facility Personnel
41. Annual Miscellaneous Supplies and Equipment
42. Annual Outside Support Services
43. Annual General and Administrative Costs
44. Annual Coolant Makeup
45. Annual Process Materials
46. Annual Fuel Handling Costs
47. Annual Miscellaneous
50. Annual First Wall/Blanket Component Replacement
51. Annual Replacement of Other Reactor Components
02. Annual Fuel Cost
03. Annual Fuel Cycle Materials Cost

TABLE 7.1-2

TOTAL BUS-BAR ENERGY COST COMPONENTS

- Annualized Cost of Capital (Account 99)
- Operations and Maintenance (Accounts 40-47)
- Scheduled Component Replacement (Accounts 50-51)
- Fuel (Accounts 02-03)

Total Annual Cost

Cost of Electricity (COE) (mills/kWeh)

7.1.1. Economic Guidelines and Assumptions. To assure a consistent, uniform and complete economic evaluation of stellarators, the DOE guidelines[3] for costing fusion systems were adopted to the maximum extent for this study. This procedure assists in an evaluation of stellarators that is consistent with procedures used for alternate energy systems. To insure that all data are consistent and easily comprehended, the study guidelines follow those of the EBTR study[2] unless otherwise noted. These guidelines apply both to design and economic analyses. All costs quoted in this report are referenced to 1980

dollars unless defined otherwise. It is assumed that the user of the power plant will be an investor-owned utility.

7.1.2. Level of Technology. The stellarator design philosophy adopts the state-of-the-art technology for all BOP systems except where incorporation of specific advances in technology will enhance the performance, schedule, and/or cost. An example is the thermal-cycle efficiency consistent with the use of three stages of moisture separation for the steam turbine rather than the current practice of using one stage; for this study the stellarator turbine cycle efficiency is assumed to be $\eta_{TH} = 0.35$. For the construction time frame envisaged, it is likely that this improvement would be a then-current technology. Another example is the use of multiplex cabling and distributed microprocessors to reduce schedule constraints and system costs. Most of the BOP systems selected for stellarator represent current PWR technology (i.e., the Steam Generators, Turbine and Electric Plant Equipment, Condensing and Heat Rejection Equipment, and most of the Miscellaneous Plant Equipment). The EBTR building cannot be adapted for stellarator use because of the smaller major radius of the latter systems, precluding placement of steam generators inside the reactor torus. All other buildings are also considered to be of conventional design.

As with the EBTR, three levels of technology compose the RPE. The first level represents technologies that have been demonstrated for a commercial power plant. Typical of this level is the Primary and Closed Coolant Systems, power supplies, portions of the Radioactive Waste Treatment and Disposal system, and most of the Other Reactor Plant Equipment. The second level of technology represents technologies that have been demonstrated in existing power plants, but the application, design, and/or configuration is new or unique. This level is only a modest extrapolation of the existing state of the art; examples are elements of the shielding, the Atmospheric Tritium Cleanup System, elements of the Maintenance Equipment, Special Heating Systems, Inert Atmosphere System, and Reactor I&C System. The third level of technology is yet to be demonstrated in a commercial power plant, but the technology may have been commercially demonstrated by other industries. All these systems and related technologies are assumed to have been commercially demonstrated in power plants by the time EBTR is constructed (i.e., first-wall/blanket/limiter systems, the superconducting coils, rf power amplifiers, waveguides, large vacuum cryopumps, rf-heating/startup system components,

cryogenic cooling, tritium processing and storage, and special remote maintenance equipment).

Another aspect of the level of technology involves the design and operational philosophy of remote maintenance. This philosophy will require a re-evaluation of present power plant design criteria, procurement procedures, and operational practices. Designs will have to be modified or redesigned for modular replacement and firmer control will have to be enforced on specifications and interchangeability of parts. This philosophy represents an evolutionary change in the power industry, but it will be necessary in the future.

It is implied in all of the foregoing discussions that the stellarator, like EBTR and STARFIRE, is not the first-of-a-kind fusion power plant. Specifically, it has been assumed that these systems are the "10th-of-a-kind" power plant based on a specific design technology and that all systems have been proved thoroughly. Equipment R&D costs, therefore, are not included, and the equipment is costed with appropriate learning curves applied. Engineering and Construction Management Services (Cost Account 92) are reduced to a degree that reflects the design standardization of the reactor and BOP. No tooling costs are included in the cost estimate as all initial tooling costs are amortized over the previously constructed stellarator fusion power plants. Learning curve design allowance and site assumptions are consistent with EBTR and STARFIRE.

A contingency allowance is added to a cost estimate to account for the difference between the sum of individual estimated costs and the total amount that is reasonably expected to be spent, considering the degree of uncertainties in the estimated quantities, prices, and labor productivity. This contingency allowance is intended to reduce the risk of an overrun. The stellarator estimate uses the recommended value of 15% for Accounts 21, 22, 23, 24, and 25 from Ref. 3.

Any power plant requires a supply of spare parts that must be held in inventory in order that the plant quickly recover operation in event of a breakdown. Spare parts do not include equipment that is permanently connected in the systems to assure a desired level of redundancy. The spare parts are considered capital cost items that must be held in reserve for use during unexpected breakdowns or scheduled maintenance actions. The spare-parts

inventory should be increased to assure adequate supplies if lead times are unusually long.

The spare-parts allowance is assumed to be a percentage of direct equipment cost. The spare-parts allowances adopted from Ref. 3 are

Cost Account	Spare-Parts Allowance
21, 22, 23	2%
24	4%
25	3%
Others	0%

7.1.3. Indirect Cost Allowances. The indirect cost allowances are expenses resulting from the support activities required to design, fabricate, assemble, and check out the entire power plant. The three major accounts are Construction Facilities, Equipment and Services (Account 91), Engineering and Construction Management Services (Account 92), and Other Costs (Account 93). Appendix G of Ref. 2 gives additional detail for specific items included in each account.

Construction Facilities, Equipment and Services (Account 91) is somewhat different from fission plants in that more modular plant equipment is planned for EBTR with assembly and major checkout being conducted offsite. These preassembled modules will be much larger than most fission reactor components with the exception of the PWR pressure vessel. The cost estimate of the Construction Facilities, Equipment and Services adopts an allowance of 10% of the total direct cost. This approach was selected because the plant size and power output are only slightly larger than a current PWR, whereas the estimate is being scaled as a percentage of the direct cost, which is considerably larger than the direct cost of a current PWR power plant. Most of the high cost items (magnets, blanket, or shields) require very little handling and no field construction, with the clear exception of a continuous torsatron coil.

Engineering and Construction Management Services (Account 92) consists of the expenses for reactor and plant engineering and construction management services. The design philosophy of applying the current and envisaged power plant technology will certainly reduce the required engineering for the BOP and the heat transfer and transport systems. Also the 10th-of-a-kind reactor will require reduced engineering services. The only engineering services

being considered are those which are necessary for site development, utility requirements, new or updated regulatory guides, and design improvements. Services required of the construction management will be eased somewhat because of familiarity with the PWR systems and the assumed nine prior stellarator systems. Offsetting those advantages is the management of the construction of a large reactor building, the handling of large and expensive equipment, and the coordination of potentially more complex tasks. Based upon these considerations and the capital-intensive cost base, it was concluded that Account 92 costs could be estimated to be a factor of 8% of the TDC.

Associated with other costs (Account 93) are taxes, insurance, staff training, plant startup, and owner's General and Administrative (G&A) costs. Most of these items scale directly with the direct capital expense, and the stellarator estimate, therefore, adopted the recommended 5% of the Total Direct Cost for Other Costs.[3]

7.1.4. Time-Related Costs. Time-related costs are incurred because the fabrication, installation, construction, checkout, and startup occur over a finite period of time. These expenses are related to the opportunity cost of money and the changes in the purchasing power of the dollar with respect to time. Account 94 represents the allowance for funds used during construction (AFDC) or interest during construction (IDC). The IDC is the expense of the interest charges of financing the debt, the charges on the equity (common stock) portion of the financing, and any administrative charges on the financing. The interest during construction is determined by three elements: the total direct and indirect capital cost of the facility, the time distribution of the capital expenditures, and the aggregate interest rate on all financing charges. The direct and indirect costs are estimated using current-1980-dollar price levels. The time distribution of the capital expenditures is dependent upon the construction schedule, the construction techniques, the material and equipment purchases and progress payments, and the checkout and startup schedule. The expenditure pattern[3] shown in Fig. 7.1-1 is adopted by this study. At a point 60% through the construction period, one-half of the direct costs have been incurred.

The aggregate interest rate is representative of a privately owned utility. The following assumptions[3] are used as a basis for determining the cost of capital:

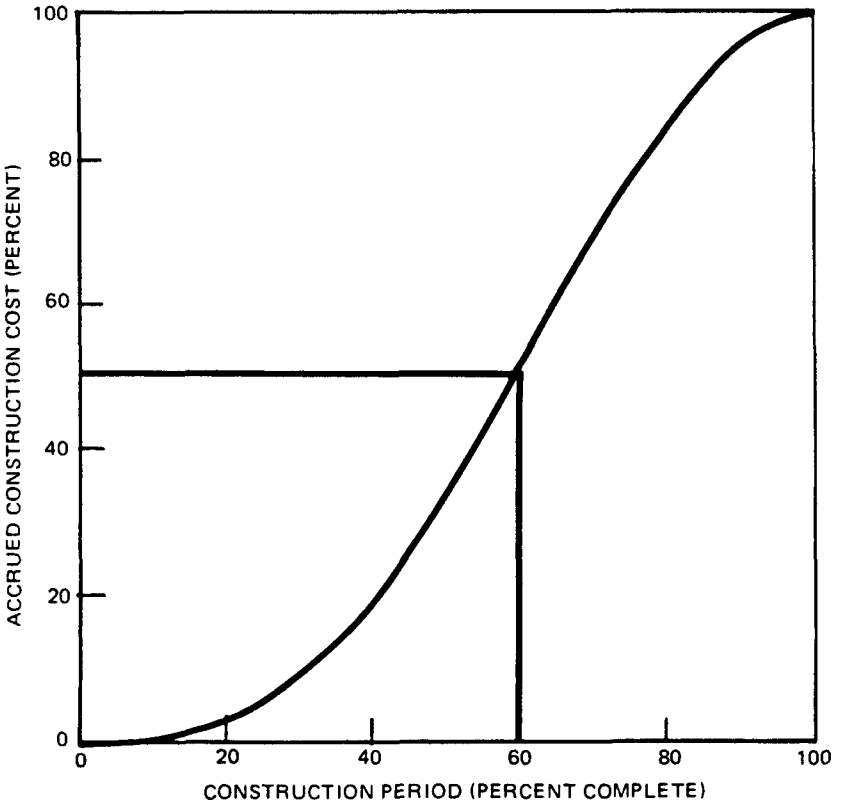

Fig. 7.1-1. Fusion power plant expenditure pattern.[3]

- Utility is investor owned.
- Capital structure is 53% debt financing and 47% equity (common stock) financing.
- Nominal cost of debt financing is 8% per year.
- Nominal cost of equity financing is 14% per year.
- Power plant economic lifetime is 30 yr with no salvage value.
- Cost escalation and general inflation is 5% per year.

Given these assumptions, the nominal cost of capital is 10% per year and the real (deflated) cost of capital is 5% per year.

Two modes of economic analysis are utilized in this study. The first mode is a "constant-dollar" mode, which assumes the purchasing value of the dollar remains constant over time. This constant-dollar analysis will express the cost in 1980 dollars. The inflation is assumed to be zero and the cost of

capital is 5% per year. The second analysis uses the "then-current-dollar" mode which assumes that purchasing value changes over time (inflation rate is not zero). The cost of capital for this mode is 10% per year, and the escalation is 5% per year. Figure 7.1-2 illustrates the means by which interest and escalation are additive to the direct and indirect cost of capital. Alternative schemes are available.[4] The specific values assumed for interest and escalation have been standardized[3] for comparison purposes with other fusion studies and are not intended to reflect actual interest and inflation fluctuations. The multipliers of the direct cost as a function of construction time are illustrated in Fig. 7.1-3. All costs reported in Accounts 20 through 26 and 91 through 93 are presented in 1980 dollars, and

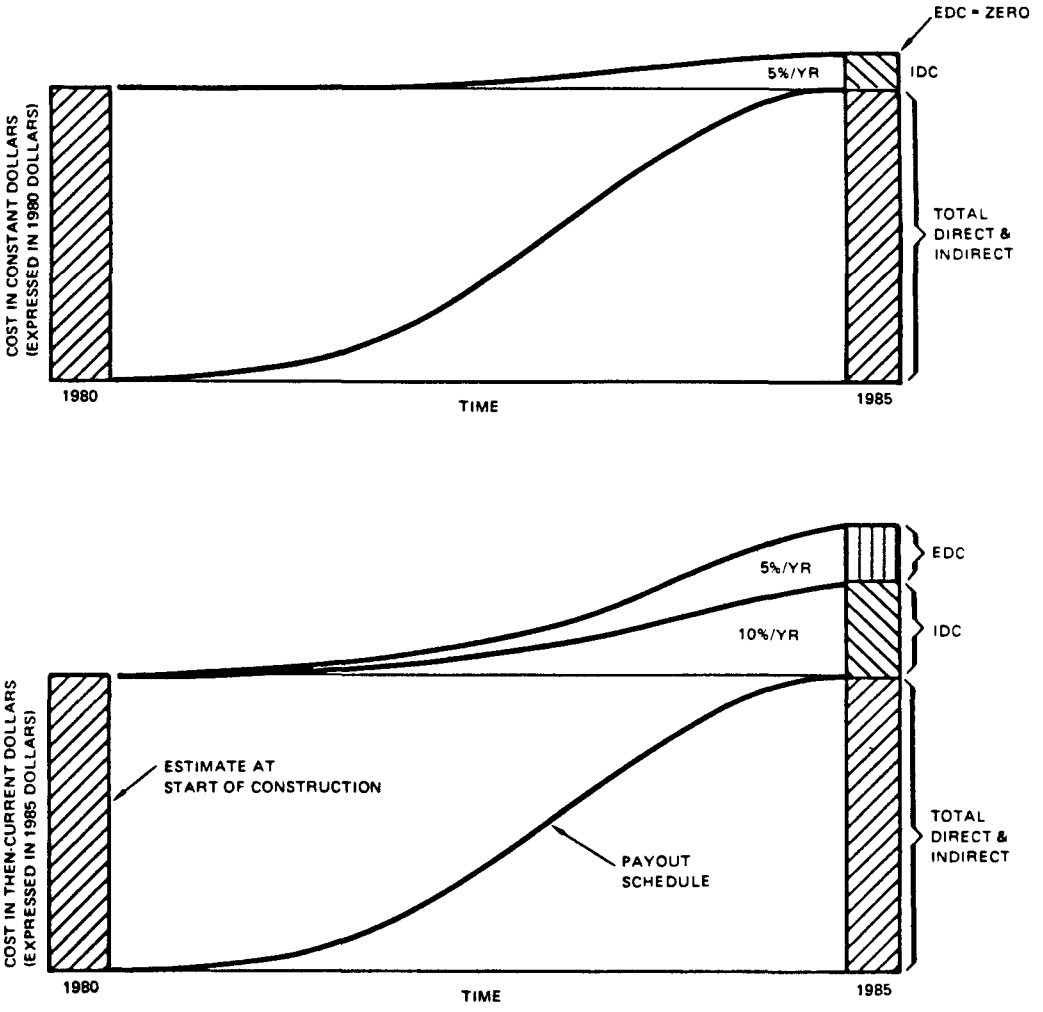

Fig. 7.1-2. Comparison of constant and then-current dollar analyses for a 5-yr construction period.[4]

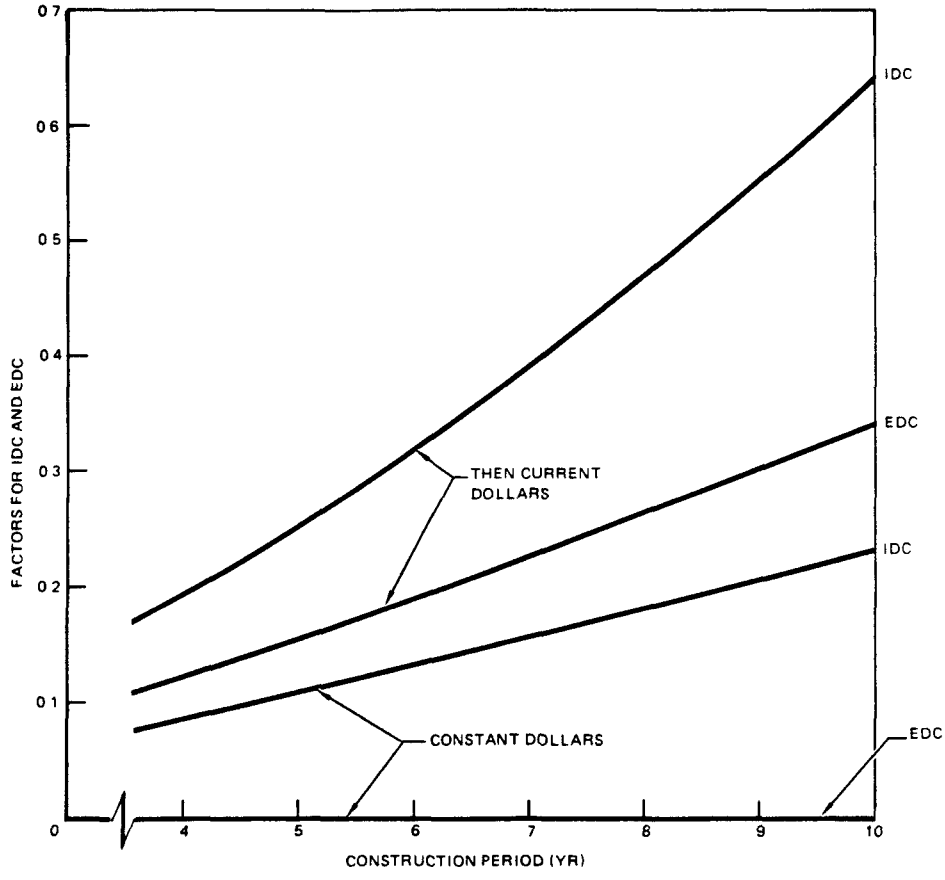

Fig. 7.1-3. Factors used for Interest During Construction (IDC) and Escalation During Construction (EDC) as a function of construction duration.

all effects of cost of capital and escalation during construction are reported, respectively, in Accounts 94 and 95 as factors of total direct and indirect costs.[3] The then-current-dollar analysis gives essentially a nominal first-year facility cost, with escalation only computed during construction.

Considerable care should be exercised when comparing the cost of stellarator to that of other energy sources. Key factors involve the cost basis of the estimate (usually the start of construction), the length of construction, the basis for the cost of capital and escalation, and the presentation mode of the facility economics (e.g., constant, then-current, or levelized). Any new energy source starting construction now will certainly cost more than an existing energy source as a result of inflation. Therefore, any comparison should only consider new starts on alternative energy sources.

Also, the preliminary nature of the present stellarator cost estimates, based on incomplete engineering designs, is again emphasized.

7.1.5. Key Design, Performance, and Operational Features. Several key features of a power plant directly influence the capital and operational cost. Table 7.1-3 lists the major design, performance, and operational features that can significantly affect the power plant economics.

The stellarator design philosophy reflects a mature fusion energy industry (i.e., 10th of a specific design). Several design features reflect this philosophy: steady-state operation, enhanced maintenance access, rf heating rather than neutral-atom beams, and limiter/vacuum impurity-control system. These features remain to be thoroughly demonstrated, but they have been shown to be feasible and would be typical of the design features to be found on a mature fusion power plant.

Steady-state operation of the stellarator reactor relieves thermal-fatigue problems and increases the system reliability. Steady-state operation also eliminates the need for thermal and electrical energy storage. Commercial operation also requires adequate maintenance access and other provisions not required in experimental devices or demonstration machines. The stellarator design incorporates accessible and maintainable wall/blanket

TABLE 7.1.3

KEY STELLARATOR DESIGN, PERFORMANCE, AND OPERATIONAL FEATURES

- Tenth-of-a-kind of a specific design technology
- Moderate aspect ratio device
- Enhanced maintenance access
- Steady-state operation
- Lower hybrid heating (LHH) for plasma startup
- Limiter/vacuum impurity-control system
- Stainless steel first-wall and blanket structural material
- Moderate neutron wall loading
- Reactor thermal power output of 4000-5000 MWt
- Pressurized-water primary coolant
- No intermediate coolant loop
- High efficiency steam turbine generator
- High plant availability
- Low fuel cost

sectors, as well as providing adequate space around the reactor for maintenance equipment. The decision to incorporate fully remote maintenance in the reactor building and hot cell represents another strong influence on system economics. This decision anticipates that the nuclear regulatory process will result in and require fully remote maintenance by the time fusion becomes a commercial reality. Remote handling is currently undergoing rapid development, and it is anticipated that the necessary equipment has been developed and is being utilized. The use of rf heating in place of neutral-atom beams and the use of limiter/vacuum impurity control in place of a magnetic divertor were selected for reasons of design simplification, enhanced maintainability and improved performance. Added benefits of these approaches are systems that are less expensive than the alternatives.[2]

It has been shown that power reactors exhibit an economy of scale; larger reactors have lower COE. Three important utility considerations, however, limit the desirable power rating. The first consideration is the difficulty of raising the capital for larger power plants. The second consideration relates to the cost of reserve electric power capacity that the utility must provide in order to compensate for scheduled and unscheduled outages; the impact on the electrical grid of an unscheduled outage for a large power plant represents another concern. The cost of reserve capacity increases with the size of the individual power plant. The third consideration is the maximum capacity of a single turbine generator by the year 2000, which is postulated to be in a range around 1400 MWe(gross). The most desirable power rating at present, therefore, is in the range of 3000-4000 MWt [~1250 MWe(net)] for electrical power;[1,2] the power level for the higher beta stellarator designs was targeted within this range. The low-beta stellarators violate this constraint.

The selection of the first-wall and blanket structural material is a significant element of the conceptual design. A key factor in this choice is the anticipated integral neutron wall loading or wall fluence ($MWyr/m^2$). A trade study was conducted in conjunction with the STARFIRE design,[1] which concluded that a fluence limit of 16 $MWyr/m^2$ for PCASS was acceptable from the viewpoint of radiation damage and would yield reasonable economic results. The neutron wall loading also has a substantial impact on the physical size of the reactor. For the same fusion power, higher neutron wall loading results in a smaller surface area, higher power density, smaller reactor volume, and

potentially lower cost. This obvious correlation underlines the motivation for developing designs with higher neutron wall loadings. Limitations exist, however, on the ability to produce and use high wall loadings. The upper limits on neutron wall loadings are dictated primarily by the first-wall cooling capability and the structural lifetime. Constraints imposed by the maximum operating temperature and thermal stresses establish an upper bound on the allowable neutron wall loading. For a given lifetime fluence, the neutron wall loading must assure that the frequency of structure replacement is not excessive. For a given structural material and a fluence lifetime, the loss of energy production associated with high neutron wall loading and the resultant short wall lifetime must be weighed against the economic gain realized by designing a small size reactor.

Plant availability is one of the most economically influential features of any power plant. A reduction in availability from a nominal 76 to 75% increases the COE almost 1.0 mills/kWeh for a capital-intensive facility like the stellarator. The reactor design was developed to permit all scheduled maintenance to occur during the maintenance of the BOP that typically operates with an availability of 60 to 80%. System redundancy, steady-state operation, ease of component replacement, and development of reliable components should permit the assumed overall plant availability of 76% for the stellarator designs. This plant availability also includes a major 120-day shutdown every 10 yr. Steady-state operation of the stellarator should considerably improve reliability for the application of economically optimum engineering safety factors. The plant availability factor is defined as the ratio of the expected amount of energy generation and the amount of energy generation that would occur if the plant operated 100% of the time at design power level. The availability is reduced from 100% because of outage time for scheduled, t_s, and unscheduled, t_u, maintenance periods. The plant availability equals $(365-t_u-t_s)/365$, where t_u and t_s are expressed in days. The scheduled outage time has been estimated as 28 days per year for reactor and BOP and 120 days every 10 yr for turbine generator overhaul and TF-coil anneal. To achieve the target availability of 76%, the unscheduled outage is set at 48 days per year. The availability factor has a strong influence on the COE.

The periodic first-wall and blanket replacement is an important operational feature. An integral neutron wall loading of 16 $MWyr/m^2$, a neutron wall load of 2 MW/m^2, and an overall plant availability of 76% yield a

first-wall life of approximately 10.5 calendar years. The maintenance procedure calls for replacing 12 of the 108 modules during the annual maintenance period in the last 9 yr of any 10-yr cycle. This expenditure is taken into account under the Annual Scheduled Component Replacement costs. The remote maintenance equipment is designed to accomplish the required replacement within the annual maintenance period. The resultant impacts of remote maintenance on the reactor and hot cell have been incorporated in both the design and cost analyses.

Another attractive feature of a DT fusion power plant is the low cost of fuel. Deuterium is currently estimated to cost in the range of $2000/kg.[3] If the reactor consumes 0.5 kg/day, the annual deuterium cost is approximately $300,000. Adequate tritium would be bred by the reactor and, therefore, is not considered as a cost item. The future tritium cost will be dependent upon the then-current supply and demand for tritium but will probably never decrease below the cost of processing and handling. The startup cost for tritium has not been taken into account; several years of plant operation may be required before the plant becomes intrinsically self-sufficient for tritium.

All the prior analyses are utilized in preparing the necessary data to calculate the bus-bar cost of energy available from the stellarator fusion power plant. This energy cost is the most important evaluation tool to compare alternative energy sources. Both constant-1980 and then-current-1990 dollar analyses are used to evaluate the stellarator economic parameters. The general equation for bus-bar energy cost is given by

$$COE = \frac{C_{AC} + (C_{O\&M} + C_{SCR} + C_F)(1 + E)^P}{(PC)(P_F)(10^{-3})} , \qquad (7.1\text{-}1)$$

where

COE = Cost of electricity in constant or then-current dollars (mills/kWeh).

C_{AC} = Annual capital cost charge = total capital cost multiplied by fixed charge rate (0.10 for constant-~dollar analysis or 0.15 for then-current-~dollar analysis).

$C_{O\&M}$ = Annual operations and maintenance cost = $C_{40} + C_{41} + \ldots + C_{47}$.

C_{SCR} = Annual scheduled component replacement cost = $C_{50} + C_{51}$.

C_F = Annual fuel costs = C_{02} and C_{03}.

E = Escalation rate equals 0.0 for constant-dollar analysis and 0.05 for then-current-dollar analysis.

P = Construction period (years).

PC = Plant capacity (kWeh).

P_F = Plant availability factor (%/100).

The degree of detailed design effort applied to the STARFIRE and EBTR allowed itemized cost estimates beyond the level available to the present stellarator reactor study. For the present effort, homogenized unit-cost averages were applied to the first-wall/blanket, shield, and coil subsystems of the Fusion Power Core (FPC). The assumed stellarator unit costs (1980 dollars) are displayed in Table 7.1-4 and compared with the comparable numbers derived from the STARFIRE and EBTR designs.

TABLE 7.1-4

FUSION POWER CORE HOMOGENIZED UNIT COSTS ($/kg)

	STARFIRE[1]	EBTR[2]	STELLARATOR
First-Wall/Blanket	53.3	41.2	42.0
Shield	13.9	14.6	15.0
Coils	20.8	21.3	25.0
Total	19.0	19.0	22-24

The stellarator FW/B/S values are similar to but slightly higher than those for the EBTR. The unit cost for stellarator coils is somewhat larger than for the other two systems to reflect the additional cost of out-of-plane winding. In addition to the general commonalty of unit costs indicated here for the FPC, the BOP cost models are essentially identical functions of thermal power.[3,5] The cost data base, as summarized in Table 7.1-5, has also been found to be comparable to that implemented independently in the Westinghouse COAST code.[6]

TABLE 7.1-5

SUMMARY FUSION REACTOR COST DATA BASE[a]

ACC. NO	ACCOUNT TITLE	(M$, 1980)
20.	Land and land rights	3.3
21.	Structure and site facilities	
21.1	Site improvements and facilities	11.15
21.2	Reactor building	$7(10)^{-4}V_{RB}$
21.3	Turbine building	34.43
21.4	Cooling structures	$7.13(P_{ET}/1000)^{0.3}$
21.6	Miscellaneous buildings	76.5
21.5	Power supply and energy storage	9.16
21.6	Miscellaneous buildings	76.5
21.7	Ventilation stack	1.81
21.98	Spare parts (2%)	
21.99	Contingency (15%)	
22.	Reactor Plant Equipment	
22.1	Reactor Equipment	
22.1.1	Blanket and first wall	$4.2(10)^{-2}\ M_{BL}$
22.1.2	Shield	$1.5(10)^{-2}\ M_{SHD}$
22.1.3	Magnets	$2.5(10)^{-2}\ M_{C}$
22.1.4	Supplemental heating	0.0
22.1.5	Primary structure and support	$0.16\ V_{STR}$
21.1.6	Reactor vacuum	$0.0051\ V_{VAC}$
22.1.7	Power supply (switching & energy storage)	$0.04\ P_{ET}$
22.1.8	Impurity control	$0.0026\ V_{VAC}$
22.1.9	Direct energy conversion	0.0
22.2	Primary coolant	$0.0175\ P_{TH}$
22.3	Auxiliary cooling	$6.7(10)^{-4}P_{TH}$
22.4	Radioactive waste treatment	$1.2(10)^{-3}\ P_{TH}$
22.5	Fuel handling and storage	$9.65(10)^{-3}\ P_{TH}$
22.6	Other reactor plant equipment	$1.09(10)^{-2}\ P_{TH}$
22.7	Instrumentation and control	23.41
22.98	Spare parts allowance (2%)	
22.99	Contingency allowance (15%)	
23.	Turbine plant equipment	
23.1	Turbine-generators	$59.9\ (P_{ET}/1000)^{0.7}$
23.2	Main steam system	$4.80\ (P_{TH}/2860)$
23.3	Heat rejection systems	$33.0\ (P_{TH}/2860)^{0.8}$
23.4	Condensing system	$13.8\ (P_{ET}/1000)^{0.9}$
23.5	Feed heating system	$7.55\ (P_{TH}/2860)$
23.6	Other turbine plant equipment	$40.9\ (P_{ET}/1000)^{0.6}$
23.7	Instrumentation and control	$7.80\ (P_{ET}/1000)^{0.3}$
23.98	Spare parts allowance (2%)	
23.99	Contingency allowance (15%)	
24.	Electric plant equipment	
24.1	Switchgear	$8.6\ (P_{ET}/1000)$

TABLE 7.1-5 (cont)

ACC. NO	ACCOUNT TITLE	(M$, 1980)
24.2	Station service equipment	18.0 (P_{ET}/1000)
24.3	Switchboards	5.4 (P_{ET}/1000)
24.4	Protective equipment	2.11
24.5	Electrical structures and wiring containers	17.4
24.6	Power and control wiring	35.99
24.7	Electrical lighting	8.2
24.98	Spare parts allowance (4%)	
24.99	Contingency allowance (15%)	
25.	Miscellaneous plant equipment	
25.1	Transportation and lifting equipment	15.68
25.2	Air and water service systems	12.35
25.3	Communications equipment	6.22
25.4	Furnishings and fixtures	1.12
25.98	Spare parts allowance (3%)	
25.99	Contingency allowance (15%)	
26.	Special Materials	
90.	Total direct cost (TDC)	
91.	Construction facilities, equipment, and services (10%)	
92.	Engineering and construction management services (8%)	
93.	Other costs (5%)	
94.	Interest during construction, IDC (10%/yr)	
95.	Escalation during construction, EDC (5%/yr)	
99.	Total reactor cost	

(a) Gross electric, P_{ET}, net electric, P_E, and total thermal, P_{TH}, powers given in MW. Volumetric V(m^3) abbreviations or corresponding mass M(tonne) costs for the fusion power core (FPC) and related items are given as

Reactor building, $V_{RB} = 20\pi(R_T + r_c + 15)^2$.
Blanket, M_{BL}
Shield, M_{SHD}
Magnet, M_C
Structure, V_{STR}
Vacuum, $V_{VAC} = 2\pi R_T \pi r_w^2$.

Stellarator annual costs (operations and maintenance, fuel, and component replacement) are estimated to be 2% of the total reactor cost.[3] More detailed analyses in Refs. 1-2 suggest this is a reasonable, conservative estimate for preliminary cost analyses such as the present effort.

7.2. Cost Estimates and Comparison with Other Fusion Systems

The cost data base summarized in the previous section has been used to estimate the costs of the four flagship stellarator design points. Results are summarized in Table 7.2-1 and compared with the STARFIRE[1] and EBTR[2] study results. It is again emphasized that the stellarator estimates are based on much more poorly detailed design points and must, therefore, be considered preliminary estimates. The conservatively assumed stellarator construction time is 10 yr in contrast to 6 yr for STARFIRE and 5 yr for EBTR. It may be noted that the recommended value[3] is 13 yr and that long construction times exert a considerable multiplication of the direct costs in determining the total costs (Fig. 7.1-3).

The $\langle\beta\rangle = 0.04$ cases, MSR-IIA and TR-A, have higher output (P_{TH} = 5.1 GWt) than the $\langle\beta\rangle = 0.08$ cases, MSR-IIB and TR-B (P_{TH} = 4.0 GWt), and, therefore, exhibit an economy-of-scale advantage in unit costs and COE. Substitution of the continuous-helical-coil set of the TR-A case for the modular-coil set of the MSR-IIA case results in somewhat higher costs. No specific optimization or "tuning" of the TR-A design point was performed. In contrast, the TR-B3 case was tuned to take advantage of the common B_{CM} = 12 T peak-coil-field limit, resulting in lower values of coil radius, mass, and consequently lower costs. Both $\langle\beta\rangle = 0.08$ cases result in lower direct costs than those found for the STARFIRE and EBTR systems, as was generally anticipated by the Ref. 13 parametric studies. The assumed longer construction time of the stellarator system results in higher relative total costs, particularly for the then-current-dollar-analysis option. The lower recirculating-power fractions for the stellarators ($\varepsilon = f_{AUX} = 0.07$), when contrasted to the STARFIRE with current drive [($\varepsilon = 0.167$) ($f_{AUX} = 0.06$)] and the EBTR with ring drive [($\varepsilon = 0.15$) ($f_{AUX} = 0.07$)], result in comparable COE estimates. This effect may be interpreted to allow the longer construction times without incurring a COE penalty or a clearer advantage for stellarators constructed more quickly than in a decade.

TABLE 7.2-1

FUSION REACTOR COST COMPARISON[a]

	ACCOUNT TITLE	STARFIRE[1]	EBTR[2]	MSR-IIA	TR-A	MSR-IIB	TR-B3
20.	Land and land rights	3.3	3.3	3.3	3.3	3.3	3.3
21.	Structures	346.6	289.8	286.3	286.3	255.0	250.5
22.	Reactor plant equipment	968.6	1425.7	1686.8	1899.2	967.6	792.9
23.	Turbine plant equipment	249.7	249.7	298.0	298.0	249.9	249.9
24.	Electric plant equipment	117.3	100.5	143.8	143.8	129.1	129.1
25.	Miscellaneous plant equipment	40.8	39.6	41.8	41.8	41.8	41.8
26.	Special materials	0.3	0.3	0.3	0.3	0.3	0.3
	Direct cost	1726.5	2108.8	2460.3	2672.8	1647.0	1467.8
91.	Construction, facilities, equipment, and service (10%)	172.7	210.9	246.0	267.3	164.7	146.8
92.	Engineering and construction management service (8%)	138.1	168.7	196.8	213.8	131.8	117.4
93.	Other costs (5%)	86.3	105.4	123.0	133.6	82.4	73.4
	Base Cost	2123.6	2593.9	3026.1	3287.5	2025.9	1805.4
	Construction time, P (years)	6	5	10	10	10	10
94.	Interest during construction [5%/yr(10%/yr)]	276.7(671.7)	278.1(650.8)	668.8(1948.9)	726.5(2117.2)	447.7(1304.6)	399.0(1162.7)
95.	Escalation during construction [0%/yr(5%/yr)]	0.0(462.6)	0.0(403.1)	0.0(1022.9)	0.0(1111.2)	0.0(684.7)	0.0(610.2)
99.	Total Cost	2400.3(3197.9)	2871.9(3647.7)	3695.0(5998.0)	4014.1(6515.9)	2473.6(4015.2)	2204.5(3578.4)
	Recirculating power fraction, ε	0.167	0.15	0.07	0.07	0.07	0.07
	Plant availability factor, P_f	0.75	0.76	0.76	0.76	0.76	0.76
	Net electrical power, P_E (MWe)	1200	1214	1660	1660	1302	1302
	Unit direct cost ($/kWe)	1439	1737	1482	1610	1265	1127
	Unit base cost ($/kwe)	1770	2137	1823	1980	1556	1387
	Total unit cost ($/kWe)	2000(2665)	2366(3005)	2226(3613)	2418(3925)	1900(3084)	1693(2748)
	10%/yr(15%/yr) capital return (mills/kWeh)	NA	NA	33.5(81.5)	36.4(88.6)	28.6(69.6)	25.5(62.0)
	2%/yr operating cost (mills/kWeh)	NA	NA	5.8(9.3)	6.4(10.1)	5.1(8.0)	4.6(7.3)
	Cost of electricity (mills/kWeh)	35.1(67.1)	38.9(71.7)	39.3(90.8)	42.8(98.7)	33.7(77.6)	30.1(69.3)

[a] Paired entries indicate constant (1980) and then-current (at end of construction) costs. Units are M$ for entries above Account 99.

A more detailed comparison of reactor fusion power core (Account 22.1.1-3) masses and costs is presented in Table 7.2-2. Included are the mass utilization, defined as the mass, M, of the fusion power core normalized by the total thermal power output, P_{TH}; the fractional cost of the FPC relative to the RPE and TDC is also shown as is the UDC. When reactor net power output is normalized to P_E = 1000 MWe, a strong linear correlation between mass utilization and UDC has been identified, as is shown on Fig. 7.2-1. The UDC increases linearly with M/P_{TH}, as expected, with an average unit FPC cost being \$30/kg. The mass utilization is apparently a good indicator of increasing plant cost. The equipment and structural mass (including rebar in both physics and technology) for the BOP is 10-15 tonne/MWt. A FPC mass utilization of 10 tonne/MWt approximately doubles the plant mass (again, excluding concrete), and a commensurate doubling of direct cost is expected. The correlation of UDC with mass utilization was used in Ref. 13 to motivate the search for stellarator design points with $\langle\beta\rangle \simeq 0.08$, consistent with $M/P_{TH} \simeq 5$ tonne/MWt to be competitive with the mainline STARFIRE tokamak design. The greater elongation of the plasma cross section at $\langle\beta\rangle = 0.08$ when compared with $\langle\beta\rangle = 0.04$ implies that the MSR-IIB mass cannot be reduced relative to the MSR-IIA as much as can the TR-B3 mass compared to the TR-A. Elliptical-bore modular coil would help the MSR-IIB in this respect. More vigorous application of the correlation motivates the investigation of compact fusion systems[5] with mass utilizations, power densities, and unit direct costs approaching those of contemporary Light Water Reactor (LWR) fission central power stations.

It is concluded on the basis of this preliminary economic analysis based on a somewhat preconceptual design that stellarator reactors will require $\langle\beta\rangle \simeq 0.08$ to be economically competitive with the mainline fusion systems. Lower recirculating power fractions for the stellarators offset some of the higher direct costs to give more comparable values of COE. However, design effort was insufficient in this study to distinguish between modular and torsatron stellarator configurations on the basis of cost in order to choose a preferred development route. However, important engineering considerations (Sec. 5.) dictate a preference for the modular approach at the commercial reactor level.

TABLE 7.2-2

FUSION POWER CORE COMPARISON[a]

	STARFIRE[1]	EBTR[2]	MSR-IIA	TR-A	MSR-IIB	TR-B3
Mass (tonne):						
First Wall/Blanket	1574	4116	5151	5987	2060	1699
Shield	13360	13110	16272	22254	10275	5859
Coils	8240	26150	21233	20740	14149	12037
Total FPC Mass, M	23117	43376	42656	48981	26484	19595
Mass Utilization, M/P_{TH} (tonne/MWt)	5.7	10.8	8.4	9.6	6.6	4.9
Cost (M$):						
21.1.1 First Wall/Blanket	82.4	174.5	228.4	264.6	91.1	74.5
21.1.2 Shield	186.1	191.5	244.1	333.8	154.1	87.9
21.1.3 Coils	171.6	556.9	530.8	518.5	353.7	300.9
Total FPC Cost	440.1	922.9	1003.3	1116.9	598.9	463.3
Cost Figures of Merit:						
FPC/RPE	0.45	0.65	0.59	0.59	0.62	0.58
RPE/TDC	0.56	0.68	0.69	0.71	0.59	0.54
FPC/TDC	0.25	0.44	0.40	0.42	0.37	0.32
UDC ($/kWe)	1439	1737	1482	1610	1265	1127

[a]Paired entries indicate constant (1980) and then-current (at end of construction) costs.

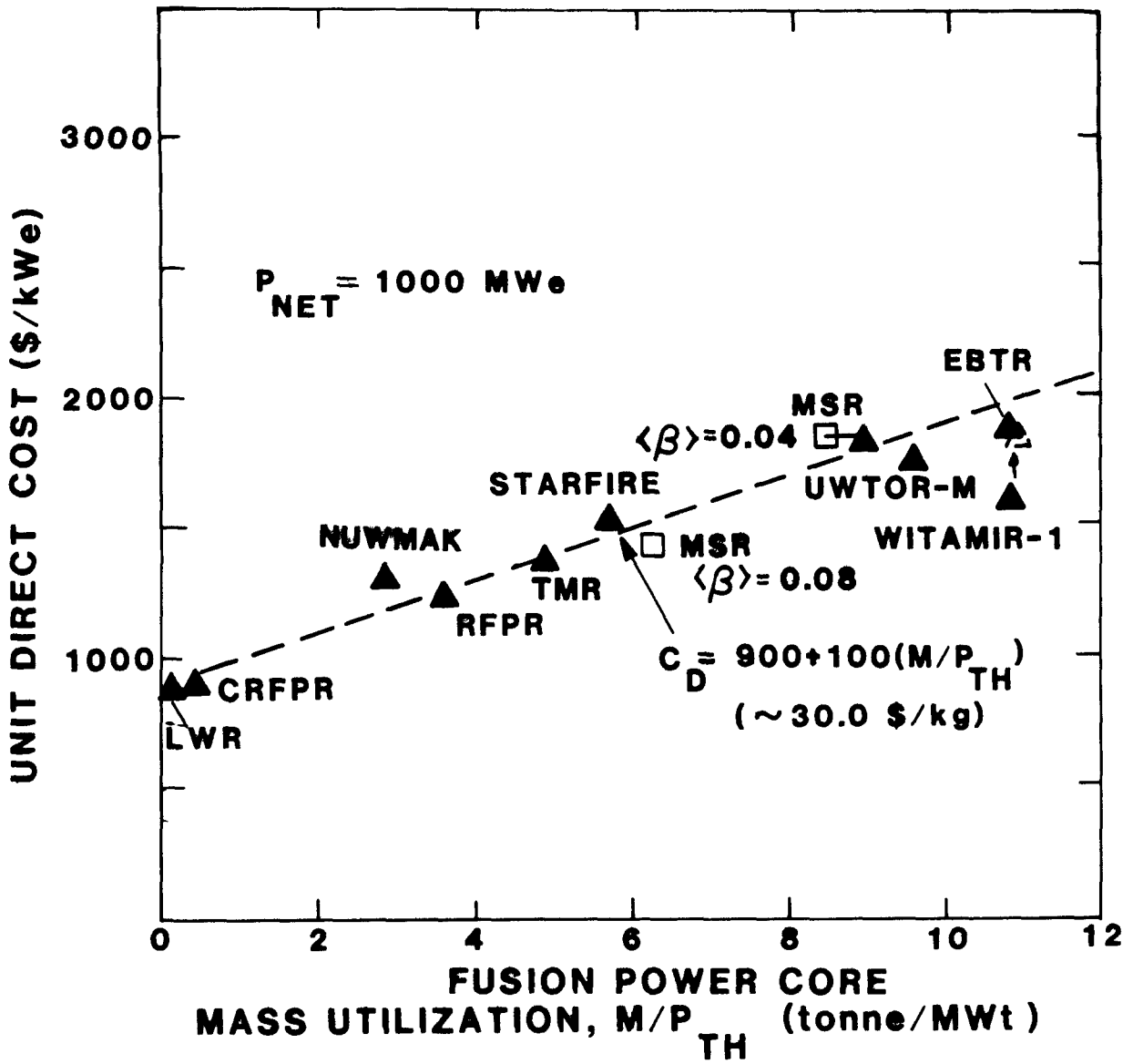

Fig. 7.2-1. Correlation of mass utilization factor, M/P_{TH} (tonne/MWt), with unit direct cost (UDC). Reactor design points shown are: LWR;[7] Compact Reversed-Field Pinch Reactor (CRFPR);[5] Reference Reversed-Field Pinch Reactor, RFPR;[8] STARFIRE tokamak reactor;[1] NUWMAK tokamak reactor;[9] Tandem Mirror Reactor (TMR);[10] Modular Stellarator Reactor (MSR); WITAMIR-III; UWTOR-M;[12] and ELMO Bumpy Torus Reactor (EBTR);[2] Costs have been adjusted to 1980 dollars. The UDC values given here do not include indirect costs (typically 23%), interest during construction (IDC), or escalation during construction (EDC).[3] Reactor unit costs have been normalized using a 0.4 power law to a common net electric output P_{NET} = 1000 MWe.

REFERENCES

1. C. C. Baker, M. A. Abdou, D. A. DeFreece, C. A. Trachsel, D. W. Graumann, et al., "STARFIRE - A Commercial Tokamak Fusion Power Plant Study," Argonne National Laboratory report ANL/FPP-80-1 (September 1980).

2. C. G. Bathke, D. J. Dudziak, R. A. Krakowski, W. B. Ard, D. A. Bowers, J. W. Davis, et al., "ELMO Bumpy Torus Reactor and Power Plant Conceptual Design Study," Los Alamos National Laboratory report LA-8882-MS (August 1981).

3. S. C. Schulte, W. E. Bickford, C. E. Willingham, S. K. Ghose, and M. G. Walker, "Fusion Reactor Design Studies - Standard Unit Costs and Cost Scaling Rules," Pacific Northwest Laboratory report PNL-2987 (September 1979).

4. D. L. Phung, "A Method for Estimating Escalation and Interest During Construction," Institute for Energy Analyses, Oak Ridge Associates Universities (October 1977).

5. R. L. Hagenson and R. A. Krakowski, "Compact Reversed-Field Pinch Reactors (CRFPR): Sensitivity Study and Design-Point Determination," Los Alamos National Laboratory report LA-9389-MS (July 1982).

6. D. A. Sink and E. M. Iwinski, "User's Manual for COAST-4, A Code for Costing and Sizing Tokamaks," Westinghouse Electric Corporation report WFPS: TME-79-023 (September 1979).

7. C. Komanoff, Power Plant Cost Escalation (Komanoff Energy Associates, New York, 1981).

8. R. L. Hagenson, R. A. Krakowski, and G. E. Cort, "The Reversed-Field Pinch Reactor (RFPR) Concept," Los Alamos Scientific Laboratory report LA-7973-MS (August 1979).

9. B. Badger, K. Audenaerde, H. I. Avci, J. Beyer, D. Blackfield, R. W. Boom, et al., "NUWMAK - A Tokamak Reactor Design Study," University of Wisconsin report UWFDM-330 (March 1979).

10. G. A. Carlson, "The Design of Tandem Mirror Reactors with Thermal Barriers," Proc. 4th ANS Top. Meeting on the Technology of Controlled Nucl. Fus. III, 815-824 (October 14-17, 1980).

11. B. Badger, K. Audenaerde, J. B. Beyer, D. Braun, J. D. Callen, G. A. Emmert, et al., "WITAMIR-I: A Tandem Mirror Reactor Study," University of Wisconsin report UWFDM-400 (September 1980).

12. B. Badger, I. N. Sviatoslavsky, S. W. Van Sciver, G. L. Kulcinski, G. A. Emmert, et al., "UWTOR-M: A Conceptual Modular Stellarator Power Plant," University of Wisconsin report UWFDM-550 (October 1982).

13. R. L. Miller, R. A. Krakowski, and C. G. Bathke, "Parametric Systems Analysis of the Modular Stellarator Reactor (MSR)," Los Alamos National Laboratory report LA-9344-MS (May 1982).

8. CONCLUSIONS

A number of recent reactor studies of the stellarator concept have addressed the fundamental physics, engineering, and economic implication aspects of these systems. These generally conservative studies, taken collectively, demonstrate credible, competitive solutions to the crucial lingering problems that contributed to the de-emphasis of stellarator reactor work about a dozen years ago. Guidance has been provided to the near-term theoretical and experimental program indicating parameter sets and design direction that would seem to promise an attractive fusion power system worthy of vigorous pursuit. The crucial coupling between specific coil designs (i.e., torsatron versus modular, winding law, aspect ratio, etc.), resultant magnetics performance (i.e., rotational transform, shear, well, ripple etc.), and beta as limited by equilibrium/stability is the key driver in fixing the optimum stellarator reactor configuration.

The following conclusions have emerged from the MSR study.

- Modular-coil configurations sacrifice magnetics performance relative to continuous-coil configurations [rotational transform (~2% less), shear (comparable at high transform), volume utilization (~2% less), peak coil field (~10% higher for same B_o), B_{CM}/B_o (~10% less), etc.] in return for fabrication/maintenance advantages and lower stored energy.

- Radial forces are larger for the torsatron, while lateral forces are smaller when compared to modular coils. Access is diminished primarily proportionally to the lateral forces; the modular-coil approach is adversely affected most by the lost access as B is increased but has the option of coil movement as part of the routine maintenance scheme.

- Access to first-wall/blanket components for fixed modular or torsatron systems is comparable, suggesting a similar routine maintenance scheme that does not require coil movement.

- Modular-coil and torsatron configurations with similar plasma performance (size, field, beta, etc.) are comparable in terms of access and cost. Modular coils are preferable if life-of-plant (LOP) coils cannot be assumed. Availability of LOP coils and desire to maximize plasma performance (beta) would favor torsatron coils. Availability of breakable joints without LOP coils favors torsatron coils. Marginally competitive MSR designs are available for $\langle\beta\rangle$ as low as 0.04 at $\gtrsim$25% higher power. Designs that are competitive with STARFIRE at lower power output would require $\langle\beta\rangle$ of at least 0.08. The magnetics performance of simple, modular coils raises questions about

obtaining the latter, based on current understanding of stability/equilibrium beta limits.

- Beta remains the major issue for S/T/H reactors from the viewpoint of stability and equilbrium.
  - If high transform and shear are required, torsatron or advanced modular configurations (e.g., M&S or Heliac) are preferable.
  - Reactor performance is critically coupled to the magnetics performance of the coil set.
- Startup using modest power from the electrical grid avoids the cost of rarely used on-site power sources but constrains the startup transient. This critical aspect of the MSR study was not investigated.
- As for many MFE approaches, energy confinement projections for S/T/H reactors are subject to large uncertainties, leading to uncertainties in startup trajectories as well as reactor size and power density. Plasma performance evaluations should include the effects of the self-consistent ambipolar electric fields on orbits and transport, which may lead to significantly reduced plasma and reactor sizes.

ACKNOWLEDGMENTS

The authors gratefully acknowledge neutronics computations performed for this study by R. J. LaBauve and M. E. Battat of Los Alamos. We also thank I. N. Sviatoslavsky and J. L. Shohet of the University of Wisconsin; J. L. Johnson and T. K. Chu of the Princeton Plasma Physics Laboratory; O. Motojima of Kyoto University; H. Nakashima of Kyushu University; I. Yanagisawa of Mitsubishi Atomic Power Industries, Inc.; and J. H. Harris, J. F. Lyon, and J. A. Rome of Oak Ridge National Laboratory for useful discussions and other cooperation.

We are especially appreciative of the efforts of Olivia Moss of Los Alamos for her cheerful and expert typing and composition of this report.

APPENDIX: Table of MSR-IIB Design Parameters

This table contains the comprehensive and uniform design data for the MSR-IIB. The format of this table follows the DOE/OFE guidelines.[1] Superscripted numbers in parentheses refer to notes found at the end of this table.

TABLE OF REACTOR DESIGN PARAMETERS

Parameter	Unit	Value
1. Characteristic Machine Dimensions		
1.1. Reactor envelope(1)		
1.1.1. Height (coil outside diameter)	m	9
1.1.2. Width (coil outside diameter)	m	9
1.1.3. Length (major circumference)	m	145
1.1.4. Volume of reactor envelope	m^3	6677
1.2. Plasma chamber		
1.2.1. Major radius, R_T	m	23.0
1.2.2. Minor radius	m	0.5 to 1.4
1.2.3. Plasma volume, V_p	m^3	298
1.2.4. Plasma chamber volume (actual)	m^3	468
1.2.5. Wall surface area (actual)	m^2	1480
1.2.6. Number of sectors, N	-	36
2. Plasma Parameters (Steady State)		
2.1. Plasma dimensions		
2.1.1. Major radius, R_T	m	23.0
2.1.2. Average minor radius, r_p	m	0.81
2.1.3. Minor radius at coil plane, r_{CP}	m	0.82
2.1.4. Minor radius at midplane, r_{MP}	m	0.84
2.2 Average ion density, n_i	$10^{20}/m^3$	3.64
2.3 Average alpha-particle density, n_α	$10^{20}/m^3$	0.2
2.4 Energy confinement time, τ_E	s	0.94
2.5 Electron confinement time, τ_{pe}	s	1.9
2.6 Ion confinement time, τ_{pi}	s	1.9
2.7 Average Lawson parameter, $n_i\tau_E$	10^{20} s/m^3	3.4
2.8 Average toroidal beta(2a), $\langle\beta\rangle$	-	0.08
2.9. Average plasma toroidal current	MA	0.
2.10. Average ion temperature, $\langle T_i \rangle$	keV	8.0

Parameter	Unit	Value
2.11. Average electron temperature, $\langle T_e \rangle$	keV	8.0
2.12. Average alpha-particle energy, $\langle T_\alpha \rangle$	keV	80
2.13. Effective plasma ion charge[2b], Z_{eff}	-	1.1
2.14. Reactor cycle		
2.14.1. Burn pulse length	s	Steady state
2.14.2. Total pulse length	s	Steady state
2.15. Fuel cycle	-	DT/Li
2.16. Plasma heating method	-	TBD
2.16.1. Plasma heating power[2c]	MW	TBD
2.16.2. Plasma heating frequency[2d]	GHz	TBD
2.17. Plasma energy gain[2h], Q_p	-	∞ (ignited)
3. Power Output		
3.1. Plasma fusion power, P_F	MWt	3713
3.1.1. 14.1-MeV neutron power, P_N	MWt	2963
3.1.2. 3.5-MeV alpha-particle power, P_α	MWt	740
3.2. Reactor thermal power	MWt	4000
3.2.1. Power to first wall	MWt	660
3.2.2. Power to limiter	MWt	90
3.2.3. Power to blanket	MWt	3620
3.2.4. Power from blanket ($M_N \simeq 1.1$)	MWt	3910
3.2.5. Power to shield	MWt	TBD
3.3. Blanket power amplification factor, M_N	-	~1.1
3.4. Plasma chamber power density (total cycle time average)[3a]	MWt/m^3	7.9
3.5. Plasma power density[3b]	MWt/m^3	12.4
3.6. Engineering power density[3c]	MWt/m^3	0.60
3.7. Blanket power density[3d]	MWt/m^3	6.3
3.8. Total thermal power to conversion cycle[3e], P_{TH}	MWt	4000
3.9. Plant gross electrical output, P_{ET}	MWe	1400
3.10. Plant net electrical output, P_E	MWe	1302
3.11. Thermal cycle efficiency, η_{TH}	-	0.35
3.12. Net plant efficiency, $\eta_p = \eta_{TH}(1-\varepsilon)$	-	0.33
3.13. Recirculating power fraction, ε	-	0.07

Parameter	Unit	Value
4. Reactor Coolant System		
4.1. Blanket coolant	-	H_2O(liquid)
4.2. Blanket outlet temperature (hot leg)	K	593
4.3. Blanket inlet temperature (cold leg)	K	553
4.4. Blanket outlet pressure	MPa	TBD
4.5. Blanket inlet pressure	MPa	15
4.6. Blanket coolant flow rate (total)	kg/s	TBD
4.7. Blanket coolant-tube material[4a]	-	Modified PCASS
4.8. First-wall coolant type	-	H_2O
4.9. First-wall outlet temperature	K	TBD
4.10. First-wall inlet temperature	K	TBD
4.11. First-wall outlet pressure	MPa	TBD
4.12. First-wall inlet pressure	MPa	TBD
4.13. First-wall-coolant flow rate (total)	kg/s	TBD
4.14. Total number of blanket-coolant loops	-	4
4.15. Type of blanket coolant circulator		Vertical, 1 stage
4.16. Power input to each circulator[4b]	MWe	4.25
4.17. Peak temperature in case of loss-of-coolant-flow		
4.17.1. First wall	K	TBD
4.17.2. Blanket multiplier	K	TBD
4.17.3. Breeder	K	TBD
4.18. Energy storage	J	Not required
5. Intermediate Coolant System		Not required
6. Steam Generation (SG) System		
6.1. Steam outlet temperature	K	TBD
6.2. Steam outlet pressure	MPa	TBD
6.3. Steam flow rate (total)	kg/s	TBD
6.4. Feedwater temperature	K	TBD
6.5. Number of steam generators (SG) per loop	-	1
6.6. Number of reactor sectors per SG (2 modules/sector)	-	9
6.7. SG materials, shell/tube	-	Low carbon steel/ Inconel 600

Parameter	Unit	Value
7. Shield Coolant System[7a]		
7.1. Total power deposited in the shield	MWt	50
7.2. Shield coolant type	-	H_2O
7.3. Shield outlet temperature	K	333
7.4. Shield inlet temperature	K	316
7.5. Coolant outlet pressure	MPa	0.34
7.6. Coolant inlet pressure	MPa	0.48
7.7. Coolant flow rate (total)	kg/s	700
8. Reactor Auxiliary System		
8.1. Vacuum pumping system		
8.1.1. Plasma chamber pressure[8a]	Pa	10^{-3}
8.1.2. Plasma chamber volume	m^3	468
8.1.3. Total vacuum volume	m^3	TBD
8.1.4. Number of vacuum pumps (cryogenic)	-	72 (36 on-line, 36 regenerating)
8.1.5. Regeneration interval	h	2
8.1.6. Helium pumping speed (per pump)	m^3/s	TBD
8.2. Magnet cooling system		
8.2.1. Helium cooling load (total)	kWt	TBD
8.2.2. Nitrogen cooling load	kWt	TBD
8.3. Plasma-heating-system cooling load	MWt	TBD
8.4. Plasma fueling system		
8.4.1. Type	-	DT Pellet
8.4.2. Fuel composition	-	50% D, 50% T
		TBD
8.4.4. Pellet diameter	mm	TBD
8.4.5. Pellet injection frequency	s^{-1}	TBD
8.5. Tritium processing and recovery system		
8.5.1. Total tritium inventory	kg	TBD
8.5.2. Vulnerable tritium inventory	kg	TBD
8.6. Impurity Control System		Pumped limiter
9. Reactor Components		
9.1. First wall/blanket		
9.1.1. Structural material	-	Modified PCASS[4a]
9.1.2. Breeding material		Li_2O (natural Li)

	Parameter	Unit	Value
9.1.3.	Neutron multiplier material	-	Be
9.1.4.	Breeding ratio[9a]	-	~1.1
9.1.5.	Number of modules (3 per sector)	-	108
9.1.6.	Weight of modules (3 per sector)	tonnes	60
9.1.7.	Weight of largest single component	tonnes	60
9.1.8.	Dimensions of largest component	m	5 × 4 × 1.5
9.1.9.	First-wall power loading		
9.1.9.1.	14.1-MeV neutron flux	MW/m^2	2.0
9.1.9.2.	Alpha-particle flux	MW/m^2	TBD
9.1.9.3.	Radiation, charge-exchange, and conduction power to first wall	MW/m^2	0.44
9.1.9.4.	Radiation, charge-exchange, and conduction/convection power to limiter	MW/m^2	2.5
9.1.9.5.	First-wall life	$MWyr/m^2$	16
9.2.	Shielding		
9.2.1.	Material		W/Pb, 304 SS, TiB_2 TiH_2,H_2O
9.2.2.	Number of modules (3 per sector)		108
9.2.3.	Weight of each module	tonnes	60
9.2.4.	Weight of largest single component	tonnes	NA
9.2.5.	Dimensions of largest component	m	5 × 4 × 1.5
9.3.	Magnets		
9.3.1.	Superconducting		yes
9.3.2.	Conductor material		Cu/NbTi/Nb_3Sn
9.3.3.	Structural material		316L SS
9.3.4.	Operating temperature	K	4.0
9.3.5.	Coolant		He-I
9.3.6.	Mean stress in coil	MPa	TBD
9.3.7.	Maximum force transmitted to building	MN	TBD
9.3.8.	Maximum field	T	11.6
9.3.9.	Field on axis (coil-plane)	T	6.5
9.3.10.	Field on axis (midplane)	T	6.4

	Parameter	Unit	Value
9.3.11.	Number of magnets	-	36
9.3.12.	Mean coil radius	m	3.31
9.3.13.	Total stored energy (full torus)	GJ	108
9.3.14.	Weight of largest single component	tonnes	390
9.3.15.	Dimension of largest single component	m	7 × 7 × 4
9.4.	Energy transfer and storage		Not required
9.5.	Plasma heating		Required only for startup(2e)
9.5.1.	Type	-	LHH
9.5.2.	Frequency	GHz	TBD
9.5.3.	Power to the plasma	MW	TBD
9.5.4.	Transmission method	-	TBD
9.5.5.	Power reflected from plasma	MW	TBD
9.5.6.	Power loss in transmission	MW	TBD
9.5.7.	Power loss in amplifiers	MW	TBD
9.5.8.	Power loss in power supplies	MW	TBD
9.5.9.	System input power	MW	TBD
9.5.10.	Heating time	min	TBD
9.5.11.	Number of waveguide grills	-	4 (90° around torus)
9.5.12.	Number of amplifiers	-	TBD
10.	Electrical Power Requirements		
10.1.	Cold-plasma startup-power from grid	MWe/s	TBD
10.2.	Auxiliary power requirements (normal operation)	MWe	98
10.2.1.	Electrical energy storage	MWe	none required
10.2.2.	Magnet power supply (other than energy storage)	MWe	TBD
10.2.3.	First-wall/blanket circulators	MWe	TBD
10.2.4.	Limiter-coolant circulators	MWe	TBD
10.2.5.	Shield-coolant circulators	MWe	TBD
10.2.6.	Refrigeration system	MWe	TBD
10.2.7.	Vacuum system (roughing)	MWe	TBD
10.2.8.	Miscellaneous reactor plant auxiliaries	MWe	TBD

Parameter	Unit	Value
10.2.9. Feedwater pump system	MWe	not required (turbine driven)
10.2.10. Condensing system	MWe	TBD
10.2.11. Heat rejection system	MWe	TBD
10.2.12. Miscellaneous BOP auxiliaries	MWe	TBD
11. Buildings		
11.1. Reactor Building		
11.1.1. Characteristic dimensions	m	~85(diam) × ~10(ht)
11.1.2. Enclosed volume		
11.1.2.1. Free volume[11a]	m^3	TBD
11.2.1.2. Total volume	m^3	110,000
11.1.3. Minimum wall thickness for shielding	m	1.5
11.1.4. Internal pressure, normal/accident[11b]	MPa	TBD
11.1.5. Containment atmosphere	-	CO_2
11.2. Turbine Building		
11.2.1. Characteristic dimensions	m	110 × 50 × 35
11.2.2. Enclosed volume	m^3	192,500
11.3. Reactor Service Building		
11.3.1. Characteristic dimensions	m	110 × 69 × 24
11.3.2. Special functions (i.e., hot cells, blanket processing equipment, etc.)		Tritium handling, radwaste, hot cells, cryogenics and helium storage, maintenance and storage
12. Reactor Maintenance		
12.1. First-wall/blanket/shield replacement		
12.1.1. Annual percentage	% area/yr	11
12.1.2. Area	m^2/yr	165
12.1.3. Weight[12a]	tonnes/yr	
12.2. Radioactive material storage for life of plant (30 yr)		
12.2.1. Total long-term storage (>> 30 yr)	m^3/tonnes	870/6900[1.2b]

Parameter	Unit	Value
12.2.2. Remaining recycled blanket storage	m^3/tonnes	TBD
12.2.3. Total recycled reactor equipment[12c] (after plant decommissioning)	m^3/tonnes	TBD
12.3. Reactor availability		TBD
12.4. Overall plant availability		0.76

Footnotes for Reactor Design Table

1. Characteristic Machine Dimensions

   The reactor envelope encloses the modular coils and has the dimensions given with a circumference (length) of 145 m (at the major toroidal radius of 23 m).

2. Plasma Parameters

   (a) Includes average alpha-particle pressure.

   (b) Based only on steady-state alpha-particle density.

   (c) Startup only, overall system efficiency to be determined.

   (d) Frequency varied to optimize startup efficiency as temperature varies.

   (e) Design point specifies $Q_p \to \infty$.

3. Power Output

   (a) Based on fusion power (3703 MWt) divided by vacuum chamber volume (468 m^3).

   (b) Based on fusion power (3703 MWt) divided by plasma volume (298 m^3).

   (c) Based on total thermal power (4000 MWt) and net volume (6677 m^3) enclosed by and including magnets.

   (d) Based on blanket volume (624 m^3) and thermal power actually delivered to primary coolant (3692 MWt).

   (e) Includes a portion of primary-coolant pumping power.

4. Reactor Coolant System

   (a) PCASS is primary candidate alloy, stainless steel.

   (b) Each coolant loop uses two circulators, for a total of 8 circulators or 34-MWe total circulation power.

7. Shield Coolant System

(a) Following EBTR parameters (Ref. 2).

9. Reactor Components

(a) Theoretical breeding ratio; does not include losses, decay, first-wall area reduction.

11. Buildings

(a) Includes volume of reactor hall and primary-coolant component room; value used to calculate overpressure in event of coolant line rupture.

(b) Normal operating pressure is slightly less than atmospheric, as in the present-day nuclear power plants. The accident condition is assumed to be the loss of primary coolant into the containment building.

12. Reactor Maintenance

(a) Based on replacing 1/9 of first wall and blanket (i.e., 12 of 108 total FW/B/S modules) during each of the last 9 yr of a 10-yr cycle.

(b) Includes first-wall, blanket, and limiter PCASS components.

(c) Includes blanket and first wall, all shielding, modular coils, primary structure and support, limiters, and vacuum cryopumps but excludes long term storage in Item 12.2.1.

REFERENCES

1. C. R. Head, "Standard Fusion Reactor Design Study Contents," Department of Energy, Office of Fusion Energy letter RS&A:CRH:#478 (March 7, 1979).

2. C. G. Bathke, D. J. Dudziak, R. A. Krakowski, W. B. Ard, D. A. Bowers, J. W. Davis, et al., "ELMO Bumpy Torus Reactor and Power Plant Conceptual Design Study," Los Alamos National Laboratory report LA-8882-MS (August 1981).

☆U.S. GOVERNMENT PRINTING OFFICE: 1983-0-676-026/70